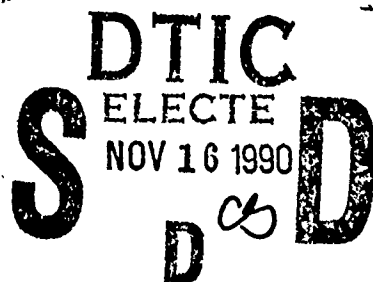


AD-A228 557



R. C. Hansen



DTIC FILE COPY

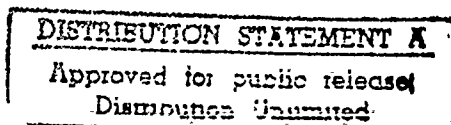
2nd Annual Review of Progress in

APPLIED COMPUTATIONAL ELECTROMAGNETICS

at the
Naval Postgraduate School
Monterey, CA

March 18-20, 1986

Conference Proceedings



90 11 15 142

*Some of the papers contained in these Proceedings are in the form of abstracts and/or viewgraphs. If possible, the full text of the papers will be published in a future Newsletter.

Some of the material presented at the Second Annual Review of Progress in Applied Computational Electromagnetics has not yet been released by the sponsors for public distribution. Other work is still in progress and results presented at the Conference are considered preliminary.



Accession For	
NTIS	CRACI ✓
DTIC	TAB []
Unannounced	[]
Justification	
By <i>per AD-A224563</i>	
Distribution/	
Availability Codes	
Dist	Avail and/or Special
<i>A-1</i>	

(A)

Contents: **SESSION I - "APPLICATIONS OF COMPUTER EM MODELING"**

Session 2 - Modeling of Structures Near Lossy Earth;
Session 3 - Code Development; Session 4 - Code Validation;

"Solution of Large Method of Moments Problems Using Banded Matrix Iteration: Destroyer Case Study"

D.E. Thomas

The BDM Corporation

"Analyzing Large Structures Using the NEC-BSC"

Ronald J. Marhefka

OSU-ElectroScience Laboratory

"Micro computer Computation of Electromagnetic Scattering By Stratified Anisotropic Media"

M. Morgan

Office of Naval Research

D. Fisher

Edwards Air Force Base

E. Milne

Naval Postgraduate School

"Application of NEC to EMP-Analyses"

M. Wurm and K. Müller

Industrieanlagen-Betriebsgesellschaft

"Use of MININEC to Determine the Optimum Placement of Insulators on a VLF Top-Loaded Monopole"

T.D. Poston and B.G. Hagaman

Kershner, Wright & Hagaman

T.L. Simpson

University of South Carolina

"A Comparison of Thin-Wire EM Modeling Codes for the Case of Scattering From a Cross"

Richard W. Adler

Naval Postgraduate School

"Efficient Computation of the Far Field of Offset Reflector Antennas With Offset Feeds"

Larry Q. Bowers and John Hoover

Martin Marietta Denver Aerospace

"Thin Aperture Modeling Using an FDTD Code"

Kenneth R. Demarest

U of Kansas-Remote Sensing Laboratory

"Time Domain Finite Difference Modeling on the Floating Point System 264 Array Processor"

Karl Kunz, Jim Breakall & Stephen Pennock

Lawrence Livermore National Lab

"Scattering By a Lossy Dielectric and Magnetic Body of Arbitrary Cross-Section"

J.L. Lin

Boeing Military Airplane Co.

"Selected Pattern Measurements of Four Full-Scale Tactical HF Antennas"

David Faust

Eyring Research Institute

"Bandwidth Optimization for Specified Antenna Gain Patterns"

Robert Bevensee

Lawrence Livermore National Lab

Session 5 - Numerical Aspects of Input/Output;
Session 6 - Numerical (Electromagnetic Code) Applications;
Session 7 - Computational Electromagnetic Modeling. (KR)

SOLUTION OF LARGE METHOD OF MOMENTS PROBLEMS USING
BANDED MATRIX ITERATION : DESTROYER CASE STUDY

D. E. THOMAS
THE BDM CORPORATION
1801 RANDOLPH ROAD SE
ALBUQUERQUE, NM 87106

The Method of Moments formalism is routinely used to reduce an integral equation to a set of simultaneous linear equations

$$AX = b$$

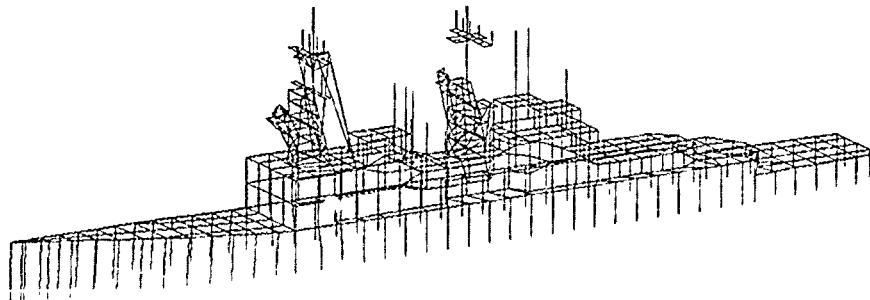
where A is the NxN impedance matrix, X is the column vector of unknown coefficients in the current expansion, and b is the excitation column vector. Normally, X is solved for with Gaussian elimination; however, this becomes impractical for problems with a large number (say, $N > 1000$) of matrix interactions. An alternative technique, Banded Matrix Iteration (BMI), will be explored in this paper. The BMI technique requires that all the large matrix elements in A be contained in a narrow bandwidth centered on the main diagonal of the interaction matrix; physically, this requirement is satisfied if wire segments which are actually close to each other have, in addition, segment numbers which are relatively close to one another. The matrix is then written as $A = L + B + U$, where B is the banded matrix, and L and U are the portions of A below and above B respectively. The original matrix equation can then be written as

$$BX = b - (L+U)X ;$$

it is solved iteratively with the scheme

$$BX_{n+1} = b - (L+U)X_n, \quad n=0,1,2,\dots,K.$$

Numerical results (current distributions and field patterns) for an NT-66047 35-foot whip antenna, driven at 7 MHz, and located in-place on a "Spruance" class destroyer, will be presented. The results were obtained with the GEMACS (General Electromagnetic Model for the Analysis of Complex Systems) code; the ship model (of more than 1200 segments) was generated with the GCAD (Gemacs Computer Aided Design) modeling code; and outputs were made with the WHIZ and PATPLOT codes.



SOLUTION OF LARGE METHOD OF MOMENTS PROBLEMS USING
BANDED MATRIX ITERATION : DESTROYER CASE STUDY

D. E. THOMAS
THE BDM CORPORATION
1801 RANDOLPH ROAD SE
ALBUQUERQUE, NM 87106

ABSTRACT- In this paper, the technique of Banded Matrix Iteration (BMI) for solving Method of Moments problems with a large number of unknowns will be explored. The results for the BMI technique will be compared to those for the traditional Gaussian Elimination ("SOLVE") solution for a simple geometry (monopole mounted on a box); in addition, BMI results for a very complex, large geometry (a "Spruance" class destroyer) will be presented.

I. INTRODUCTION.

The Method of Moments formalism is routinely used to reduce an integral equation to a set of simultaneous linear equations

$$AX = b, \quad (1)$$

where **A** is the $N \times N$ impedance interaction matrix, **X** is the column vector of unknown coefficients in the current expansion, and **b** is the excitation vector. Normally, **X** is solved for with Gaussian elimination; however, this becomes impractical for problems containing a very large number of unknowns. Gaussian elimination (hereafter referred to as a "SOLVE" solution) is the technique which requires the smallest number of operations for an exact solution to the set of linear algebraic equations; however, 6 or 12-digit accuracy for the matrix solution is often "overkill", considering the assumptions and approximations inherent in modeling complex structures with wire-grid models. Many problems in antenna design or placement do not require this kind of accuracy; in fact, solutions accurate to within a few decibels are often quite adequate. The Banded Matrix Iteration (BMI) technique can be used to obtain solutions with this range of accuracy, and often in much less computer time than the Solve method would require. However, the BMI technique has its own intricacies and pitfalls, and requires a good deal of expertise on the part of its practitioners.

II. THEORY.

The basic approach for the BMI technique is to separate the matrix **A** into two parts : a "banded" matrix **B**, which is centered on the main diagonal of the interaction matrix, and which ideally contains all of the large matrix elements of **A**; and, a second matrix **L + U**, where **L** and **U** are the portions of **A** below and above **B** respectively. The original matrix equation (1) can then be written as

$$BX = b - (L+U)X \quad (2)$$

Equation (2) is solved iteratively using the scheme

$$B_{n+1} X_n = b - (L+U) X_n, \quad n = 0, 1, 2, \dots, K. \quad (3)$$

The matrix B is decomposed into a product of lower and upper triangular matrices, but (it is hoped!) with less computer time than is required to decompose the full matrix A. If the lower and upper triangular decompositions of B are referred to as B_L and B_U respectively, then the solution of (3) can be obtained by pivoting on the main diagonal elements of B. This is accomplished by using forward elimination in

$$B_{Lj} Y_j = b_j - (L+U) X_j, \quad (4)$$

followed by back substitution in

$$B_{Uj+1} X_j = Y_j \quad (5)$$

With pivoting on the main diagonal elements of B, the cost of decomposition is proportional to

$$\frac{2}{3} NM - \frac{2}{3} M^2$$

where M is the "bandwidth". In addition, the cost of solving equation (3) is proportional to the square of N for each iteration. Since the cost for a "SOLVE" (Gaussian elimination) is proportional to 1/3 the cube of N, an efficiency of BMI to SOLVE solutions can be defined as

$$g = \frac{(N/3)^3}{(NM - \frac{2}{3} M^2 + KN^2)} \quad (6)$$

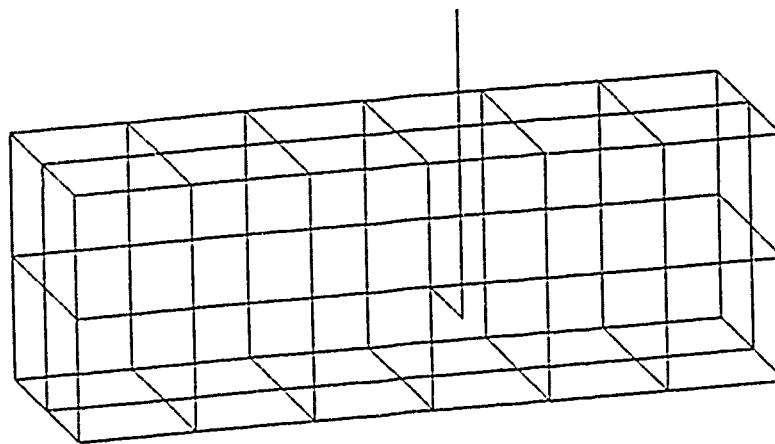
For problems with small numbers of unknowns, BMI solution times may be as long (or even a bit longer) as the corresponding SOLVE solution times; however, BMI can be used to solve very large moments problems in a fraction of the time required for Gaussian elimination.

For the BMI technique to be successful, the banded matrix B must contain all of the large interaction matrix elements, leaving small elements in the portion L+U. Physically, this requirement is satisfied if wire segments which are in close proximity to one another have their matrix interaction elements located nearby the main diagonal of the impedance matrix; in other words, the segment numbers which identify the wires should be fairly close to each other. This requirement can be achieved for certain types of geometries (especially long, slender shapes) by re-numbering the entire model. A detailed example of such a re-numbering is given in the next section, which deals with a simple problem involving a quarter-wave monopole mounted on the side of a box-shaped structure.

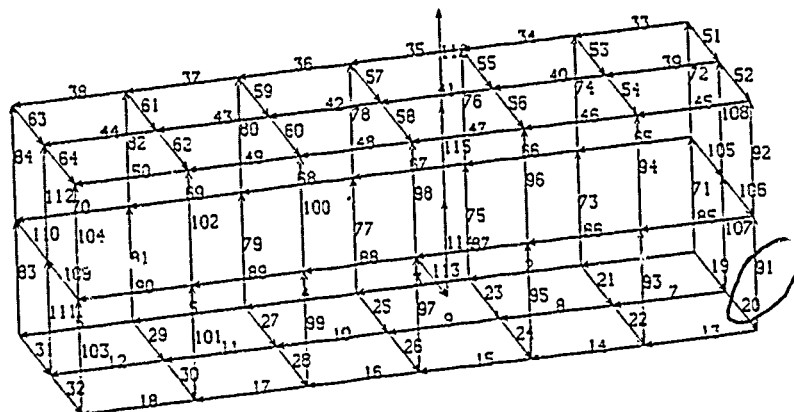
III. COMPARISON OF BMI TO SOLVE : MONOPOLE ON A BOX.

In this section, results for a quarter-wave monopole (7 MHz) hanging off the side of a rectangular box will be presented, for both SOLVE and BMI solution methods. The basic geometry of the box and the antenna is shown in Figure 1-a. The wire-grid model used with the SOLVE technique appears in Figure 1-b ; this model was generated with the GCAD (GEMACS Computer Aided Design) program. The box was generated in an orderly fashion : the first side to be created was the bottom, followed by the top, back, front, left, and right sides, and finally, the antenna itself. The model used with the BMI technique is displayed in Figure 1-c : this model was produced from the original model using the Re-number feature of the GCAD program, which allows the order of segment numbers to be determined with respect to segment proximity to a user-supplied (x,y,z) location. In this case, the (x,y,z) point used was a large distance to the left of the model in Figure 1-c; the segment numbers can be seen to advance from left to right in the re-numbered model. The effect of this re-numbering on the BMI technique is shown in Figure 2, which contains sketches of the locations of some matrix interactions in the impedance matrix. The adjacent segments 20 and 91 of the as-generated model of Figure 1-b are seen to be outside the "band" indicated in Figure 2-a, while the same segments (now with segment numbers 109 and 114) for the re-numbered model appear well inside the "band" indicated in Figure 2-b. In general, the BMI method works best if the model can be re-numbered along the axis of "minimum rotational inertia"; however, not all shapes are conducive to this technique (for example, a sphere). The solutions for both models were obtained with the GEMACS (General Electromagnetic Model for the Analysis of Complex Systems) code, and are displayed in Figure 3. The current maps of Figure 3, which show the currents in the cross-sectional planes containing the antennas for each model, were produced with the WHIZ program. Because there was a small number of unknowns, the solution times for both BMI and SOLVE methods were about the same; however, the agreement is excellent. A bandwidth of 60 was used for the BMI portion of the analysis. The far-field patterns in the YZ plane (the same plane which contains the antennas) are given in Figure 4; the BMI and SOLVE solutions are practically indistinguishable. In fact, reasonable far-field can be found from current distributions which may be in error as much as 30 percent. The patterns were produced from GEMACS output with the aid of the PATPLOT program.

(a)



(b)



(c)

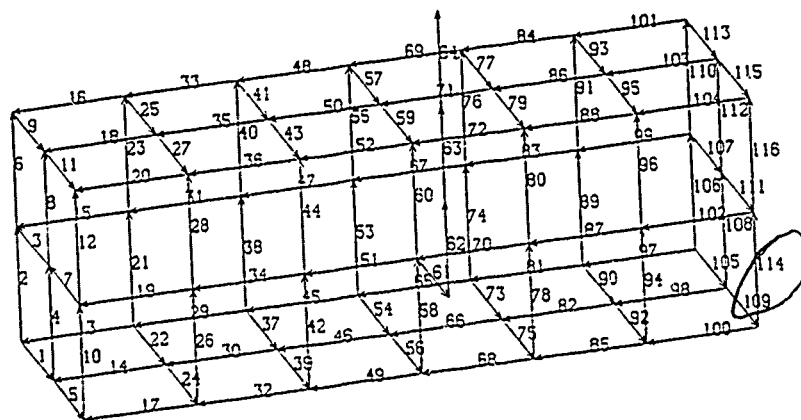


Figure 1. (a) The Wire-Grid Model of a Rectangular Box; a Quarter-Wavelength Monopole is Attached to the Front Side of the Box. (b) The Box Model, As Generated with the GCAD Program, for Use with SOLVE Method; Segments 20 and 91 (Circled) are Adjacent. (c) The Same Box, Now Re-Numbered with the GCAD Program, for Use with BMI Solution; Segments 109 and 114 (Circled) are Adjacent.

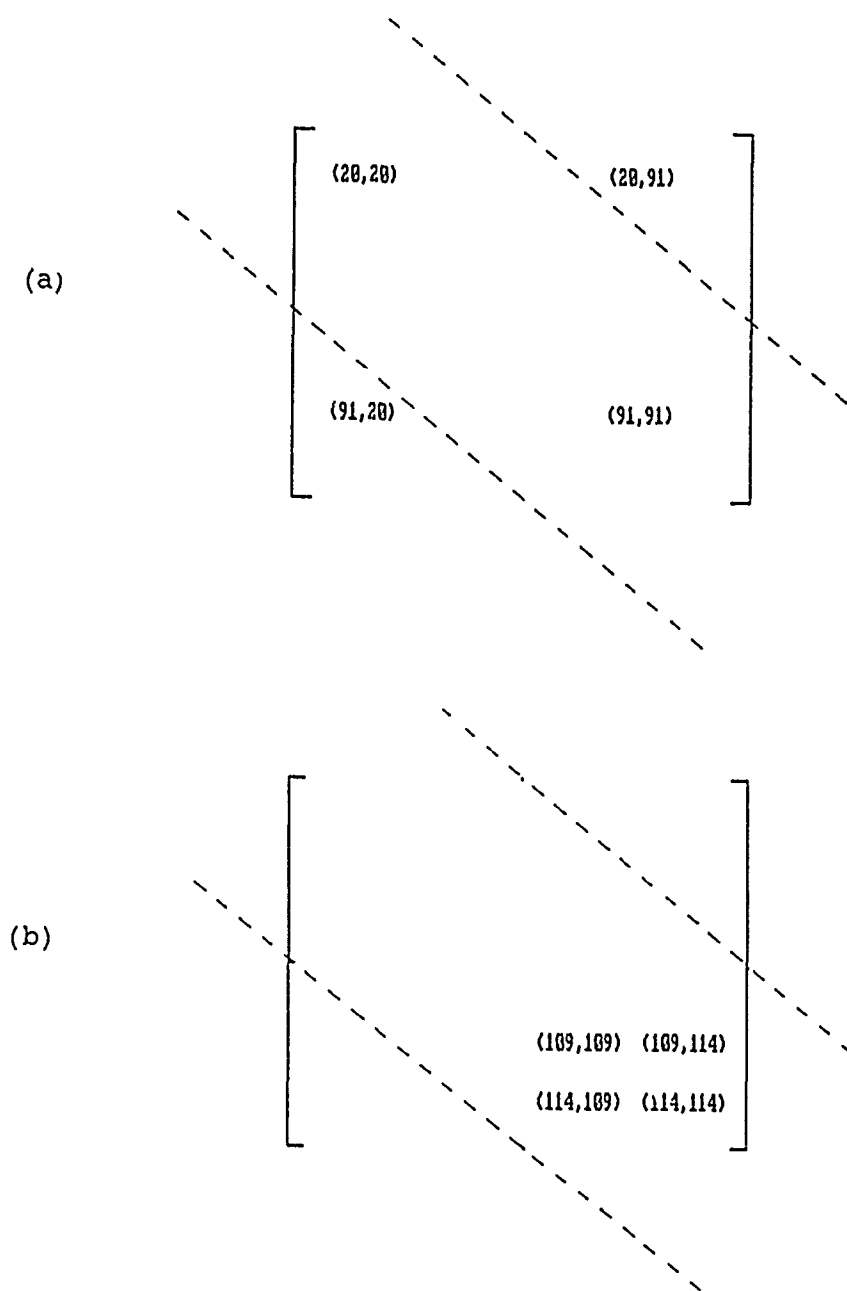


Figure 2. Sketches of the Interaction Matrix for the Models Shown in Figures 1-b and 1-c : (a) Segments 20 and 91 of the As-Generated Model (Figure 1-b), While Adjacent, are Separated by 71 Segment Numbers, and so Their Interaction Falls Outside of the "Band" ; (b) Adjacent Segments 109 and 114 of the Re-Numbered Model (Figure 1-c) are Separated by Only 5 Segment Numbers, and so Their Interaction Falls Well Inside the "Band" .

SOLVE SOLUTION

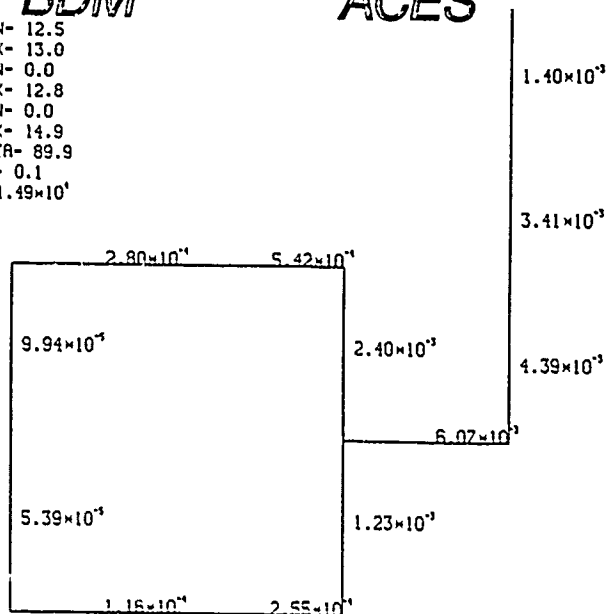
(GEMACS.THOMAS)DD967 16-MAR-86 09:29:02

BDM

ACES

XMIN- 12.5
XMAX- 13.0
YMIN- 0.0
YMAX- 12.8
ZMIN- 0.0
ZMAX- 14.9
THETA- 89.9
PHI- 0.1
R- 1.49×10^4

(a)



BMI SOLUTION

(GEMACS.THOMAS)DD967 16-MAR-86 09:32:39

BDM

ACES

XMIN- 12.5
XMAX- 13.0
YMIN- 0.0
YMAX- 12.8
ZMIN- 0.0
ZMAX- 14.9
THETA- 89.9
PHI- 0.1
R- 1.49×10^4

(b)

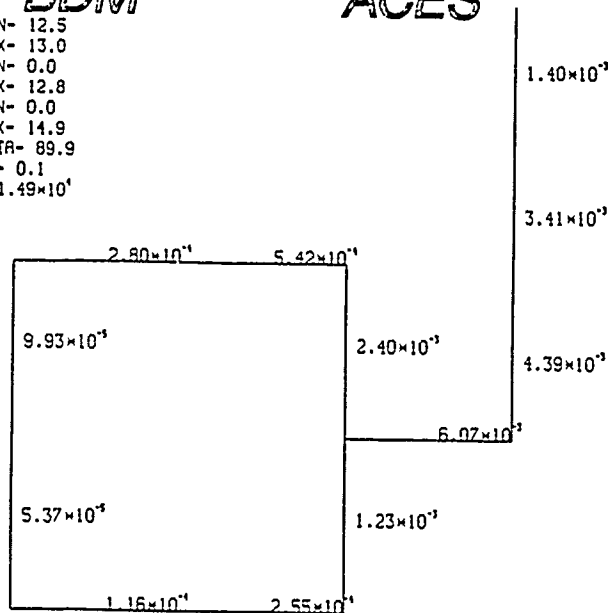
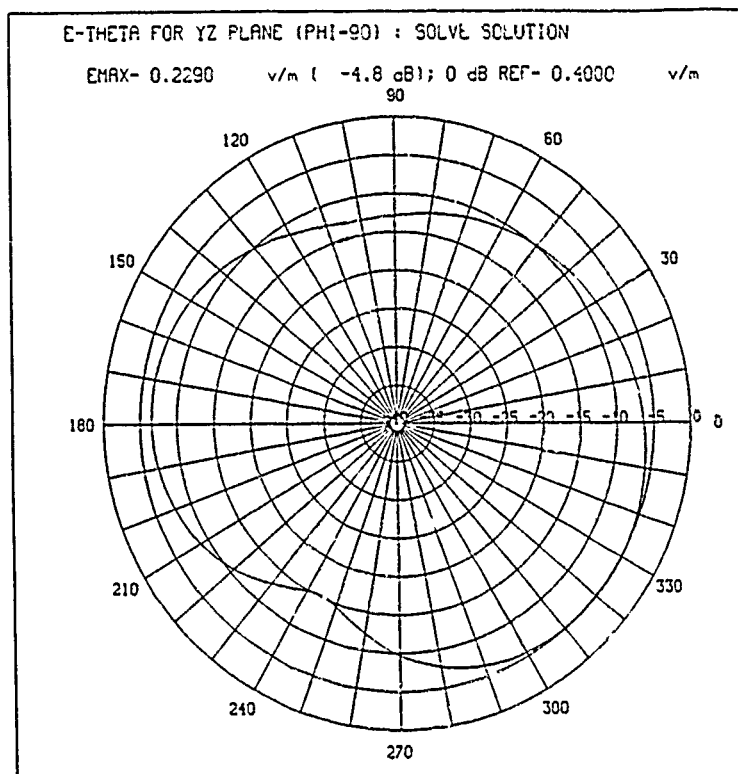


Figure 3. WHIZ Current Maps for the Cross-Section of the Box of Figure 1-a Containing the Quarter-Wave Monopole : (a) The SOLVE Solution Currents, for the As-Generated Model of Figure 1-b ; (b) The BMI Solution Currents, for the Re-Numbered Model of Figure 1-c, With a Bandwidth of 60. Note the Similarity of the Different Solutions.

(a)



(b)

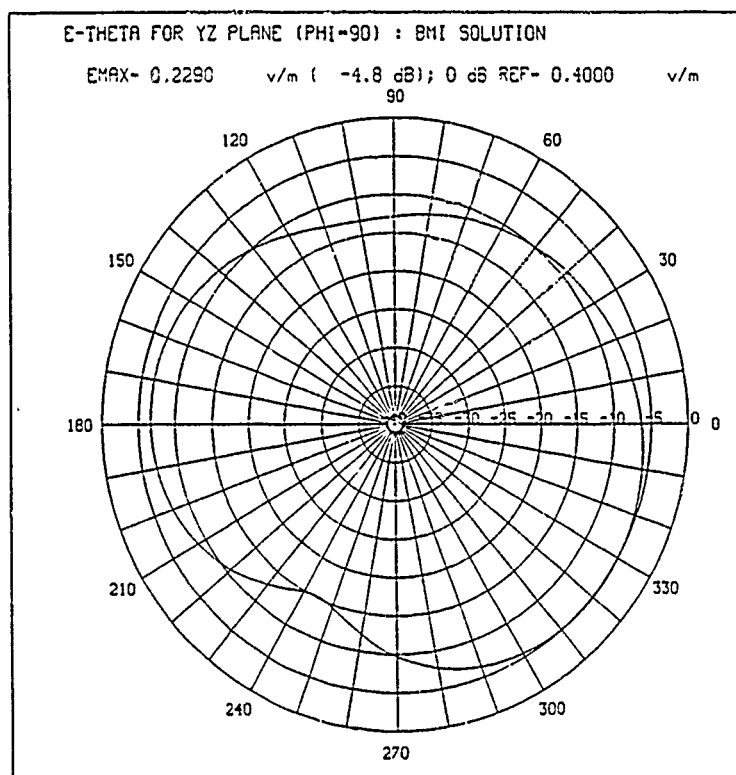


Figure 4. PATPLOT Field Patterns for the Box/Monopole of Figure 1-a : (a) The SOLVE Solution Pattern, for the As-Generated Model of Figure 1-b ; (b) The BMI Solution Pattern, for the Re-Numbered Model of Figure 1-c, With a Bandwidth of 60.

IV. DESTROYER CASE STUDY.

As an example of the utility of the BMI method, an NT-66047 35-foot whip antenna was modeled in-place on a "Spruance" class destroyer. The geometry data for the model was obtained from IGES files (see Figure 5), along with photographs and 3-D diagrams. The GCAD modeling program was a key part of the modeling process, since it allowed the model to be developed in portions, which were then pieced together interactively. Some of the stopping points during the development phase are shown in Figure 6. The final model, with 1222 wire segments, is shown in various views in Figure 7. The whip antenna itself appears in Figure 8-a; a portion of the forward mast is displayed in Figure 8-b. Figures such as these were used to determine which wire segments represented antennas or guy wires, and allowed such wires to be modeled with their actual radius (as opposed to the standard surface-mesh radius of average segment length over 2 times PI). Once antenna wires have been identified, the GCAD program sets up the radius tables and tags automatically.

The BMI bandwidth used was 300 (equivalent to approximately half a wavelength). However, this was not sufficient to place all of the large interactions within the band, and the solution was only accurate to 10 percent when it began to diverge. This illustrates one of the caveats for using the BMI technique : convergence is not guaranteed. Future research is planned to estimate the optimum bandwidth for this very large problem.

The solution process using the BMI technique took 15.4 hours of CPU time (VAX 11/750) ; in comparison, the CPU time for the SOLVE method, based on experience with problems having 500-700 unknowns, and using the N-cubed proportionality of the SOLVE solution, is estimated to be on the order of 50 hours. The input impedance for the whip antenna was calculated at 232 ohms. The distribution of currents for the destroyer as a whole was produced with the WHIZ program, and is shown in Figure 9. The far field for the E-THETA component (vertical) in the yaw (horizontal) plane is shown in Figure 10.

V. CONCLUSION.

The Banded Matrix Iteration method can be used to solve method of moments (MOM) problems having a very large number of unknowns. Future research plans include optimization of the bandwidth, and comparisons of the BMI solutions for large problems to hybrid Geometrical Theory of Diffraction (GTD) / Method Of Moments (MOM) solutions; a hybrid GTD/MOM methodology is already implemented in GEMACS. The author wishes to acknowledge the patient and willing assistance of R. J. Balestri during the preparation of this paper.

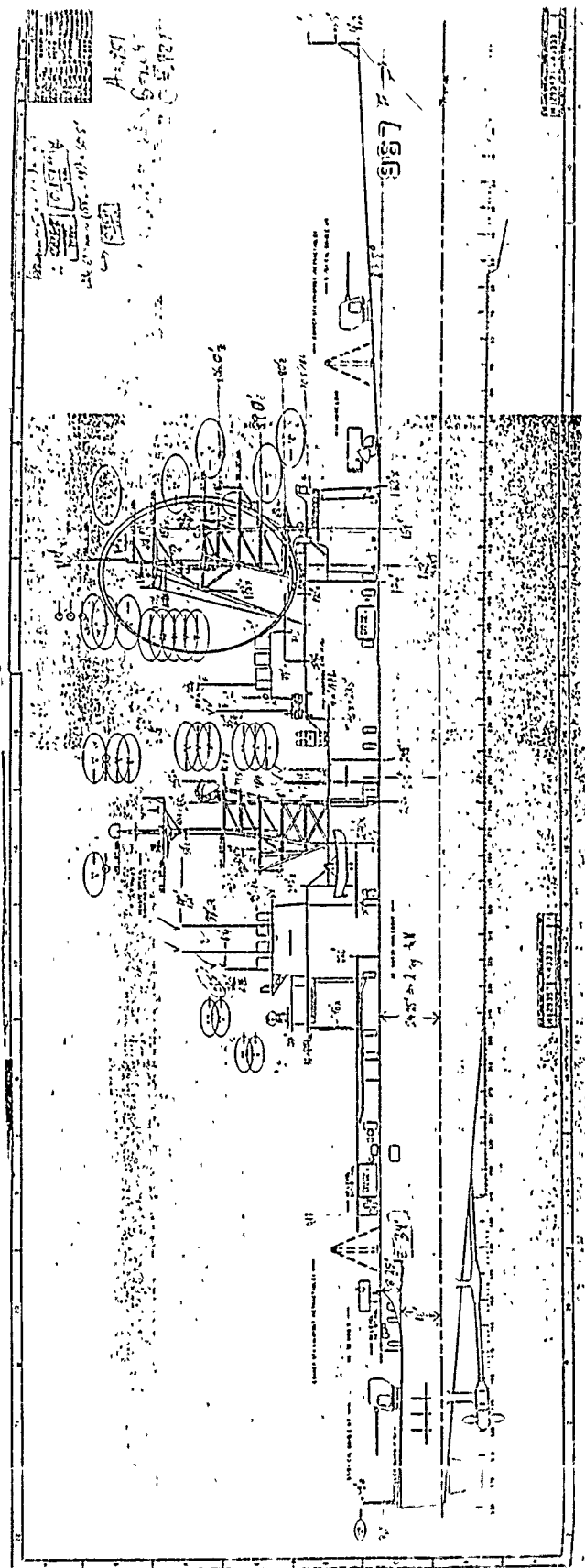


Figure 5. One of the IGES Files Used to Formulate the Geometry of a "Spruance" Class Destroyer for Input to the GCAD Modeling Program; Photographs and 3-D Diagrams Were Used As Well.

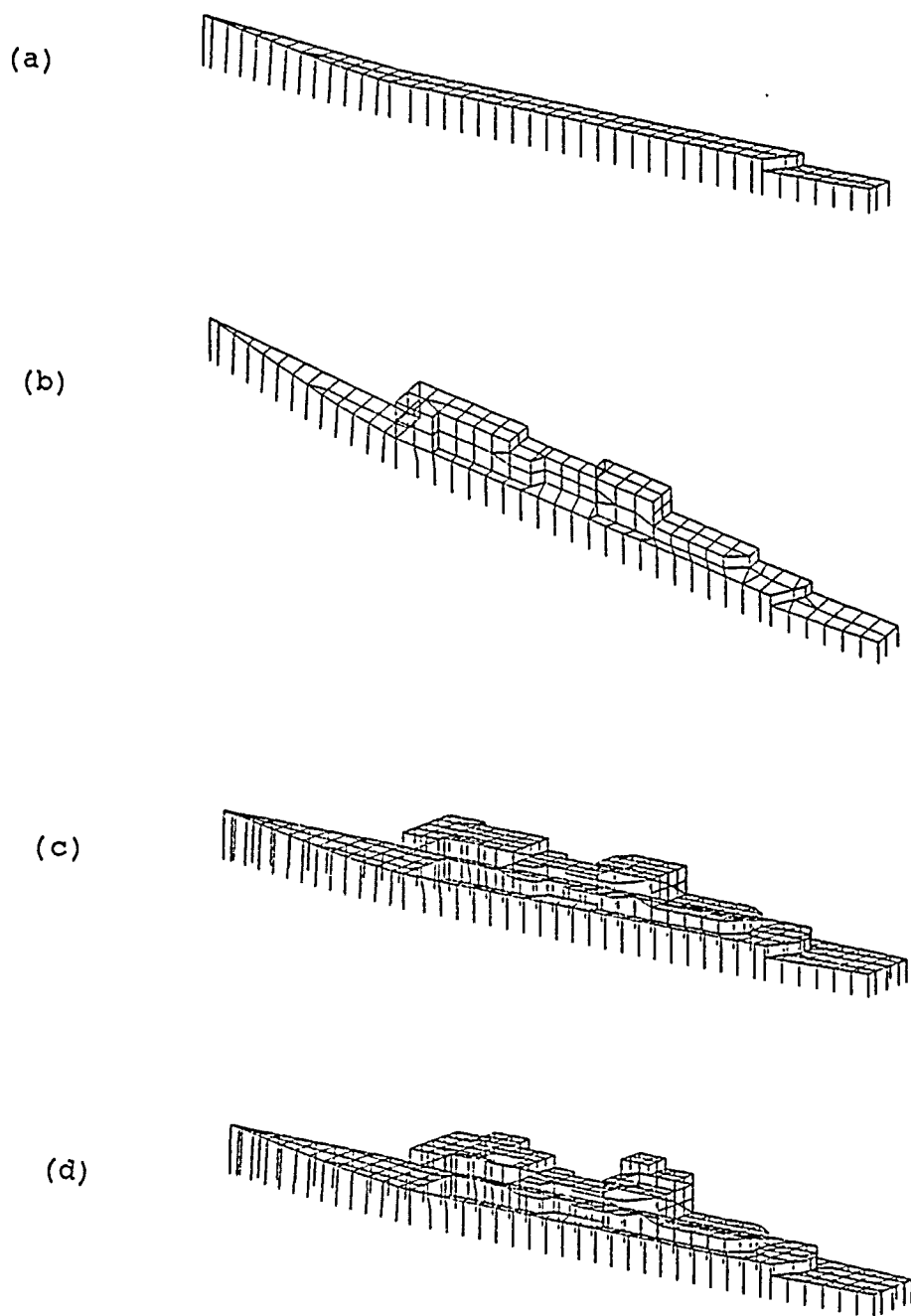


Figure 6. Several Way Stations for the Development of the Destroyer Wire-Grid Model : (a) the Port Side of the Basic Deck; (b) the Port Side, with Mid-ship Structures Added; (c) The Symmetrical Basic Ship Structure, Formed by Reflection of the Port Side; (d) The Basic Ship Structure, with Some of the Asymmetrical Structures Added.

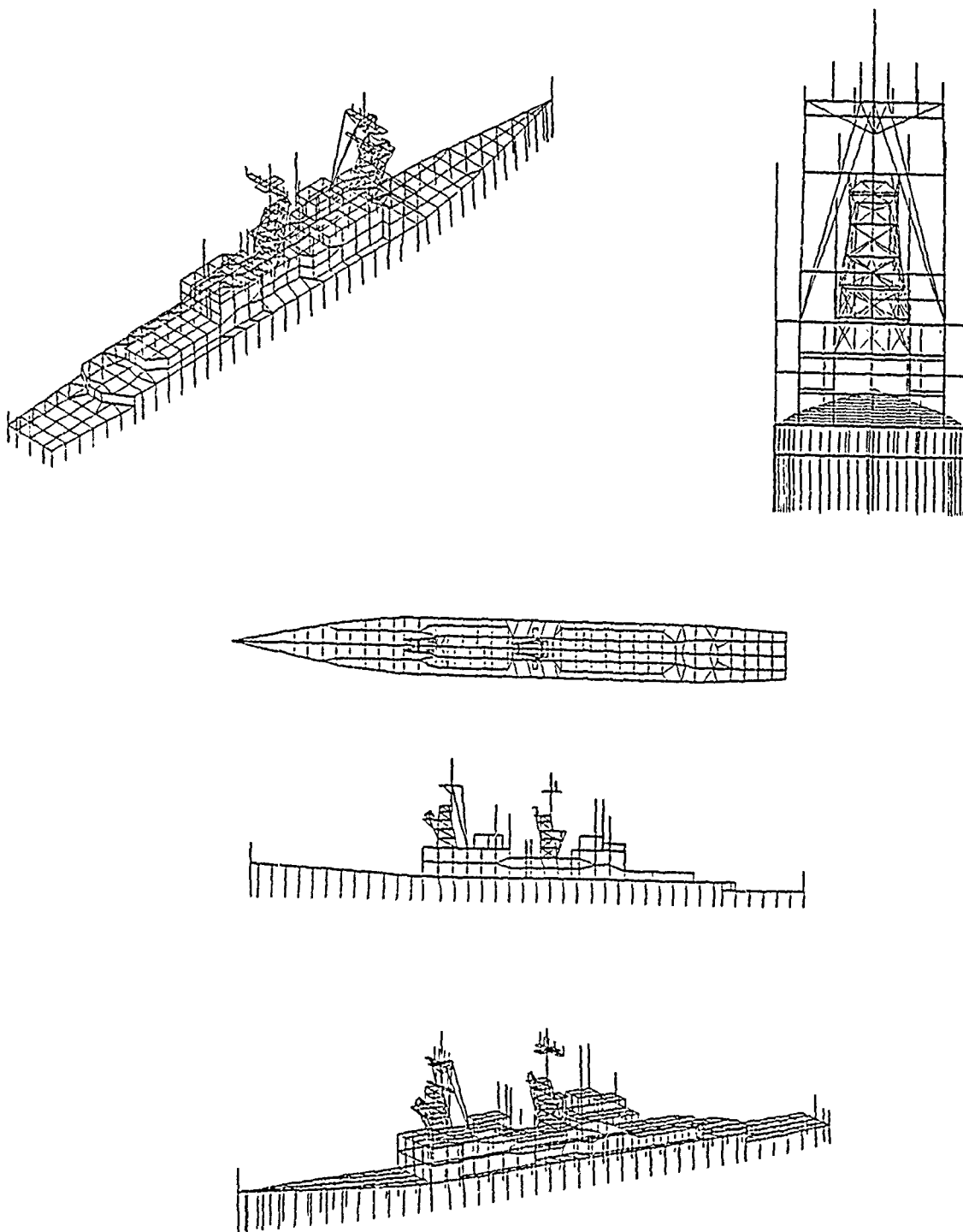


Figure 7. Several Views of the Final Destroyer Model, Showing the Masts, Antennas, and Guy Wires. The Model Contains 1222 Wire Segments.

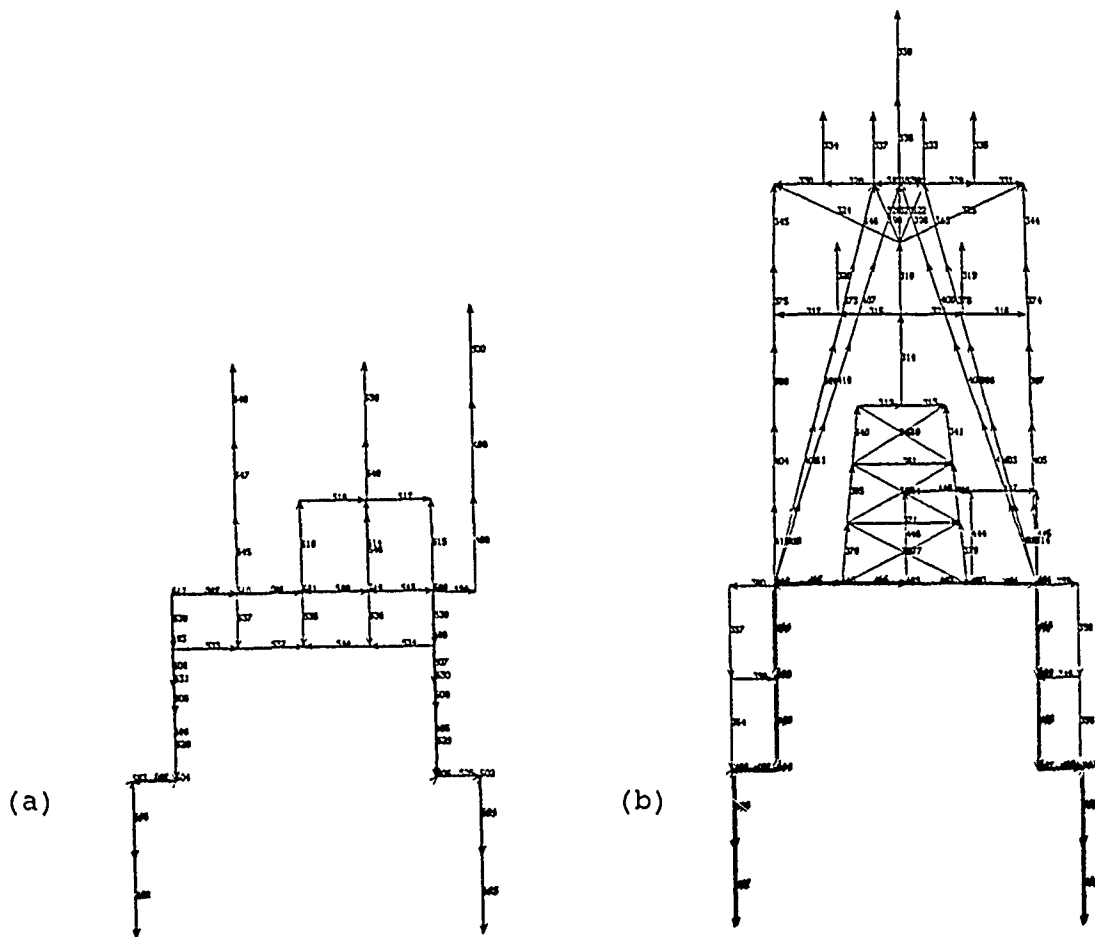
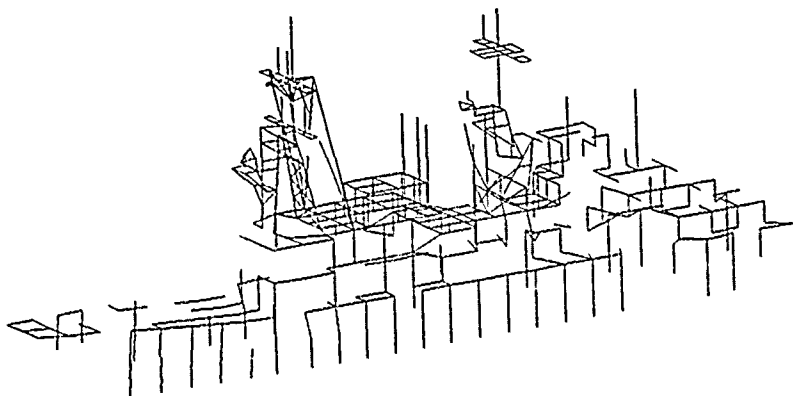


Figure 8. Cross-Sectional Views of the Destroyer, Used to Identify Antenna/ Guy-Wire Segments. (a) A Cross-Section Approximately Half-way Between the Two Masts; the Antenna at the Upper Right is the NT-66047 35-Foot Whip to be Analyzed using Banded Matrix Iteration. (b) A Cross-Section of the Area Near the Forward Mast, Showing Several Antennas and Guy Wires.

(a)



(b)

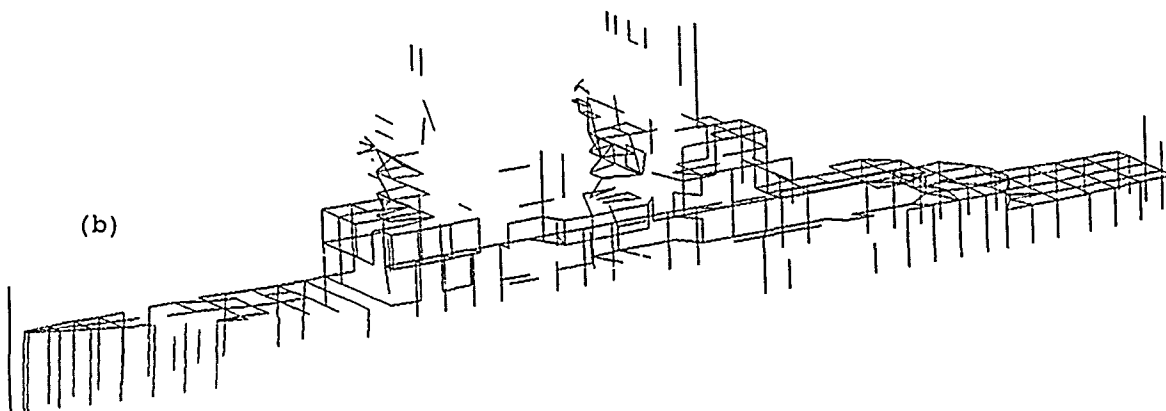


Figure 9. WHIZ Current Map for the Destroyer, Showing the Currents Induced by Driving the Base of the 35-Foot Whip Antenna of Figure 9-a at 7 Megahertz; a Bandwidth of 300 Was Used for the BMI Solution. The "Hot" Currents (Above $2.5e-4$ Amps) Appear in Figure 9-a ; the "Cold" Currents (Below $2.5e-4$ Amps) are Shown in Figure 9-b.

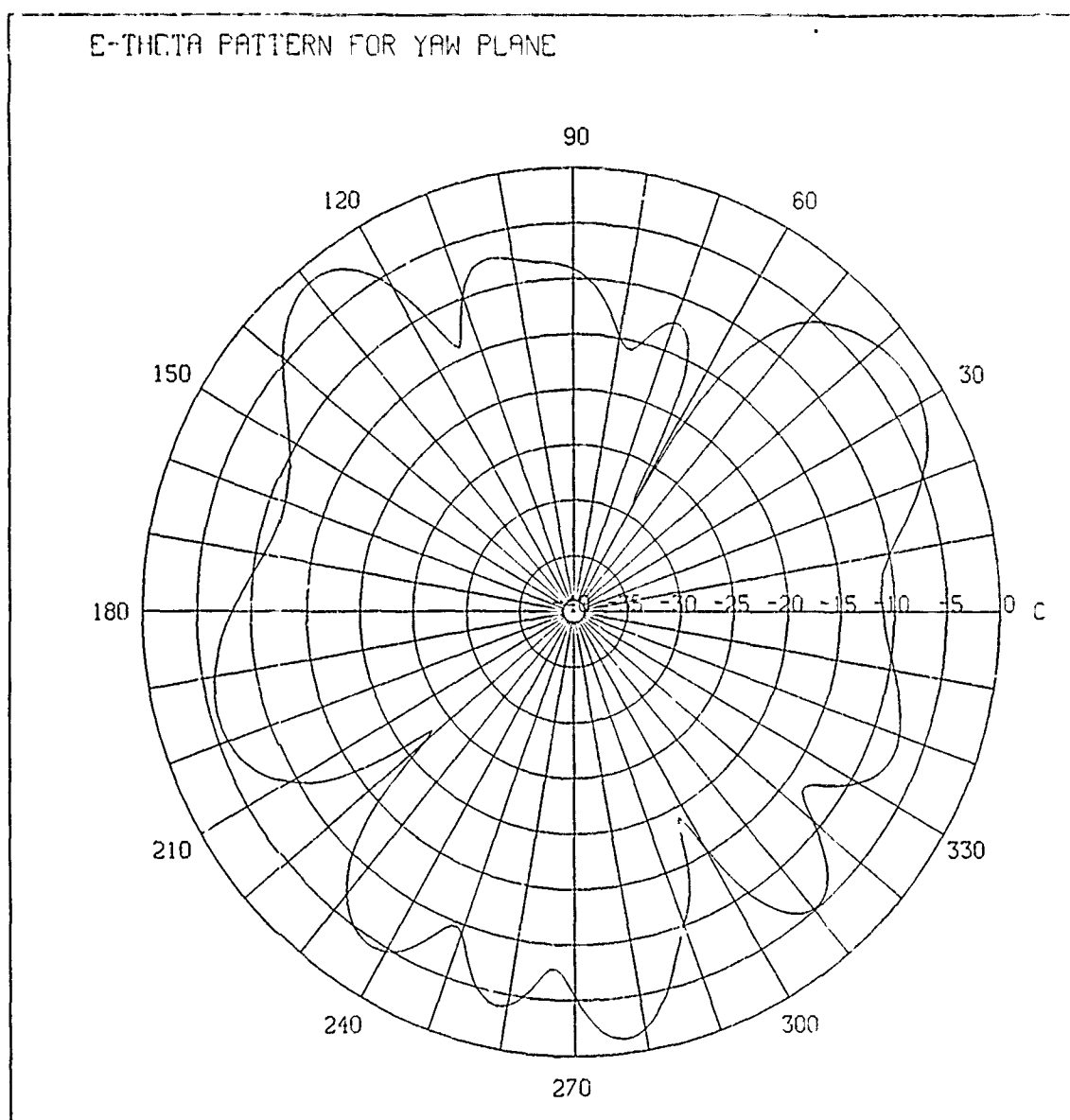


Figure 10. A Field Pattern for the 35-Foot Whip Antenna. Here, E-THETA (Vertical Component) is Plotted in the Yaw Plane.

VI. REFERENCES.

- (1) "Banded Matrix Iteration in Moments Problems", T. R. Ferguson, IEEE/AP-S International Symposium, June 1975, pp. 146-149.
- (2) "Efficient Solution of Large Moments Problems : Theory and Small Problem Results", T. R. Ferguson, T. H. Lehman, R. J. Balestri, IEEE Transactions on Antennas and Propagation, March 1976, pp. 230-235.
- (3) "Solution of Large Wire Grid Moments Problems", T. R. Ferguson, R. J. Balestri, IEEE International Symposium on Electromagnetic Compatibility, July, 1976, pp. 290-294.
- (4) Shipboard Antennas, Preston E. Law, Artech House, Inc., Dedham, Maryland, 1983.
- (5) "Operational Assessment of a Spruance Class Destroyer", J. P. Geddes, International Defense Review, 6/1976, pp. 34-40.

ANALYZING LARGE STRUCTURES USING THE NEC-BSC

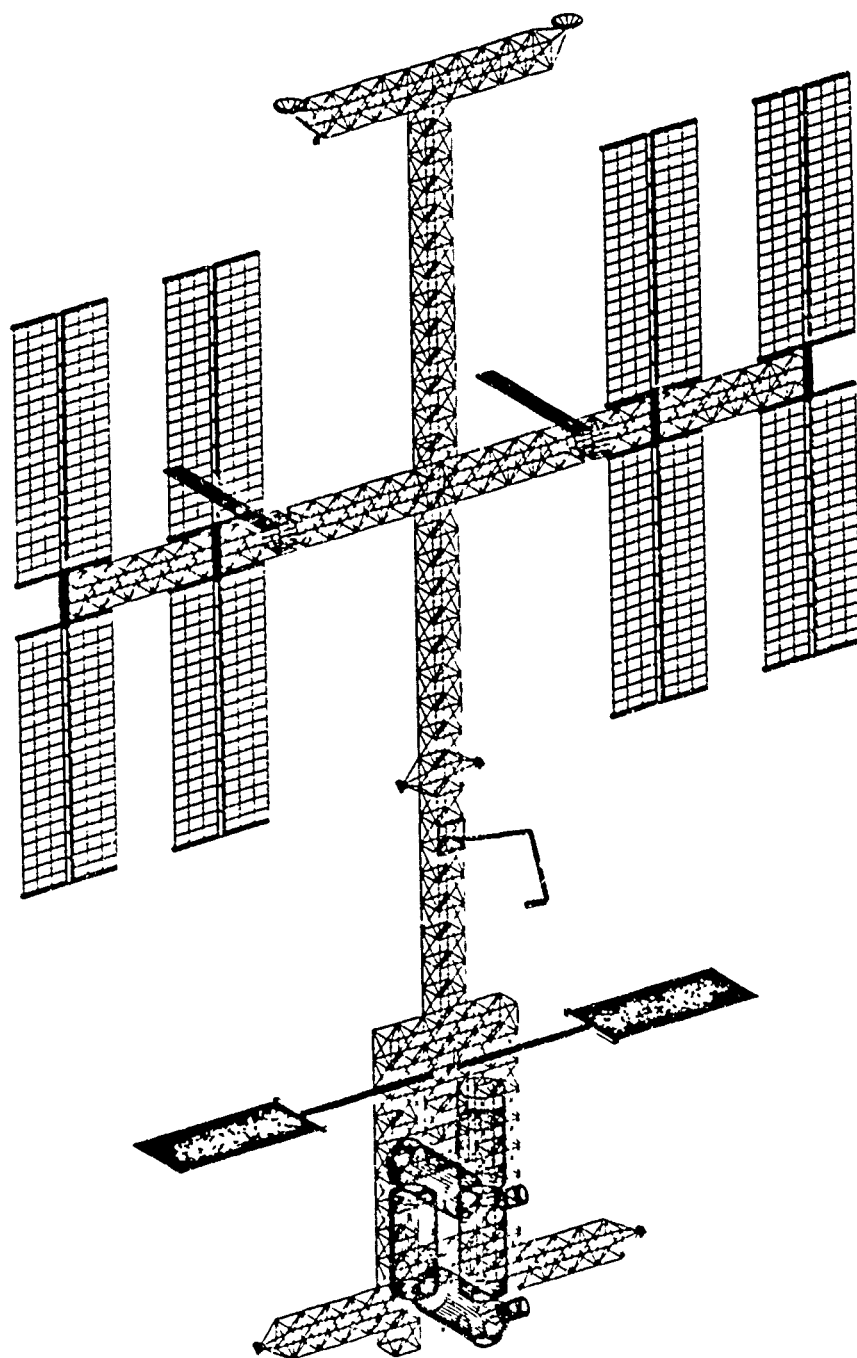
R. J. Marhefka
The Ohio State University
ElectroScience Laboratory
1320 Kinnear Road
Columbus, Ohio 43212

In the initial design phase, when the minimum number and placement of antennas on large structures, such as a space station, is being considered, it is desirable to study a large number of possibilities in a short amount of time. In addition, the entire volumetric pattern should be available in order to determine if an unobstructed view of an orbiting satellite can be obtained, for example. When analyzing models with many plate and cylinder type structures, the NEC-BSC code can be rather time consuming to calculate complete volumetric patterns for many different antenna sighting locations. An obscuration code has been designed to complement the NEC-BSC to overcome this time limitation. Of course, after an optimized location is found, the NEC-BSC needs to be run to confirm the conclusions and to determine that the gain and ripple levels are appropriate.

The obscuration code uses a generalized version of the NEC-BSC input set to produce a shadow map of the defined plates and cylinders on the far zone sphere. Any angular area of space and resolution can be specified. It calculates a map in the order of a few minutes instead of hours for the original code. An algorithm that efficiently allows the outer edges of the plates and cylinders to be projected onto the far zone sphere and an efficient pixel fill procedure accounts for this savings in time.

Because of the short turn around time, an interactive feature has been added to the obscuration code. It is based on command language handlers in version 4 of the DEC VAX VMS operating system. It also allows the definition of the VT100 type keypad to execute the commands. This method of creating interactive commands to control a code will be briefly discussed as a possible interesting way for engineers using VAX's to improve the user friendliness of their computer codes.

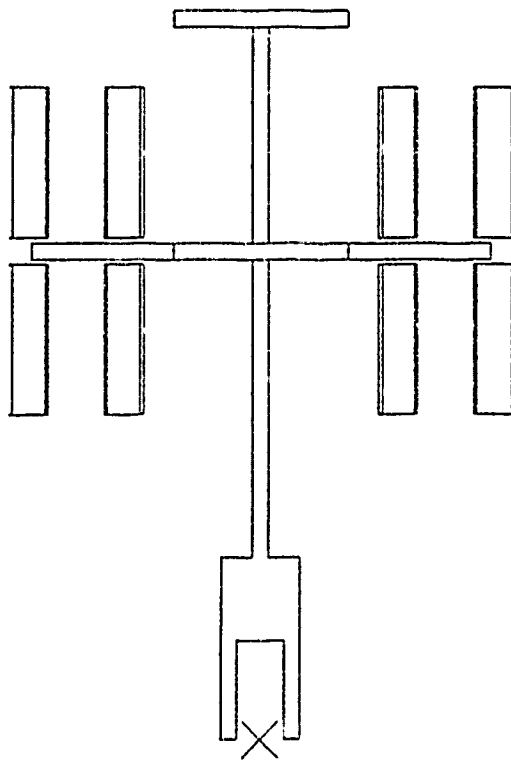
In addition, some of the new improvements and features planned for future versions of the NEC-BSC will be briefly presented.



LARGE SPACE STATION



TOP



FRONT



SIDE

LARGE SPACE STATION MODEL
USING NEC-BSC

Outline of Presentation

1. Discussion of Problem - Modeling the Space Station.
2. Potential NEC-BSC2 modeling considerations.
3. New Obscuration Code to complement NEC-BSC.
4. DEC VAX/VMS command language handler for interactive use.
5. Some improvements and features planned for future versions.

Statement of Problem

- Analysis of antenna placement on structures of large size with many plate and cylindrical pieces.
- Volumetric patterns needed to determine number of antennas needed and their placement to achieve uninterrupted communications.
- Many possible candidate locations may need to be tested in initial design stages.
- Measurements may not be economical because of the size of structure (far zone considerations) and because the exact design of the structure could be changing frequently making model redesign costly.
- NEC-BSC will be able to determine if gain and ripple levels of pattern will be within acceptable bounds.
- NEC-BSC can help determine if antennas in a multiple antenna system will interfere with one another.

NEC-BSC Considerations

- When running NEC-BSC, on complicated structures code may give warped plate warning. Solution is to define corners more carefully, change code to allow more warp or use triangular plates.
- Errors such as non-symmetries may occur due to logic bound tests failing when large subtended angles due to large distances between scattering centers. Simple solution is to move the source slightly, or take pattern in slightly different plane.

- NEC-BSC being based on UTD is efficiently designed for large structures, however, computer run time could take hours for structures with 40 plates, 5 cylinders, theta from 2 to 178 in steps of 2 degrees and phi from 0 to 360 in step of 2 degrees.
- Run the full code when verification of the location is needed. Use minimum number of field terms at first to accomplish point being studied. A obscuration code has been written to give run interactively to speed up one of the first considerations. Where is the best locations to place an antennas for an unobstruted view of the source from the receiver.

The Obscuration Code - "SHADOW"

1. Efficiently produces shadow map of structure on far zone sphere for a near zone source.
2. Based on extension of NEC-BSC input set.
3. Any area or resolution of the far zone sphere can be chosen.
4. Individual parts of the structure can be tagged.
5. Interactive input control option using VAX VMS like commands or keypad.

Outline of Method

1. Project boundary of plate or cylinder onto far zone sphere.
2. Use variable step around edge based on distance of source from edge.
3. Pixelize theta and phi result and store in map using special character.
4. Scan down map and do shadow test at mid point between markers.
5. If shadowing occurred, fill with character between markers.
6. Get another plate or cylinder and start process again.

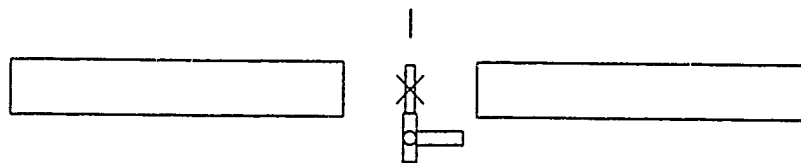
SIMPLER
SPACE STATION MODEL



SIDE VIEW



FRONT VIEW

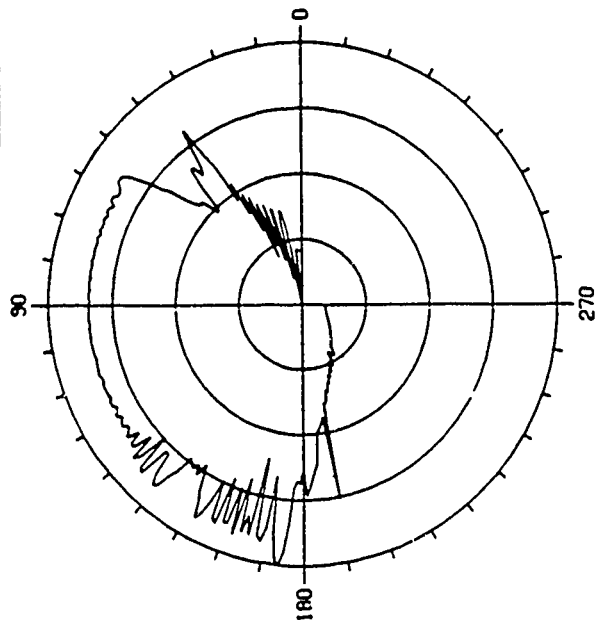


TOP VIEW

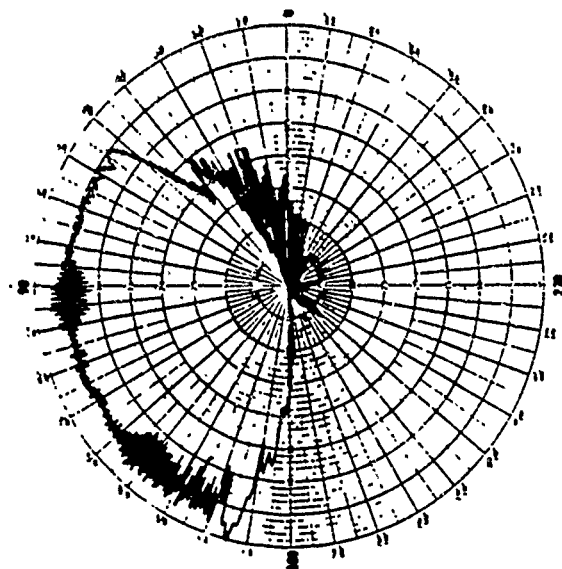
2.2 GHZ CIRCUMFERENTIAL SLOT ON UTILITY MODULE
OF CDG CONFIGURATION (SIMPLE MODEL)

dB - 1

ELEVATION PATTERN



CALCULATED



MEASURED

Projection of boundary

- The boundary of the structures are traced onto the far zone sphere by defining a vector from the source position, \bar{R}_s , to some position along its outer boundary, \bar{R}_i , such that

$$\bar{R} = \bar{R}_i - \bar{R}_s.$$

- The vector can then be transformed onto the two dimensional far zone sphere by

$$\theta = \arctan(\hat{\rho} \cdot \bar{R} / \hat{z} \cdot \bar{R})$$

and

$$\phi = \arctan(\hat{y} \cdot \bar{R} / \hat{x} \cdot \bar{R}).$$

- Assuming that the resolution increment is small and the distance is relatively large, the value of the edge increment is given by

$$\delta t = \delta \alpha R \sin \theta.$$

The new edge point then becomes

$$\bar{R}_{i+1} = \bar{R}_i + \delta t \hat{e}.$$

Plate Shadowing

- The shadow test for a plate is made by first projecting the vector chosen at the mid point of the scan line, \hat{r} , onto the plane of the plate to find its intersection point,

$$\bar{R}_t = \bar{R}_s - \frac{[\hat{n} \cdot (\bar{R}_s - \bar{C}_1)] \hat{r}}{\hat{n} \cdot \hat{r}}.$$

- Now, using an idea based on Cauchy's formula from complex variables, that is,

$$\oint_C f(z) dz = \begin{cases} 0, & \text{no pole in } f(z) \\ 2\pi j, & \text{one pole in } f(z) \end{cases}.$$

the intersection point can be tested to see whether or not it falls within the limits of the plate.

- It is easy to show that

$$\theta_m = \arctan \left[\frac{[(\bar{C}_m - \bar{R}_t) \times (\bar{C}_{m+1} - \bar{R}_t)] \cdot \hat{n}}{(\bar{C}_m - \bar{R}_t) \cdot (\bar{C}_{m+1} - \bar{R}_t)} \right]$$

which leads to the test, if

$$\left| \sum_{m=1}^M \theta_m \right| = \begin{cases} < \pi, & \text{no hit occurs} \\ > \pi, & \text{a hit occurs} \end{cases}.$$

Cone Frustum Shadowing

- A vector on the surface of the cone frustum can be represented as

$$\bar{R}_c = \bar{R} + \bar{R}_s$$

or

$$\begin{aligned} \bar{R}_c = & (R \cos \phi \sin \theta + x_s)^2 \hat{x} + (R \sin \phi \sin \theta + y_s)^2 \hat{y} \\ & + (R \cos \theta + z_s)^2 \hat{z}. \end{aligned}$$

- The point defined by \bar{R}_c should satisfy the equation for a cone, that is,

$$\begin{aligned} 0 = & \frac{(R \cos \theta + x_s)^2}{a_j^2} + \frac{(R \sin \phi \sin \theta + y_s)^2}{b_j^2} \\ & - \lambda_j^2 (R \cos \theta + z_s) \end{aligned}$$

where

$$\lambda_j (R \cos \theta + z_s) = \left[1 + \frac{1}{a_j} \tan \theta_j (R \cos \theta + z_s - z_j) \right].$$

- The distance R is unknown in this equation, since we know the direction to the observer, θ and ϕ , but not the distance to the hit point. We can solve for R , however, from the above equations using

$$\alpha R^2 + 2\beta R + \gamma = 0,$$

where

$$\begin{aligned} \alpha = & \frac{\cos^2 \phi \sin^2 \theta}{a_j^2} + \frac{\sin^2 \phi \sin^2 \theta}{b_j^2} - \frac{\tan^2 \theta_j \cos^2 \theta}{a_j^2}, \\ \beta = & \frac{x_s \cos \phi \sin \theta}{a_j^2} + \frac{y_s \sin \phi \sin \theta}{b_j^2} - \tan \theta_j \cos \theta \lambda_j(z_s), \end{aligned}$$

and

$$\gamma = \frac{x_s^2}{a_j^2} + \frac{y_s^2}{b_j^2} - \lambda_j^2(z_s).$$

- If the value of R is real, then the hit point is on the finite cone frustum and therefore the ray from the source to observer is shadowed.

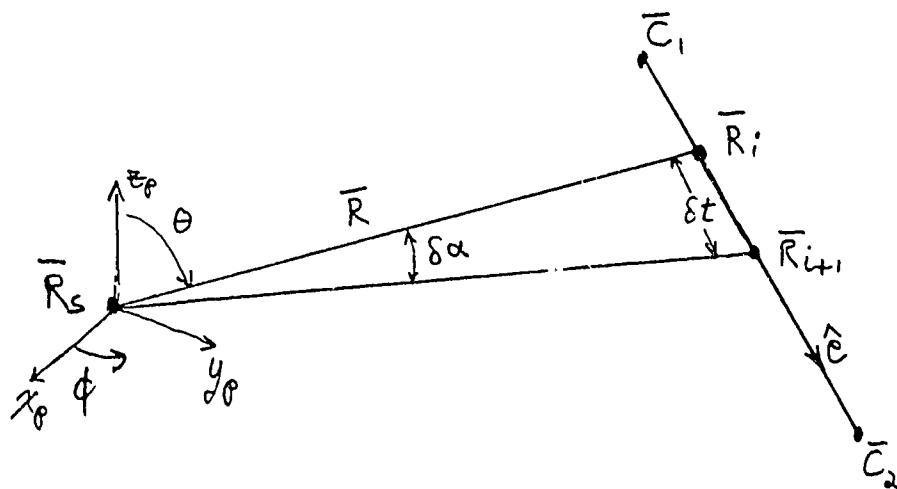
Fill Procedures

1. Place desired character in pixel to indicated shadowing.

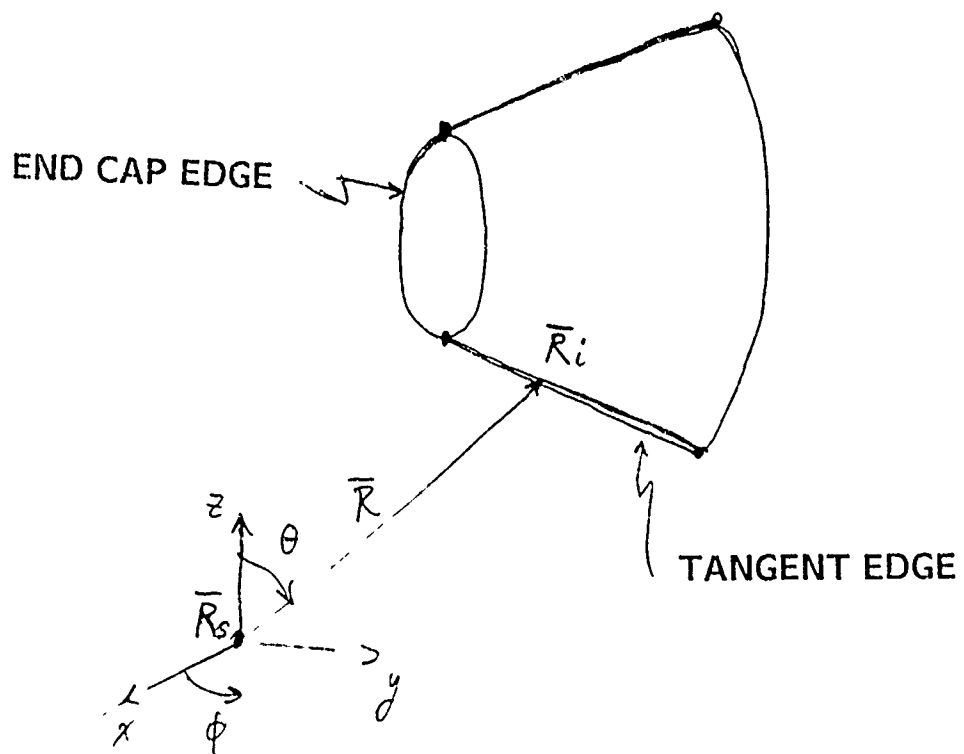
2. If desired, highlight particular plate with a different character.
3. If desired place different character in pixel for each plate or cylinder.

DEC VAX VMS Interactive Language Control

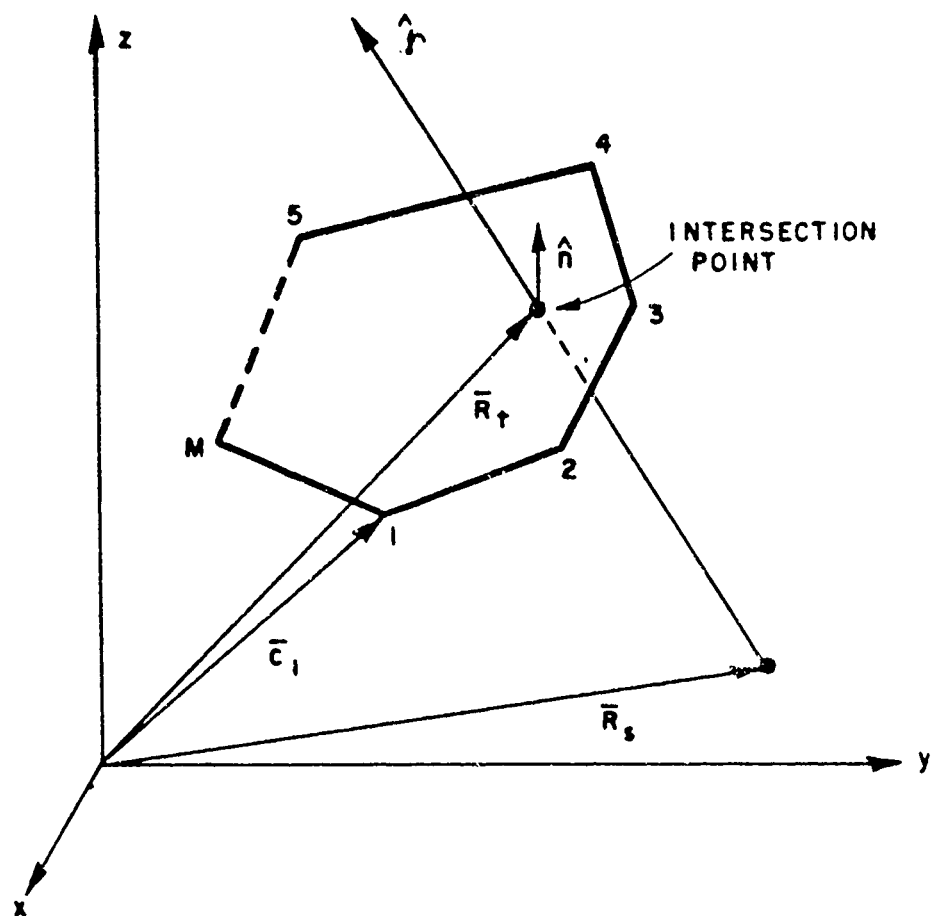
1. VAX VMS system service subroutines allow simulation of VMS commands for interaction with code.
2. Definition of the commands are made in a command table through file SHADOW.CLD.
3. Key pad can be used as a substitute for typing the command names.
4. Definition of the key pad key names are made in the file SHADOW.KPD.



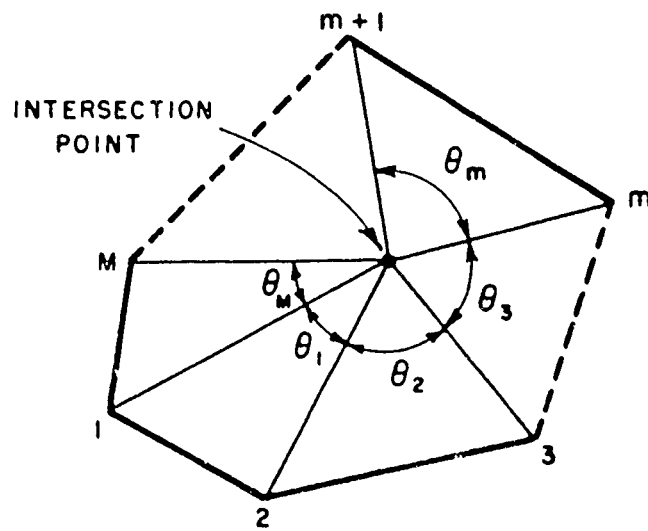
GEOMETRY FOR PROJECTING PLATE
EDGE ONTO FAR ZONE SPHERE



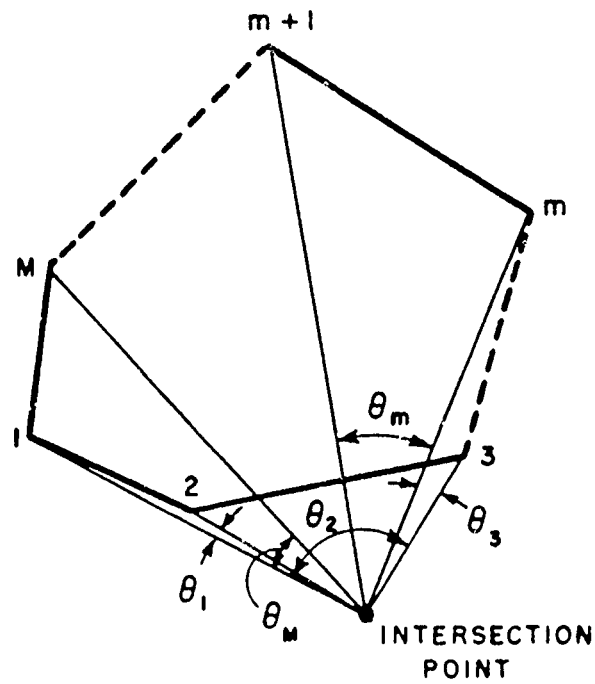
GEOMETRY FOR PROJECTING CONE FRUSTUM
ONTO FAR ZONE SPHERE



Intersection of scatter direction ray with plate.

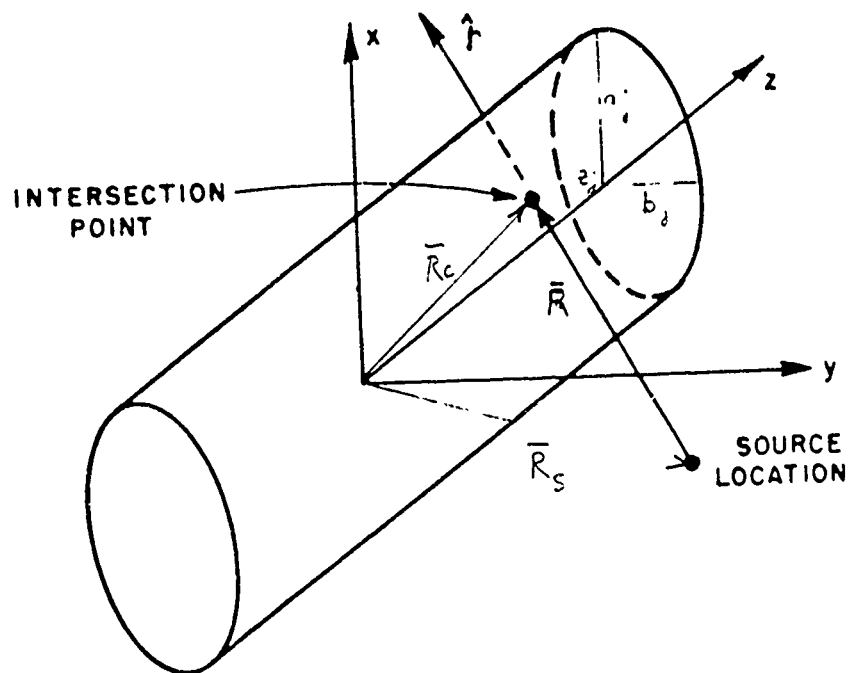


(a) RAY HITS PLATE



(b) RAY DOES NOT HIT PLATE

Geometry for deciding whether ray does or does not hit plate.



Geometry of intersection point of ray
in three dimensions.

Interactive Commands for SHADOW Code

- EXIT - exit code.
- HELP - online help definitions of commands.
- SPAWN - use of DCL from code.
- SET ANTENNA.LOCATION - define x,y,z position of source.
- SET COORDINATES - define rotate - translate coordinates
- SET FILL.CHARACTERS - define characters to be used to fill shadow.
- SET INPUT.SET - define non-interactive NEC-BSC input set to be read.
- SET KEYPAD.MODE - define whether keypad is to be used for numbers or command input.
- SET OUTPUT - define name of output files.
- SET PATTERN.CUT - define axes of the pattern cut coordinate system.
- SET SCALE.FACTOR - define scale factor for source location input.
- SET UNITS - define units for source location input.
- SET WINDOW - define range of theta and phi for the shadow window and the resolution.
- SHADOW - execute the SHADOW Code to produce a shadow map.
- SHOW etc. - For each of the above SET commands there is a corresponding SHOW command that indicates the values chosen.

Key Pad for SHADOW Code

PF1 gold	PF2 HELP	PF3 SHADOW	PF3 nokeypad SET KEYPAD
7 show SET OUTPUT	8 show SET INPUT	9 show SET ANTENNA	- show SET WINDOW
4 show SET SCALE	5 show SET UNITS	6 show SET COORD	show SET PATTERN
1 show SET FILL	2 /cylin FILL /PLATE	3 show FILL /SEQUEN	Enter RETURN
0 SPAWN		EXIT	

Example Interactive Run

This example is a four-cornered plate centered at the origin and situated in the X-Y plane. The antenna is located on the positive Z axis. It was generated with the following input files and commands. The commands were:

```
$ RUN SHADOW
SHADOW> SET OUT  PLAEX1/NCPLOT/PRINT
SHADOW> SET INP  PLAEX
SHADOW> SET UNI  METERS
SHADOW> SET WIND
          90, 180
          1.0
          0., 360
          5.
SHADOW> SET ANT
SHADOW> 0,0,8
SHADOW> SHADOW
SHADOW> EXIT
$
```

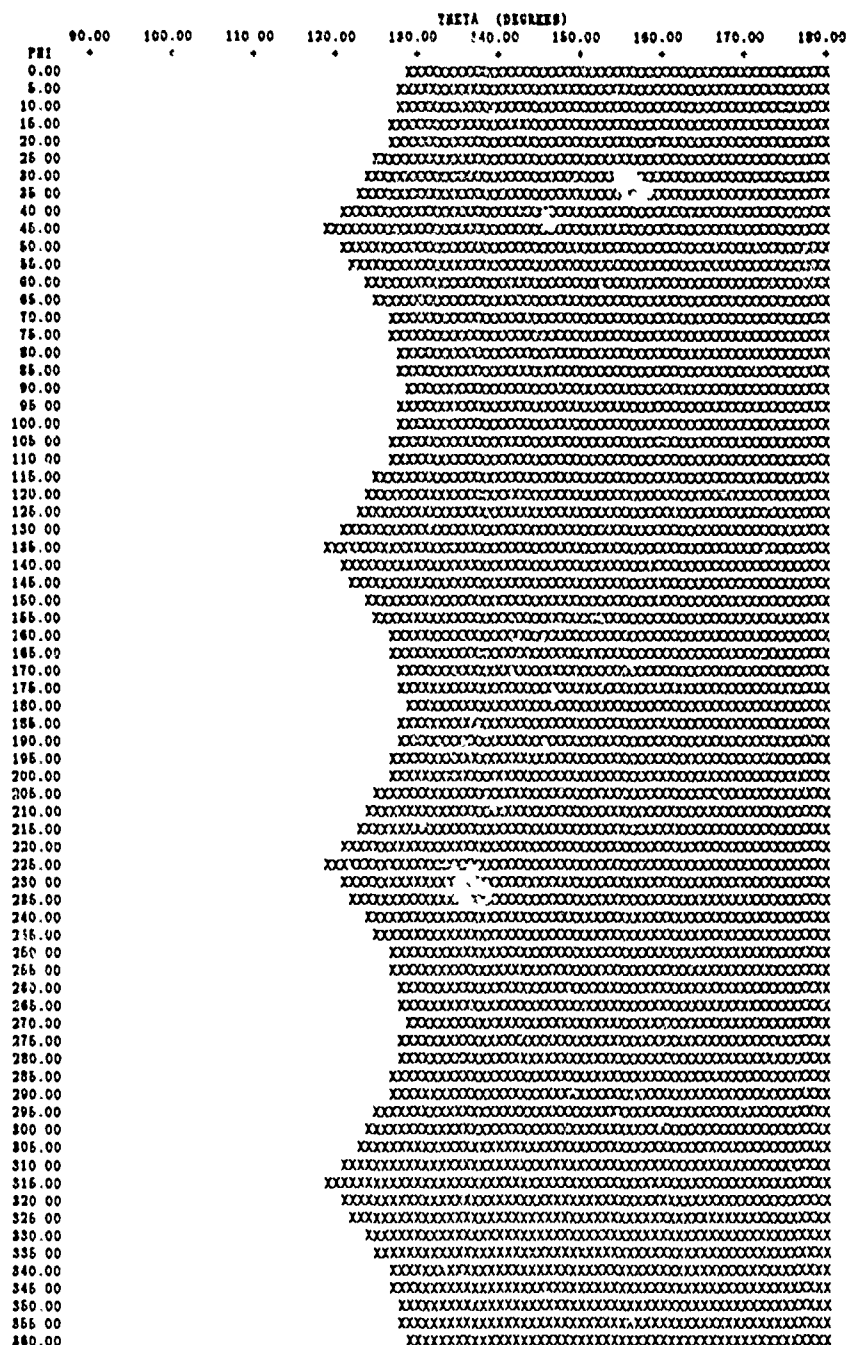
Non-interactive Input Set of Example

The input set defining the plate was the following:

```
CE:  SIMPLE PLATE TEST SET
UN:
1
PG: THE PLATE IS 400 SQUARE-METERS.
4.0
-10.0, +10.0, 0.0
-10.0, -10.0, 0.0
+10.0, -10.0, 0.0
+10.0, +10.0, 0.0
XQ:
EN:
```

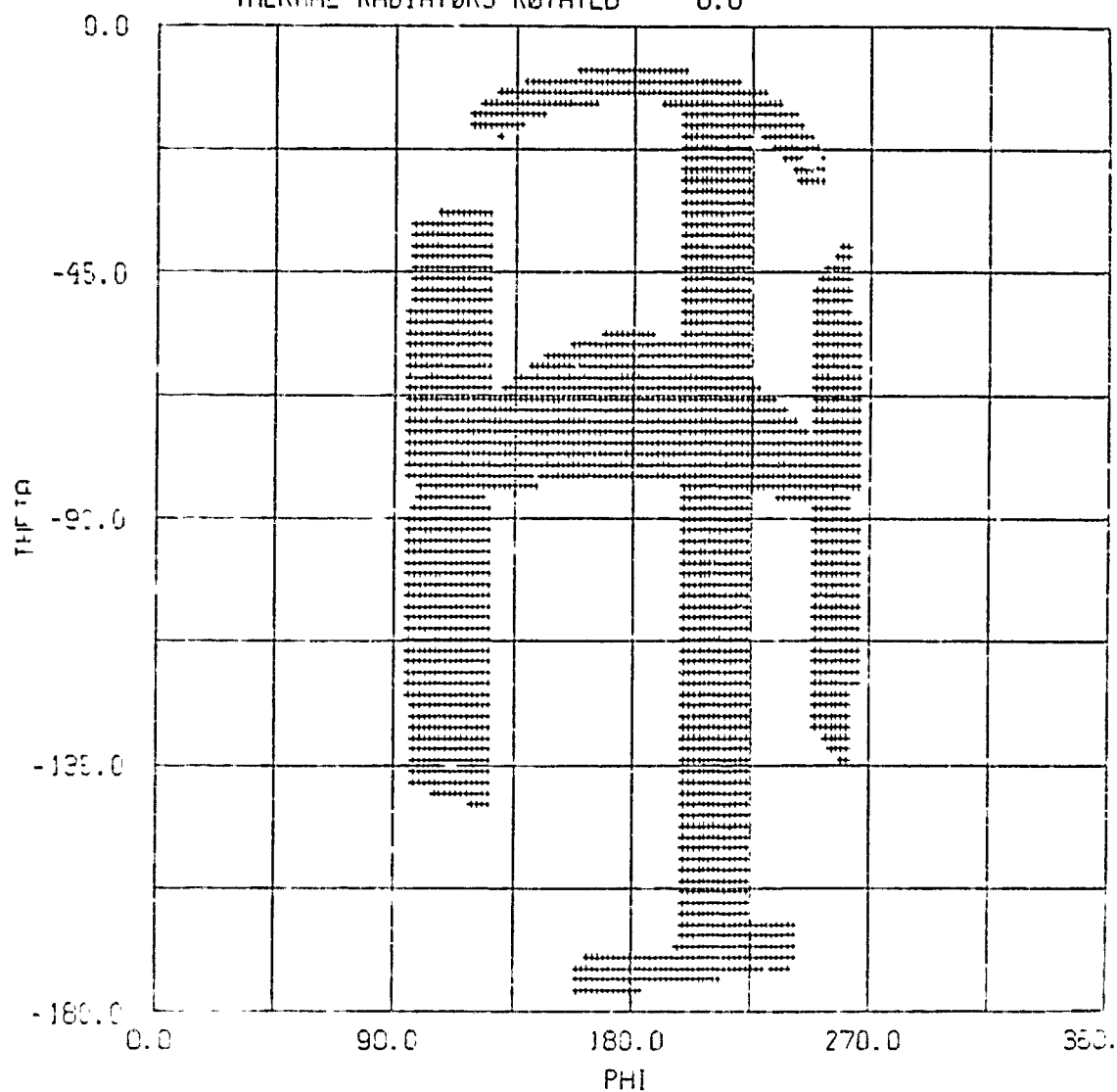
The output this produced was the following:

ANTENNA (RCS) = (0.0000, 0.0000, 8.0000) IN METERS INPUT SET: USER1:[LJM.NAS.MAN]PLAEX.INP:5



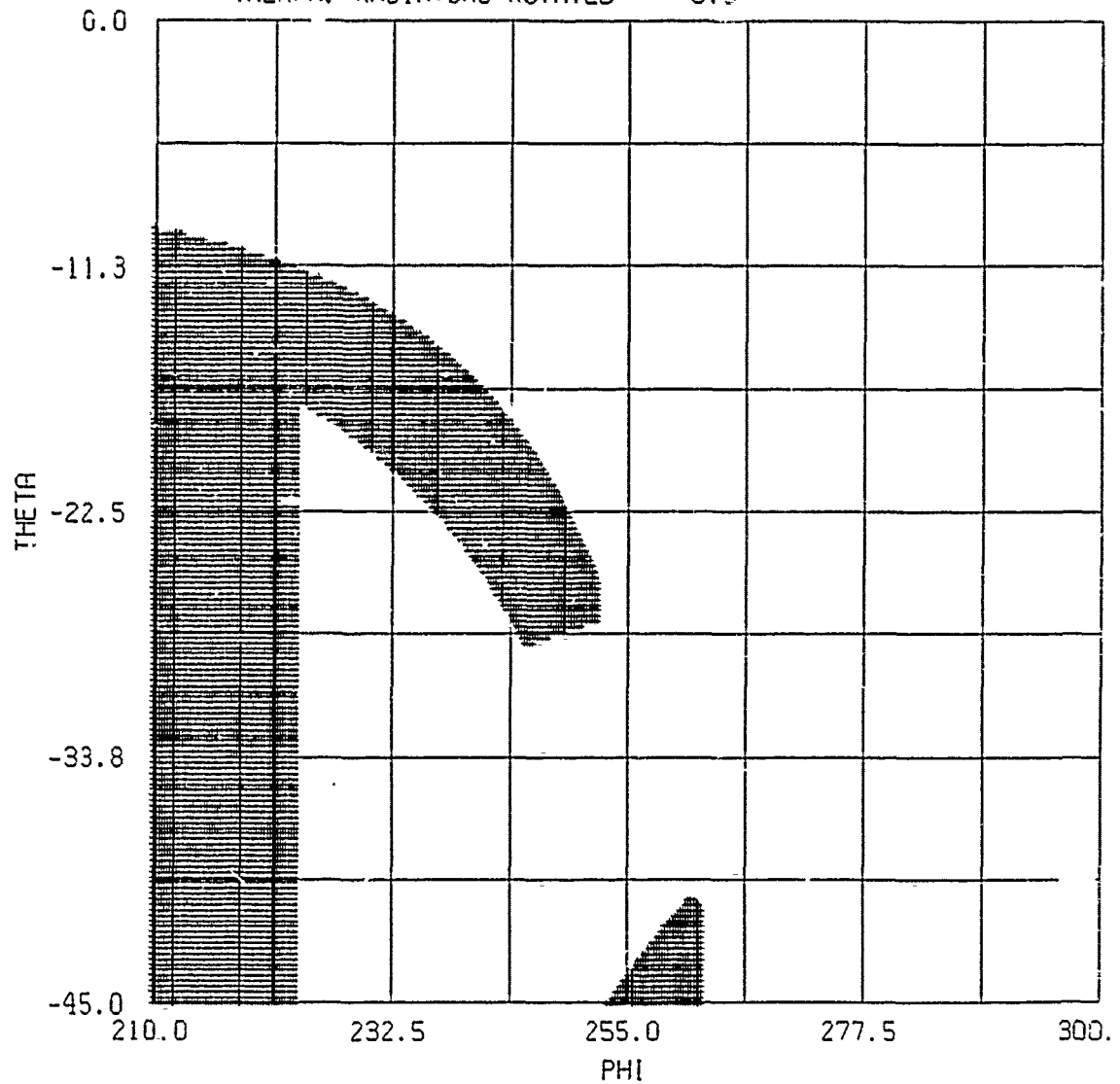
OUTPUT OF SHADOW CODE FOR SIMPLE PLATE EXAMPLE

SHADOW TEST FOR CASE ANSS1
 ANTENNA LOCATED AT 25.0, 15.0, 256.5
 ANTENNA ORIENTATION 0.0, 0.0, 90.0, 0.0
 SOLAR PANELS ROTATED 0.0, -52.0
 THERMAL RADIATORS ROTATED 0.0



OUTPUT PLOT FROM SHADOW CODE FOR
 LARGE SPACE STATION

SHADOW TEST FOR CASE ANSS1
 ANTENNA LOCATED AT 25.0, 15.0, 256.5
 ANTENNA ORIENTATION 0.0, 0.0, 90.0, 0.0
 SOLAR PANELS ROTATED 0.0, -52.0
 THERMAL RADIATORS ROTATED 0.0



OUTPUT PLOT FROM SHADOW CODE FOR LARGE
 SPACE STATION (SMALLER VIEW WINDOW)

VAX dependent interactive subroutines

C-----

SUBROUTINE INTRAC

```
!
!++
! FACILITY:  INTERACTIVE TERMINAL COMMAND INTERFACE
!
! ABSTRACT:
!
!   This procedure prompts a terminal for input and parses/dispatches
!   through CLI$ routines.
!
! ENVIRONMENT: VAX/VMS Version 4.x
!
! AUTHOR:  Laszlo Takacs  CREATION DATE: 20-AUG-1985
!
! MODIFIED BY:
!
! 1-001 -  Original, LAT 20-AUG-1985
!--
      IMPLICIT NONE
      INCLUDE '($RMSDEF)'
      INCLUDE '($SMGDEF)'
      EXTERNAL
      + COMMAND_TABLES,  ! User-defined command language.
      + GET_INPUT        ! The I/O routine at the bottom.
!
      INTEGER KBDID, KEYTBL
      INTEGER*4 STS, READ_STS,
      + CLI$PRESENT, CLI$DISPATCH, CLI$DCL_PARSE, CLI$GET_VALUE,
      + SMG$LOAD_KEY_DEFS, SMG$CREATE_KEY_TABLE,
      + SMG$DELETE_VIRTUAL_KEYBOARD, SMG$CREATE_VIRTUAL_KEYBOARD
!
      COMMON /TERCOM/ KBDID, KEYTBL
!
! Make a key definition table.
!
      STS = SMG$CREATE_KEY_TABLE( KEYTBL )
      IF (.NOT. STS) CALL LIB$SIGNAL( %VAL(STS) )
!
```

```

! Load the definitions from the key definition file.
! Ignore "file not found".
!
      STS = SMG$LOAD_KEY_DEFS( KEYTBL, 'SHADOW.KPD' )
      IF ((.NOT. STS) .AND. (STS .NE. RMS$_FNF)) THEN
        CALL LIB$SIGNAL( %VAL(STS) )
      ENDIF
!
! Get a handle on SYS$INPUT.
!
      READ_STS = SMG$CREATE_VIRTUAL_KEYBOARD( KBDID )
!
! The main processing loop.
! Keep reading input until the user types EOF.
!
      DO WHILE ( READ_STS .NE. RMS$_EOF )
!
! Read from input and parse the command.
!
      READ_STS = CLI$DCL_PARSE(,COMMAND_TABLES, GET_INPUT,
+   GET_INPUT, 'SHADOW> ')
!
! If the command parse was successful, execute the command-routine.
!
      IF ( .NOT. (.NOT. READ_STS) ) CALL CLI$DISPATCH()
!
      END DO
!
! Get rid of the virtual keyboard.
!
      STS = SMG$DELETE_VIRTUAL_KEYBOARD( KBDID )
      IF ( .NOT. STS ) CALL LIB$SIGNAL( %VAL(STS) )
!
! Return
!
      RETURN
      END

```

C-----

```

      INTEGER*4 FUNCTION GET_INPUT( COMMAND, PROMPT, LENGTH )
C!!!

```

C!!! This routine does all the reading for the terminal interface.
 C!!! It has the same calling format as LIB\$GET_INPUT except that
 C!!! optional parameters may not be omitted.
 C!!!

```

    INCLUDE '($RMSDEF)'
    EXTERNAL SMG$_EOF ! The linker finds this.
    CHARACTER*(*) COMMAND, PROMPT
    INTEGER KBDID, KEYTBL, LENGTH*2, SMG$READ_COMPOSED_LINE*4
    COMMON /TERCOM/ KBDID, KEYTBL
  
```

```

!
! Read a (composed) line and return the status to CLI$ stuff.
!
    GET_INPUT = SMG$READ_COMPOSED_LINE (KBDID, KEYTBL, COMMAND,
+ PROMPT, LENGTH)
    IF ( GET_INPUT .EQ. %LOC( SMG$_EOF ) ) GET_INPUT = RMS$_EOF
!
    RETURN
  END
  
```

C-----

```

    INTEGER*4 FUNCTION PUT_OUTPUT ( STRING )
  
```

C!!!
 C!!! This routine does all the writing for the terminal interface.
 C!!! It has the same calling format as LIB\$PUT_OUTPUT.
 C!!!

```

    CHARACTER*(*) STRING
    INTEGER*4 LIB$PUT_OUTPUT
  
```

```

!
! Read a line.
!
    PUT_OUTPUT = LIB$PUT_OUTPUT ( STRING )
!
! There should be no errors here. Signal if there are any.
!
    IF (.NOT. PUT_OUTPUT) CALL LIB$SIGNAL( %val(PUT_OUTPUT) )
!
! Return.
!
    RETURN
  END
  
```

Some Future Plans for the NEC-BSC

1. Volumetric pattern control.
2. Independent movement of source and receivers.
3. More source and receiver type options.
4. More curve surface options (cones, ellipsoids, etc.)
5. More UTD interaction field terms.
6. Direct control over all UTD field terms.
7. Easier access to scattering center positions.

MICROCOMPUTER COMPUTATION OF ELECTROMAGNETIC SCATTERING BY STRATIFIED ANISOTROPIC MATERIALS

Michael A. Morgan
Office of Naval Research, Code 1114SE
800 North Quincy Street
Arlington, VA 22217-5000

Dean L. Fisher
6520 Test Group/ ENVB, Stop 239
Edwards Air Force Base, CA 93523

Edmund A. Milne
Physics Dept. Code 61 Mn
Naval Postgraduate School
Monterey, CA 93943

ABSTRACT

A microcomputer program is described for the computation of scattering and transmission by planar layered anisotropic material. A 4×4 transformation matrix approach is employed, being an extension of a 2×2 matrix formulation for stratified isotropic media. Computational results are displayed in a pseudo 3D format showing specular scattering versus frequency and incidence angle. Cross coupling between orthogonal incident polarizations is considered. Validations are presented for special cases which can be independently computed.

INTRODUCTION

Our goal in this effort was to develop a general purpose formulation and efficient numerical algorithm for scattering and transmission calculations involving stratified anisotropic media, [1]. By combining this algorithm with a numerical optimization procedure it will become possible, in a continuing effort, to synthesize multiple layered structures to achieve desirable polarization filtering characteristics for a postulated range of incident field wave-vectors.

The methodology described herein is an extension of the technique developed by Ruck, et al [2] for use with isotropic material. Maxwell's equations are cast into a 4×4 matrix formulation which is equivalent, but not identical, to that in [3]. Solution procedures based upon both eigenfunction expansions and a new finite-difference approach are considered. A computer program is described and the various means of validating its performance is discussed along with accompanying sample computations.

GENERAL FORMULATION

The geometry being considered is shown in Figure 1, wherein a one-dimensionally inhomogeneous planar anisotropic region is bounded by homogeneous isotropic material half-spaces for $z < 0$ and $z > d$. A monochromatic plane wave is obliquely incident from the left half-space (region 1) with arrival angle θ_1 in the $x - z$ plane of incidence. Using an $\exp(j\omega t)$ time convention, the complex phasor fields may be written in the separable product form

$$\mathcal{E}(x, z) = E(z) \exp(-jk_x x) \quad (1a)$$

$$\mathcal{H}(x, z) = H(z) \exp(-jk_x x) \quad (1b)$$

where $k_x = k_1 \sin \theta_1$ is the x -component of the incident field wave vector.

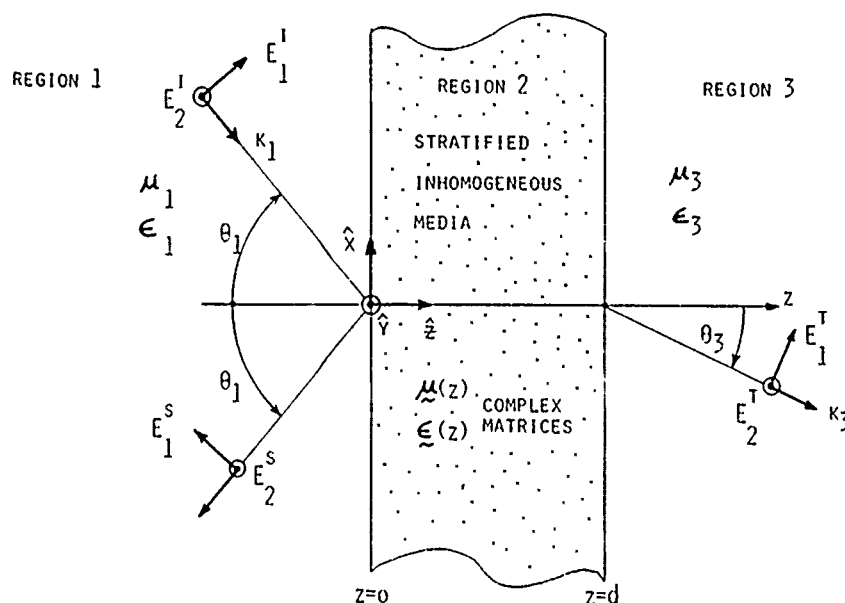


Figure 1 Scattering and Transmission from Stratified Anisotropic Material.

By defining a state vector in terms of the transverse field components of E and H in (1),

$$\Psi(z) = \begin{bmatrix} E_x(z) \\ E_y(z) \\ H_x(z) \\ H_y(z) \end{bmatrix} \quad (2)$$

Maxwell's equations can be reduced to coupled ordinary differential equations, expressed in matrix notation by

$$\frac{d}{dz} \Psi(z) = \Gamma(z) \cdot \Psi(z) \quad (3)$$

The elements of the 4×4 Γ -matrix can be easily derived [6].

The overall diffraction problem, including specular scattering and refractive transmission, can be solved by first undertaking the computation of the complex 4×4 *transition matrix*, A , defined by

$$\Psi(0) = \underset{\sim}{A} \cdot \Psi(d) \quad (4)$$

Using the hypothetical A -matrix we can solve the diffraction problem in a direct manner. By introducing tangential field matrices,

$$E_T(z) = \begin{bmatrix} E_x(z) \\ E_y(z) \end{bmatrix} \quad (5a)$$

$$H_T(z) = \begin{bmatrix} H_x(z) \\ H_y(z) \end{bmatrix} \quad (5b)$$

and using i , s and t superscripts to denote respective incident, scattered and total fields, we define 2×2 complex scattering and transmission matrices, S and T , by

$$E_T^s(0) = \underset{\sim}{S} \cdot E_T^i(0) \quad (6)$$

$$E_T^t(d) = \underset{\sim}{T} \cdot E_T^i(0) \quad (7)$$

By partitioning the 4×4 transition matrix into four 2×2 quadrant sub-matrices,

$$\underset{\sim}{A} = \begin{bmatrix} \underset{\sim}{Q}_1 & \underset{\sim}{Q}_2 \\ \underset{\sim}{Q}_3 & \underset{\sim}{Q}_4 \end{bmatrix} \quad (8)$$

there results from (4) and (5),

$$E_T^i(0) + E_T^s(0) = \underset{\sim}{Q}_1 \cdot E_T^t(d) + \underset{\sim}{Q}_2 \cdot H_T^t(d) \quad (9a)$$

$$H_T^i(0) + H_T^s(0) = \underset{\sim}{Q}_3 \cdot E_T^t(d) + \underset{\sim}{Q}_4 \cdot H_T^t(d) \quad (9b)$$

To solve the scattering problem, we introduce wave impedance

matrices for the homogeneous half-spaces in regions 1 and 3,

$$E_T^i(0) = \tilde{Z}_1 \cdot H_T^i(0) \quad (10a)$$

$$E_T^s(0) = -\tilde{Z}_1 \cdot H_T^s(0) \quad (10b)$$

$$E_T^t(d) = \tilde{Z}_3 \cdot H_T^t(d) \quad (10c)$$

where, for $m = 1$ or 3 ,

$$\tilde{Z}_m = \begin{bmatrix} 0 & \eta_m \cos \theta_m \\ -\eta_m \sec \theta_m & 0 \end{bmatrix} \quad (11a)$$

$$\text{and} \quad \eta_m = \sqrt{\frac{\mu_m}{\epsilon_m}} \quad (11b)$$

$$\sin \theta_3 = \sqrt{\frac{\mu_1 \epsilon_1}{\mu_3 \epsilon_3}} \sin \theta_1 \quad (11c)$$

The S and T matrices may be obtained via simple matrix algebra,

$$\tilde{S} = (\tilde{Z}_a + \tilde{Z}_b)^{-1} \cdot (\tilde{Z}_a - \tilde{Z}_b) \quad (12)$$

$$\tilde{T} = 2 \tilde{Z}_3 \cdot (\tilde{Z}_a + \tilde{Z}_b)^{-1} \quad (13)$$

where we have defined new impedance matrices,

$$\tilde{Z}_a = \tilde{Z}_1 \cdot \tilde{Z}_3 + \tilde{Q}_2 \quad (14a)$$

$$\tilde{Z}_b = \tilde{Z}_1 \cdot (\tilde{Q}_3 \cdot \tilde{Z}_3 + \tilde{Q}_4) \quad (14b)$$

For the important case of a perfect conductor in region 3, with $\tilde{Z}_3 = 0$, the T - matrix becomes zero and the scattering matrix simplifies to

$$\tilde{S} = (\tilde{Q}_2 + \tilde{Z}_1 \cdot \tilde{Q}_4)^{-1} \cdot (\tilde{Q}_2 - \tilde{Z}_1 \cdot \tilde{Q}_4) \quad (15)$$

TRANSITION MATRIX COMPUTATION

Consider the special case of the anisotropic media in region 2 being composed of N homogeneous layers, as illustrated in Figure 2, where $z_1 = 0$ and $z_{N+1} = d$. The incident field half-space (region 1) will be denoted as the zeroth layer while the left half-space (region 3) is enumerated as the $N+1$ layer. Our initial goal will be to describe procedures for obtaining *local* transition matrices relating the state vectors at adjacent "n" and "n-1" interfaces,

$$\tilde{\Psi}(z_{n-1}) = A_n \cdot \tilde{\Psi}(z_n) \quad (16)$$

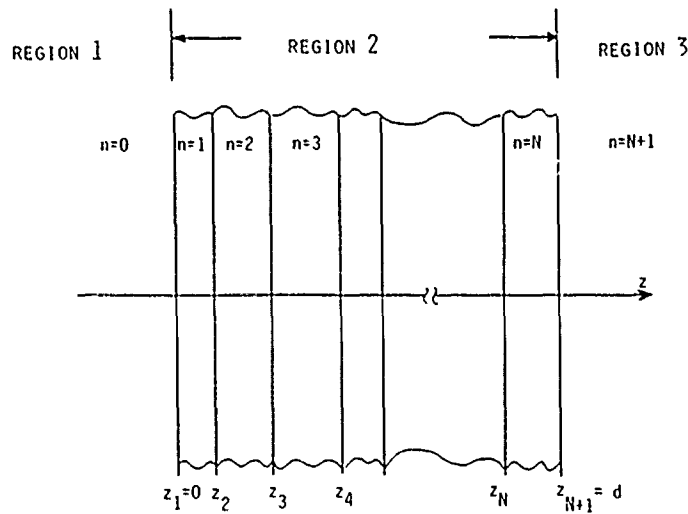


Figure 2 Anisotropic Region Composed of N Homogeneous Layers.

Since $\tilde{\Gamma}(z) = \tilde{\Gamma}_n$ is constant within the n -th layer, the resultant state vector solutions of (3) will have the form of non-uniform plane waves

$$\tilde{\Psi}_n(z) = \tilde{V}_n \exp(\gamma_n z) \quad (17)$$

where \tilde{V}_n is a constant vector. Acceptable complex z -directed wavenumbers, γ_n are found by first substituting (17) into (3) to produce the eigenvalue system

$$[\tilde{\Gamma}_n - \gamma_n \tilde{I}] \tilde{V}_n = 0 \quad (18)$$

with \tilde{I} being the 4×4 identity matrix. The eigenvalue wavenumbers may be found as the roots of the quartic characteristic equation obtained by setting the determinant of the bracketed matrix in (18) to zero. Efficient procedures exist for evaluating eigenvalues and eigenvectors, [4].

Once the sets of eigenvalue-eigenvector pairs have been found within the n -th layer we can represent the state-vector as a weighted summation of the eigen-basis functions which were postulated in (17),

$$\tilde{\Psi}_n(z) = \sum_{m=1}^4 C_n^m \tilde{V}_n^m \exp(\gamma_n^m z) \quad (19)$$

It can be shown through substitution of (19) into (16), followed by simple matrix manipulations, that

$$\tilde{A}_n = \tilde{V}_n \cdot \tilde{U}_n(-d_n) \cdot \tilde{V}_n^{-1} \quad (20)$$

where \tilde{V}_n has its m -th column formed from the components of \tilde{V}_n^m while $\tilde{U}_n(z)$ is a 4×4 diagonal matrix with non-zero elements given by $\exp(\gamma_n^m z)$ and d_n is the thickness of the n -th layer.

An alternative method for obtaining the local transition matrix in each layer is through a finite difference algorithm. Consider partitioning the region within the n -th homogeneous layer into L_n sub-layers, each having equal thickness $h_n = d_n/L_n$. A piecewise linear approximation for each of the four components of the state-vector may be employed, as illustrated in Figure 3.

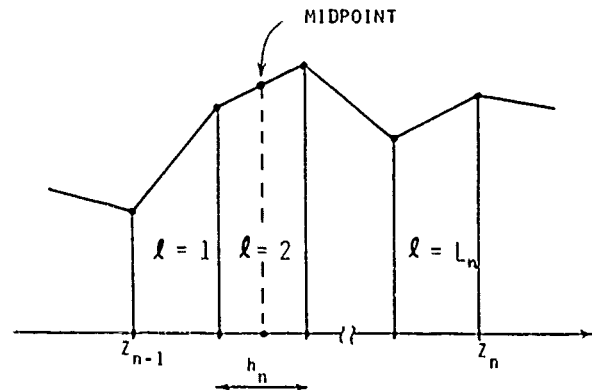


Figure 3 Piecewise Linear Approximation in the n -th Layer.

Enforcing (3) at the midpoint of the ℓ -th sub-layer, yields

$$\Psi_n(\ell-1) = \mathcal{P}_n \cdot \Psi_n(\ell) \quad (21)$$

where the sub-layer localized 4×4 transition matrix is given by

$$\mathcal{P}_n = \left(\mathcal{I} + \frac{h_n}{2} \mathcal{J}_n \right)^{-1} \cdot \left(\mathcal{I} - \frac{h_n}{2} \mathcal{J}_n \right) \quad (22)$$

As a result of equal intervals being chosen for the sub-layers, h_n , this transition matrix remains constant throughout the n -th homogeneous layer. The local transition matrix can be found in terms of successive self-multiplications,

$$\mathcal{A}_n = \prod_{\ell=1}^{L_n} \mathcal{P}_n = [\mathcal{P}_n]^{L_n} \quad (23)$$

The selection of the sub-layer interval, h_n , will depend upon the maximum expected rate of change of the state vector fields therein. This interval should be small enough to allow accurate tracking of the set of exponential basis functions in (17). A simple analysis shows that h_n should be made small compared to the reciprocal of the magnitude of the largest (in modulus) complex eigenvalue,

$$h_n \ll 1 / \{ \max |\gamma_n^m| \} \quad (24)$$

The *power method* can be used to estimate this magnitude without the need to solve for the smaller eigenvalues [14].

Once the local transition matrices are obtained for the various layers, the complete transition matrix can be computed as the product,

$$\tilde{A} = \prod_{n=1}^N \tilde{A}_n \quad (25)$$

This matrix is then used to find the scattering and transmission matrices, using the procedure described in the previous section.

The extension of the finite-difference algorithm to continuously stratified media in region 2 embodies the use of an approximate model composed of thin homogeneous layers. The layer thicknesses can be made locally dependent upon the material properties through estimates of maximum wavevectors. Enhancements of this approach can be made by implementing more optimized numerical methods such as that of Runge-Kutta [14].

COMPUTATIONAL VERIFICATION

The algorithm was implemented on a microcomputer using the finite-difference approach to compute the transition matrix. As input to this program, the user must specify the number and thicknesses of each layer within region 2 followed by the entry of the complex matrix elements within each layer for the permittivity and permeability tensors. The material in region 1 is assumed to be free-space while that of region 3 can be specified as either free-space or a perfect electric conductor (p.e.c.). Further inputs are required as to range and increments of both temporal frequencies and incident aspect angles. Scattering computations are performed for two incident orthogonal linear polarizations, having the incident E-field either parallel or normal to the x - z plane of incidence.

The computer program was checked in three steps. First, simple cases were run to verify that no obvious errors were present. Next, several test cases involving complicated layered material configurations composed of lossy isotropic media were compared to the results of a previously developed computer program. This separate program, which used the 2 x 2 matrix formulation for isotropic material, had been extensively checked against independent results [2]. The final validation was for a metal backed (p.e.c. in region 3) homogeneous lossy anisotropic layer whose scattering could be computed by analytic means.

An example of the results from the initial set of computations involving free space in region 2 is shown in the pseudo-3D plot of Figure 4. In computing the transition matrix, region 2 was partitioned into multiple layers (based on the

criterion discussed in the previous section) and the diagonal elements of the permittivity and permeability matrices within each layer were set to their respective free space values, with other elements set to zero. The independent variable axes are normalized frequency, $k_0 d$ and incident aspect angle (0° is normal to the surface). In this plot the case of a p.e.c. in region 3 is considered which, of course, should yield complete reflection, $|S_{11}| = 1$. When region 3 was considered as free space, the computed S-matrix was found to be identically zero while the resultant transmission matrix had unit diagonals and zero off-diagonal elements.

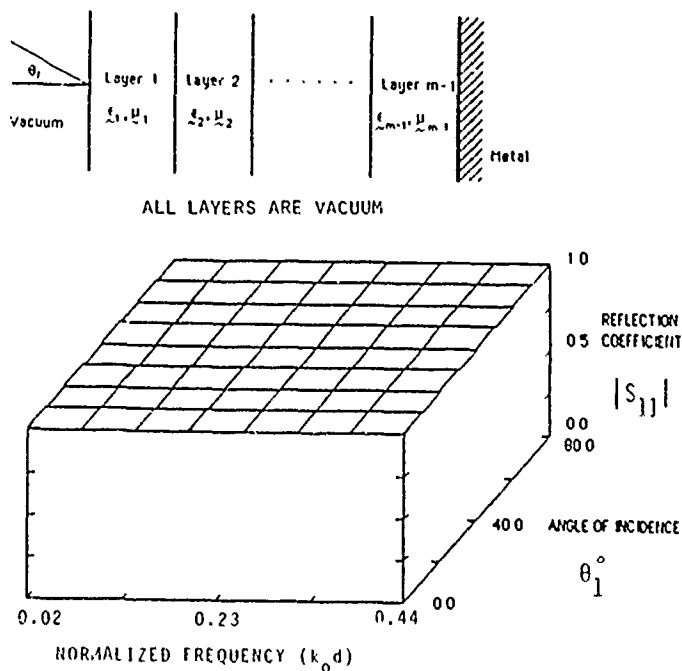


Figure 4 Scattering Computation Using Multiple Free Space Layers Over a Metal Plane.

An example of the computational comparisons made between the general anisotropic program and the specialized isotropic program is shown in Figure 5. This case is that of a single electrically thin layer of lossy dielectric bounded by a vacuum on both sides. S-matrix values are shown for a range of aspects and frequencies. Differences of the various validating computations were in the realm of a fraction of one-percent in each case.

To test the accuracy of the general program for anisotropic material in region 2, a comparison was made to our analytical solution for normal incidence upon a metal-backed layer of magneto-plasma. With a z-directed static magnetic field, the

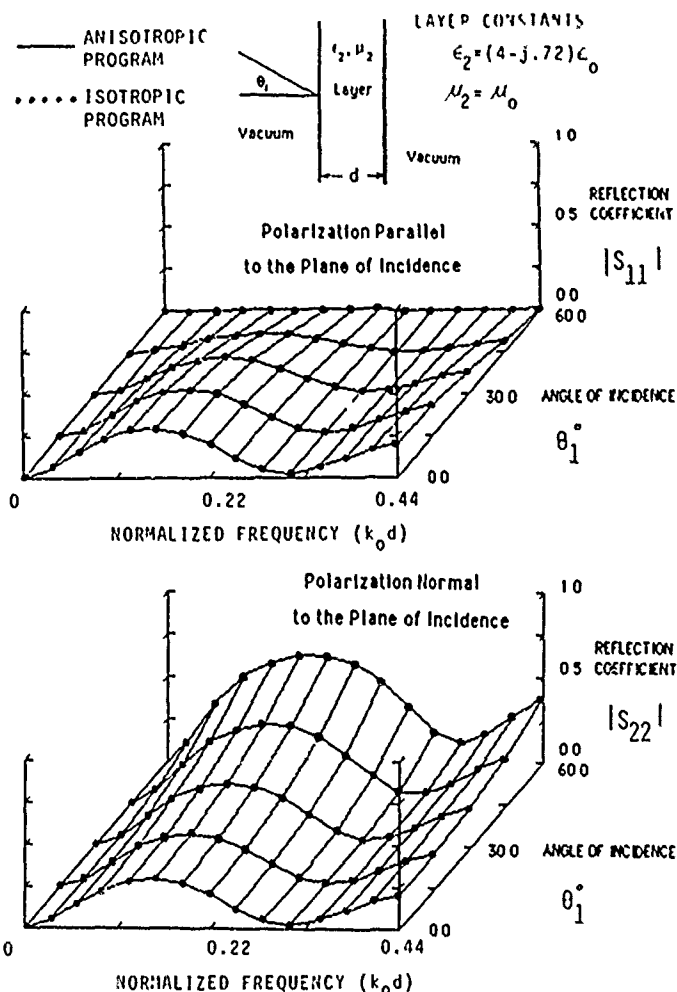


Figure 5 Magnitudes of S_{11} and S_{22} for a Lossy Isotropic Dielectric Coating on a Metal Plane.

permittivity tensor has the Hermitian form, [5],

$$\underline{\epsilon} = \begin{bmatrix} \epsilon_a & j\epsilon_b & 0 \\ -j\epsilon_b & \epsilon_a & 0 \\ 0 & 0 & \epsilon_c \end{bmatrix} \quad (26)$$

It can be shown by way of an eigenvalue solution [7] which is similar to that in the general formulation, that for the case of normal incidence the basis functions for $E(z)$ are circularly polarized waves propagating in the $+z$ and $-z$ directions,

$$E_1^{\pm} = C_1^{\pm} (\hat{x} + j\hat{y}) \exp(\mp j\beta_1 z) \quad (27a)$$

$$E_2^{\pm} = C_2^{\pm} (\hat{x} - j\hat{y}) \exp(\mp j\beta_2 z) \quad (27b)$$

where

$$\beta_2 = k_0 \sqrt{\frac{\epsilon_a + \epsilon_b}{\epsilon_0}} \quad (27c)$$

An application of the cogent boundary conditions on E and H at the outer interface, $z = 0$, and at the p.e.c., $z = d$, provides four simultaneous equations that can be solved to yield the scattering matrix elements,

$$S_{11} = S_{22} = \frac{a_1}{a_1 + b_1} + \frac{a_2}{a_2 + b_2} - 1 \quad (28a)$$

$$S_{12} = -S_{21} = \frac{a_1}{a_1 + b_1} - \frac{a_2}{a_2 + b_2} \quad (28b)$$

$$\text{with} \quad a_n = [1 - \exp(-j2\beta_n d)] \quad (28c)$$

$$\text{and} \quad b_n = [1 + \exp(-j2\beta_n d)] - \frac{\beta_n}{k_0} \quad (28d)$$

A comparison of S-matrix magnitudes is given in Figure 7 for a particular case of magneto-plasma coated metal. The complex permittivity matrix in (31) has non-zero elements $\epsilon_a = 100 \epsilon_0$, $\epsilon_b = 50 \epsilon_0$ and $\epsilon_c = \epsilon_0$. Further comparisons are pending, with use of experimental scattering data for multilayered magnetic materials.

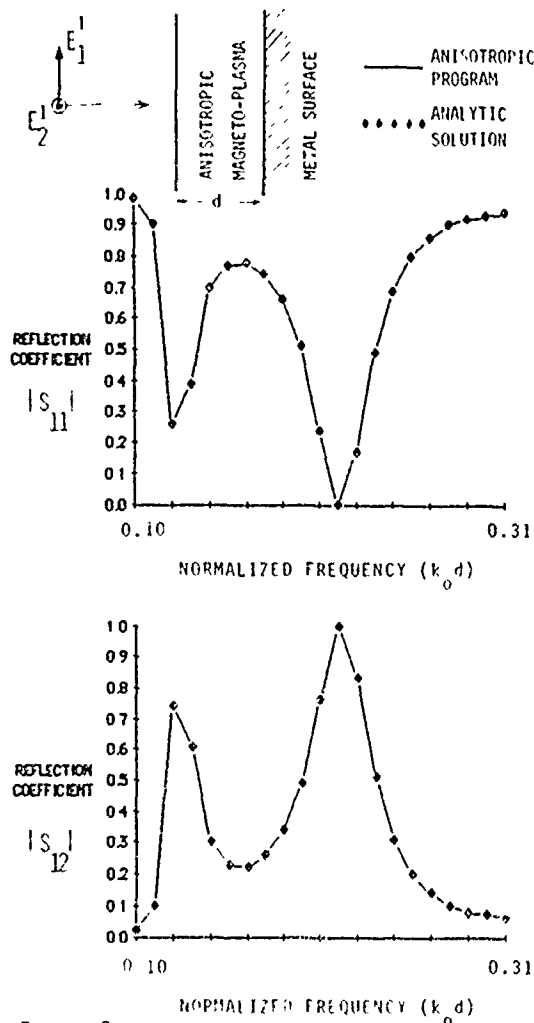


Figure 6

S Matrix Magnitudes for a Lossy Anisotropic Magneto Plasma Coating on a Metal Plane.

CONCLUSION

A general analytic formulation has been described for scattering and transmission problems involving lossy stratified anisotropic material. The method employs a 4×4 transition matrix combined with impedance boundary conditions at the entrance and exit planes of the stratified region. A new finite-difference approach is employed for field solutions within homogeneous layers of the structure. Scattering and transmission matrices are obtained for ranges of frequency and aspect angle for incident plane wave fields.

Extensive accuracy checks were performed on the general numerical algorithm. This included comparisons with results from an earlier program which was designed to handle only isotropic media. An anisotropic case was considered, using an independent analytical solution for scattering by a layer of magneto-plasma covering a planar metallic surface.

A continuing effort is underway for incorporating the algorithm described here into an optimization program for use in the design of transmission and/or reflection structures. Input specifications include bounds on the characteristic behavior of the scattering and/or transmission matrix elements for a range of incident aspect angles and harmonic frequencies.

REFERENCES

- [1] D.L. Fisher, "Investigation of Electromagnetic Scattering from Anisotropic Materials," M.S. Thesis, E.C.E. Dept., Naval Postgraduate School, Monterey, CA, Sept. 1985.
- [2] G.T. Ruck, D.E. Barrick, W.D. Stuart and C.K. Krishbaum, *Radar Cross Section Handbook, Vol. 2*, New York: Plenum Press, 1970, pp. 473-484.
- [3] D.W. Berreman, "Optics in Stratified and Anisotropic Media: 4×4 Matrix Formulation," *J. Opt. Soc. Am.*, vol. 62, no. 4, pp. 502-510, April 1972.
- [4] E. Isaacson and H.B. Keller, *Analysis of Numerical Methods*, New York: Wiley, 1966.
- [5] C.C. Johnson, *Field and Wave Electrodynamics*, New York: McGraw Hill, 1965, pp. 398-400.
- [6] M. A. Morgan, "Scattering by Stratified Anisotropic Media," Naval Postgraduate School, 17 July 1985, Unpublished.
- [7] M. A. Morgan, "Scattering from a Metal-Backed Layer of Magneto-Plasma, 11 Sept 1985, Unpublished.

APPLICATION OF NEC TO EMP-ANALYSES

M. Wurm, K. Mueller
Industrieanlagen-Betriebsgesellschaft mbH
Department SOE
Einsteinstr. 20
D-8012 Ottobrunn /West-Germany

The assessment of surface currents in three-dimensional structures with metallic surfaces is an important issue in the field of EMP-interaction analysis. To obtain sufficient information about magnitude, direction, frequency - and time dependence upon these currents, the NEC code system - consisting of NEC-2 and the supplementary code SOMNEC for the calculation on the Sommerfeld integral in the case of finite conductivity of the earth - was implemented on different computer systems. Furthermore the code system was expanded by a pre- and post-processor which enables the user to apply NEC also for analyses in the time domain.

As NEC operates in the frequency domain, it is first necessary to transform the time-dependent EMP into the frequency domain, i.e. to calculate the EMP-spectrum. This Fourier-Transformation is done by an appropriate "post-processor", using either analytical or numerical methods (fig. 1).

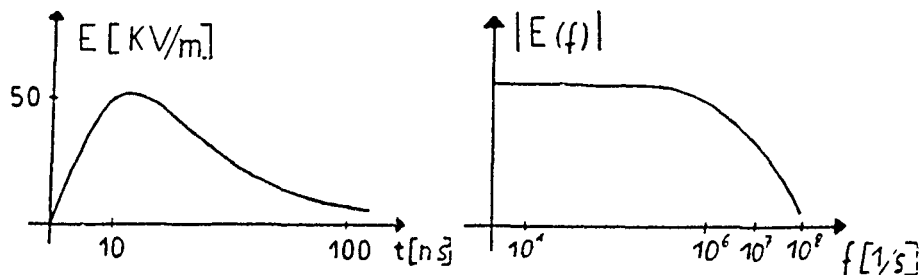


Fig. 1: EMP in time- and frequency domain

NEC-2 has then to be applied for each frequency of this spectrum.

To gain first experience with the application of NEC to the problem mentioned above, a parallelepiped with metallic surfaces was chosen and modeled as a wire-grid structure consisting of 292 elements. Finite electric conductivity of the earth was assumed and taken into account by the SOMMERFELD-NORTON option. The object was illuminated by a linear polarized electromagnetic wave with a frequency of 10 MHz (fig.2).

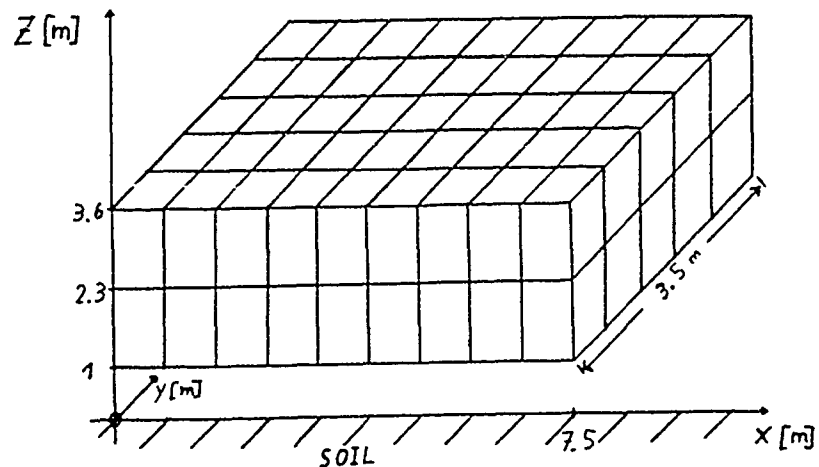


Fig. 2: Wire-grid model of a parallelepiped

The surface currents in each element, some near fields and radiation patterns were calculated. The calculations were performed at 4 different computer systems:

CDC CYBER 835/855	60-bit machine
SIEMENS 7551	32-bit machine
SIEMENS 7980	32-bit machine
SIEMENS/FUJITSU VP200	VECTOR HARDWARE

The elapsed CPU-times vary in a wide range as follows:

CPU-time on various computer-systems running NEC-2, SOMNEC

Wire-grid-model of a parallelepiped consisting of 292 elements	CYBER 835/855 60-bit machine single precision	SIEMENS 7551 double precision	SIEMENS 7890 double precision	SIEMENS 7890 double precision skalar performance running at VP 200	SIEMENS/FUJITSU VP 200 double precision vector perform. auto-vectorization
SOMNEC	84 sec	432 sec	14 sec	8 sec	
NEC-2	528 sec	6318 sec	188 sec	112 sec	102 sec (30 sec without ground option)
TOTAL FOR EACH FREQUENCY	612 sec	6750 sec	202 sec	120 sec	110 sec

=====

Running the code on the 32-bit mainframes with "single precision" inaccurate results were achieved compared with those from the 60-bit machine Cyber 835/855.

Using the "double precision" option on the 32-bit machines - which can be achieved through compiler-options - produced identical results with those from the Cyber-machine.

Running the code on vector hardware VP200 offered a time-reduction of factor 5 by mere auto-vectorization of the FORTRAN source-code by the compiler. It is expected to achieve still more time-saving for each frequency-run by a source-code modification with respect to the special requirements of the vector hardware ("hand-vectorization").

After having calculated the wire-currents in each segment for each frequency of interest, it is necessary to "add up" the frequency-dependent currents to obtain the results in the time-domain. This is achieved by the reverse Fourier-Transformation done by the post-processor. This transformation generally cannot be performed analytically. To avoid time-consuming numerical direct methods, the application of the Fast-Fourier-Transformation (FFT) was chosen.

However, as FFT requires equidistant frequencies, and the available results have normally not been computed at equidistant frequencies, it is first necessary to apply an interpolation routine (spline-interpolation, fig. 3).

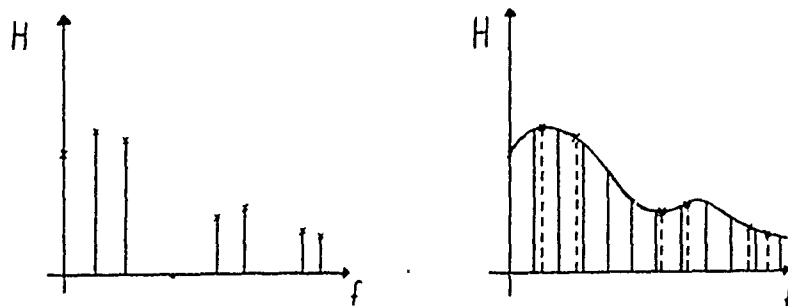


Fig. 3: Spline-interpolation

The required equidistance in the frequency range is then available and FFT can be performed. (An example testing merely the FFT against direct methods showed that the FFT is faster by a factor of 12, using approx. 500 frequencies).

To visualize the achieved results a 2-dimensional plot is generated to give a first but easy to survey impression of the currents in the structure. The currents are represented by arrows whose heads indicate the current-direction and whose length is directly related to the magnitude of the currents.

To demonstrate this method, the EMP-induced currents flowing in a wire-grid model of a cross-bar are shown in fig. 4.

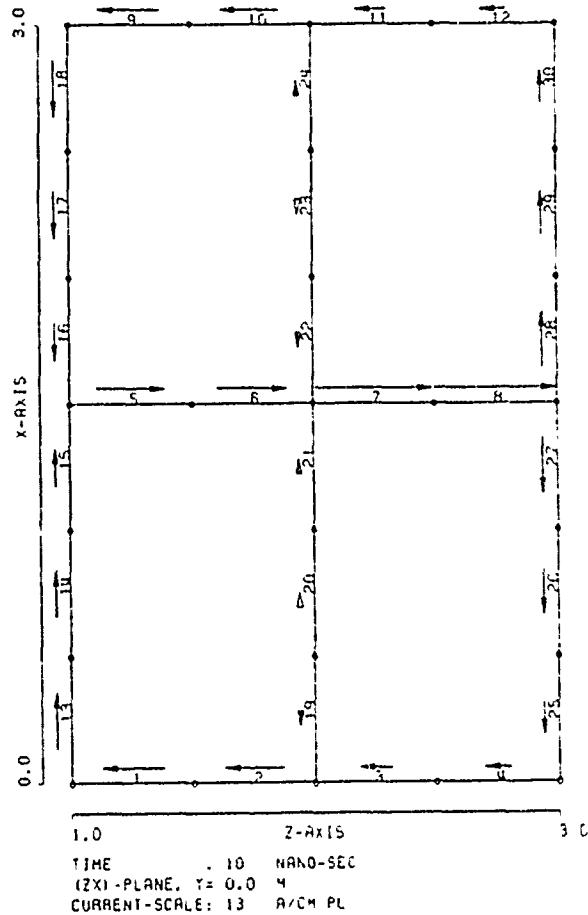


Fig. 4: Currents in a wire-grid structure

Use of MININEC to Determine the Optimum Placement of Insulators on a VLF Top-Loaded Monopole

T. D. Poston & B. G. Hagaman
Kershner, Wright & Hagaman, P.C.
5730 General Washington Drive
Alexandria, Virginia 22312

T.L. Simpson
College of Engineering
University of South Carolina
Columbia, South Carolina 29208

ABSTRACT

The possibility of using MININEC to determine the optimum placement of insulators on a top-loaded monopole antenna has been investigated. The MININEC results are compared with two alternate techniques: a computer program based on an electrostatic analysis and an experimental method using a scale model placed in an electrolytic tank. All three methods require that some approximations be made. Comparison of the methods seem to indicate that MININEC might eventually be used to solve this problem if the structure is accurately modeled. However, the present results are only slightly encouraging. Evidently, a large number of segments and close attention to insulator lengths and impedances will be required in order to get an adequate solution.

INTRODUCTION

The problem of how to determine the optimum insulator placement on the guys of a base-fed, top-loaded-vlf monopole antenna has existed for years and continues to be a problem as new antennas are designed and as damaged insulators are replaced. The high power and corresponding high voltage levels (up to 250 kV) require large insulators that are expensive and heavy. Their weight

reduces the guy efficiency and appreciably affects the tower's structural design. Fail-safe insulators are commonly used in the primary guy system. If the porcelain in a fail-safe insulator assembly should fail, then the structural integrity will be maintained by the assembly's hardware. Insulators are rated in terms of their wet flashover voltages. As a safety factor, the operating voltage across an insulator should not be greater than one-half the wet flashover rating. Therefore, optimum choice of the number of insulators and their location occurs when each insulator (or string of several insulators) is operating at one-half of its wet flashover rating. Underinsulation will result in having to operate at reduced power during unfavorable weather to prevent arcs from developing across the insulators. In the past, this type of antenna may have been overinsulated since a good technique to calculate insulator voltages did not exist.

The voltage across an insulator can be determined from the potential on the wire sections on each side of the insulator or from the guy wire current and the insulator impedance. These insulators are primarily capacitive. Since this type of antenna is electrically small, a static analysis could be an accurate method to calculate the voltages on the guys. A quasistatic analysis of a scaled model placed in an electrolytic tank is an experimental method to determine the guy wire voltages [1]. This technique has been used in the past. For a time-varying analysis, method of moments programs such as MININEC and NEC can be used to calculate the current in the guys. The product of the current and the insulator impedance yields the voltage drop across an insulator.

This paper presents an attempt at using MININEC as a numerical approach to optimize insulator placement. A comparison is made between the results of three techniques: a static program, measurements made in an electrolytic tank, and MININEC. The general modeling problems

of each method are also discussed. For an example, a 365.8 m monopole with 12 top-loading radials and radiating 100 kW at 27 kHz is examined. The tower is modeled as a cylinder with a radius of 1.27 m. The radials have a radius of 1.43 cm. This antenna has three sets of primary guys at 91.4 m, 182.9 m, and 274.3 m with radii of 1.59 cm, 1.43 cm, and 1.75 cm respectively. The guys for the top radials have a radius of 1.27 cm. The fail-safe insulators being considered have a wet flashover rating at 60 Hz of 100 kV for a single insulator, 150 kV for a string of two, 185 kV for a string of three, and 285 kV for a string of four with a suitable grading ring.

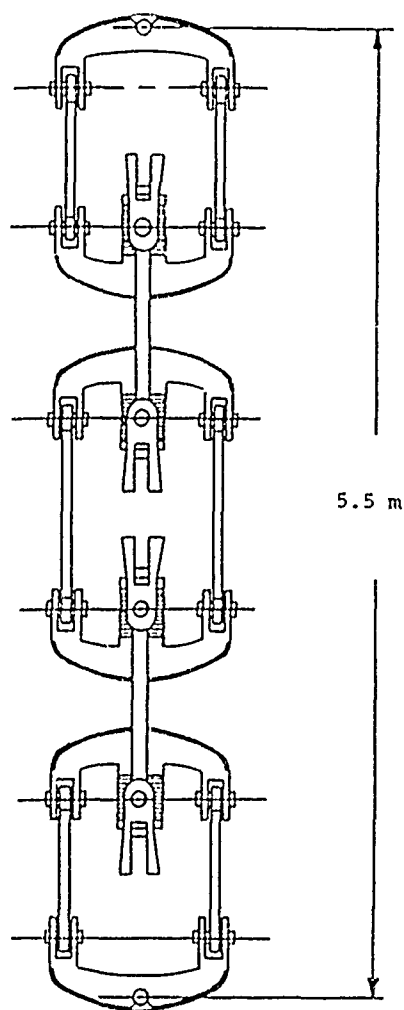


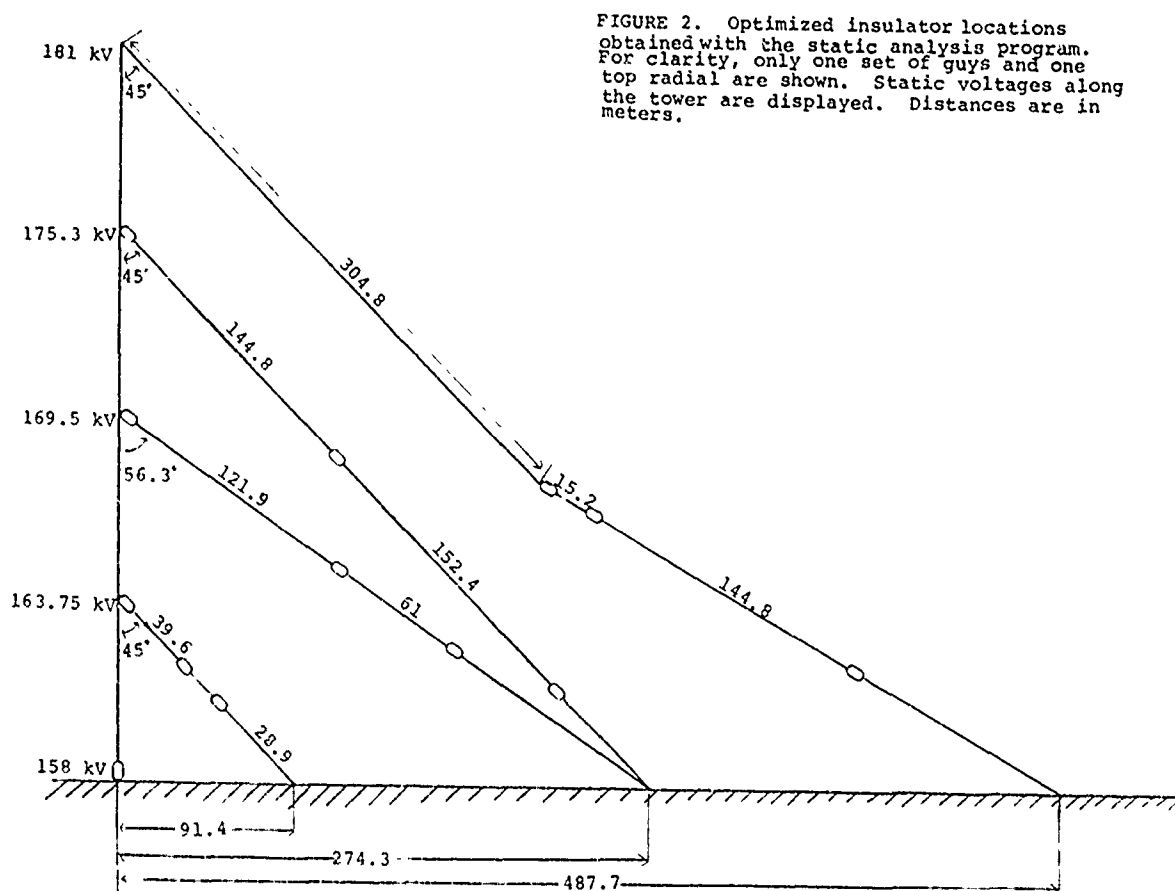
FIGURE 1. A string of four fail-safe insulators. (Lapp Insulator Catalog 590).

The estimated capacitance of one insulator is 25 pF. A sketch of a string of four insulators is displayed in Figure 1 to indicate the general structure of these insulators and the associated hardware.

ELECTROSTATIC ANALYSIS

A microcomputer program has been written to perform an electrostatic analysis of the antenna and one guy at a time. The insulators are modeled with spheres to yield approximately the same capacitance as the actual insulators. To minimize run times, the charge distribution on the antenna is solved for first. And then this information is used to solve for the charge distribution on the guy segments and the insulators, neglecting any affect the guy has on the antenna. Note that each guy section is an equipotential surface and that the last section is grounded. Also the sum of the insulator voltages must equal the tower voltage at the point where the guy attaches to the tower. The base voltage and the top hat voltage can be calculated from the antenna solution [2]. A straight-line approximation can be used to estimate the tower voltage at any height.

This technique has several problems. The program treats the support guys as being located directly beneath a top radial, when for this example they are offset by 15 degrees. Also, it is impractical to model the insulators rigorously. This problem is obvious from the sketch of a string of four insulators shown in Figure 1. Nevertheless, this program was used to try to optimize the insulator placement and to get some values for comparing the three techniques. Figure 2 shows this initial set of string locations, lengths of guy sections, and static tower voltages at the guy attachment levels. The number of insulators in each string and the calculated insulator voltages are displayed in Table I.



ELECTROLYTIC TANK MEASUREMENTS

A model with a scale factor of 1/850 has been constructed and placed in an electrolytic tank in order to measure the voltage on the guy sections. This experimental method uses small pieces of a dielectric (such as plastic beads) to model the insulators. With the model placed in a tank of ordinary tap water, the antenna was driven with a signal generator operating at a relatively low frequency (1 kHz). The measured voltage on each section of guy wire can be related to the full scale voltage by the voltage on the model tower and the static tower voltages. The model was designed using the dimensions shown in Figure 2.

The primary problem with this technique is that it is not efficient for design purposes since modification of the model is so time consuming. Also, some error may be introduced by modeling all of the insulator strings with the same sized pieces of dielectric. As with any experimental technique, it is subject to various measurement errors. The results of the model measurements are displayed in Table I.

MININEC

MININEC can be used to compute the current distribution along a guy wire and lumped loads can be placed at the insulator positions. The guy must connect to the tower's center at a junction

between two tower segments. Therefore, it is convenient to model the tower with two wires that join where the guy attaches to the tower. The desired lengths of guy wire sections can be specified by using a separate wire for each guy section. A current pulse will be placed at the junction of the wires [3]. If a lumped load equal to the reactance of the insulator is placed at that pulse, then the voltage across the insulator is the product of the reactance and the value of the current pulse given by MININEC.

The primary difficulty with this method is determining the proper impedance value to use for the insulator and where to place the load. The insulator manufacturer can usually provide the approximate capacitance of a single insulator assembly and sometimes the capacitance of a string of insulators. Any error in the accuracy of the capacitance value would of course cause error in the MININEC results. Also, a lumped load does not consider the length of the insulator or the field due to the insulator assembly which could be significant. Another source of error is that the guy wire must attach to the tower's center instead of its surface.

A modified version of MININEC(2) was used to improve the treatment of the very thin wires [4]. Since MININEC does not take advantage of any symmetry a large number of segments must be used. But even though the code was compiled, the minimum possible number of segments must still be used in order to keep run times reasonable. Only one guy was considered at a time to help keep the number of segments low (≈ 50). The following segmentation values were chosen: six segments on the tower, two segments on each radial, and three segments on each guy section. The dimensions in Figure 2 were used with the exception that the insulator lengths were shifted to the lowest guy link. The capacitances of the multiple insulator strings were estimated from the charge distributions given by the static program. The use of several more segments on the guy sections and the five closest radials did not significantly change the results that are presented in Table I.

CONCLUSIONS

The values in Table I indicate that MININEC is not a simple solution to the insulator placement problem. The results of the static program and the

TABLE I
RESULTS OF THREE DIFFERENT METHODS OF DETERMINING INSULATOR VOLTAGES

Each case used approximately the same guy section lengths shown in Figure 2.

Level (m)	Insulators per String	Static Program	String Voltages (kV)	
			Tank Measurements	MININEC
91.4	3	82.7	85.1	68.6
	1	40.8	37.1	46.5
	1	40.2	41.6	47
182.9	3	82.8	84.8	79
	1	42.1	41.7	29.1
	1	44.6	43	42.4
274.3	2	63.2	67.1	59.4
	2	64.9	59.6	64.6
	1	47	48.6	48.6
365.8	4	133	127.3	---
	1	26.1	22.6	---
	1	21.9	32.5	---

electrolytic tank measurements agree reasonably well when the differences between the two methods are taken into consideration. The MININEC results are not in close agreement with the other techniques except for the voltages on the lowest guy section on the 182.9 m and 274.3 m level guys. However, the MININEC results are encouraging enough to continue investigating this application. Possibly the use of more segments, more attention paid to adjusting the guy section lengths to compensate for neglecting the insulator lengths, and more accurate values of the insulator capacitances would yield better results. MININEC(3) which is to be released soon may have some features that would be helpful for this application. In addition, NEC could be used in a similar fashion. It would enable the use of more segments and possibly allow more detailed modeling of the tower and the insulator assemblies.

REFERENCES

1. R.C. Johnson and H. Jasik Antenna Engineering Handbook, 2nd Edition, New York: McGraw-Hill, Chapter 24, 1984.
2. A.D. Watt, VLF Radio Engineering, Oxford: Pergamon Press, 1967.
3. S. T. Li, J. W. Rockway, J. C. Logan, and D. W. S. Tam, Microcomputer Tools for Communications Engineering, Dedham, Mass.: Artech House, Chapter 4, 1983.
4. T. D. Poston and S. W. Kershner, "Modification to MININEC for the Analysis of Wire Antennas With Small Radius to Wavelength Ratios", 2nd Annual Review of Progress in Applied Computational Electromagnetics, Monterey, CA, 1986.

"A COMPARISON OF THIN-WIRE EM MODELING CODES FOR THE CASE OF SCATTERING FROM A CROSS"

Richard W. Adler
Naval Postgraduate School
Code 62AB
Monterey, CA 93943

This paper looks at the performance of six thin-wire theory antenna codes in representing the current distribution on a crossed-dipole scatterer. Measurements by Burton are used as a reference. The structure is a $3/4$ wave high vertical cylinder with a half wave horizontal cross-arm located at the half wave high point. Illumination is via a vertically polarized plane wave.

The results raise questions concerning the application of continuity of current at the junction region by the antenna codes. The thin-wire azimuthally uniform current assumption may also be responsible for some of the differences observed.

INTRODUCTION

One method of validation of thin-wire antenna codes is comparison of calculations to measurements of surface currents on a thin cylindrical structure. Most numerical modelers use one thin-wire code exclusively - the one they have invested the most time in and have the greatest experience with. Some engineers have developed their own codes and these are considered proprietary and therefore not available to the general public. This paper compares current amplitude and relative phase for a crossed dipole scatterer, as obtained from measurement and from calculation via six different thin-wire codes, two of which are not in the public domain.

Figure 1 shows a thin-wire crossed dipole scatterer with a three-quarter wavelength vertical shaft and a half wavelength horizontal arm, located one-half wavelength up from the infinite, perfect ground plane. The radius of all elements is 0.185185 wavelengths. The measurements were provided by R.W. Burton and appear in Reference 1. The measured and calculated current amplitudes were presented for this investigation as relative dB. values and the phase as relative values also. Calculated values were plotted and adjusted vertically on each graph to obtain the most favorable match to the measured values.

The crossed-dipole structure provides a tough test of the thin-wire codes. The junction, which requires continuity of current and equal charge per unit length on the connecting arms, is treated in several different manners by the codes. The usual thin-wire approximations adhered to by antenna codes are:

1. The currents on cylindrical surfaces can be assumed to flow on the surface of the perfect conductor and only in the axial direction and to be constant circumferentially at a given cross-section.
2. The current and charge densities can be approximated by filaments at the geometrical center of the wire.
3. The boundary conditions on tangential electric field intensity require zero value on the wire surface and can be applied to just the axial component.
4. The current at the ends of the cylindrical surfaces is approximately zero.
5. The distance from the observation point to the source point for field calculations must always be greater than or equal to the radius of the cylinder.
6. The summation of all the currents at a junction must equal zero.

The equation of continuity for a surface equates the divergence of surface current density at a point to the time rate of reduction of surface charge density. If a large scale equivalent of the equation of continuity is applied to a spherical volume surrounding the crossed dipole junction, the result is equating the algebraic sum of the currents flowing out in the cylindrical wires to the negative time rate of change of charge, if any, accumulating at the junction. Kirchoff's first law, as used in classical circuit theory, equates the current sum to zero, a static condition. For a sufficiently large volume, this seems valid, but if the radius of the sphere approaches the diameter of the cylinder surface, charge must be permitted at the junction.

The thin-wire approximation states negligible circumferential currents and circumferential invariance of axial current density. Near the junction of two or more wires, no matter how thin, there will not be rotational symmetry around each wire. These considerations give rise to questions of reliability of currents and fields near junctions obtained with thin wire programs.

THIN-WIRE PROGRAMS USED

Each of the six thin-wire codes exercised for the crossed-dipole scatterer are Method of Moments applications of a thin-wire integral equation. K.K. Mei and J.H. Richmond, in 1965, suggested methods of thin-wire solutions, as did R.F. Harrington in 1967. In applying the Moment Method, some code developers have used a Galerkin procedure and some the method of colocation. For the six codes used in this study, the basis functions and testing method are listed in Table 1.

<u>CODE NAME/AUTHORS</u>	<u>BASIS FUNCTION</u>	<u>TESTING METHOD</u>
OSU/Richmond	Piecewise Sine	Galerkin
Syracuse/Chao & Strait	Piecewise Linear	Galerkin
"MININEC3"/Logan, et al	Piecewise Constant	Galerkin
TCI/Tanner & Andreason	Three Term	Colocation
"BIGANT"/Arens	Three Term	Colocation
"NEC3"/Burke, et al	Three Term	Colocation

TABLE 1. CODES USED IN THIS STUDY

The TCI and BIGANT codes are proprietary and were run by their owners. The remaining programs are in various stages of public domain and are discussed in Reference 2. Figures 2 through 25 show the measures relative current amplitude in dB. and relative phase for the horizontal and vertical portions of the cross. Code results were adjusted vertically for best visual match. The bottom, junction, top and end are labeled B,J,T, and E respectively.

OBSERVATIONS

1. The measured horizontal arm current magnitude was most closely matched by BIGANT. The other codes did not predict the shape of the current distribution as well as BIGANT with typical differences 3 to 5 dB.

2. The horizontal arm current phase correlation was quite good, with BIGANT showing the poorest prediction, but still within 20 degrees of the measurement.

3. For the vertical current amplitude, measurements show a drop of approximately 1 1/2 dB. as the observation point passes upward through the junction. All codes missed the junction value by 2-5 dB. None predicted the drop at the junction and the Syracuse code actually predicted a rise of 8 dB. at the junction. It also missed the ground plane current by 12 dB.

4. Vertical current phase shows a sharp rise for the measured values at the quarter-wave high point with another small rise through the junction. All codes predict a phase jump near the quarter-wave point, but only the Ohio State code and NEC3 approximate the junction phase changes. The TCI phase change is in the wrong direction and the BIGANT phase prediction is the widest ranging and shows the greatest difference from measured. The Syracuse code phase change at the junction is in the correct direction but overshoots. BIGANT and MININEC3 have no junction phase ramps.

CONCLUSION

The estimated current distributions in a crossed-dipole scatterer are shown in Figure 26 and are verified by the measured currents of Burton. The choice of arm lengths and location of the junction force a condition of maximum current (minimum charge) at the ground plane and at the junction. Kirchoff's current law applies for this case and as such it should favor thin-wire antenna codes. Six popular codes' calculations of complex current distribution on the cross reveal that junction behavior of current magnitude is rather poorly predicted and only two codes were reasonably close on phase distribution.

If the geometry were changed to the case of a vertical 3/4 wave from the ground plane to the junction with a 1/2 wave top and 1/2 wave horizontal arms, maximum charge will exist at the junction with a much more uniform junction current distribution. Finally, the case of current discontinuities in both the vertical and horizontal arms, 1/2 wave long top section, 1/4 and 1/2 wave horizontal arms, and 3/8 wave bottom vertical section should cover the range of junction currents and charges of interest. Code developers wishing to improve junction performance could use these cases as benchmarks to test their code's accuracy.

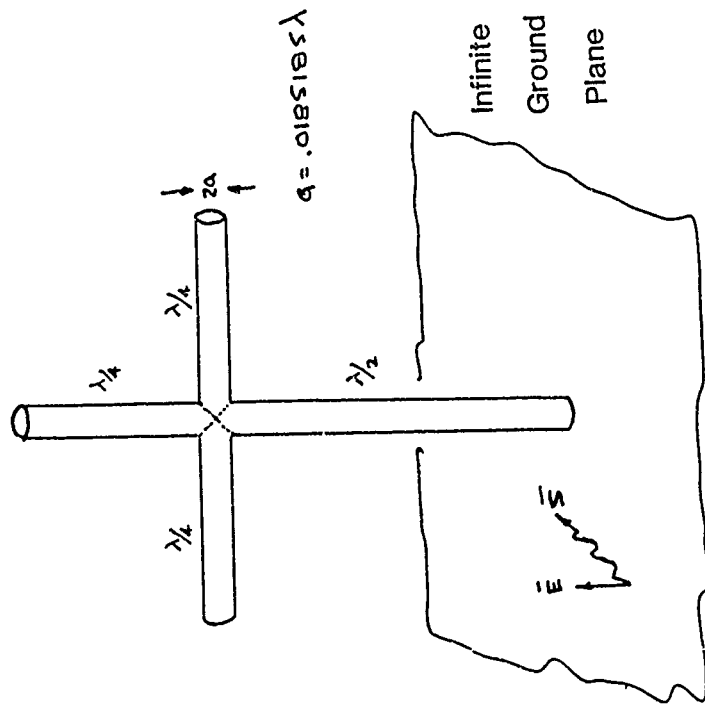
The application of Kirchoff's Law and charge conditions and the lack of rotational symmetry at junctions are apparently important factors in the crossed-dipole performance by thin-wire antenna codes.

ACKNOWLEDGEMENTS

James Logan provided the Syracuse code results, Virgil Arens the BIGANT calculations, and R.L. Tanner the predictions by the TCI code. The MININEC3 calculations were from a developmental version of February 1986.

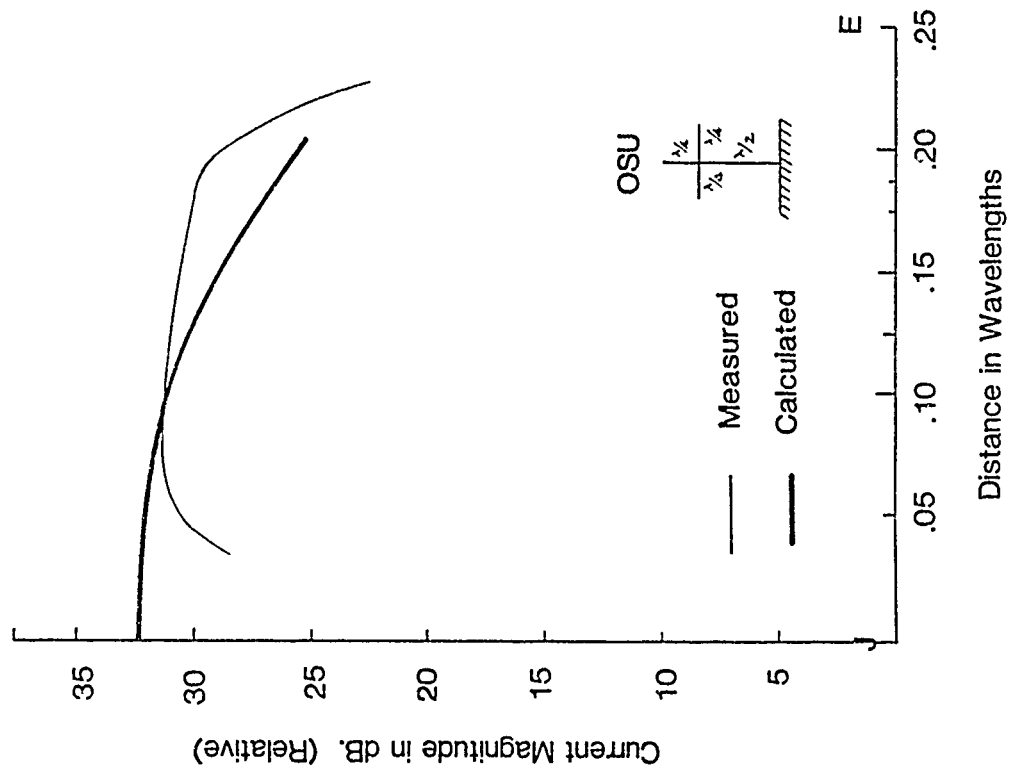
REFERENCES

1. R.W. Burton and R.W.P. King, "Measured Current and Charges on Thin Crossed Antennas in a Plane Wave Field," IEEE Trans., AP-23, No. 5, Sept. 1975, pp. 657-664.
2. E.K. Miller and others, An Evaluation of Computer Programs Using Integral Equations for the Electromagnetic Analysis of Thin Wire Structures, UC Lawrence Livermore Laboratory, March 1974.



CROSSED DIPOLE SCATTERER

Figure 1



Horizontal Element

Figure 2

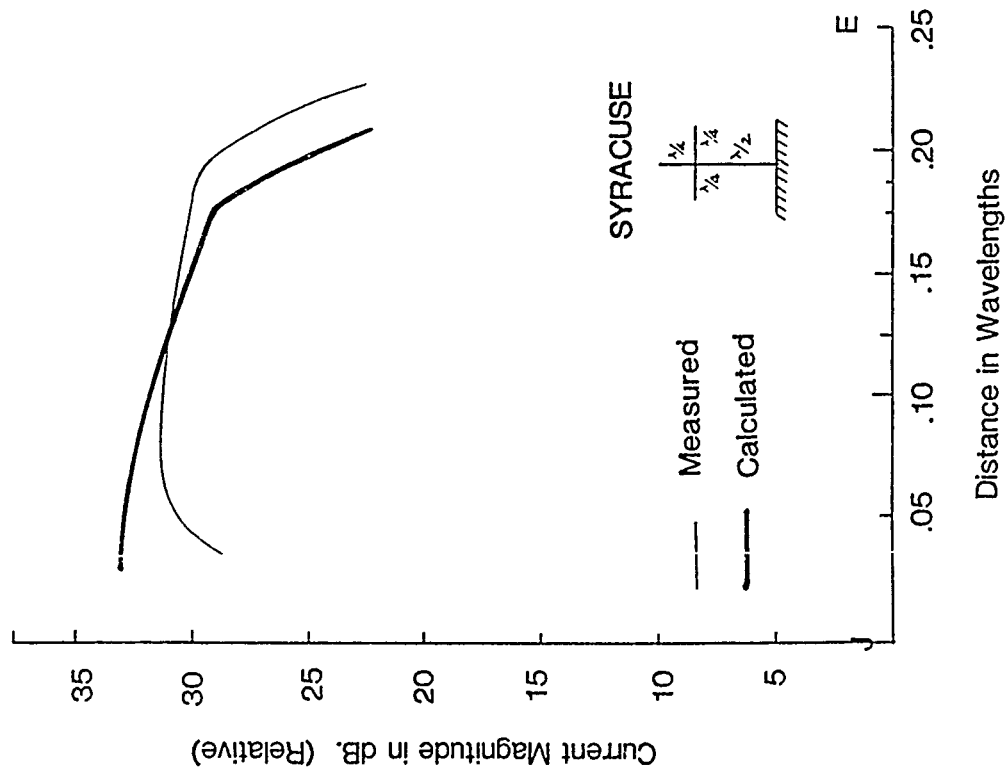


Figure 3

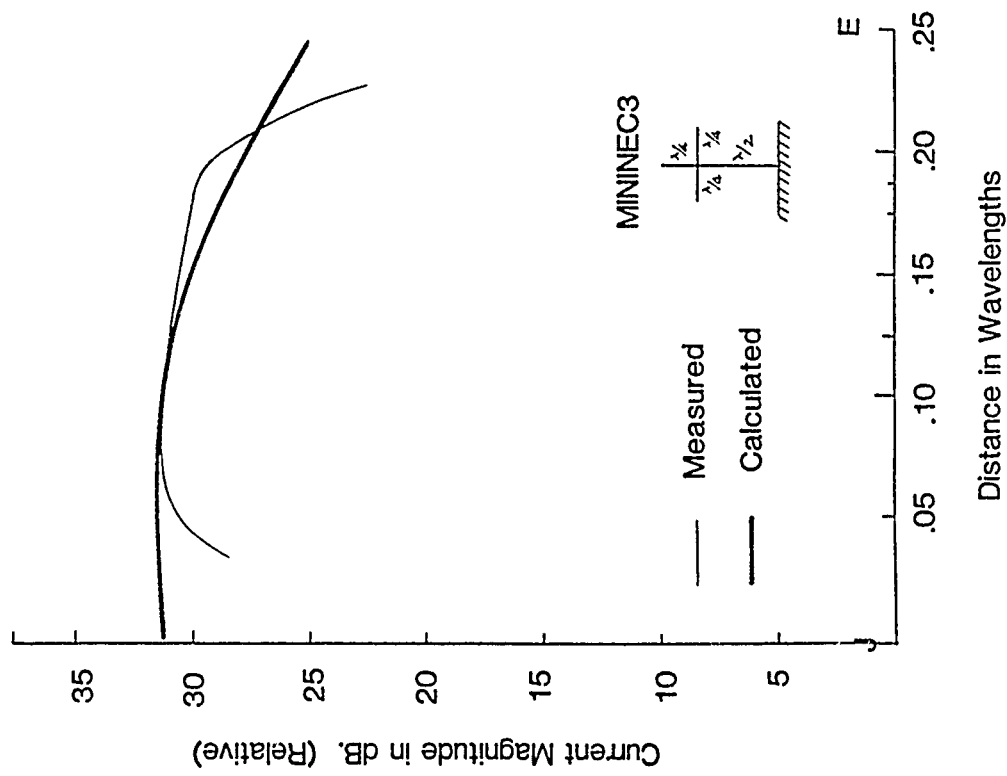
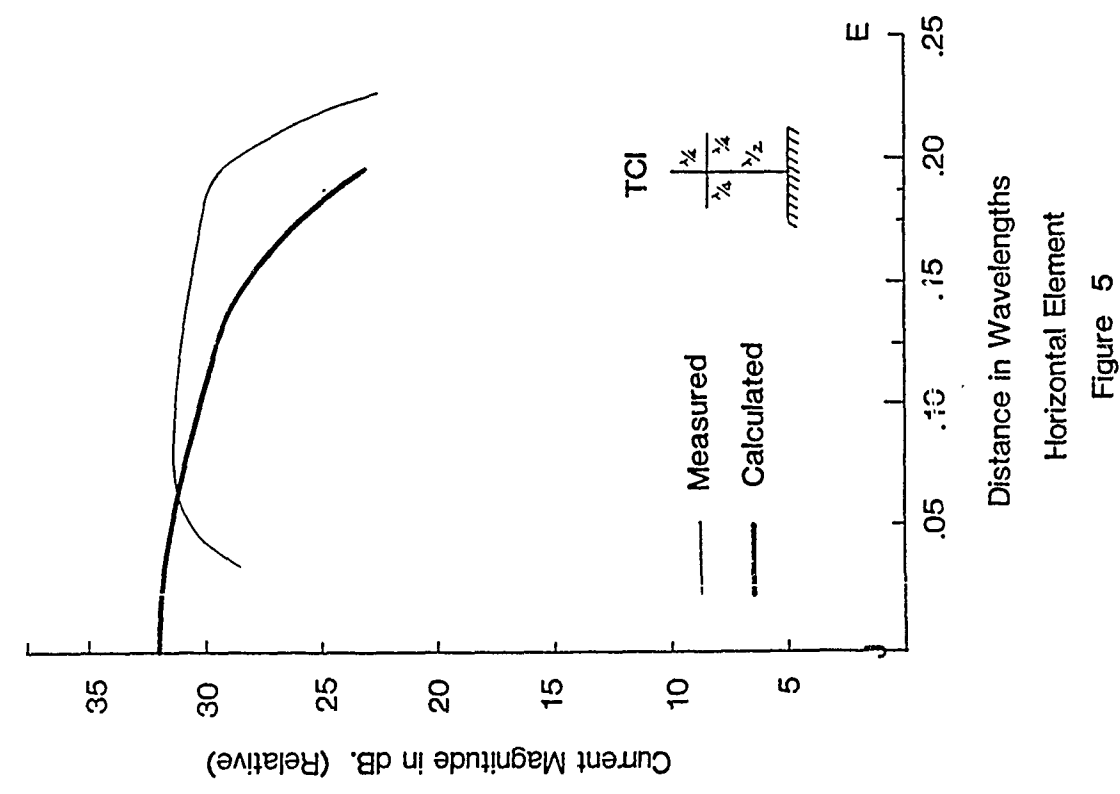
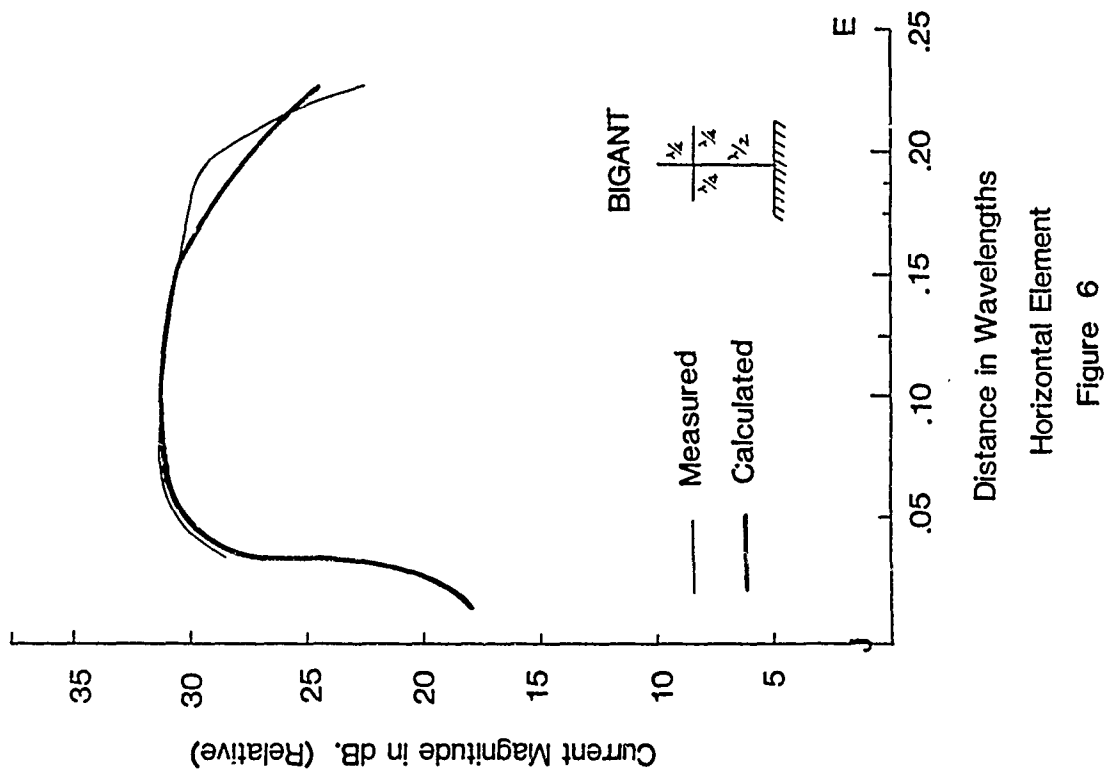


Figure 4



Horizontal Element
Figure 5



Horizontal Element
Figure 6

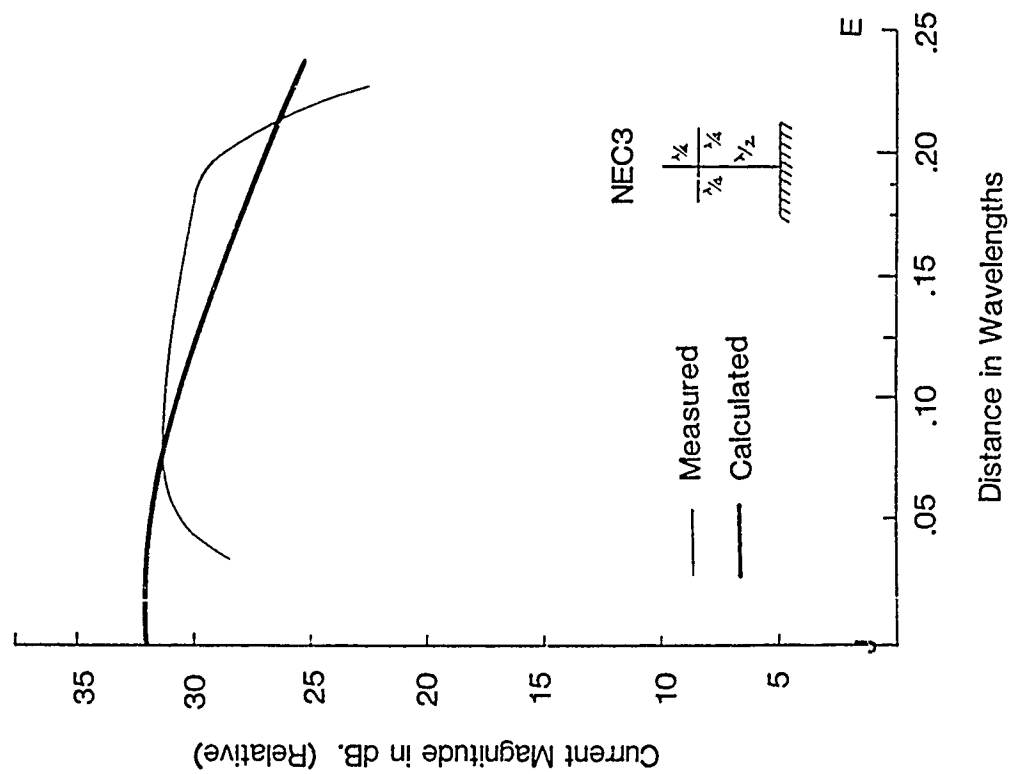


Figure 7

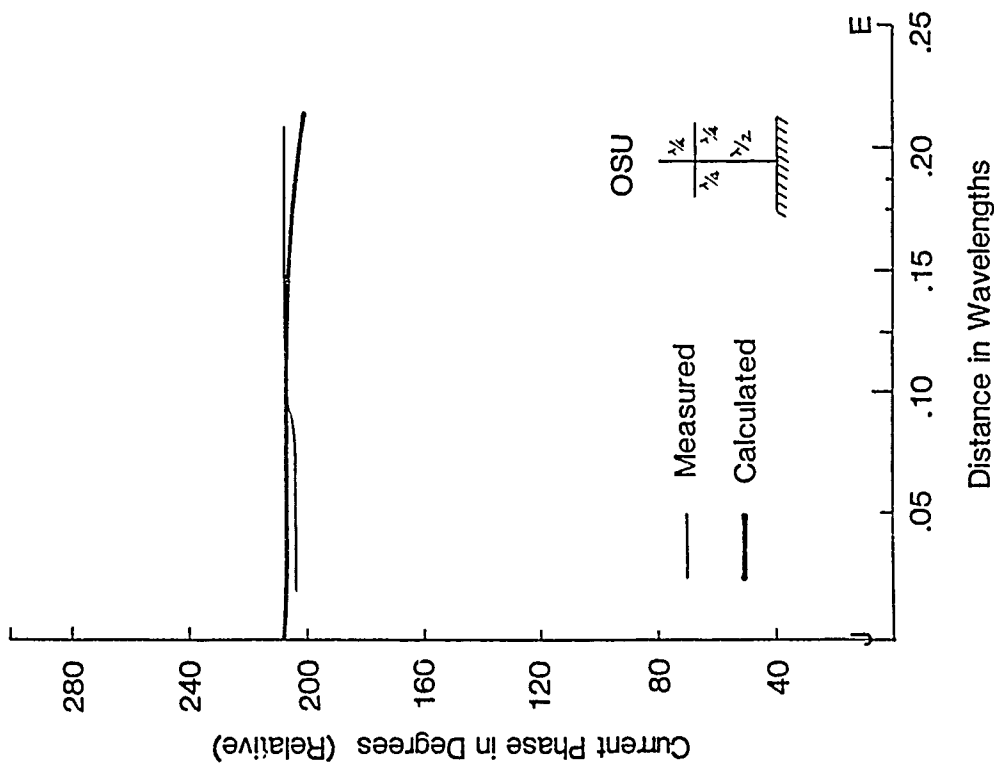


Figure 8

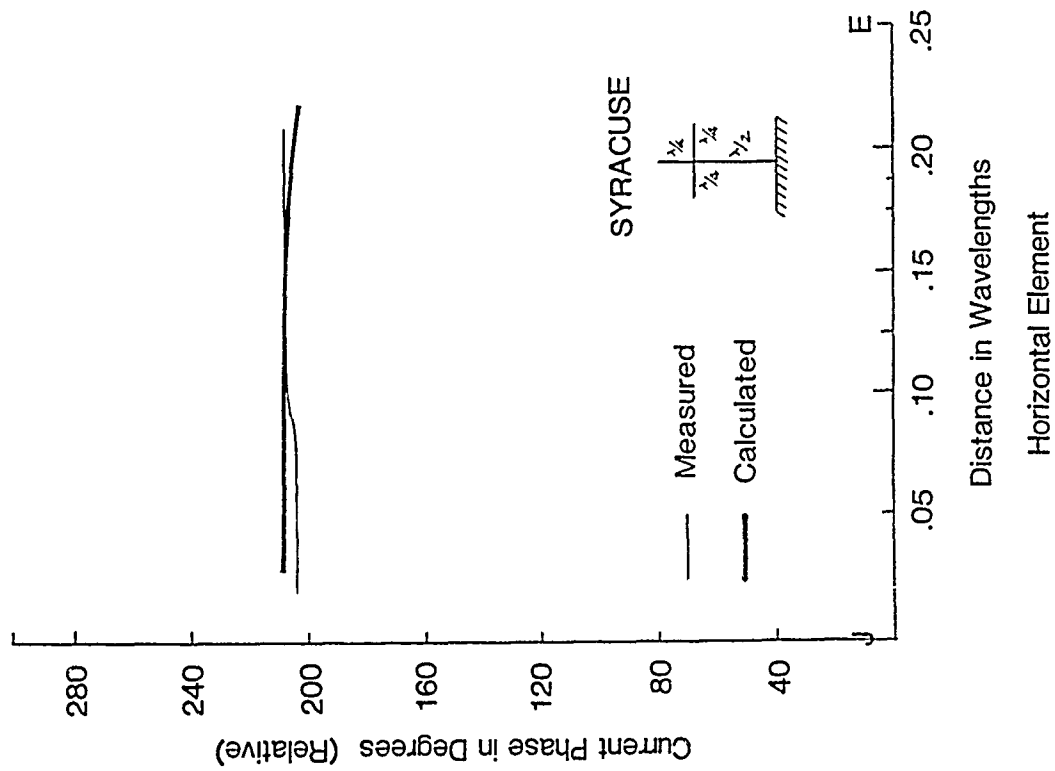


Figure 9

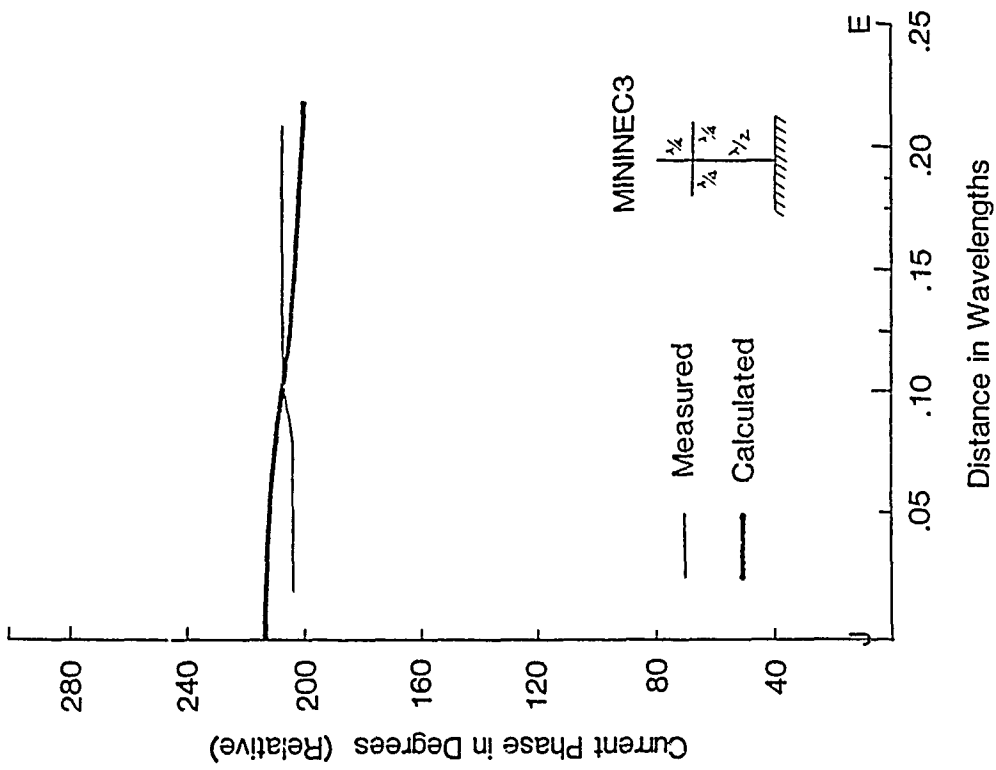
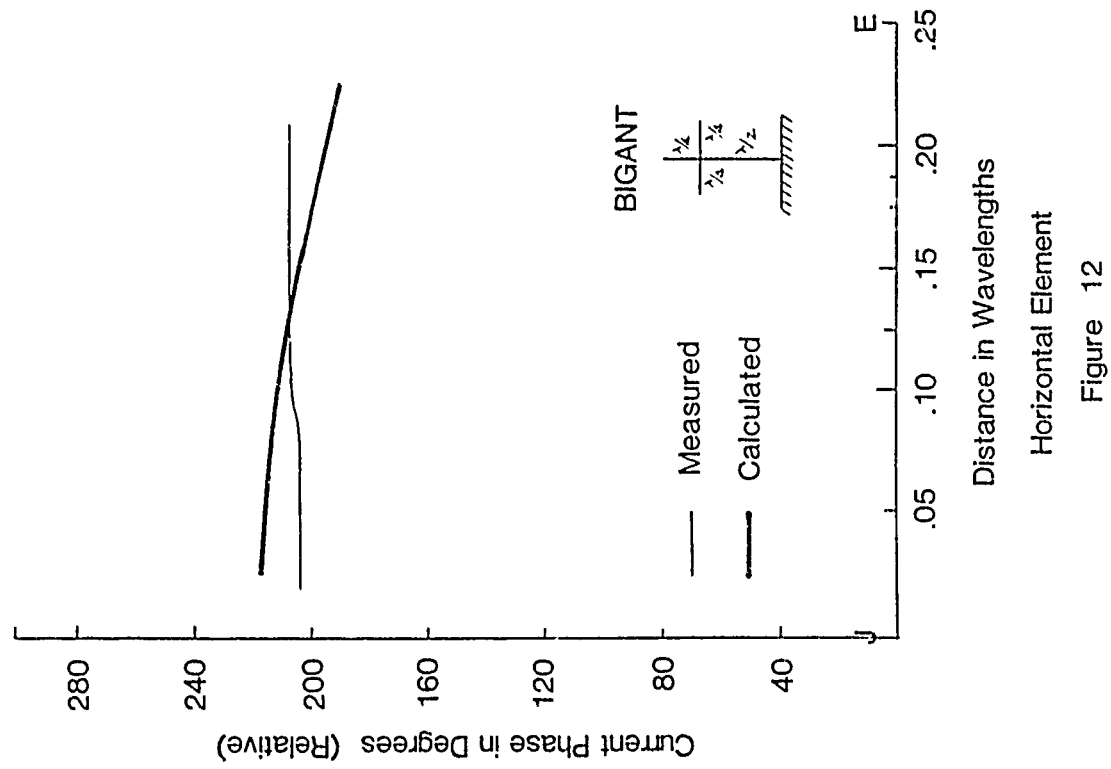
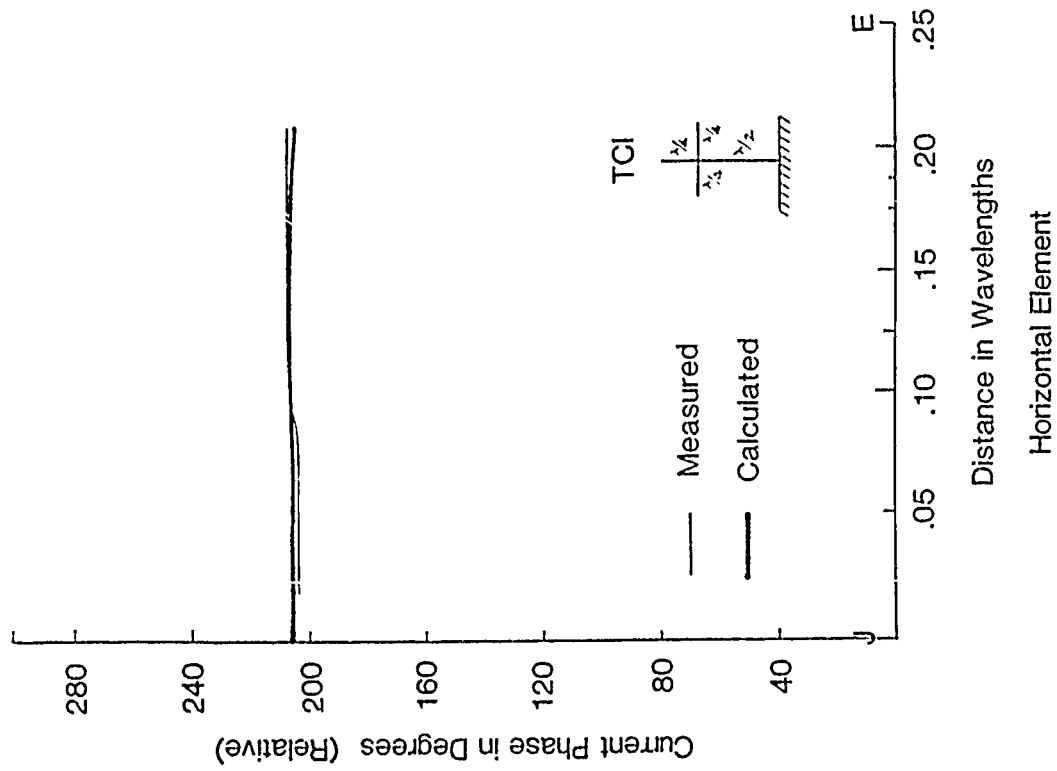
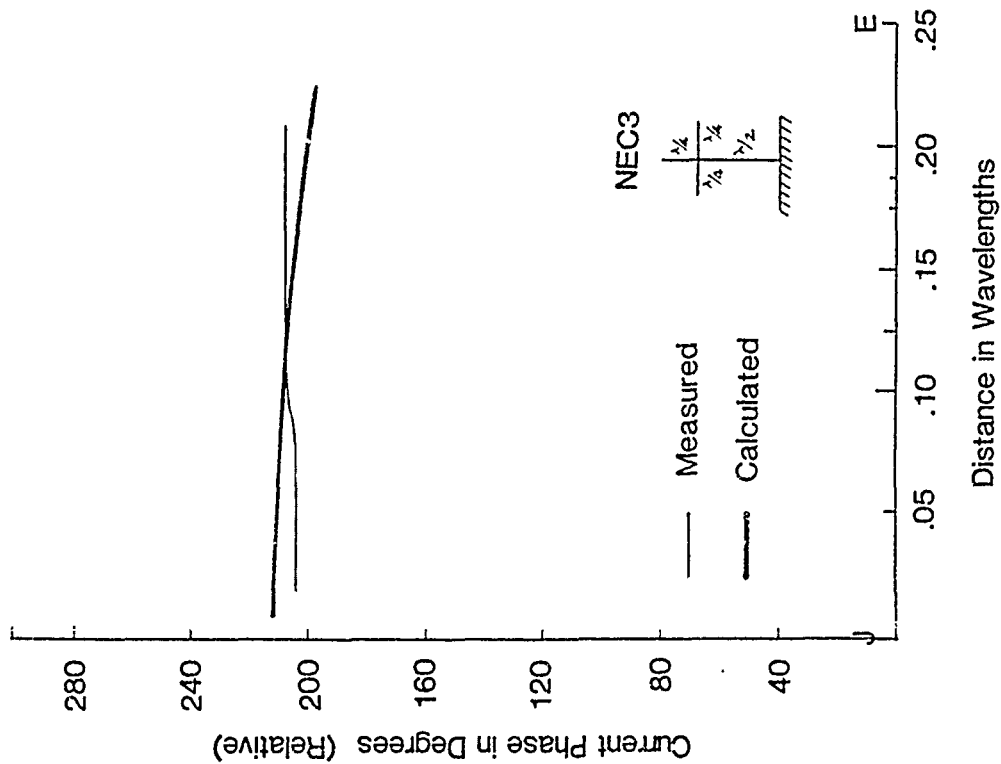


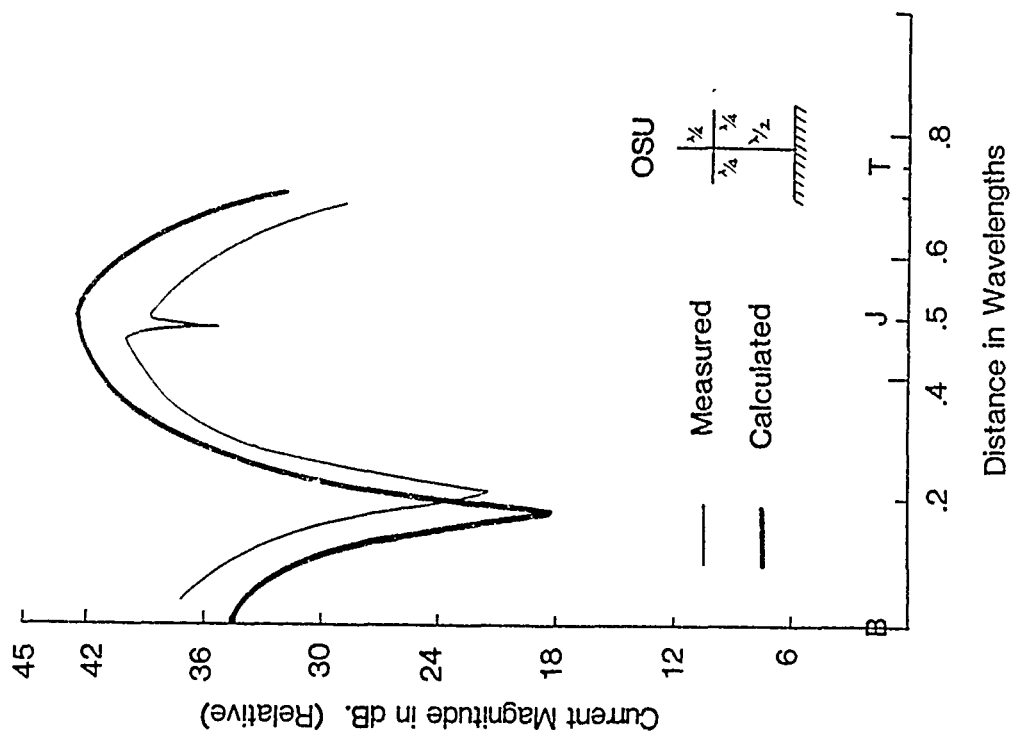
Figure 10





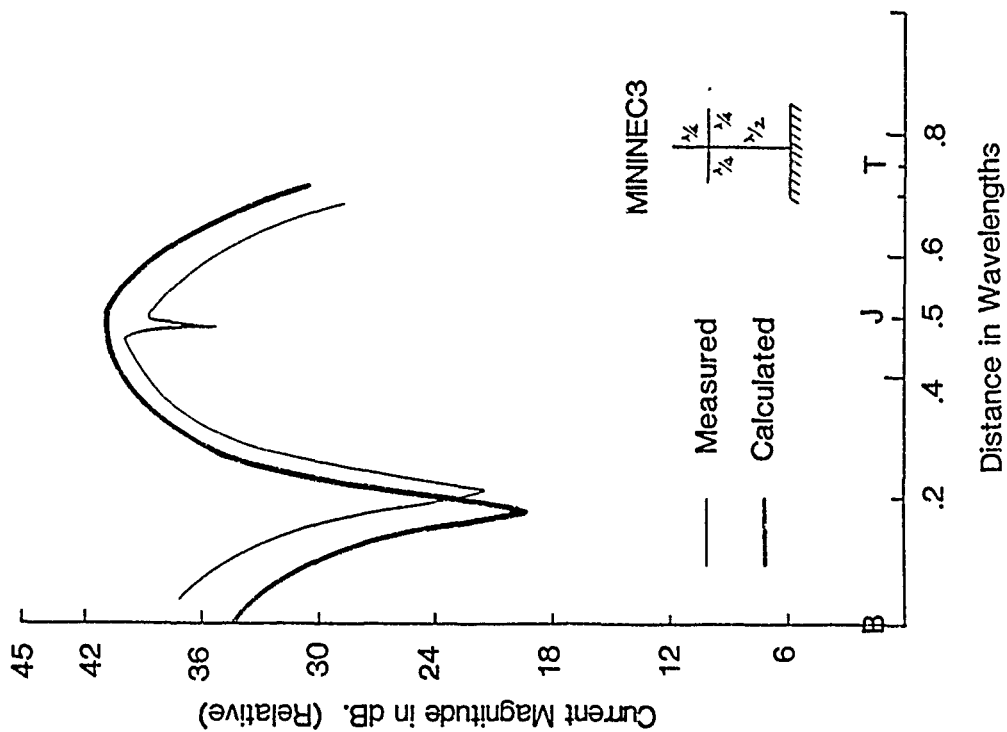
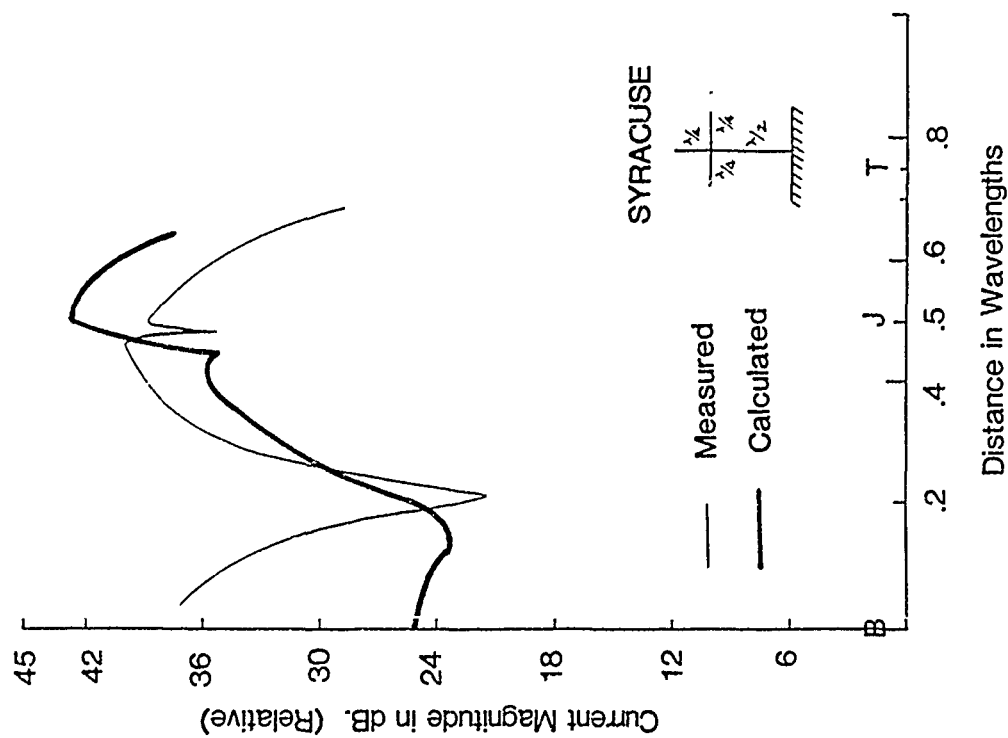
Horizontal Element

Figure 13



Vertical Element

Figure 14



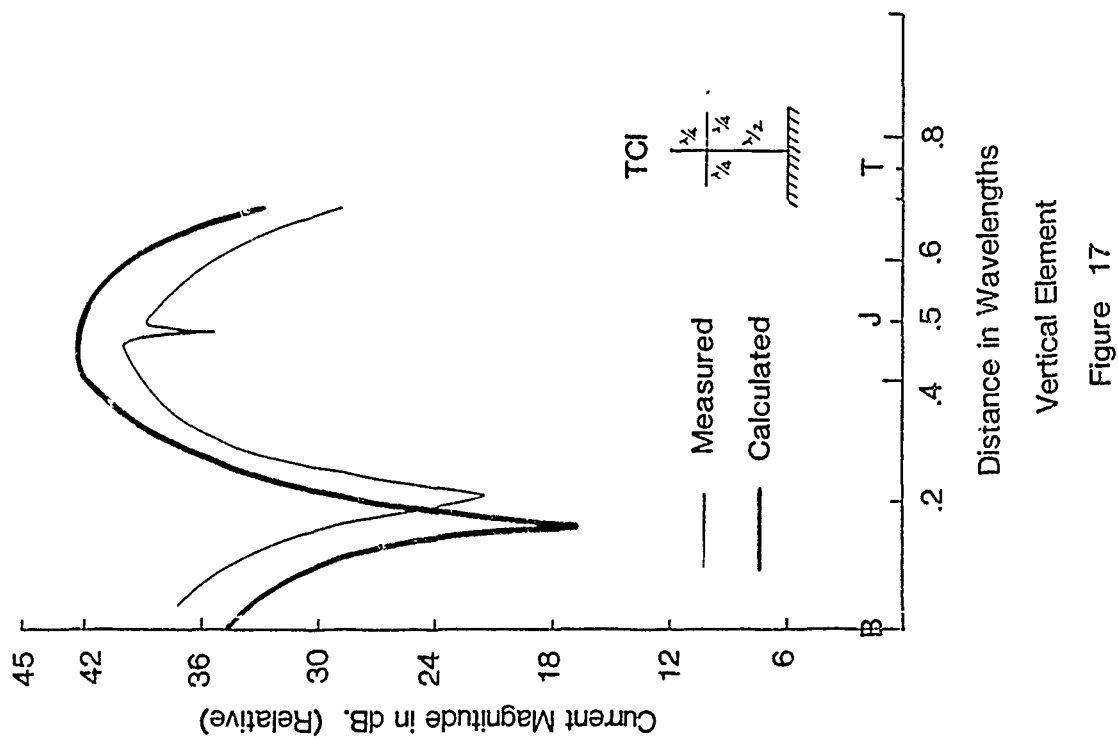


Figure 17

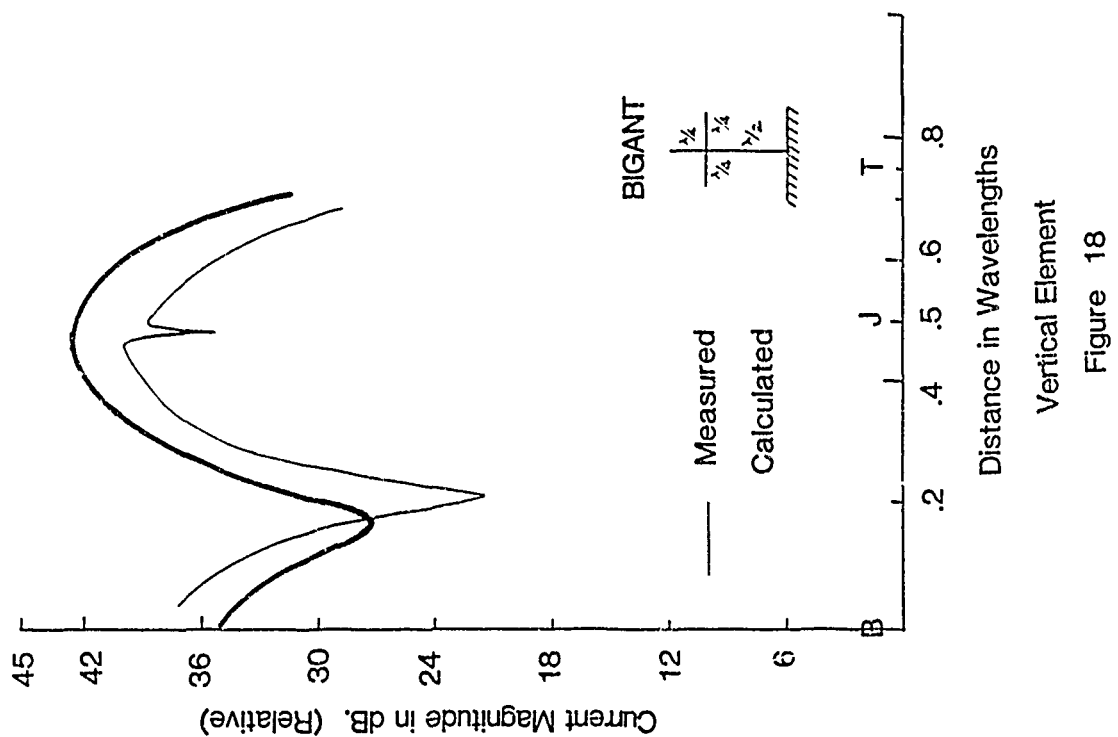
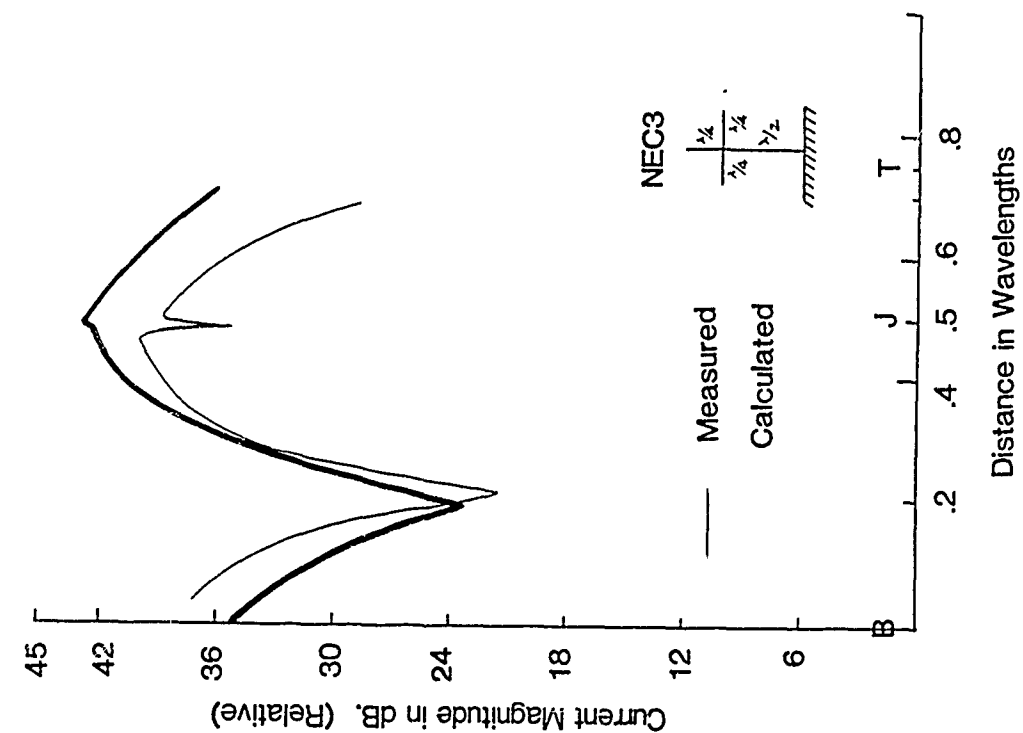
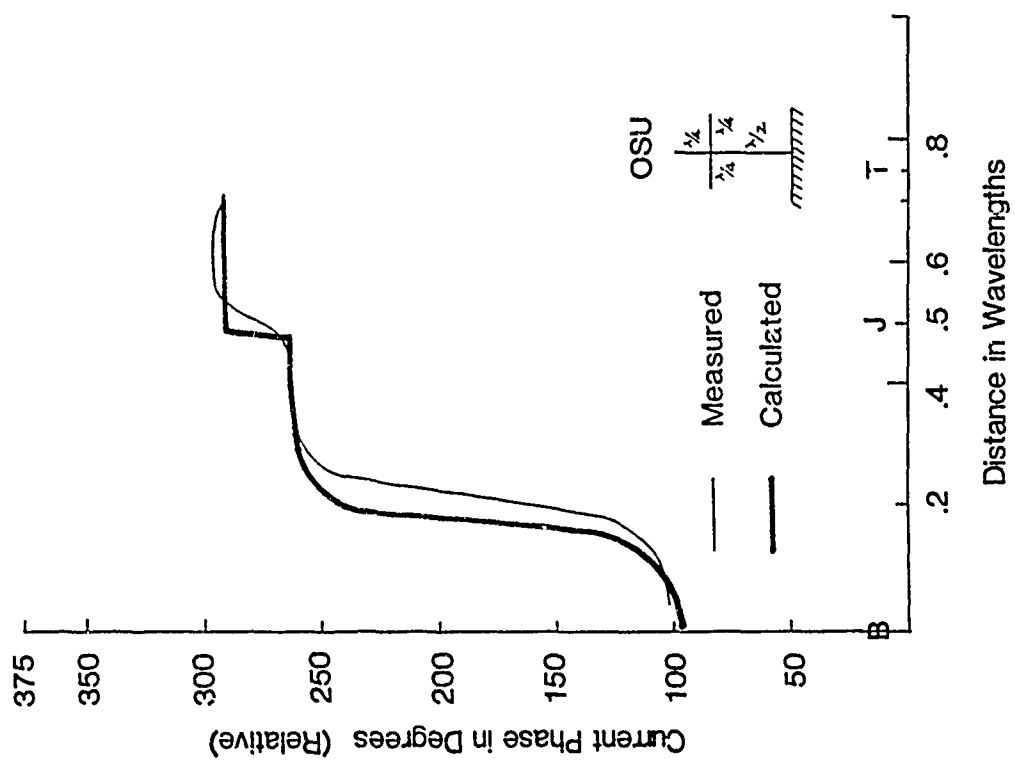


Figure 18



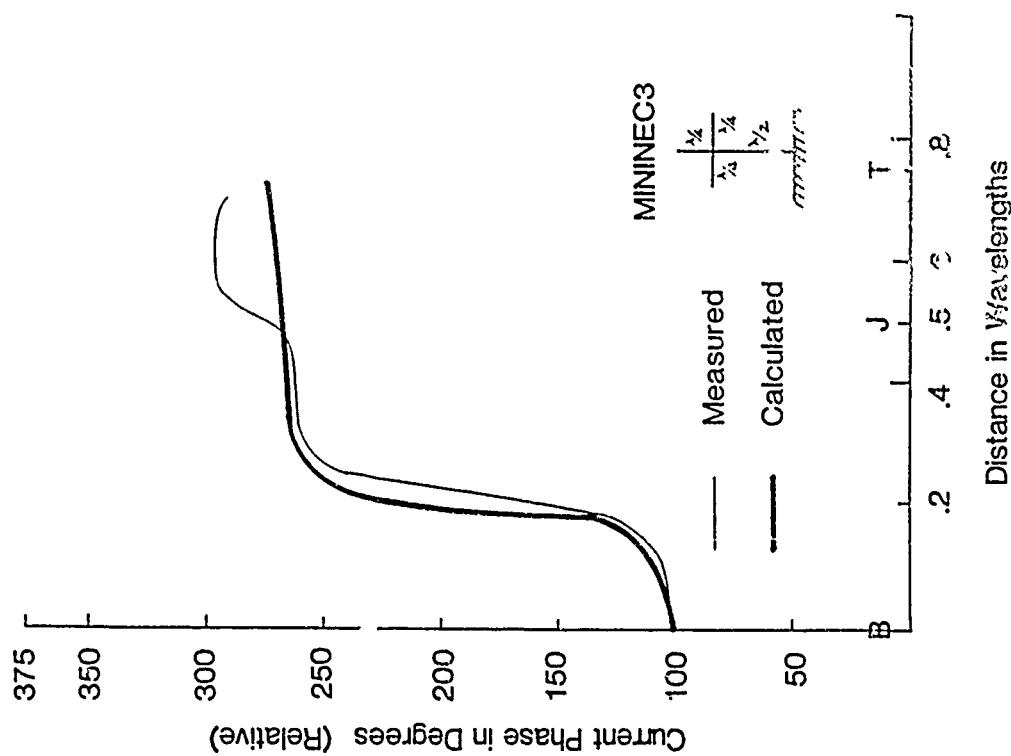
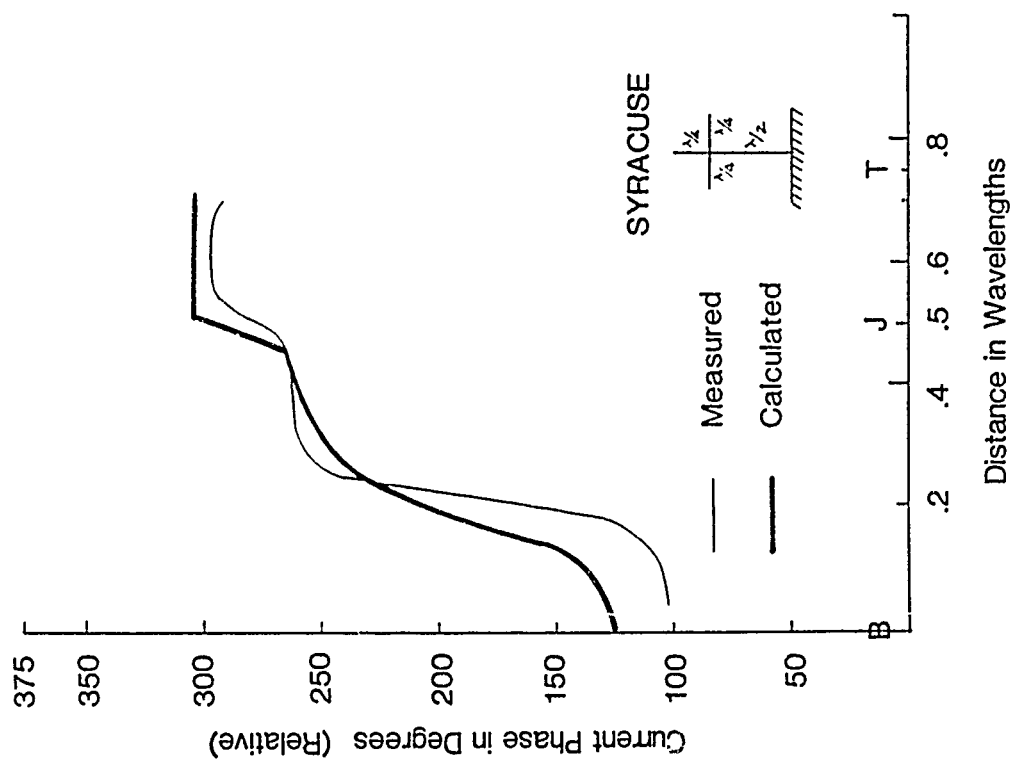
Vertical Element

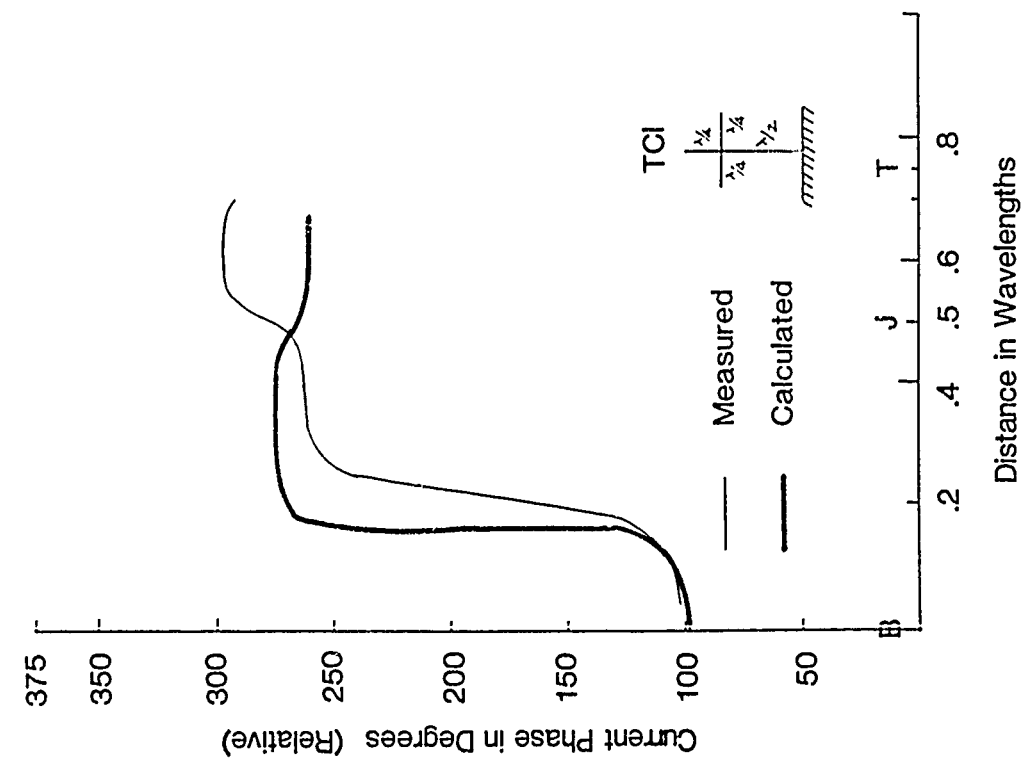
Figure 19



Vertical Element

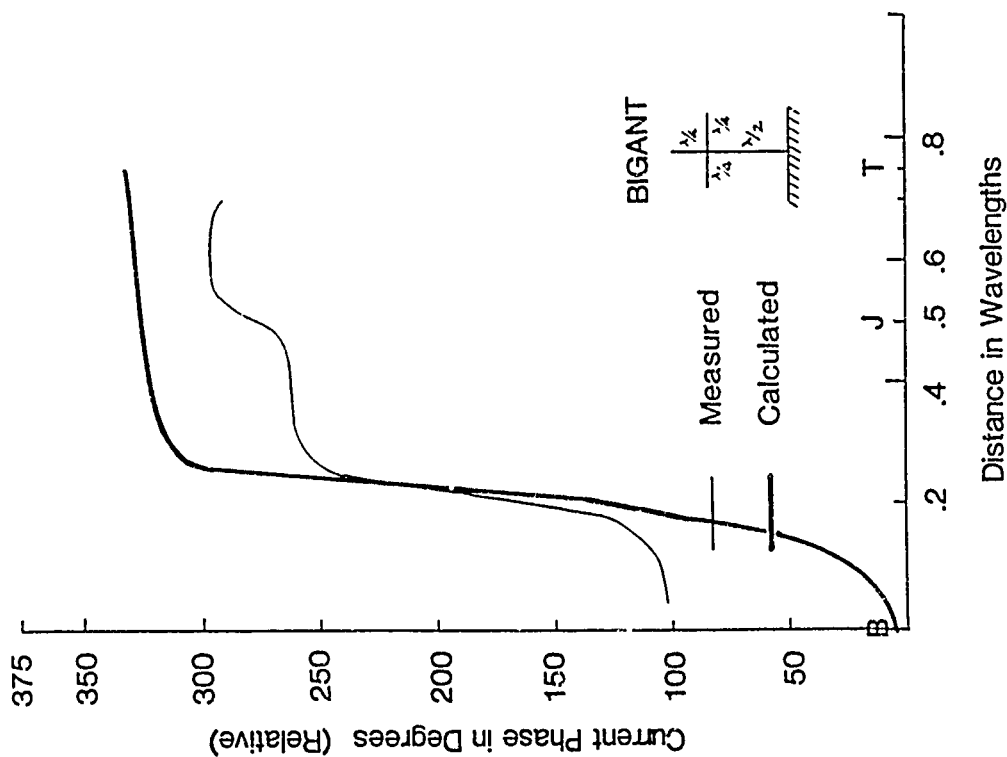
Figure 20





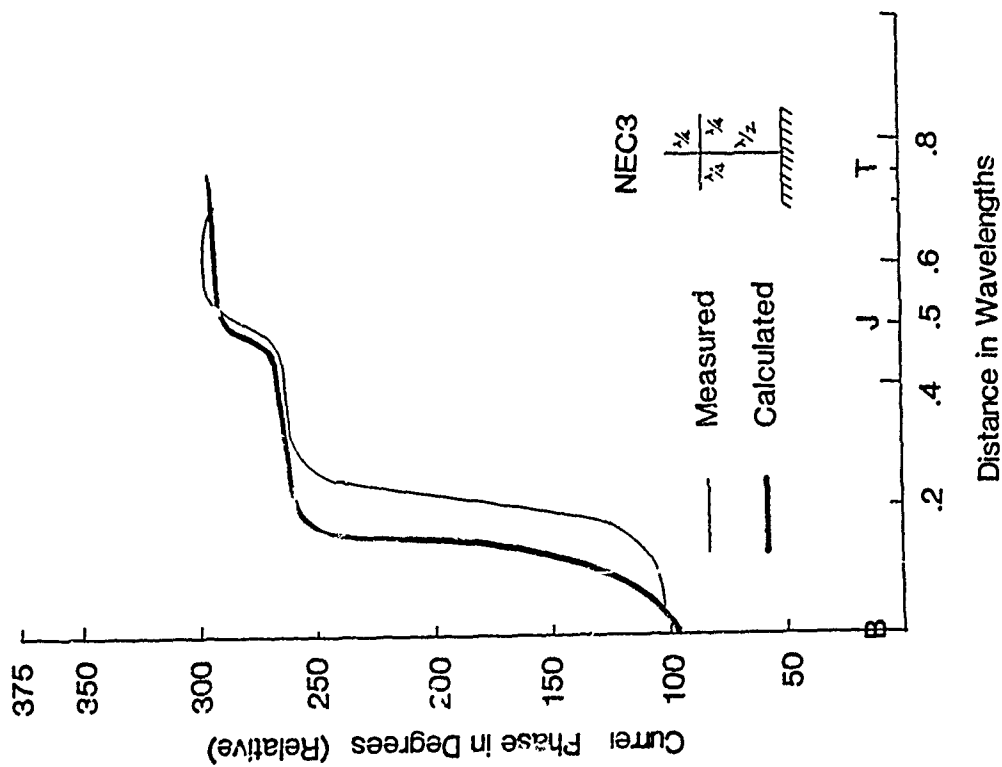
Vertical Element

Figure 23

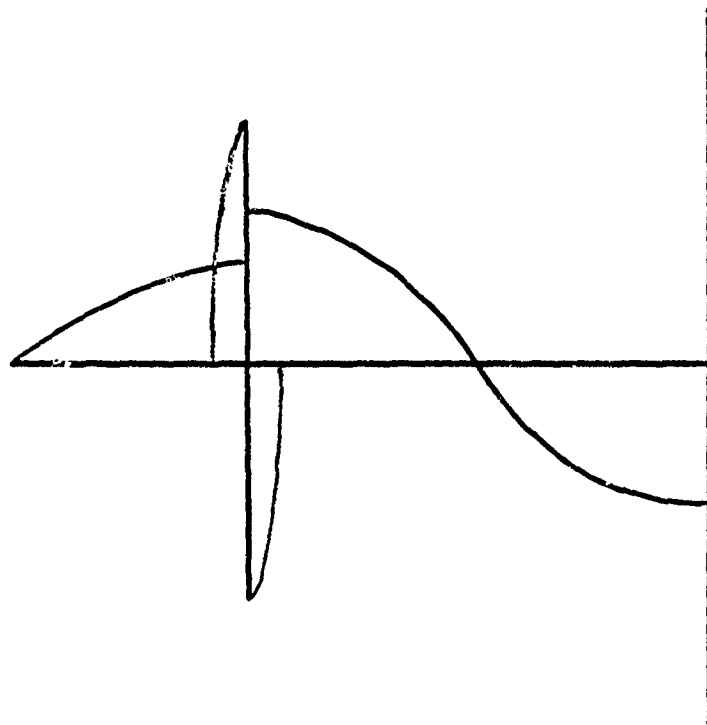


Vertical Element

Figure 24



Vertical Element
Figure 25



CROSSED DIPOLE ARM CURRENTS

Figure 26

EFFICIENT COMPUTATION OF THE FAR FIELD OF OFFSET
REFLECTOR ANTENNAS WITH OFFSET FEEDS

Larry Q. Bowers John Hoover
P. O. Box 179 MS-8080
Martin Marietta Denver Aerospace
Denver, CO. 80201

I. INTRODUCTION

An efficient method of computing the far field of offset reflector antennas with offset feeds has been developed and implemented on a VAX 11/780 and an IBM-PC. The method relies upon the use of Geometrical Optics to evaluate the vector field in the aperture of the reflector on a grid of equally spaced points. For a specific feed, reflector, and aperture geometry, the reflected field is determined at successive grid points in the aperture. The associated reflection point is located numerically using an efficient algorithm which effectively minimizes the distance function between the feed point and the aperture point via the reflector surface. Typically, convergence is reached after 1 to 3 iterations so that most of the computer time is spent evaluating the reflected field as opposed to searching for reflection points.

Once the aperture fields have been computed, two-dimensional discrete Fourier Transform techniques are used to rapidly compute the far field radiation patterns and contours for both the co- and cross-polarized components. Modified algorithms have also been developed to compute single plane cuts of on- and off-principle plane far fields directly from the aperture field data. A modified form of the Cooley-Tukey FFT algorithm allows densely spaced far field data computation over a specified angular range, making no unnecessary intermediate calculations.

The techniques and algorithms described above will be discussed in detail and results presented. Comparison with measurements made in the MMMA Planar Near Field Facility will also be discussed. Computer run time benchmarks will be presented for comparison with other analysis methods, and future improvements to the existing software will be summarized.

II. EVALUATION OF THE APERTURE FIELD

Figure 1 illustrates the specification of the general offset paraboloidal reflector antenna geometry. Although the aperture need not be circular, this assumption is made for simplicity. In this way, the reflector is fully characterized by the focal length and the two angles ϕ , and ϕ_0 shown in Figure 1. The reflector profile can then be expressed as:

$$\rho = \frac{f}{\cos^2(\psi/2)}$$

where ψ is the angle between the axis of rotation and a line connecting the focus and a point on the reflector, f is the focal length, and

$$\begin{aligned}\psi_1 &\leq \psi \leq \psi_2 \\ \psi_1 &= \phi_0 - \phi/2 \\ \psi_2 &= \phi_0 + \phi/2\end{aligned}$$

The aperture plane is positioned perpendicular to the axis of the paraboloid a distance Z_p from the vertex of the parent paraboloid (see Figure 1). Equally spaced grid points in the aperture plane are centered about the circular aperture as shown in Figure 2. Grid spacing is generally chosen to be a half wavelength, however, there are no specific restrictions on the distance between points so long as it is constant.

In order to evaluate the Geometrical Optics vector reflected field at each of the aperture grid points, the associated reflection points on the reflector surface must be determined. For electrically large apertures, this can be a formidable task since there is no "closed form" solution for arbitrary aperture and feed point locations. In one form or another, a numerical algorithm is required to determine the point by successive iteration. The technique employed here effectively minimizes the distance function defined by the sum of the distance from the feed to the reflection point and the distance from the reflection point to the aperture point. Since the reflection point must correspond to a local minimum in the distance function, (by Fermat's Principle) the solution can be found by a process of numerical minimization.

Figure 3 illustrates reflection from the paraboloid, and Figures 4 and 5 illustrate the minimization algorithm conceptually. From Figure 3, the distance function is defined as

$$D = s' + s$$

or

$$D = |\overline{SP}| + |\overline{PO}|$$

Assuming the point P is a potential reflection point lying on the parent paraboloid, its location can be described by the quantities r , and ϕ defined in Figure 4. With this definition, the paraboloid can be described by

$$r^2 = 4fz$$

where

$$r^2 = x^2 + y^2$$

and

$$\phi = \tan^{-1}(y/x)$$

From Figure 4 it can be seen that the \hat{r} and $\hat{\phi}$ directions are perpendicular (independent) and correspond to the principle directions of the surface of the paraboloid. The \hat{r} direction is along the parabolic arc and the $\hat{\phi}$ direction corresponds to the direction of rotation about the z-axis. The algorithm described here takes advantage of these independent directions and makes use of gradient calculations to step toward the minimum in the distance function in both the \hat{r} and $\hat{\phi}$ directions. This procedure is illustrated in Figures 5 and 6. The first step in the process is to choose a point P which is in the vicinity of the actual reflection point, Q_R . Next, the distance function is evaluated at P and two successive closely spaced points in each of the principle directions. These values are then used to form approximations of the gradient of the distance function. In the \hat{r} direction (corresponding to Figure 6) these quantities are

$$\left. \frac{\partial D}{\partial r} \right|_{\phi_r + \frac{4r}{2}} \quad \text{and} \quad \left. \frac{\partial D}{\partial r} \right|_{\phi_r + \frac{3\Delta r}{2}}$$

These values of the gradient are then used to project "back" to the zero crossing of the gradient function assuming approximate linearity. Since a zero crossing in the gradient corresponds to a local minimum (or maximum) in the distance function, convergence on the reflection point is achieved, provided the initial guess is in the vicinity of the true reflection point. This process is performed sequentially in both the \hat{r} and $\hat{\phi}$ directions and a new point P is determined. The gradient calculations are repeated until P is within a specified error bound of the reflection point, Q_R . This procedure is extremely efficient in that convergence is typically achieved in one to three iterations. Once the reflected field at the aperture point is determined, the process is repeated at an adjacent aperture grid point. Since aperture grid points are numerous and usually closely spaced, the reflection point associated with the previous grid point is a good initial guess for the next grid point.

Once the reflection point associated with an aperture grid point has been determined, the Geometrical Optics Vector reflected field is computed. As given by Kouyoumjian [1] the reflected field is

$$\bar{E}_R = \bar{E}_i(Q_R) \cdot \bar{R} \cdot A(s) e^{-jks}$$

where

$$\bar{E}_i(Q_R) = \frac{\bar{E}_0 e^{-jks'}}{s'}$$

$$\bar{R} = \begin{bmatrix} 1 & 0 \\ 0 & -1 \end{bmatrix}$$

$$A(s) = \sqrt{\frac{\rho_1^r \rho_2^r}{(\rho_1^r + s)(\rho_2^r + s)}}$$

$\bar{E}_i(Q_R)$ is the vector incident field at the point of reflection resolved into the components which permit the use of the reflection dyad, \bar{R} . $A(s)$ is the divergence coefficient which describes the divergence of the wavefront as it reflects from Q_R and radiates outward. As such, the quantities ρ_1^r and ρ_2^r are the principle radii of curvature of the reflected wavefront evaluated at Q_R . For spherical wave incidence they can be found from:

$$\frac{1}{\rho_1^r} = \frac{1}{s'} + \frac{1}{\cos \theta_i} \left[\frac{R_1}{\sin^2 \theta_2} + \frac{R_2}{\sin^2 \theta_1} \right] \pm \sqrt{\frac{1}{\cos^2 \theta_i} \left[\frac{R_1}{\sin^2 \theta_2} + \frac{R_2}{\sin^2 \theta_1} \right]^2 - \frac{4}{R_1 R_2}}$$

where

$$\begin{aligned} \theta_i &= \cos^{-1} [-\hat{s}' \cdot \hat{N}] \\ \theta_1 &= \cos^{-1} [\hat{s}' \cdot \hat{r}] \\ \theta_2 &= \cos^{-1} [\hat{s}' \cdot \hat{\phi}] \end{aligned}$$

R_1 is the radius of curvature of the reflector surface (at Q_R) in the \hat{r} direction, and R_2 is the radius of curvature in the $\hat{\phi}$ direction. These quantities are easily found from geometrical considerations.

Once the vector reflected field has been determined, it can be resolved into co- and cross-polarized components so that these components can be treated separately in the far field. Either the co- or cross-polarized components of the far field may be examined independently.

A limitation associated with this method arises from the nature of the Geometrical Optics formulation. The solution is not valid at or near caustic regions of the reflected field. As a result, some care must be taken in the placement of the aperture plane so that caustic regions are avoided. For some feed locations, it may not be possible to avoid caustics and in these instances, conventional stationary phase methods can be employed. In general, the aperture plane should be placed as close to the reflector edge as possible.

III. EVALUATION OF THE FAR FIELD

Once the vector reflected field has been evaluated in the aperture plane, the data must be transformed to the far field. Conventional aperture integration and FFT techniques can be employed, however, they are usually computationally intensive for even moderately sized apertures. The primary

purpose for performing the analysis described here is to examine the changes in the far field pattern when the main beam is steered by moving the feed relative to the reflector. Of primary interest is the effective reduction in gain and increase in coma lobe, or first sidelobe in the steered plane when the feed is moved a given distance from the focus of the reflector. Other pattern features which can be studied using this analysis include the change in cross-polarized pattern in the vicinity of the main beam. All of these effects occur in close proximity to the main beam of the far field pattern, and they may be most accurately viewed and easily understood in terms of standard far field pattern plots, namely a graph of far field amplitude as a function of either azimuth angle with constant elevation or elevation angle with constant azimuth. A scheme of fast computation of single plane far-field patterns from the two-dimensional near-field array has therefore been implemented. This technique uses certain features found in two-dimensional Fast Fourier transform algorithms, but is itself not a true FFT.

A form of the discrete Fourier transform [2] used to compute far-field plane wave component, or far field pattern value, from a rectangularly sampled near-field array may be written

$$A(k_x, k_y) = \sum_{j=1}^M \sum_{i=1}^N E(x_i, y_j) e^{-j2\pi k_x i/N} e^{-j2\pi k_y j/M} \quad (1)$$

where

(x_i, y_j) is the near-field sample location

E is the complex field at that location

(k_x, k_y) is the far-field location in two dimensional wave number

A is the complex far-field value

The rectangularly sampled near-field array is stored in the computer as records corresponding to matrix rows. For example, record 1 is

$$E(1,1), E(2,1), E(3,1), \dots E(N,1)$$

and record 2

$$E(1,2), E(2,2), E(3,2), \dots E(N,2)$$

for record j from 1 to M . When a single cut of the far-field pattern is to be computed, for example $A(0, k_y)$ for $-\frac{\pi}{\lambda} < k_y < \frac{\pi}{\lambda}$ ($+30^\circ$), the two dimensions of the transform are applied independently. First the rows (records) of the matrix are read from mass storage, and the inner summation of equation 1 is computed for the constant k_x value of 0. Each row is thus accumulated as a single value of

$$B(j) = \sum_{i=1}^N E(i,j) e^{-j2\pi(0)i/N} \quad (2)$$

where j (in $E(i,j)$ and $B(j)$) is the row number currently being read and integrated.

In this case, the complex values $E(i,j)$ for each row are simply summed together, but if a constant k_x value other than 0 were desired, it would be included in place of the zero in equation (2). Then after all rows have been read from mass storage, the $B(j)$ exist as a single dimension of data, and the second dimension of the transform may be applied,

$$A(0, k_y) = \sum_{j=1}^M B(j) e^{-j2\pi k_y j/M} \quad (3)$$

for the desired sampling within $-\frac{\pi}{\lambda} < k_y < \frac{\pi}{\lambda}$.

By applying this technique, the brute force method of aperture integration (or the 2-d FFT) has been avoided, with the restriction that either azimuth or elevation angle must be held constant. This allows the antenna designer to investigate many more alternatives in a shorter period of time than has been previously possible.

An additional time savings is realized by storing all complex values in rectangular format, that is real and imaginary parts rather than as amplitude and phase. Finally, the real and imaginary parts of the Fourier transform multipliers, (shown in equations 1 through 3) are computed only once, then indexed from a table, minimizing the number of trigonometric operations performed.

IV. RESULTS

The techniques described above have been implemented on a VAX 11/780 as well as an IBM-PC equipped with an 8087 numeric co-processor. Benchmark execution times which follow apply only to the IBM-PC, however they can be extrapolated to other larger computer systems.

Three programs are used to generate far-field patterns given the reflector geometry:

1. P1 - near-field computation in the aperture plane
2. P2 - far-field data computation from near-field
3. P3 - far-field hard copy plots of far-field data.

The first program is by far the code with the longest execution time due to the iterative reflection point calculation, the geometrical optics computations, and the large number of data values to compute. On an IBM-PC with floating point co-processor, the near fields are computed typically in 100 msec per sample location. A 128 X 128 near-field array can thus be computed in about 30 minutes. This time can be reduced by approximately a factor of two with the implementation of machine-code subroutines for the basic geometrical operations, namely, the dot product, cross product, and 3 dimensional distance computation.

The second program which computes the far-field patterns, requires approximately 100 msec for each far-field value calculated in addition to the time required to read the entire near-field array from storage. Due to the large amount of data in the near-field array, (a 128 X 128 point array requires 131 kbytes), accessing all data in the array takes an appreciable amount of time, depending on the mass storage media used.

The last program, which plots the data on paper, is limited in speed only by the plotting hardware. The plots shown in this paper were generated on an Epson RX-80 dot matrix printer and were produced in about two minutes. Faster dot-matrix printers or the use of a pen plotter could reduce this time considerably.

The example patterns which follow correspond to a full scale developmental space-deployable antenna built by General Dynamics Convair Division for Intelsat. A sketch of the antenna is shown in Figure 7. A sketch of the reflector geometry, illustrating the parameters pertinent to the analysis, is shown in Figure 8. The reflector is a 5 meter diameter mesh surface, held in place with periodically spaced cords. The feed associated with this reflector is a 3.4 GHz linearly polarized circularly symmetric corrugated horn with 17 dB taper at the reflector edge.

Figure 9 shows the co-polarized far-field pattern of this antenna with the feed positioned at the focal point of the parent paraboloid. Note the 32 dB first sidelobes. Figure 10, in contrast, shows the pattern when the feed is moved laterally 10 wavelengths to steer the beam 8.5 degrees from boresight. Because the General Dynamics antenna has such a high focal length to diameter ratio (F/D of 1.3) the familiar coma lobe is not readily visible. The degradation to the main beam, however can be clearly seen. The first sidelobes, previously at -32 dB relative to the peak of the main beam, have degenerated into shoulders perturbing the main beam at approximately -10 dB below the beam peak.

Some results of this analysis have been compared to actual measured patterns associated with this antenna taken in the Martin Marietta near-field chamber. Figure 11 shows an overlay of the computations vs actual measurement of the antenna when the 3.4 GHz feed is at the reflector focus position. The main beam shows good agreement, but sidelobes do not. This is a result of the non-ideal surface of the reflector, producing higher sidelobes than those associated with the illumination profile. Figure 12 demonstrates this effect by comparing the computations with measured data in which the surface deformation effects have been mathematically removed. The sidelobe envelope and individual sidelobe width and position now show good agreement with those from the analysis.

V. CONCLUSIONS

An efficient method of computing the far field of offset reflector antennas with offset feeds has been developed, and the utility of the method demonstrated. Although they have not been discussed here, many of the design problems and issues associated with this class of antennas can be addressed and studied using the techniques described. The versatility and speed of these techniques allows the antenna designer to vary a wide range of parameters in a short period of time in the process of developing the best antenna system design for a given set of requirements.

In conclusion, it should also be noted that this method easily lends itself to enhancements which improve the accuracy and broaden the range of application of these techniques. One such improvement is the computation of the edge diffracted field by the Geometrical Theory of Diffraction [3]. This would allow an extension of the near field aperture plane and greatly improve the accuracy of the far field computations in the far out sidelobe region of the antenna. Another useful extension involves the modeling of array feeds. Each feed element can be modeled independently (as opposed to a single feed with equivalent phase center) allowing the application of superposition and the ability to optimize combining networks for specific applications.

In addition, surface deformation effects can be modeled effectively as near field phase deviations (proportional to surface deviations) so long as the deviation is a slowly varying one, and the aperture plane is positioned close to the reflector edge. Finally, this method can be applied to other reflector geometries and configurations such as shaped reflectors and divergent reflectors simply by accounting for the change in geometry in the reflected field computations. These improvements and enhancements are presently being investigated and implemented.

VI. REFERENCES

- (1) R. G. Kouyoumjian, P. H. Pathak, "A Uniform Geometrical Theory of Diffraction for an Edge in a Perfectly Conducting Surface", Proc IEEE, Vol 62, pp 1448 - 1461, November 1974.
- (2) E. Brigham, The Fast Fourier Transform, Prentiss Hall Inc, 1974.
- (3) R. G. Kouyoumjian, P. H. Pathak, "The Dyadic Diffraction Coefficient for a Curved Edge", NASA CR-2401, June 1974.

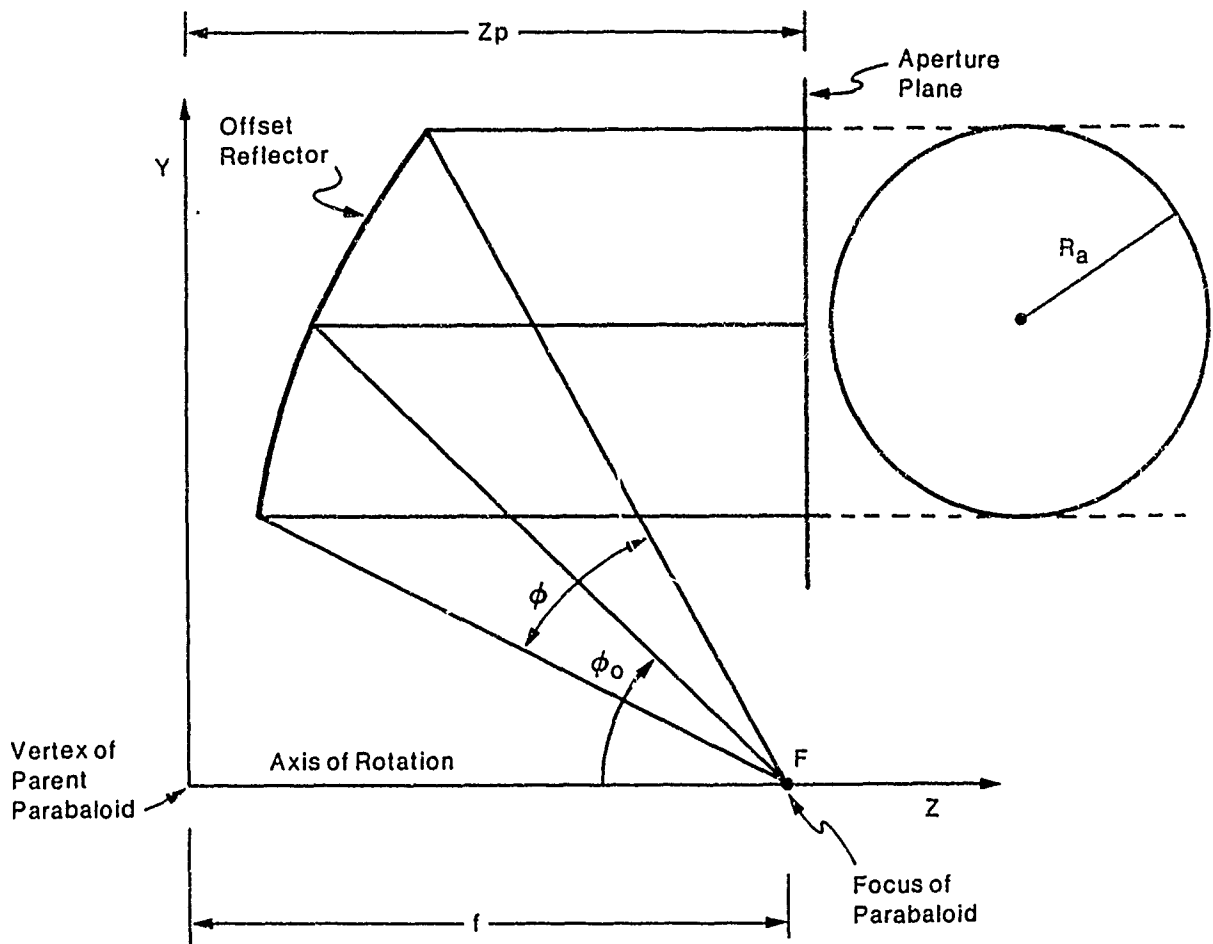


Figure 1 - Specification of the Offset Reflector Antenna

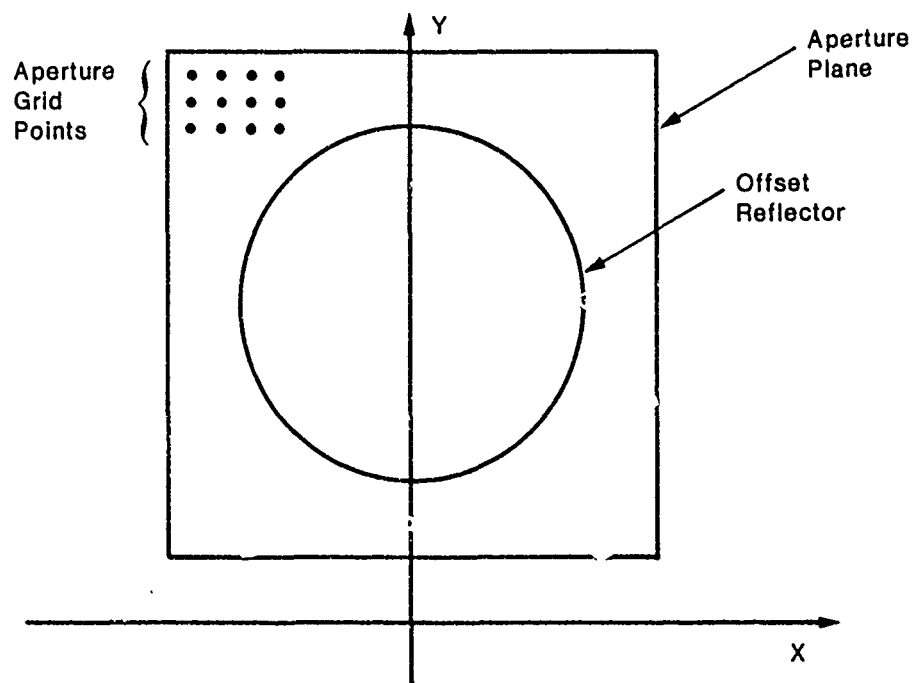


Figure 2 - Aperture Geometry

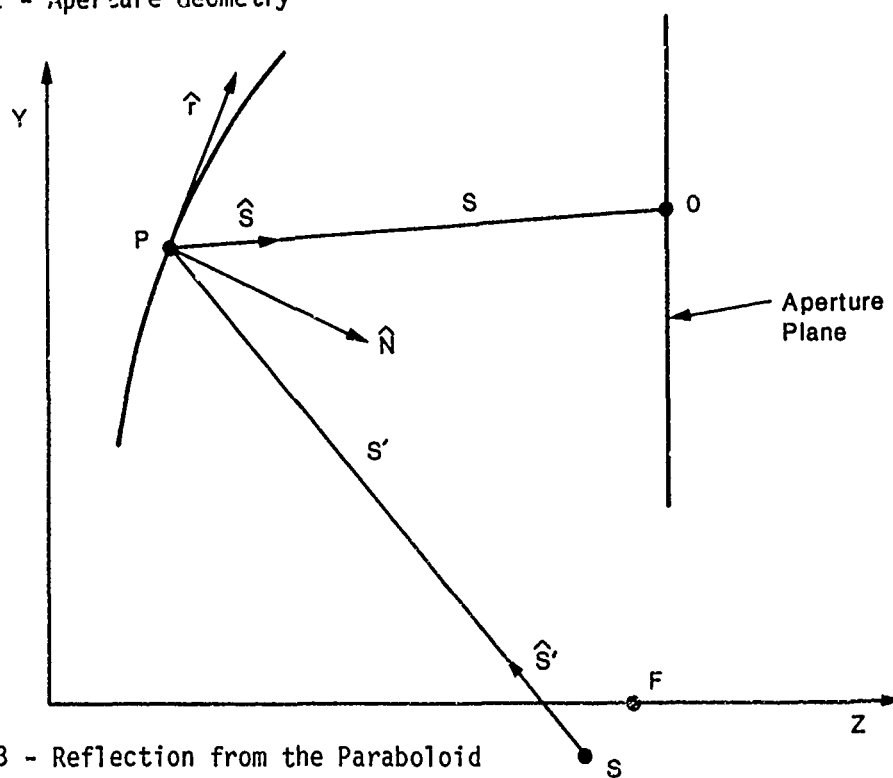


Figure 3 - Reflection from the Paraboloid

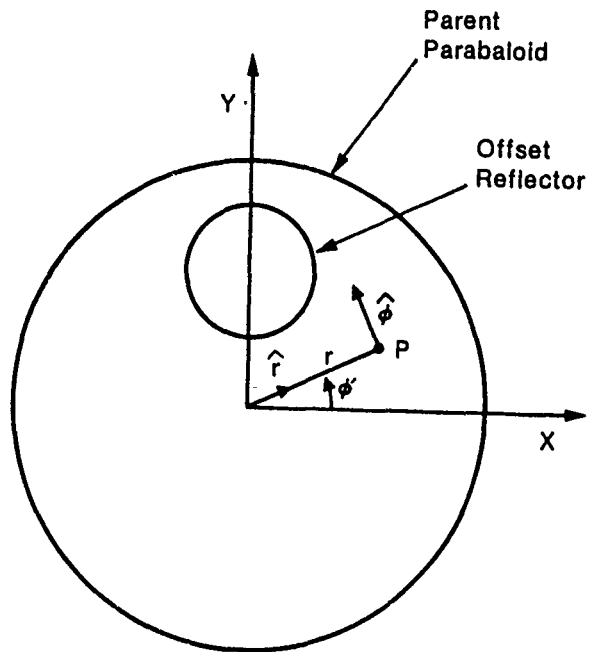


Figure 4 - Principle Directions of the Reflector Surface

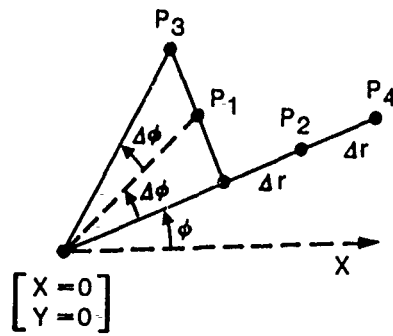


Figure 5 - Approximate Evaluation of the Distance Function Gradient

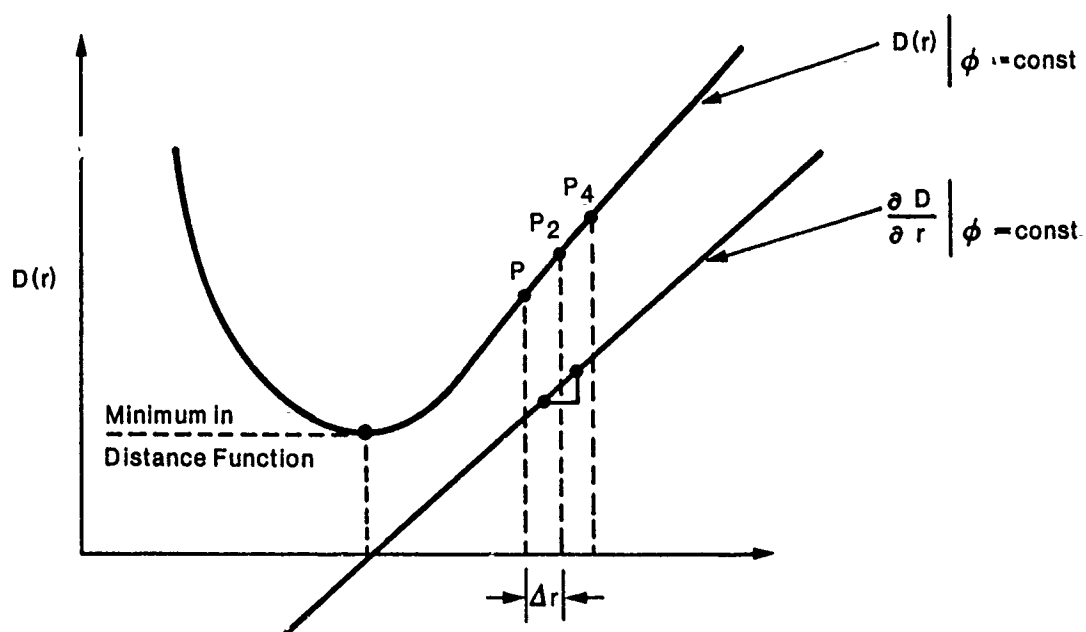


Figure 6 - Distance Function Gradient Computations

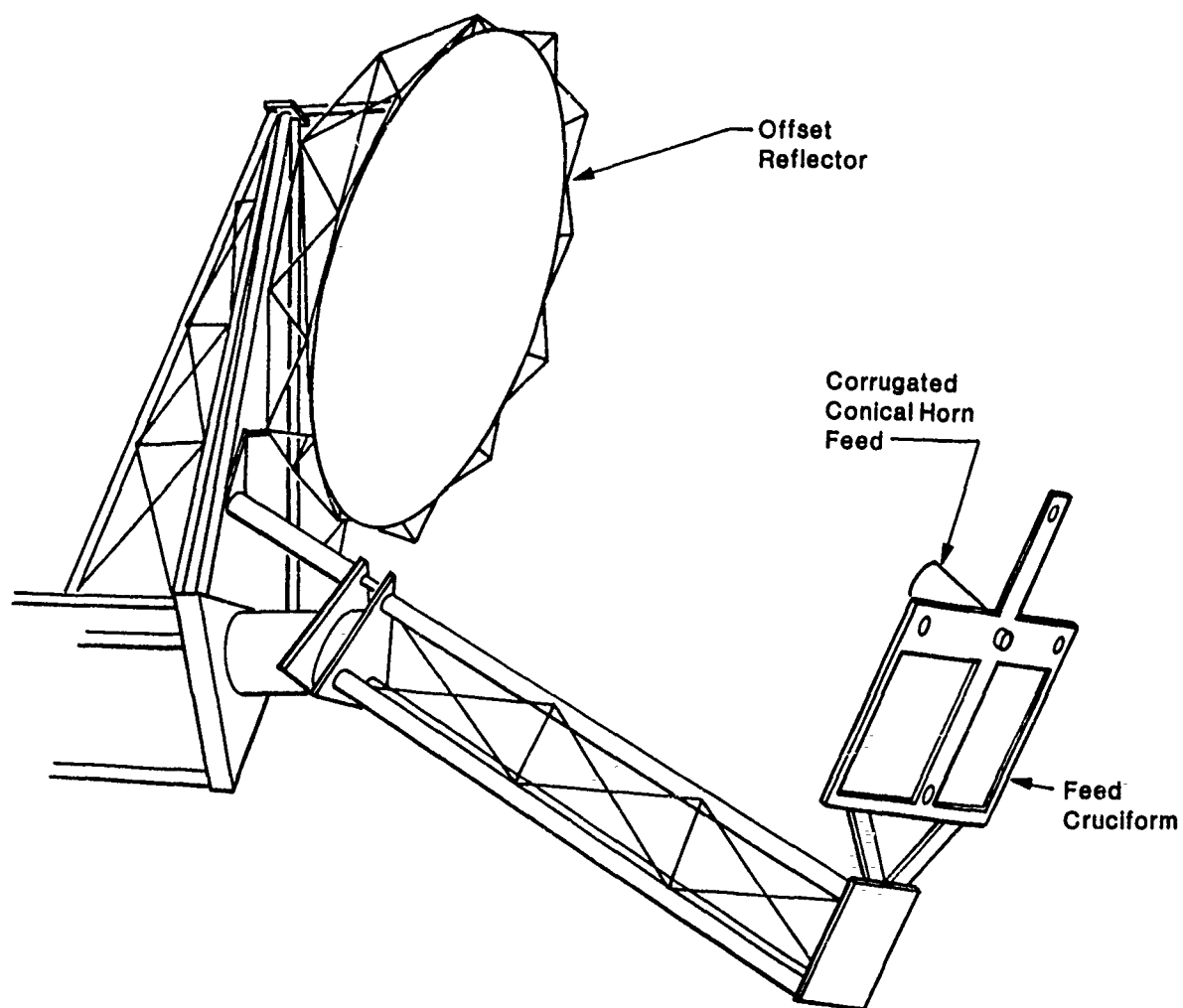


Figure 7 - Illustration of General Dynamics Offset Reflector

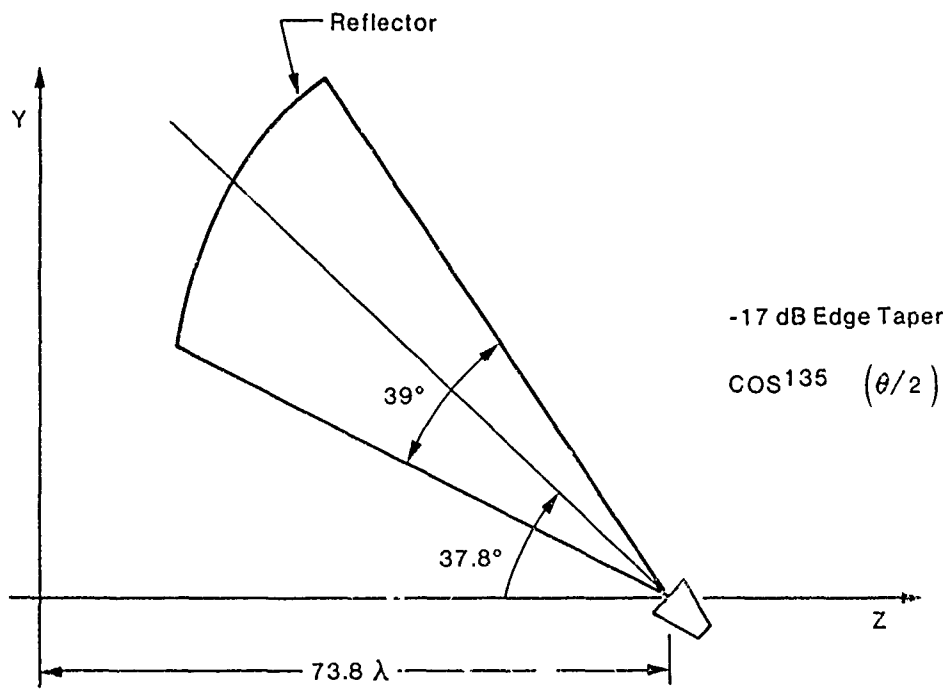


Figure 8 - General Dynamics Reflector Geometry

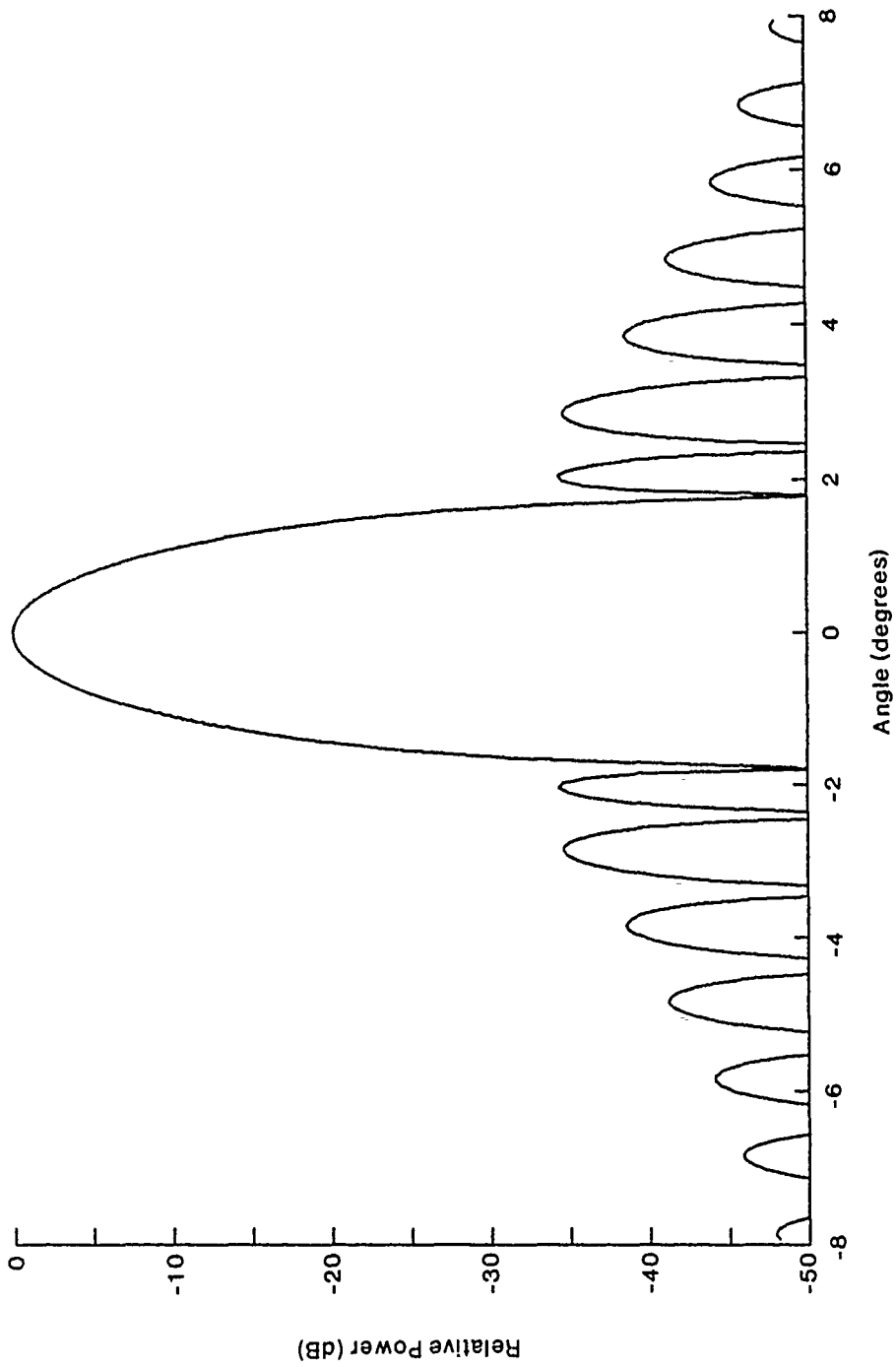


Figure 9 - Focused Far Field Pattern

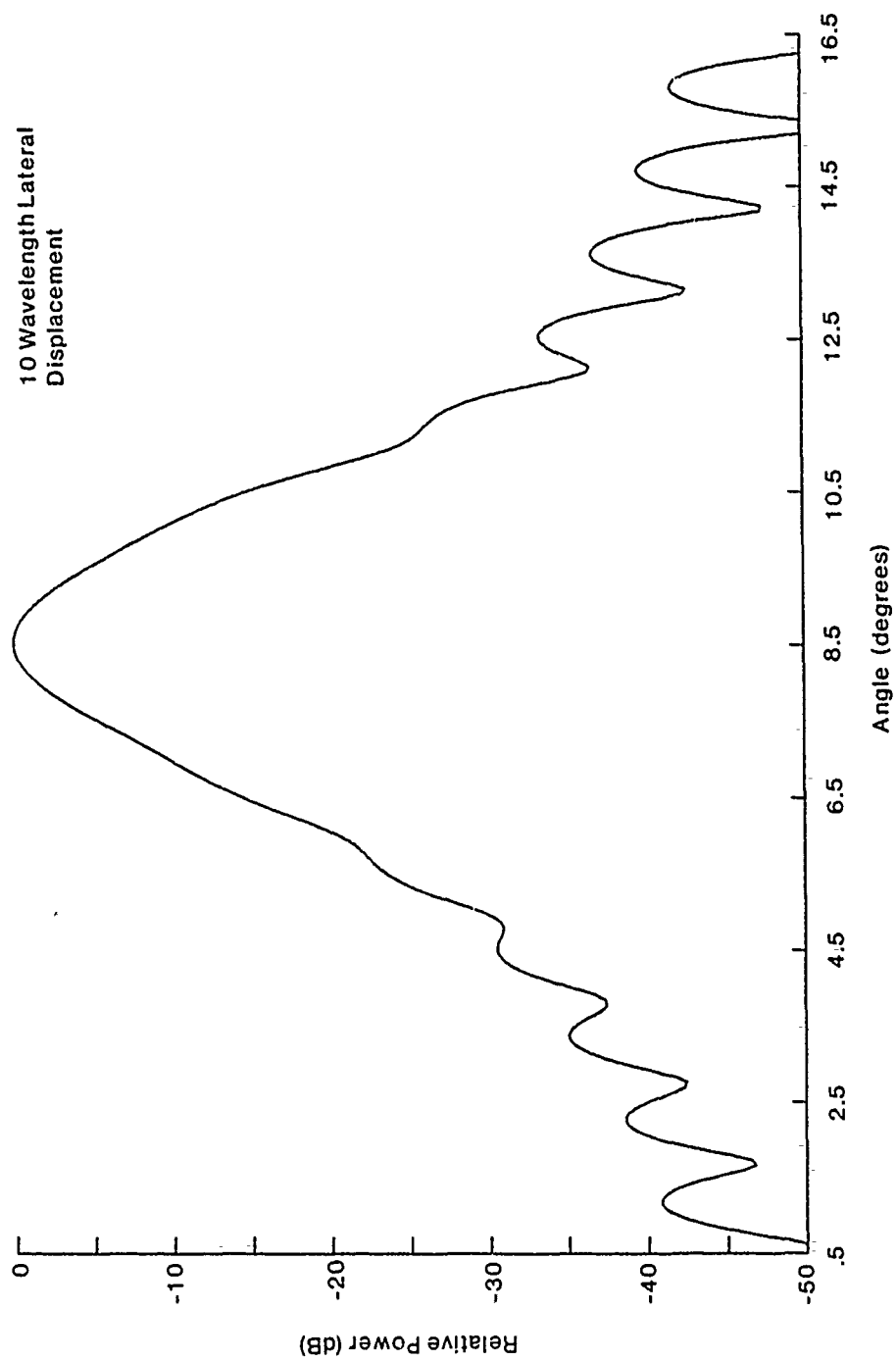


Figure 10 - Defocused Far Field for 10 Wavelength Lateral Displacement

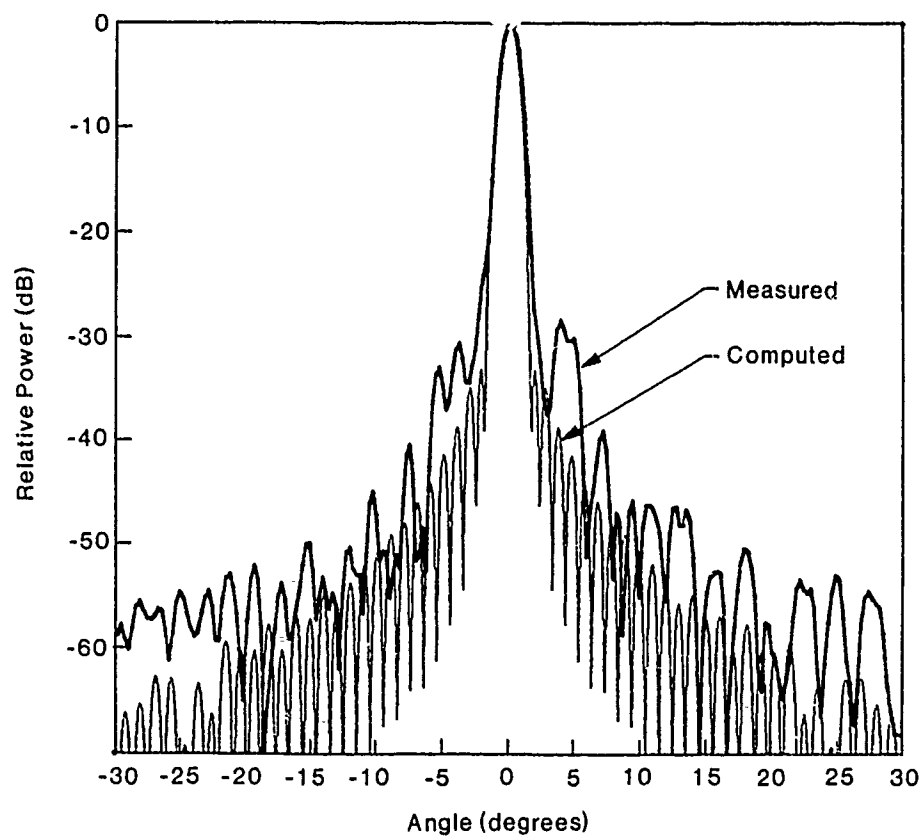


Figure 11 - Comparison of Measurements and Computations

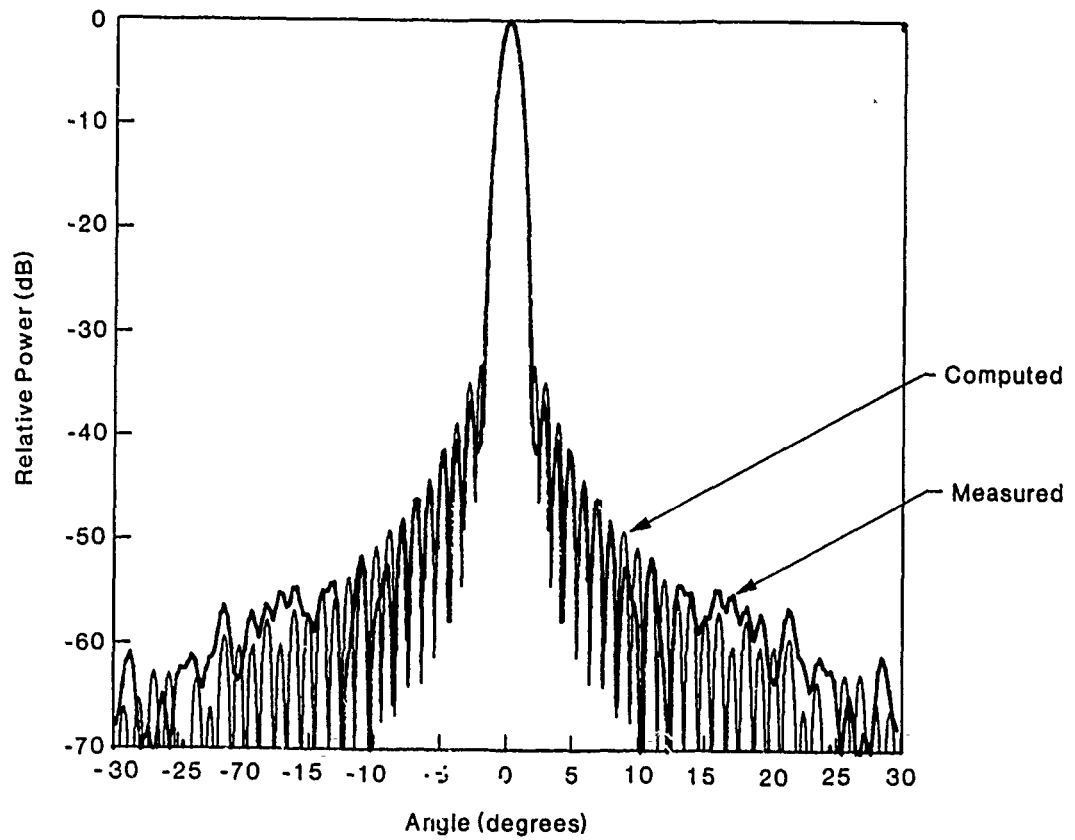


Figure 12 - Comparison of Measurements and Computations

Thin Aperture Modeling Using an FDTD Code

Kenneth R. Demarest
Radar Systems and Remote Sensing Laboratory
The University of Kansas Center for Research, Inc.
Lawrence, Kansas 66045-2969

The topic of electromagnetic penetration through apertures has been a subject of intense interest in recent years. This interest stems from the great number of practical problems that arise in both military and civilian applications where it is necessary to determine the coupling from one region to another. Increased concern caused by broadband threats such as lightening and NEMP have heightened the interest in developing accurate techniques for analyzing penetration problems involving small apertures.

The Finite-Difference Time-Domain (FDTD) technique has proven to be a valuable tool for the calculation of the transient and steady state scattering characteristics of relatively complex scatterer and source configurations. Among its attractive characteristics are its ability to model a very large variety of conducting and dielectric geometries, numerical straight-forwardness, the ability to model nonlinearities, and the production of direct time domain results.

In spite of the attractive attributes of the FDTD technique, it is well known that it is not well suited to geometries that exhibit variations in shape or consistency that are small with respect to wavelength. To counter this, various schemes have been developed to allow the FDTD technique to model fine detail such as thin wires, points, and apertures.

This paper describes an FDTD code that incorporates augmentations that allow the modeling of geometries containing multiple wires (including the possible junctions) and long thin apertures. The wire technique used in this code is a variation of one developed by Simpson and Holland [1]. The aperture technique utilizes the generalized Babinet's principle to decouple the interior and exterior regions on both sides of an aperture, thus allowing for the analysis of geometries containing long thin apertures, backed by cavities that might contain fine detail [2, 3].

View-graphs 1-3 illustrate the basics of the FDTD technique. Here, the scatterer is modeled as a collection of rectangular cells and immersed in a numerical grid in both time and space. In each cell, all three components of

the electric and magnetic fields are calculated. The positions of the electric fields are interlaced in both time and space so as to allow Maxwell's two curl equations to advance the electric and magnetic fields alternately in time to produce time marching solutions.

View-graph 4 summarizes the way in which apertures of various sizes can be modeled in an FDTD code. Generally, in order for an aperture to be modeled directly by an unaltered FDTD code, it must extend over an area of at least 4 square cells. For apertures that are somewhat smaller, a technique has been developed [4] whereby a second computational run is made over a portion of the geometry using a finer numerical grid (usually 4 times smaller), thus allowing the modeling of apertures that are approximately one cell in dimension in the original grid. For long and thin apertures (such as cracks and seams), the aperture is often too narrow to be resolved by the numerical grid, but can be modeled by utilizing the generalized Babinet's principle (the subject of this paper). Finally, for extremely small holes, Bethe hole theory could probably be applied to adequately calculate the coupling.

The calculation sequence that this code uses to invoke Babinet's principle and calculate the interior fields of a geometry containing a cavity backed by a small aperture is shown in View-graph 5. Here, the top figure shows the entire geometry to be analyzed, and the remaining figures are the sub-geometries that are modeled sequentially to find the cavity fields of the original geometry. The first geometry modeled is that of the entire external geometry with the aperture short circuited. The purpose of this step is to calculate and store the external surface currents at all points except along the aperture plane.

In the next calculation, the fields of the external surface currents radiating into free space are found. Then, the fields of these same currents radiating in the presence of the complement of the aperture plane (i.e. free space where conductor had been and magnetic conductor where free space had been) are found. During this calculation, the narrow magnetic strip is modeled as a narrow wire and the dual of Holland and Simpson's wire technique is used.

The fields in the aperture of the top geometry of View-graph 5 are then found from Babinet's principle by taking the difference between the aperture fields of the "incident" and "magnetic" field cases. These aperture fields can then be used as the sole driving sources for a final computation that

involves only the cavity. Since the external geometry need not be included in this calculation, the numerical grid used can be much smaller and thus result in sufficient spatial resolution to model cavities with fine detail. Configurations of wires in these cavities can also be modeled.

Summaries of the way in which electric and magnetic wires are modeled in this code are shown in View-graphs 6 and 7. Basically, they are simply duals of each other. In both cases, the way in which the fields are advanced in cells containing wires must be altered in order to account for the distributed inductances and capacitances associated with these structures. Also, junctions are handled by forcing the charges at these junctions to distribute themselves according to the capacitances on all sides of the junctions.

View-graph 8 shows a comparison of the aperture current (with the aperture short circuited) and the aperture field for a hollow, "fuselage like" geometry with a narrow aperture on top that is excited by an injected current pulse on lightning channel (modeled as a wire). Note that the current waveform is that of a pulse washing back and forth across the aperture. The aperture field waveform, however, shows high frequency components not present in the current waveform which result from the rapid discharging of the aperture.

View-graph 9 shows a comparison of the fields 2m above and 2m below the aperture. Here, we note a phase reversal and diminished amplitude of the interior fields. View-graph 10 depicts the peak field strength in the cavity as a function of the aperture width. As expected, there is a logarithmic decrease.

View-graph 11 shows a comparison of electric fields calculated for the same exterior geometry as in View-graph 9, but each with different size cavities. In these waveforms, we notice the higher "ring" frequencies associated with the smaller cavities. Also, we notice smaller amplitudes in the smallest cavity due to the decreased energy in the aperture fields at the high ring frequency of this cavity.

View-graph 12 depicts that capability of this code to model wires within cavities. As can easily be seen, the presence of the wire causes the initial response close to the bottom of the cavity to be somewhat lower than when it is not present due to partial shielding. Later, however, the wire rings at its resonant frequency, which is much lower than the first resonance of the cavity.

Finally, View-graph 13 is an example of the multiple wire (with junctions) geometries that can be modeled by this code. Here, three wires of different lengths and diameters intersect at right angles. This configuration is excited by a current pulse on the far right side of the horizontal wire. The four current waveforms shown depict several characteristics that would be expected from such a geometry, including the positive reflection of the incident pulse at the wire junction, and the subsequent negative reflections off of the wire ends as the incident pulse passes through the junction. We also see that the injected currents across the junctions are largest for the largest diameter wires.

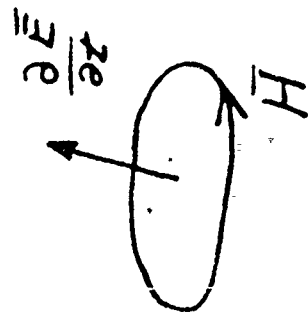
REFERENCES

- [1] Holland, R. and L. Simpson, "Finite-Difference Analysis of EMP coupling to Thin Struts and Wires," IEEE Trans. Electro. Compat., vol. EMC-23, no. 2, pp. 88-97, May 1981.
- [2] Demarest, K., "A Finite Difference-Time Domain Technique for Modeling Narrow Apertures in Conducting Scatterers," submitted to the IEEE Trans. on Antennas and Propagation.
- [3] Demarest, K., "Time-Domain Finite-Difference Modeling of Thin Apertures," 1985 URSI Symposium Proceedings, Vancouver, pp. 122.
- [4] Kunz, K.S. and Simpson, "A Technique for Increasing the Resolution of Finite-Difference Solutions of the Maxwell Equation," IEEE Trans. Electro. Compat., vol. EMC-23, no. 4, pp. 175-178, November 1981.

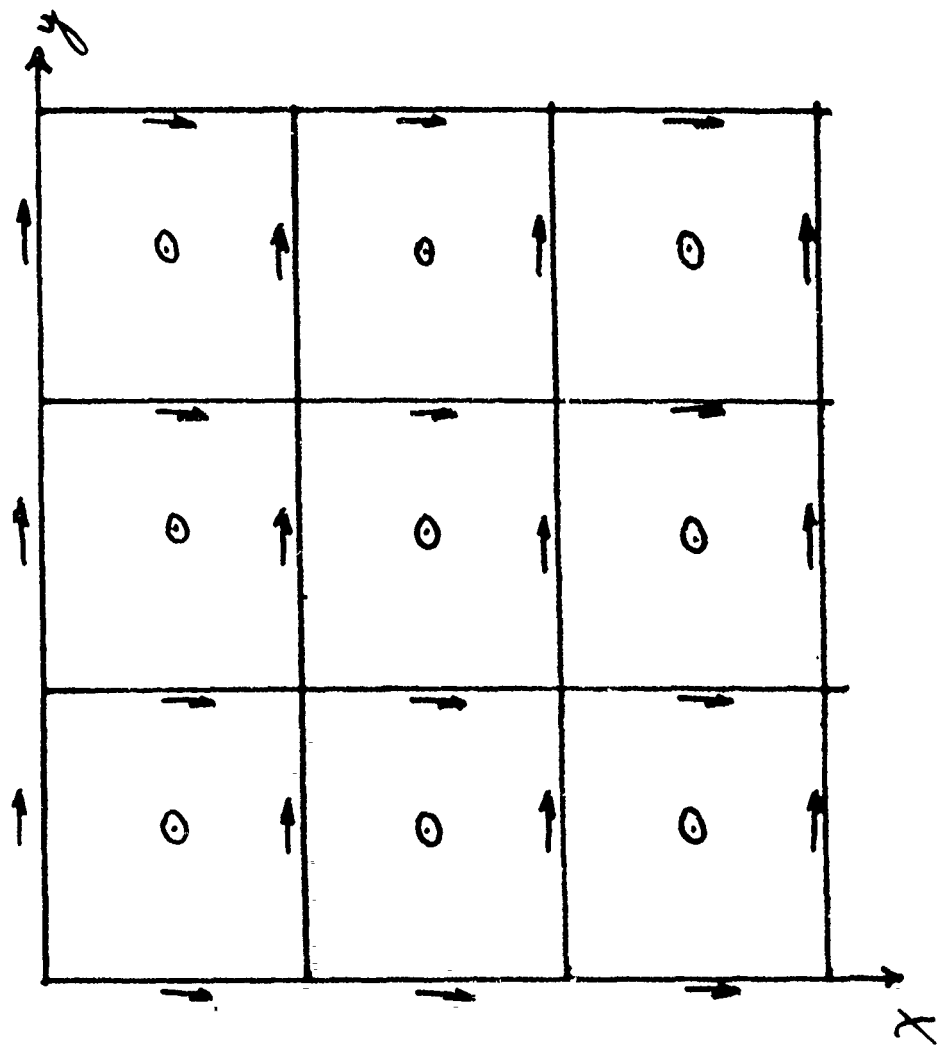
TIME DOMAIN SOLUTIONS

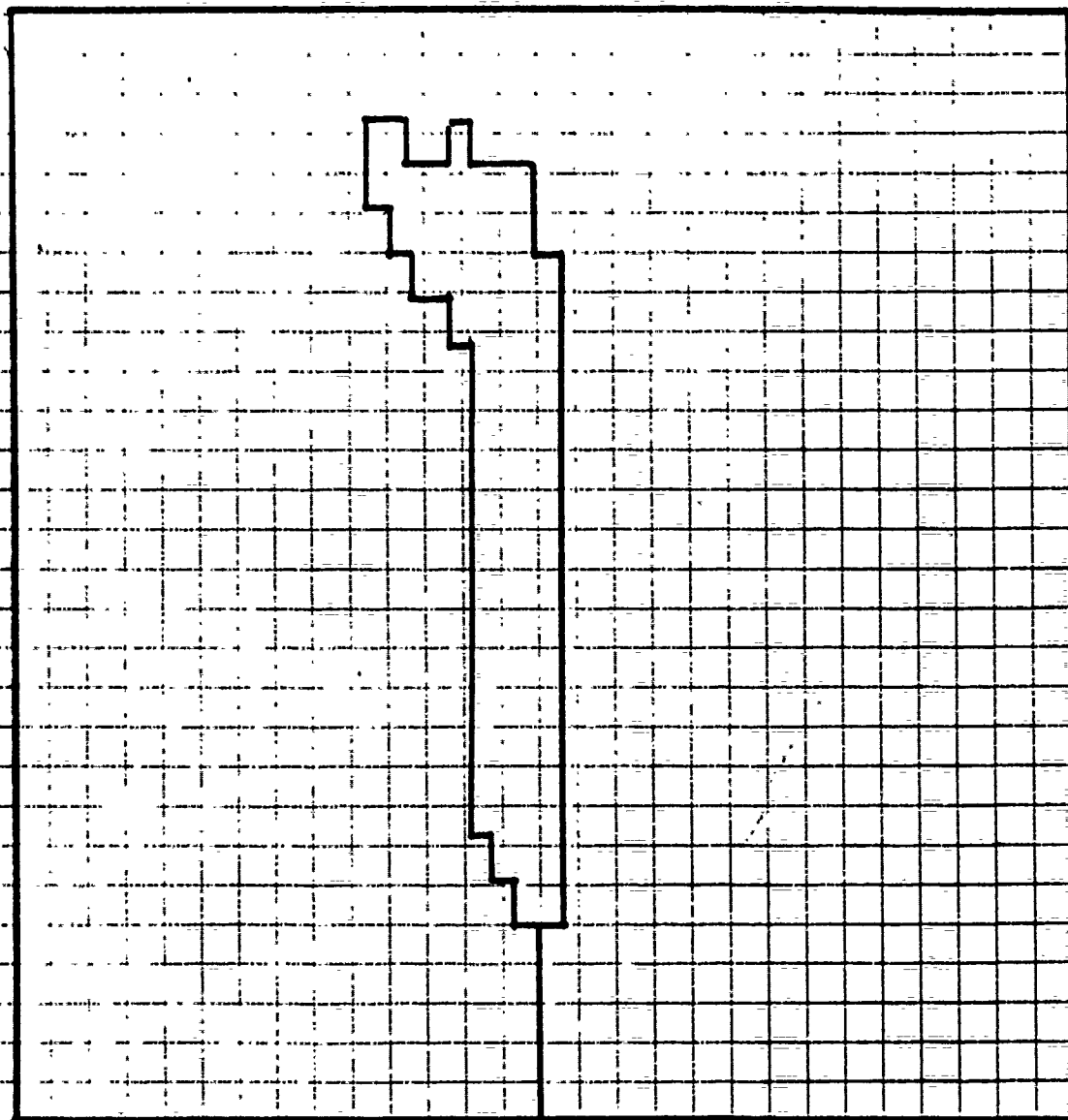
$$\nabla \times \bar{E} = -\mu \frac{\partial \bar{H}}{\partial t}$$

$$\nabla \times \bar{H} = \epsilon \frac{\partial \bar{E}}{\partial t}$$



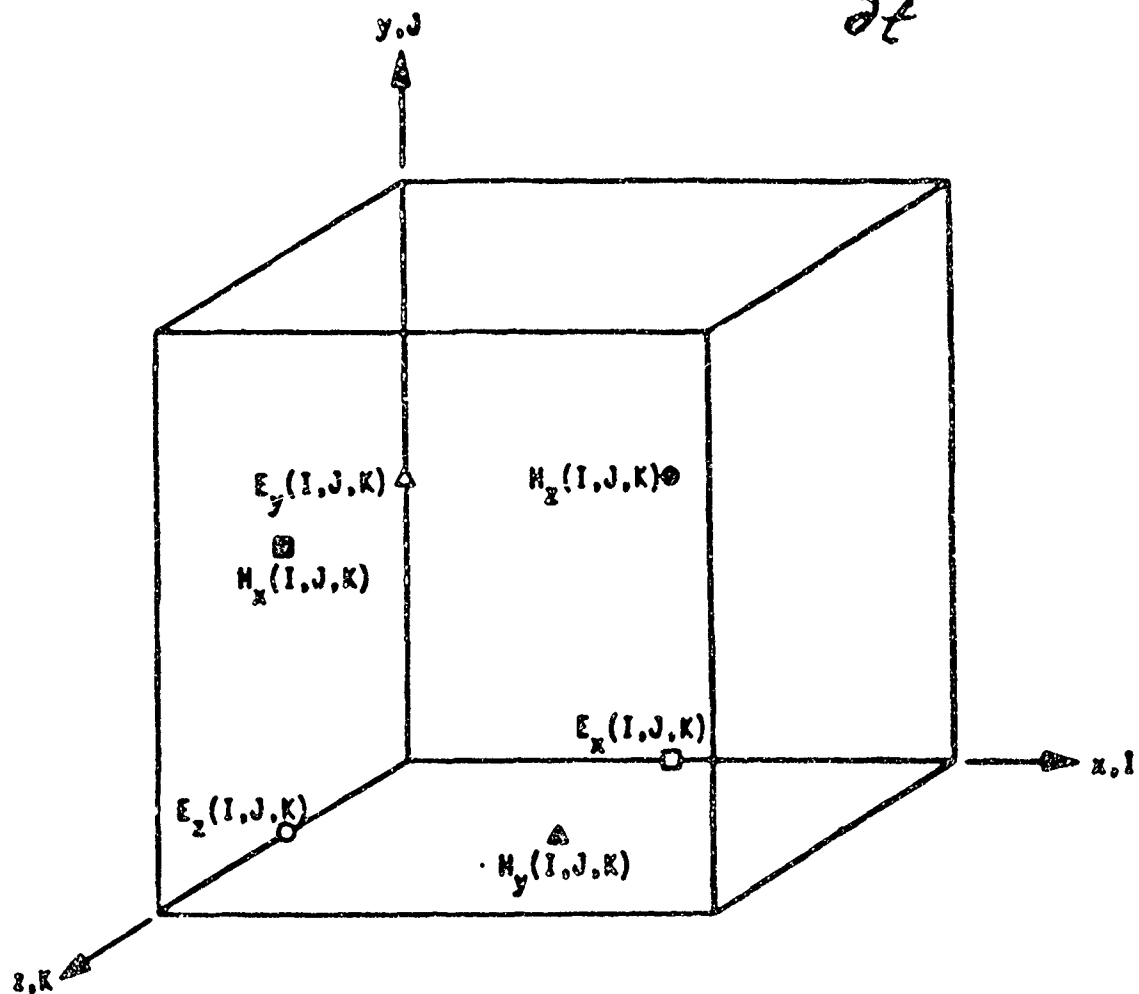
$$-\bar{H}^n - \bar{E}^{n+1/2}$$





$$\nabla \times \vec{E} = -\mu \frac{\partial \vec{H}}{\partial t}$$

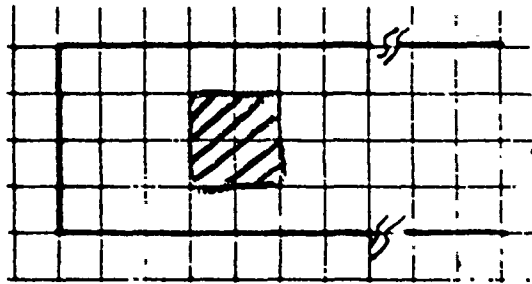
$$\nabla \times \vec{H} = \epsilon \frac{\partial \vec{E}}{\partial t}$$



Location of the Six Field Evaluation Points in a Typical Cell

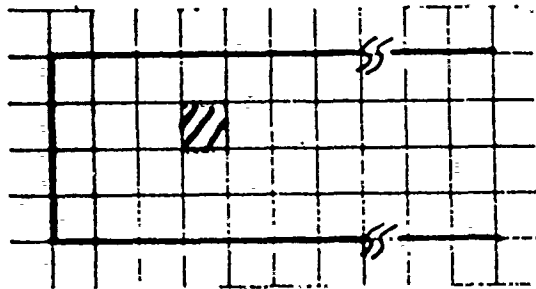
Aperture Classes

**VERY
LARGE**



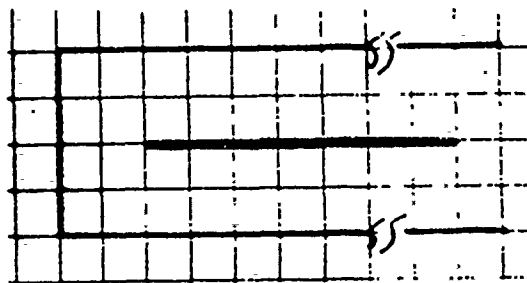
DIRECT 3-D RUN

LARGE



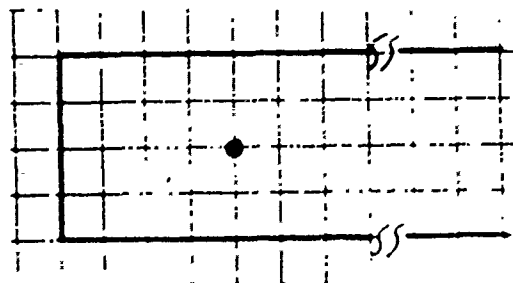
EXPANDED 3-D RUN

**LONG &
NARROW**



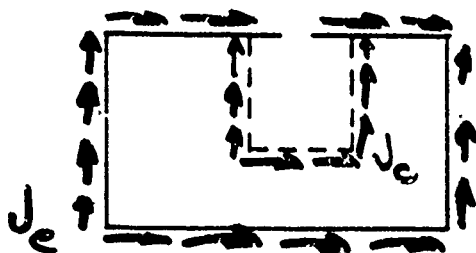
BABINET'S PRINCIPLE

SMALL

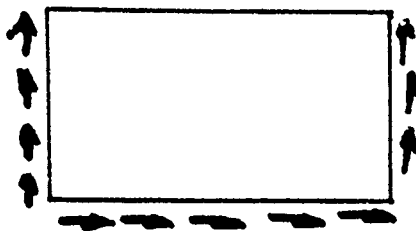


**BETHE HOLE
THEORY**

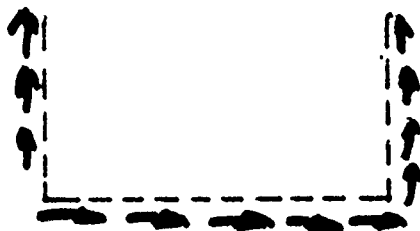
CALCULATION SEQUENCE



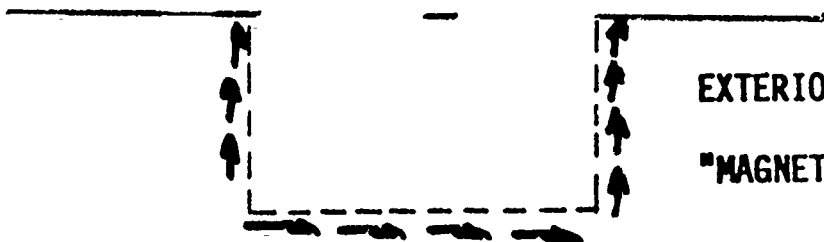
GEOMETRY TO BE SOLVED
CAVITY FIELDS DESIRED



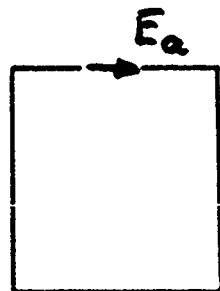
EXTERIOR CURRENTS
CALCULATED AND STORED



EXTERIOR CURRENTS FORCED
"INCIDENT FIELDS" CALCULATED

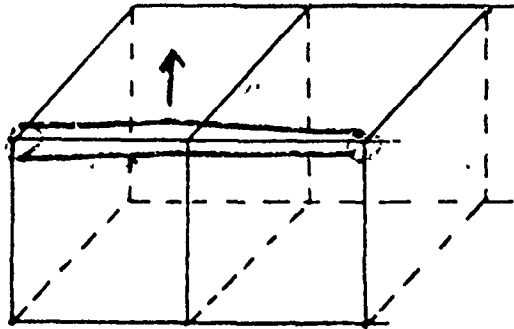


EXTERIOR CURRENTS FORCED
"MAGNETIC FIELDS" CALCULATED



APERTURE FIELDS FORCED
CAVITY FIELDS CALCULATED

Electric Wire Equations



$$\nabla \times \vec{E} = -\mu \frac{\partial \vec{H}}{\partial t}$$

H FIELD ADVANCE

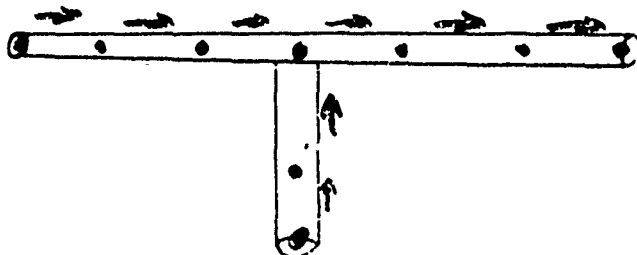
$$\langle E_z \rangle = L \frac{\partial I}{\partial t} + \frac{1}{C} \frac{\partial \phi}{\partial z}$$

WIRE CURRENT &
CHARGE ADVANCE

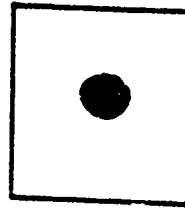
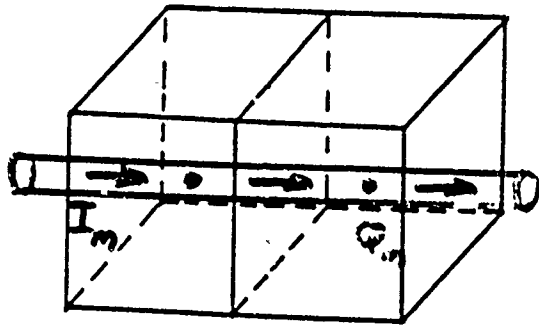
$$\frac{\partial I}{\partial z} = - \frac{\partial \phi}{\partial z}$$

$$\nabla \times \vec{H} = \frac{I}{45} + \epsilon \frac{\partial \vec{E}}{\partial t}$$

E FIELD ADVANCE



MAGNETIC WIRES



$$\nabla \times \vec{H} = \epsilon \frac{\partial \vec{E}}{\partial t}$$

E FIELD ADVANCE

$$\langle H_z \rangle = L_m \frac{\partial I_m}{\partial t} + \frac{1}{C_m} \frac{\partial Q_m}{\partial z}$$

CURRENT ADVANCE

$$\frac{\partial Q_m}{\partial t} = - \frac{\partial I_m}{\partial z}$$

CHARGE ADVANCE

$$\nabla \times \vec{E} = - \frac{I_m}{4\pi} - \mu \frac{\partial \vec{H}}{\partial t}$$

H FIELD ADVANCE

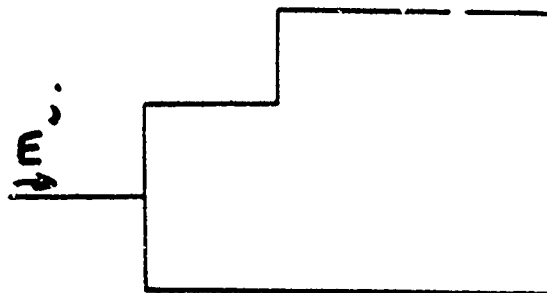
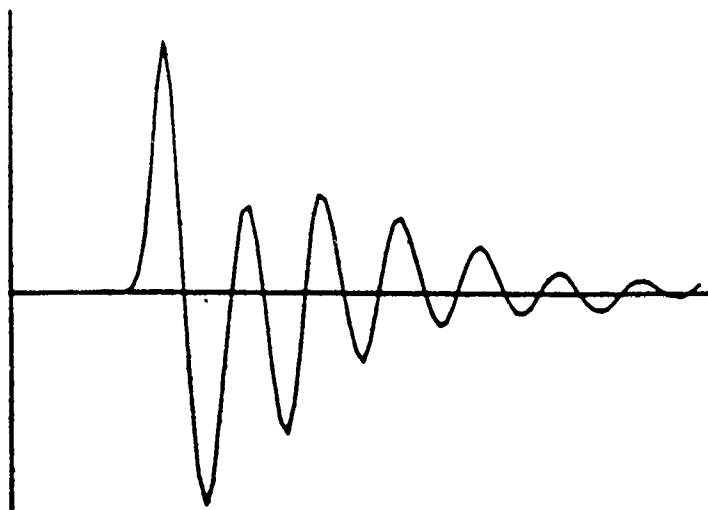
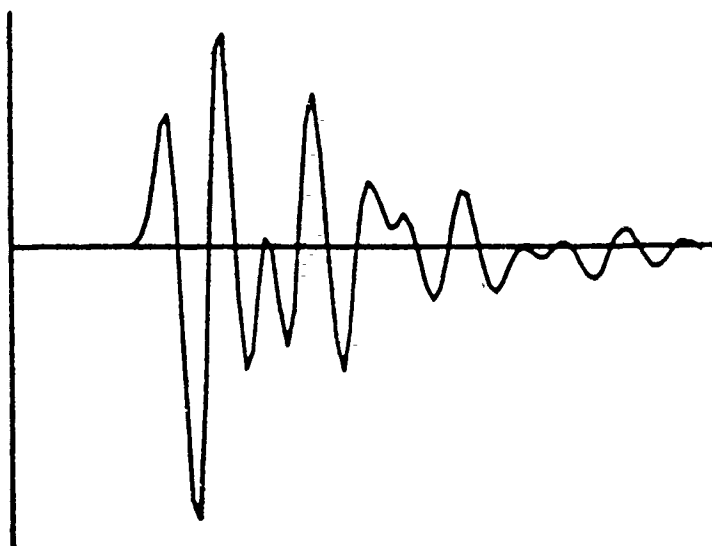


PLATE
CURRENT

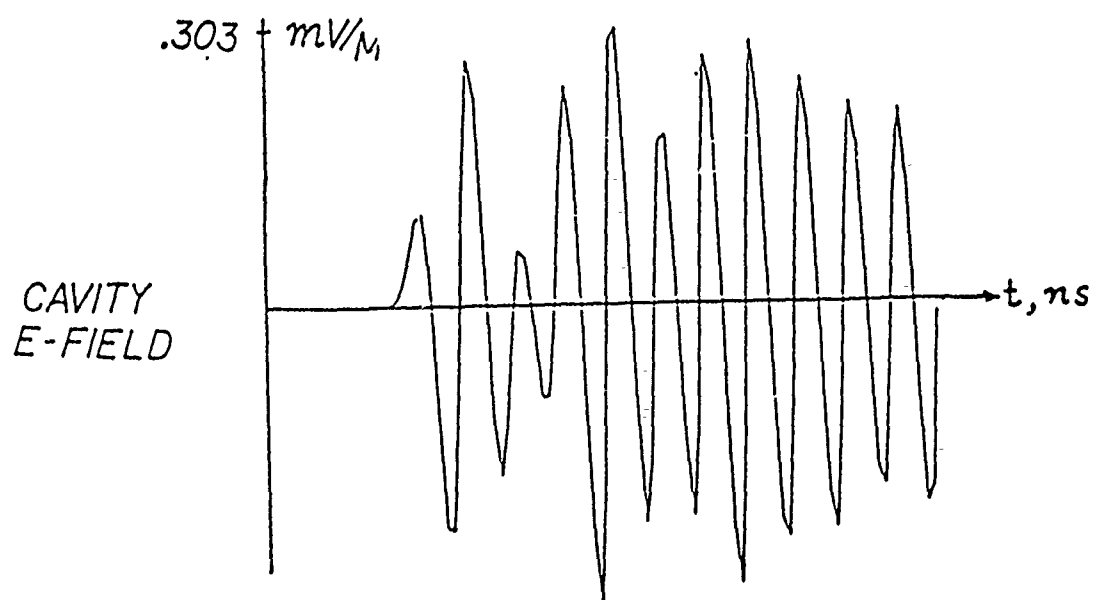
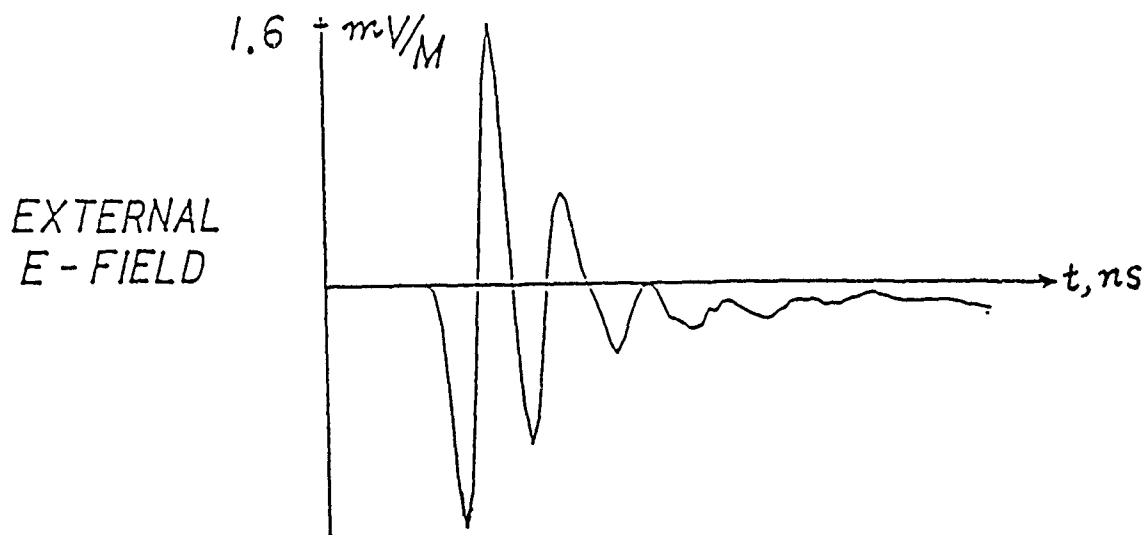
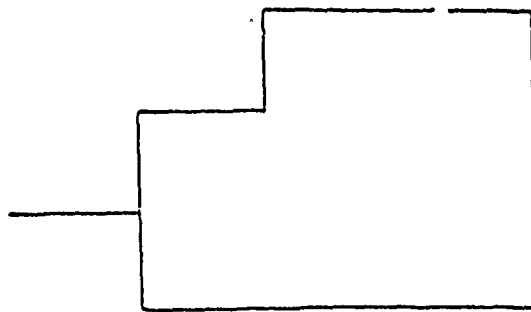


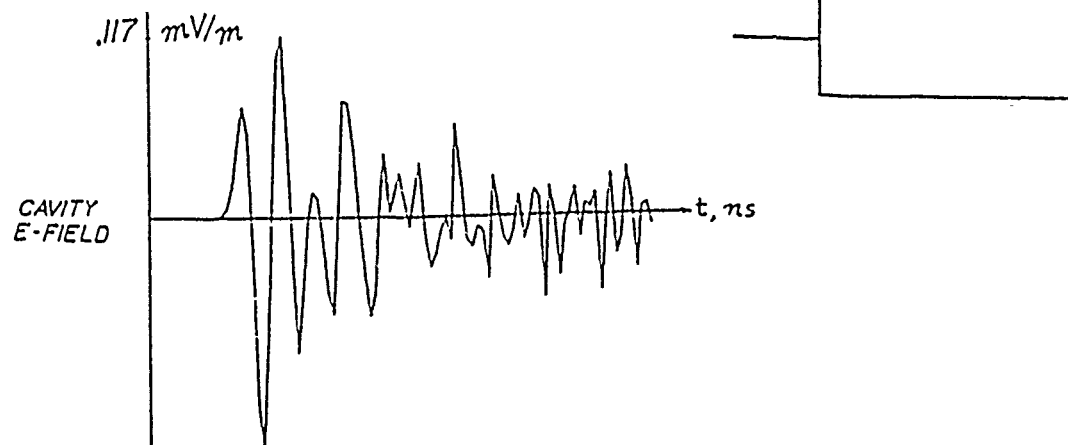
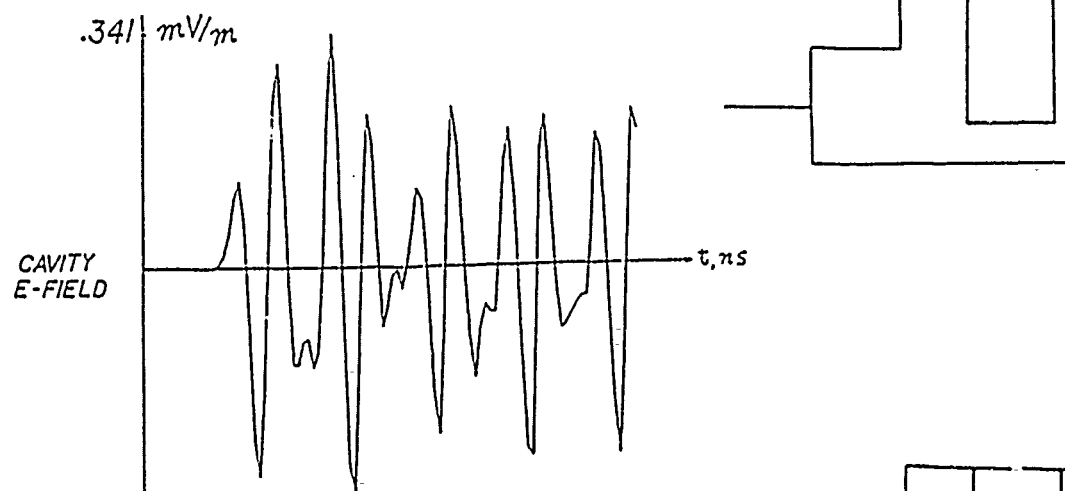
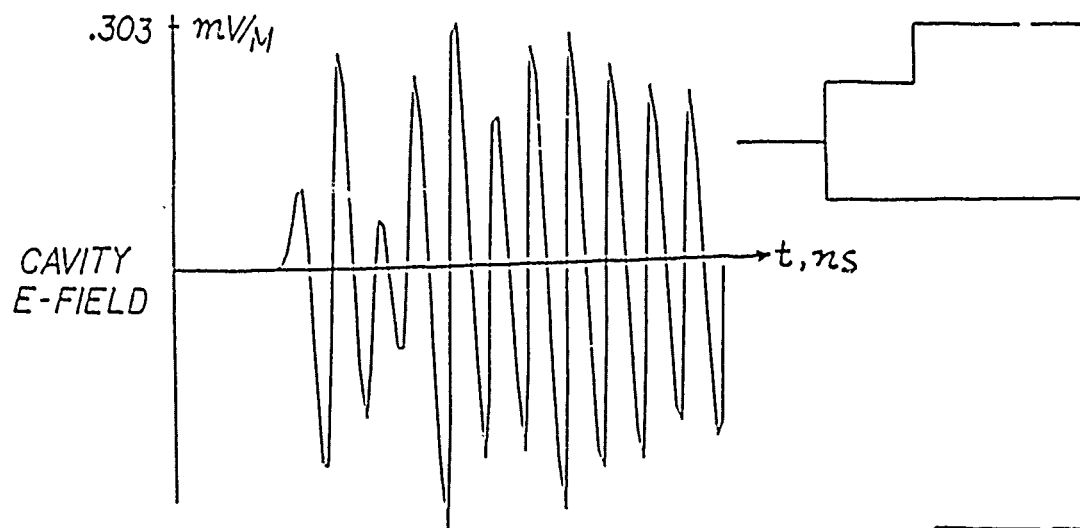
APERTURE
FIELD

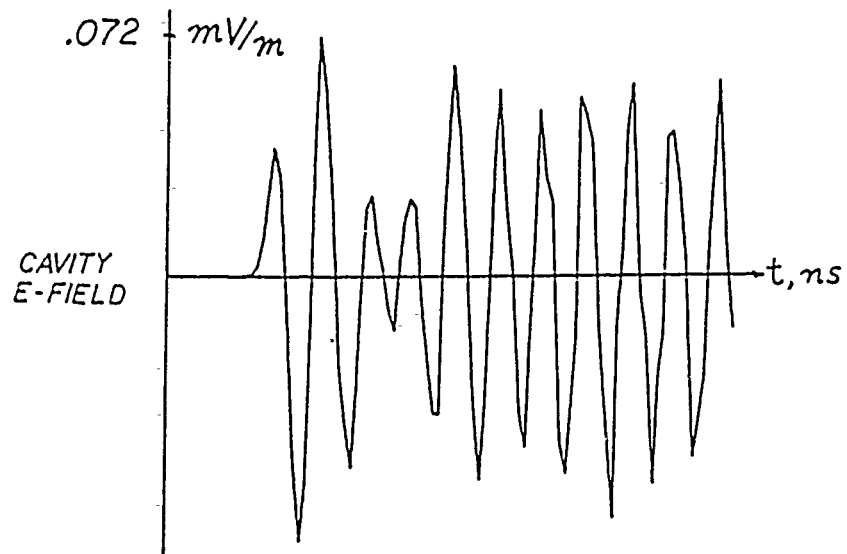
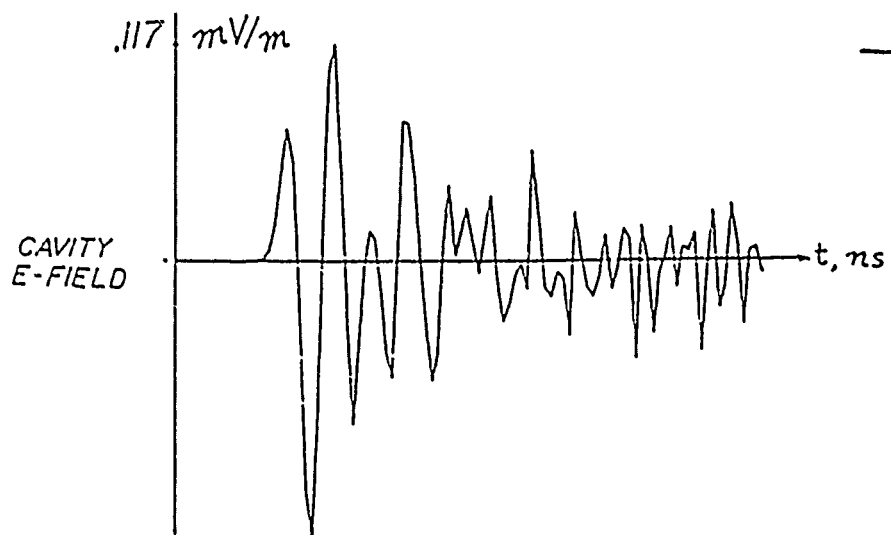


APERTURE
WIDTH $d = 0.2 \text{ M}$

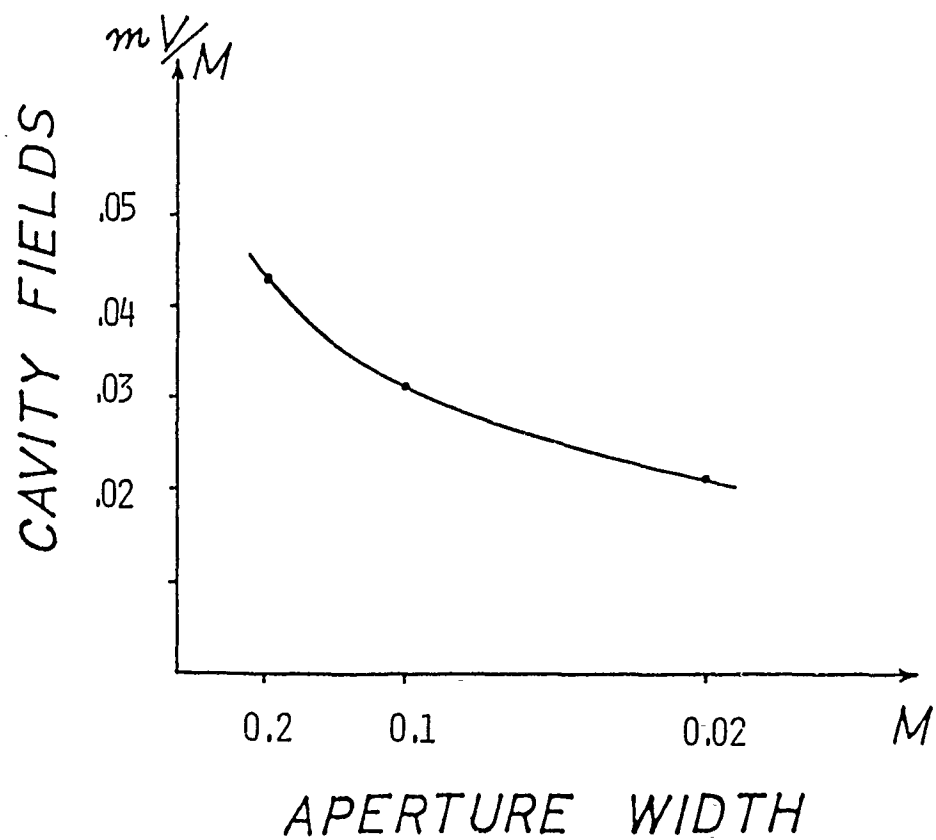
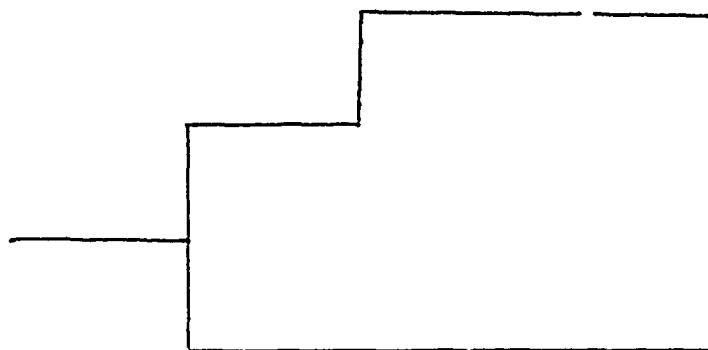
$$\frac{d}{\lambda} \ll 1$$

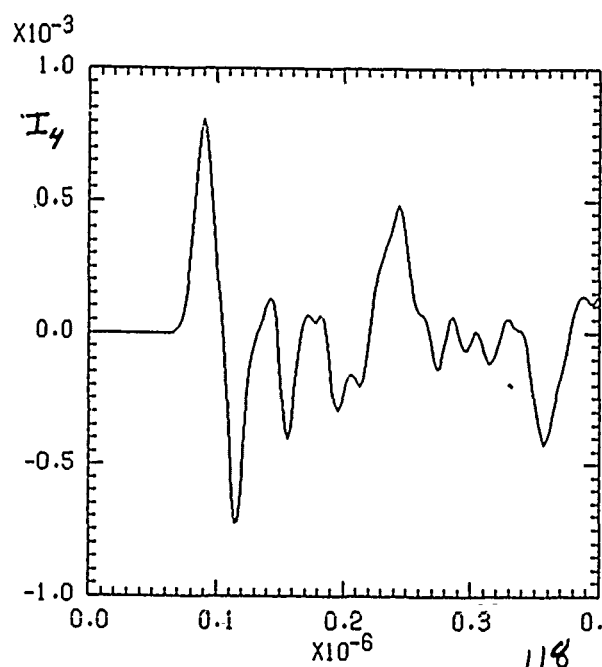
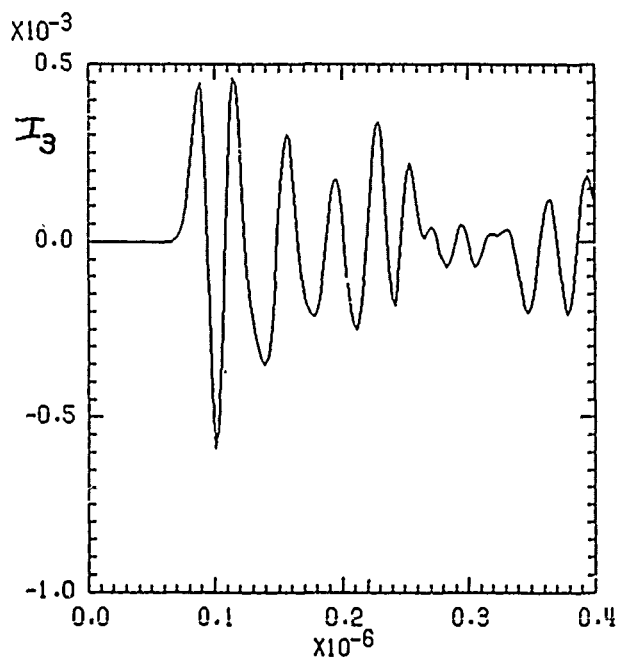
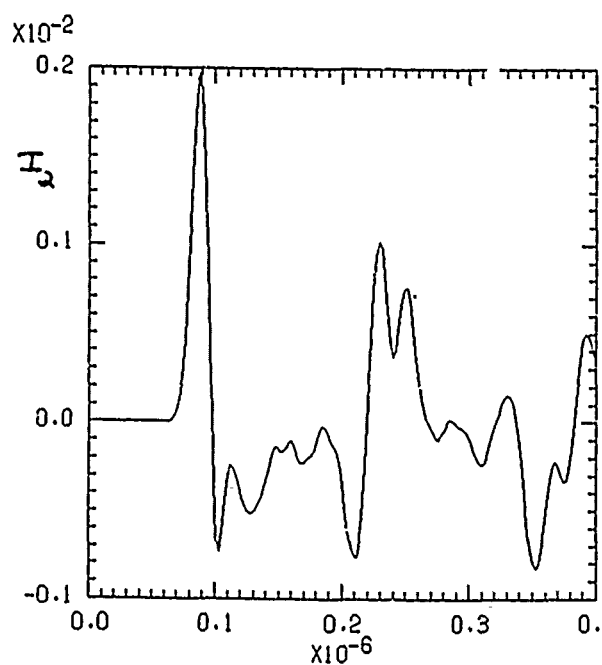
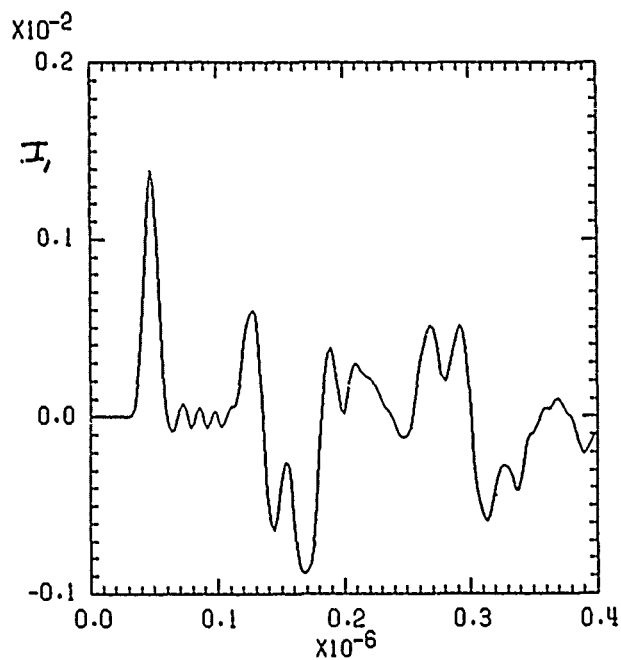
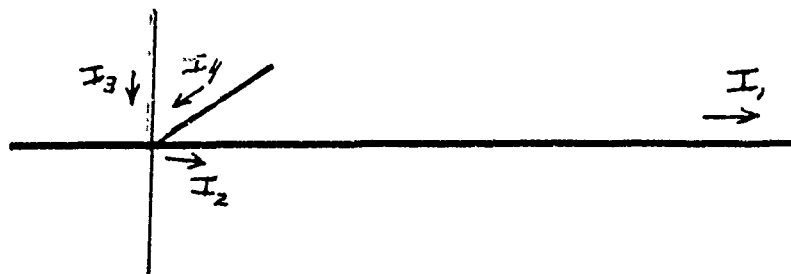






APERTURE SHIELDING





TIME DOMAIN FINITE DIFFERENCE MODELING ON THE FLOATING POINT SYSTEM 264 ARRAY PROCESSOR

K.S. Kunz, S.T. Pennock, and J.K. Breakall
Lawrence Livermore National Laboratory
P.O. Box 808, L-156
Livermore, CA 94550

A time domain finite difference electromagnetics code using the separate field formation first espoused by Yee (Ant. and Prop. Vol. AP-14, pp. 302-307, May 1966) has been implemented on the newly acquired Floating Point System 264 Array Processor within the Engineering Research Division at Lawrence Livermore National Laboratory. This machine provides 30 times the speed of a VAX 11/780 equipped with floating point accelerator. Such a speed approaches that of an early CRAY computer. With two million sixty-four bit words, a problem space on the order of $128 \times 64 \times 64$ cells can be modeled without resorting to virtual memory with the attendant performance loss.

Modeling of 10:1 scale model generic test objects is possible with a 0.3125 cm (1/8") cell size for an upper frequency limit of 12 GHz, using an eight-cell to a wavelength criterion. A day long run produces a 100 ns or 16,000 time step record that transforms into spectral data with a 10 MHz spacing. This is an adequate, not overly refined, resolution as determined experimentally. Data storage requirements are also extremely large, easily running up to 100 MB or more. From these considerations and the very low cost of computations on the FPS 264, a present day performance envelope can be assigned to this type of computation.

*Work performed under the auspices of the U.S. Department of Energy by the Lawrence Livermore National Laboratory under contract number W-7405-ENG-48.

TIME DOMAIN FINITE DIFFERENCE MODELING ON THE
FLOATING POINT SYSTEM 264 ARRAY PROCESSOR

K. S Kunz, S. T. Pennock and J. K. Breakall

Lawrence Livermore National Laboratory

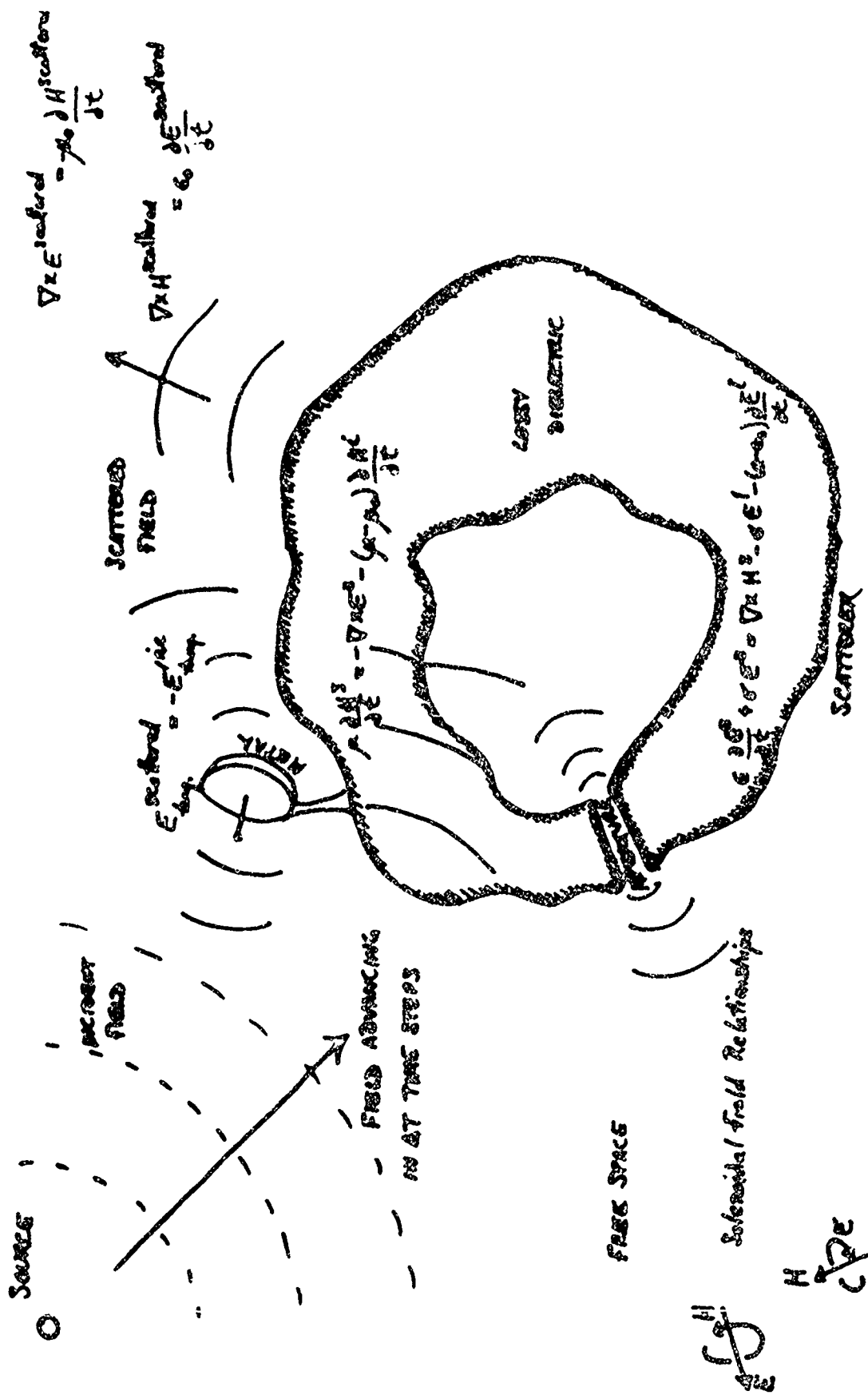
P.O. Box 808, L-156

Livermore, CA 94550



TIME DOMAIN FINITE DIFFERENCE (TDFD) MODELING

- o Description
- o Uses
- o Limitations



FDTD FORMALISM



$HX(I, J, K) = HX(I, J, K) - DTXMU * ((EZ(I, J+1, K) - EZ(I, J, K)) * DYOI(J)$
 $1 - (EY(I, J, K+1) - EY(I, J, K)) * DZOI(K))$

SAMPLE TDFD APPLICATIONS



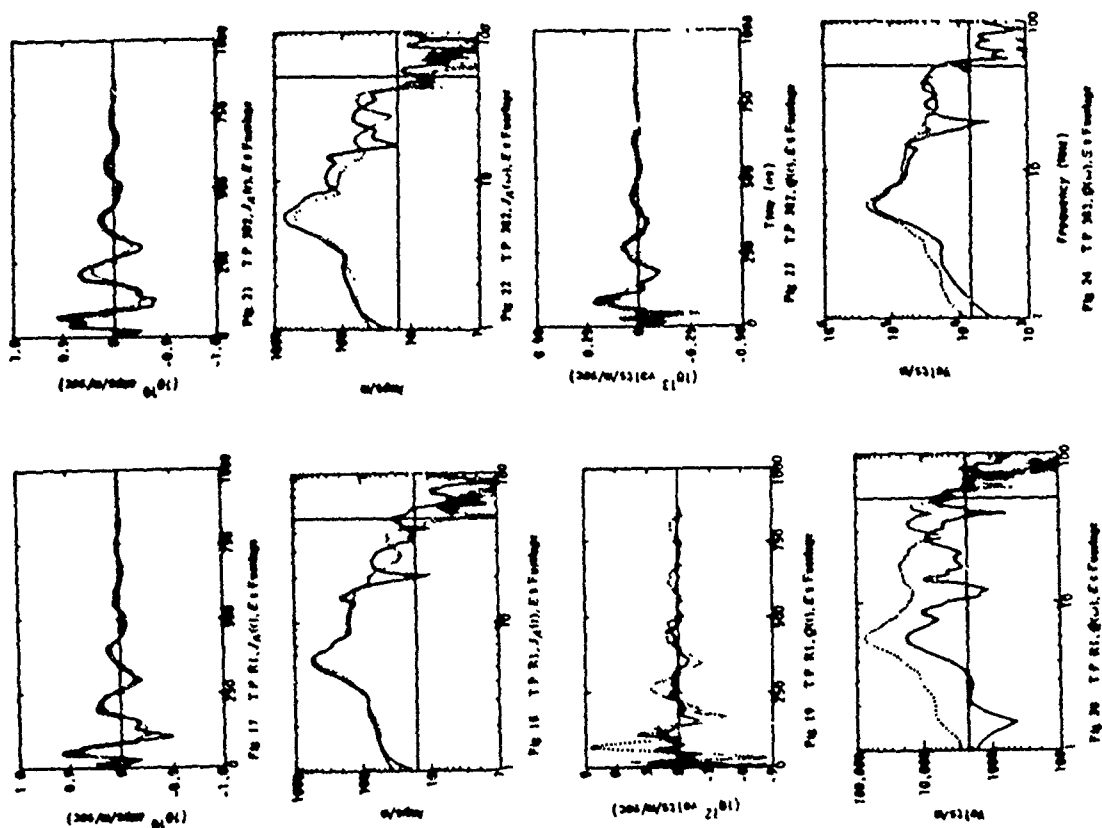


Figure 2. Sample of Predicted vs Measured F-111 Responses

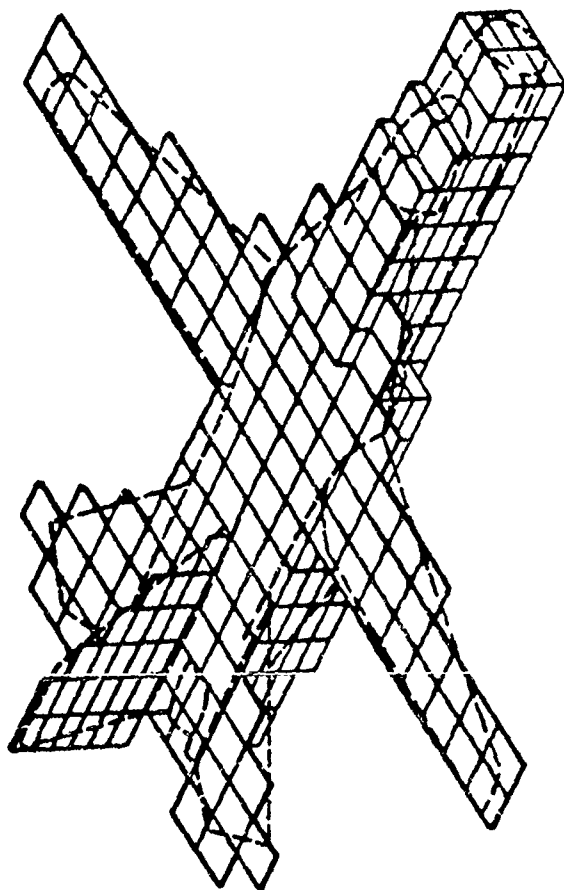


Figure 1. F-111 Finite Difference Model

LOSSY DIELECTRIC CAPABILITIES

The lossy-dielectric version of TIREDIE is based upon

$$\mu \frac{\partial \mathbf{H}}{\partial t} + \sigma \mathbf{H} = -\nabla \times \mathbf{E} - \sigma \mathbf{H} - (\mu - \mu_0) \frac{\partial \mathbf{H}}{\partial t}$$

$$\epsilon \frac{\partial \mathbf{E}}{\partial t} + \sigma \mathbf{E} = \nabla \times \mathbf{H} - \sigma \mathbf{E} - (\epsilon - \epsilon_0) \frac{\partial \mathbf{E}}{\partial t}$$

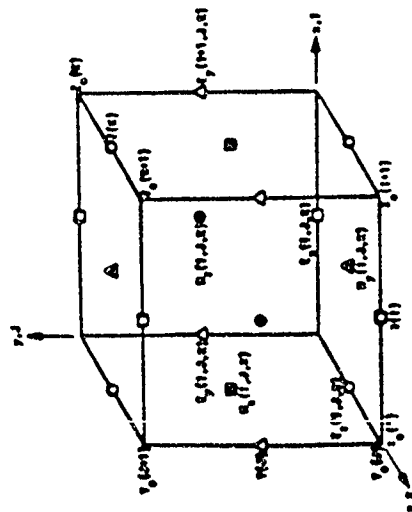


Fig. 1. Convention for labeling the (i, j, k) indices on the (x, y, z) problem space, and location of the six field evaluation points in a typical cell

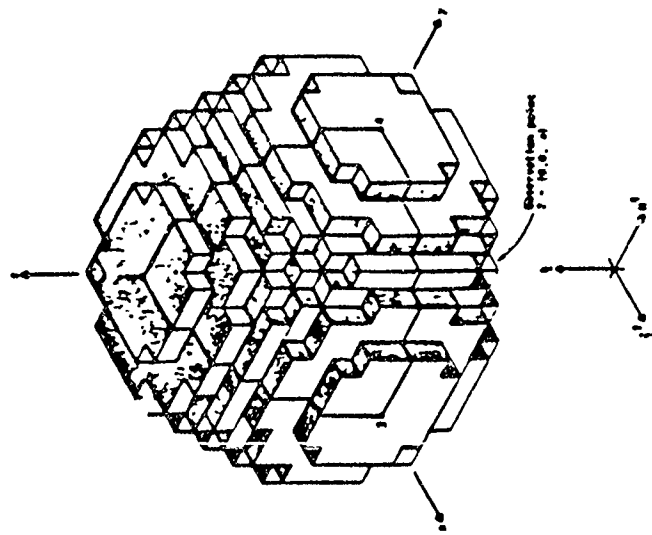


Fig. 2. TIREDIE model of a dielectric sphere with incident field and observation points indicated. The numerical observation points marked in this figure refer to the observation points used in Figs. 1, 2, 3.

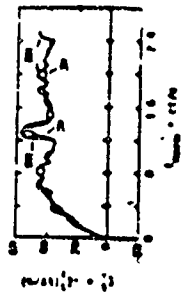


Fig. 3. $E_y^d = -E_y^i$ at observation point 2 (pole of illuminated hemisphere) for $\epsilon = 9\epsilon_0$.

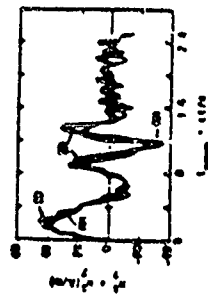


Fig. 6. $H_y^d = +H_y^i$ at observation point 2 for $\epsilon = 9\epsilon_0$.

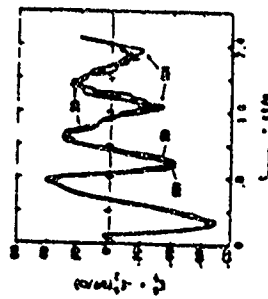


Fig. 7. $E_y^d = -E_y^i$ at observation point 1 for $\epsilon = 9\epsilon_0$.

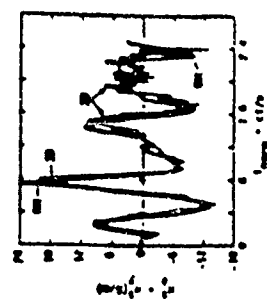


Fig. 8. $H_y^d = +H_y^i$ at observation point 1 for $\epsilon = 9\epsilon_0$.

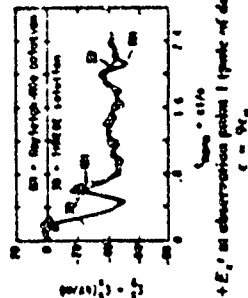


Fig. 3. $E_y^d = +E_y^i$ at observation point 1 (pole of dark hemisphere) for $\epsilon = 9\epsilon_0$.

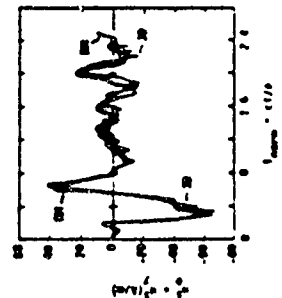


Fig. 4. $H_y^d = +H_y^i$ at observation 1 for $\epsilon = 9\epsilon_0$.

FIGURE 3.

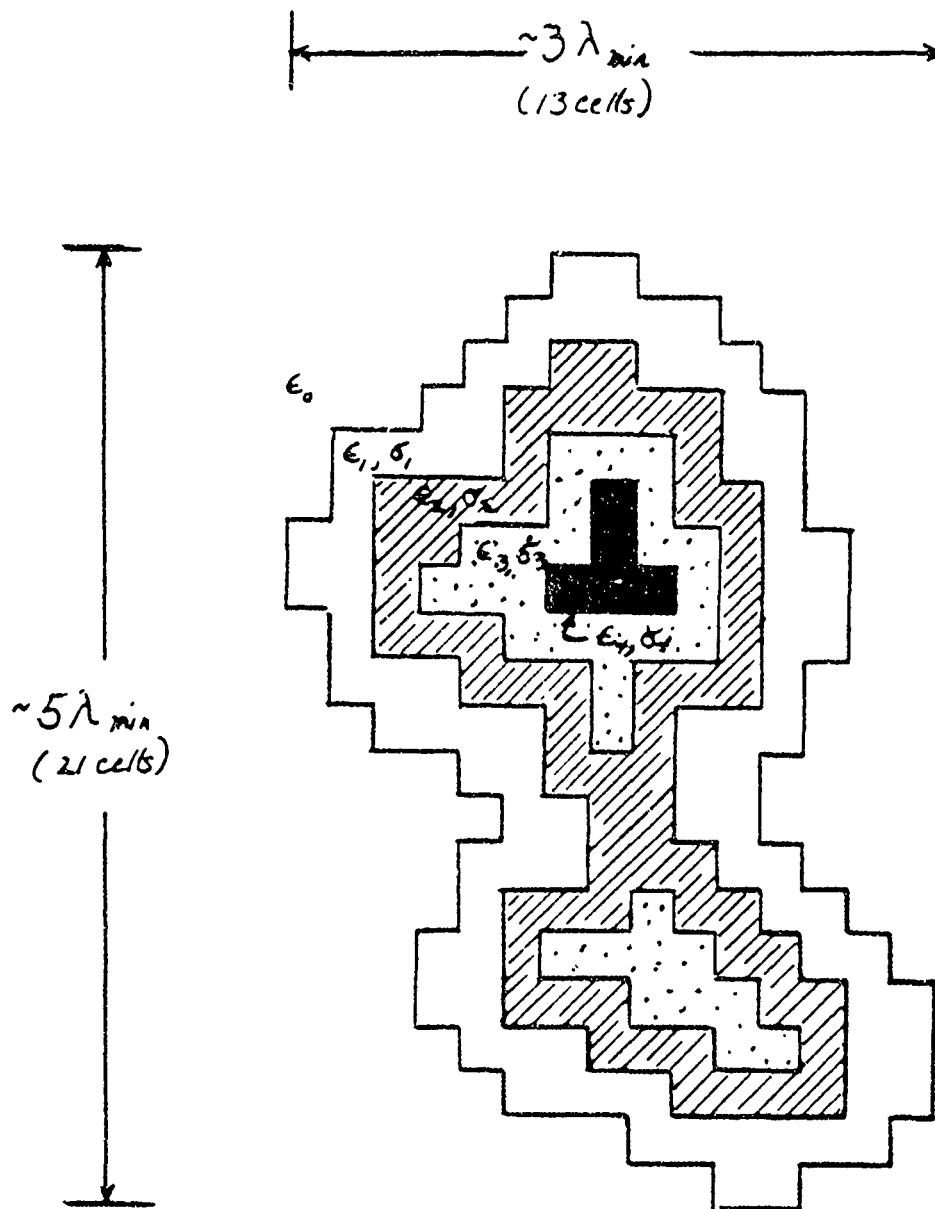


Figure 12. Aerosol Particle of Generalized Shape and Composition

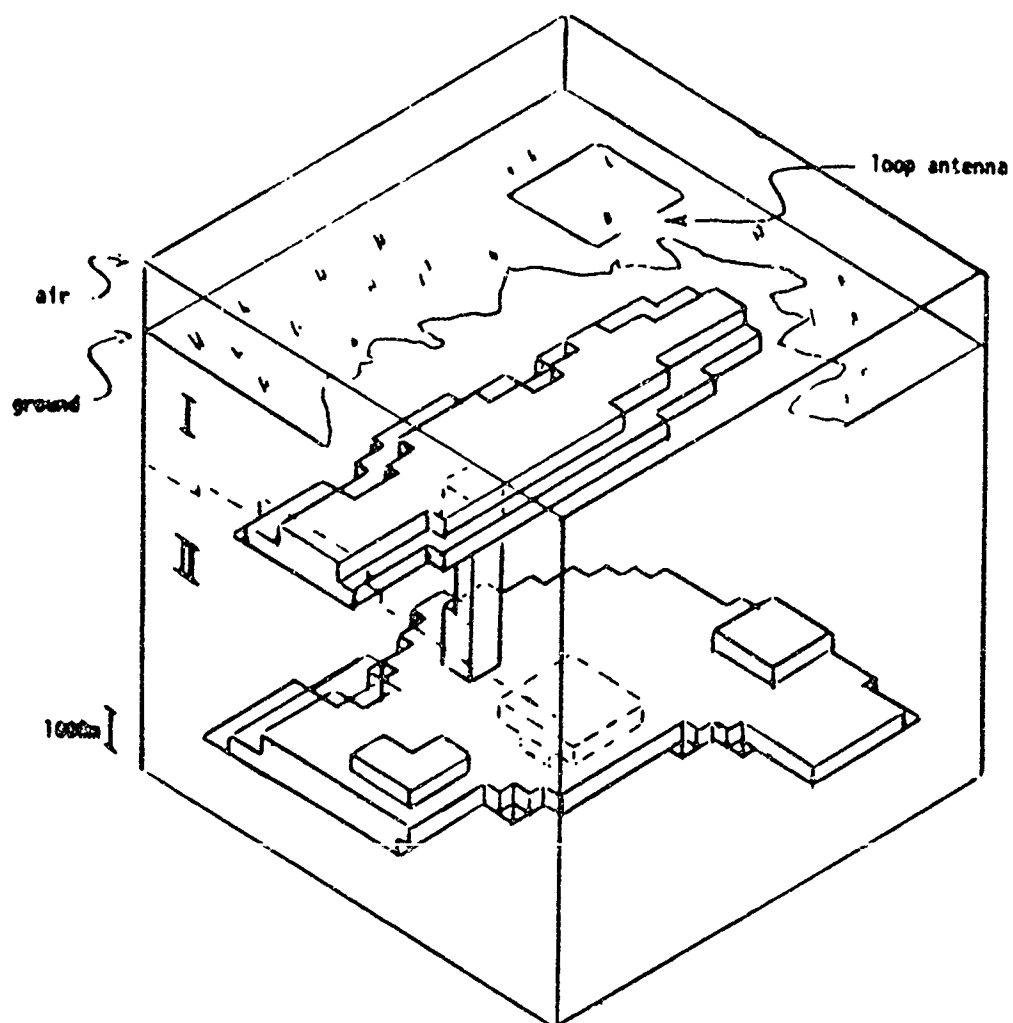
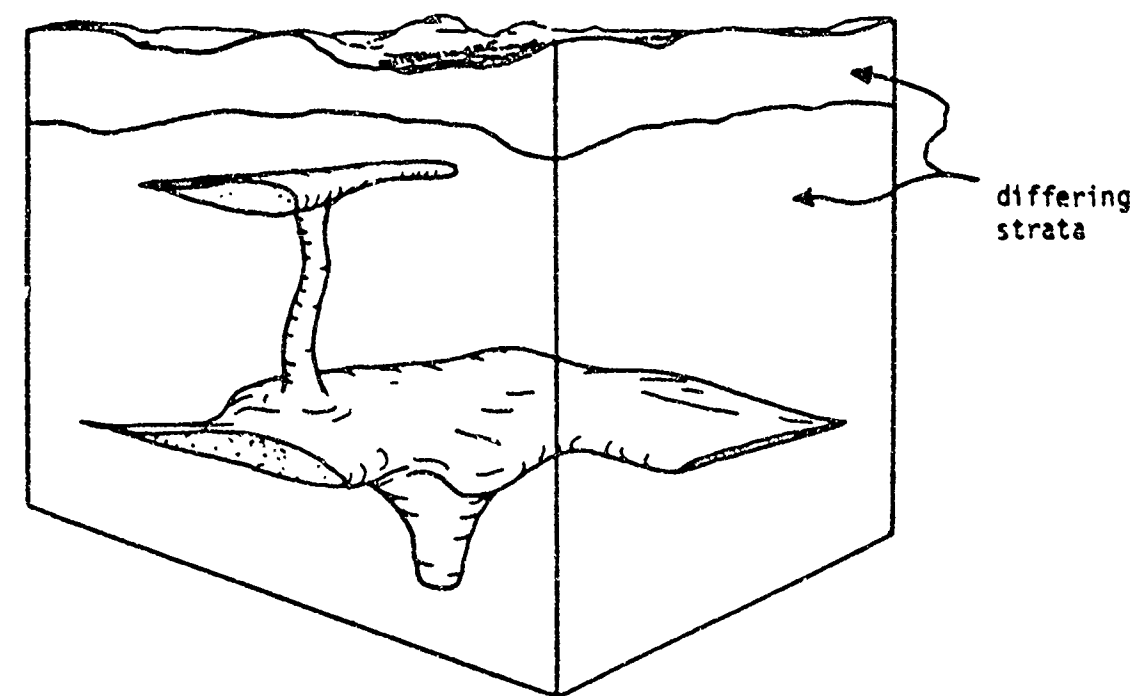
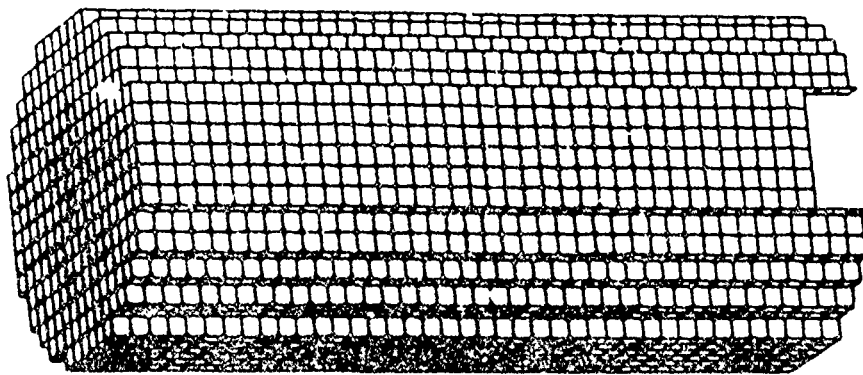
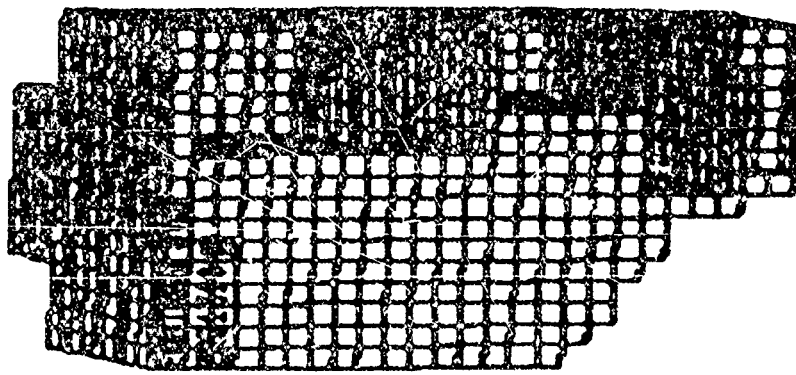


Figure 13. LDFD Model of a Buried Magma Deposit

LIMITATIONS



- o Speed (turnaround)
- o Memory (problem size)
- o Mass Storage (response characterization)
- o Graphics (geometry generation)



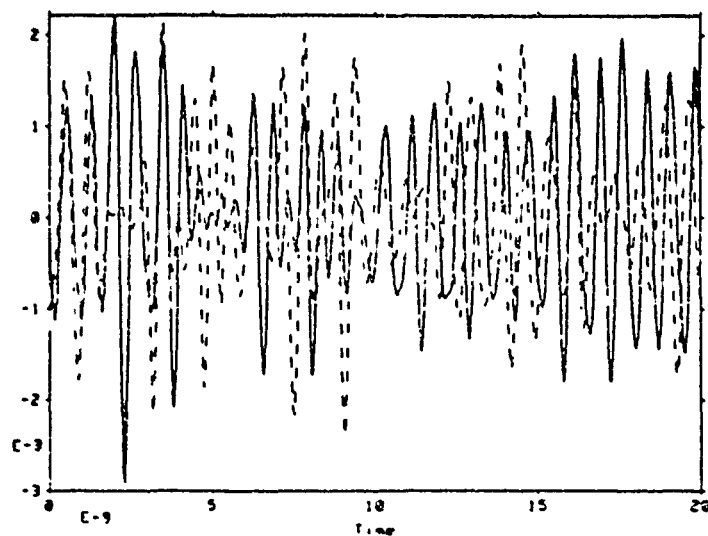


Figure 3-54 Time Domain Comparisons at Test Point 3, Experimental (Solid) and Compensated Computed (Dashed).

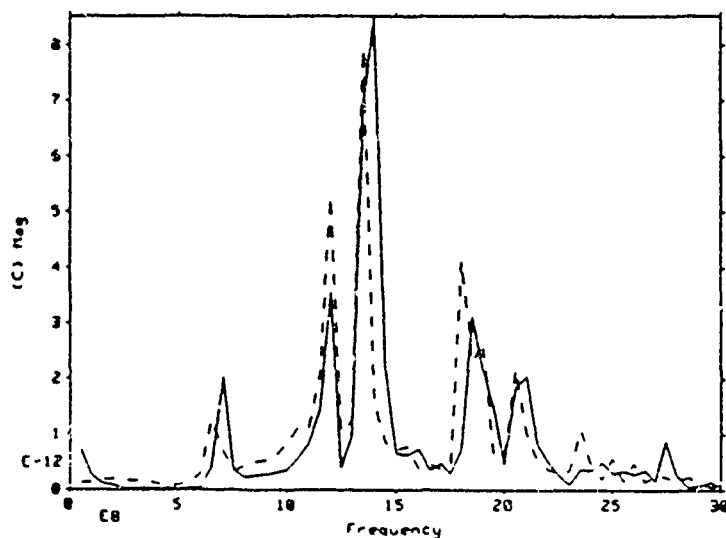


Figure 3-55 Fast Fourier Transform Comparisons at Test Point 3, Experimental (Solid) and Compensated Computed (Dashed).

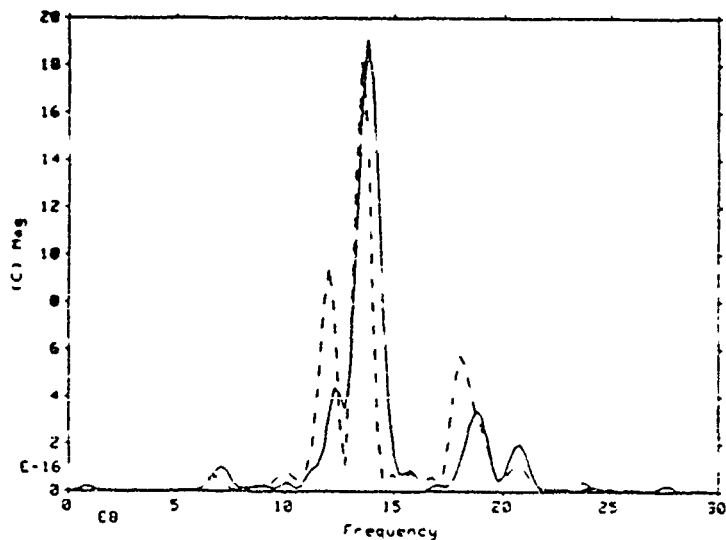


Figure 3-56 Power Spectral Density Comparisons at Test Point 3, Experimental (Solid) and Compensated Computed (Dashed).



- o Description
- o Uses at LLNL
- o Capabilities for TDFD Modeling

FPS 264 HARDWARE DESCRIPTION



- o Array Processor
- o 2 M Word (64 bit) Memory
- o "Transparent" to VAX



PERFORMANCE MEASUREMENTS

Program Execution Time (seconds)
Processor: VAX11/785 , FPS264/SJE/APFTN64/OPT=3

	<u>VAX 11/785</u>	<u>FPS-264</u>	<u>CPU RATIO</u>

		NEC, number of segments = 101	

FILL	57.60	2.04	28.2
FACTOR	22.4	0.188	119
TOTAL	80.0	2.224	32

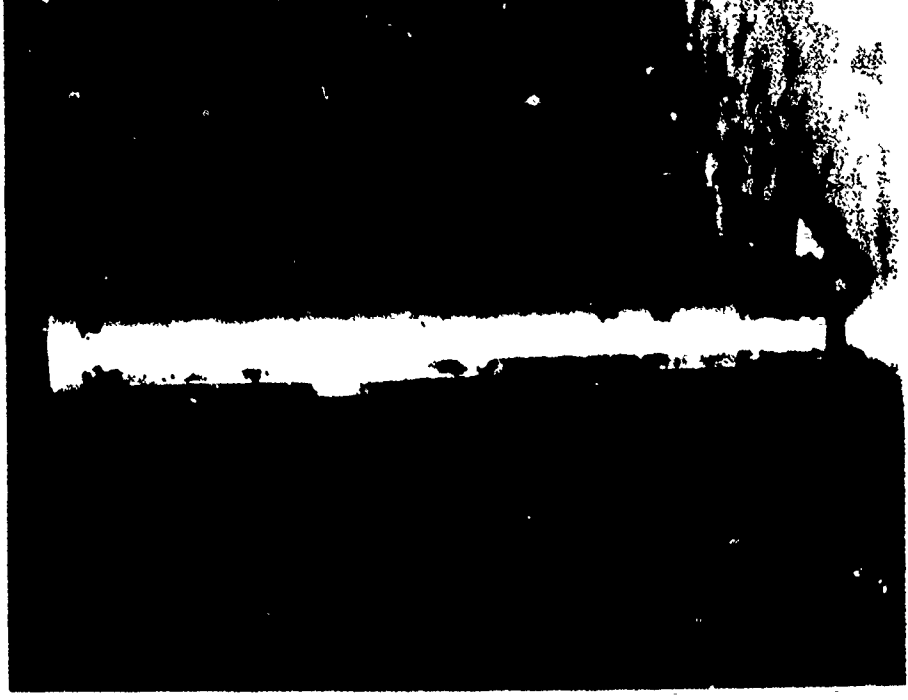
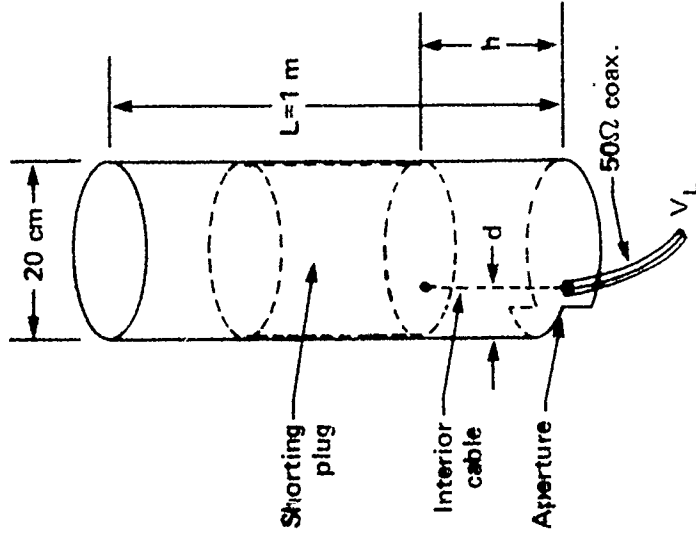
		NEC, number of segments = 299	

FILL	484	16.4	29.5
FACTOR	588	4.43	132.7
TOTAL	1072	20.83	49.5

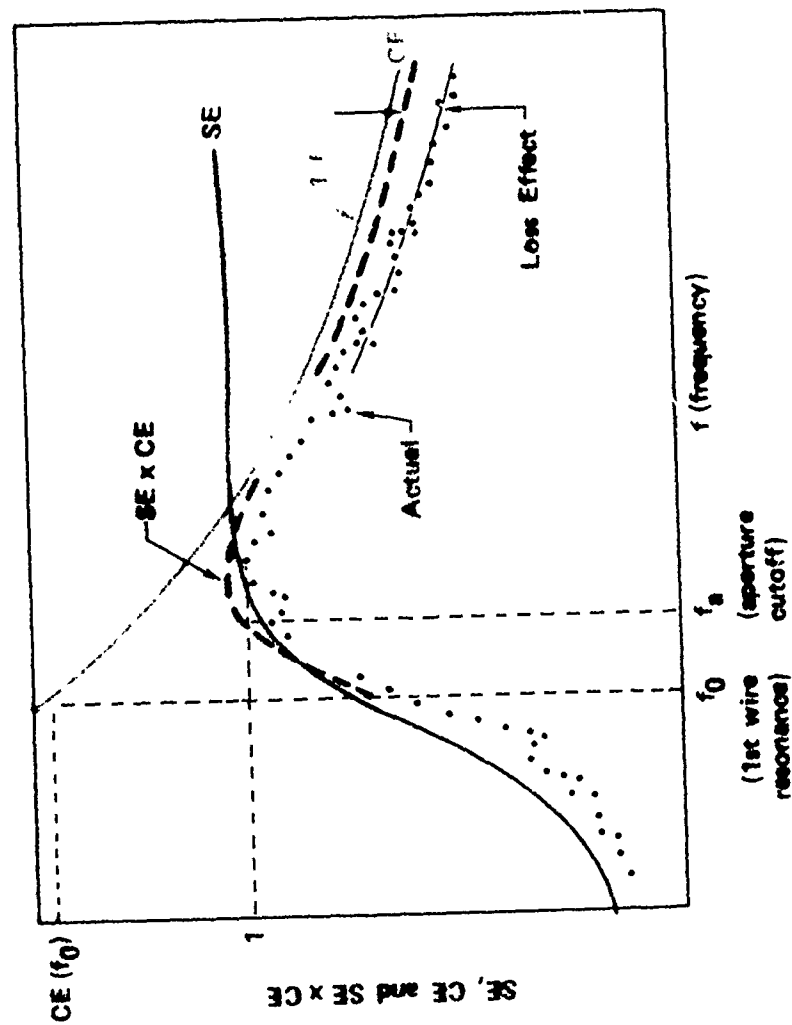
	G3DXL3, 89 * 33 * 33 space with 51 time steps		

	1226	38.4	31.9

PLUTO is a versatile generic test object



Given some basic topologic features, a predictive model bounds the coupled response



SE x CE Modeled Response Envelope

MODELING REQUIREMENTS FOR ADVANCED FPS 264 APPLICATIONS



- o Interior coupling to generic object
- o Interior wire resonances above and below (at least three) aperture cutoff
- o Thin aperture (10:1) modeled at least two cells high
- o 10 GHz or better upper frequency limit for 10:1 scale model
- o 10 MHz frequency domain spectrum resolution

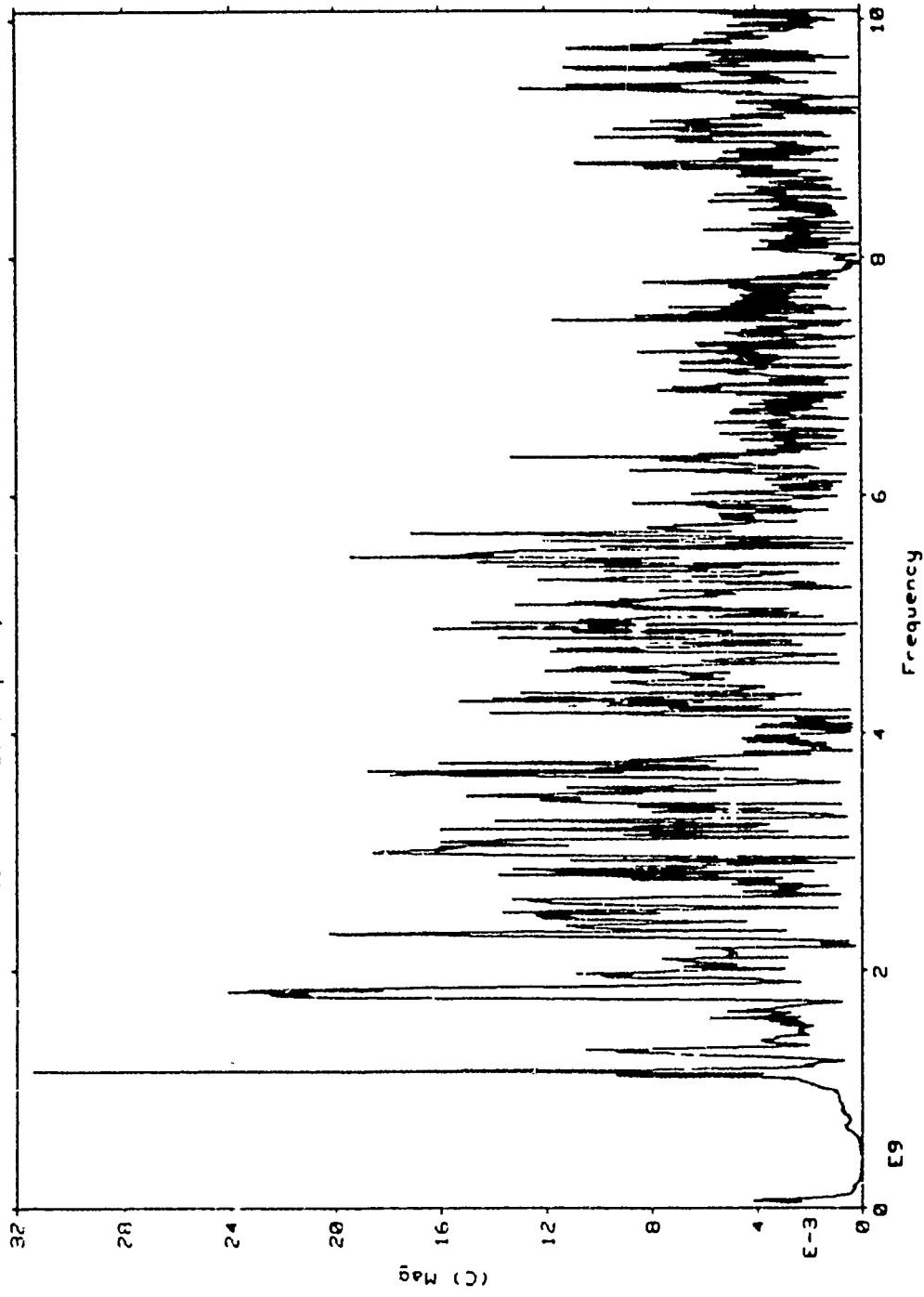
EXPERIMENTAL DATA OF VARYING RESOLUTION



..UDWIGSEN.PLUTO.L10DEC

21-FEB-86 15:02:05

DS #5 VI/EInc(aper), PLUTO A3T3L1 HI-Res

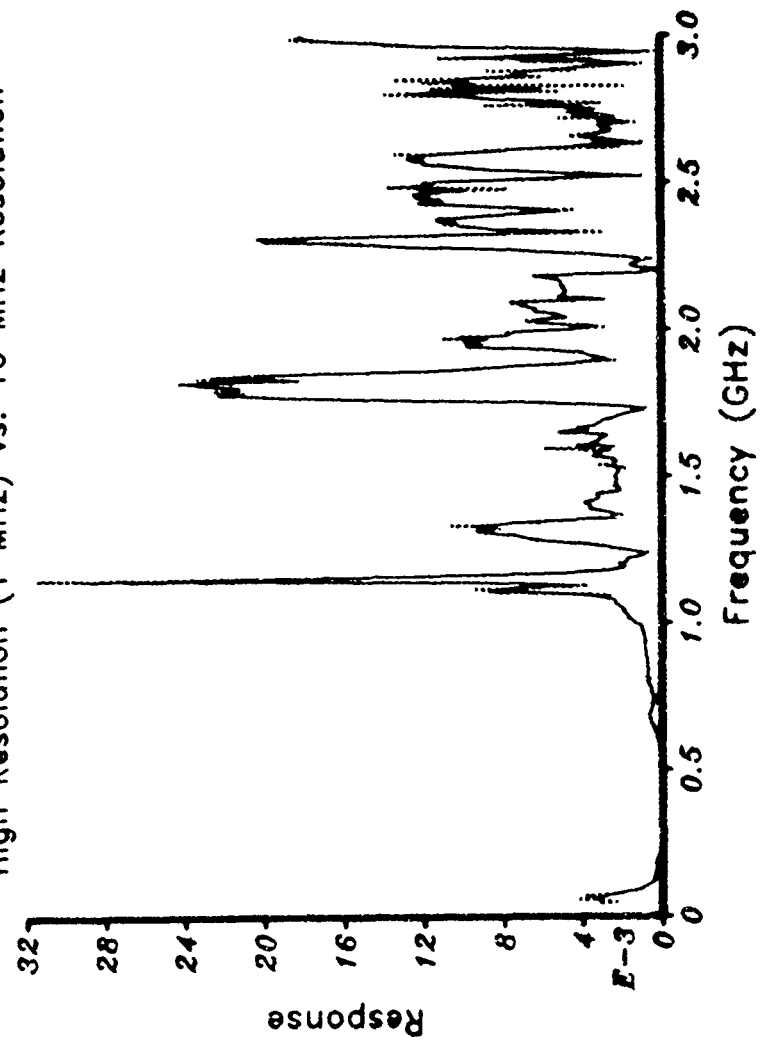


sig

21-FEB-86 16:08:26

IIREZ PLUTO MEASUREMENT A3T3L1
RD131::USER2_DISK:(HUDSON.PLUTO.L10DEG.8510.HIREZ)
IS NUMBER(S) 201 5

High Resolution (1 MHz) vs. 10 MHz Resolution



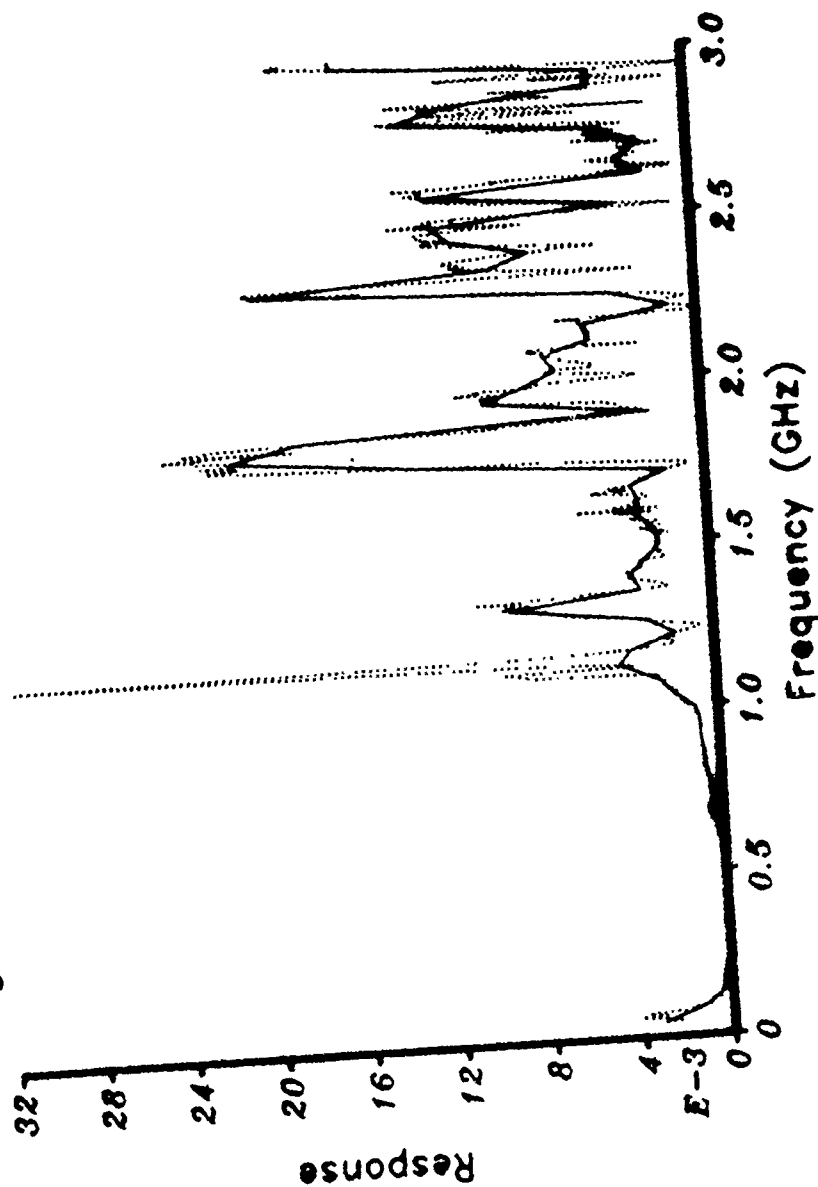
LEGEND

10MHz RES
1 MHz RES

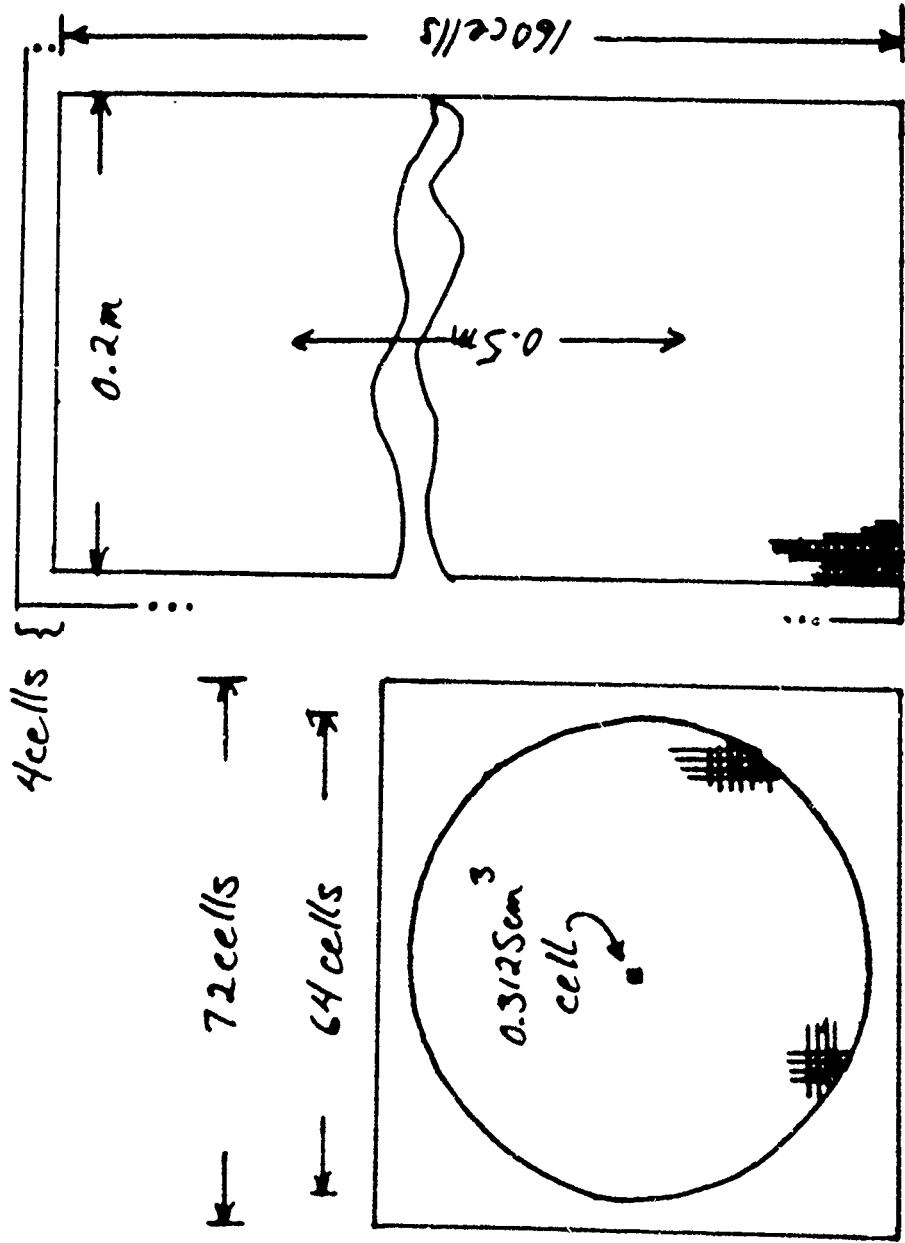
21-FEB-86 16:41:51

REZ PLUTO MEASUREMENT A3T3L1
D131::USER2_DISK:[HUDSON.PLUTO.L10DEG.8510.HIREZ]
NUMBER(S) 202 5

High Resolution (1MHz) vs. 45MHz Resolution



MODIFIED PLUTO FOR ADVANCED APPLICATIONS



COMPUTATIONAL PARAMETERS



- o Problem Space

$72 \times 72 \times 164$

- o Cell Size

0.3125 cm ($1/8''$)

12 GHz upper frequency limit at $\lambda = 8 \Delta X$

- o Time Steps

16,000 for 100 ns record and 10 MHz resolution

~ 1 day run time

COMPUTATIONAL PARAMETERS (Cont'd)



- o **Storage**

24 MB/slice (every 4th time step and every other spatial point)

- o **Cost**

Free (at present) on FPS

\$8,000/run for 8 hours of CRAY X-MP at ~\$1,000/hour

**SCATTERING BY A LOSSY DIELECTRIC
AND MAGNETIC BODY OF ARBITRARY
CROSS-SECTION**

JUANG-LU LIN
BOEING MILITARY AIRPLANE COMPANY
P.O. Box 3707
Seattle, WA 98124-2207

Scattering by a two-dimensional lossy dielectric and magnetic body of an arbitrary cross-section is investigated numerically and experimentally for both E and H polarized incident waves. Application of superposition and duality principles results in coupled integral equations for the unknown electric and magnetic field intensities within the body material. Following the conventional method of moments technique, the entire body is divided into electrically small cells such that the integral equations can be converted into a set of linear equations by pulse expansion and point matching at the center of each cell. The radar cross sections are then computed based on the scattered fields maintained by the fields within the body material. To check the accuracy of the results, computations on the echo area are compared with either the exact solutions or measurements.

SCATTERING BY A LOSSY DIELECTRIC AND MAGNETIC BODY OF ARBITRARY CROSS-SECTION

1. INTRODUCTION

In recent years much research has been conducted on reducing the radar cross section of metallic objects. The widely adopted techniques include the use of radar absorbing material and reshaping of the body. In this connection, it is highly desirable that a computer code be available to compute the effect of reshaping the body or changing the parameters in the absorbing material. As a result, much effort has been expended in the past on developing a computer program which can predict the backscatter of an aero-shaped body such as an airfoil composed of a conducting surface covered with lossy dielectric foam and magnetic radar absorbing material (RAM) over the frequency range of 2 to 18 GHz. Unfortunately, most body shapes of interest possess irregular geometries and the materials used are often lossy. Also it is often required to know the backscatter of an object illuminated by both the E- and H-polarized plane waves. These factors complicate the problem. A careful analysis and a proper measurement for verification are indispensable to insure the numerical procedures and approximations yield sufficiently accurate results.

As a result, a computer code, LINKS, was developed at the Boeing Company, which solves the electromagnetic scattering problems of two-dimensional lossy dielectric and magnetic bodies illuminated by both the E and H polarized plane waves as shown in Figure 1. The theory is based on the integral equations and numerical solution is obtained by applying the Method of Moments (MOM). Details of the theoretical development is available elsewhere (1) and will be omitted here.

The objective of this paper is to show the comparisons between prediction and measurement on certain types of test objects used. With the uncertainty in the material electromagnetic parameters, the results obtained are considered satisfactory within specified frequency ranges. The test objects include a conducting plate, a conducting plate with a resistive card, a conducting ogive, a conducting ogive coated with a magnetic material, a conducting ogive coated with a magnetic material and with the leading edge covered by a lossy dielectric foam.

2. Comparisons between prediction and measurement.

To check the accuracy of the computer code, a series of measurements were made at Boeing's indoor ranges for various shapes, materials, frequencies, and polarizations.

(i) Case 1 A plane slab, a wedge, a wedge-cylinder made of a plexiglass.

Plexiglass is a lossless dielectric with a relative permittivity of 2.6 at the frequency range used in the measurements. The dimensions of the test objects are as shown in Figure 2. Figure 3 and 4 show comparisons between prediction and measurement at 3.16 GHz for the plexiglass

slab illuminated by an E-polarized and H-polarized wave, respectively.

In general, they compare very well. It appears that the discrepancy largely comes from the material inhomogeneity and imperfect construction of the test object.

In the same manner, the RCS of a plexiglass wedge with enclosed angle 30° was measured and compared very well with the computations shown in Figure 5 for E-polarized wave at 3.16 GHz.

Figure 6 shows the comparisons between the computations and measurements on RCS for a plexiglass wedge cylinder of enclosed angle 30° illuminated by an H-polarized wave. The difference in the comparison shows within 2 dB.

(ii) Case 2 Conducting Rectangular Plate with a Resistive Card (Figure 7).

The scattering body is a conducting plate of cross-section dimensions $1/16"$ x $9.25"$ ($\times 12"$ long) with a $3.15"$ resistive card attached to one end of the plate as shown in Figure 7. The resistances in Ω/\square were chosen specifically to reduce the traveling wave. They were implemented by 9 resistive strips of $0.35"$ wide with Ω/\square of 21, 89, 251, 489, 830, 1190, 1760, 2700, and 3500 as shown in the resistivity vs displacement plot in Figure 7. The RCS is also plotted as a function of aspect angle at 6 GHz. In modeling the conducting plate, a box formed by four conducting surfaces is utilized to include the effect of the plate thickness. Because of this special treatment on the thickness, the comparisons near the grazing angle ($\theta \approx 0^\circ$) improve to within a dB or so. As can be seen, the traveling wave peak at 25° has been reduced by 10 dB and agreement between measurement and computation is good. The results shown in Figure 7 also confirm the fact that the resistive card at the rear end reduces the traveling peak of the H-polarized wave looking at the front end. The RCS looking at the rear end is essentially unchanged from that of a plate without a resistive card.

(iii) Case 3 A conducting ogive of $1.25" \times 10"$ (Figure 8)

A series of measurements were made for this ogive ranging from 2 to 18 GHz. Comparisons were made in Figure 8 with the computations for 3, 7, and 14 GHz. The ogive is made of solid aluminum with good machine finish. The agreement is within 1 - 2 dB.

(iv) Case 4 A conducting Airfoil of $1.5" \times 10"$ with leading edge angle 30° and trailing angle 11° (Figures 9 and 10).

The airfoil is of irregular shape, and therefore, it requires

a more thorough inspection of the design drawing and the finished product. For example, we started with the design drawing as shown in Figure 9 to compute RCS as a function of aspect angle at 3.5 GHz. Based on past experience, we expected to obtain a better agreement than this. With a careful examination of the test body, we found that the constructed shape was somewhat different from the design drawing. Therefore, we used the actual test body as the model and re-computed the RCS. Comparison is shown in Figure 10. Much better agreement was then obtained. With the same constructed model, the agreement between the computation and measurement looks fairly good at 5 GHz. This is a good example of emphasizing the importance of using the test body as a final check on the computational model in use.

- (v) Case 5 These cases included magnetic material and lossy foam applications to conductive ogives. Comparisons of computed and measured data are contained elsewhere (2) and are classified confidential. The results are good and agreements are usually within 1-3 dB after the error for phase front curvature in the measurements (near field) are removed.

3. CONCLUSIONS

Theoretical formulation is presented for backscattering from two-dimensional lossy dielectric and magnetic bodies. Integral equations are formulated and solved by the method of moments. A series of measurements were made for various frequencies, polarizations and combinations of materials to verify the theory. The test bodies evaluated include a conducting plate; a conducting plate with a resistive card; a conducting ogive; a conducting ogive coated with a lossy magnetic material; a conducting ogive covered with lossy dielectrics; and, a conducting ogive coated with a lossy magnetic material and the leading edge covered by lossy dielectric foam. The numerical results compare favorably with the measurements in most cases.

4. REFERENCES

1. J. L. Lin "Electromagnetic Scattering from Two-Dimensional Lossy Dielectric and Magnetic Bodies", BAC Memo No. 2-3745-RHW-012 dated April 5, 1985.
2. BAC 1984 IR&D year end report.

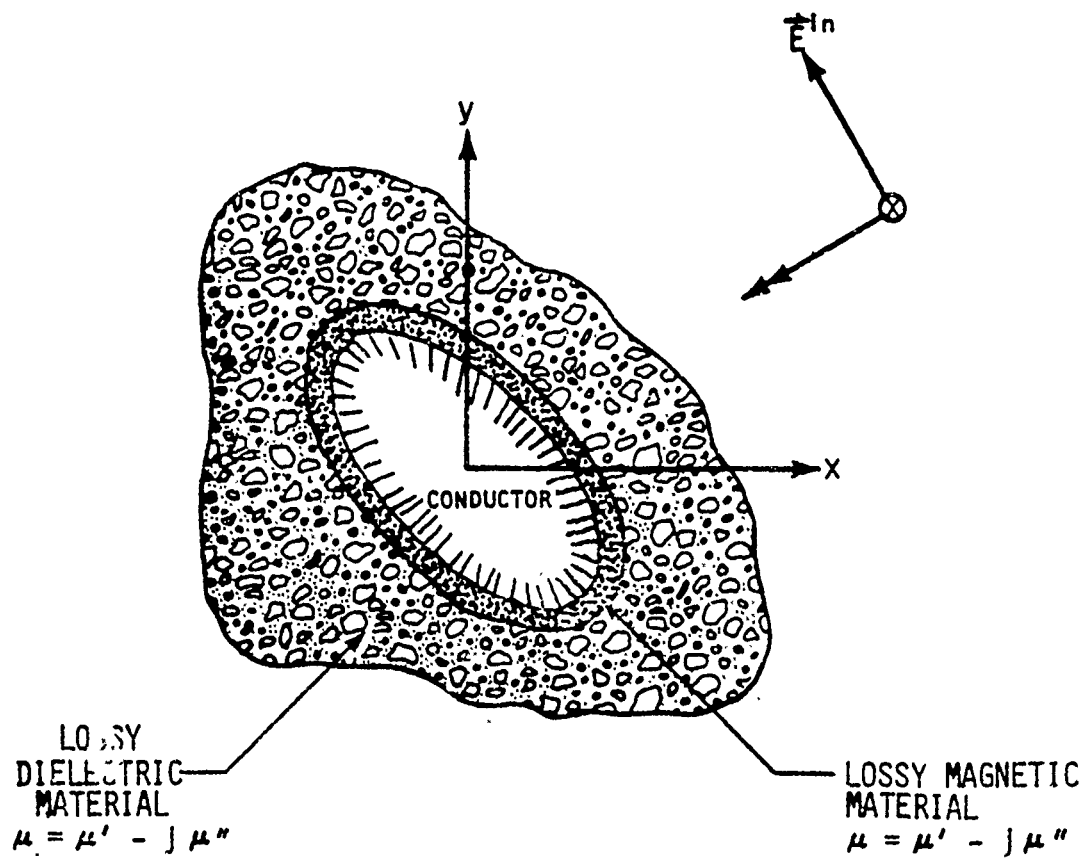


Figure 1. Geometry for Object with Conductor and Lossy Dielectric and Magnetic Material for H Polarized Wave

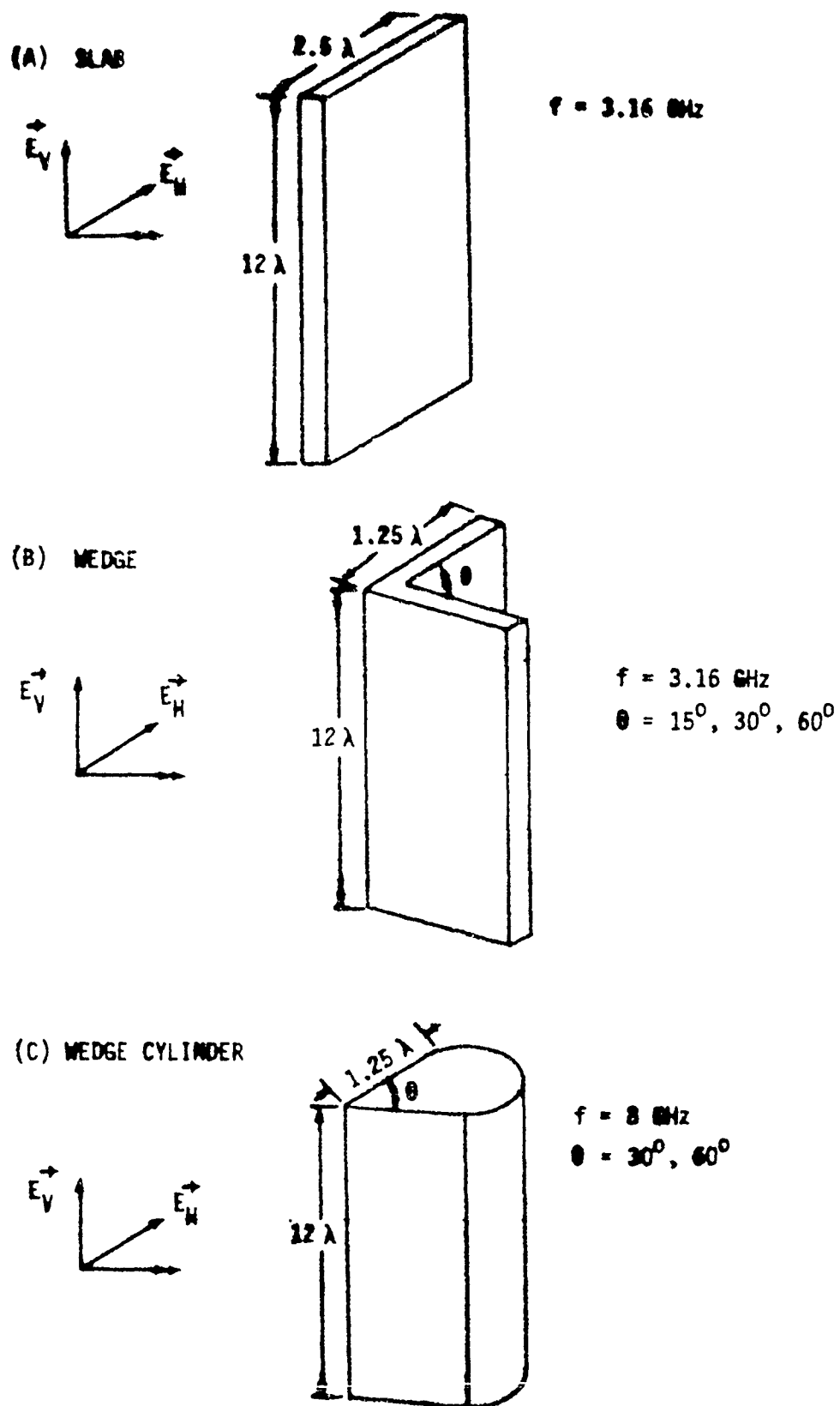


Figure 2. Dimensions and Geometries of the Test Objects

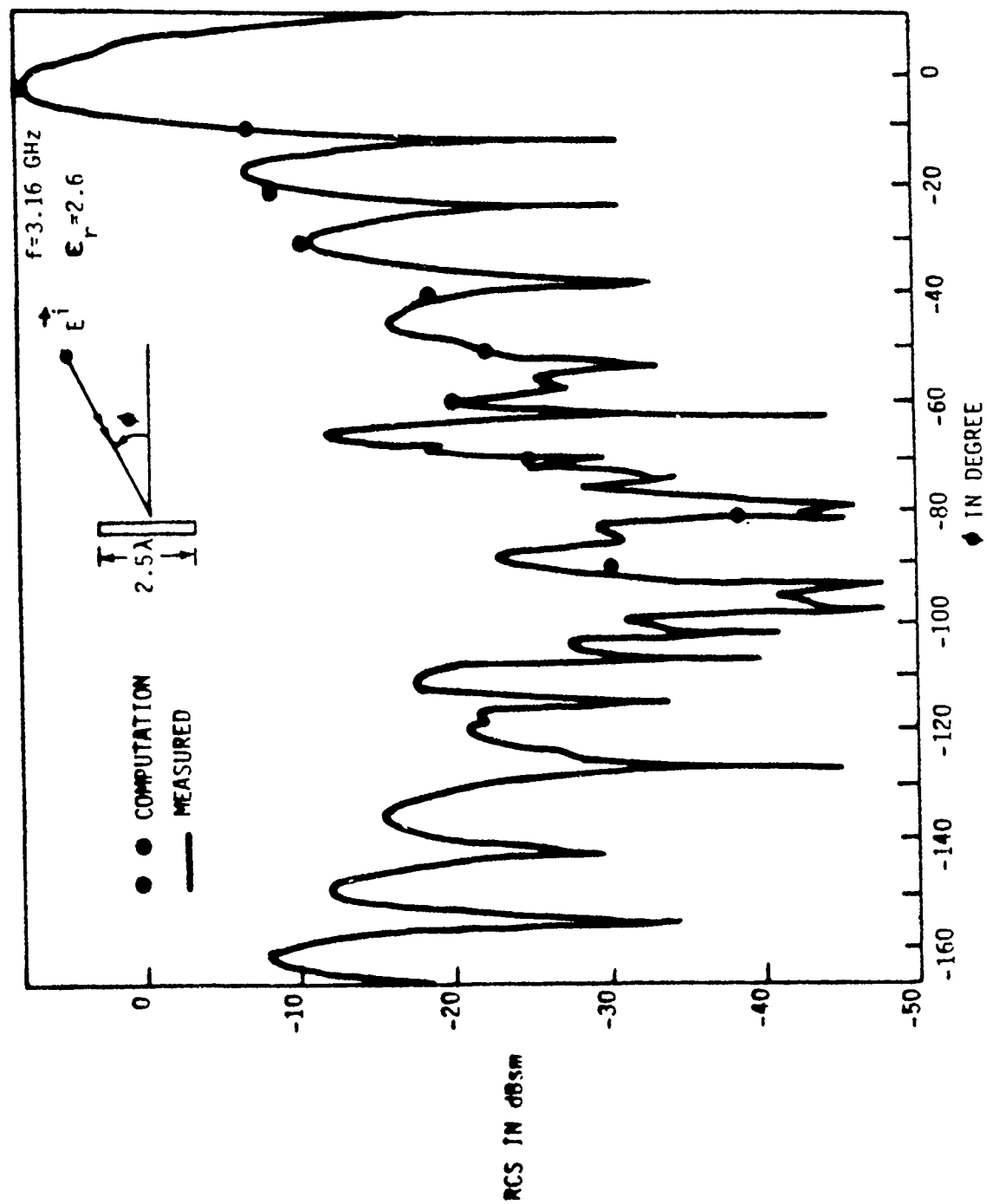


Figure 3. Computed and Measured RCS of a Plexiglas Slab for E-Polarized Incident Wave

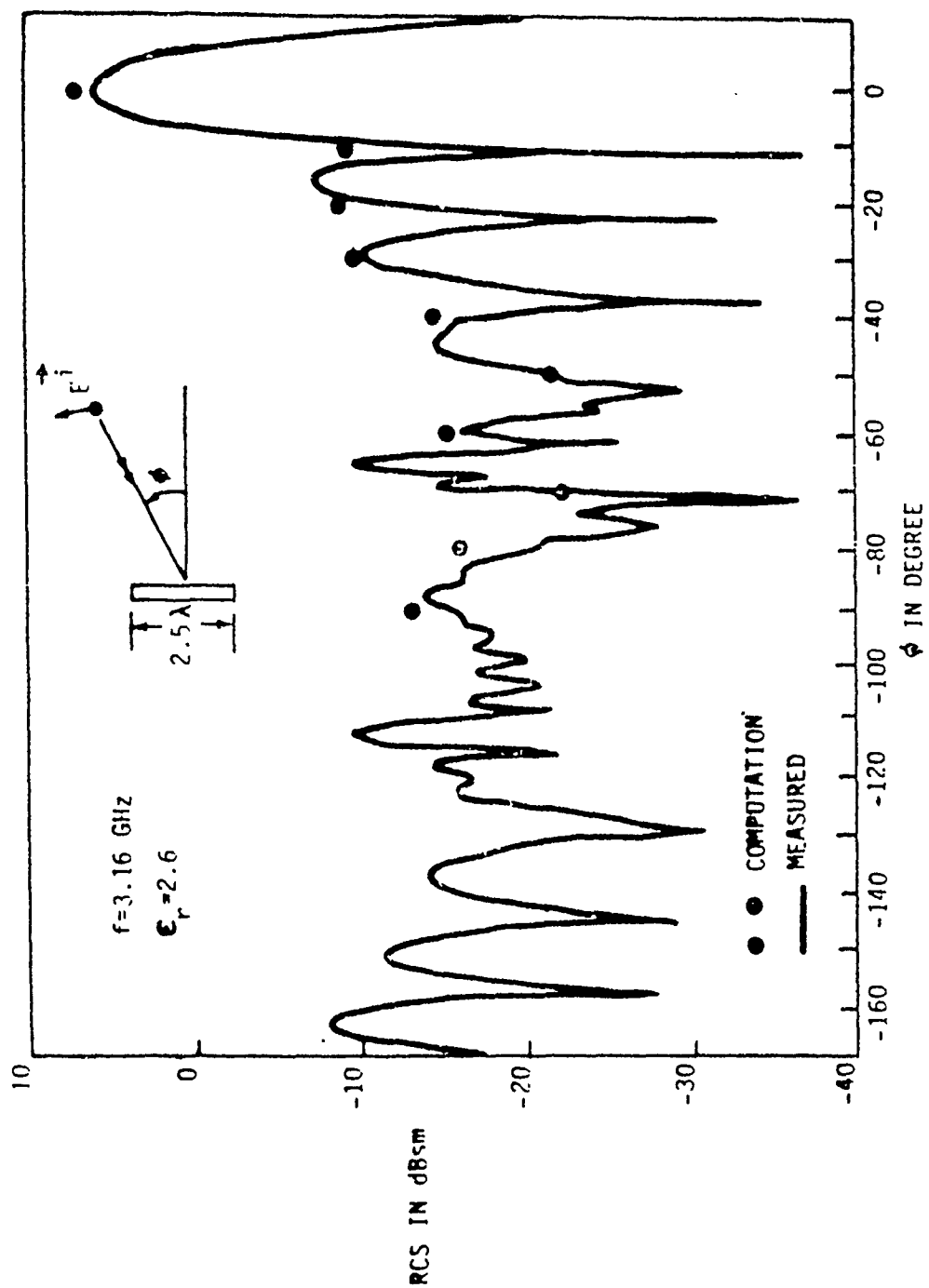


Figure 4. Computed and Measured RCS of a Plexiglas Slab for H-Polarized Incident Wave

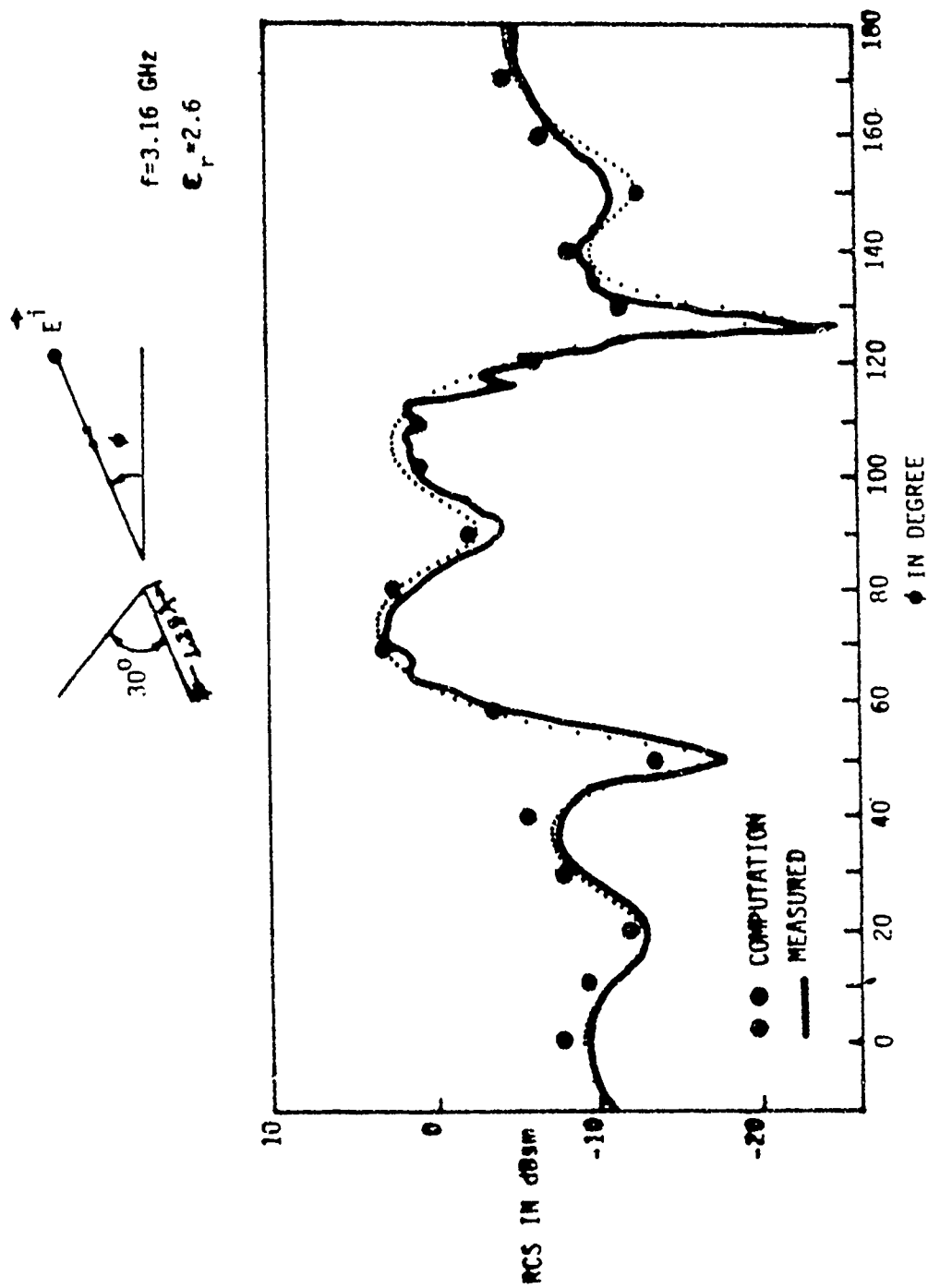


Figure 5. Computed and Measured RCS of a Plexiglas Wedge of Enclosed Angle 30° for E-Polarized Incident Wave

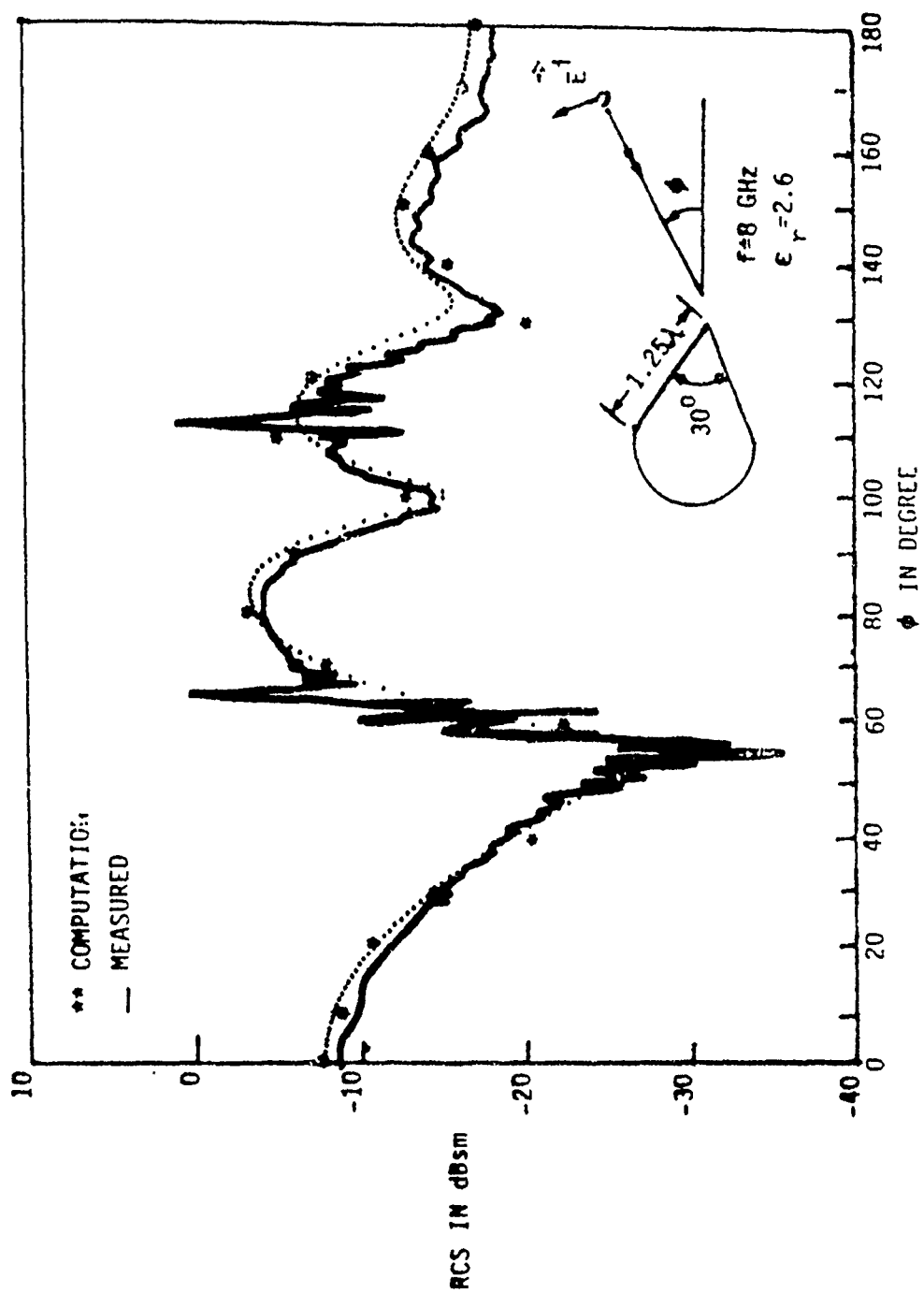


Figure 6. Computed and Measured RCS of a Plexiglas Wedge Cylinder for H-Polarized Incident Wave

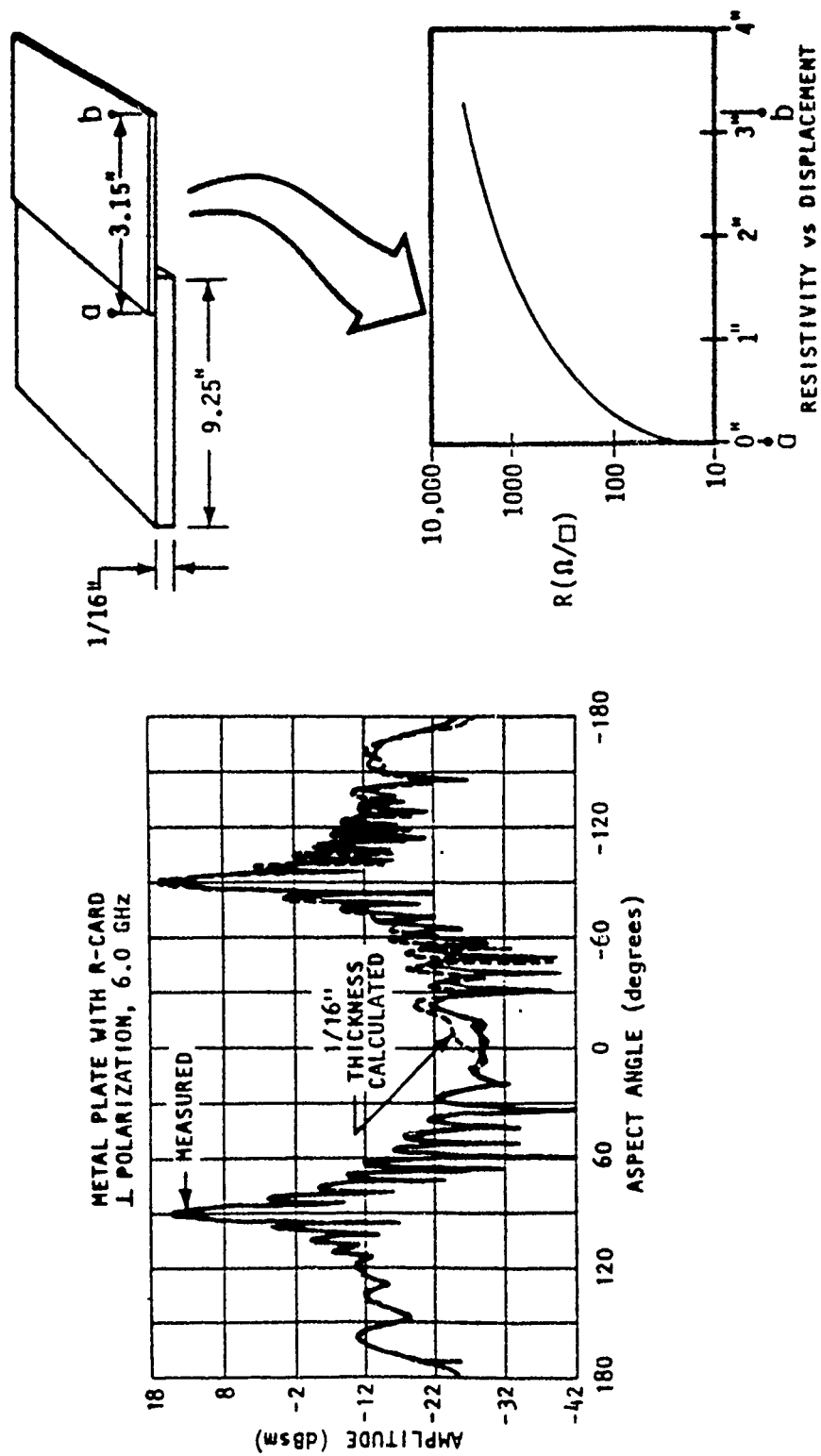


Figure 7. R-Card Traveling Wave Treatment (Example Links Verification)

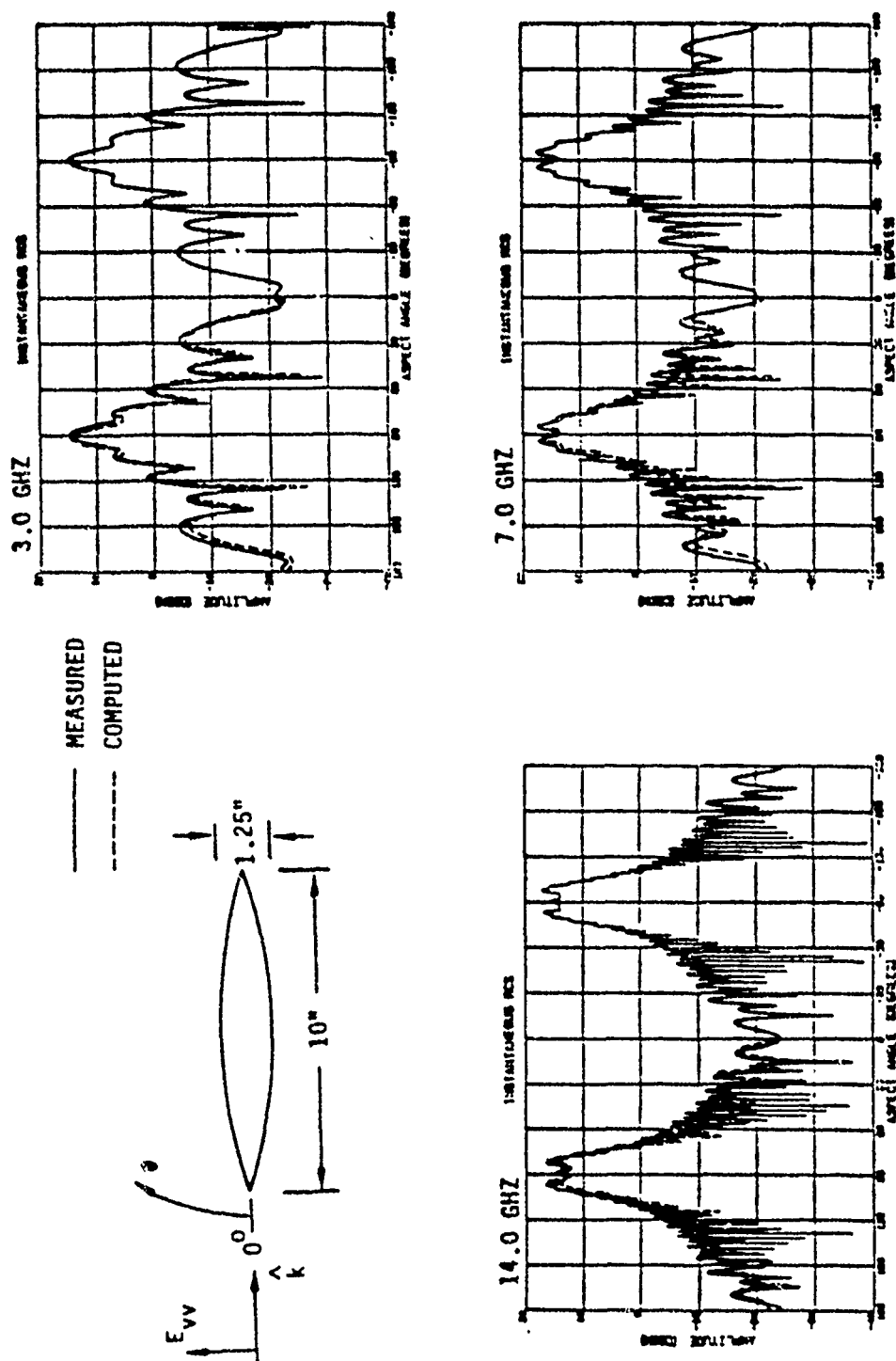
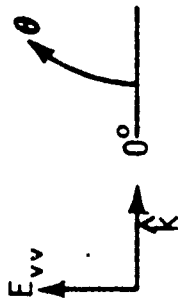


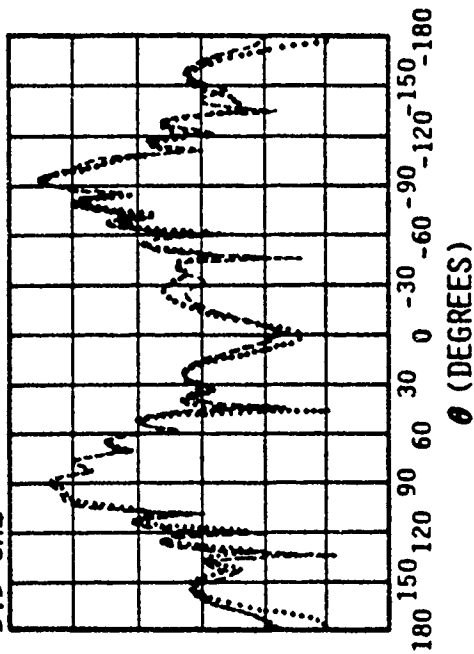
Figure 8. Metal Ogive Links Verification



— DRAWING



3.5 GHz



--- MEASURED

..... COMPUTER
(DRAWING)

Figure 9. Metal Wing Section-Links Verification

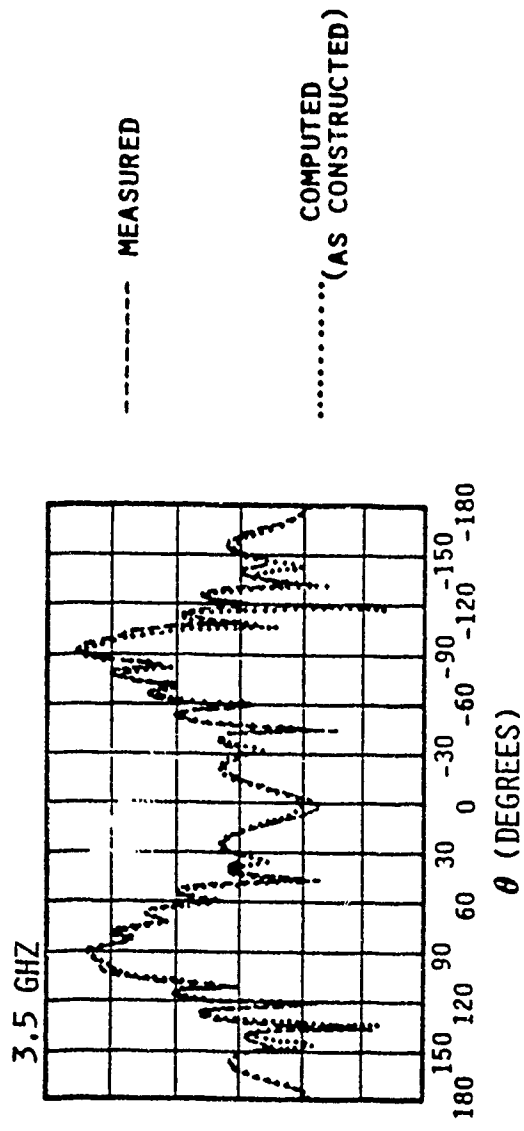


Figure 10. Metal Wing Section-Links Verification

SELECTED PATTERN MEASUREMENTS OF FOUR
FULL-SCALE TACTICAL HF ANTENNAS

By David L. Faust

Advanced Systems Research Group
Eyring Research Institute
Provo, Utah 84601

Abstract

Selected pattern measurements are presented for a 500-foot, broadbanded sloping longwire antenna; a 500-foot, broadbanded sloping vee antenna with a 30-degree apex angle; a 500-foot, broadbanded vertical half-rhombic antenna; and a broadband, receive-only orthogonal dipole pair. The three 500-foot antennas used rapid deployment, 46-foot steel support towers. The gain patterns presented are "textbook style" azimuth and elevation plots scaled in dBi of antenna response to vertically or horizontally polarized beacons. The patterns are compared to each other as well as to reference monopoles and dipoles. The measurements were obtained by a helicopter towed elementary dipole beacon.

The measurements were performed in the fall of 1985 at the Eyring Research Institute test facility located at the Cedar Valley Airport, Cedar Valley, Utah.

BANDWIDTH OPTIMIZATION FOR SPECIFIED ANTENNA GAIN PATTERNS*

R. M. Bevensee
Lawrence Livermore National Laboratory

Summary

An expression for the two-sided fractional bandwidth B (assumed $\leq 100\%$) of a lossless metal antenna in free space has been derived, in terms of a rigorously defined time-average "reactive stored energy," W_R , at centerfrequency ω_0 . We express it, as well as time-average power radiated, P_{rad} , as a quadratic form involving the current moments on the antenna. We express antenna gain $G(\theta, \phi)$ and B as ratios of quadratic forms. Specializing to $G = G_0$, unidirectional, and using an eigenfunction expansion for the current moments, we describe the B - G_0 behavior of an antenna as a function of a single parameter which characterizes the current-moment distribution.

We discuss computational issues and describe a computer code implemented on the VAX for studying the B - G_0 behavior of a class of antennas synthesized by thin dipoles, all parallel to the z -axis of a coordinate system in which G_0 is measured along the x -axis.

We describe the dipole distribution with the best B - G_0 behavior for a spherical working volume of radius $a/\lambda = 1$.

Theory

One obtains the bandwidth for a lumped circuit around a centerfrequency ω_0 by computing the rate of change of reactance $\partial X/\partial \omega|_{\omega_0}$ as

$$\operatorname{Im} \left. \frac{\partial V(\omega)}{\partial \omega} \right|_I I^* = |I|^2 \frac{\partial X}{\partial \omega} \quad * = \text{complex conjugate} \quad (1)$$

where Re , Im means real, imaginary part, $V = ZI$, and $\operatorname{Re} Z = R$ is essentially constant near series resonance. The fractional bandwidth B is then $(\omega_2 - \omega_1)/\omega_0$, where $\omega_{1,2}$ are the two frequencies at which $|(\omega - \omega_0)\partial X/\partial \omega| = R$.

We can compute the bandwidth for an antenna by analogy from a "reactive stored energy," W_R , defined as

* Work performed under the auspices of the U.S. Department of Energy by the Lawrence Livermore National Laboratory under contract number W-7405-ENG-48.

$$W_R = -\frac{1}{4} \text{Im} \int_S \frac{\partial \hat{E}_\omega}{\partial \omega} \times \hat{H}_\omega^* \cdot d\vec{S} \Big|_{\hat{J}} \quad (2)$$

where \hat{E}_ω , \hat{H}_ω are the complex amplitudes of the fields induced by current distribution \hat{J} (held fixed) on antenna surface S and $d\vec{S}$ points out of the volume. One can prove that the bandwidth of a voltage source driving all the current elements through a series circuit of ideal transformers shown in Fig. 1 is given by [1]

$$B = \frac{P_{\text{rad}}}{\omega_0 W_R} \quad (3)$$

(neglecting stored energy in the feed circuit).

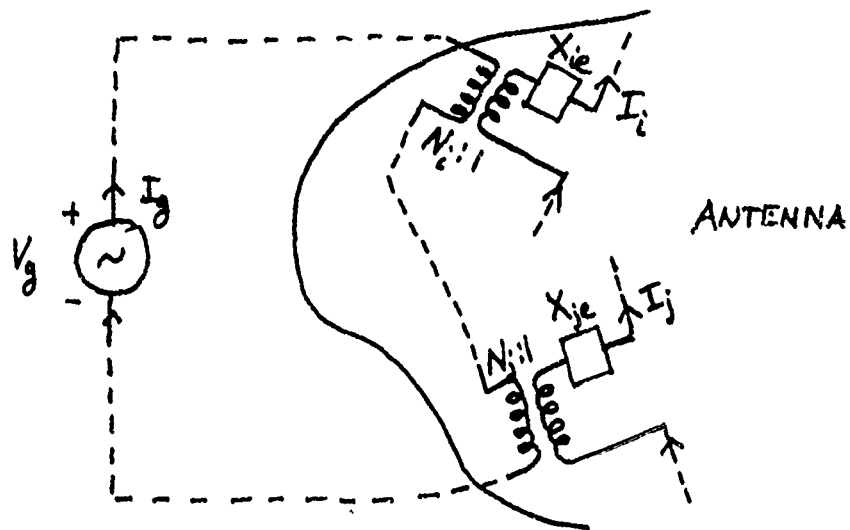


Fig. 1. The distributed driving circuit for the antenna, showing two "ports" coupled to the source via ideal transformers. X_{ie} is an external reactance inserted to cancel the reactance of the i th port at centerfrequency.

By a lengthy, detailed evaluation of (2) with the fields given by integrals of the Panofsky-Phillips expressions [2] for sinusoidal currents, we obtain

$$W_R = \frac{1}{16\pi\epsilon_0} \text{Re} \left\{ \iint_S \frac{\hat{J}(\vec{r}) \cdot \hat{J}^*(\vec{r}') e^{-jkR}}{R} (1+jkR) dS dS' + \right. \\ \left. + \frac{1}{c^2} \iint_S \frac{\hat{J}(\vec{r}) \cdot \hat{J}^*(\vec{r}') e^{-jkR}}{R} (1-jkR) dS dS' \right\} \quad (4)$$

where

$$R = |\vec{r} - \vec{r}'|, \quad \hat{g}(\vec{r}) = \nabla \cdot \hat{J}(\vec{r}) / -j\omega \quad (5)$$

In a method-of-moments expansion of the currents for wires, which will concern us here,

$$\mathbf{I} = \sum \mathbf{I}_n \mathbf{f}_n \quad (6)$$

we can write W_R as the quadratic form

$$W_R = \frac{\mu_0}{16\pi\lambda_0} \underset{\sim}{M}^{\dagger} \underset{\sim}{W} \underset{\sim}{M} \quad \dagger = \text{transpose conjugate} \quad (7)$$

$\underset{\sim}{M}$ being the matrix of current moments. The mth one is $\mathbf{I}_n L_n$, length $L_n = \int \mathbf{f}_n d\mathbf{l}$ along the wire.

We can write the time-average radiated power either as

$$\begin{aligned} P_{\text{rad}} &= \frac{1}{2} \sqrt{\frac{\epsilon_0}{\mu_0}} \iint |\hat{E}(r_0, \theta, \phi)|^2 r_0^2 \sin\theta d\theta d\phi \\ &= \frac{1}{2} \sqrt{\frac{\epsilon_0}{\mu_0}} \left(\frac{\omega \mu_0}{4\pi} \right)^2 \sum_i |\mathbf{L}_i|^2, \quad \sum_i |\mathbf{L}_i|^2 = \underset{\sim}{M}^{\dagger} \underset{\sim}{P}_S \underset{\sim}{M} \end{aligned} \quad (8)$$

on the radiation sphere, in Sahalos' notation [3], or as

$$P_{\text{rad}} = \frac{1}{2} \sum_{ij} \mathbf{I}_i^* R_{ij} \mathbf{I}_j = \frac{1}{2} \sum_{ij} \mathbf{M}_i^* \frac{R_{ij}}{L_i L_j} \mathbf{M}_j \quad (9)$$

in terms of $\underline{R} = \text{Re } \underline{Z}$. This latter expression may be cast into the same form as (8) but with a different \underline{P} replacing \underline{P}_S .

With (7) and either (8) or (9) for P_{rad} , we have for (3)

$$\mathbf{B} = \frac{\underset{\sim}{M}^{\dagger} \underset{\sim}{P} \underset{\sim}{M}}{\underset{\sim}{M}^{\dagger} \underset{\sim}{W} \underset{\sim}{M}} \quad (10)$$

Specializing to directional gain G_0 in the $\theta_0 = \frac{\pi}{2}$, $\phi_0 = 0$ direction along the x-axis of a spherical coordinate system, in which we take all the current elements parallel to the z-axis, we can write

$$G_0 = 4\pi \frac{|T_1^T M|^2}{M^T P M} \quad (11)$$

Here $T_1 = e^{-jkx_1}$ of the i th current moment. The $G_0 B$ product is

$$G_0 B = 4\pi \frac{|T_1^T M|^2}{M^T W M} \quad (12)$$

Expansion in Eigenfunctions

We can obtain much information about the behavior of G_0 and B from an expansion of M in eigenvectors X_i of the eigenvalue equation

$$P X_i = \beta_i W X_i \quad (13)$$

where P , W are real symmetric and W is positive definite. β_i is the value of B for the i th "eigenstate" with the current moments M_1, \dots, M_N given by X_i . If we substitute the expansion for M

$$M = \sum a_i X_i \quad (14)$$

into the "objective function" F :

$$F = \frac{M^T P M}{M^T W M} + \gamma_0 \left(\frac{|M^T T|^2}{M^T P M} - g_0 \right), \quad g_0 = \frac{G_0}{4\pi} \quad (15)$$

and make F stationary for small changes in the complex a_i , γ_0 being a Lagrange multiplier, we obtain

$$a_i = \frac{\kappa_0}{1 - \alpha \beta_i} \tilde{X}_i^T \tilde{T} \quad (16)$$

Here κ_0 may be taken 1 and α is a running parameter over $(-\infty, \infty)$ which traces a complicated curve in the B- G_0 plane.

When we substitute (14) and (15) into (10) and (11), we find

$$B = \frac{\sum_i |\tilde{T}^T \tilde{X}_i|^2 \beta_i / (1 - \alpha \beta_i)^2}{\sum_i |\tilde{T}^T \tilde{X}_i|^2 / (1 - \alpha \beta_i)^2} \quad (17)$$

$$G_0 = 4\pi \frac{[\sum_i |\tilde{T}^T \tilde{X}_i|^2 (1 - \alpha \beta_i)^2]^2}{\sum_i |\tilde{T}^T \tilde{X}_i|^2 \beta_i / (1 - \alpha \beta_i)^2} \quad (18)$$

In this representation one can quite easily show that

$$(G_0)_{B_{\max}} \leq (G_0)_{\max} (G_0 B) \quad (19)$$

Computational Issues

We found that when we employed 0.2λ dipoles of radius a and total length $2L$ such that $a/L \leq 1/8$, with f_n a triangle function T_n , that the W_{mn} element of (7) was ($k = \omega/c$)

$$W_{mn} = \frac{\lambda}{L^2} \left[\frac{1}{k^2} \iint \frac{\partial f_m(z')}{\partial z'} \frac{\partial f_n(z)}{\partial z} \left(\frac{\cos kR}{R} + k \sin kR \right) dz dz' \right. \\ \left. + \iint f_m(z') f_n(z) \left(\frac{\cos kR}{R} - k \sin kR \right) dz dz' \right] \quad (20)$$

We easily modified subroutine CALZ of Kuo and Strait [4] based on R. Harrington's formulas for interacting triangle functions. However, to evaluate the self-element W_{ii} sufficiently accurately, we expanded $\cos kR/R + k \sin kR$ as $1/R = k^2/2R$, $\cos kR/R - k \sin kR = 1/R - 3k^2/2R$, used the exact $R^2 = (z-z')^2 + [2a \sin(\frac{\phi-\phi'}{2})]^2$, integrated over ϕ' trivially, integrated exactly over Z and Z' , then tediously expanded terms and retained predominant ones. After integrating over ϕ , we obtained

$$W_{ii} = \frac{4\lambda}{L} \left[\frac{1}{(kL)^2} \left(\ln \frac{L}{ea} + \frac{6}{\pi} \frac{a}{L} \right) + \frac{1}{3} \ln \frac{8L}{a} - \frac{7}{9} \right] \quad (21)$$

for $L/a \geq 5$, $e = 2.71828\dots$

We also corrected the expression for dipole self impedance Z_{ii} , and the result is

$$Z_{ii} = 20(kL)^2 - j \frac{120}{kL} \left\{ \ln \frac{L}{ea} + \frac{6}{\pi} \frac{a}{L} - (kL)^2 \left[\frac{1}{3} \ln \frac{8L}{a} - \frac{7}{9} \right] \right\} \quad (22)$$

If two dipoles overlapped by L , half their length, it was not necessary to correct the mutual Z .

Computer Code

The basic code GOB.FOR;1 for the VAX consists of MAIN, CALW, CALP or CALZ, depending on which form of P was employed, and RSG. MAIN reads the number of z-directed wires, number of points on the wires (a triangle function extends over five of them), wire radius a , and $k = 2\pi/\lambda$. It also reads the first point on each wire, its x- and y-coordinates, and the z-coordinates of the remaining points on the wire. Subroutine CALW defines the triangle T-functions and their derivatives TP and computes the W_{mn} -elements of (20). CALP obtains the P_{mn} elements of (8); CALZ was taken from the Kuo-Strait code and modified for the more accurate Z_{ii} . RSG from Eispack computes the X_i and β_i of (13). Finally, MAIN verifies the orthonormality $X_i^\dagger W X_j = \delta_{ij}$, defines the T_i , and solves for B and G_0 for (a) max $G_0 B$ for $\alpha = 0$, (b) all the eigenstates, and (c) $(G_0)_{\max}$ and corresponding B for $\alpha = \pm\infty$. Then it computes $(G_0)_{\max}$ by Sahalos' formula. A later version of GOB.FOR allowed computations of B and G_0 for any specified α , as well as lines of dipoles with prescribed spacing between the ends of neighboring dipoles and x-y separations between lines.

The computer code was checked to see if it obeyed the scaling law: increase of all dimensions by a factor and decrease of frequency by that

factor yielded the same $B-G_0$ performance, vs α . There is no absolute dependence on frequency, as implied by one recently published article.

The Antenna with the Best $B-G_0$ Behavior [5] for $\alpha/\lambda = 1$

With G_0 measured in the x-direction and all the dipoles parallel to the z-axis within a spherical working volume of $\alpha/\lambda = 1$, we found that the distribution with the highest B for given G_0 , and vice versa, consisted of lines of overlapping (0.2λ) dipoles in three planes, one bisecting the sphere at $y = 0$, the other two at $y = \pm .43$ (units of λ). In each line of dipoles the ends overlapped 0.01 (thus reducing the qq-portion of W_R). There were six lines at $y = 0$: $x = -.12, 0, .12, .24, .36, .48$; two lines at $y = -.43$: $x = 0, .12$; and two similar lines at $y = +.43$. Wire radius/L = .25 and there were 94 dipoles in all.

We found that, for high $B-G_0$ performance, the reactive stored energy matrix \underline{W} of (7) is nearly nonpositive definite, so that some of the eigenvalues in (13) are computed to be slightly negative. Double precision computations do not change the situation qualitatively. The result is an overly optimistic $B-G_0$ behavior computed by (8) (\underline{P} on the radiation sphere) which extends into the supergain region: $G_0 \geq ka(ka+2)$. However, with \underline{P} represented by (9) (proportional to $\text{Re}\underline{Z}$) the $B-G_0$ behavior showed negligible B in the supergain region.

The interesting and pragmatic aspect of this type of analysis is that it yielded the same antenna with the best $B-G_0$ behavior regardless of which way P_{rad} was represented!

References

1. R. M. Bevensee, "Fundamental Limitations of Antennas in Terms of Gain, Bandwidth and Volume," Report to Ft. Monmouth under Army MIPR CS-4-V0113-CS-WA, September, 1984.
2. W. K. H. Panofsky and M. Phillips, Classical Electricity and Magnetism, Addison Wesley, 1962, p. 246 et. seq.
3. J. Sahalos, "On the Optimum Directivity of Antenna Consisting of Arbitrarily Oriented Dipoles," IEEE Trans. Ant. Prop., AP-24, pp. 322-327, 1976.

4. D-C Kuo and B. J. Strait, "Improved Programs for Analysis of Radiation and Scattering by Configurations of Arbitrarily Bent Thin Wires," Scient. Rept. No. 15, Dept. of Elect. and Comp. Eng., Syracuse University, January 15, 1972. See also H. H. Chao and B. J. Strait, "Computer Programs for Radiation and Scattering by Arbitrary Configurations of Bent Wires," Scient. Rept. No. 7, Dept. of Elect. and Comp. Eng., Syracuse University, September 15, 1970.
5. R. M. Bevensee, "Fundamental Limitations of Antennas in Terms of Gain, Bandwidth and Volume," Report to Ft. Monmouth under Army MIPR No. 85-CS010, February, 1986.

SESSION II - "MODELING OF STRUCTURES NEAR LOSSY EARTH"

"A Comparison of Computer Codes and the Real World"

Virgil Arens

Arens Applied Electromagnetics, Inc.

Al Christman

Ohio University

"Gain & Pattern Measurements Examples of a Low Profile HF Antenna Array"

David Faust and Neil Skousen

Eyring Research Institute

"Moment Method Analysis of Wire Antennas Located Over Layered Ground: Using Sommerfeld Theory"

Gerald Burke

Lawrence Livermore National Lab

Edward Miller

University of Kansas

"A Surface Wave Code for Modeling Antennas Over Irregular Terrain, Inhomogeneous Terrain"

Robert Bevensee

Lawrence Livermore National Lab

A COMPARISON OF COMPUTER CODES AND THE REAL WORLD

Virgil R. Arens
Arens Applied Electromagnetics, Inc.
P.O. Box 329, Gaithersburg, MD 20877

and

Alan Christman
329 Stocker Center
Electrical & Computer Engineering Department
Ohio University
Athens, Ohio 45701

This paper compares the prediction of BIGANT and NEC-3 with full scale measurements at 29 MHz. The test antenna was a vertical half-wavelength delta-fed dipole located over sea water. Relative measurements of field strength were made at several elevations, using a lighter-than-air vehicle. Both codes gave good results and clearly demonstrate the need to use the double precision version of NEC-3. Since these two codes can model radiating structures over a finitely conductivity planar earth, comparisons such as these are both practical and meaningful.

Introduction (The Real World)

In December of 1932 an article entitled "The Radiation Characteristics of a Vertical Half-Wave Antenna" (Stratton and Chinn, Proceedings of the IRE, vol. 20, #12, pp. 1892-1913) was published showing actual measured values of electric field intensity radiated by a vertically oriented half-wave dipole (see Figure 1). The dipole was fed through a delta-match and open-wire transmission line, which was link-coupled to a transmitter operating at 29 MHz. The antenna and transmitter were mounted on a wooden platform floating in sea water 200 meters (about 20 wavelengths) from shore, in the vicinity of MIT's Round Hill Experimental Station near Boston. Vertical electric field strength measurements were taken during a series of flights made in a dirigible provided by the Goodyear-Zeppelin Corporation. Horizontal distances up to 8km (800 wavelengths) and elevations up to 730 meters were used.

BIGANT

BIGANT is a computer code that is an extension of the approach used by Dr. Anderson in the late 1960's. It is an integral equation approach using point matching on wire surfaces. A three term Fourier Series representation of the current on each segment is used. Rather than extrapolating to the adjacent segments centers to express the weights in terms of the unknown currents, the weights are expressed in terms of the unknown currents at the sample points and at the ends of the wire. In so doing this, the current and its first spatial derivative are forced to be continuous as one moves across the segment interface.

Sources and sinks are applied only at the junction of wires, or wires and a perfect ground plane. Schelkunoff's techniques are used to handle the source and junction problem. Electric fields in the presence of a finitely conducting ground are calculated using the Sommerfeld integrals as expressed by Banos.

Using the Codes

The dimensions of the antenna system, including the delta match, were fed into both computer codes BIGANT in 1972, and NEC-3 this year, along with suitable values of conductivity and dielectric constant. The 1932 article states that "the measured conductivity of the sea water was 0.41 mhos per centimeter cube," But this is clearly in error and should be 0.041 mhos/cm. or 4.1 mhos/m, the value used by the authors. The dielectric constant of sea water was taken as 81. Both codes were set up to calculate the total radiated field (sky wave and ground wave) and the vertical component was extracted from the data for plotting purposes. The driving voltage used with BIGANT was 100 volts peak.

Results

The outcome of the comparison is shown on the three graphs (Figures 2,3, and 4) representing vertical electric field intensity at various horizontal distance from the antenna at altitudes of 1 meter, 40 meters, and 540 meters. Since the measured data had been normalized the original graphs were plotted using the predicted voltages from BIGANT and the normalized measured data was positioned vertically to give the best agreement. As can be seen in these figures there is excellent agreement on the shape of the two curves. Recall that these plots were made in April 1972.

The NEC-3 output was obtained using both the single precision and double precision versions. Dr. Adler furnished the double precision results. For both cases, the driving point voltage used was 150 volts. The results of the NEC-3 calculations are overlayed on the earlier charts. As the graphs show the double precision version also gives excellent agreement. We plan to investigate the reason for the different required voltages. It looks like a peak/r.m.s. problem. The NEC-3 single precision output is also quite good at short distances from the antenna, but becomes poorer as one moves further from the radiator. This is especially pronounced at an altitude of 40 meters (Figure 3), where the NEC-3 value at a distance of 800 wavelengths is off by 75%. At a height of 540 meters, agreement between NEC-3 and the measurements is very good, even at large distance from the antenna. At a height of 1 meter, NEC-3 agreements at large distances is only fair, this erratic behavior - good agreements at high and low altitudes with poor correspondence at intermediate elevations - is puzzling, and no explanation can be offered at the present time. We plan to compare these results with the approximations of Norton in the near future.

Conclusions

It is always interesting to see how well a numerical model can perform when real-world measurement data is available as a standard of reference. In this particular instance, two codes were used, and both did rather well. The ability of both codes to model antennas over "real ground" is of significant importance, and makes them much more useful than programs which are limited to "free space" or "perfect earth". Readers with access to other codes are urged to analyze the Stratton and Chinon antenna on their own systems to see how their "pet program" stacks up with the two codes described here.

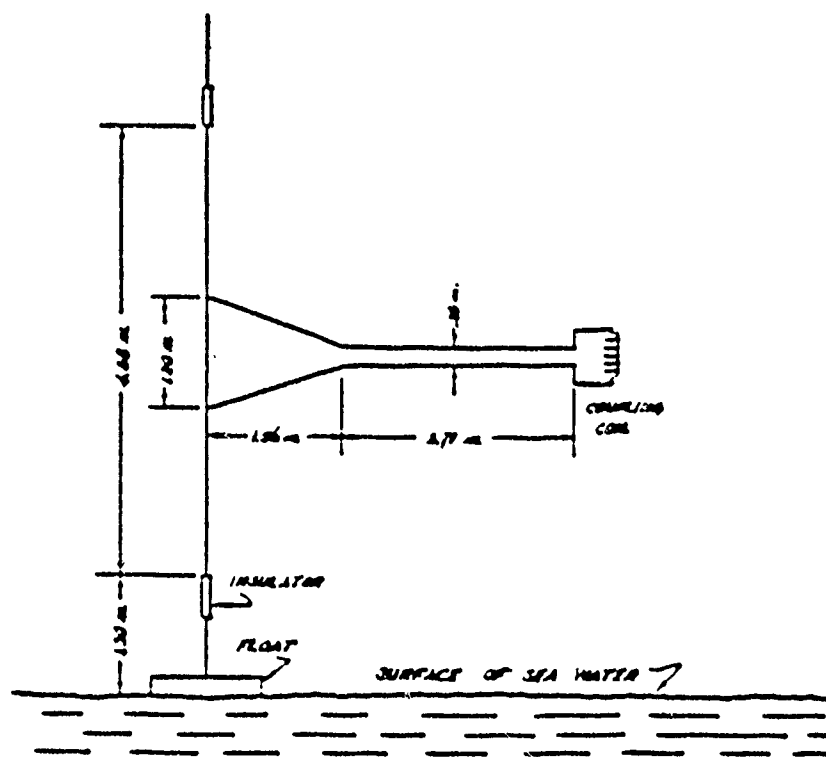


Fig. 1—Details of half-wave, vertical antenna used for the experimental work on 29 megacycles

VERTICAL FIELD INTENSITY VS DISTANCE

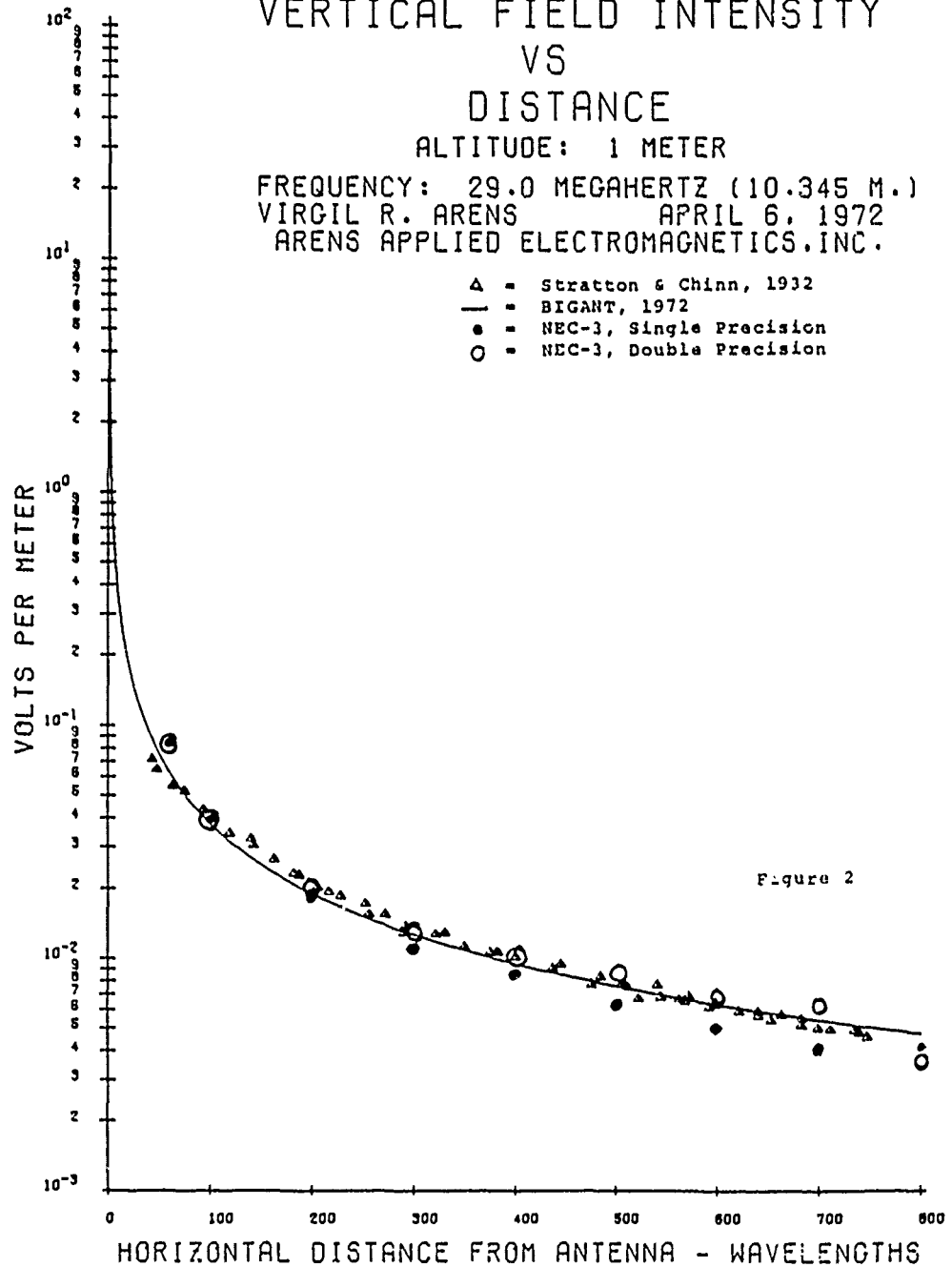
ALTITUDE: 1 METER

FREQUENCY: 29.0 MEGAHERTZ (10.345 M.)

VIRGIL R. ARENS APRIL 6, 1972

ARENS APPLIED ELECTROMAGNETICS, INC.

- Δ - Stratton & Chinn, 1932
- - BIGANT, 1972
- - NEC-3, Single Precision
- O - NEC-3, Double Precision



VERTICAL FIELD INTENSITY VS DISTANCE

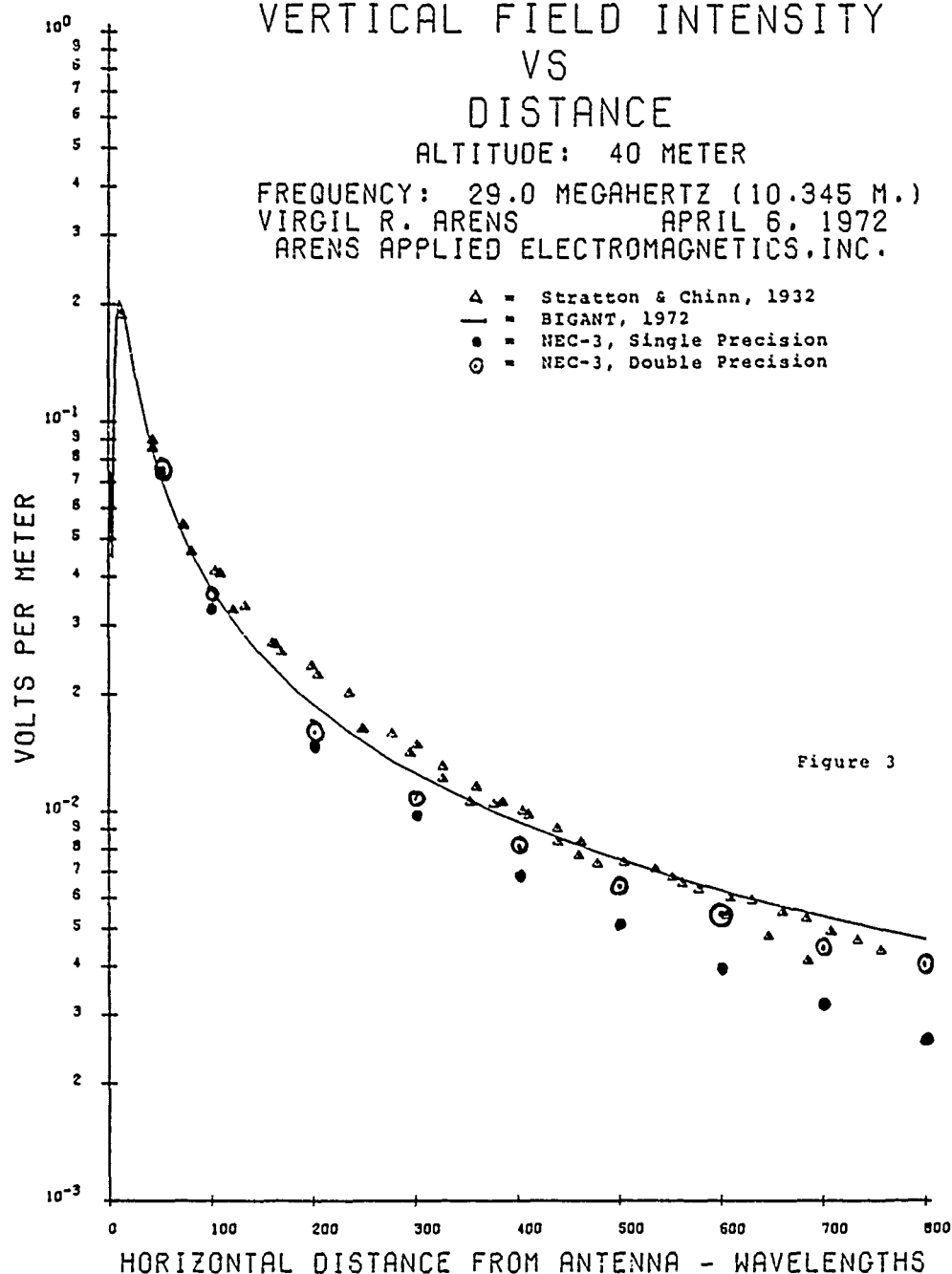
ALTITUDE: 40 METER

FREQUENCY: 29.0 MEGAHERTZ (10.345 M.)

VIRGIL R. ARENS APRIL 6, 1972

ARENS APPLIED ELECTROMAGNETICS, INC.

- △ = Stratton & Chinn, 1932
- = BIGANT, 1972
- = NEC-3, Single Precision
- ⊙ = NEC-3, Double Precision



VERTICAL FIELD INTENSITY VS DISTANCE

ALTITUDE: 540 METERS

FREQUENCY: 29.0 MEGAHERTZ (10.345 M.)
VIRGIL R. ARENS APRIL 6, 1972
ARENS APPLIED ELECTROMAGNETICS, INC.

- △ = Stratton & Chinn, 1932
- = BIGANT, 1972
- = NEC-3, Single Precision
- ⊙ = NEC-3, Double Precision

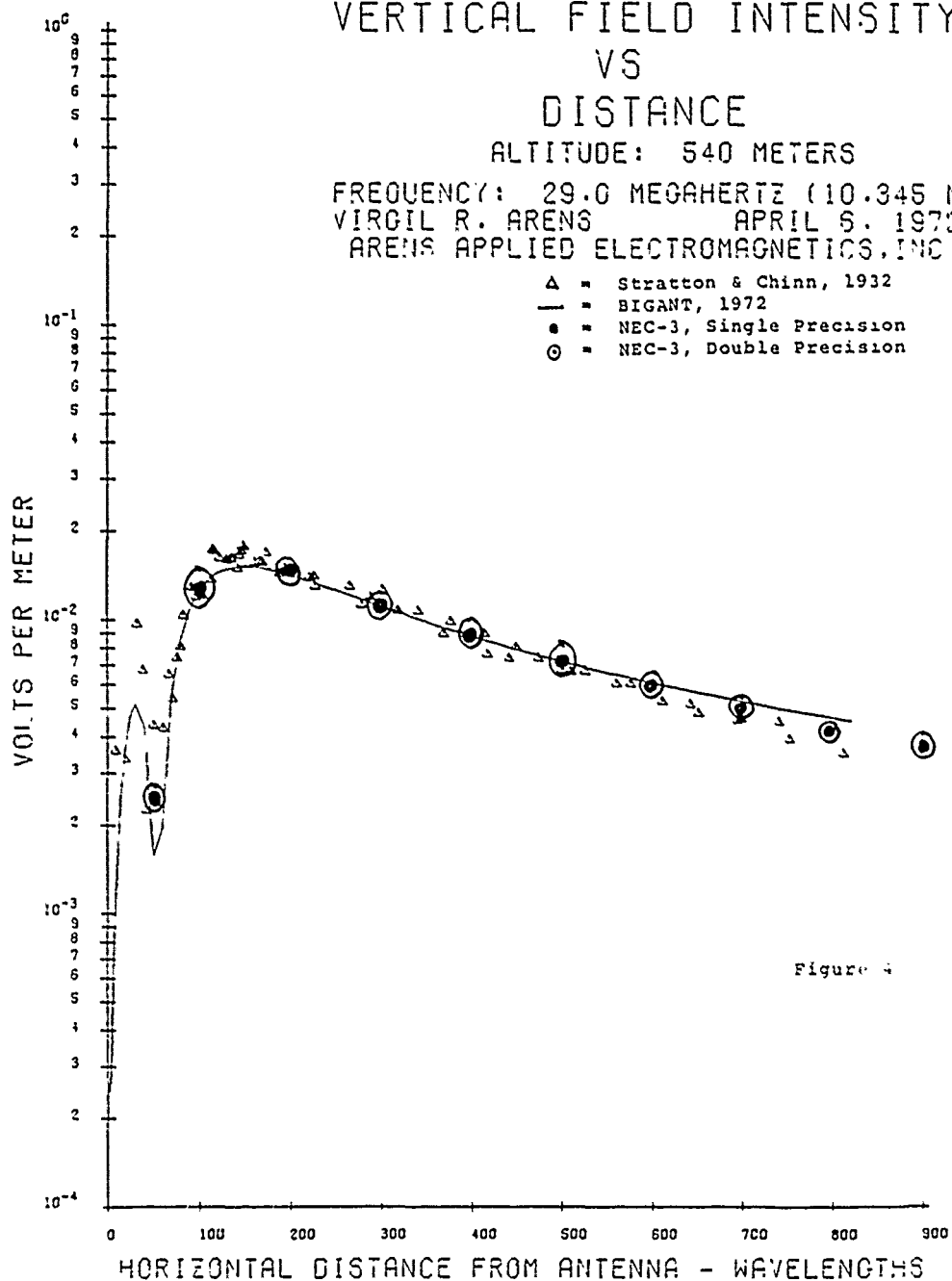


Figure 4

GAIN AND PATTERN MEASUREMENTS EXAMPLES OF
A LOW PROFILE HF ANTENNA ARRAY

By

David L. Faust
O. Niel Skousen

Advanced Systems Research Group
Eyring Research Institute
Provo, Utah 84601

Abstract

Measurement data is presented for several configurations of the Eyring Low Profile Antenna (ELPA). The antenna can be classed as an arrayed, broadband antenna with a controlled ground interaction. Examples will demonstrate bandwidth, azimuth patterns, elevation patterns and layout conditions. Eight-element arrays will be compared to typical broadband tactical antennas at several frequencies.

The measurements were obtained by a helicopter-towed elementary dipole beacon. The measurements were performed at the Eyring Research Institute, Cedar Valley Airport Test Facility in Utah in the fall of 1985.

MOMENT-METHOD ANALYSIS OF WIRE ANTENNAS LOCATED OVER LAYERED GROUNDS USING SOMMERFELD THEORY

G.J. Burke
Lawrence Livermore National Laboratory
P.O. Box 808, L-156
Livermore, CA 94550

E.K. Miller
University of Kansas
Department of Electrical Engineering
Lawrence, KA 66045-2228

A model for wire objects of arbitrary geometry above a planar interface was developed in the code NEC-2 and extended to wires buried or penetrating the interface in NEC-3. The electric-field integral equation with Sommerfeld integrals to account for the effect of the interface is solved numerically using the Method of Moments. Interpolation and model-based parameter estimation is used to reduce the computer time needed to evaluate the Sommerfeld portion of the integral-equation kernel. The total computer time is 4-8 times that required for the same object located in free space to be solved with comparable numerical accuracy.

The homogeneous, half-space model can provide a starting point in developing an approach for more general ground problems where various kinds of lateral and vertical inhomogeneities can occur. In this paper, we describe an extension of the above procedure to handle wire objects located above a layered half-space. The extension is reasonably straightforward, with the Sommerfeld fields above ground now involving transmission-line like terms for multiple-interface reflections. Once these fields have been obtained, the approach follows that previously used for the single interface. A new "SOMNEC" code was developed for layered ground. The field produced is read by an interpolation routine that can be linked with NEC-2, NEC-3, or NEC-GS. Results are shown for several layered half-space problems, including the case where there is a salt water half-space at a variable depth beneath the ground-air interface, to study the effect of tidal change on the behavior of low-frequency antennas sited near a sea coast. Also discussed is generalization of the basic model to antennas penetrating into or buried in a layered half-space.

* Work performed under the auspices of the U.S. Department of Energy by the Lawrence Livermore National Laboratory under contract number W-7405-ENG-48.

MOMENT-METHOD ANALYSIS OF WIRE ANTENNAS LOCATED OVER LAYERED GROUNDS USING SOMMERFELD THEORY

G. J. BURKE
E. K. MILLER

LAWRENCE LIVERMORE NATIONAL LABORATORY

PREVIOUS CODES MODELED A HOMOGENEOUS
HALF SPACE -

- NEC-2 FOR WIRES ABOVE GROUND
USED TABLE LOOK-UP FOR SOMMERFELD
INTEGRAL VALUES (BIVARIATE-CUBIC INTERPOLATION)
AND ASYMPTOTIC APPROXIMATION
- NEC-3 FOR WIRES BURIED OR PENETRATING
THE GROUND SURFACE USED -
 - TRIVARIATE INTERPOLATION
 - LEAST-SQUARES APPROX. (PARAMETER ESTIMATION)
 - ASYMPTOTIC APPROXIMATION

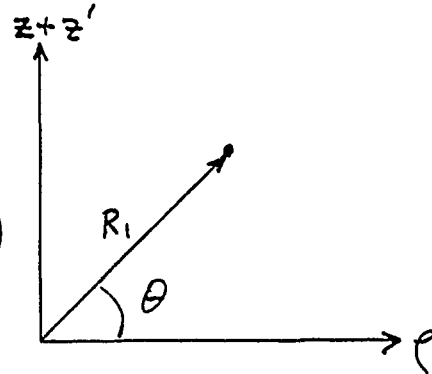
THE SINGULARITY AND PHASE FACTOR ARE SUPPRESSED FOR INTERPOLATION -

$$\vec{E} = \vec{E}_{\text{DIRECT}} + \frac{k_1^2 - k_z^2}{k_1^2 + k_z^2} \vec{E}_{\text{IMAGE}} + \frac{e^{-jk_z R_1}}{R_1} \vec{E}_S$$

SOMMERFELD INTEGRALS \rightarrow

\vec{E}_S IS FINITE AS $R_1 \rightarrow 0$

$$\lim_{R_1 \rightarrow 0} \vec{E}_S(R_1, \theta) = \vec{E}_S(0, \theta)$$



THE INTERPOLATION GRID IN R_1, θ CAN INCLUDE $R_1 = 0$.

A "STATIC" APPROXIMATION FOR THE FIRST INTERFACE IS SUBTRACTED FROM THE INTEGRAND -

$$\pi \approx \frac{m}{4\pi} \frac{k_1^2 - k_0^2}{k_1^2 + k_0^2} \frac{e^{-jkR}}{R}, \quad R = [e^2 + (z+z')^2]^{1/2}$$

$$\frac{e^{-jkR}}{R} = \int_0^\infty \frac{\lambda}{u_0} e^{-u_0 |z+z'|} J_0(\lambda e) d\lambda$$

THIS HELPS TO -

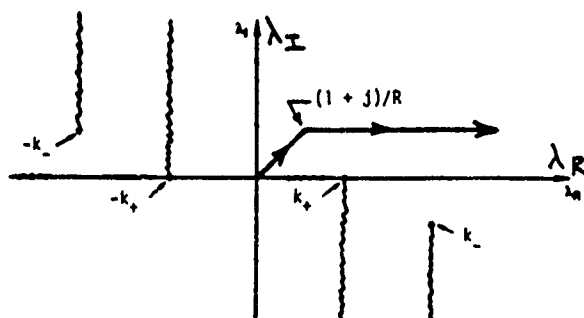
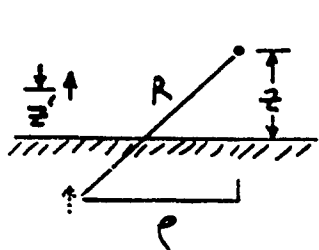
- REDUCE THE SINGULARITY TO AID TABLE-LOOK UP, INTERPOLATION
- IMPROVE CONVERGENCE OF THE INTEGRAL
- REDUCE ACCURACY LOSS DUE TO CANCELLATION IN INTEGRAND

THE INTEGRALS ARE EVALUATED NUMERICALLY
ALONG CONTOURS IN THE λ PLANE.

FOR A SINGLE INTERFACE -

$$\pi_0 \propto 2 \int_0^{\infty} F(\lambda) \exp[-u_0(z+z')] J_0(\lambda \rho) \lambda d\lambda$$

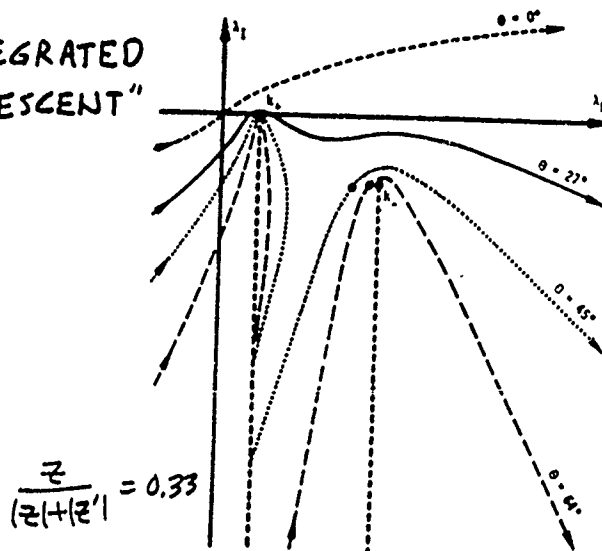
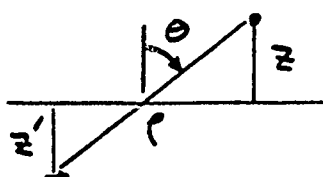
WHEN $|z+z'| \gg \rho$ A CONTOUR PARALLEL TO
THE REAL AXIS IS EFFECTIVE



WHEN $|z|+|z'|$ IS SMALL RELATIVE TO ρ THE
INTEGRALS ARE MORE EASILY EVALUATED IN THE
FORM

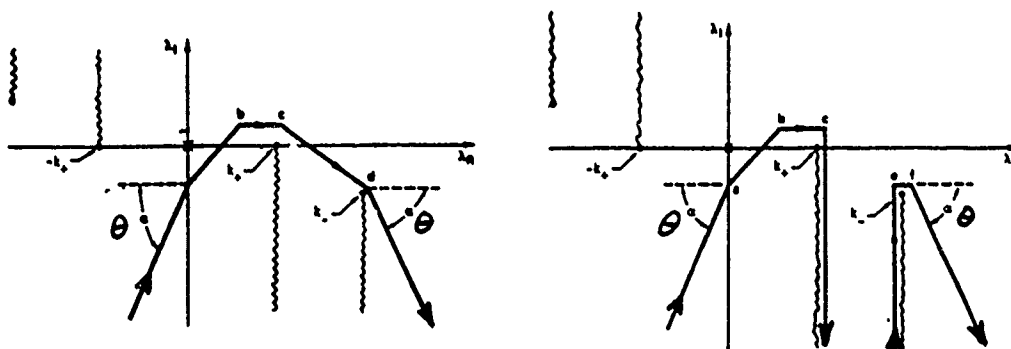
$$\pi_0 \propto \int_{-\infty}^{\infty} F(\lambda) \exp[-u_0|z| - u_1|z'|] H_0^{(2)}(\lambda \rho) \lambda d\lambda$$

WHICH CAN BE INTEGRATED
ALONG "STEEPEST DESCENT"
CONTOURS -



NUMERICAL INTEGRATION CONTOURS ARE CHOSEN TO APPROXIMATE THE STEEPEST DESCENT CONTOURS FOR LARGE $|\lambda|$

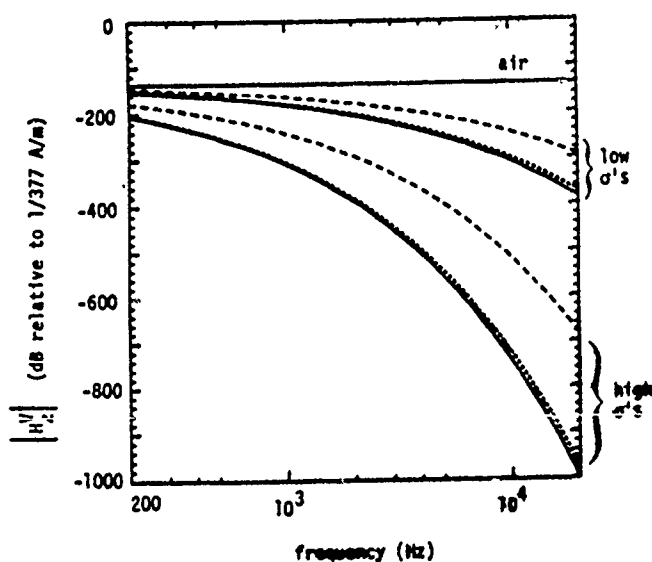
FOR SMALL $k\rho$: OR FOR LARGE $k\rho$:



A CODE WAS DEVELOPED TO COMPUTE THE FIELD OF A POINT SOURCE IN A STRATIFIED GROUND BY EVALUATING "SOMMERFELD INTEGRALS"

SOURCE DEPTH : 2500'

air			$\uparrow H_z^V$
1	$\sigma=0.005-0.1 \text{ S/m}$	200'	
2	$\sigma=0.002-0.07 \text{ S/m}$	1000'	
3	$\sigma=0.10-1.0 \text{ S/m}$	750'	
4	$\sigma=0.05-0.2 \text{ S/m}$	150'	
5	$\sigma=0.01-0.04 \text{ S/m}$	1200'	
6	$\sigma=0.05-0.2 \text{ S/m}$		



FOR A HORIZONTAL MAGNETIC DIPOLE IN LAYER ZERO
THE X COMPONENT OF HERTZ POTENTIAL IN LAYER i IS

$$\pi_{ix} = \frac{m}{4\pi} \int_0^\infty \left[\delta(1)\lambda/u_0 \exp(-u_0|z+d|) \right. \\ \left. + D_{ix}(\lambda) \exp[-u_i(z-z_i)] + U_{ix}(\lambda) \exp[u_i(z-z_i)] \right] J_0(\lambda\rho) d\lambda$$

WHERE, IN THE SOURCE LAYER, U_{0x} AND D_{0x} ARE:

$$U_{0x}(\lambda) = \frac{\lambda}{u_0} R_{10}^+ \cdot \frac{\exp(-u_0 d) + R_{10}^- \exp[u_0(d-2h_0)]}{1 - R_{10}^+ R_{10}^- \exp(-2u_0 h_0)}$$

$$D_{0x}(\lambda) = \frac{\lambda}{u_0} R_{10}^- \exp(-2u_0 h_0) \cdot \frac{\exp(u_0 d) + R_{10}^+ \exp(-u_0 d)}{1 - R_{10}^+ R_{10}^- \exp(-2u_0 h_0)}$$

$$u_i = (\lambda^2 - k_i^2)^{1/2} \quad \sigma_i' = \sigma_i + j\omega\epsilon_i \quad k_i^2 = -j\omega\mu_i \sigma_i'$$

U AND D IN OTHER LAYERS ARE OBTAINED BY
APPLYING PROPAGATION AND CONTINUITY CONDITIONS

REFLECTION COEFFICIENTS IN LAYER i AT THE
+ OR - INTERFACES ARE -

$$R_{1i}^\pm = \frac{K_i - Y_i^\pm}{K_i + Z_i^\pm} \quad R_{1i}^\pm = \frac{N_i - Y_i^\pm}{N_i + Y_i^\pm}$$

SURFACE Y AND Z ARE
FOUND BY RECURSION:

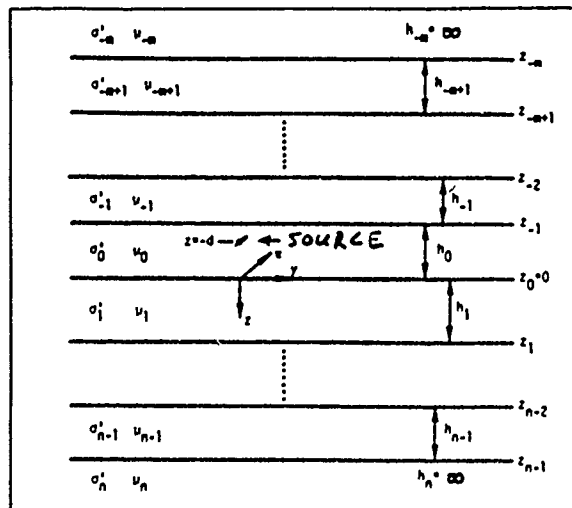
$$Y_{i+1}^\pm = N_i \frac{Y_i^\pm + N_i \tanh(u_i h_i)}{N_i + Y_i^\pm \tanh(u_i h_i)}$$

$$Z_{i+1}^\pm = K_i \frac{Z_i^\pm + K_i \tanh(u_i h_i)}{K_i + Z_i^\pm \tanh(u_i h_i)}$$

where $N_i = u_i / j\omega\mu_i$ $K_i = u_i / \sigma_i'$

$$u_i = (\lambda^2 - k_i^2)^{1/2}$$

$$k_i^2 = -j\omega\mu_i \sigma_i' \quad \sigma_i' = \sigma_i + j\omega\epsilon_i$$



AT TOP AND BOTTOM INTERFACES

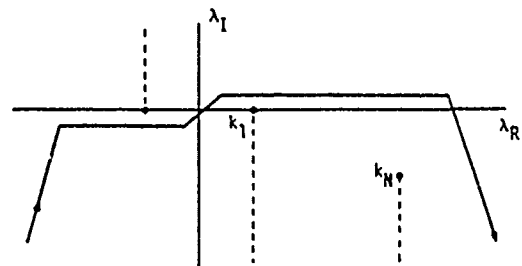
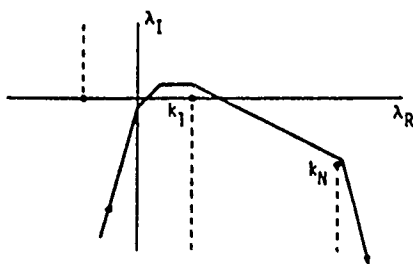
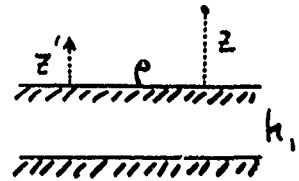
$$Y_{n-1}^+ = Y_n^+ = N_n \quad \text{and} \quad Z_{n-1}^+ = Z_n^+ = K_n$$

$$Y_{-m+1}^- = Y_{-m}^- = N_{-m} \quad \text{and} \quad Z_{-m+1}^- = Z_{-m}^- = K_{-m}$$

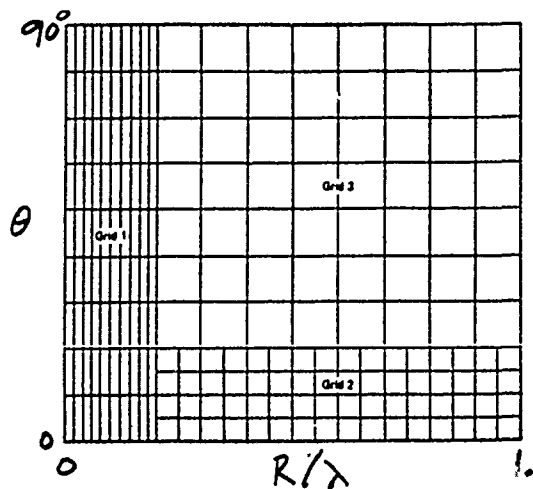
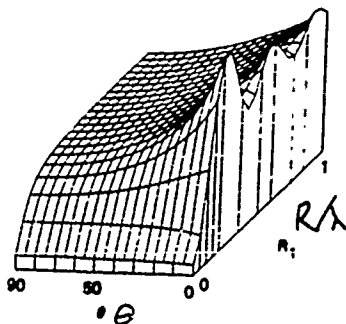
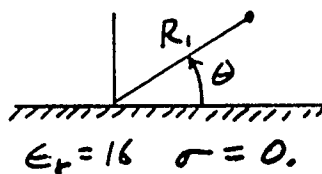
FOR A TWO-INTERFACE MEDIUM THE INTEGRAL FORM IS -

$$\pi_0 \propto \int_{-\infty}^{\infty} F(\lambda) \left[\frac{a_1(\lambda) e^{2u_1 h_1} + a_2(\lambda)}{a_3(\lambda) e^{2u_1 h_1} + a_4(\lambda)} \right] e^{-u_0(z+z')} H_0^{(z)}(\lambda e) d\lambda$$

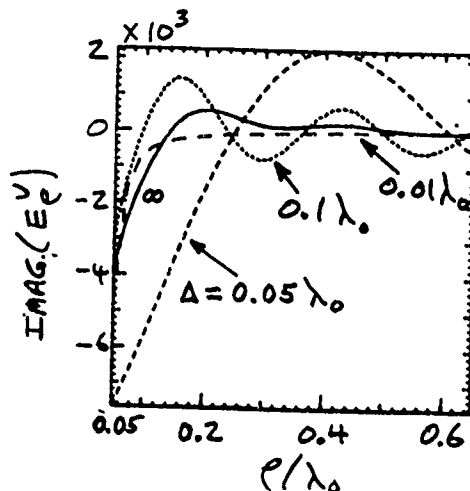
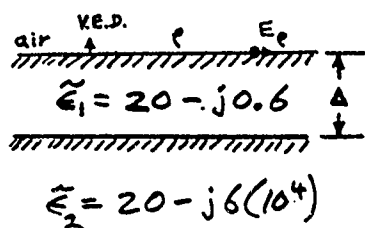
THE CONTOUR IS MODIFIED TO GET CONVERGENCE WHILE AVOIDING POLES, BRANCH CUTS AND EXCESSIVE OSCILLATIONS



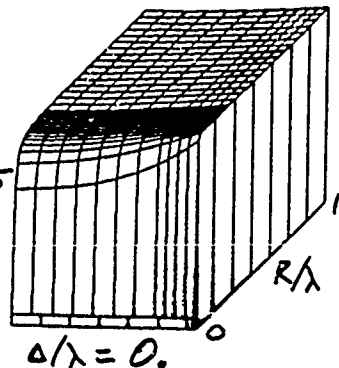
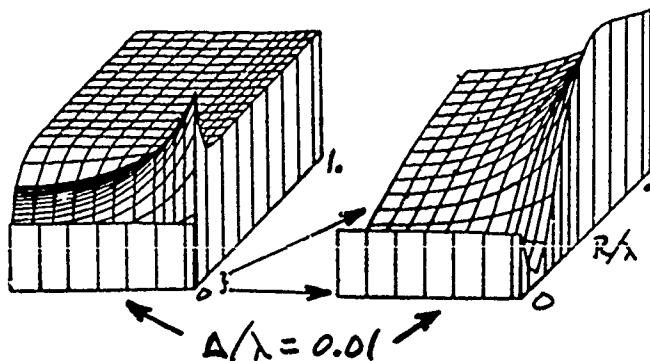
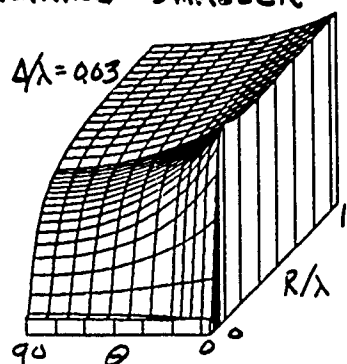
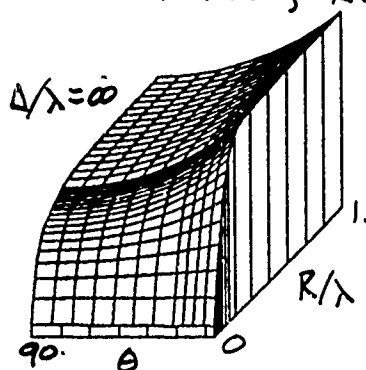
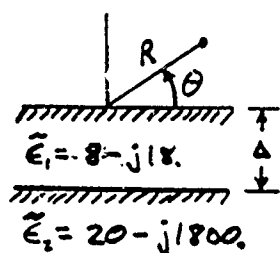
AN INTERPOLATION SCHEME WAS CHOSEN BY EXAMINING THE BEHAVIOR OF THE FUNCTION



CHANGES IN FIELD BEHAVIOR WITH LAYER THICKNESS MAY REQUIRE ALTERATION OF THE INTERPOLATION GRID



AS THE LAYER THICKNESS IS REDUCED THE INTERPOLATED FUNCTION DEVELOPES A SPIKE, REQUIRING SMALLER INTERVALS



SUBROUTINE SFLDS FROM NEC-2 WAS MODIFIED
TO INTERFACE THE NEC-2 INTERPOLATION
ROUTINES WITH NEC-3 AND NEC-65

NEC-3 :

```

SUBROUTINE SFLDS (T,E)                                SL  1
C                                                       SL  2
C SFLDS RETURNS THE FIELD DUE TO CURRENT IN THE PRESENCE OF GROUND SL  3
C THE CURRENT ELEMENT IS AT T RELATIVE TO THE SEGMENT CENTER. THE SL  4
C MAIN FUNCTION OF SFLDS IS TO TRANSFORM COORDINATES AND COMBINE SL  5
C FIELD COMPONENTS.                                     SL  6
C                                                       SL  7
C COMPLEX E,ERV,EZV,ERH,EZH,EPH,T1,EOK,EYK,EZK,EXS,EYS,EZS,EXC,EYC,E SL  8
12C,XXU,XXL,ETAU,ETAL,ZRAT2,FRAT1,XX,RX,SPAC           SL  9
COMMON /DATA1/ S,B,XJ,YJ,ZJ,CABJ,SABJ,SALPJ,EOK,EYK,EZK,EXS,EYS,EZ SL 10
1S,EXC,EYC,EZC,RXH,IEOK,IND1,IND2,IPGND              SL 11
COMMON /GND/ XXU,XXL,ETAU,ETAL,ZRAT2,FRAT1,CL,CH,SCRWL,SCRWR,NRADL SL 12
1,KSYMP,IFAR,IPERF,T1,T2,GSCAL                       SL 13
1,KSYMP,IFAR,IPERF,T1,T2,GSCAL                       SL 14

```

NEC-2 :

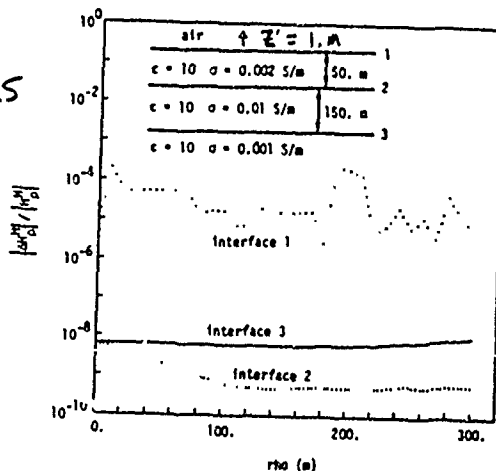
```

SUBROUTINE SFLDS (T,E)                                SL  1
C                                                       SL  2
C SFLDX RETURNS THE FIELD DUE TO GROUND FOR A CURRENT ELEMENT ON SL  3
C THE SOURCE SEGMENT AT T RELATIVE TO THE SEGMENT CENTER         SL  4
C                                                       SL  5
C COMPLEX E,ERV,EZV,ERH,EZH,EPH,T1,EOK,EYK,EZK,EXS,EYS,EZS,EXC,EYC,E SL  6
12C,XX1,XX2,U,U2,ZRAT1,ZRAT12,FRAT1,ER,ET,HRV,HZV,HRH     SL  7
COMMON /DATA1/ S,B,XJ,YJ,ZJ,CABJ,SABJ,SALPJ,EOK,EYK,EZK,EXS,EYS,EZ SL  8
1S,EXC,EYC,EZC,RXH,IEOK,IND1,IND2,IPGND              SL  9
COMMON /GND/ XXU,XXL,ETAU,ETAL,ZRAT2,FRAT1,CL,CH,SCRWL,SCRWR,NRADL SL 10
1,KSYMP,IFAR,IPERF,T1,T2,GSCAL                       SL 11
COMMON /GND/ XXU,XXL,ETAU,ETAL,ZRAT2,FRAT1,CL,CH,SCRWL,SCRWR,NRADL SL 12
1,KSYMP,IFAR,IPERF,T1,T2,GSCAL                       SL 13
1,KSYMP,IFAR,IPERF,T1,T2,GSCAL                       SL 14

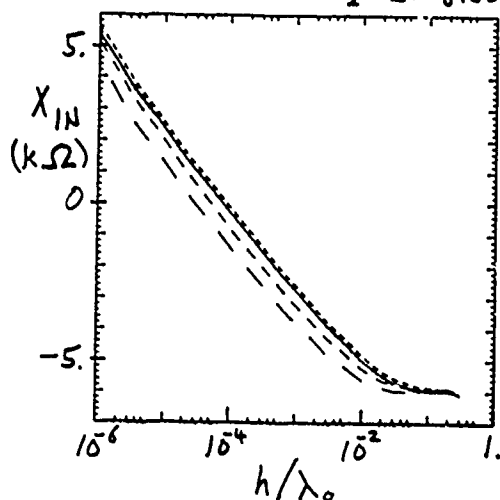
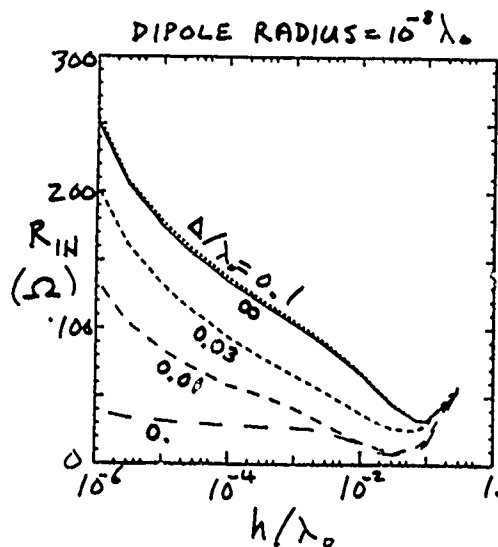
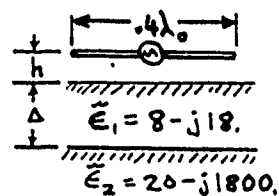
```

ACCURACY WAS CHECKED BY TESTING —

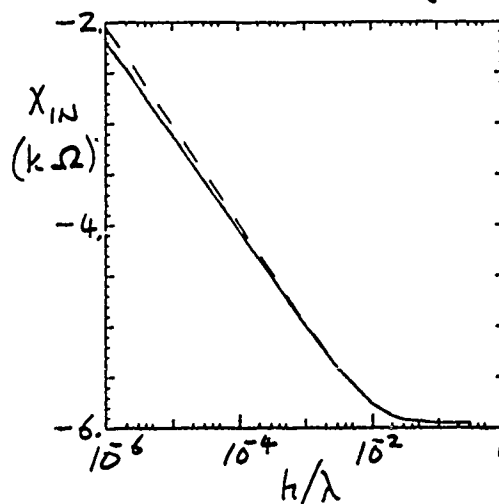
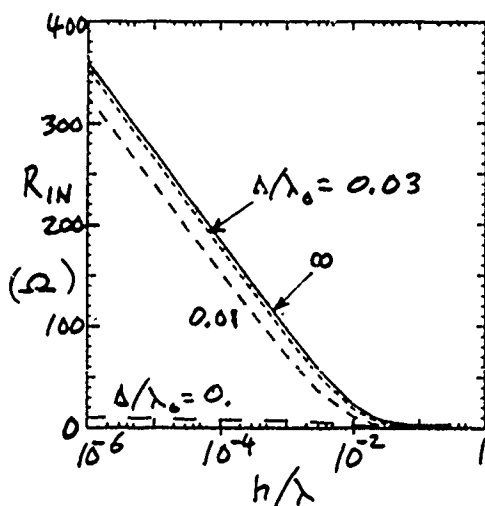
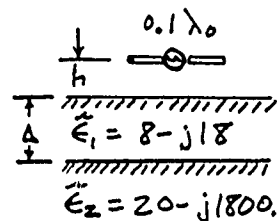
- CONTINUITY AT INTERFACES
- FINITE DIFFERENCE EVALUATION OF MAXWELL'S CURL EQUATIONS
- CONSISTENT RESULTS FROM DIFFERENT INTEGRATION CONTOURS
- AGREEMENT WITH HALF-SPACE CODE



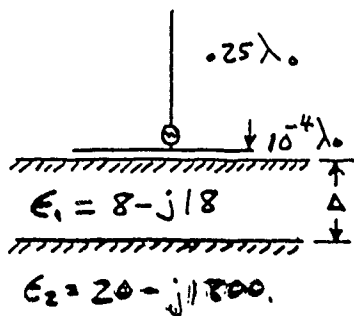
INPUT IMPEDANCE OF A DIPOLE OVER GROUND
WAS COMPUTED FOR VARYING HEIGHT WITH LAYER
THICKNESS A PARAMETER



A SHORTER DIPOLE SHOWS LESS EFFECT OF THE
LOWER MEDIUM

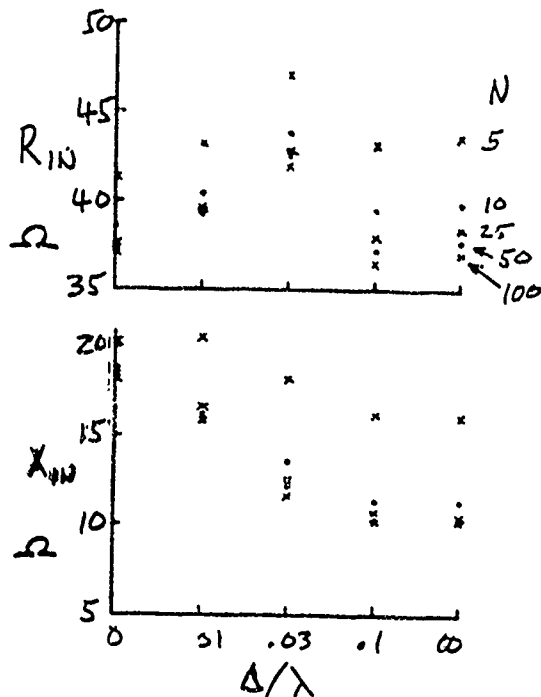


A MONOPOLE ON A RADIAL WIRE GROUND SCREEN
SHOWS THE EFFECT OF THE LOWER INTERFACE
DEPTH ON INPUT
IMPEDANCE

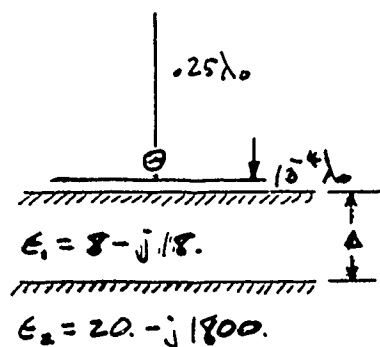


SCREEN RADIUS = $0.2\lambda_0$

N = NUMBER OF RADIALS

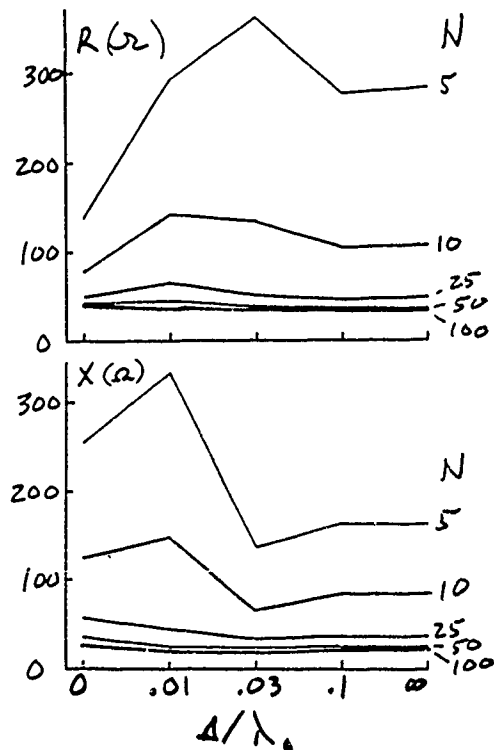


WITH A SCREEN RADIUS OF $0.35\lambda_0$ (ABOVE GROUND)
THE DEPENDENCE OF Z_{IN}
ON Δ IS REDUCED
FOR LARGE N .



SCREEN RADIUS = $0.35\lambda_0$

N = NUMBER OF RADIALS



A SURFACE WAVE CODE FOR MODELING ANTENNAS OVER IRREGULAR, INHOMOGENEOUS TERRAIN

R. M. Bevensee
Lawrence Livermore National Laboratory

Summary

We outline the highlights of a comprehensive report treating work on surface wave propagation done by others and recently at the Lawrence Laboratory (LLNL). The report is intended to serve as a comprehensive reference for future surface wave work.

We describe a Compensation Theorem integral equation for propagation of the TM_0 field from vertical current sources over irregular terrain of varying surface impedance. It depends on the field over irregular terrain of constant impedance, obtained from R. H. Ott's integral equation with distributed source terms.

Several NEC-WAGNER computer codes are described for computing an antenna current distribution over flat, homogeneous terrain and the surface wave it induces over the more distant irregular, inhomogeneous terrain.

The Report

The above mentioned report [1] reviews pertinent past work on surface wave propagation over irregular and/or inhomogeneous terrain and presents some new analyses and conclusions about the best way to compute surface wave propagation over general terrain. Part 1 reviews the concept of surface impedance for flat or locally flat terrain in terms of the exact Sommerfeld field expressions [2] and approximate ones of R. W. P. King [3]. Part 2 defines the "Relative Communication Effectiveness" (RCE) for any test antenna relative to a reference antenna. The usefulness of RCE for computing test antenna propagation from flat-homogeneous to irregular and/or inhomogeneous terrain is pointed out. Various properties of RCE are discussed and various antennas studied at LLNL are compared on the basis of their maximum RCE for four different flat-homogeneous earths.

Part 3 of the Report treats surface wave generation by one-dimensional Volterra integral equations, neglecting backscatter and sidescatter. Three Volterra equations are considered: R. H. Ott's equation [4, 5] for irregular terrain, a "modified" equation obtained by changing the constant relative surface wave impedance Δ to $\Delta(x)$ in Ott's attenuation function W , and a "self-consistent W " equation obtained by S. H. Cho [6] for flat inhomogeneous terrains. This last does not seem to generalize to irregular, inhomogeneous terrains. We conclude the most general -- and elegant -- treatment of the general problem is by the Compensation Theorem [7]. A Volterra integral equation was derived for $f'_1(x)$, the relative field function perturbed by $\Delta(x)$, in terms of the unperturbed $f_1(x)$ for reference Δ_r and $f_2(x)$ from a test dipole at x . These last two are computed by Ott's integral equation for irregular, homogeneous terrain.

Part 4 briefly reviews past work on surface wave propagation. Part 5 presents the full three-dimensional Compensation Theorem analysis of the perturbed field on flat (or irregular) earth surface due to prescribed variations in surface impedance $\Delta(x, y)$. The unperturbed fields may be computed by the NEC code. The integral equations for the perturbed $E'_{\tan}(x, y)$ and $H'_{\tan}(x, y)$ are given for a vertical electric dipole and horizontal electric dipole source.

The Compensation-Theorem Volterra Equation for General Terrain

For surface wave propagation in one direction, x , neglecting sidescatter and backscatter, illustrated in Fig. 1 we have derived the following expression for $f'_1(x)$ (the prime denotes a relative field perturbed away from $f_1(x)$ for irregular, homogeneous terrain by the effect of $\Delta(x)$ for inhomogeneous terrain) for vertical current sources, TM_p -field,

$$f'_1(x) = f_1(x) - i2\omega\epsilon_0 \int_0^x [\Delta(\xi) - \Delta_r] f'_1(\xi) f_2(x-\xi) \cdot e^{-ik\omega(\xi, x)} \sqrt{\frac{x}{\xi(x-\xi)}} d\xi \quad (1)$$

The time variation is $e^{i\omega t}$ and f is related to the field function ϕ defined by Ott [4] as

$$\begin{pmatrix} \phi_1(\xi) \\ \phi_1'(\xi) \end{pmatrix} = 2 \begin{pmatrix} f_1(\xi) \\ f_1'(\xi) \end{pmatrix} \exp \left[-ik \left(\xi + \frac{\eta^2}{2\xi} \right) \right] / \sqrt{\xi} \quad (2)$$

ϕ is proportional to H_ϕ for these V-polarized sources. A similar equation applies for H-polarization, TM_ρ -field in the direction of the sources. The H-polarized TE_ρ -field broadside is more involved and cannot be solved by the same integral equation. But this field decays initially as x^{-2} rather than x^{-1} so it is of lesser interest.

In (1) we have

$$\omega(\xi, \eta; \kappa, z) = \frac{1}{2} \left[\frac{[z(x) - \eta(\xi)]^2}{\kappa - \xi} + \frac{\eta^2}{\xi} - \frac{z(x)^2}{x} \right] \quad (3)$$

$f_1(x)$ is obtained by solving Ott's integral equation with $\Delta =$ reference Δ_r , constant, without any $W \cdot (\Delta - \Delta_r)$ -terms. For distributed sources ($k = 2\pi/\lambda$)

$$\begin{aligned} f_1(x) = & \sqrt{\frac{\pi}{2ik}} 60 \sum_{\xi} \left(\int I(\vec{r}_s) d\vec{r}_s \right) e^{ik[\kappa_2 + Qz - \vec{r}_s \cdot \vec{r}_s / 2x]} \\ & \cdot W_{\Delta_r}(\kappa_s, \vec{r}_s; \kappa, z) \\ & - \sqrt{\frac{i}{\lambda}} \int_0^x f_1(\xi) e^{-ik\omega(\xi, \eta; \kappa, z)} \left\{ \frac{\partial \eta(\xi)}{\partial \xi} W_{\Delta_r}(\xi, \eta; \kappa, z) \right. \\ & \left. - \frac{z(x) - \eta(\xi)}{\kappa - \xi} \right\} \sqrt{\frac{x}{\xi(x - \xi)}} d\xi. \end{aligned} \quad (4)$$

The sum is over dipole moment sources, $I(\vec{r}_s)$ centered at \vec{r}_s . The field f_2 ($\kappa_2 = x - \zeta$) is obtained

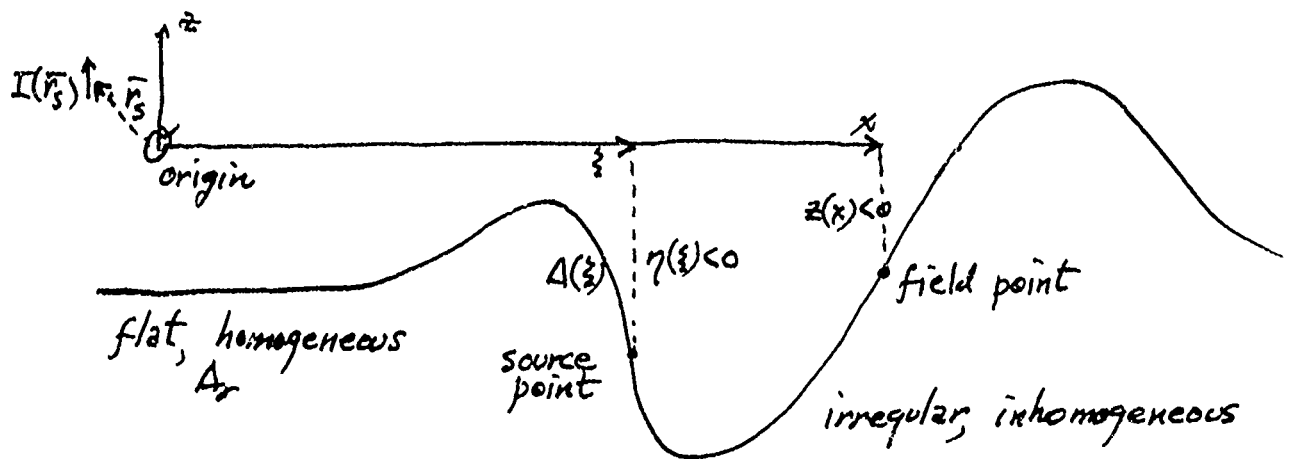


Fig. 1. Terminology for describing propagation by the integral equations. Δ_r is Ott's reference normalized surface impedance; $\Delta(\xi)$ is the inhomogeneous impedance.

by replacing the distributed source by a vertical electric dipole of moment $K_2^0 = 1$ at x and solving (4) backward from x .

If the terrain over $(0-x)$ were flat and we use the relation

$$f_2(x-\xi) = \sqrt{\frac{\pi}{2ik}} 60 W^F(x, \xi), \quad W^F(x, \xi) = W^F(\xi, x)$$

then (1) would read

$$f_1'(x) = f_1(x) - \sqrt{\frac{i}{\lambda}} \int_0^x [\Delta(\xi) - \Delta_r] f_1'(\xi) e^{-ik\omega(\xi, x)} W^F(\xi, x) d\xi \quad (5)$$

To solve for the surface wave over general terrain one must run a computer code thrice -- for $f_1(\xi)$ and $f_2(x-\xi)$ over irregular, homogeneous terrain of Δ_r , and then for $f_1'(\xi)$, $0 \leq \xi \leq x$, for the correct relative field by (1).

The Computer Codes

Computer code WAGNER has been written by Ott [4] to solve (4) for a point source when the initial terrain under the antenna is flat and homogeneous.

That equation is of the form

$$f(x) = g(x) - c \int_0^x f(s) K(x, s) ds \quad (6)$$

Wagner [8] showed that the solution will be unique and continuous if $g(x)$ is bounded and continuous and if

$$\int_0^x |K(x, s)| ds \leq L < \infty \quad (7)$$

The integral equation is solved by a stepwise computation that divides the interval $(0, x)$ into sub-intervals of arbitrary width. $f(s)$ is represented by a polynomial over the first 3 intervals.

$$f(s) = \alpha_0 + \alpha_1 s^{1/2} + \alpha_2 s + \alpha_3 s^{3/2}, \quad 0 \leq s \leq x_3 \quad (8)$$

and by

$$f(s) = a_0 + a_1 s + a_2 s^2, \quad x_3 \leq s \leq x_n \quad (9)$$

The α_i are solved by requiring the polynomial to pass through the first three known points (where the earth is flat), and the a_j are found, when solving for $f(x_i)$ by requiring (9) to pass through x_{i-2} , x_{i-1} , and x_i . With these relations $f(x_n)$ is solved stepwise forward, each new value being a linear combination of preceding values.

We have written two special versions of NEC to solve (4) and (1) after NEC computes the current distribution on a wire antenna above flat, homogeneous ground. The source term in (4) is resolved into three spatial moments,

$$\begin{aligned}
M_0 &= \sum_s \int I(\vec{r}_s) dl_s e^{ikx_s} \\
M_x &= \sum_s \int I(\vec{r}_s) dl_s x_s e^{ikx_s} \\
M_z &= \sum_s \int I(\vec{r}_s) dl_s z_s e^{ikx_s}
\end{aligned} \tag{10}$$

which need be computed only once. The source term in (4) is replaced by

$$\sqrt{\frac{\pi}{2ik}} 60 \left[(M_0 + ik \frac{z(x)}{x} M_z) W_0(0,0; x, z) + M_x \frac{\partial W(x, 0; x, z)}{\partial x_s} \right. \\
\left. + M_z \frac{\partial W(0, z_s; x, z)}{\partial z_s} \right]_0 \tag{11}$$

(more moments may be included if necessary) and W_0 and its derivatives are evaluated for each new point x in the spatial stepping.

The first version of NEC-WAGNER solves (4) with the source term (11), with the terrain profile, conductivity and relative dielectric distributions stored in subroutines. The Compensation Theorem version of NEC-WAGNER solves (1) after solving and storing $f_1(\zeta)$ in the forward direction and $f_2(x-\zeta)$ in the backward direction.

References

- [1] R. M. Bevensee, "Report on the Status of Numerical Modeling of Groundwave Excitation and Propagation," informal report for Lawrence Livermore National Laboratory, March 1, 1986.
- [2] G. J. Burke and A. J. Poggio, "Numerical Electromagnetics Code (NEC) - Method of Moments," Tech. Doc. 116, Vol. 1, NOSC, Jan., 1981, Sec. IV, Effect of a Ground Plane.
- [3] R. W. P. King, "Electromagnetic Surface Waves: New Formulas and Applications," IEEE Trans. Ant. Prop., AP-33, Nov., 1985, pp. 1204-1212.

- [4] R. H. Ott, "A New Method for Predicting HF Ground Wave Attenuation Over Inhomogeneous Irregular Terrain," OT/ITSRR 7, U.S. Department of Commerce, Office of Telecommunications, Inst. Telecommunication Sciences, Jan. 1971.
- [5] R. H. Ott, "An Alternative Integral Equation for Propagation Over Irregular Terrain (Part 2)," Radio Science, 6, 1971, pp. 429-435.
- [6] S. H. Cho, "Electromagnetic Wave Propagation Over Nonuniform Surface Impedance Planes," Ph.D. Thesis, Elec. Eng., Univ. Wisconsin, 1975, pp. 93 et. seq.
- [7] R. Mittra, "The Vector Compensation Theorem and Its Applications to Boundary Value Problems," Scient. Rept. 2, AFCRL 575, Univ. Colorado, June 15, 1961. Also R. J. King, private notes, 1978.
- [8] C. Wagner, "On the Numerical Solution of Volterra Integral Equations," J. Math. Phys., 32, 1953, pp. 289-401.

SESSION III - "CODE DEVELOPMENT"

"An Insulated Wire Capability for NEC"

Gerald Burke

Lawrence Livermore National Lab

"User-Friendly Electromagnetics Software"

Edward Miller

U of Kansas-ECE Department

"A Topside Antenna Case Study with DIDEK and Spectrum: Model Generation and Current Display Codes"

S.J. Kubina and Colin Larose

Concordia University

"Error Bounds on Direct and Indirect Solution of EM Scattering Problems"

V.P. Cable

California Microwave, Inc.

"MININEC to MICRONEC, The Next Generation"

Lewis Thomas

Lockheed Missile and Space Company

"An Implicit Algorithm for Solving Maxwell's Equations in Non-Linear Conducting Media"

W.E. Page

Air Force Weapons Lab

R.L. Knight and R.W. Clemens

Applied Physics, Inc.

"Computer Program for Designing Large Phased Array Radiating Elements"

H.K. Schuman and G.A. Bright

Atlantic Research Services Corporation

"Computational Resources and Convergence for MM Calculations with Electrically Large Scatterers"

John W. Williams

Booz, Allen & Hamilton Inc.

J.S. Yu

Sandia National Laboratories

AL: INSULATED WIRE CAPABILITY FOR NEC

G.J. Burke
Lawrence Livermore National Laboratory
P.O. Box 808, L-156
Livermore, CA 94550

The code NEC-3 has been modified to model an insulated wire in air or a lossy medium. The equivalent radial current approach taken by Richmond and Newman (Radio Science, January 1976) was adapted to the spline current basis and point matching in NEC. For an insulated wire in a conducting medium, the NEC current expansion is modified to improve convergence. Insulated wires may be located above or below the ground surface.

Results are compared with published measurements for insulated wires in air and water and with a transmission line approximation. The power balance of input, radiated and dissipated power, is also examined. The effect of insulation on the radiation efficiency of a buried antenna is demonstrated.

* Work performed under the auspices of the U.S. Department of Energy by the Lawrence Livermore National Laboratory under contract number W-7405-ENG-48.

NUMERICAL SOLUTION FOR AN INSULATED WIRE INCLUDING THE EFFECT OF AN INTERFACE

G. J. BURKE
E. K. MILLER

LAWRENCE LIVERMORE NATIONAL LABORATORY

A METHOD OF MODELING AN INSULATED WIRE USING
AN EQUIVALENT RADIAL POLARIZATION CURRENT*
IS BEING ADAPTED TO THE NUMERICAL
ELECTROMAGNETICS CODE (NEC-3)

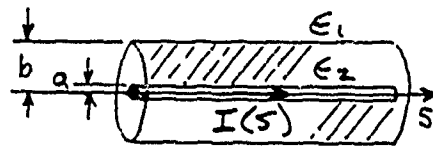
PRELIMINARY RESULTS ARE COMPARED WITH -

- RICHMOND & NEWMAN'S CODE
- A TRANSMISSION LINE MODEL (RWP. KING)
- MEASUREMENTS

* J.H. RICHMOND, E. H. NEWMAN - RADIO SCI. 1976

AS DONE BY RICHMOND AND NEWMAN (R. SCI. 1976)
AN INSULATING SHEATH IS REPLACED BY AN
EQUIVALENT CURRENT SOURCE IN THE AMBIENT
MEDIUM

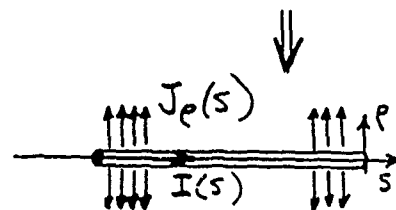
$$\vec{J}_{eq} = j\omega(\tilde{\epsilon}_2 - \tilde{\epsilon}_1)(\vec{E}_s + \vec{E}_I)$$



WE ASSUME -

$$|\vec{E}_s| \gg |\vec{E}_I|$$

$$\vec{E}_s \approx \frac{j I'(s)}{2\pi\omega\epsilon_2 \rho} \hat{\rho}$$



THEN

$$\vec{J}_{eq} \approx \vec{J}_e = \frac{-(\epsilon_2 - \epsilon_1)}{2\pi\epsilon_2 \rho} I'(s) \hat{\rho} \quad a < \rho < b$$

\vec{J}_e PRODUCES AN ADDITIONAL AXIAL FIELD -

$$E_s^p(s_0) = \frac{-j\eta}{4\pi k_1} \hat{s}_0 \cdot \int_a^b \int_0^{2\pi} \int_{s_1}^{s_2} \rho \vec{J}_e(\rho, \phi, s) \cdot$$

$$(\nabla\nabla + k_1^2 \vec{I}) \frac{\exp(-jk_1 R)}{R} ds d\phi d\rho$$

$$\approx \frac{j\eta(\epsilon_2 - \epsilon_1)}{2\pi k_1 \epsilon_2} I''(s_0) \ln \frac{b}{a}$$

WHICH IS INCLUDED IN THE INTEGRAL EQUATION

$$\int_S \hat{s}_0 \cdot \vec{G}(\vec{r}_0, \vec{r}') \cdot \vec{I}(s') ds' + E_s^p(s_0) = -\hat{s}_0 \cdot \vec{E}_I(s_0)$$

IN NEC, THE CURRENT IS EXPANDED IN SPLINE BASIS FUNCTIONS

$$I(s) = \sum_{j=1}^N X_j F_j(s)$$

$$F_j(s) = \sum_{\ell} [A_{j\ell} + B_{j\ell} \sin k_1(s-s_\ell) + C_{j\ell} \cos k_1(s-s_\ell)]$$

WITH POINT MATCHING, THE MATRIX EQ. IS

$$\sum_{j=1}^N X_j [G_i[F_j] + K_{ij} F_j''(s_i)] = -E^I(s_i) \cdot \hat{s}_i \quad i=1, \dots, N$$

$$\text{WHERE } K_{ij} = \frac{j\omega(\epsilon_2 - \epsilon_1)}{2\pi k_1 \epsilon_2} \ln \frac{b}{a} \quad \begin{array}{l} \text{IF } F_j \text{ EXTENDS} \\ \text{ONTO SEGMENT } i \end{array}$$

$$= 0 \quad \text{OTHERWISE}$$

$$G_i[F_j] = \hat{s}_i \cdot \vec{E} \text{ AT } s_i \text{ DUE TO CURRENT } F_j(s)$$

FOR THE REACTION INTEGRAL EQUATION
WITH PIECEWISE-SINUSOIDAL CURRENT
BASIS - $R_i(s)$, $i=1, \dots, N$

AS USED BY RICHMOND & NEWMAN

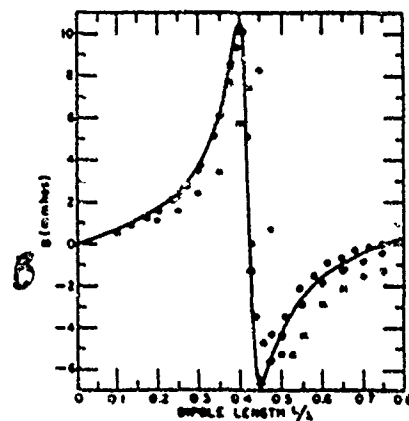
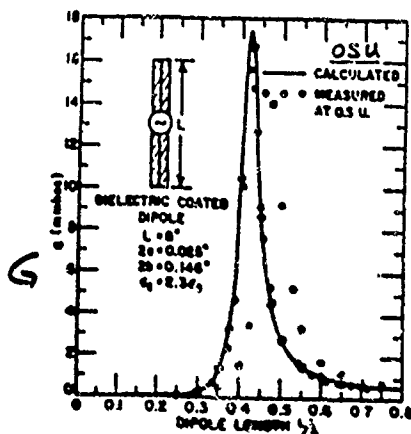
THE EXTRA MATRIX TERM FOR AN INSULATED
WIRE IS -

$$\Delta Z_{mn} = \frac{-(\epsilon_2 - \epsilon_1) \ln b/a}{2\pi j\omega \epsilon_1 \epsilon_2} \int_{mn} R'_m(\ell) R'_n(\ell) d\ell$$

WHERE THE INTEGRAL IS OVER THE REGION
SHARED BY R_m AND R_n

NEC RESULTS FOR A DIELECTRIC COATED DIPOLE
IN AIR ARE IN GOOD AGREEMENT WITH
RICHMOND'S CODE AND MEASUREMENTS

- NEC DIELECTRIC COATED WIRE
- NEC BARE WIRE

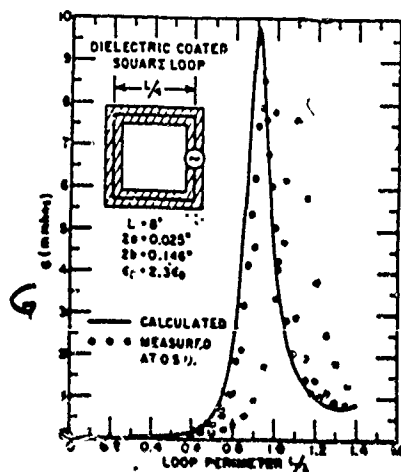
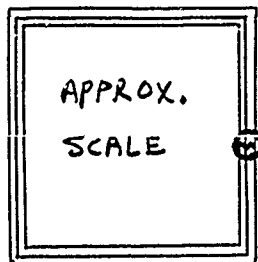


FOR A DIELECTRIC COATED LOOP, NEC RESULTS
ARE SHIFTED FROM 0.5 U.

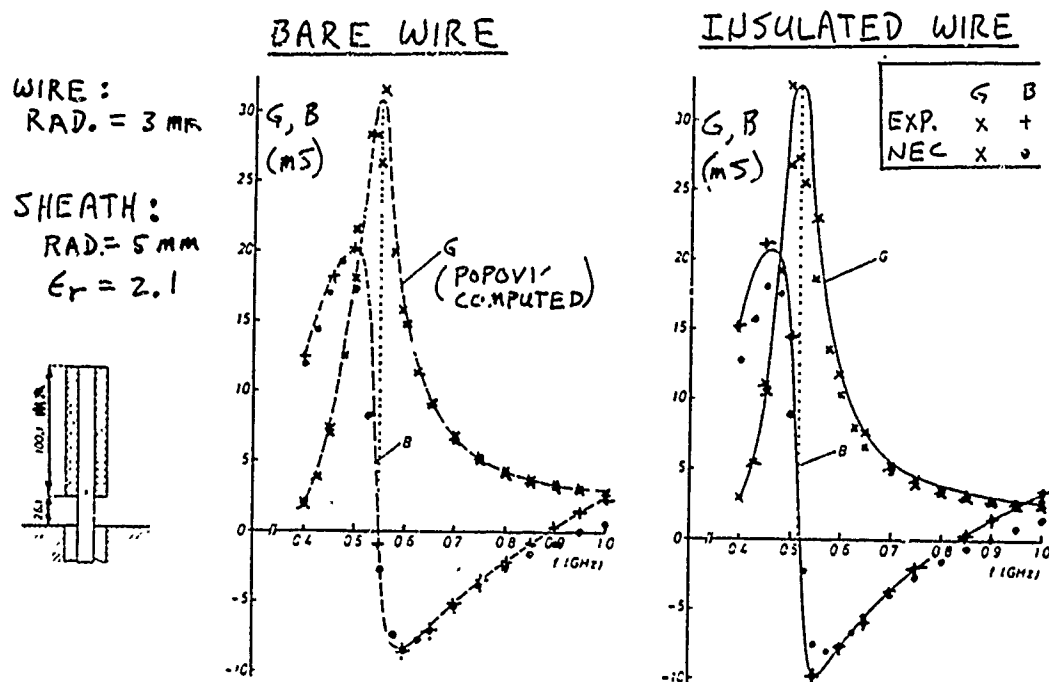
BUT IN REASONABLE AGREEMENT WITH EXPERIMENT

THIN WIRE APPROXIMATION MAY BE QUESTIONABLE

- NEC COATED WIRE
- NEC BARE WIRE



POPOVIC ET AL. HAVE MEASURED AND COMPUTED Y_{IN}
FOR SEVERAL INSULATED ANTENNAS -



THE FIELD COMPONENTS FROM INTERPOLATION
ARE USED TO EVALUATE THE GREEN'S FUNCTION
IN THE POCKLINGTON THIN-WIRE INTEGRAL
EQUATION

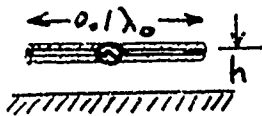
$$\hat{s} \cdot \int_L \left[\vec{G}_{\text{DIRECT}}(\vec{r}, \vec{r}') + \vec{G}_{\text{GROUND}}(\vec{r}, \vec{r}') \right] \cdot \vec{I}(s) ds = -\hat{s} \cdot \vec{E}^{\text{INC}}(s)$$

WHICH IS SOLVED BY MEANS OF THE METHOD
OF MOMENTS

RESULTS FOR AN INSULATED WIRE NEAR AN INTERFACE LOOK REASONABLE

GROUND:
 $\tilde{\epsilon}_g = 10 - j10$

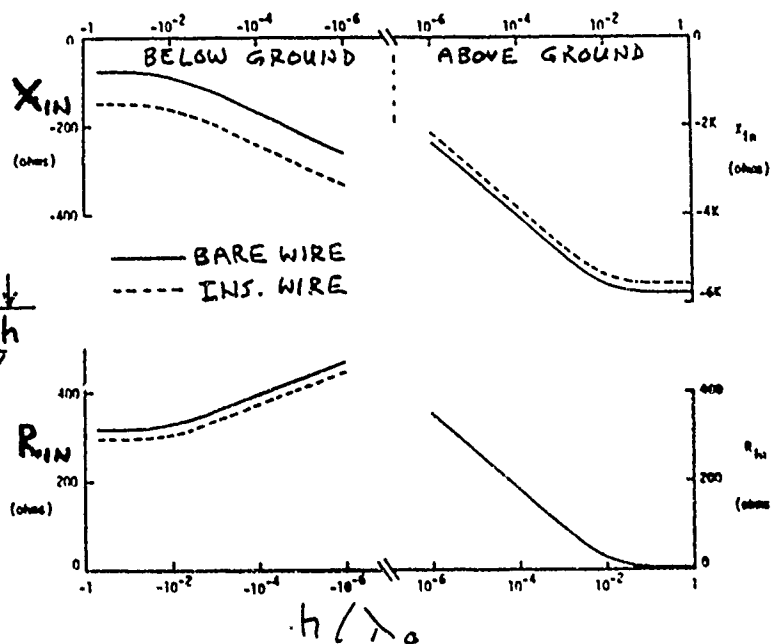
WIRE:
 RADIUS = $10^{-8} \lambda_0$



INSULATION:

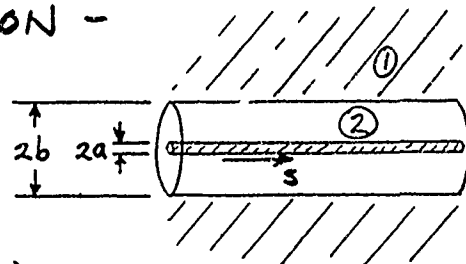
RADIUS = $2(10^{-8})\lambda_0$

$\epsilon_r = 3$
 $\sigma = 0$



FOR AN INSULATED WIRE IN A CONDUCTING MEDIUM A SIMPLE TRANSMISSION LINE MODEL FROM KING & SMITH, ANTENNAS IN MATTER WAS USED FOR COMPARISON -

PROPAGATION CONSTANT AND CHAR. IMPEDANCE ARE :



$$k_L \approx k_2 \left[1 + \frac{H_0^{(2)}(k_1 b)}{k_1 b \ln(b/a) H_1^{(2)}(k_1 b)} \right]^{1/2}$$

$$Z_c = \frac{\omega \mu k_L}{2\pi k_2^2} \ln(b/a)$$

VALID FOR $k_1 \gg k_2$

FOR A DIPOLE WITH LENGTH $2h$

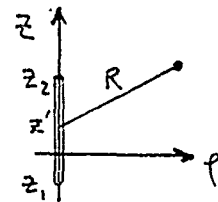
$$I(s) \approx \frac{jV_0}{2Z_c} \frac{\sin k_L(h-|s|)}{\cos(k_L h)}$$

TO IMPROVE CONVERGENCE NEC WAS MODIFIED
TO USE k_L FROM KING'S T. L. MODEL IN
THE CURRENT EXPANSION

$$F_j(s) = \sum_l [A_{jl} + B_{jl} \sin k_L (s - s_l) + C_{jl} \cos k_L (s - s_l)]$$

WHEN $k_L \neq k$ IN THE MEDIUM, ADDITIONAL
INTEGRALS APPEAR IN THE EXPRESSIONS
FOR THE FIELD OF A STRAIGHT SEGMENT

FOR CURRENT $I(z') = \begin{pmatrix} \sin k_s z' \\ \cos k_s z' \end{pmatrix}$
AND k = WAVE NUMBER IN THE MEDIUM
THE FIELDS ARE :



$$E_p(\rho, z) = \frac{-jnI_0}{4\pi k \rho} \left\{ \left[\begin{pmatrix} \sin k_s z' \\ \cos k_s z' \end{pmatrix} [1 - (z - z')^2 (1 + jkR)] \frac{1}{R^2} + k_s \begin{pmatrix} \cos k_s z' \\ -\sin k_s z' \end{pmatrix} (z - z') \right] \frac{e^{-jkR}}{R} \right\}_{z_1}^{z_2}$$

$$- \frac{(k^2 - k_s^2) \int_{z_1}^{z_2} \begin{pmatrix} \sin k_s z' \\ \cos k_s z' \end{pmatrix} (z - z') \frac{e^{-jkR}}{R} dz'}{\quad}$$

$$E_z(\rho, z) = \frac{-jnI_0}{4\pi k} \left\{ \left[\begin{pmatrix} \sin k_s z' \\ \cos k_s z' \end{pmatrix} (z - z') (1 + jkR) \frac{1}{R^2} - k_s \begin{pmatrix} \cos k_s z' \\ -\sin k_s z' \end{pmatrix} \right] \frac{e^{-jkR}}{R} \right\}_{z_1}^{z_2}$$

$$+ \frac{(k^2 - k_s^2) \int_{z_1}^{z_2} \begin{pmatrix} \sin k_s z' \\ \cos k_s z' \end{pmatrix} \frac{e^{-jkR}}{R} dz'}{\quad}$$

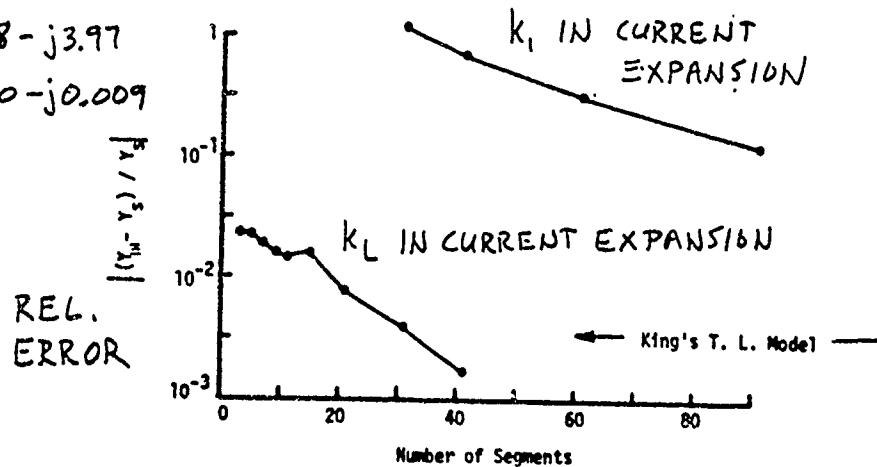
THE ADVANTAGE OF USING k_L IN THE CURRENT EXPANSION CAN BE SEEN IN THE CONVERGENCE RATE OF THE SOLUTION -

18 m. DIPOLE IN SEA WATER 1 MHz

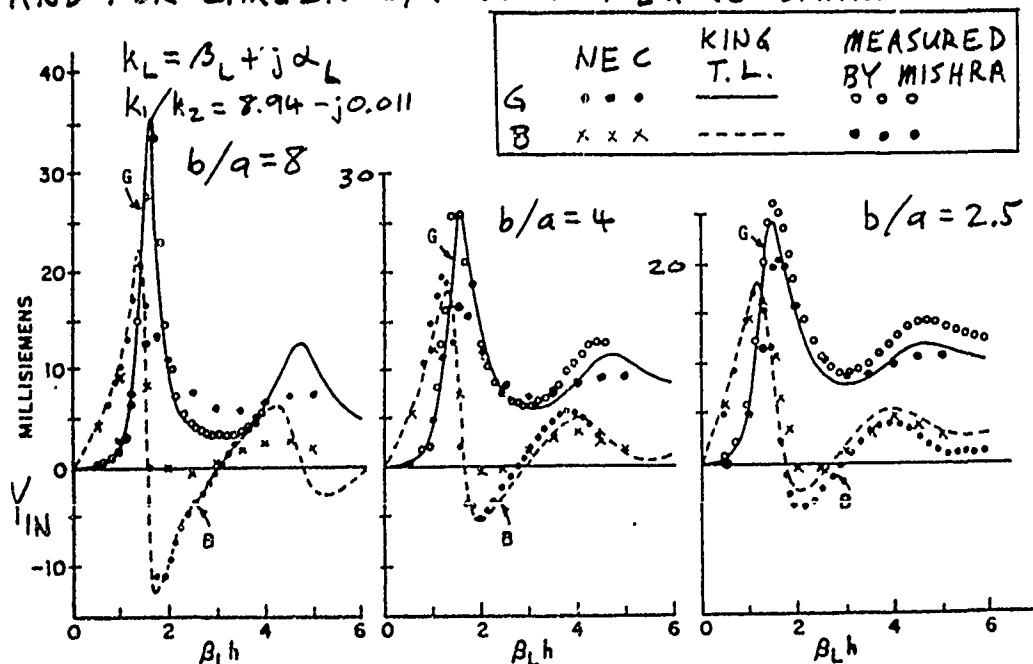
$Y_S = Y_{IN}$ FOR 61 SEGMENTS USING k_L

$$k_1 = 3.98 - j3.97$$

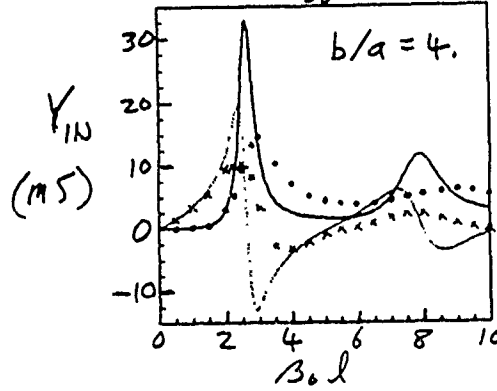
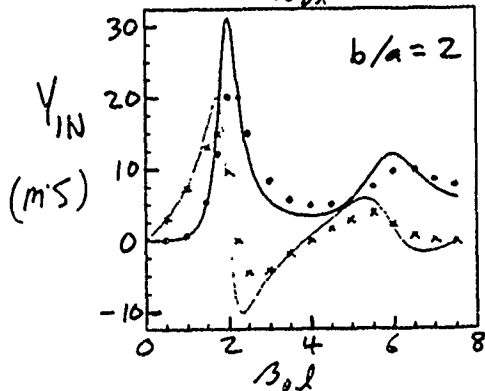
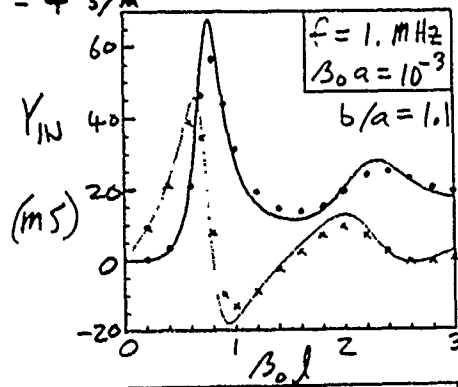
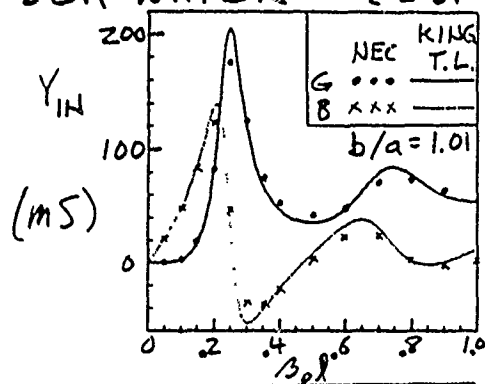
$$k_L = 0.20 - j0.009$$



MEASURED Y_{IN} FOR A MONOPOLE IN LAKE WATER
CONFIRMS NEC RESULTS FOR SMALL b/a
AND FOR LARGER b/a WHEN $\beta_L h$ IS SMALL



SIMILAR RESULTS ARE OBTAINED FOR A DIPOLE IN SEA WATER. $\epsilon = 81$ $\sigma = 4 \text{ S/m}$



RADIATION EFFICIENCY OF A BURIED DIPOLE IS INCREASED BY INSULATION

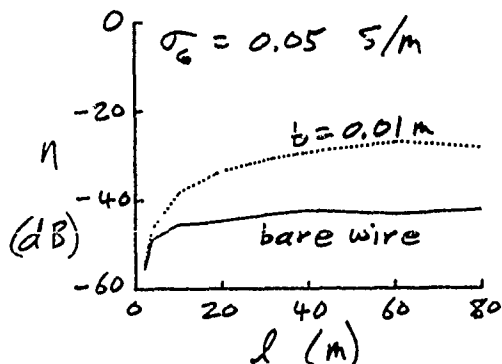
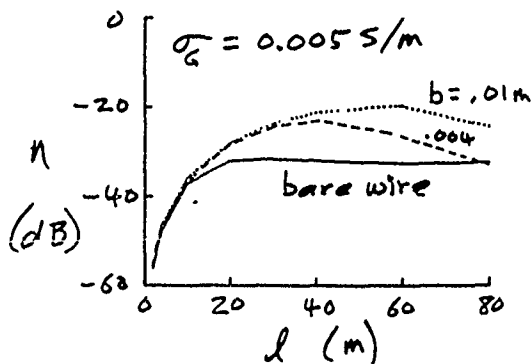
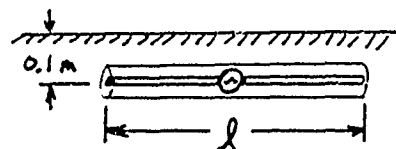
$$\eta = \int P_{RAD} / P_{IN} d\Omega$$

FREQ. = 2. MHz

WIRE RADIUS = a

SHEATH " = b (air)

GROUND: $\epsilon = 8$, σ_g



POWER LOSS IN THE SHEATH CAN BE COMPUTED AS

$$P_s \approx \int_l \int_a^b \int_0^{2\pi} \sigma |E_r|^2 \rho d\phi dr dl$$

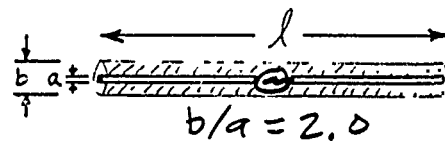
$$\approx \frac{1}{4\pi\omega^2} \int_l \frac{\sigma}{|\epsilon_z|^2} \ln \frac{b}{a} |I'|^2 dl$$

P_s IS MAXIMUM WHEN LOSS TANGENT IN SHEATH (ϵ_z) IS ONE.

$P_s \rightarrow 0$ FOR $\sigma \rightarrow 0$
OR $\sigma \rightarrow \infty$

POWER BALANCE PROVIDES A CHECK ON SOLUTION ACCURACY

SHEATH: $\epsilon = 3$, $\sigma = 0.05$
Freq. = 300 MHz



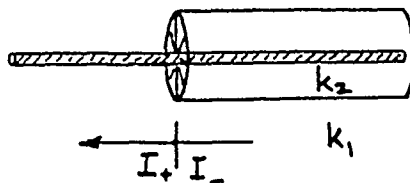
a/λ	0.01	0.02	0.05	0.1	0.2	0.3	0.4	0.5	0.6	0.8	
10^{-8}	5.65 0.005	1.89 0.04	2.37 0.57	6.09 4.44	28.92 27.83	58.34 57.75	77.53 77.15	87.14 86.78	91.51 91.09	93.27 92.65	η_1 η_2
10^{-6}	6.45 0.005	2.11 0.04	2.53 0.57	6.19 4.41	28.94 27.79	58.43 57.82	77.62 77.24	87.14 86.78	91.38 90.95	92.86 92.21	
10^{-4}	17.99 0.004	4.53 0.03	3.65 0.54	6.74 4.30	29.07 27.64	58.68 58.01	77.84 77.43	87.07 86.67	90.94 90.45	91.64 90.88	
10^{-3}	16.88 0.006	12.37 0.006	15.80 0.31	10.52 3.82	29.98 27.19	59.40 58.27	78.21 77.61	86.78 86.23	89.97 90.31	89.44 88.45	
10^{-2}	56.85 0.02	42.64 0.16	25.20 1.12	15.80 5.65	20.23 9.67	47.18 41.44	69.40 61.03	76.98 71.52	78.39 74.10	75.35 71.72	

$$\eta_1 = (P_{IN} - P_{SHEATH LOSS}) / P_{IN} \times 100.$$

$$\eta_2 = \int_{4\pi} P_{rad.} d\Omega / P_{IN} \times 100.$$

AT A JUNCTION BETWEEN BARE AND INSULATED WIRE A CONDITION IS NEEDED ON I'

I IS CONTINUOUS.



$$I'_+ / I'_- = k_1^2 / k_2^2 \quad ?$$

$$k_1^2 / k_2^2 \quad ?$$

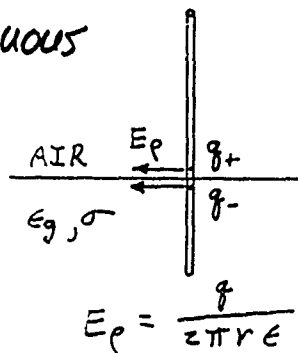
$$\frac{k_1 / z_{c1}}{k_2 / z_{c2}} \quad ?$$

AT THE INTERFACE -

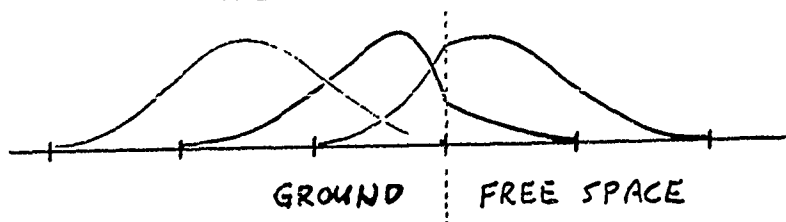
- E_r IS CONTINUOUS
- CHARGE DENSITY IS DISCONTINUOUS

$$q_- / q_+ = \epsilon_g$$

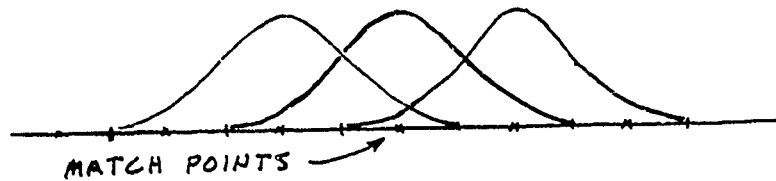
$$I'_- / I'_+ = \hat{\epsilon}_g = (\epsilon_g - j \frac{\sigma}{\omega \epsilon_0})$$



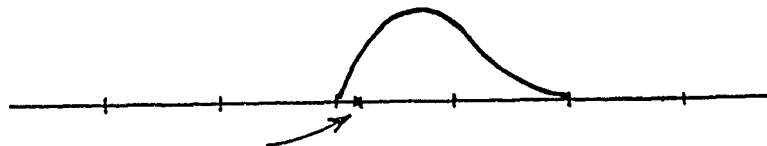
THE BASIS FUNCTIONS HAVE DISCONTINUOUS DERIVATIVES AT THE INTERFACE



THE CONDITION ON I' CAN BE LEFT AS AN UNKNOWN
TO BE DETERMINED IN THE NUMERICAL SOLUTION
IN ADDITION TO THE NORMAL SPLINE BASIS FUNCTIONS



A BASIS FUNCTION WITH DISCONTINUOUS DERIVATIVE
IS INCLUDED -



AND AN ADDITIONAL MATCH POINT TO DETERMINE
ITS AMPLITUDE

AT THIS POINT NEC WILL MODEL -

- INSULATED WIRES IN AIR OR CONDUCTING MEDIUM
- INSULATED WIRES NEAR AN INTERFACE FOR
DISTANCE TO INTERFACE \gg INSULATION RADIUS
- INSULATED WIRE WITH GROUNDED ENDS FOR
STUB LENGTH = $\lambda/4$ IN MEDIUM ?

MORE WORK IS NEEDED -

- CAREFUL NUMERICAL TREATMENT
- ANALYSIS OF DISCONTINUOUS SHEATH PROBLEM
- SOLUTION FOR AN INFINITE WIRE
- VALIDATION - MEASUREMENTS
MODEL WITH FINITE DIFFERENCE CODE

USER FRIENDLY ELECTROMAGNETICS SOFTWARE

E. K. MILLER

Department of Electrical and Computer Engineering
The University of Kansas
Lawrence, KS 66045

The evolution of electromagnetics modeling software may be concluded to involve up to three generations in its development. The first-generation stage, which is where most software development actually ends, is that which involves a feasibility demonstration for a particular modeling approach. Most codes that do not go beyond this stage could be characterized as research tools developed for a specific purpose the utility of which was expected to be limited. A few codes reach the second-generation stage through being documented and distributed and thereby reaching fairly widespread application. Such second-generation codes could usually be expected to have received ongoing improvement through funding and through the fairly continuous involvement of one or more of their developers. NEC is an example of one of these second-generation codes whose continued evolution into a third generation as part of the NEEDS (Numerical Electromagnetics Engineering Design Systems) is the topic of this discussion.

The major initial goal of NEEDS is to improve the utility of NEC as an EM analysis and design tool. This is to be accomplished by making the basic code easier to use, maintain and update. Of particular concern is the need to have access to a growing variety of modeling tools beyond what is now in NEC so that more modeling choices are provided to the user. One example is a NEC-GTD hybrid model to enable both techniques to be used in combination where appropriate. Another concern is that of providing more error checking and results' validation so that the modeling tools included in NEEDS can be used more reliably. Finally, graphics-based pre- and post-processors are planned to make input data preparation easier and more accurate, and output data interpretation more convenient and insightful. Various of these issues will be discussed in this presentation.

USER-FRIENDLY ELECTROMAGNETICS SOFTWARE

Edmund K. MILLER

The University of Kansas

Second Annual Review of Progress in Applied Computational Electromagnetics

Naval Postgraduate School

Monterey, CA

March 18-20, 1986

PRESENTATION ADDRESSES SOME OF THE ISSUES INVOLVED IN DEVELOPMENT AND APPLICATION OF COMPUTATIONAL ELECTROMAGNETICS SOFTWARE ...

- *DEGREE OF CODE MATURITY
 - FIRST, SECOND, THIRD GENERATION
- *CRITERIA FOR DEVELOPMENT
 - ACCURACY, EFFICIENCY, UTILITY
- *STRATEGY FOR DESIGN
 - AGGREGATION VS. RE-WRITE
- *MEASURE OF PERFORMANCE
 - VALIDATION, CALIBRATION, ERROR ANALYSIS

... IN THE CONTEXT OF NEEDS

EM MODELING CODES CAN BE CHARACTERIZED IN TERMS OF THEIR GENERATIONS OF DEVELOPMENT

- *FIRST GENERATION
 - FEASIBILITY DEMONSTRATION
 - MINIMAL DOCUMENTATION, DISTRIBUTION, ASSISTANCE
 - RESEARCH APPLICATIONS
- *SECOND GENERATION
 - ONGOING DEVELOPMENT AND IMPROVEMENT
 - CONTINUITY OF SPONSORS AND ORIGINATORS
 - BETTER DOCUMENTATION, WIDER DISTRIBUTION, MORE ASSISTANCE
 - ANALYSIS APPLICATIONS
- *THIRD GENERATION
 - EXTENDED MODELING CAPABILITIES
 - ON-LINE HELP AND GUIDANCE, IMPROVED DOCUMENTATION
 - MORE AUTOMATED
 - DESIGN APPLICATIONS

NEEDS IS ONE EXAMPLE OF EVOLUTION TOWARDS A THIRD-GENERATION CODE

- *BRACT (1968-1972)
 - FIRST-GENERATION RESEARCH APPLICATION
 - MAIN-FRAME BATCH
 - MODEST DISTRIBUTION
 - MBASSOCIATES
- *AMMP---AMP---NEC (1972-1984)
 - SECOND-GENERATION ANALYSIS APPLICATIONS
 - HINTS OF INTERACTIVITY, MINI-NEC
 - BROAD DISTRIBUTION, "DE-FACTO" STANDARD
 - MBASSOCIATES, LAWRENCE LIVERMORE, ...
- *NEEDS (1984-?)
 - THIRD-GENERATION DESIGN APPLICATIONS
 - INTERACTIVE, WORK-STATION ORIENTED
 - LAWRENCE LIVERMORE, ...

GOALS FOR NEEDS DEVELOPMENT ARE STRAIGHTFORWARD . . .

- 1) ACCURACY
 - QUANTIFIABLE (KNOWN)
 - SPECIFIABLE (USER SELECTABLE LEVEL)
 - ALLOCATEABLE (MOST CRITICAL QUANTITIES MOST ACCURATELY KNOWN)
- 2) EFFICIENCY
 - COMPUTATIONAL (NUMBER CRUNCHING)
 - APPLICATIONAL (USER-EFFORT REQUIRED)
- 3) UTILITY
 - BREADTH OF CAPABILITIES (PROBLEMS SOLVEABLE)
 - EASE OF USE AND INTERPRETABILITY (INPUT AND OUTPUT)

. . . AND INTERDEPENDENT

MORE SPECIFIC OBJECTIVES FOR IMPROVING USER FRIENDLINESS INCLUDE . . .

- ERROR ANALYSIS
 - HINTS FOR WHAT MIGHT BE THE CAUSE OF INCORRECT RESULTS
 - SUGGESTIONS FOR CORRECTING THE PROBLEM
- CALIBRATION
 - PERIODIC REASSURANCE THAT CODE OPERATION IS UNCHANGED
- TEST CASES FOR VALIDATION
 - PROVIDED AS PART OF THE SOFTWARE PACKAGE
 - MODELS AND RESULTS
- MODEL LIBRARY
 - GROWING SET OF COMMONLY ENCOUNTERED PROBLEMS
- ON-LINE DOCUMENTATION
- WORK-STATION INTERFACE
 - GRAPHICAL INPUT AND OUTPUT
 - COMMON FORMAT FOR ALL MODELING TOOLS

APPLICATIONS' ERRORS CAN BE ASSIGNED TO FOUR CATEGORIES . . .

- LEVEL 0, CODE "BOMBS"
 - SYSTEM SOFTWARE OR MODELING CODE
 - GENERALLY EASY TO FIND
- LEVEL 1, CODE RUNS PRODUCING OBVIOUSLY WRONG RESULTS
 - SYSTEM SOFTWARE OR MODELING CODE
 - FORMULATION, IMPLEMENTATION OR CODING ERROR
 - FINDING AND CORRECTING MORE DIFFICULT
- LEVEL 2, CODE RUNS PRODUCING PHYSICALLY PLAUSIBLE RESULTS THAT ARE WRONG
 - SYSTEM SOFTWARE OR MODELING CODE
 - INSIDIOUS HAIR PULLERS
 - PROBABLY MOST DIFFICULT TO HANDLE BECAUSE NOT OBVIOUS
- LEVEL 3, CODE PRODUCES USEFUL RESULTS MISINTERPRETED, MISTRUSTED OR MISUSED
 - UNREALISTIC EXPECTATIONS
 - UNWARRANTED SKEPTICISM
 - BLIND FAITH

ACCURACY MUST BE CONSIDERED THE FOREMOST ATTRIBUTE REQUIRED . . .

- INACCURATE BUT EFFICIENTLY AND EASILY OBTAINED RESULTS HAVE NO VALUE
 - RESULTS OF UNKNOWN ACCURACY HAVE SIMILARLY DEGRADED VALUE
 - ACCURACY SHOULD BE A "DIALABLE" QUANTITY
 - TRADE-OFFS BETWEEN ACCURACY AND EFFICIENCY SHOULD BE EXPLICITLY ALLOWED
- PHYSICAL- AND NUMERICAL-MODELING ERRORS NEED CONSIDERATION
 - INADEQUATE MATHEMATICAL REPRESENTATION OF THE REAL PHYSICAL PROBLEM
 - INADEQUATE NUMERICAL SOLUTION OF THE MATHEMATICAL REPRESENTATION

. . . FOR WHICH VARIOUS APPROACHES ARE AVAILABLE

INTERNAL CHECKS PROVIDE A MEASURE OF MODEL SELF-CONSISTENCY WITH RESPECT TO MAXWELL'S EQUATIONS AND THE NUMERICAL TRENDS

- INPUT DATA CHECK
 - IS INPUT CONSISTENT WITH CODE REQUIREMENTS AND ASSUMPTIONS?
 - UNINTENTIONAL VIOLATION OF MODELING GUIDELINES?
- NUMERICAL BEHAVIOR OF THE COMPUTATION
 - CONDITION NUMBER OF THE IMPEDANCE MATRIX
 - EQUATION ERROR, i.e., IS THE LINEAR SYSTEM SATISFIED?
 - SOLUTION ERROR, i.e., IS THE SOLUTION CONVERGED?
- PHYSICAL BEHAVIOR REQUIRED OF A VALID SOLUTION
 - ENERGY AND POWER CONSERVATION, e.g. $P_{rad} \sim I^2 R_{in}$
 - RECIPROCITY, e.g., *Receiving Pattern* = *Radiation Pattern*
 - BOUNDARY CONDITIONS, e.g.,
$$\int E_{tan} \cdot s \, ds \approx 0$$

EXTERNAL CHECKS PROVIDE INDEPENDENT CONFIRMATION CONCERNING THE VALIDITY OF CODE RESULTS . . .

- EXPERIMENTAL
 - CAN PROVIDE MEASURE OF PHYSICAL MODELING ERROR
 - PROBABLY MOST REASSURING
- ANALYTICAL
 - CAN PROVIDE MEASURE OF NUMERICAL MODELING ERROR
 - CANONICAL PROBLEMS RIGOROUSLY SOLVED
- COMPUTATIONAL
 - ALTERNATE TREATMENTS
 - PROVIDES MUTUAL CONFIDENCE

... AND ARE MUTUALLY COMPLEMENTARY

MEANINGFUL WAYS OF QUANTITATIVELY COMPARING RESULTS FROM TWO OR MORE SOURCES ARE REQUIRED WHEN THEY . . .

- YIELD DIFFERENT BUT EQUIVALENT DATA
 - DIFFERENT SAMPLING FUNCTIONS
 - Linear vs. sinusoidal
 - DIFFERENT FIELD MODELS
 - Integral vs. differential equations
- ARE QUALITATIVELY SIMILAR BUT QUANTITATIVELY DIFFERENT DUE TO FREQUENCY, ANGLE, TIME, . . . , SHIFTS
 - USE INTEGRAL OR GLOBAL RATHER THAN LOCAL OR POINTWISE MEASURES
 - USE REFERENCE-BASED PARAMETER VARIATIONS
 - COMPARE APPROPRIATE MODELS
 - CALIBRATE USING KNOWN RESULTS

CAPABILITY TO SPECIFY ACCURACY WOULD BE EXTREMELY HELPFUL . . .

- REDUCE UNCERTAINTY, BUILD CONFIDENCE
 - COULD LEAD TO EXPLICIT COST-ACCURACY TRADEOFF
 - WOULD PROMOTE "DESIGN TO SPECIFICATION"
- ... AS WOULD ITS ADAPTIVE ALLOCATION THROUGHOUT THE PROBLEM
- GIVE GREATEST ATTENTION TO MOST CRITICAL QUANTITY
 - PAY FOR WHAT'S MOST NEEDED

THERE ARE TWO MEASURES OF EFFICIENCY THAT ARE IMPORTANT FOR DESIGN APPLICATIONS . . .

- COMPUTATION EFFICIENCY
 - RECEIVES EXPLICIT CONSIDERATION
 - COMPUTER-RESOURCE COST IN TIME AND STORAGE
 - UPPER LIMIT ON MAXIMUM SIZE THAT IS MODELABLE
- APPLICATION EFFICIENCY
 - TENDS TO BE OVERLOOKED
 - PEOPLE-RESOURCE COST IN TIME AND FRUSTRATION
 - UPPER LIMIT ON MAXIMUM COMPLEXITY THAT IS MODELABLE

... HAVING SOME MIX THAT MINIMIZES THE OVERALL COST OF COMPUTER MODELING

COMPUTATION EFFICIENCY MIGHT BE IMPROVED USING VARIOUS ALTERNATIVES

- FORMULATION
 - MODELS MORE APPROPRIATE FOR PROBLEM REQUIREMENTS
 - COMPUTE ONLY WHAT IS NEEDED
 - HYBRID MODELS
 - MORE USE OF MODAL CONCEPTS
- APPROXIMATION
 - NEAR-NEIGHBOR APPROACH
 - HIGH-FREQUENCY TECHNIQUES
 - PERTURBATION AND ESTIMATION PROCEDURES
- NUMERICAL
 - MATRIX SOLUTION, e.g., LINEAR PREDICTION
 - ADAPTIVE SAMPLING
 - ERROR ESTIMATION

APPLICATION EFFICIENCY RELATES TO NON-SOLUTION ASPECTS OF MODELING . . .

- FOCUS ON APPLICATION AND NOT THE PROCESS
 - DEVELOP ERGONOMIC SOFTWARE DESIGN
 - PROVIDE COMMON-SENSE USER ASSISTANCE
 - Stored models, nominal parameter selection, . . .
 - ACCEPT ENGINEERING ORIENTED PROBLEM DESCRIPTION
 - CONSIDER EXPERT-SYSTEM APPROACH
- DEVELOP HANDBOOK OF SOLVED PROBLEMS
 - DEMONSTRATE WHAT IS FEASIBLE
 - CATALOG "TRICKS OF THE TRADE"
 - GIVE GUIDANCE FOR NEW PROBLEMS
- PROVIDE ANALOG OUTPUT
 - MORE GRAPHICAL OPTIONS
- BORROW FROM WHAT WORKS IN THE EXPERIMENTAL WORLD

... AND SUGGESTS COMPUTATION SHOULD BE VIEWED AS JUST ANOTHER WAY TO GET AN ANSWER

THE UTILITY OF A COMPUTER MODEL IS ESTABLISHED BY SEVERAL FACTORS . . .

- EASE OF USE
- SCOPE OF APPLICABILITY
- OVERALL COSTS INVOLVED
- RELIABILITY OF RESULTS
- INTEGRATABILITY WITH OTHER RESULTS

... WHICH ARE ULTIMATELY DRIVEN BY APPLICATIONS' REQUIREMENTS

HYBRID COMPUTATIONAL MODELS CAN INVOLVE MORE THAN ONE LEVEL OF HYBRIDIZATION . . .

- FAR-FIELD ONLY
 - FAR-FIELDS COMPUTED INDEPENDENTLY AND SUMMED
- FAR-FIELD INTERACTION
 - FAR FIELDS OF ONE MODEL ARE MODIFIED BY ANOTHER
 - e.g., Moment-Method fields scattered by GTD model
 - DOES NOT CHANGE MOMENT-METHOD IMPEDANCE OR ADMITTANCE MATRICES
- NEAR-FIELD INTERACTION
 - SOURCE DISTRIBUTIONS OF TWO (OR MORE) MODELS MUTUALLY MODIFIED
 - INTERACTION MATRICES ARE CONSEQUENTLY CHANGED

. . . FOR WHICH COMMON PROBLEM DESCRIPTION IS ESSENTIAL

SOFTWARE PERFORMANCE STANDARDS ARE NEEDED IF EM COMPUTATIONAL TOOLS ARE TO SATISFY THEIR POTENTIAL . . .

- GOES BEYOND SOFTWARE WRITING--
 - LANGUAGE, STYLE, STRUCTURE, FORMAT
- TO OUTPUT-ORIENTED FOCUS ON SUCH ISSUES AS--
 - IS THE CODE WORKING AS INTENDED?
 - IS IT PRODUCING PHYSICALLY REALISTIC AND VALID RESULTS?
- BY PROVIDING A QUANTITATIVE FIGURE-OF-MERIT FOR THE RESULTS PRODUCED IN MODELING APPLICATIONS--
 - USING INTERNAL CHECKS
 - COMPARISON WITH EXTERNAL DATA
- AND BY COMPARISON WITH STANDARD TEST CASES AND CANONICAL PROBLEMS

AT LEAST TWO DESIGN PATHS COULD BE CONSIDERED FOR A THIRD-GENERATION CODE . . .

- AN AGGREGATED APPROACH
 - COMBINE/HYBRIDIZE VARIOUS MODELING CODES
 - Minimize internal modification
 - Exploit basic functionality of each
 - ONE INPUT-OUTPUT INTERFACE
 - INTERNAL TRANSLATORS FOR CODE-TO-CODE INTERACTIONS
 - Provide unique data needs
 - Avoid unpredictable/uncontrollable influences
 - MORE EXPEDIENT
- A RE-WRITE APPROACH
 - COMMON FORMAT AND STRUCTURE
 - "TIGHTER" MORE EFFICIENT CODE
 - NON-TRIVIAL TASK
 - Replicate original functionality
 - LONGER TO ACHIEVE AND MORE EXPENSIVE
 - PROBABLE EVENTUAL APPROACH

. . . WITH NEEDS DEVELOPMENT HAVING CHANGED DIRECTION OVER TIME

- ORIGINAL MOTIVATION WAS TO MAKE NEC EASIER TO MODIFY AND UPDATE
 - SPECIFIC GOAL WAS E-FIELD SURFACE MODELING
- DESIRE TO HYBRIDIZE CAUSED RE-THINKING
 - GTD/MOM MODEL BECAME IMPORTANT GOAL
 - MAGNITUDE OF TASK BECAME DISTRESSINGLY CLEARER
- ALTERNATIVE TO RE-WRITING WAS NEEDED
 - QUICKER RESULTS WERE ENVISIONED
 - NO OBVIOUS BEST WAY TO RE-WRITE
 - DID NOT RULE OUT RE-WRITING EVENTUALLY

A MODEL OF THE MODELING PROCESS IS ESSENTIAL IF
THE RE-WRITING APPROACH IS TO BE EMBARKED ON
WITH CONFIDENCE

- TO IDENTIFY THE IRREDUCIBLE MINIMUM OF UNIVERSALLY
ENCOUNTERED MODELING STEPS

- WHAT IS NEEDED AS INPUT DATA?

- HOW IS INPUT TRANSFORMED VIA MAXWELL'S EQUATIONS TO THE
DESIRED OUTPUT?

- WHAT IS THE COMPUTATIONAL COST OF SEEKING UN-NEEDED
INFORMATION?

- TO PROMOTE MORE EFFICIENT HYBRIDIZATION

- DEVELOP A GENERALLY APPLICABLE PROCEDURE RATHER THAN

- CASE-BY-CASE TAILORING

- PERMIT USE OF INDEPENDENT INFORMATION OBTAINED FROM
EXPERIMENTAL, ANALYTICAL AND COMPUTATIONAL APPROACHES

PRESENTATION HAS DISCUSSED A FEW OF THE ISSUES
INVOLVED IN ACHIEVING USER-FRIENDLY
ELECTROMAGNETICS SOFTWARE

- DEGREE OF CODE-DEVELOPMENT MATURITY

- SOME CRITERIA FOR DEVELOPMENT

- STRATEGIES FOR DESIGN

- NEED FOR PERFORMANCE MEASURES

A TOPSIDE ANTENNA CASE STUDY
WITH DIDEK AND SPECTRUM:
MODEL GENERATION AND CURRENT DISPLAY CODES

S. J. Kubina and Colin Larose
EMC Laboratory, Concordia University
7141 Sherbrooke St. W.
Montreal, Que., Canada H4B 1R6

A classic problem in ships' topside design is the location of communications antennas where their desired patterns will suffer minimum distortion from nearby structures. Practical layouts of all the desired antenna systems lead to configurations that are bound to result in compromised pattern performance. Seasoned designers use their previous experience and intuition in the selection of initial antenna locations. It is hoped that these can be verified by scale model measurements at an early date so that practical adjustments can be made prior to a design freeze. If however, a commitment must be made prior to measurement, it is desired to have some quantitative assessment of pattern distortion. This paper describes such a dilemma for the case of a UHF antenna installation and a nearby support mast. In this case NEC and a GTD code were exploited to predict the likely result.

The model of the major portion of the tubular grid mast was developed with the use of DIDEK (P. Bhartia, S. J. Kubina et al., EMC Symposium, Tokyo, Oct. 1984) which has been described at the First Annual NEC review. Since that time, the display of segment currents, is being done by a separate program called SPECTRUM. It allows faster execution and additional file manipulation capabilities that are useful in attempting to understand the segment current contributions to pattern results.

Examples of model generation and the display of results are presented in a representative sequence for three frequencies in the UHF band. The NEC results are compared to those obtained from a simplified GTD analysis.

ERROR BOUNDS ON DIRECT AND INDIRECT SOLUTION OF EM SCATTERING PROBLEMS

V. P. Cable
P.O. Box 2800
California Microwave, Inc.
Woodland Hills, CA 91365

I. INTRODUCTION

Numerical difficulties in matrix solutions have long been discussed in the numerical analysis literature [1,2] as well as in the EM literature [3,4]. The purpose of this paper is to present a brief review of the classical LU direct method [5] plus an error bound on solving such systems based on the Doolittle method [6]. This bound takes into account accumulated roundoff, machine precision and "condition" of the coefficient matrix; convergence trends for certain EM scattering problems are computed with this bound. A general error bound for indirect solutions is also presented and applied to the "sphere of influence" iterative technique, a linear, 1st order, block technique (Cable); these results are also presented for a similar scattering problem.

II. THE EM PROBLEM

The matrix solution considered is for plane wave EM scattering by perfectly conducting thin flat plates and thin wire structures. The Moment Method [7] is used with piecewise sinusoidal, subsectional bases and Galerkin's method [8] to transform an EM integral equation into a system of simultaneous, linear, algebraic equations whose solution, under rather broad conditions, is exact if taken to the limit. This system of equations is usually then written in the familiar impedance matrix form given by

$$Z I = V \quad (1)$$

where $Z=[z_{kl}]$, $k,l=1,N$ is a $N \times N$ matrix of self and mutual impedances between subsectional modes, $I=[i_k]$, $k=1,N$ is a $N \times 1$ vector of unknown coefficients which determine the magnitude and phase of each current mode and $V=[v_k]$, $k=1,N$ is a $N \times 1$ vector representing plane wave excitation of the structure. The general solution to Eq. 1 is given by,

$$I = Z^{-1} V \quad (2)$$

The set of equations in Eq. 1 is not, in general, sparse since all mutual interactions are considered significant and the manner of numbering these interactions is arbitrary. Both direct and indirect solutions will be used to solve Eq. 1 and certain of these results appear in a subsequent section.

III. THE DIRECT LU SOLUTION AND ERROR BOUND

While the solution to Eq. 1 requires a nonsingular Z , it does not require that the actual inverse matrix Z^{-1} in Eq. 2 be found. The LU "decomposition" of Z is one method which represents a class of compact algorithms including the Crout, Doolittle and Cholesky methods (Westlake). None of these methods require storage of intermediate matrices during the solution process and for this reason, they are widely used in EM computations.

The LU decomposition (or factorization) of Z is based on the LU Theorem which states that, if Z^k represents the k^{th} principal submatrix of Z formed by eliminating $N-k$ rows and columns from Z and, if

$$\det Z^k \neq 0, \quad k = 1, 2, \dots, N-1, \quad (3)$$

then there exist two unique triangular matrices $L = [l_{ij}]$ and $U = [u_{ij}]$, with L being unit lower triangular (i.e., ones on the main diagonal and zeros above the main diagonal), such that

$$Z = L U \quad (4)$$

with

$$\det Z = \prod_{i=1}^N u_{ii} \quad (5)$$

The factored form of Z given by Eq. 4 is often referred to as the Doolittle decomposition of Z and details of computing L and U can be found elsewhere (Stewart). This technique leads to an optimum method with minimum roundoff when inner products are accumulated in double precision and rounded to single precision prior to storage.

Equation 1 can now be restated as

$$L U I = V \quad (6)$$

and the solution is begun by setting

$$U I = I' \quad (7)$$

in Eq 6 and solving for I' by forward substitution, then substituting back into Eq. 7 and solving for I by backward substitution. Also, if Z is symmetric, Cholesky's method (Square-Root method) can be used and Z takes the form

$$Z = G G^T \quad (8)$$

where T denotes transpose and the determinate is given by

$$\det Z = \prod_{i=1}^N (g_{ii})^2 \quad (9)$$

Relative solution error can be expressed by

$$E = \frac{\|I - \tilde{I}\|}{\|I\|} \quad (10)$$

where I and \tilde{I} represent the exact and the computed solutions, respectively, and $\| \cdot \|$ signifies an appropriate vector norm. The actual problem solved in the numerical process can be restated in the form given by

$$(Z + \delta Z) \tilde{I} = V + \delta V \quad (11)$$

where \tilde{I} is now the exact solution to the perturbed system. The δZ and δV terms are found by a process referred to as backward error analysis which yields the following relative error bound for the Doolittle algorithm,

$$E \leq \frac{1.01 K \gamma \varphi(N) \text{cond}\{Z\}}{1 - 1.01 K \gamma \varphi(N) \text{cond}\{Z\}} \quad (12)$$

where

$$K = \max_{i,j,k} \frac{|z_{ij}^{(k)}|}{\|Z\|} \quad (13)$$

$$\gamma = .5 \tau^{1-t} \quad (14)$$

and

$$\varphi(N) = 1.003 N^3 + 2.006 N^2 + 0.0026 N \quad (15)$$

with the restriction that

$$1.01 K \gamma \varphi(N) \text{cond}\{Z\} < 1 \quad (16)$$

The K factor in the above expressions is related to the "growth" of elements during triangularization, τ is the machine base (modulo), t is the number of bits carried in the mantissa, $\varphi(N)$ is derived from the forward and backward substitution phases and the condition of Z is given by

$$\text{cond}\{Z\} = \|Z^{-1}\| \|Z\| \quad (17)$$

The matrix norm assumed here is given by

$$\|Z\| = \max_i \sum_{j=1}^N |z_{ij}| \quad (\text{max row sum}) \quad (18)$$

IV. THE INDIRECT SOLUTION AND ERROR BOUND

A general form for i^{st} order, linear, stationary iteration is given by

$$I^{(m)} = H I^{(m-1)} + V \quad (20)$$

where H is referred to as the iteration matrix. An alternative form for this same process can be written as

$$I^{(m)} = I^{(m-1)} + d^{(m)} \quad (21)$$

where correction term $d^{(m)}$ is given by

$$d^{(m)} = Z^{-1} r^{(m-1)} \quad (22)$$

and "residual" $r^{(m)}$ by

$$r^{(m)} = V - Z I^{(m-1)} \quad (23)$$

The inverse of Eq. 22 is often called a psuedo inverse and simply represents a set of rules for computing $d^{(m)}$.

A new indirect technique called the sphere of influence (SOI) technique is based on dividing a large problem into a reasonable number of smaller problems and solving each of these directly (e.g., Doolittle). The psuedo inverse of Eq. 22 in this case is the set of implicit inverses of N ($m_i \times m_i$) submatrices $Z(m_i)$. Elements of the i th submatrix satisfy

$$c |z_{ii}| < |z_{ip}|, \quad p = 1, 2, \dots, N, \quad p \neq i \quad (24)$$

and each submatrix thus defines a unique region of influence around a subsectional domain. All N regions are then used iteratively to solve the original larger problem, assuming of course that the solution converges. The constant c in Eq. 24 is in the range $0 < c < 1$ and determines the size of each influence region and therefore the convergence rate.

The residual $r^{(m)}$ (Eq. 23), after $(m-1)$ iterations, appears to be a natural measure of convergence (or error) since $r^{(m)} = 0$ implies $I^{(m-1)}$ is the exact solution. On the other hand, to say small $r^{(m)}$ implies $I^{(m-1)}$ is near the exact solution may be an overstatement and an appropriate bound on the relative error which illustrates this is given by

$$E^{(m)} = \frac{\|I - I^{(m)}\|}{\|I\|} \leq \frac{\|r^{(m)}\|}{\|V\|} \text{cond}\{Z\} \quad (25)$$

where $\|\cdot\|$ again represents an appropriate vector norm. Norms of $r^{(m)}$ defined by Eq. 23, however, do not necessarily decrease monotonically when the process is convergent; they often oscillate or increase and, as in the previous bound, this bound is also sensitive to the $\text{cond}\{Z\}$.

A useful form for the bound of Eq. 25 is the normalized average residual defined by

$$\epsilon^{(m)} = \frac{\| r^{(m)} \|_1}{N \| V \|_1} \quad (26)$$

where

$$\| r^{(m)} \|_1 = \sum_{i=1}^N |r_i^{(m)}| \quad (\text{sum norm}) \quad (27)$$

and

$$\| V \|_1 = \max_i |v_i| \quad (\text{max norm}) \quad (28)$$

V. RESULTS

Calculations for two EM scattering problems are presented; 1) scattering by a thin, perfectly conducting, flat plate and 2) scattering by a random array of thin, perfectly conducting, straight wires (dipoles). Only square plates with unknown current I , expanded in strips of overlapping, cosinusoidal, surface patch modes [9], are considered. The random array model is defined with the uniform probability density function. Each dipole is approximately resonant and, hence, only one piecewise sinusoidal, filamentary, current mode is used per dipole. The total number of modes N on each structure therefore determines the number of simultaneous equations per given geometry. Also, all data presented here were computed on a 24 bit mantissa machine using standard FORTRAN double precision (approximately 11 decimal digits) and solution of simultaneous equations used only Cholesky's method.

Combined results for $\text{cond}\{Z\}$ (Eq. 17) and E (Eq. 12) for three plate sizes ($h = 1, 2$ and 3 wavelengths) are presented in Figure 1. The overlapping patch mode structure is also illustrated in the figure, where the number of strips per plate is held equal to the number of overlapping modes per strip. Cyclic peaks in E in Figure 1 appear to be loosely correlated with $\text{cond}\{Z\}$, at least at $N = 49$, however, without additional analysis, the exact cause of this behavior can only be speculated.

Computed $\text{cond}\{Z\}$ and E verses number of modes for three random arrays (average densities = 1, 8 and 64 dipoles per cubic wavelength) are presented in Figure 2. Placement of the dipoles and numbering of the Z matrix elements are random and increased N corresponds to the simple addition of dipoles. The monotonic behavior of $\text{cond}\{Z\}$ and E with N in Figure 2 does not appear to be a result of the randomness since similar calculations for single longer wires (Cable) exhibit this same behavior.

The $\epsilon^{(m)}$ error bound (Eq. 26) on SOT has been computed for a single random array geometry. Figure 3 illustrates this bound as well as the corresponding backscatter cross section verses iteration number for a 100 dipole array with an average density of 8 dipoles per cubic wavelength. Convergence is indicated for

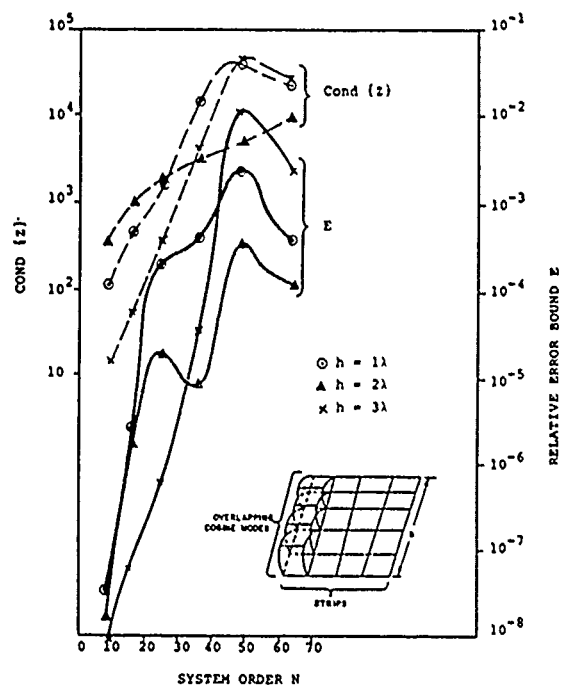


Figure 1. $\text{Cond}(Z)$ and E verses N for thin flat plates.

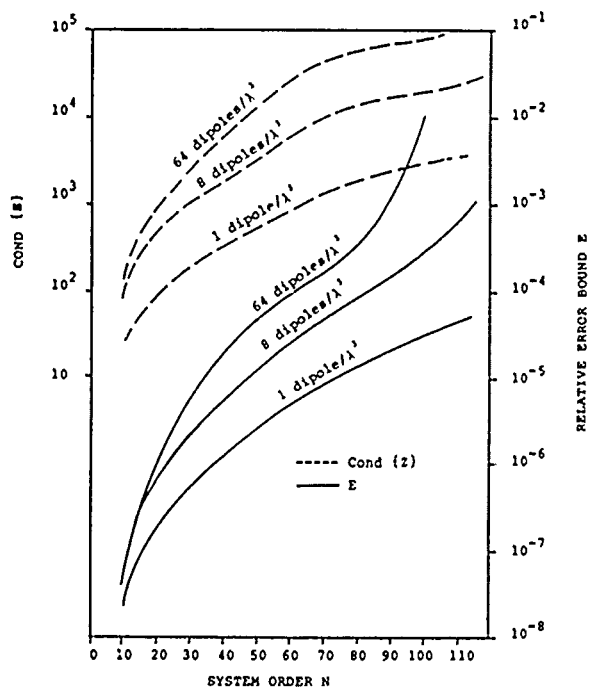


Figure 2. $\text{Cond}(Z)$ and E verses N for random arrays of resonant wires.

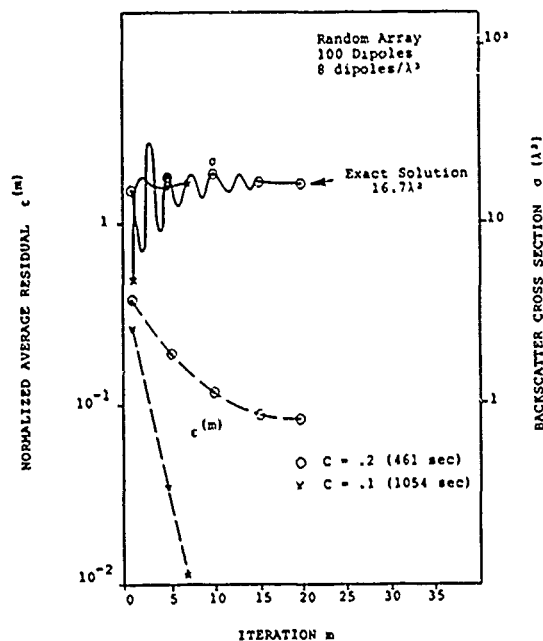


Figure 3. $\epsilon^{(m)}$ and σ verses m for a random array using SOI iteration.

both values of "influence" coefficient ($c=.2$ and $c=.1$). Computation times are also given. Note, the $c=.1$ case took only 7 iterations, as compared to 15 for $c=.2$, however, the $c=.2$ case was faster since the submatrices were smaller and computations for Cholesky's method increase as $1/6 N^3$.

VI. SUMMARY

This paper has presented upper bounds on relative solution error arising from roundoff and finite precision in certain direct and indirect numerical matrix solutions. These solution methods are commonly used in a wide variety of EM calculations resulting from application of Moment Methods. While systems of equations of this type are generally considered well suited to the digital computer, storage as well as time requirements often limit this technique to obstacle sizes on the order of a few wavelengths or less. This is particularly true when the numerical solution requires the complete coefficient matrix to be resident in fast access memory. On the other hand, if larger, faster machines (e.g., the Cray series) are used, data presented here indicate that the potential for roundoff and precision induced errors must not be forgotten.

REFERENCES

- [1] Stewart, G.W., Introduction to Matrix Computations, Academic Press, New York, 1973.
- [2] Wilkinson, J.H., "The Solution of Ill-conditioned Linear Equations," Mathematical Methods for Digital Computers, vol. 2, ed. A. Ralston, Wiley and Sons, New York, 1967.
- [3] Klein, C.A. and R. Mittra, "Stability of Matrix Equations Arising in Electromagnetics," *IEEE Trans. AP-S*, Nov., 1973.
- [4] Sarkar, T.K., K.R. Siarkiewicz and R.F. Stratton, "Survey of Numerical Methods for Solution of Large Systems of Linear Equations for Electromagnetic Field Problems," *IEEE Trans AP-S*, Nov., 1981.
- [5] Westlake, J.R., A Handbook of Numerical Matrix Inversion and Solution of Linear Equations, Wiley and Sons, New York, 1968.
- [6] Cable, V.P., "Application of Linear Iteration to Electromagnetic Scattering by Random Arrays of Wires," Report 3401-2, The Ohio State University, ElectroScience Laboratory, prepared under Contract AF33615-72-C-1435 for AFAL., Sep., 1975.
- [7] Harrington, R.F., Field Computation by Moment Methods, MacMillan Company, New York, 1968.
- [8] Richmond, J.H., "Radiation and Scattering by Thin Wire Structures in the Complex Frequency Domain," Report 2902-10, The Ohio State University, ElectroScience Laboratory, prepared under Grant NGL 36-008-138 for NASA, Jul., 1973.
- [9] Wang, N.N. and J.H. Richmond, et al., "Sinusoidal Reaction Formulation for Radiation and Scattering from Conducting Surfaces," *IEEE Trans. AP-S*, May, 1975.

MININEC TO MICRONEC, THE NEXT GENERATION

Lewis C. Thomas
(4061) Cassia Way
Sunnyvale, CA 94086

As VLSI technology grows, computing power grows to fill the imagination of the 'computer age' enthusiast. Can you imagine MININEC in the palm of your hand?

I adapted MININEC recently to run on my HP-71 handheld computer. The HP-71 contains 17.5 kbytes of internal memory with four ports for plug-in memory or ROM's in the front of the machine. I currently have 12 kbytes for a total of 29.5 kbytes. Not very impressive by main frame or most PC standards, but with that I have run a 38 segment MININEC problem. With after market RAM which is to be available in April 86, one could increase the machine capacity to 145 kbytes and run a problem as large as 118 segments.

If you're in a great rush, your main-frame may be the only answer. However, if you can relax and get a good night's sleep while the computer grinds away, you can wake up to the solution to your problem. For a comparative check, I ran the 'T' antenna example in Jim Logan's MININEC documentation (NOSC Technical Document 516 dtd 6 Sep 82.). I used 38 segments, which was most of my available memory, and obtained pattern data which compares in the third decimal place, with an overnight run time of around nine hours.

Remember, it's handheld!

MININEC TO MICRONEC, THE NEXT GENERATION

Lewis C. Thomas
1061 Cassia Way
Sunnyvale, CA 94086

The primary objective of programming MININEC on my HP-71 handheld computer was to have MININEC in a completely portable environment and to demonstrate the HP-71's muscle!

Due to present memory limitations, I have implemented the SHORT format for the matrices. This format provides 5-digit accuracy in the stored data compared with 12 digit accuracy in the standard format for the HP-71.

Corvallis Micra Technology is developing a 32 Kbyte RAM for use with the HP-71 in the front parts of the computer. I will be obtaining four of these memory modules in April and will then have 145 Kbytes of memory and plan to compare the SHORT to standard format on the 38-40 segment "T" example.

A limited number of cases have been run, and a comparison is shown in the following table.

<u>SEGMENTS</u>	<u>FILL</u>	<u>INVERT</u>	<u>PATT/OUT</u>	<u>TOTAL</u>	<u>CONFIG.</u>	<u>COMPARISON</u>
	<u>Hr:Min</u>	<u>Hr:Min</u>	<u>Hr:Min</u>	<u>Hr:Min</u>		
38 G	6:54	2:26	0:36	9:56	"T"	1 in 3rd
20 G	2:14	:22	:19	2:55	"T"	2 in 3rd
10 F	:30	:03	:05	:37	"T"	1 in 2nd
33 F	2:24	1:28	:17	4:09	"Y"	--
22 F	1:10	:22	:46	2:18	"Y"	FED DIFF
21 F	1:10	:22	:46	2:18	"Y"	

The 38 segment utilized most of the available memory and compared favorably with Jim Logan's example. As mentioned in Jim's documentation on MININEC, one must develop a familiarity with MININEC in order to obtain maximum efficiency with the code. A 20-segment example of the same configuration took less than one-third the time of the 38-segment and compared within 2 in the third decimal place.

An exact study of the computation time has not been attempted; however, by setting "flags" I have a visual check during the matrix filling operation. At least 50% of the time is spent in computing the elliptic integral. By restructuring the code to utilize the integral computation function of the HP-71 MATH ROM (which I understand is written in assembly language), I believe that the filling time could be significantly reduced.

The code could be further optimized for the HP-71 for use with and without a printer. Since the HP-71 is a "continuous memory" machine, the results of a run are available the next time the machine is turned on. With some careful planning, one could keep a solution indefinitely and run more patterns as desired, while having most of the machine memory available for other use. A major software capability of the HP-71 is its ability to redimension a matrix within a program, which allows one to reuse available memory.

The following table compares the HP-71 with an IBM PCXT with an 8087 coprocessor. As demonstrated, the IBM PLXT runs much faster in the compiled mode and approximately 2.5 the HP-71 in the interpret mode.

	FILL Hr:Min	INVERT Hr:Min	PATT/OUT Hr:Min	TOTAL Hr:Min
INTERPRET	2:52	1:06	:15	4:13
IBM PCXT				
COMPILE	:20	:07	:02	:29
HP-71	6:54	2:26	:36	9:56

MININEC for the HP-71 exists currently on magnetic cards. If there is sufficient interest among HP-71 owners, an EPROM could be developed which would facilitate easy use of the code.

AN IMPLICIT ALGORITHM FOR SOLVING MAXWELL'S
EQUATIONS IN NONLINEAR CONDUCTING MEDIA

W.E. Page, Air Force Weapons Laboratory

R.L. Knight, Applied Physics, Inc.

R.W. Clemens, Applied Physics, Inc.

A computational analysis of EM fields produced by a pulsed neutron and gamma source at or near a ground air interface has been developed. This analysis is divided into an early time phase for the initial γ pulse formulated in γ retarded time, and a late time phase. Both assume azimuthal symmetry and operate optionally in spherical polar or prolate spheroidal coordinates. Both phases include modeling of radiation induced Compton currents, and of air conductivity using field dependent charged species rate equations. The analysis also treats frequency dependent soil parameters and includes a time domain multipole outer boundary condition and field extrapolation scheme. The late time phase of the calculation includes ground neutron effects out to many milliseconds. The time step in the early time phase of the calculation is determined by the rise time of the γ -ray pulse and is considerably increased by the transformation of Maxwell's equations to retarded time. This paper treats only the late time phase.

In the late time phase, the problem has become quasistatic and the time step would normally be determined by the Courant condition. The finite difference algorithm used, however, is fully implicit. The only limit on the maximum time step is imposed by the rate of change of the sources, and the resolution desired in the results. The finite difference algorithm and an SOR matrix solver have been optimized for treating the nonlinear source region problem on a vector machine. Calculations are typically made from a problem time of 10^{-6} sec to 0.1 sec and require about 15 minutes of Cray 1 CPU time.

Azimuthal symmetry reduces the Maxwell's equations to TM field equations. These are written in generalized orthogonal coordinates. The equations are simplified by the transformation:

$$\begin{pmatrix} H_i \\ E_i \\ j_i \end{pmatrix} = h_i \begin{pmatrix} H'_i \\ E'_i \\ j'_i \end{pmatrix} \quad (1)$$

Analytical transformations of the independent variables are introduced to provide variable zoning in the coordinate system, thus

$$\frac{\partial}{\partial u_i} = \frac{\partial x_i}{\partial u_i} \frac{\partial}{\partial x_i} = \psi_i \frac{\partial}{\partial x_i} \quad i = 1, 2, 3 \quad (2)$$

The system is set up such that the x_i increments are constant while the u_i increments can be non-uniform. The finite difference equations are written in the x_i system and the u_i system describes the physical problem space.

The Maxwell equations to be solved become

$$\frac{\partial E_1}{\partial t} + \frac{\sigma}{\epsilon} E_1 = - \frac{j_1}{\epsilon} + \frac{G_1 \psi_2}{\epsilon} \frac{\partial H_3}{\partial x_2} \quad (3)$$

$$\frac{\partial E_2}{\partial t} + \frac{\sigma}{\epsilon} E_2 = - \frac{j_2}{\epsilon} - \frac{G_2 \psi_1}{\epsilon} \frac{\partial H_3}{\partial x_1} \quad (4)$$

$$\frac{\partial H_3}{\partial t} = - \frac{G_3}{\mu} \left[\psi_1 \frac{\partial E_2}{\partial x_1} - \psi_2 \frac{\partial E_1}{\partial x_2} \right] \quad (5)$$

where G_i is a combination of metric terms

$$G_i = \frac{h_i}{h_j h_k} \quad \begin{array}{l} i = 1, 2, 3 \\ i, j, k \text{ cyclic} \end{array} \quad (6)$$

The finite difference equation for H_3 is

$$\begin{aligned} \frac{H_{3i,j}^{n+1} - H_{3i,j}^n}{\Delta t} = & - \frac{G_3}{\mu} \left\{ \frac{\psi_1}{\Delta x_1} \left[\eta \left(E_{2i,j}^{n+1} - E_{2i-1,j}^{n+1} \right) \right. \right. \\ & + (1 - \eta) \left(E_{2i,j}^n - E_{2i-1,j}^n \right) \left. \right] - \frac{\psi_2}{\Delta x_2} \left[\eta \left(E_{1i,j}^{n+1} - E_{1i,j-1}^{n+1} \right) \right. \\ & \left. \left. + (1 - \eta) \left(E_{1i,j}^n - E_{1i,j-1}^n \right) \right] \right\} \end{aligned} \quad (7)$$

Where η determines how the spatial differences are centered in time.

Each electric field equation is of the form

$$\frac{\partial E}{\partial t} + \gamma(t)E = Q(t) \quad (8)$$

this equation can be integrated to give

$$E(t) = e^{-\chi(t)} \left[E(t_0) + \int_{t_0}^t Q(t') e^{\chi(t')} dt' \right] \quad (9)$$

where

$$\chi(t) = \int_{t_0}^t \gamma(t'') dt'' \quad (10)$$

define

$$\bar{\chi} = \bar{\gamma}\Delta t = \Delta t[\gamma]_{(t + t_0)/2} \quad (11)$$

Approximating equation (9) to second order in Δt yields the finite difference equations for the electric fields

$$\begin{aligned} E_{1\ i,j}^{n+1} = & E_{1\ i,j}^n e^{-\bar{\chi}} + \phi_{1\ i,j}^n \left[\frac{1}{\bar{\chi}} (1 - e^{-\bar{\chi}}) - e^{-\bar{\chi}} \right] \\ & + \phi_{1\ i,j}^{n+1} \left[1 - \frac{1}{\bar{\chi}} (1 - e^{-\bar{\chi}}) \right] \end{aligned} \quad (12)$$

$$\begin{aligned} E_{2\ i,j}^{n+1} = & E_{2\ i,j}^n e^{-\bar{\chi}} + \phi_{2\ i,j}^n \left[\frac{1}{\bar{\chi}} (1 - e^{-\bar{\chi}}) - e^{-\bar{\chi}} \right] \\ & + \phi_{2\ i,j}^{n+1} \left[1 - \frac{1}{\bar{\chi}} (1 - e^{-\bar{\chi}}) \right] \end{aligned} \quad (13)$$

where

$$\bar{\chi} = \frac{\Delta t}{\epsilon} \sigma_{i,j}^{n+1/2} \quad (14)$$

$$\phi_1 = - \frac{j_1}{\sigma} + \frac{G_1 \psi_2}{\sigma} \frac{\partial H_3}{\partial x_2} \quad (15)$$

$$\phi_2 = - \frac{j_2}{\sigma} - \frac{G_2 \psi_1}{\sigma} \frac{\partial H_3}{\partial x_1} \quad (16)$$

The electric fields are located on the sides of the finite difference mesh cell and the magnetic fields are at the corner of the cell. Substitution of equations (12) and (13) into equation (7) leads to the symmetric system

$$\left[\frac{\mu}{G_3 \eta \psi_1 \psi_2 \Delta t} + p_{i+} + p_{i-} + p_{j+} + p_{j-} \right] H_{3i,j}^{n+1} - p_{i-} H_{3i-1,j}^{n+1} - p_{i+} H_{3i+1,j}^{n+1} - p_{j-} H_{3i,j-1}^{n+1} - p_{j+} H_{3i,j+1}^{n+1} = D_4 \quad (17)$$

Where the coefficients P and D are known from previous calculation. This algorithm relates $\partial H_3 / \partial t$ to terms similar to $\nabla^2 H_3$ at the new time. The equations that must be solved constitute a five diagonal elliptic system at the new time step. For a $n \times m$ calculational grid one has an $nm \times nm$ matrix equation to solve.

Unless one is careful, the solution of this matrix system can use over 10 times as much computer time as the remainder of the calculation. Direct methods of solution of this system lead to a fill-in of the matrix such that the size of the calculations that one can do is limited by computer memory (intermediate space would go up as n^3 while the size of the mesh only goes up as n^2). In any case, after the fill-in has occurred, arithmetic operations must be performed on the n^3 non-zero elements, and although vectorization can help, the solution is still too slow to be practical.

This led to the investigation of various iterative methods, where the problem of intermediate space and fill-in is nonexistent. The matrix to be solved is large and sparse, however the diagonal pattern of the non-zero elements can obviously be used to our advantage. A number of schemes were investigated, including Jacobi, Reduced System, and SSOR all with Conjugate Gradient or Semi-Iterative acceleration, and SOR itself. Of these the SOR proved to be the fastest, with the various acceleration schemes not making up for the additional overhead that they caused. This may be an inherent problem with the system of equations being solved. In any case, the SOR

scheme was our starting point for making the code run efficiently on the CRAY 1.

The basic operation being performed in the SOR method is a matrix multiply of the Iteration matrix and the previous iterant to give a new estimate of the solution vector. The first optimization that can be made for our system is to reorder the matrix multiply to index down the diagonals, rather than across the rows as in a standard matrix multiply. This eliminates the indexing necessary to multiply each of the five non-zero elements in a given row by the appropriate element of the column vector that is the previous iterant and gives long vector operations. We note however, that this vector multiplication is not vectorizable when 'natural' ordering is used in the calculational mesh; this is because there is a vector dependency between the element being calculated and the previous element. Various authors have noted that a Red-Black permutation of the matrix removes this dependency, allowing the SOR scheme to be vectorized. Our method is to perform this Red-Black permutation of the matrix, and then do the SOR iteration using the matrix multiply in the form just described. With these modifications the code runs 4-5 times faster than when the scalar SOR routine is used, and hence, the improvement in the SOR routine itself must be somewhat better than this.

An indication of where the time is spent in the code is of interest. For a typical calculation, the main calculational routine; which includes the electromagnetic fields algorithms accounted for about 5% of the calculational time. The most time was spent in the SOR routine which accounted for about 34% of the calculational time, the Source routine which used about 20% of the calculational time, and the system log, sin-cos, exponential and sqrt routines which accounted for an additional 27% of the time. The remaining 14% of the time spread evenly among a large number of auxiliary routines, such as the self-consistency routine which accounted for 2.5% of the calculation. Although the sin and sqrt routines are used in the calculation of the metric coefficients, and the exponential routine is needed of the calculation of coefficients for the exponential integration, the majority of the calls to these system routines are from the source routine, so the source directly and indirectly accounts for perhaps 45% of the calculational

time. Thus the Source and the Matrix solution take the majority of the computational time.

Early in the development of the code a previous matrix solution method was taking 90+ percent of the calculational time. The current method has reduced this to the point where it is no longer the largest contributor to the run time. In the future we would like to investigate ICCG (Incomplete Cholesky - Conjugate Gradient) methods, however our investigation of various CG and SI methods in the past (but without preconditioning) have shown no net gain over the basic SOR iteration. At the moment it would appear that the most significant gain could be derived from reformulating the source function in a form that is more economical to compute.

COMPUTER PROGRAM FOR DESIGNING LARGE
PHASED ARRAY RADIATING ELEMENTS*

H.K. Schuman and G.A. Bright
Atlantic Research Services Corp.
1721 Black River Blvd.
Rome, NY 13440

Abstract

Large phased array antennas are attractive candidates for use in modern radars. This is because of the rapid, multiple beam scanning capability afforded by phased arrays. Computer simulation programs are required to evaluate the performance of the varied assortment of radiating elements likely to be of consideration and to aid in optimizing the design of those elements exhibiting greatest potential. A program has been developed under contract to the Air Force's Rome Air Development Center that can be applied here. The program can be used to compute antenna radiation patterns and active impedances of large planar arrays of dipole-like radiators or microstrip radiators. The underlying theory includes mutual coupling between the radiators and applies to a wide variety of radiator physical and electrical characteristics. The program recently has been applied to spaceborne and airborne antenna array concepts. The theory and capabilities of the program are reviewed and several illustrative examples are given.

Introduction

Large phased array antennas often are under consideration for use in radar systems, especially those systems calling for rapid beam steering and stringent pattern control. Satisfactory performance of the phase shift devices necessary for beam steering will depend, in part, on the RF load that the radiating elements impart on the devices. Large phased arrays typically cause dynamic loading of the devices. This arises because the mutual coupling between elements varies with the phasing applied to the elements and the phasing must be varied to obtain beamsteering and focusing. Because the impedance loads viewed by the devices, therefore, varies with phasing and, in fact, can be significantly different from that for an isolated element, severe mismatch may occur causing erroneous phase shifter operation or even burnout. Fabrication and testing of large arrays for the purpose of evaluating (active) impedances, and radiation patterns, is an expensive time consuming task. A cost and time effective alternative can be obtained from detailed computer analysis, or a combination of computer analysis and measurement.

A computer program has been under development for use in evaluating the many types and variants of radiating elements likely to be considered for large phased array antennas. The underlying technique for analyzing radiating elements basically has two parts. The first part is the "first approximation method" with which the performance of the element in an

*This work was supported in part under Air Force Contract F30602-83-C-0077.

infinite periodic planar array is analyzed. This method accounts for the interarray coupling between face arrays in space fed lenses as well as the coupling between elements within an array. The second part is the "higher approximation method". This method improves upon the first approximation method results by solving a finite array problem iteratively whereby the first approximation results are employed as an efficient starting point. The higher approximation method accounts for nonuniformities in periodicity as occurs at array edges, failed elements, and section interfaces. Detailed descriptions of the first approximation and higher approximation methods are given in References 1 through 3.

This paper contains an overview of the program capabilities, descriptions of recent theory extension of the first approximation method, and several illustrations of application to evaluating large array antenna concepts. The new theoretical developments deal with analyzing a wide variety of microstrip patch arrays and efficient modeling of folded dipole and integrated balun feedline thin conductor radiator arrays. The examples include analysis of antenna concepts and illustrate how attractive design alternatives can be uncovered largely as a result of the versatility of the analytical modeling.

General Capabilities

The theory underlying the computer program that applies to analyzing the plane wave scattering from, and transmission through, infinite phased array antennas was described in four reports and a published paper (References 1-5). The theory applies to space fed arrays (lenses) as well as to single array antennas. For lenses, the theory includes interarray, as well as intraarray, mutual coupling effects on the illuminated side and shadow side array element radiating current distributions and on the active impedance loads viewed by the amplitude and/or phase adjust modules that may interconnect the illuminated side and shadow side array elements.

The array lattices can be rectangular or triangular (general rectilinear). The radiating elements can be thin conductors or microstrip where "thin conductors" refers to arbitrarily curved thin conducting wires or strips, such as bent dipoles and folded dipoles, including parasitic wires or strips. Scattering from the feedlines connecting the radiators to the modules is included in the theory as well.

The shapes of the microstrip elements can be circular, elliptical, or rectangular although all elements within an array must be identical. The elements can be fed at interior locations via coaxial pin-type openings in the ground screen. Shorting pins or localized loads of other sorts can be arbitrarily located within the microstrip interiors. Edge feeds, as with microstrip transmission line, and edge loading, as occurs with "fences", also can be accommodated.

The theory has three parts: "radiation," "scattering," and "interarray coupling." In the radiation theory, the active impedance and reference element radiating mode current distribution of an infinite planar array of progressively phased elements is analyzed. In the scattering theory, the reference element feed port open circuit voltage and scattering current distribution produced by a plane wave illuminating an infinite planar array is analyzed. In the interarray coupling theory, the radiating and

scattering analyses are combined with the two-port scattering parameters of the modules in arriving at the lens illuminated side and shadow side radiating mode current distributions. The current distributions are determined in terms of a reference element distribution and an associated two dimensional progressive phase. A reference element distribution and two dimensional progressive phase is sufficient to define the radiating mode current distribution on every element in the infinite array. The current distributions can be used with other programs to determine radiation power gain patterns of large, finite arrays.

In all cases the theory includes the important mutual coupling effects between radiators in an array. Although these effects are complicated functions of the radiator geometry, the generality of the radiator shapes, however, is not sacrificed. The radiator models are decomposed into "local effect" models and radiating mode models. The local effect models (e.g., transmission line mode models for folded dipoles and cavity mode models for microstrip patches) do not entail mutual coupling. The radiating mode models (e.g., simple dipole mode for folded dipoles and exterior radiation model for microstrip patches) are based upon a plane wave expansion moment method (Reference 4) that accounts for the mutual coupling. In the moment method, each array radiator is modeled as a collection of linear segments, and the array is viewed as a collection of infinite arrays of segments, each segment array comprising a reference radiator segment and the similarly located segments on all other radiators. A current expansion is defined whereby to one expansion function is associated the current on one of the segment arrays. The field from each expansion function current array is expressed as a doubly infinite sum of plane waves. A matrix equation, solvable for the coefficients of the expansion functions that best represents the radiator currents, results by specifying the E-field boundary condition along each segment of the reference radiator and integrating the resulting equation over the segment.

The radiator modeling options in the program are listed in Table 1. Some of the principal output variables are

- Active impedance (SWR, etc.)
- Active element pattern,
- Current distribution, and
- Plane wave scattering reflection coefficient.

Special graphics developed for the program includes software for a "telescoping" Smith Chart. This software aids the radiator designer by allowing output impedance data to be plotted on conveniently scaled Smith Charts.

Thin Conductor Radiator Arrays

The principal thin conductor radiator models are described here. An example of a folded dipole array analysis and design exercise is presented also.

Consider the coplanar conducting strip fed, folded dipole radiator shown in Figure 1. The radiator is excited by an amplitude and/or phase adjust "module" and is imbedded in an infinite planar array of identical

elements that are progressively phased. The feedline and radiator are composed of parallel, coplanar, thin strip conductors. The widths of the feedline strips are equal; those of the radiator generally are not equal. The dipole feed port voltage V is the module output voltage transferred to the dipole feed port via the feedline transmission line (or "balanced") mode current. The feed port active admittance is given by $y = I_0/V$ where I_0 is the balanced mode current on the "upper" conductor of the coplanar feed. The feed port voltage is modeled as an ideal source that is divided into two equal sources in series. Each source is passed through its nearest junction in accordance with standard theorems of circuit theory. The resulting model is shown in Figure 2. The feedline is shown disconnected from the ground screen because it is assumed that the module output contains a balun that suppresses the unbalanced mode feedline current at this point.

The Figure 2 model can be viewed as the "sum" of the two models shown in Figure 3. The quantities indicated are combined to yield the feed port admittance of the original model in accordance with

$$y = \frac{I_r}{2(1+\gamma)^2 V_r} - \frac{I_r'}{4(1+\gamma) V_r} + Y_t/2 \quad (1)$$

Here $Y_t = I_t/V_t$ is the transmission line mode admittance of one-half the folded dipole, and γ is a constant that is dependent on the cross section contour, spacing, and relative sizes of the excited and parasitic folded dipole arms (References 5 and 6). Y_t is given also by

$$Y_t = -jY_0 \cot(kh) \quad (2)$$

where Y_0 is the characteristic admittance of the transmission line mode of the folded dipole and h is the length of the transmission line. Equations for γ and Y_0 can be obtained from those given in References 5 and 6. (Note that corrections to the formulas in 6 are given in 5.)

Only the left hand model of Figure 3 involves radiation and mutual coupling and requires analysis by the plane wave expansion moment method. An assumption in the modeling of Figure 3 is that the cross sections of the feedline and folded dipole arms are small in wavelengths. Relations for the equivalent circular cross section conductor radii, needed in the radiating mode model of Figure 3, are given in References 5 and 6.

Other dipole/feedline antenna types can be modeled by similar procedures that separate the radiating mode and transmission line mode parts. Five models, their radiating and transmission line mode parts, and the expressions for input admittances are shown in Figure 4. The dipole arms and feedlines in the models can be arbitrarily bent or curved. This capability is a consequence of the moment method modeling. Only the radiating mode models must retain the curvature of the original models. The transmission line mode models are functions of the lengths of the integrated balun feedlines or folded dipole arms and the characteristic impedances of the integrated balun feedlines or folded dipole arms. Results from applying radiating mode models to arrays of curved feedline radiators and arrays of bent arm radiators are given in Reference 4.

The field radiated by an antenna modeled in this fashion is computed from the currents in the corresponding radiating mode model only. Also, similar models have been developed for the scattering problem.

As an illustration of the application of these models, consider an equilateral triangular lattice array of folded dipoles of the Figure 1 type. The lattice and dipole orientation are shown in Figure 5. The desired range of scan from broadside is assumed to be 60° . The feedlines are assumed to drop straight back from the dipoles to the ground screen a distance of a quarter wavelength at the center frequency. The lattice dimensions are given in wavelengths corresponding to the frequency at the upper edge of a 15% bandwidth frequency range of interest. This lattice was chosen initially as a compromise on the conflicting constraints of maintaining grating lobe singularities well beyond the scan limit and minimizing the number of elements within the array aperture by maximizing the lattice spacings. The nearest grating lobe singularities occur at a scan angle of 90° in the E-plane and in the $\phi = 30^\circ$ plane. The E-plane singularity is suppressed because of polarization mismatch for propagation along the y axis; the severest singularity, therefore, could be expected to occur in the 30° plane although the ground screen tends to suppress even this singularity. The physical dimensions of the radiators were chosen to be those resulting from a design calling for a narrower scan range (larger lattice). That design was successfully attained with the computer program discussed here.

Figure 6 shows the active impedance as a function of scan at the low end of the frequency band. The dashed line borders the impedances computed with the "coplanar feed/folded dipole" model of Figure 4 wherein feedline scattering is accounted for. A severe impedance mismatch is evident when scanning in the E-plane. This effect is known to be due, in part, by the presence of feedline scattering (Reference 4). To demonstrate this, the impedances were recomputed with the "folded dipole/no feed" model of Figure 4. The feedline is absent in this model. The active impedances computed were those bordered by the solid line in Figure 6. Clearly, the severe E-plane scan mismatch is well reduced when feedline scattering is absent. Such feedline effects can be suppressed by reshaping the radiator arms. This was demonstrated with the program as reported in Reference 4.

H-plane scans theoretically are independent of feedline scattering for straight feedlines because of polarization mismatch between the feedlines and the radiation from the dipole arms in this plane. The H-plane scan loci for the two cases shown in Figure 6, therefore, should be identical. They differ slightly because of small differences in the moment method modeling of the dipole arms for the feedline present and feedline absent models.

The results in Figure 6 apply to a folded dipole of impedance step-up ratio $(1+\gamma)^2 = 1.6$ at the low end of the frequency band. Figures 7 and 8 show the active impedance loci for dipole dimensions changed to yield 1.2 and 2.2 step-up ratios, in addition to 1.6, at the low and high ends of the frequency band respectively and for a 3.6% increase in lattice spacing (grating lobe singularity at 68.2° scan). The analytical power of the program is clearly demonstrated by these results. Broadband folded dipole designs have been generated by exercising the radiator models with other

models in the program that account for feedline length and characteristic impedance variations. Designing array radiators by modeling feedline transmission mode properties as well as those of the radiators is illustrated also in the following section.

Microstrip Radiator Arrays

The microstrip antenna array modeling theory underlying the program is described in detail in Reference 5. A brief overview is presented here followed by an example of applying the program to designing microstrip radiators.

The microstrip radiator interior fields are expressed in terms of radial waveguide modes. Since the microstrip radiator perimeter is assumed to be coincident with a constant coordinate surface of a Helmholtz equation separable coordinate system, the modes are orthogonal along the perimeter. Their respective contribution to the total field is found by matching the interior fields with the exterior fields along the perimeter. In so doing, the exterior fields are expressed in terms of a line of equivalent magnetic current coincident with the perimeter. The magnetic current and associated tangential exterior H-field is represented by a moment method subsectional basis formulation. The formulation has two forms. One applies to isolated radiators and the other to infinite planar arrays of progressively phased radiators. Both are duals of thin conducting wire formulations (References 7 and 4 respectively). These formulations account for the radiative mutual coupling of an isolated radiator and between radiators in an infinite array. Edge "fringe" capacitive effects and other edge effects resulting from complicated designs that may introduce inductance and additional capacitance for frequency tuning and broadbanding purposes are accounted for directly within the generalized multiport network representation that arises naturally as a consequence of the subsectional moment method.

A fundamental matrix equation that arises from these formulations is

$$([Y^e] + [Y^d])\underline{V} = \begin{cases} -(\underline{I}^p + [Y]\underline{V}^p) & \text{pin feed} \\ \underline{I}^{sce} & \text{edge feed} \end{cases} \quad (3)$$

where $[Y^d]$ is a diagonal matrix of modal admittances; $[Y^e]$ and $[Y]$ are square matrices relating the exterior aperture tangential E- and H-fields in the modal basis; \underline{I}^p and \underline{V}^p are column matrices containing pin excited interior aperture H- and E-fields respectively in the modal basis; \underline{I}^{sce} is a column matrix containing modal coefficients of aperture H-field arising from an edge feed; and \underline{V} is a column matrix containing aperture E-field modal coefficients. (Note that provision is made for microstrip cavity excitation via feed pins (coaxial center conductors penetrating the ground screen) or edge feeds (microstrip or strip line transmission lines connecting directly to the radiator edge).) Once (3) is solved for \underline{V} , input impedance, radiated power, radiation pattern, and multiple feed port impedance parameters (z_{ij}) are readily determined.

The matrices $[Y]$ and $[Y^e]$ contain the microstrip radiator edge effects and radiation effects including fringe capacitance and mutual coupling with other radiators in an array. These matrices are obtained by

first formulating the subsectional basis moment method representation of the exterior region coupling between magnetic current "segments" along the microstrip perimeter. The result of this formulation, the subsectional basis moment matrix $[Y']$, then is transformed into the appropriate modal bases to yield $[Y]$ and $[Y^e]$.

The matrix $[Y']$ is approximated by

$$[Y'] = 2/\eta^2 [Z] + [Y_L] \quad (4)$$

where η is the free space wave impedance, $[Z]$ is the pulse expansion/pulse weighting thin wire E-field operator generalized impedance moment matrix (References 4 and 7) and $[Y_L]$ is a diagonal matrix of susceptances that account for the protrusion of the microstrip above the ground screen. The relationship between $[Z]$ and $[Y']$ in (4) is a consequence of imaging magnetic currents in a ground screen and invoking duality. If the problem concerns an isolated microstrip radiator, $[Z]$ is computed by the procedure described in Reference 7; if an infinite array, $[Z]$ is computed by the plane wave expansion moment method described in Reference 4. In either case an equivalent thin wire radius is required. The radius usually is taken to be $d/4$ where d is the substrate thickness.

This method for determining $[Y']$ assumes that the substrate exterior to the microstrip cavity has negligible effect on the exterior fields distant from the microstrip and on the coupling to other microstrips if in an array.

An accurate, but complicated, expression for computing the elements of $[Y_L]$ is available from the development in Reference 8. A simpler expression is obtained from that for the fringe capacitance of an arbitrarily shaped microstrip as derived in Reference 9. In many applications, however, expressions for the elements of $[Y_L]$ are not needed. Instead, $[Y_L]$ can be used as an adjustment factor to resonate the microstrip at precisely the center band frequency and, in the case of scanned arrays, at a specified scan angle. Such tuning is the simulation counterpart to physically adjusting a fabricated test array. An expression for the i^{th} diagonal element of $[Y_L]$ that has been found to shift a resonance without otherwise affecting the radiator impedance variation with frequency is

$$Y_{Li} = \beta j k \epsilon_r \Delta_i / \eta$$

where k is the free space wave number, ϵ_r is the substrate dielectric constant, Δ_i is the i^{th} segment length, and β is an adjustment coefficient ranging between 0 and 1.

Consider the rectangular patch radiator (Reference 10) shown in Figure 9. The radiator is excited at two points. These appear at the centers of the gaps dividing the radiator upper conductor and the edge "fences". (The fences serve to broaden the E-plane pattern.) The fences and meander lines at the gap excitation points combine to add series inductance L_f to the edges. The gaps are excited via microstrip transmission line that uses the upper conductor as a ground plane. A coaxial feed at the center connects to the microstrip line. The line divides at the right hand excitation point to excite, in parallel, that point and a transmission line of approximately twice as much characteristic

twice as much characteristic impedance that continues on to the left hand point. The latter line is electrically one half wavelength long at the center frequency.

Models of the radiator and feed network are shown respectively in Figures 10 and 11. In 10 the microstrip interior is shown to be excited by pin type feeds located near edges. The fences appear as inductances in series with edge apertures. The generalization of the microstrip modeling theory to accommodate the edge inductances begins by defining column matrices \underline{I}' and \underline{V}' of elements that are proportional to the edge tangential H- and E-fields respectively at the segment centers of a segmented contour fit to the microstrip perimeter. The relationship between \underline{I}' and \underline{V}' as viewed from the microstrip interior outward is given by

$$\underline{I}' = -[\underline{Y}']\underline{V}' \quad (5)$$

where $[\underline{Y}']$ is the moment matrix described earlier. The introduction of series inductive edge loading is modeled by appropriately modifying $[\underline{Y}']$ only. The revised $[\underline{Y}']$ is derived below.

As defined above, $(2/\eta^2)[\underline{Z}]$ is the moment matrix representation of the radiation admittance of the microstrip aperture. If the admittance matrix $[\underline{Y}_L]$ retains its definition of representing only the local edge effects and if the diagonal impedance matrix $[\underline{Z}_L]$ is introduced to represent the series inductive edge loads due to the fence, $[\underline{Y}']$ can be determined from the network equivalent representation shown in Figure 12. The numerical subscripts in the variables of the figure correspond to the column matrix elements of \underline{V}' and \underline{I}' or the diagonal elements of $[\underline{Y}_L]$ and $[\underline{Z}_L]$. The solution of this network is found to be

$$\underline{I}' = -([\underline{U}] + ((2/\eta^2)[\underline{Z}] + [\underline{Y}_L])[\underline{Z}_L])^{-1} ((2/\eta^2)[\underline{Z}] + [\underline{Y}_L])\underline{V}' \quad (6)$$

where $[\underline{U}]$ is the identity matrix. A comparison between (5) and (6) immediately defines $[\underline{Y}']$. Note that the i^{th} diagonal element of \underline{Z}_L , which corresponds to the i^{th} perimeter segment of length Δ_i along the fence edge of width W , is given by

$$Z_{Li} = j\omega \frac{W}{\Delta_i} L_f \quad (7)$$

This relation results as a consequence of the segmented inductances combining in parallel to form the total edge inductance. The inductance per segment, therefore, increases with decreasing segment size or increasing number of segments.

The analysis of the generalized (inductive edge loaded) microstrip model yields the impedance parameters of the pin excitation ports (z_{11} , z_{12} , z_{21} , z_{22}). These parameters, in turn, are combined with the feed network model as shown in Figure 11. Note that the inductances introduced by the meander lines appear in series with the excitation ports. The feed port input impedance is computed by solving the Figure 11 network. Also determined upon solution of this network is the microstrip edge E-field from which the radiated power and radiation pattern are found. The V_i^t of Figure 12 are proportional to this E-field at the perimeter segment centers.

Figure 13 shows the comparison of computed input impedance with measured impedance (from Reference 10) for the isolated radiator designed for a bandwidth exceeding 17% as defined by $SWR < 1.5$. The radiator was experimentally redesigned for a smaller bandwidth, in excess of 10% (Reference 10). The measured impedance for the redesigned radiator is shown in Figure 14. By adjusting the transmission line impedance R_g and the edge capacitance and inductance (both fence and meander line components) in the computer model to obtain approximately the same 10% bandwidth, the computed impedances also shown in Figure 14 were generated. Computed and measured element radiation patterns at the center frequency are shown in Figures 15 and 16. The agreement is reasonably good although the computed azimuth plane (E-plane or xz plane) is not quite as broad as its measured counterpart. Diffraction caused by the finite ground screen in the measurement setup may account for some of the discrepancy.

The computed active SWR for the 10% bandwidth element imbedded in an infinite, planar, broadside scan phased array (rectangular lattice shown in Figure 10) is given in Figure 17. The isolated element SWR is shown also for comparison. Some deterioration in impedance match due to arraying the radiator is evident. Azimuth scan (out to 60°) and elevation scan (out to 40°) results are shown in Figures 18 and 19 respectively. The impedance match, although degraded, appears to vary slowly with scan angle except in the vicinity of the azimuth plane grating lobe singularity that occurs at 61° at $1.05 f_0$. This suggests that the radiator can be redesigned in an array environment to exhibit improved performance throughout most of the scan volume of interest. Figures 20, 21, and 22 show the computed performance of the radiator following readjustment of edge capacitance and meander line inductance to exhibit good performance at broadside scan. Except in the vicinity of the grating lobe singularities the 10% bandwidth performance of the radiator is good throughout much of the desired scan volume.

The results presented here demonstrate the utility of the program to predict design adjustments that may become evident from array testing and to identify the cost effective adjustments that are likely to result in satisfactory array performance.

REFERENCES

*See Authors for references.

TABLE 1

RADIATOR MODEL OPTIONS

A. ENVIRONMENT

1. Isolated
2. Array
 - General Rectilinear Lattices (Rectangular and "Triangular")
3. Phased Array Lens
 - Interconnecting Amplitude/Phase Adjust Modules
 - Interarray and Intraarray Mutual Coupling

B. TYPE

1. Thin Conductor
 - Simple Dipole Variants (Bent or Curved Arms, etc.)
 - Folded Dipole Variants
 - Feedline Balun
 - Feedline Scatterer
 - Multiple Feed/Load Ports
 - Parasitic Scatterers
 - Curved Feedlines
2. Microstrip Patch
 - Rectangular, Circular, Elliptical
 - Pin Feed (Arbitrarily Located)
 - Edge Feed (Arbitrarily Located)
 - Multiple Feeds
 - Edge Loads (e.g., Fences)
 - Shorting Pins (Arbitrarily Located)

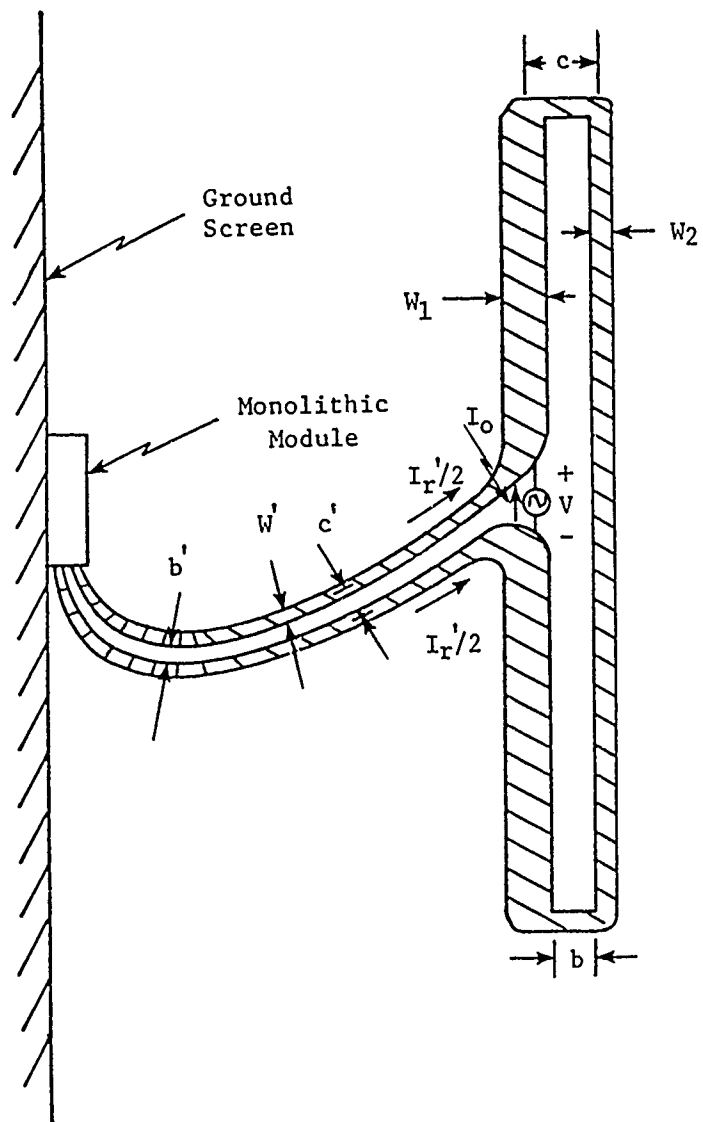


Figure 1. Coplanar Conducting Strip Fed, Folded Dipole Radiating Element

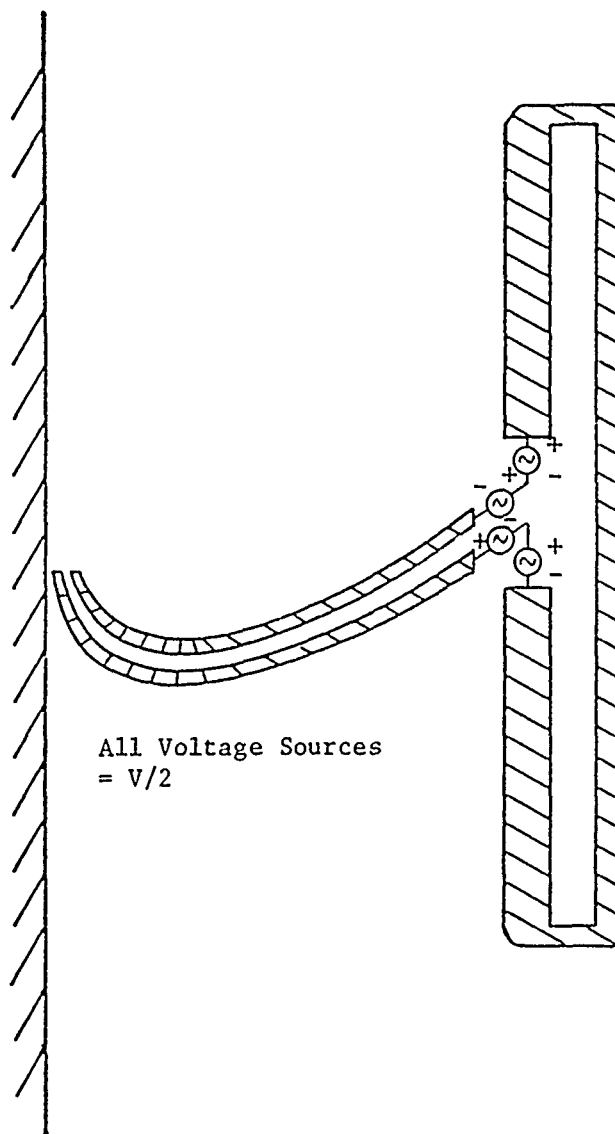


Figure 2. Equivalent Excitation Model

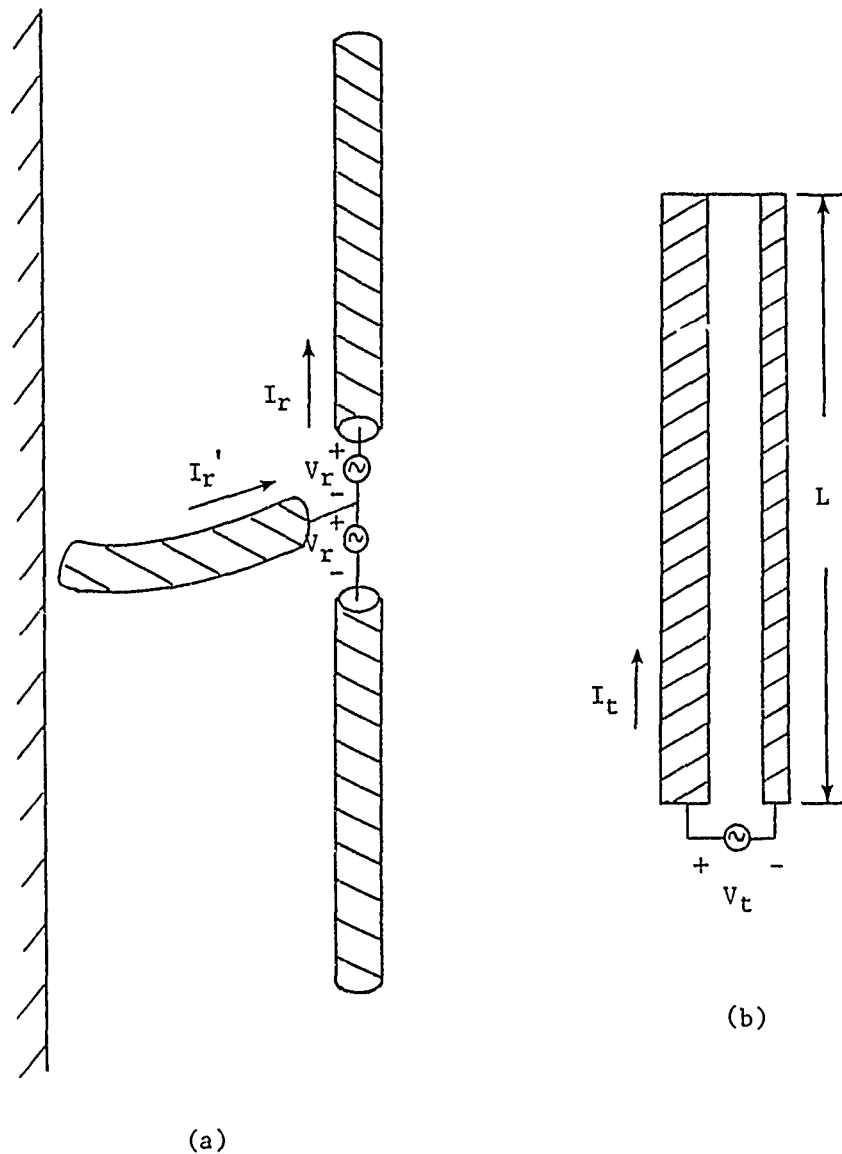


Figure 3. Folded Dipole Model Decomposition into Radiating Mode (a) and Transmission Line Mode (b)

Original Model	Radiating Mode Model	Transmission Line Mode Model	Admittance (I_o/V)
Folded Dipole/ No Feed			$\frac{I_r}{(1+\gamma)^2 V_r} + \frac{I_t}{2V_t}$
Integrated Balun Feed			$\frac{2I_r - I'_t}{4V_r} + \frac{I'_t}{V'_t}$
Integrated Balun Feed/ Folded Dipole			$\frac{I_r}{2(1+\gamma)^2 V_r} - \frac{I'_r}{4(1+\gamma)V_r} + \frac{I_t}{2V_t} + \frac{I'_t}{V'_t}$
Coplanar Feed			$\frac{2I_r - I'_r}{4V_r}$
Coplanar Feed/ Folded Dipole			$\frac{I_r}{2(1+\gamma)^2 V_r} - \frac{I'_r}{4(1+\gamma)V_r} + \frac{I_t}{2V_t}$

Figure 4. Decomposition of Thin Conductor Radiator Models

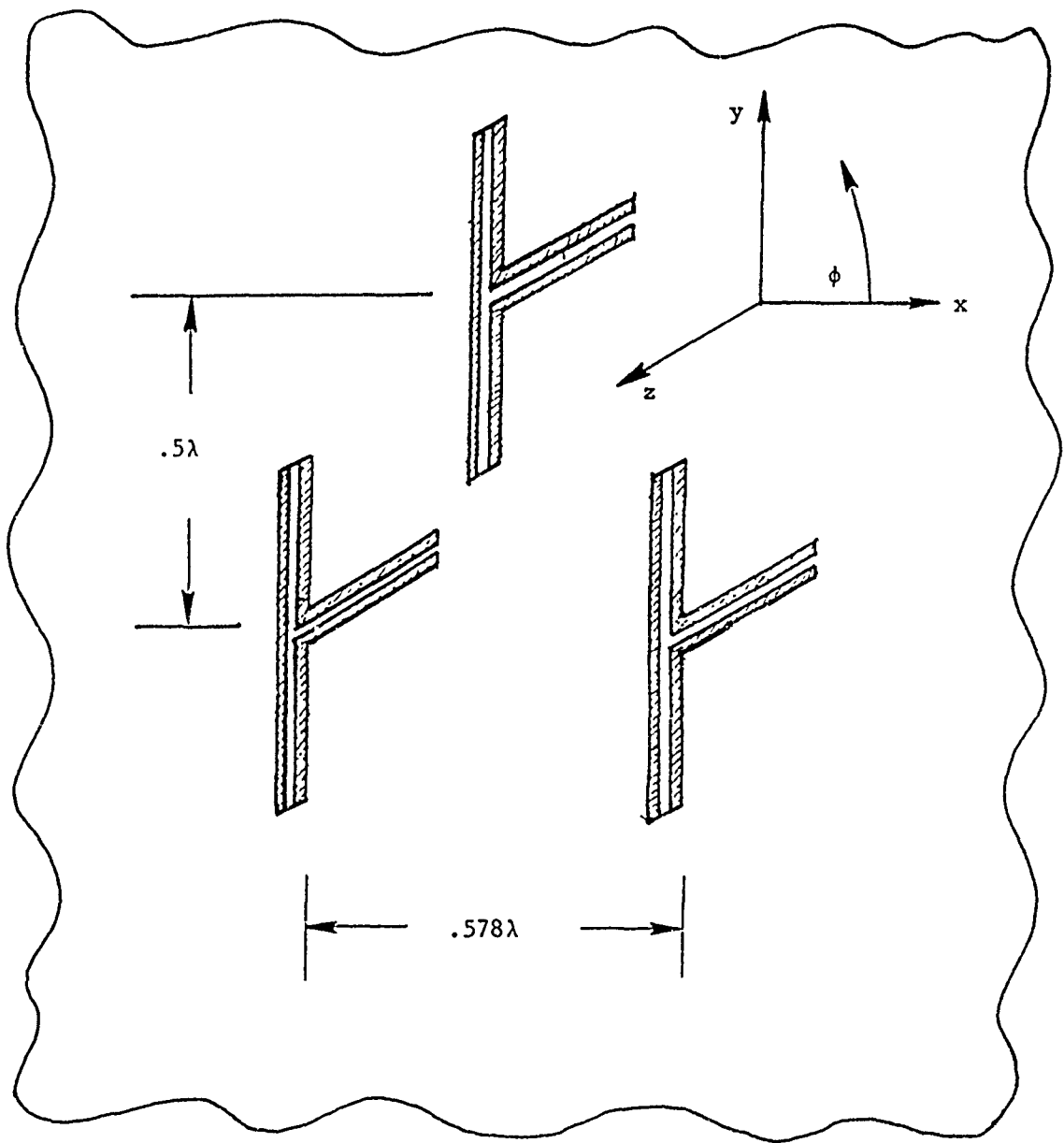


Figure 5. Equilateral Triangular Lattice Array of Folded Dipoles $\lambda/4$ in Front of Ground Screen

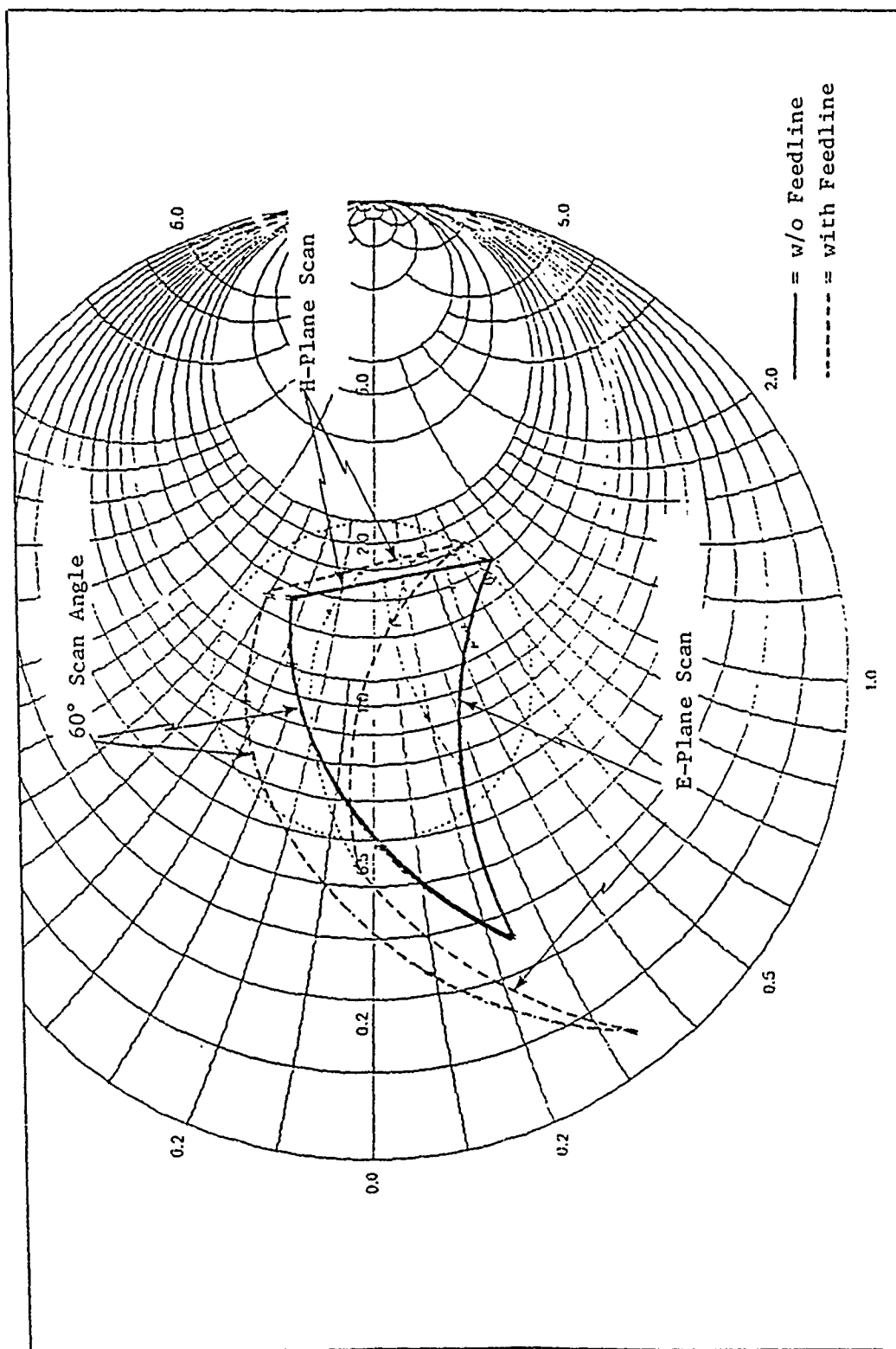


Figure 6. Folded Dipole Array Active Impedance at Low End of Frequency Band. Lattice is that of Figure 5. Normalizing Impedance = 160Ω .

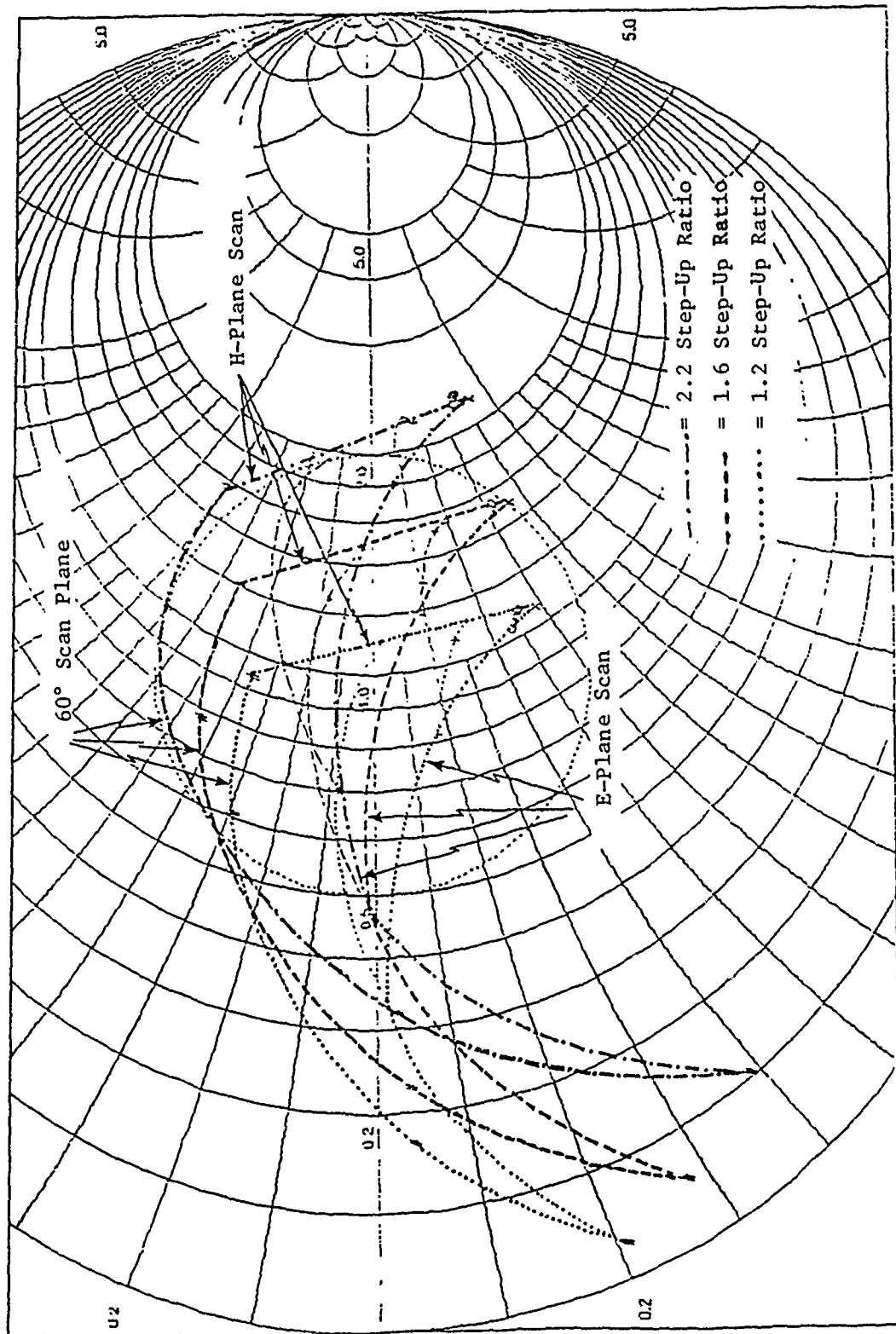


Figure 7. Folded Dipole Array Active Impedance at Low End of Frequency Band. Lattice is 3.5 Percent Larger than that of Figure 5. Normalizing Impedance = 160Ω .

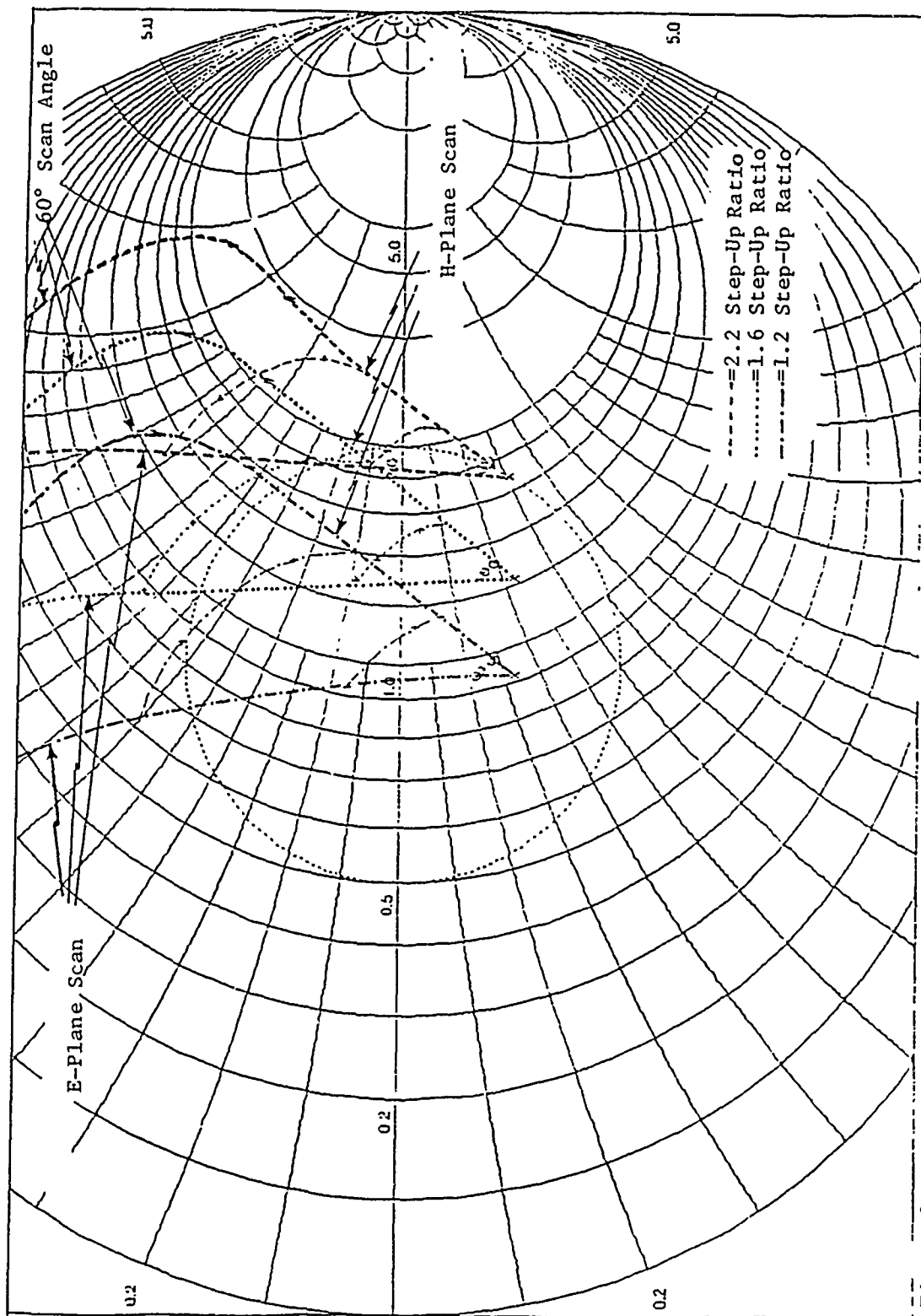


Figure 8. Folded Dipole Active Impedance at High End of Frequency Band. Lattice is 3.5 Percent Larger than that of Figure 5. Normalizing Impedance = 160Ω .

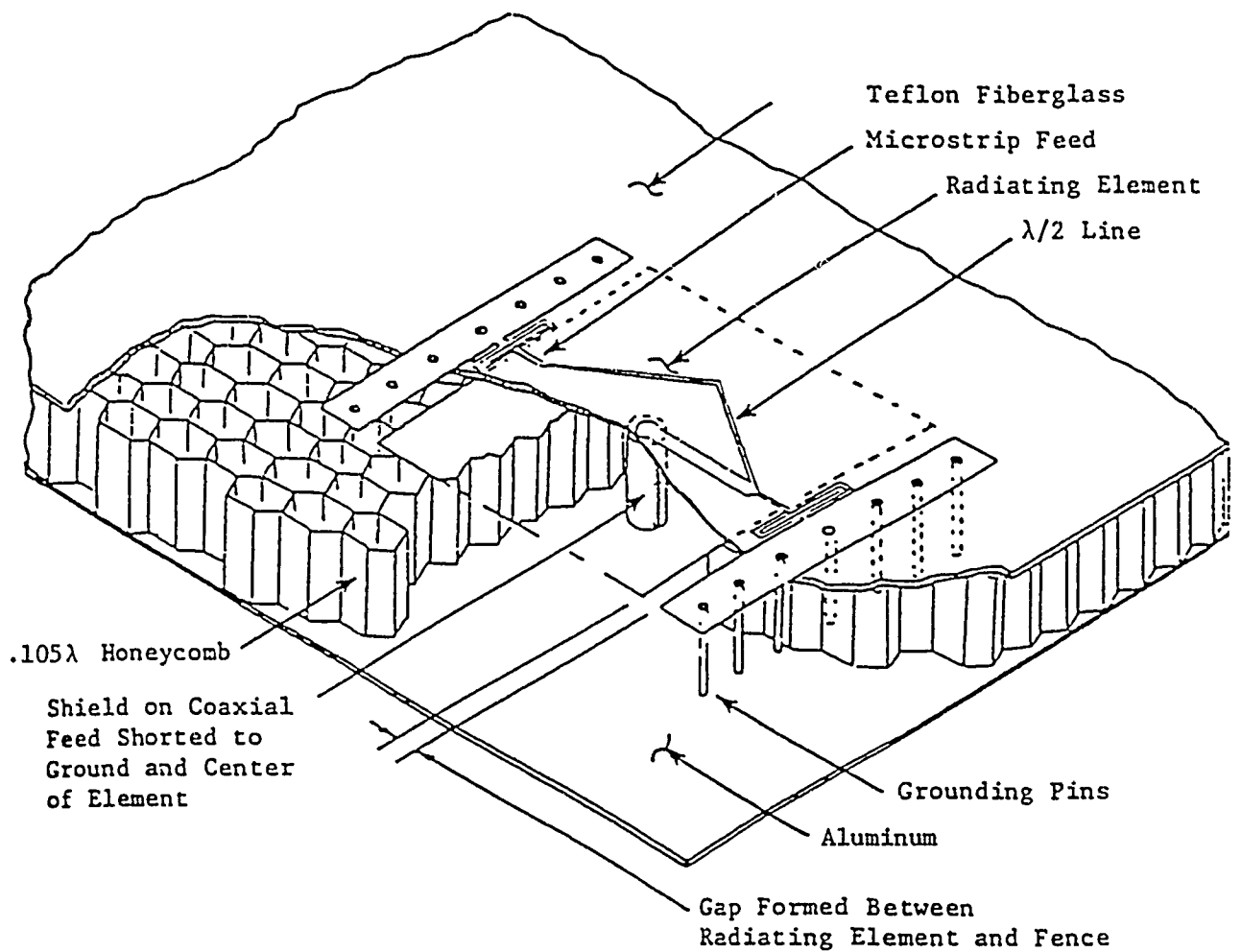


Figure 9. Microstrip Radiator

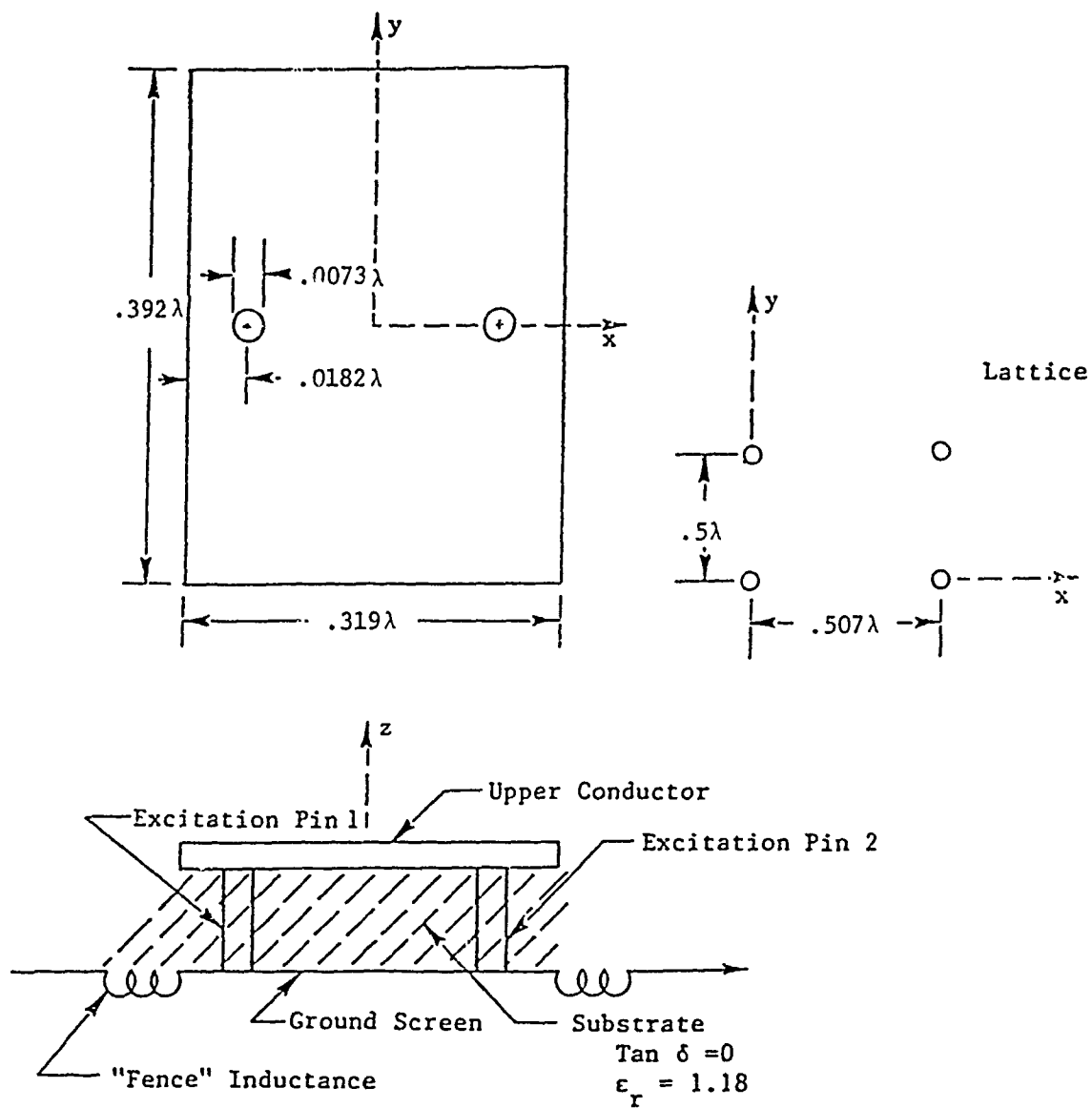


Figure 10. Microstrip Radiator Model and Array Lattice

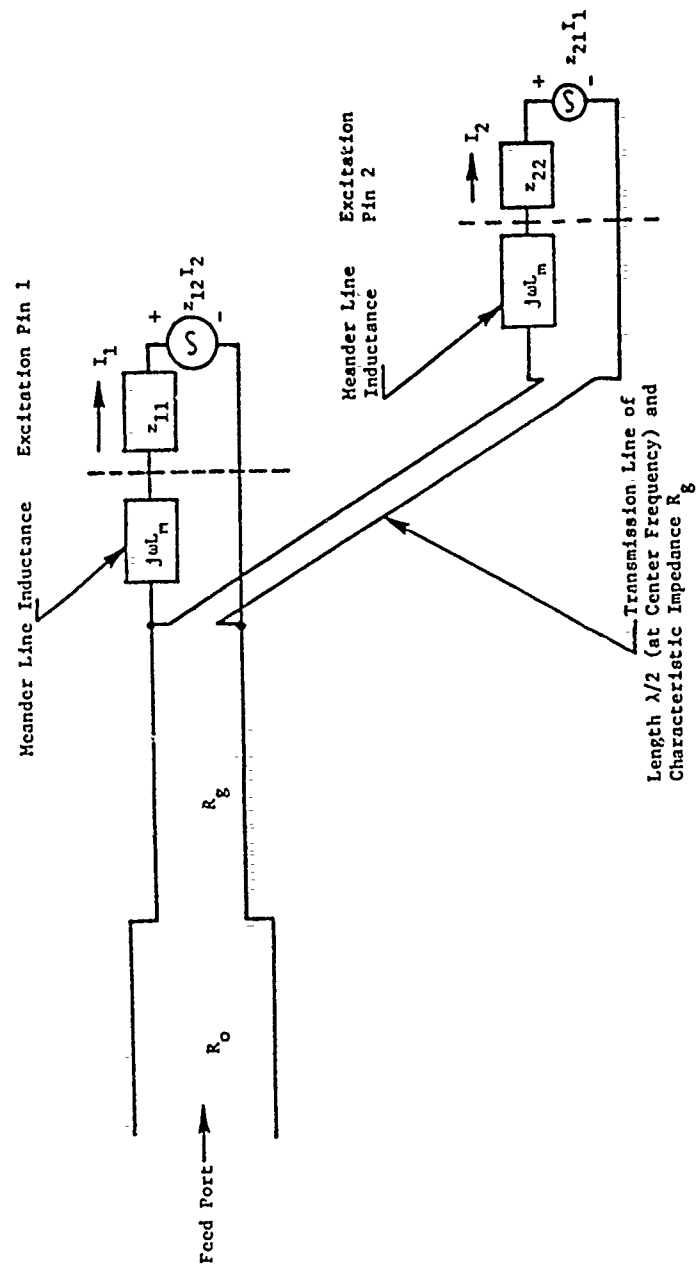


Figure 11. Feed Network Model

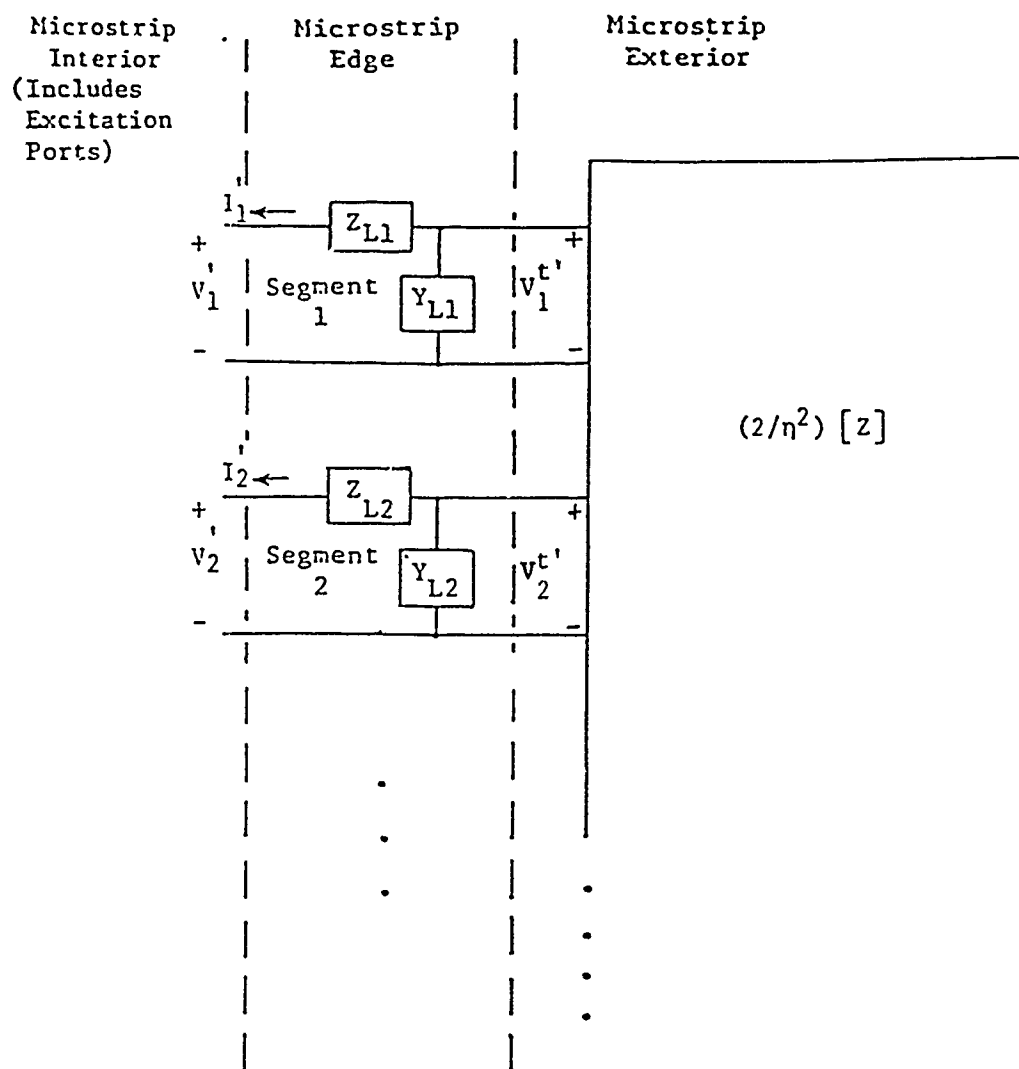


Figure 12. Network Equivalent of Microstrip

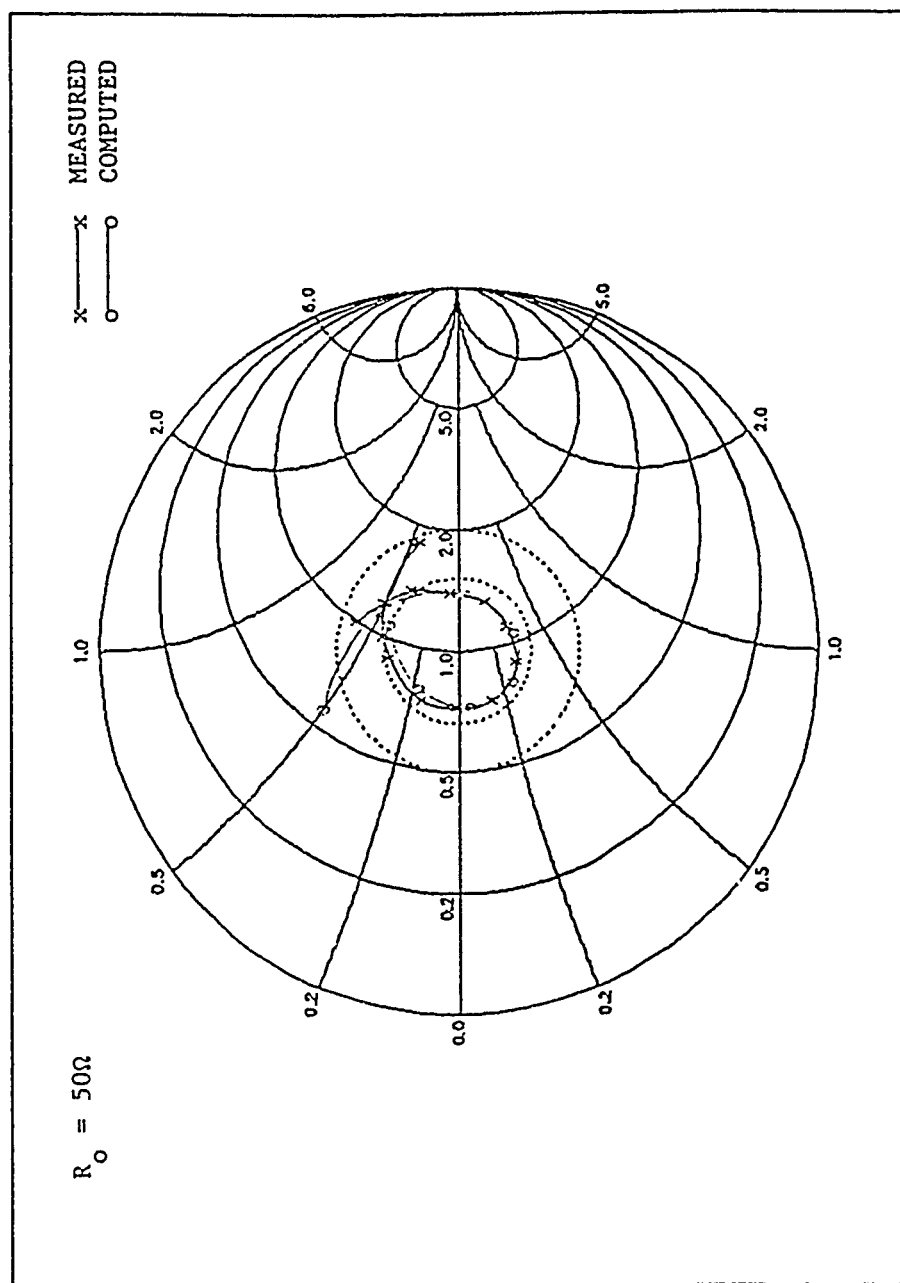


Figure 13. Isolated Radiator Impedance. 17% Bandwidth Design

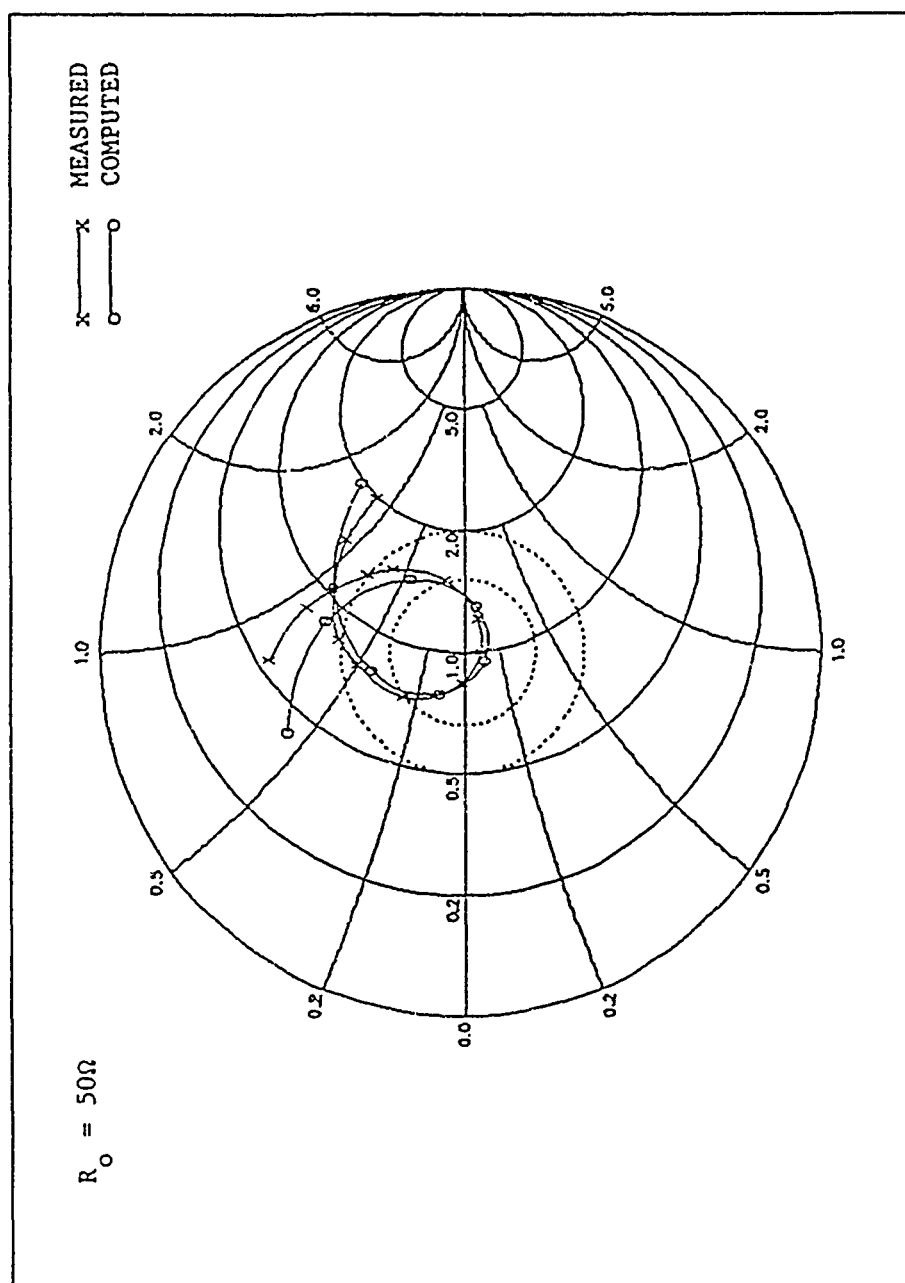


Figure 14. Isolated Radiator Impedance, 10% Bandwidth Design

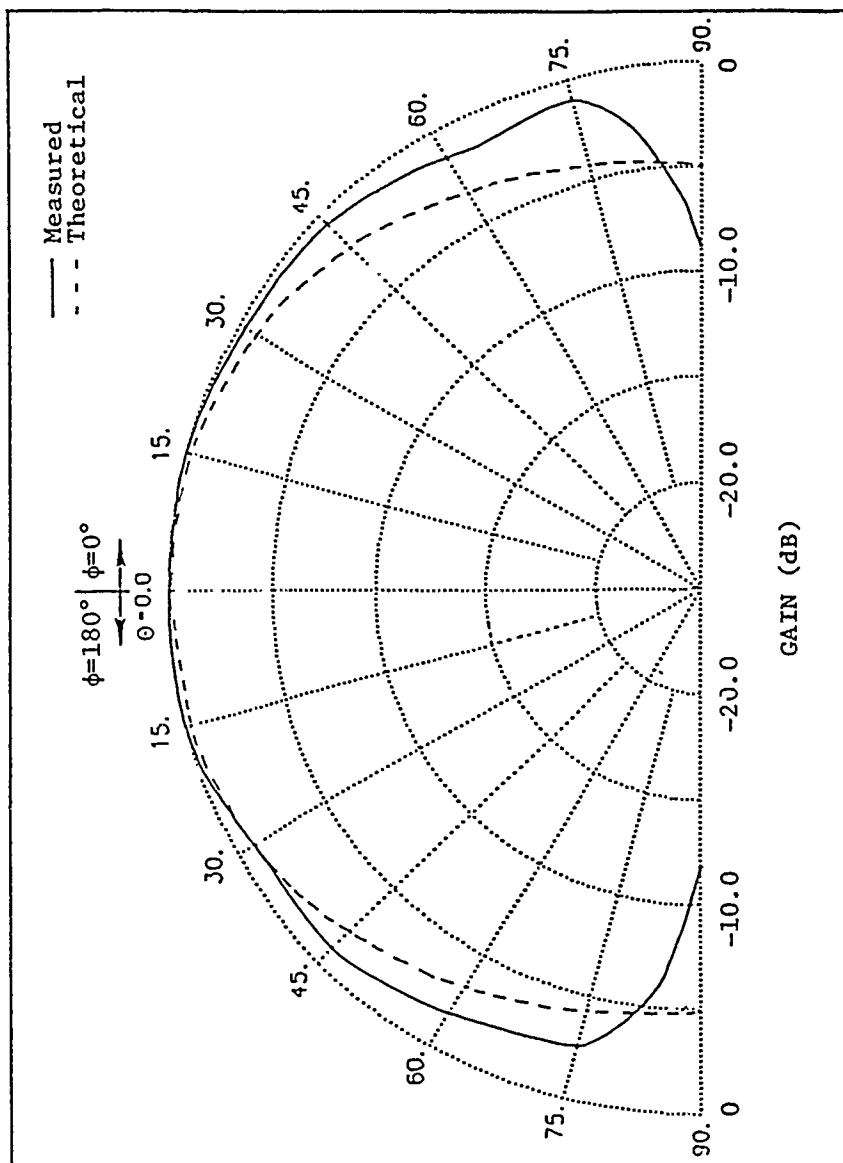


Figure 15. Isolated Radiator Normalized Pattern, E-Plane

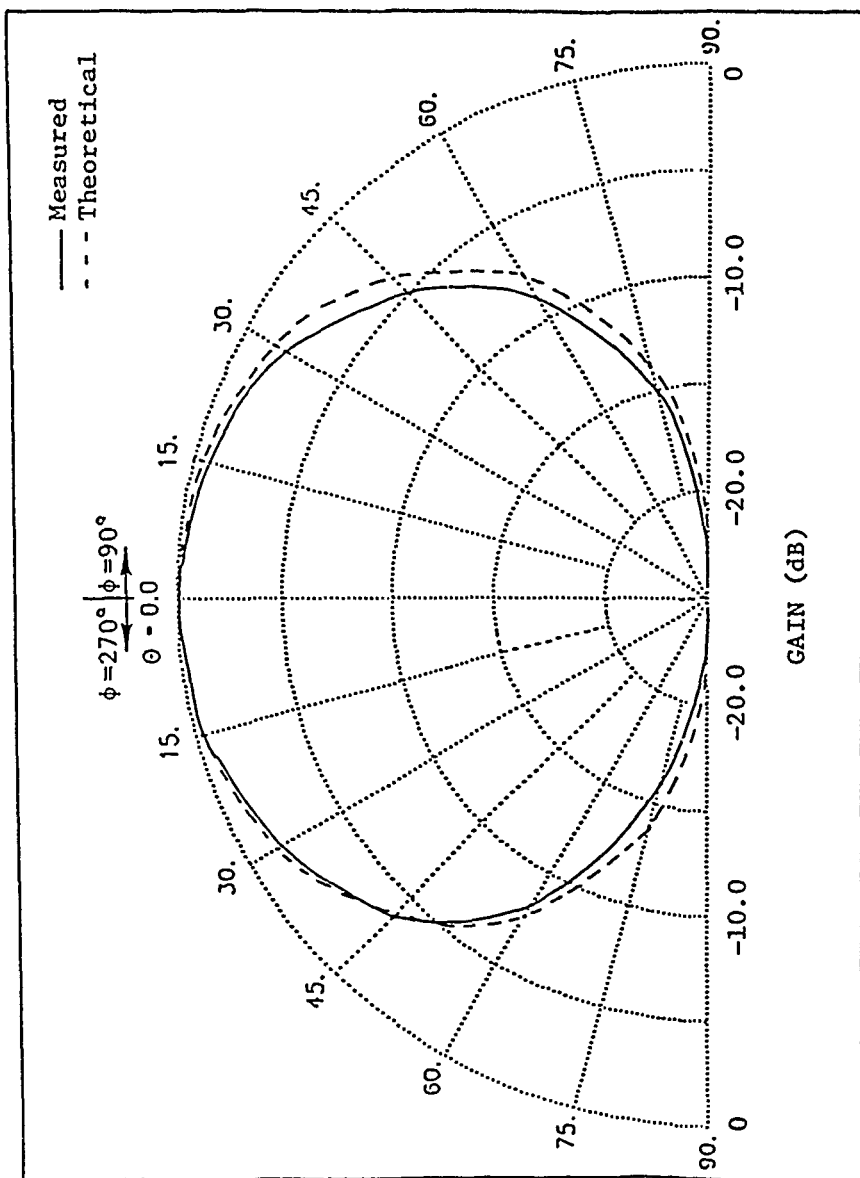


Figure 16. Isolated Radiator Normalized Pattern, H-Plane

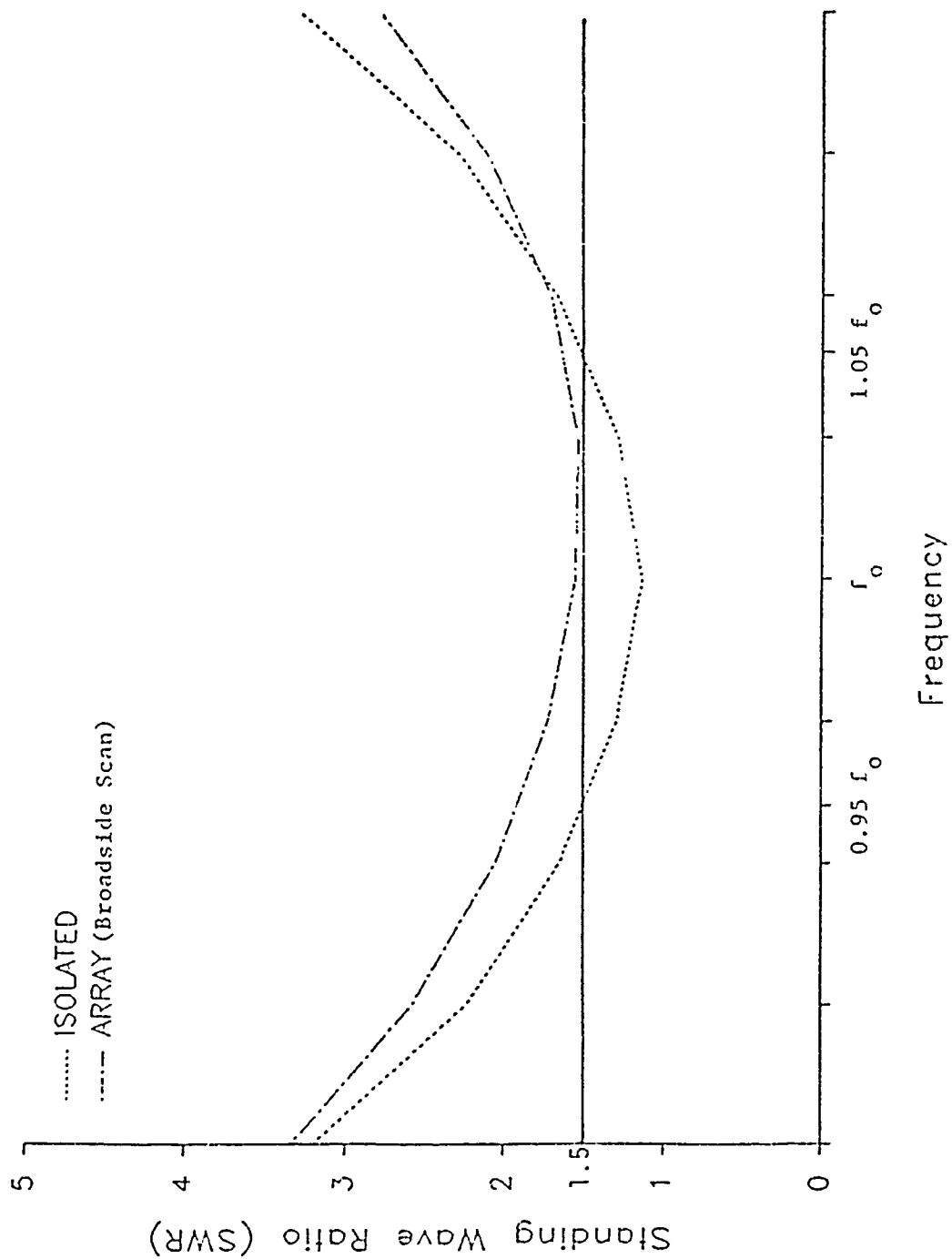


Figure 17. Standing Wave Ratio of Radiator Designed for 10% Bandwidth in Isolated Environment

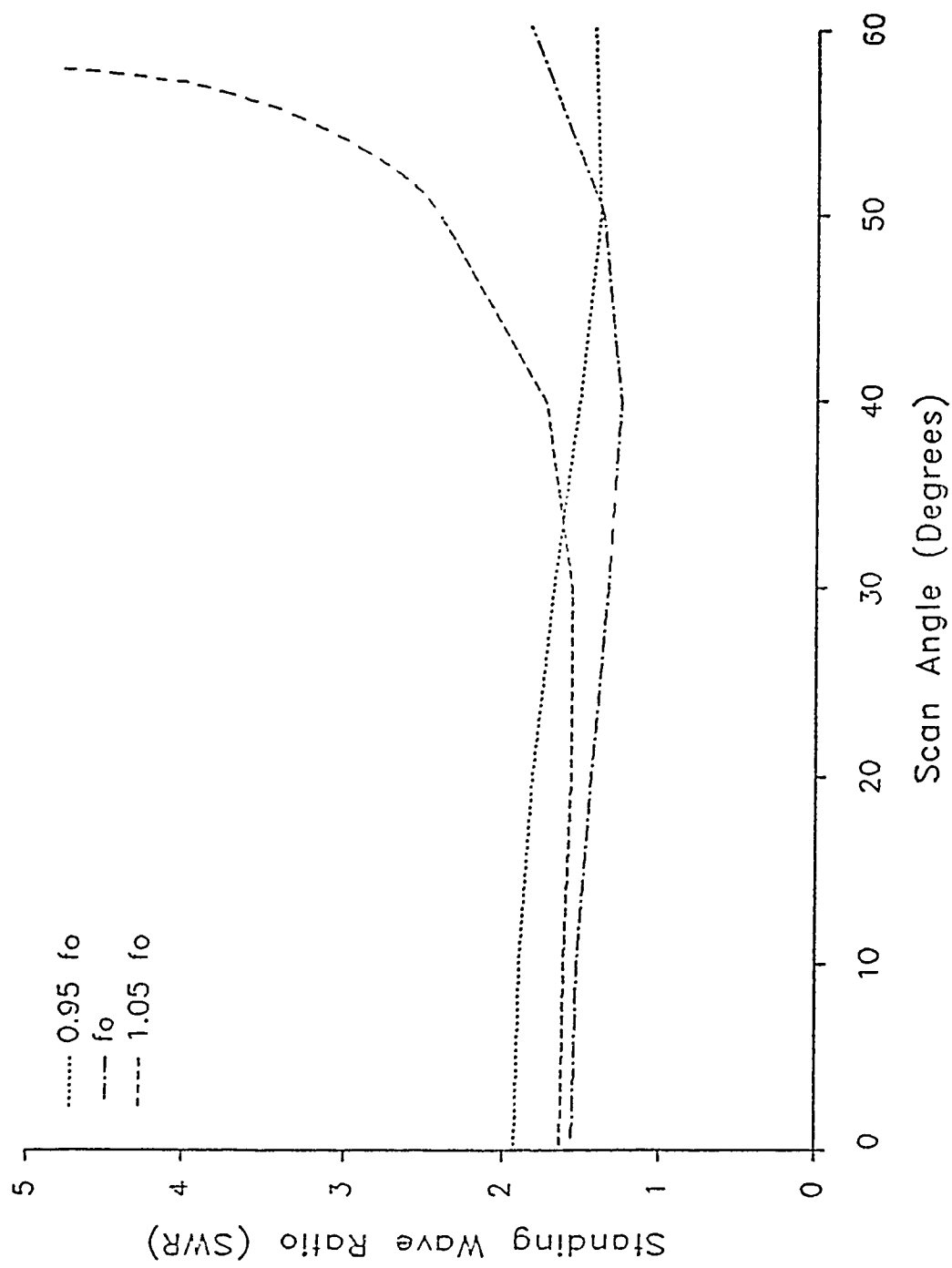


Figure 18. Azimuth Scan Active Standing Wave Ratio of Radiator
Designed for 10% Bandwidth in Isolated Environment

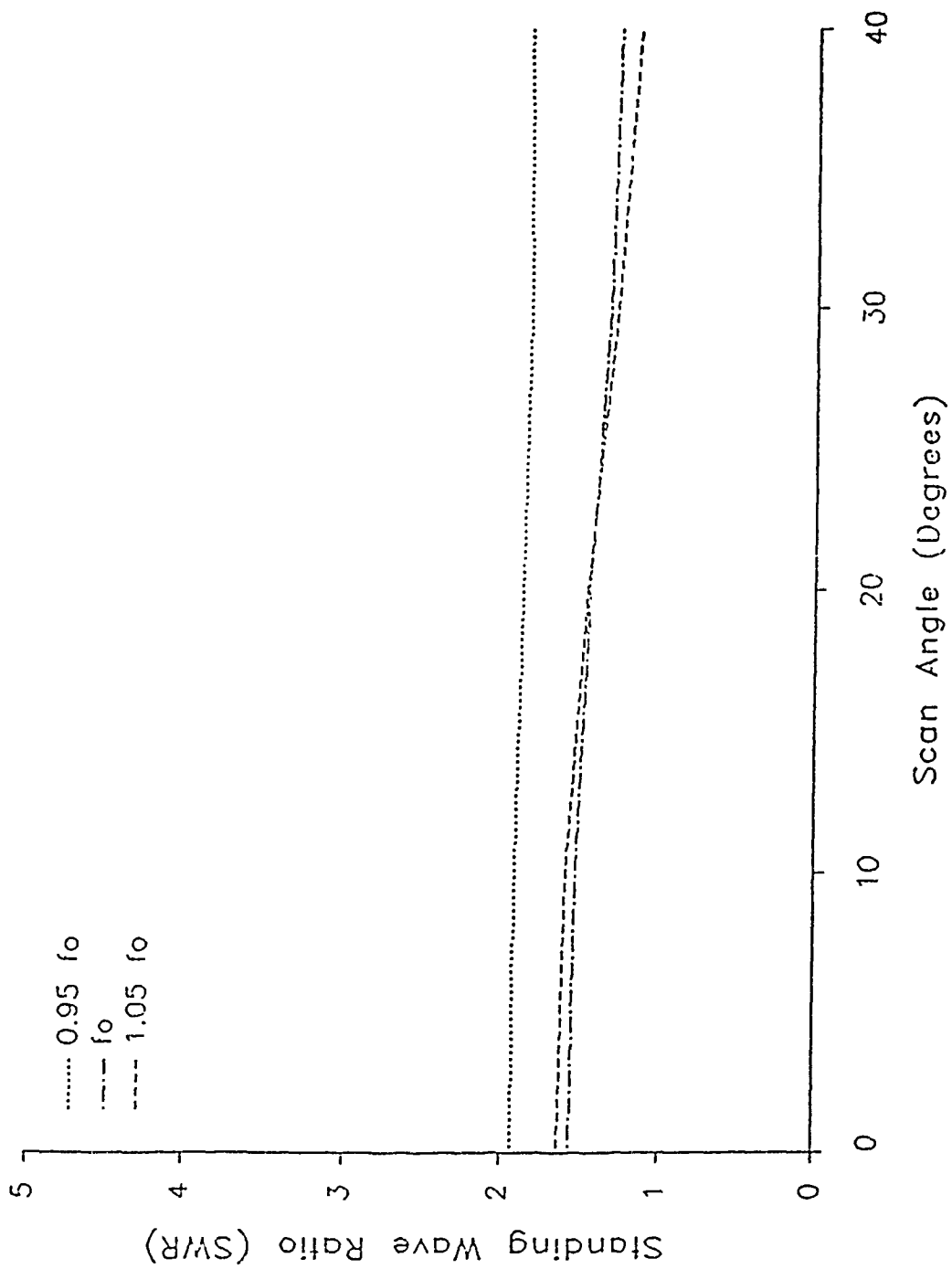


Figure 19. Elevation Scan Active Standing Wave Ratio of Radiator
Designed for 10% Bandwidth in Isolated Environment

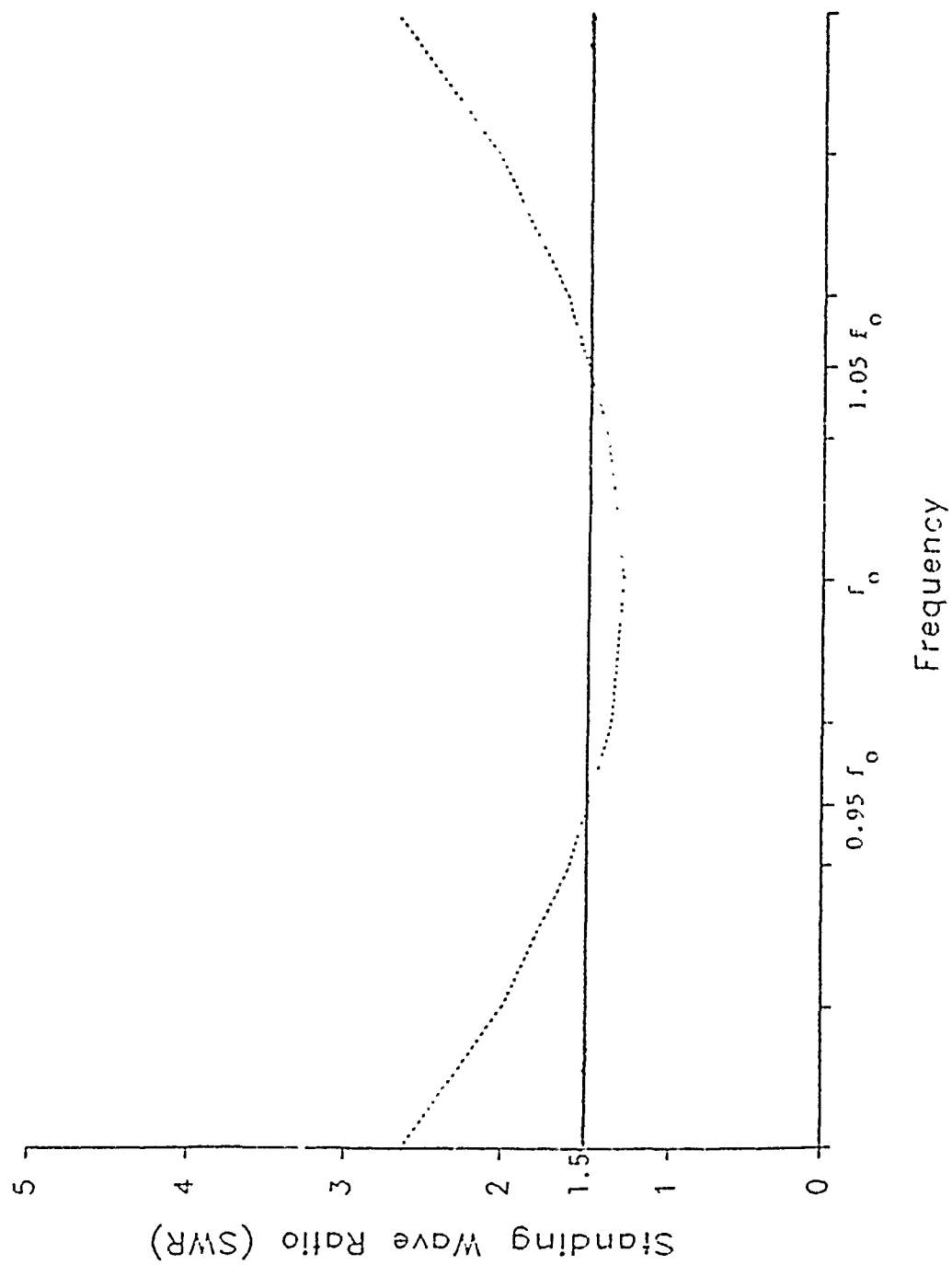


Figure 20. Broadside Scan Active Standing Wave Ratio of Radiator
Designed for 10% Bandwidth at Broadside Scan

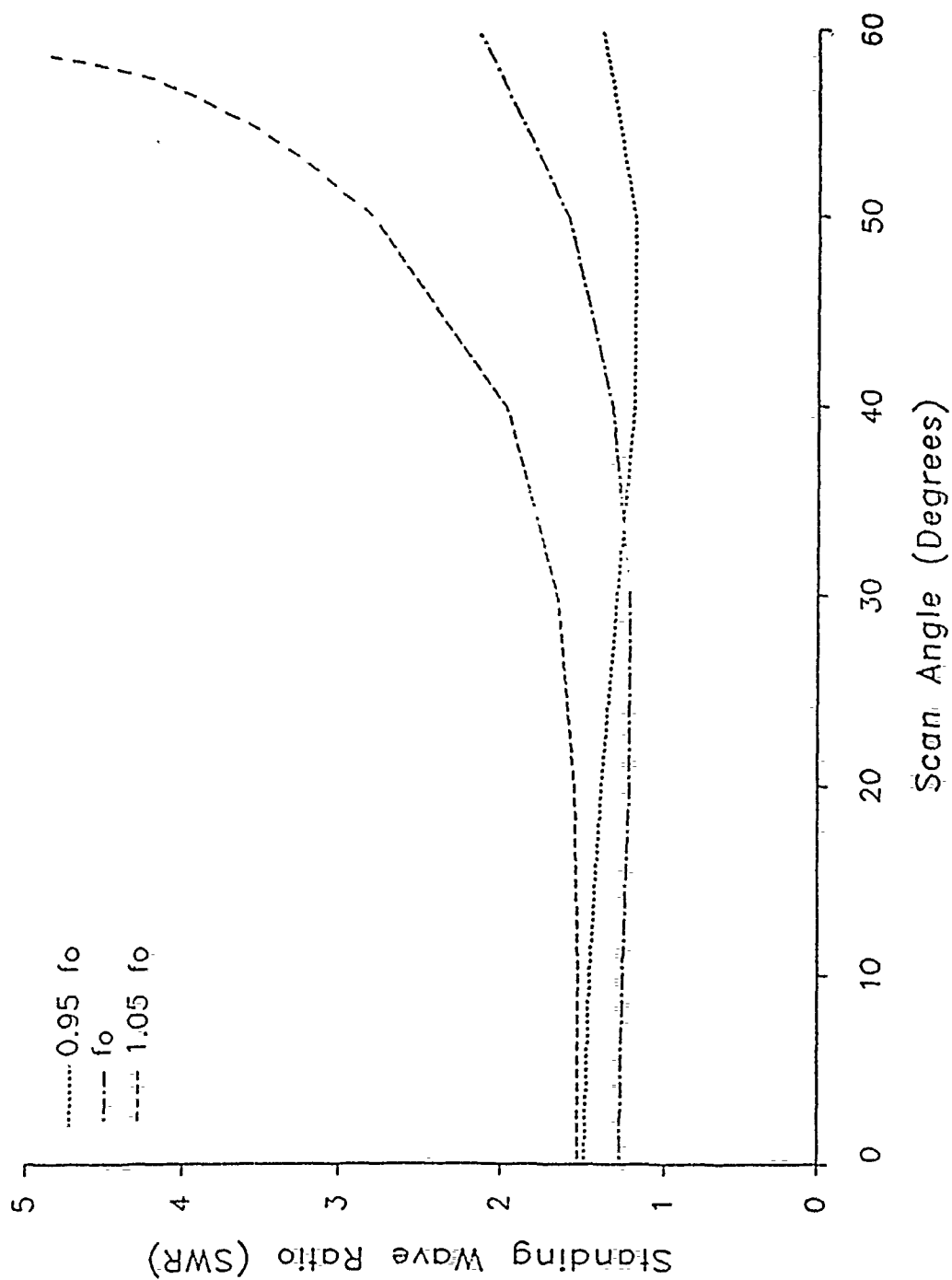


Figure 21. Azimuth Scan Active Standing Wave Ratio of Radiator for 10% Bandwidth at Broadside Scan

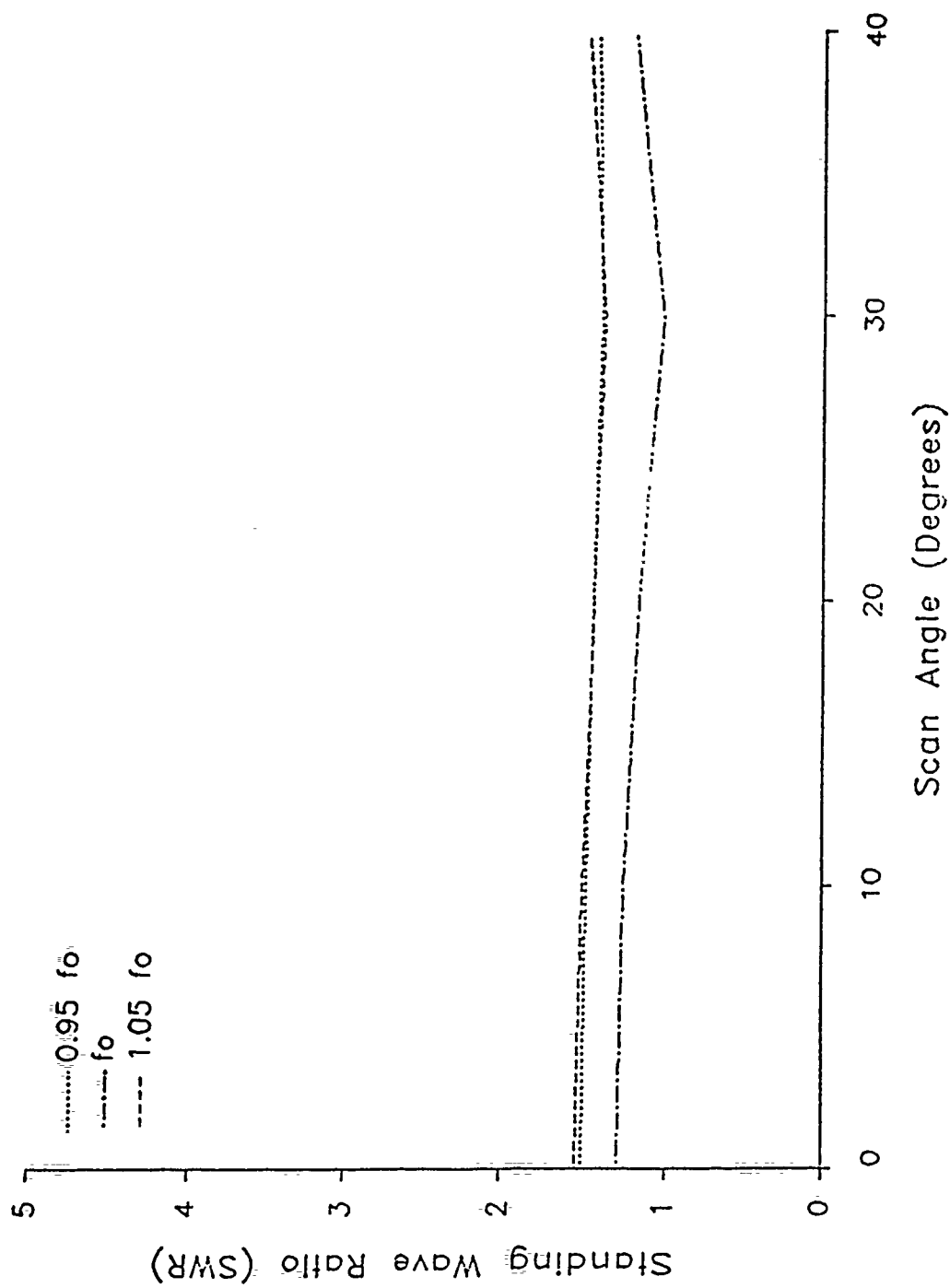


Figure 22. Elevation Scan Active Standing Wave Ratio of Radiator
Designed for 10% Bandwidth at Broadside Scan

COMPUTATIONAL RESOURCES AND CONVERGENCE FOR MM
CALCULATIONS WITH ELECTRICALLY LARGE SCATTERERS

John W. Williams
Booz, Allen & Hamilton Inc.
2309 Renard Pl., SE
Suite 301
Albuquerque, NM 87106

Jiunn S. Yu
Sandia National Laboratories
P.O. Box 5800
Division 346Z
Albuquerque, NM 87195

Abstract

Method-of-moment (MM) techniques are now widely employed for calculations of electromagnetic scattering from objects which are electrically large and possibly lossy and inhomogeneous. The availability of computer mainframes with large memory capacity combined with concurrent or vectorized processing allows application of MM techniques to increasingly large and complex scatterers. In addition, numerical instabilities, which are inherent in the electric (EFIE) and magnetic (MFIE) integral equation approaches near internal resonances, have been circumvented with a combined field integral (CFIE) formulation.

This paper presents numerical estimates of radar cross-sections (RCS) for metallic scatterers with canonical shapes. Calculations were conducted with EFIE, CFIE, and MFIE formulations and CRAY and CDC (virtual operating system) mainframes. Comparisons with experimental data and Geometrical Theory of Diffraction (GTD) calculations are employed to determine the density of expansion functions (EFs) required for convergence to the correct scattering solution. It is well known that the density of EFs necessary for accurate estimates of scattered fields depends upon the target shape. Smooth objects require fewer EFs per unit area than targets with sharp discontinuities on the surface. It is demonstrated that the required density is also dependent on electrical size of the scatterer and the polarization of the incident fields. As a result, computational resources are exhausted more rapidly than one would expect if the required expansion function density was independent of the overall electrical size of the target.

INTRODUCTION

The purpose of this paper is to present an evaluation of capabilities and limitations of MM/BOR (body-of-revolution) codes which calculate far-field scattering for axially

symmetric bodies. The original versions of these computer codes were developed by Medgyesi-Mitschang and coworkers (Ref. 1) based upon earlier investigations by Mautz and Harrington (Ref. 2 and 3). For the calculations discussed in this paper, matrix storage in the original version of computer codes CICERO and BORLAYC was expanded for execution of CRAY and CDC-855 (virtual operating system) mainframes. In order to accommodate larger objects, the original Bessel function subroutines, which were intended for computations with small arguments, were replaced with Bessel function routines from the SLATEC Mathematical Library of Sandia National Laboratories (SNL).

In the section below we will discuss the convergence of MM solutions obtained with these codes. RCS calculations are then presented for various canonical shapes. Although only metallic objects are discussed below, the computer codes also allow estimates of RCS for lossy targets. The final section summarizes the results of the calculations and provides some guidelines for selection of expansion functions for larger targets.

CONVERGENCE

In the discussion below, the term convergence means that further refinement of the model yields no significant improvement in calculated values of the RCS. For the specific models used in the computations, refinement can include: 1) increasing the number of terms in the Fourier expansion in the azimuthal coordinate, 2) increasing the sampling for Gaussian quadrature integration over the azimuthal coordinate, and 3) increasing the density of EFs (number of EFs per wavelength) along the generating curve.

The number of circumferential modes required for convergence is known to be the integer value of $ka_{\max} + 1$ (Ref. 2) where a_{\max} is the maximum radial dimension of the scatterer and k is the free space propagation coefficient. Recall that the Fourier expansion in azimuthal coordinates ϕ allows a MM solution for scattered fields in terms of a summation over n independent modes (Ref. 2). For most targets employed in this study, the calculated RCS changed by less than 0.5% when n was increased beyond the value $\text{Int}(ka_{\max}) + 1$. Figures 1 and 2 illustrate the convergence of the monostatic RCS for a metal sphere near resonance using 5 expansion functions per wavelength (5 EF/ λ). In this figure, " n " denotes the summation index over the Fourier modes from $-n$ to n . It is interesting to note that both the EFIE ($\alpha_E = 1.0$) and MFIE ($\alpha_E = 0.0$)

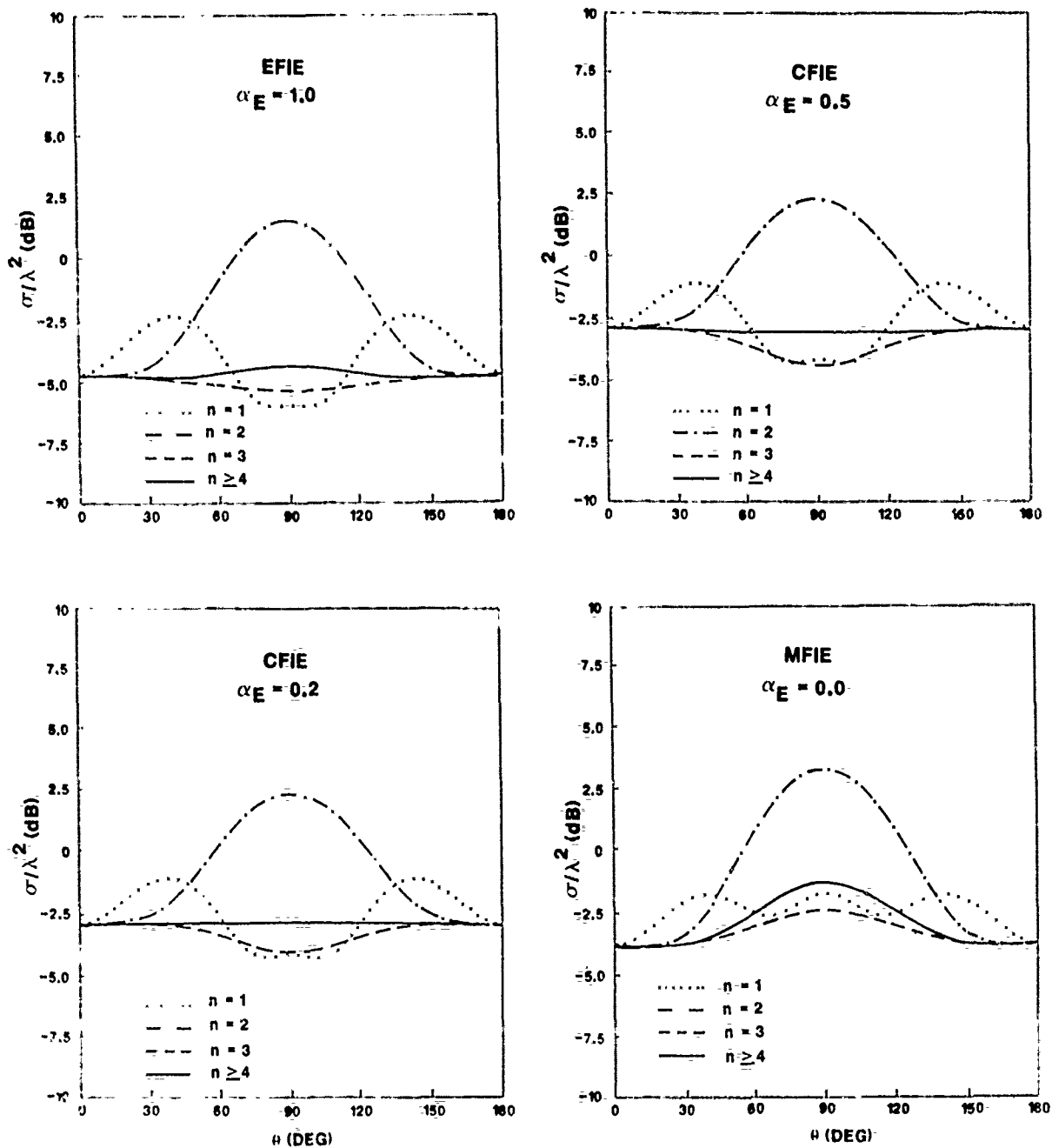


Figure 1. Vertically polarized RCS for a metal sphere near resonance ($ka = 2.770$) computed with MFIE, CFIE and EFIE Boundary Conditions

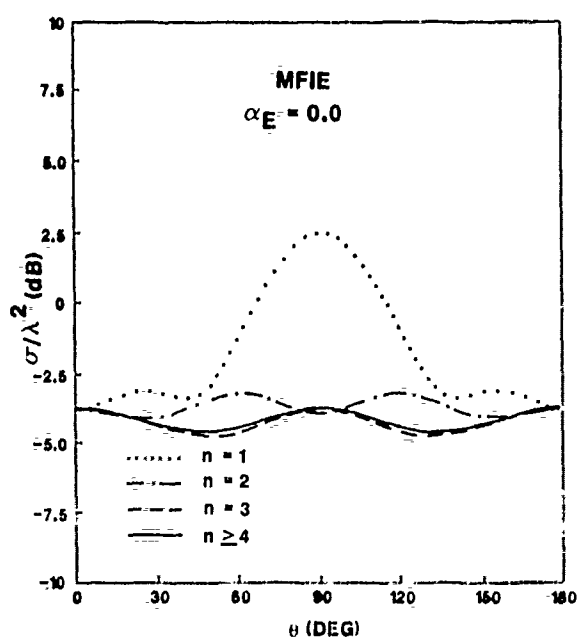
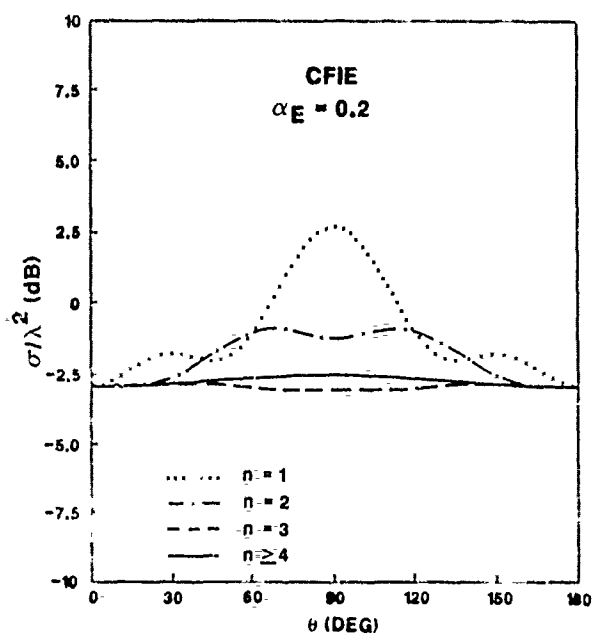
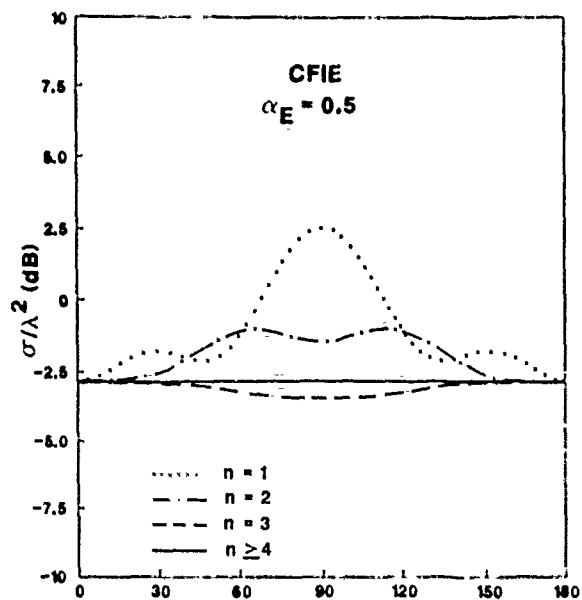
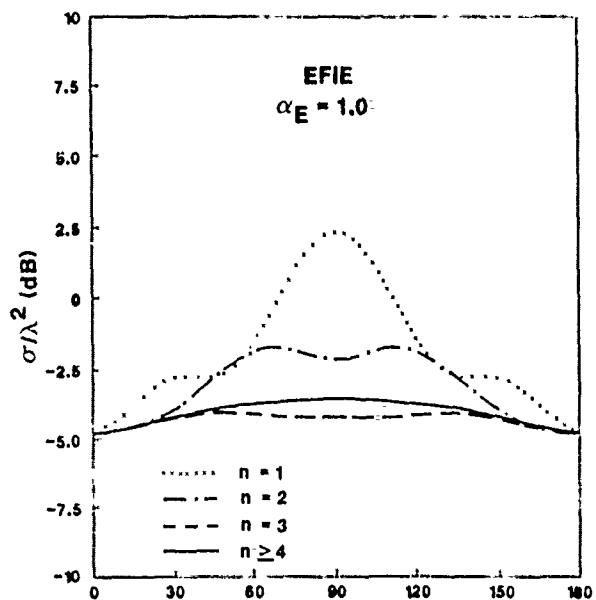


Figure 2. Horizontally polarized RCS for a metal sphere near resonance ($ka = 2.770$) computed MFIE, CFIE and EFIE Boundary Conditions

results are numerically convergent to incorrect values of the RCS. As expected, solutions obtained with the CFIE boundary condition ($\alpha_E = 0.5$ and $\alpha_E = 0.2$) are stable and tend to converge to the correct solution at all aspect angles for $n > 3$. Values of the summation index up to 10 were employed in the calculation with no significant differences observed from the RCS for $n > 3$. The point here is that for this particular code, the azimuthal convergence is easily established even when MFIE and EFIE calculations are used near internal resonance. Through numerical analysis similar to that shown in the first two figures, it was found that Gaussian quadrature integration of order $\text{Int}(4ka_{\text{max}})$ was adequate for solution convergence.

It is the third refinement mentioned above which is of primary concern. If N denotes the number of EFs employed in the model, then storage requirements increase in proportion to N^2 while the time required for full matrix decomposition will increase in proportion to N^3 (Ref. 4). Thus, the computer resources required for MM solution of the electromagnetic scattering problem can increase dramatically with the number of EFs necessary for an accurate solution. Most of the discussion below will address the density of EFs necessary for accurate estimates of the RCS for increasingly large targets.

RESULTS

As mentioned above, the number of circumferential modes employed for each configuration was selected to be $\text{Int}(ka_{\text{max}}) + 1$, and the Gaussian quadrature integration during evaluation of the Green's function was chosen to be of order $\text{Int}(4ka_{\text{max}})$. Convergence of the MM model then depends upon the density of EFs along the generating curve.

As the first example of results, Figures 3 and 4 show calculated the RCS for a metal cylinder with a length of 25.0" and a diameter of 5.5" at frequencies of 1.5 GHz, 3.0 GHz and 6.0 GHz. At these frequencies, the length of the cylinder is 3.2λ , 6.4λ , and 12.8λ , respectively. Notice that for calculations at 1.5 GHz the increase in expansion function density from 8 EF/ λ to 12 EF/ λ has little discernable effect upon the calculated RCS. However, the change in calculated RCS with increasing expansion function density becomes more noticeable as the frequency increases. Results obtained at three frequencies are summarized in Figure 5. This figure ζ shows the real part of the normalized cross-energy spectrum or (see the appendix) as a function of

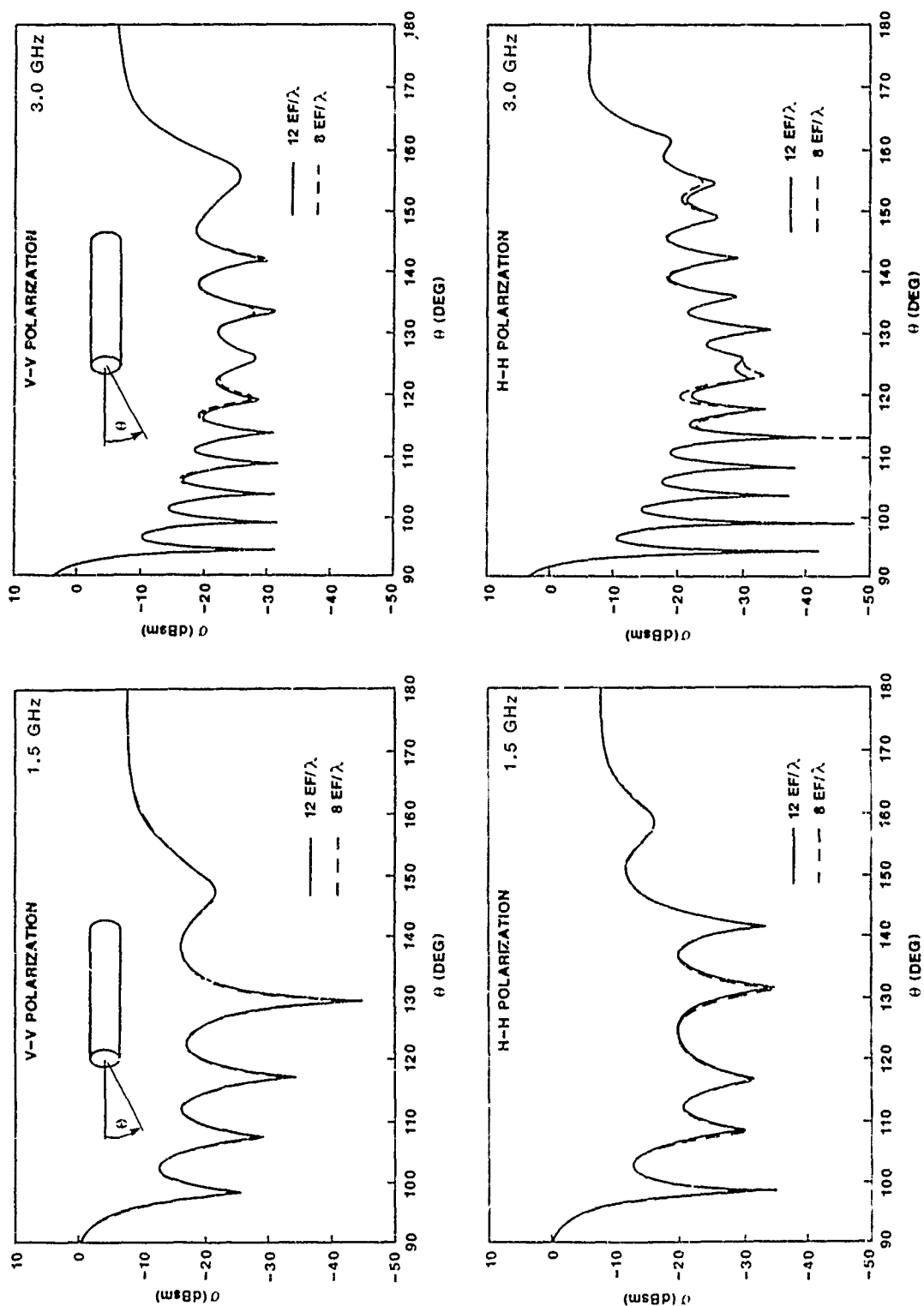


Figure 3. Monostatic RCS as a function of aspect angle for a closed metal cylinder (Dia = 5.5", Length = 25.0") calculated with $8 \text{ EF}/\lambda$ and $12 \text{ EF}/\lambda$ at frequencies of 1.5 GHz and 3.0 GHz

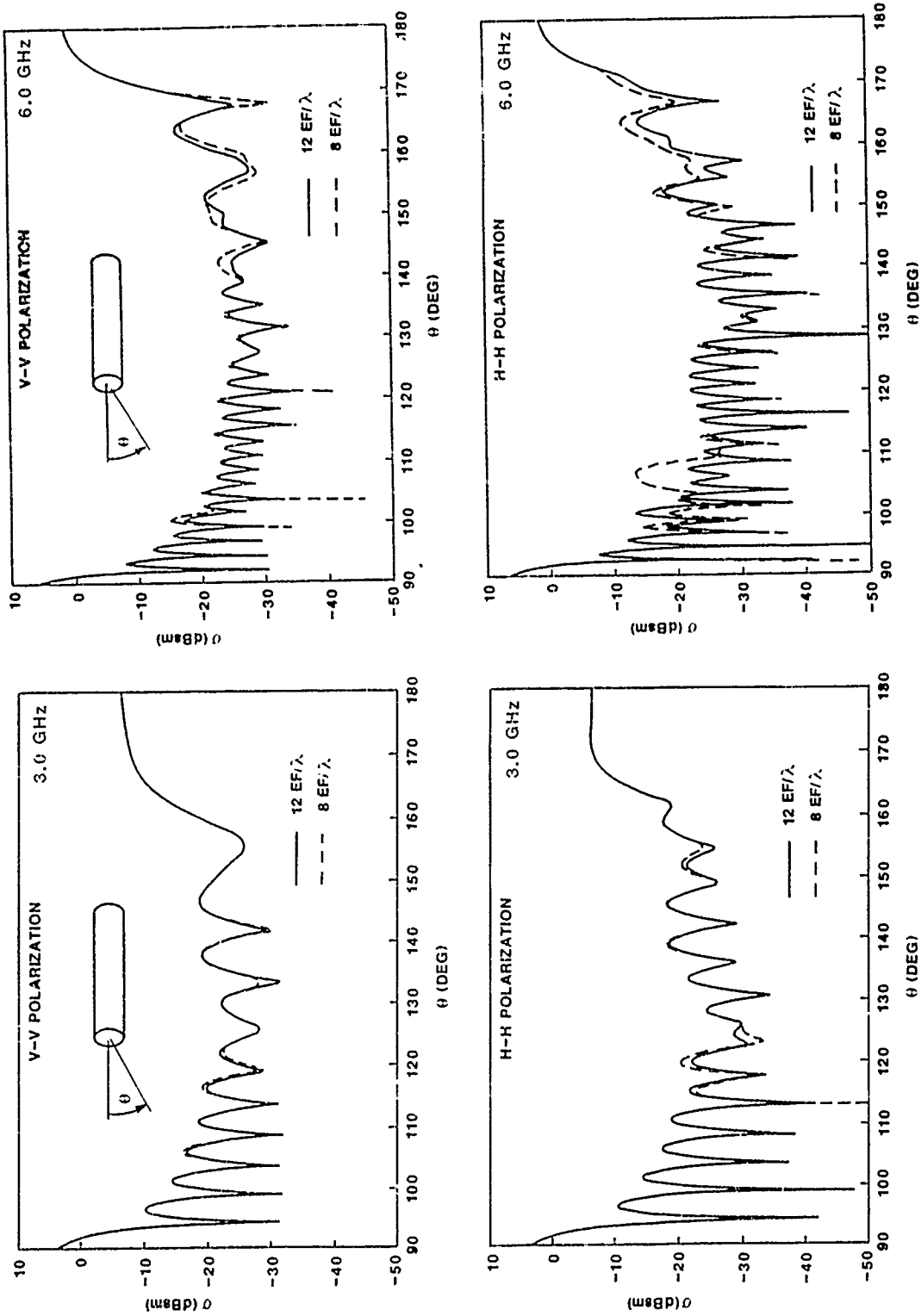


Figure 4. Monostatic RCS as a function of aspect angle for a closed metal cylinder (Dia = 5.5", Length = 25.0") calculated with 8 EF/λ and 12 EF/λ at frequencies of 3.0 GHz and 6.0 GHz

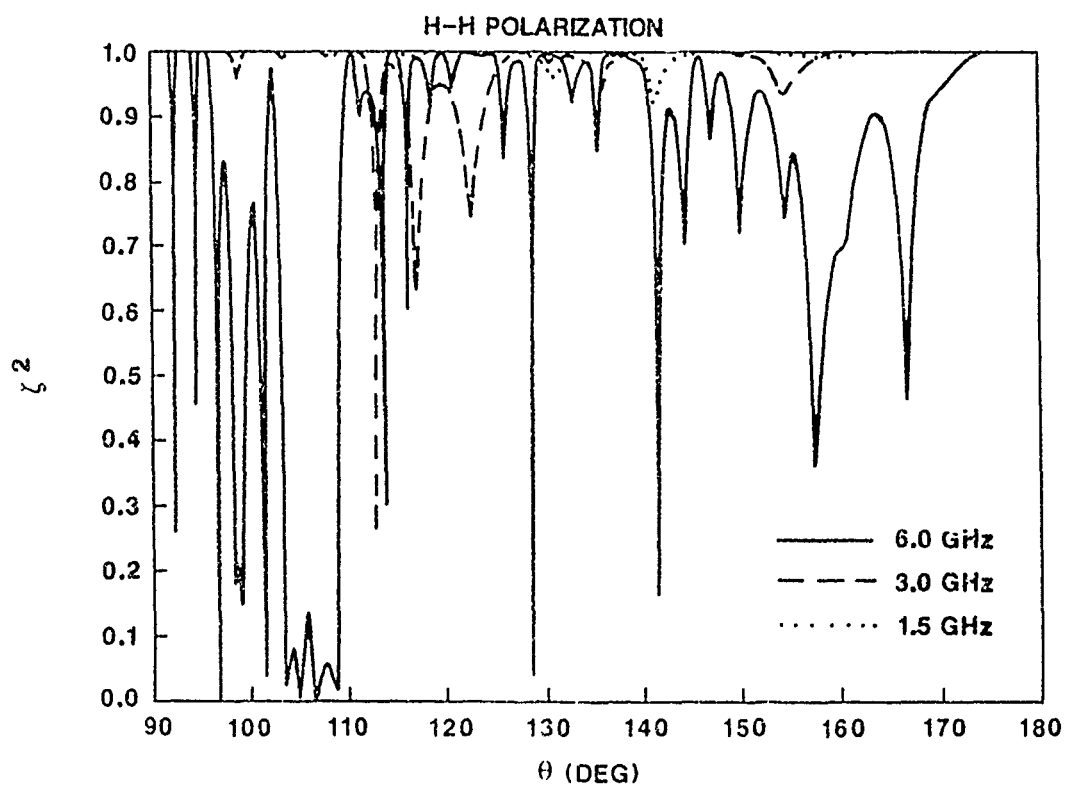
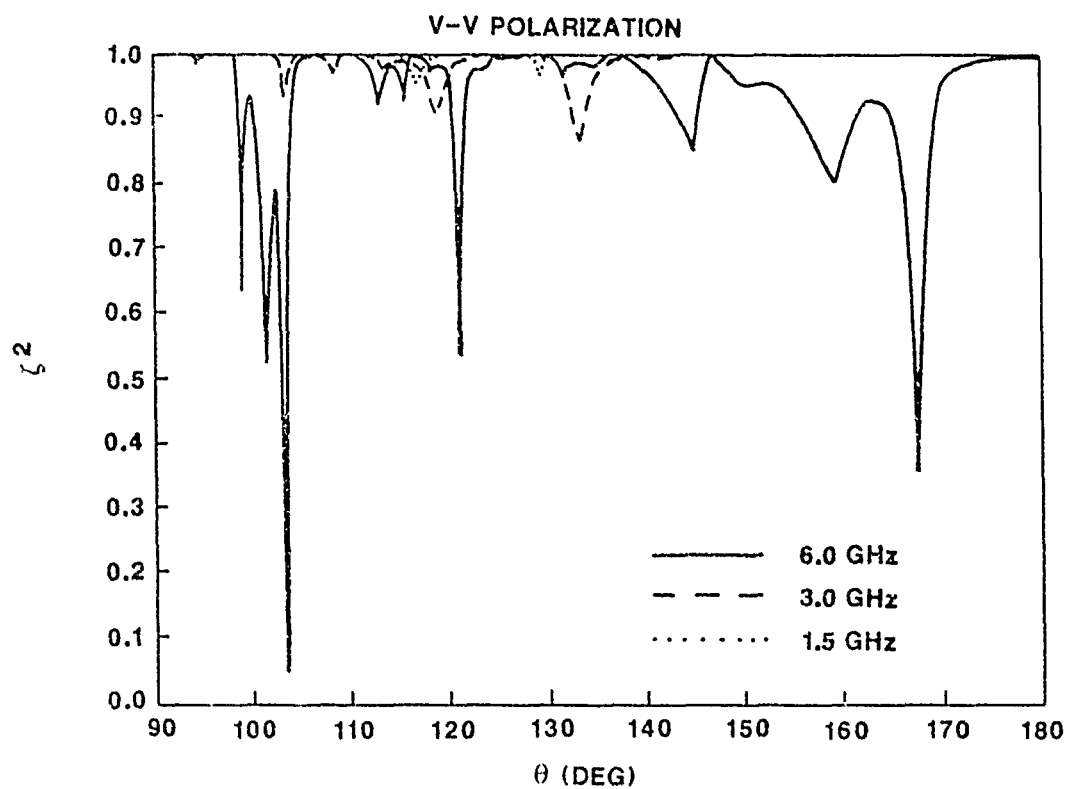


Figure 5. Real part of the normalized cross-energy spectrum for far-fields scattered from a closed metal cylinder calculated with $8 \text{ EF}/\lambda$ and $12 \text{ EF}/\lambda$

aspect angle. At a frequency of 1.5 GHz, ζ is close to one except at aspect angles where the RCS displays sharp minima. Differences in the calculated RCS at these aspect angles are only a few tenths of a dB. These differences increase noticeably with increasing frequency as evidenced by departures in the cross-energy spectrum from a value of 1. As illustrated in Figure 6, the agreement of calculations with experimental data at a frequency of 3 GHz is reasonably good except near the first minor lobe near an aspect angle of 95° and the sixth minor lobe near 120° . Based upon the agreement between GTD calculations (Ref. 5 and Figure 7), it is tentatively assumed that the discrepancy is due to the dielectric stand employed during the experiment. Additional measurements are now in progress to test this assumption. An increase in the expansion function density beyond $10 \text{ EF}/\lambda$ did not reduce the discrepancy or noticeably alter the calculated RCS.

Results of similar calculations are shown in Figures 8 through 10 for a metallic right circular cone with altitude equal to 25" and a base plate diameter of 5.5". Measurements are not yet available for this object. However, as was found for the metal cylinder, the required expansion function density for numerical convergence increased with the electrical size of the object.

Figure 11 shows the RCS computed for a metal disk of diameter 10" and a thickness of $1/4$ " at a frequency of 10 GHz. Corresponding values of the cross-energy spectrum are presented in Figure 12. The target is only 8λ in diameter, and based upon results obtained with the cylinder and cone discussed above, reasonable convergence of the numerical calculations for horizontal polarization was expected to occur for densities in the range from $10 \text{ EF}/\lambda$ to $12 \text{ EF}/\lambda$. As illustrated in the figures, convergence for vertical polarization is achieved for densities of $8 \text{ EF}/\lambda$. In agreement with calculations with the cylinder and cone, convergence is noticeably slower for the case of horizontal polarization. Figure 13 shows a comparison of the RCS measured at the SNL radar range and calculations with an EF density of $12 \text{ EF}/\lambda$. As in the comparison of measured data and calculations for the cylinder, discrepancies in amplitude for some of the sidelobes is tentatively attributed to scattering from the dielectric support during measurements. There is also a disparity between the measured and calculated results near grazing incidence for both polarizations. This difference may be partly attributable to interference from the dielectric support. Additional measurements with a modified support stand are now in progress.

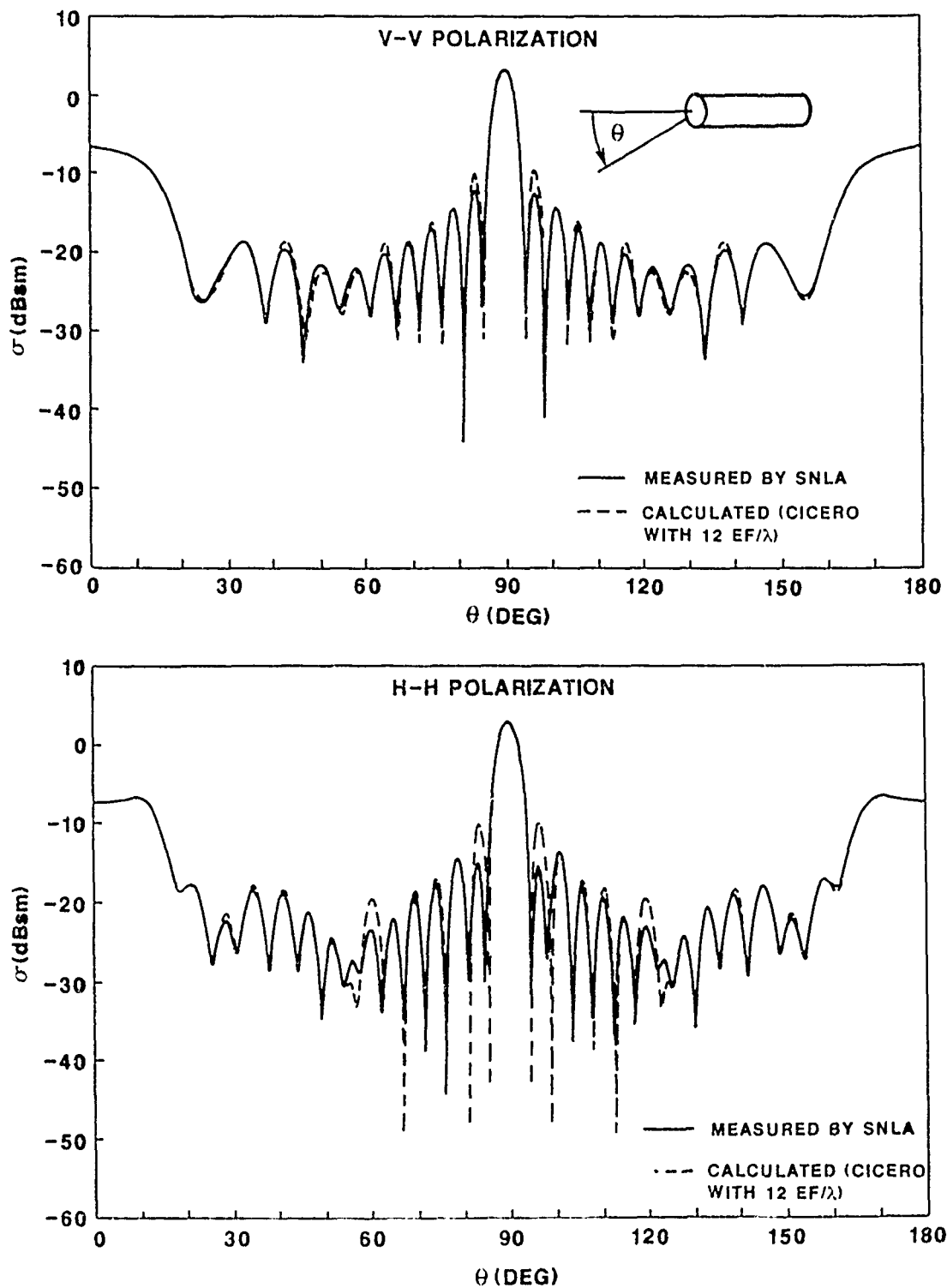


Figure 6. Comparison of measured and calculated monostatic cross sections for a closed metal cylinder (Dia = 5.5", Length = 25.0") at a frequency of 3.0 GHz

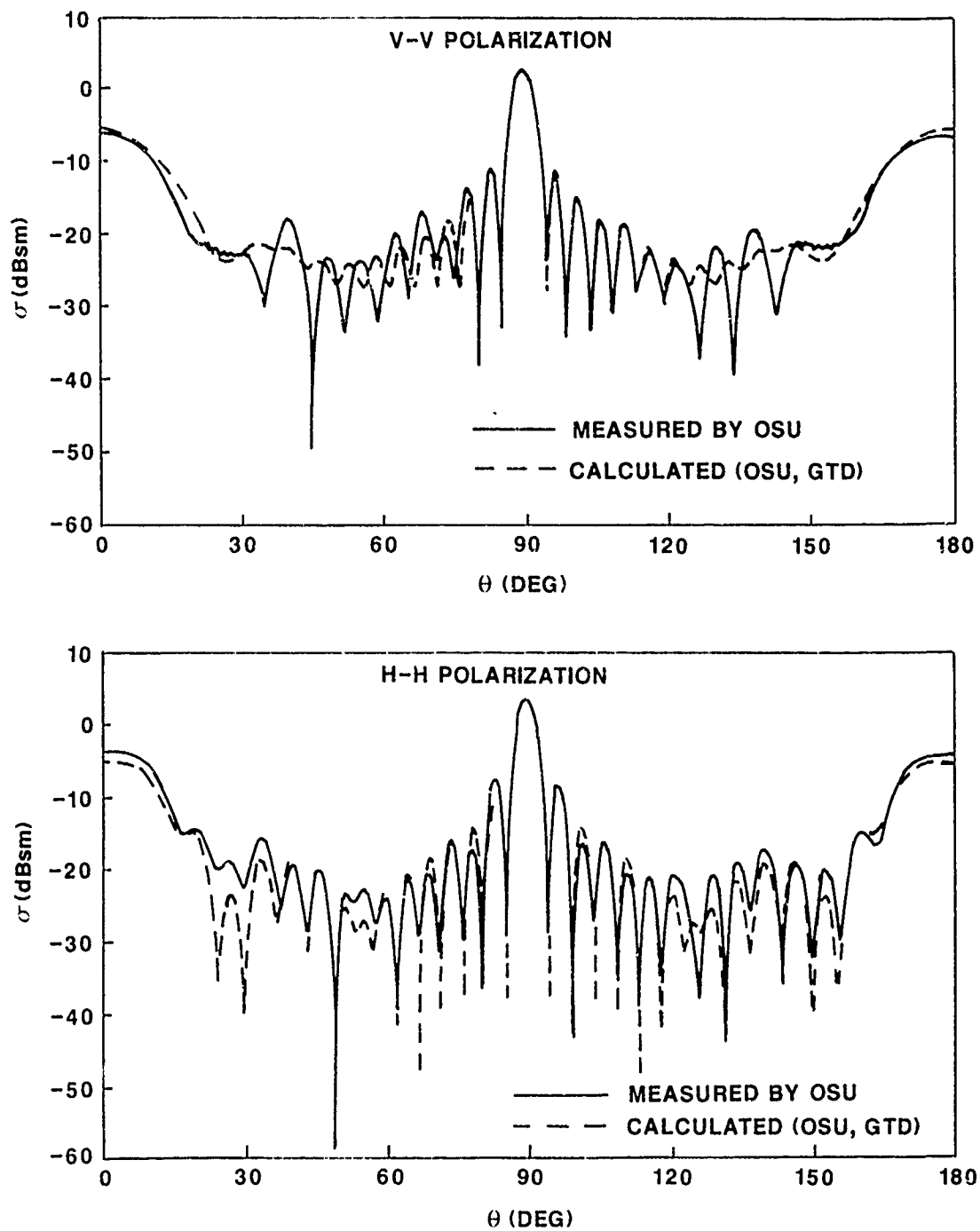


Figure 7. Comparison of measured and calculated monostatic cross sections for a closed metal cylinder (Dia = 5.5", Length = 25.0") at a frequency of 2.95 GHz (from Ref. 4)

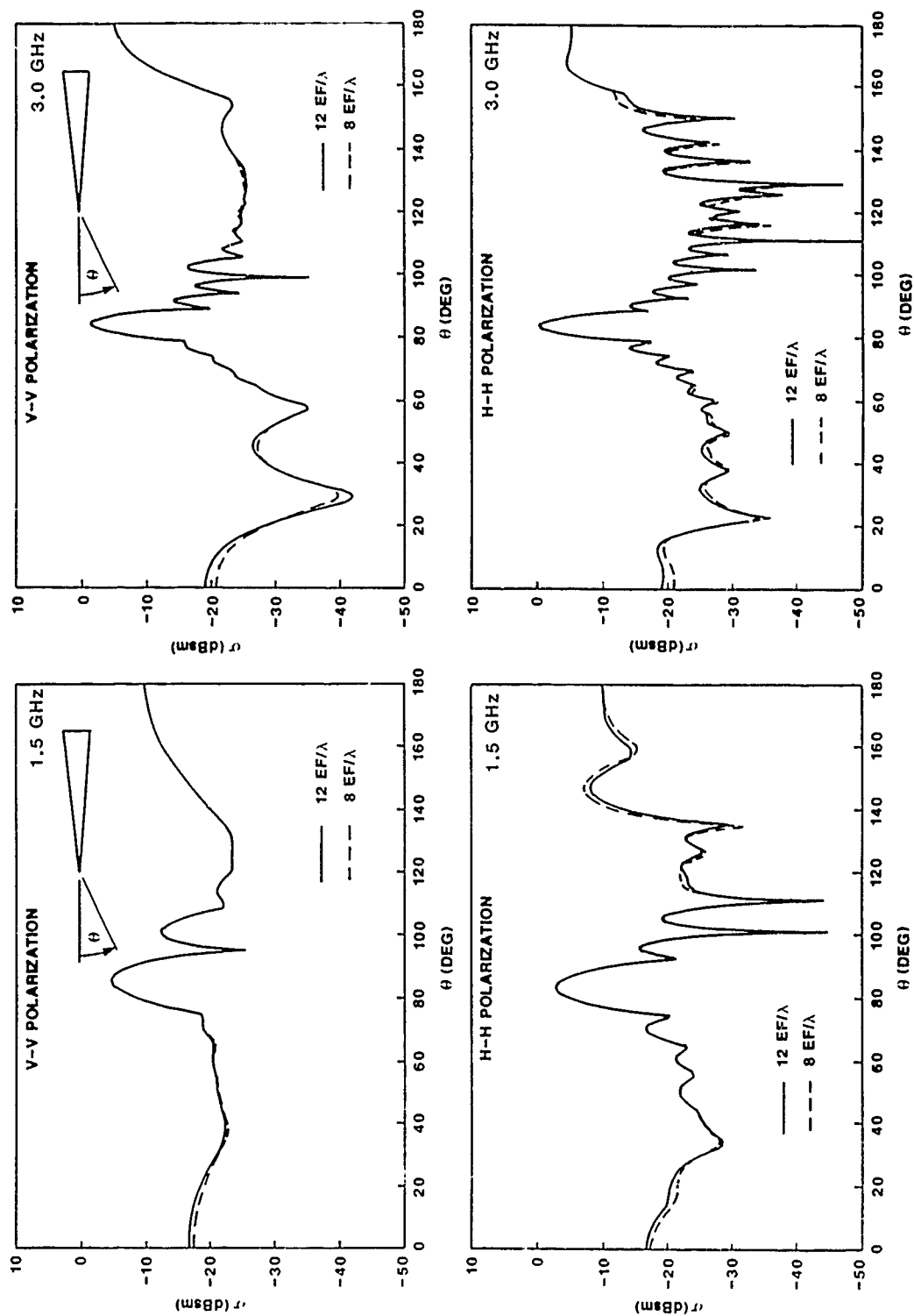


Figure 8. Monostatic RCS as a function of aspect angle for a metal cone (Dia of base plate = 5.5", altitude = 25.0") calculated with 8 EF/λ and 12 EF/λ at frequencies of 1.5 GHz and 3.0 GHz

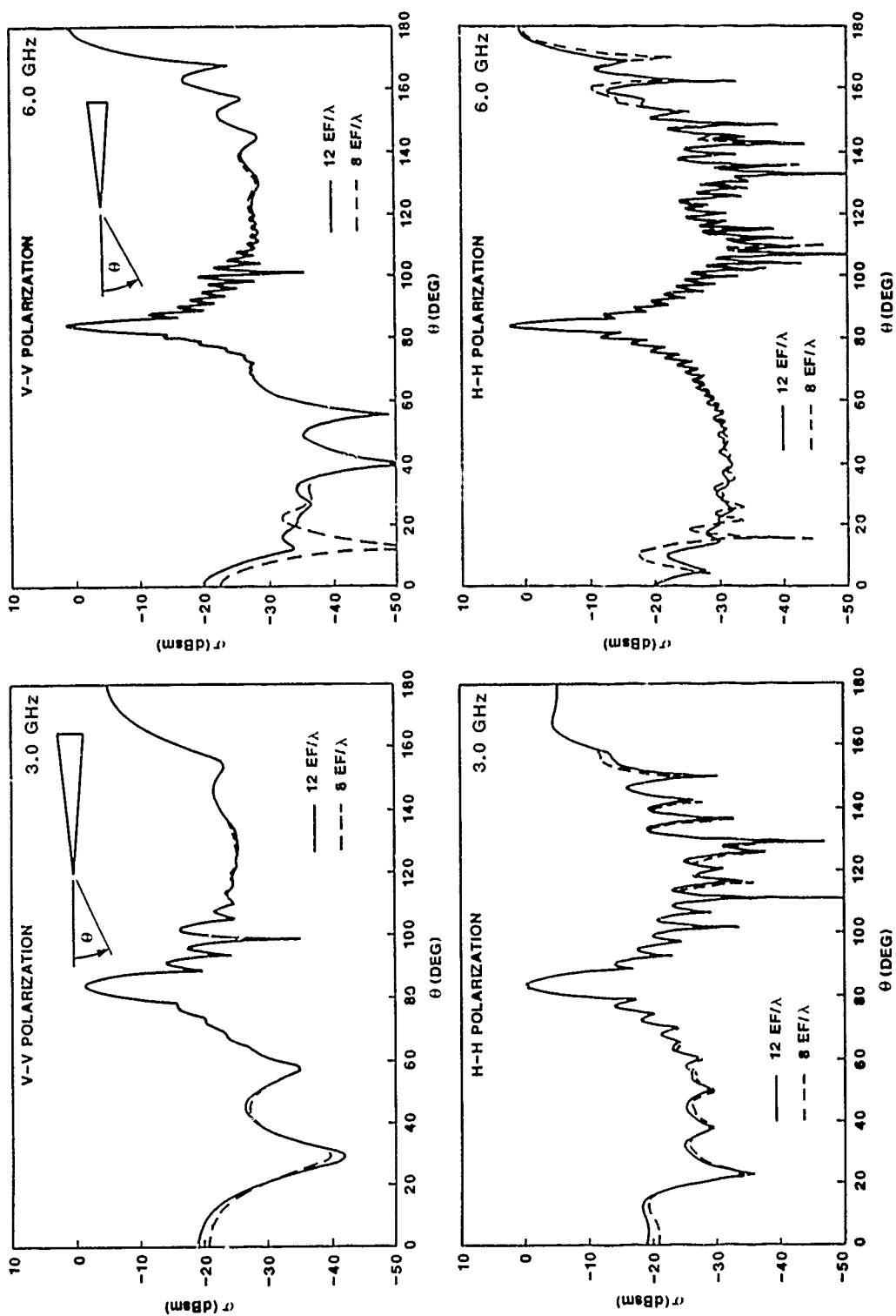


Figure 9. Monostatic RCS as a function of aspect angle for a metal cone (Dia of base plate = 5.5", altitude = 25.0") calculated with 8 EF/λ and 12 EF/λ at frequencies of 3.0 GHz and 6.0 GHz

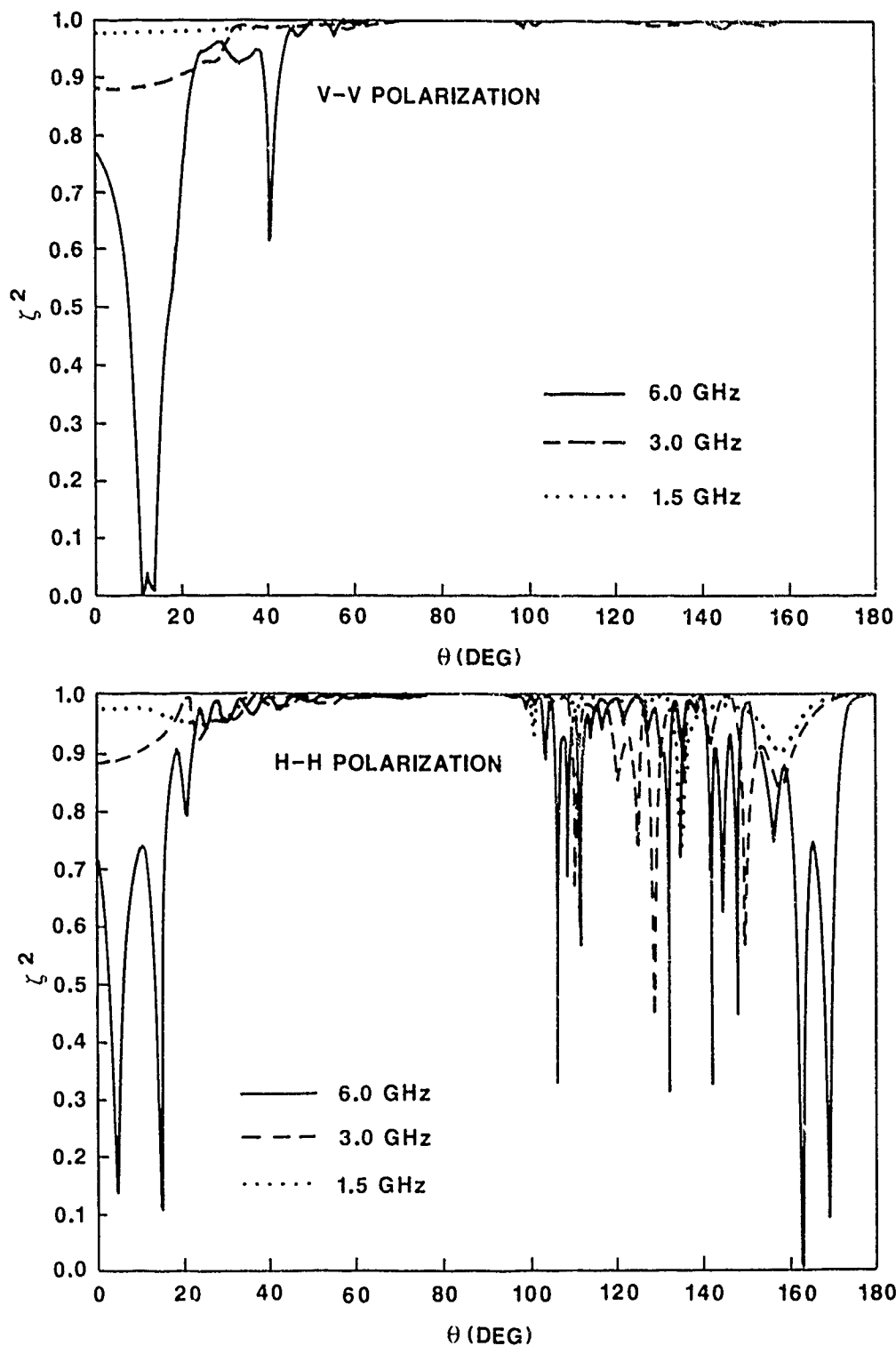


Figure 10. Real part of the normalized cross-energy spectrum for far-fields scattered from a metal cone computed with $8EF/\lambda$ and $12EF/\lambda$

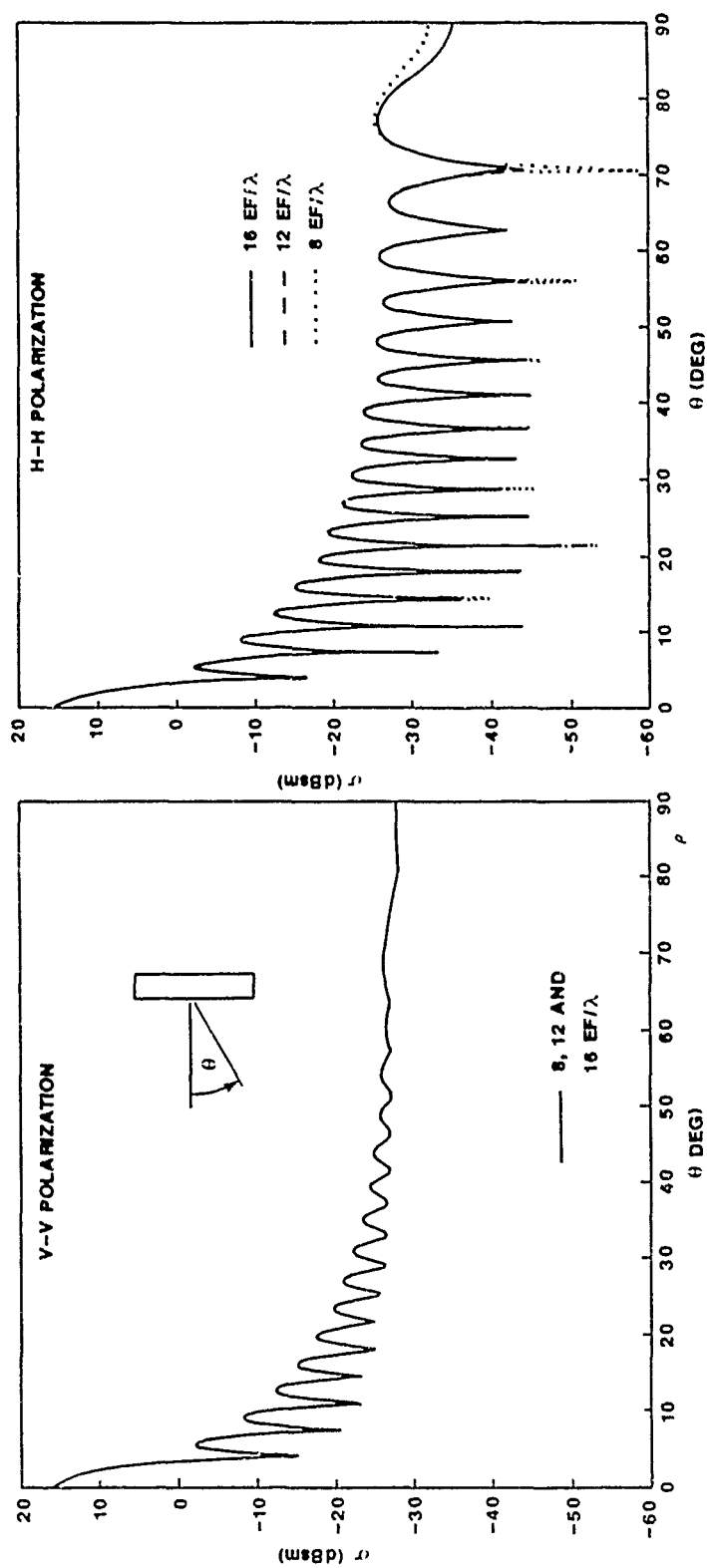


Figure 11. RCS as a Function of aspect angle for a metal disk (Dia = 10.0", thickness = $1/4$ ") calculated with 8 EF/λ and 12 EF/λ at a frequency of 10 GHz

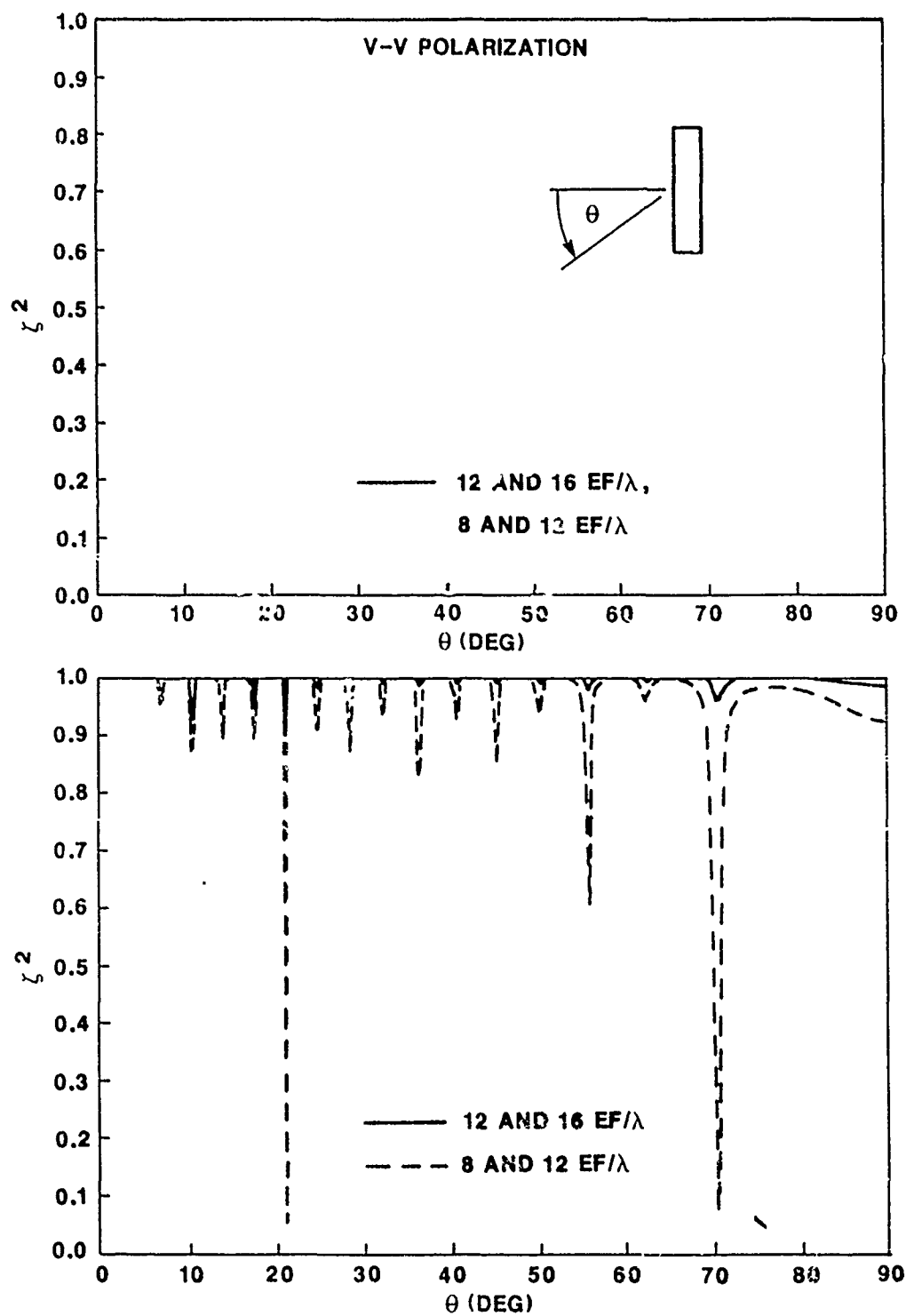


Figure 12. Real part of the normalized cross-energy spectrum for far-fields scattered from a metal disk calculated with 8 EF/ λ and 12 EF/ λ

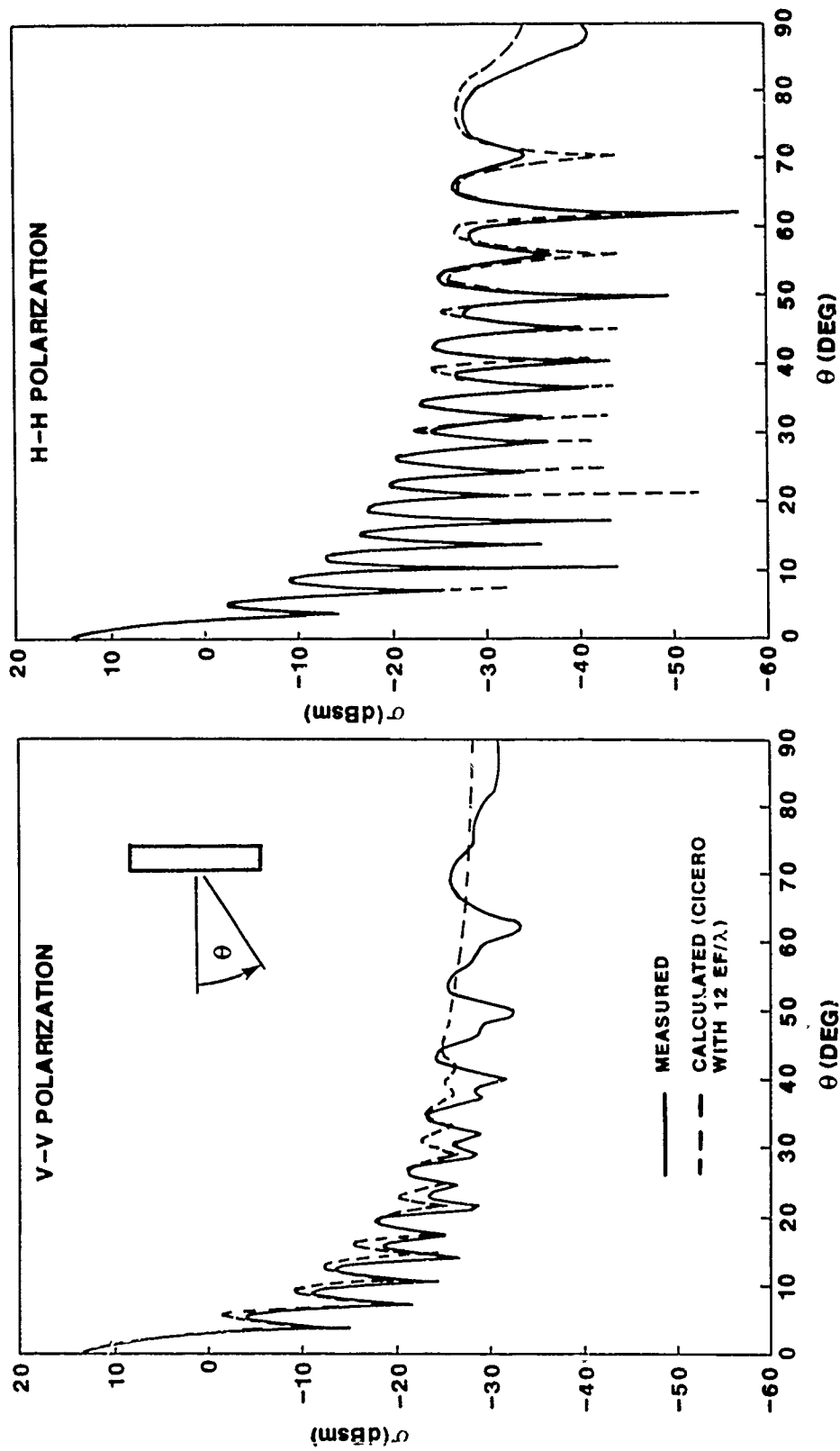


Figure 13. Comparison of measured and calculated RCS for a metal disk (Dia = 10.0", thickness = 1/4") at a frequency of 3.0 GHz

CONCLUSION

Expansion function densities required for numerical convergence are an important consideration in MM calculations because these densities have a significant impact upon computer resources necessary for solution. For the simple metallic objects discussed above, these densities were found to noticeably increase with increasing frequency. Electrically small objects with generating curves of the order of 3λ to 4λ in length required about $8 \text{ EF}/\lambda$ for convergence. Scatterers with lengths near 16λ were found to require close to $16 \text{ EF}/\lambda$. Thus, the EF densities necessary for convergence appear to vary roughly as the square root of frequency. In addition, convergence of the RCS calculations was dependent upon the polarization of the incident fields. Convergence for horizontal polarization was found to require larger EF densities than for the case of vertical polarization.

As a result of the dependence of EF densities upon electrical size and polarization, computer resources are exhausted more rapidly than one might expect as the electrical size of the target increases. Calculations with the MM/BOR codes performed on the CRAY X-MP/2 with 1.8 million words of memory are currently limited to conducting objects of length 20λ or less along the generating curve.

REFERENCES

1. Louis N. Medgyesi-Mitschang and John M. Putnam, "Electromagnetic Scattering from Axially Inhomogeneous Bodies of Revolution," IEEE Trans. Antennas Propagat. 1, AP-32, p. 797, August 1984.
2. J. R. Mautz and R. F. Harrington, "Radiation and Scattering from Bodies of Revolution," Apl. Sci. Res., 20, p. 405, June 1969.
3. J. R. Mautz and R. F. Harrington, "H-Field, E-Field, and Combined-Field Solutions for Bodies of Revolution," RADC-TR-77-109, March 1977.
4. George E. Forsythe and Cleve B. Moler, Computer Solution of Linear Algebraic Systems, Prentice Hall Inc., Englewood Cliffs, N.J., 1967.
5. M. C. Liang and R. C. Rudduck, "Calculated Near Zone Backscattering Data For Finite Cylinders," Ohio State University ElectroScience Laboratory, 715968-2, January 1985.
6. Athanasios Papoulis, The Fourier Integral and Its Applications, McGraw-Hill Book Company, New York, 1962.
7. Julis S. Bendat and Allan G. Piersol, Engineering Applications of Correlation and Spectral Analysis, John Wiley & Sons, New York, 1980.

APPENDIX

Normalized Cross-Energy Spectrum for Comparison of Far-Zone Fields

In order to display the similarities and differences between two sets of data, it is convenient to examine the real part of the normalized cross-energy spectrum (Ref. 6):

$$\zeta_{ij}(\theta) = 2 \operatorname{Re}[E_i^*(\theta)E_j(\theta)] / (|E_i|^2 + |E_j|^2). \quad (A1)$$

In this paper $E_i(\theta)$ denotes the frequency-domain spectrum of the scattered field as computed with the i th expansion function density. Under the definition in equation A1, $|\zeta_{ij}| \leq 1$. Notice that ζ_{ij} has magnitude 1 if E_i and E_j are identical or if $|E_i| = |E_j|$ and the phases differ by π radians. On the other hand, $|\zeta_{ij}|$ approaches zero if there is a large disparity between amplitudes or if the phase difference is near $\pi/2$ radians. Since phase differences in excess of $\pi/2$ radians were not found to exist for the calculations employed in this study, we have displayed the values of ζ_{ij}^2 so as to yield a number between 0 and 1. The results are graphically similar to those obtained for a coherence function (Ref. 7), although the value of ζ is constructed from only the real part of the cross-energy spectrum.

SESSION IV - "CODE VALIDATION"

"Army and Marine Antenna Engineering Handbook"

Ed Domning and James Breakall

Lawrence Livermore National Lab

"Validation of Scattering Results for a Thick Perfectly Conducting Dipole Using NEC and the Spherical-Wave Expansion Technique"

A.C. Ludwig

General Research Corporation

"A Comparison of NEC & MININEC Results with Experimental Measurements"

James Breakall and A.P. Ludwigen

Lawrence Livermore National Lab

"Use of Impedance Plots to Check Validity of NEC Models"

Don Rucker, Hang Lai and Helen Kwei

ESL, Inc.

"Full Scale HF Antenna Test Approaches Applicable to Numerical Model Validation"

David Faust and Moray King

Eyring Research Institute

"Scale and Numerical Models for a Low Profile HF Shipboard Antenna"

James Tertocha

Naval Postgraduate School

"Ground Treatment to Enhance Low Angle Radiation of High Frequency Vertically Polarized Antennas"

Carl Smith and Harold J. Braschwitz

Smith Electronics, Inc.

"Time-Domain Treatment of Maxwell's Equations in Frequency Dependent Media"

Richard Holland

Applied Physics, Inc.

Army and Marine Antenna Engineering Handbook*

Edward E. Domning and James K. Breakall
University of California
Lawrence Livermore National Laboratory

This is a brief outline of the work being done at Lawrence Livermore National Laboratory (LLNL) on a field expedient antenna handbook being developed by LLNL for the Army and Marines. Our basic task is to develop an engineering handbook that gives data and analysis of common HF field antennas. We will model these antenna with NEC3 double precision gathering our data from NEC output and putting it into a handbook format. We will then present this data to in such a manner that it can be easily combined with ease of construction data into a field handbook. This means that we must find proper field antennas and then determine what parameters define thier field capabilities.

Antennas:

The antennas chosen fall into four categories: Basic whips, half squares, long wires, and vees. Within these categories there are variations in geometry, grounding and termination. All the variations are shown or mentioned in the slides. We are using a model of a typical radio which is shown as a box in the slides. We are also using a frequency of 17MHz for all the antenna plus a frequency of 5MHz on the basic whips and half squares.

Field Parameters:

Since a command site uses computers to calculate ionospheric reflection and ground wave propagation, we can say that the command site has the ability to give minimum gain at each angle for sky wave and minimum field values for ground wave propagation needed for reliable communication. This means that field operators would just have to have data on the antennas that would tell them whether or not they meet this criteria. Given this information, field operators can then find the antenna that meet or exceed the given reliability criteria and then compare with ease of construction data on each antenna to find best antenna to erect. This means that we will have to define meaningful field parameters for both sky and ground waves.

For the sky wave we have decided that the maximum field gain and its associated azimuthal angle at each elevation angle is a good parameter defining performance. This parameter can easily be put into (or retrieved from) long distance communication codes to find what is needed for reliable communication at sites one or two hops away. The gain will be in

* Work done under auspices of the U.S. Department of Energy by Lawrence Livermore National Laboratory under contract W-7405-Eng-48.

dB over an isotropic antenna taken at one degree increments of elevation and azimuth.

Given a necessary field strength needed for acceptable communication with the command or other sites, the command site can propagate a ground wave back to a certain point from the field antenna. The point we have chosen for this is one mile away, twenty-five feet off the ground, which is reasonable for an antenna on a tower. The transmitter power is fifteen watts and the propagation is done over fair ground with relative dielectric constant of ten and a conductance of three milli-siemans per meter. Since polarization is important we will be looking for both maximum and minimum field for both vertical and horizontal waves.

The slides show some results for sky wave and ground wave for four variations of the half square antenna. We are also going to report the input impedance for each antenna to help the field operator with matching.

Other Developments(Current Output) :

When we first started to collect our data we quickly found that we were taking up a large amount of disk space when looking only sky wave data in ten degree increments. This prompted us to explore a new method of data collection; we gather our parameters from a program using current data instead of NEC output. This means that we must store the parameters needed for field calculation (in binary form for compact storage) and then write a program to access this file and do field calculations. After modifying NEC3 to write out the necessary variables, and the routine RDPAT from NEC3 to calculate fields, we were able to get radiation pattern cuts a lot easier than with the typical NEC output. This program currently makes it easy to look at different sky wave patterns of an antenna and could possibly have use in general antenna analysis. We are currently investigating including ground wave calculations in this program.

Other Developments (Ground Variations):

We have done a side study of ground variations on a dipole. We looked at a half wave dipole fed three tenths of a wavelength above the ground, over frequencies of two, ten and thirty MHz, with the following variations of dielectric constants and conductivities :

$\epsilon = 1, 15, 30 \text{ and } 100$

$\sigma = 0.0001, 0.001, 0.01 \text{ and } 0.1 \text{ siemens/meter.}$

The slides show a typical radiation pattern plot. Notice that most of the gain is between ten and thirty degrees. This is indicative of all the plots observed over all grounds. Looking at the slide of surface wave results, we find that the dB variation of the field with relative dielectric constant for two and ten MHz is very small. We also see that for thirty MHz

the variation is getting large. Looking at the dB variation of the field with conductance we find that the opposite is true; the variation is large for two and ten MHz and getting small for thirty MHz.

Looking at the sky wave results for the critical angles of ten, twenty and thirty degrees, we find that the gain varies over all these grounds from four to nine dB. Also notice that the maximum gain variation is at ten degrees ; the angle that would be most affected by ground variations.

Conclusions:

Wrapping this summary up, I would just like to mention some important products of this investigation. We have defined antennas and parameters for field handbook analysis and have begun modeling and collecting sky and ground wave parameters. We have developed a tool that gets far field plots in a manner that is easier than before making it a good tool for antenna analysis. We also looked at ground parameter variations and found that while it is important to have a good value for ground for an accurate analysis of an antenna, it is not as important for a less accurate analysis. Last, I would just like to say that an engineering handbook with an analysis of HF field expedient antennas should be completed by the end of the fiscal year.

HF ANTENNA ENGINEERING HANDBOOK



J. K. Breakall

E. E. Domning

Lawrence Livermore National Laboratory
Livermore, Ca.

Applied Computational Electromagnetics Review
March 18,19 and 20 1986

TeX

Page 1

INTRODUCTION

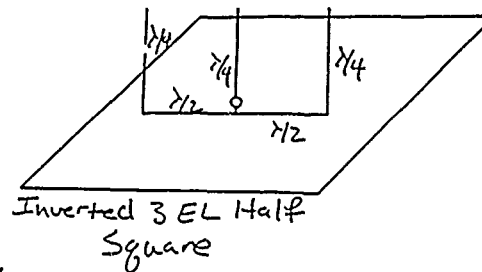
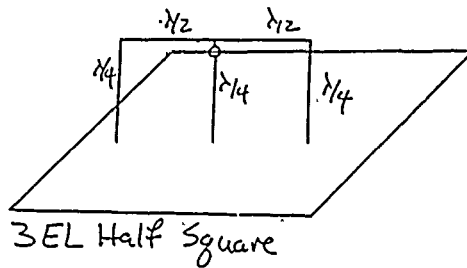
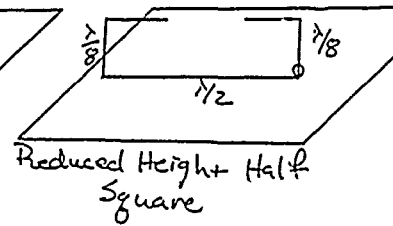
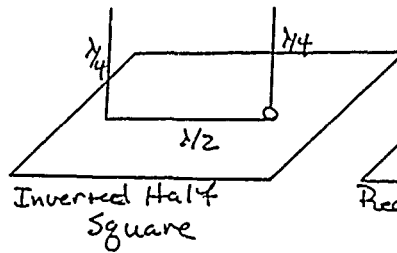
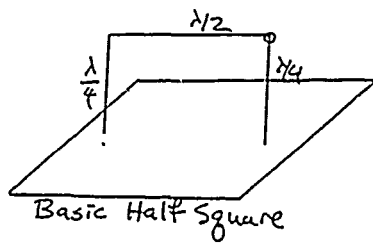


GOALS

- Construct an engineering handbook giving an analysis of HF field antennas used by the Army and Marines
- Present the electrical performance data such that it can be easily combined with ease of construction data into a field handbook
- Find proper antennas and parameters for analysis

TeX

HALF SQUARE CONFIGURATIONS



Frequencies: 5, 17, 14 & 20 MHz

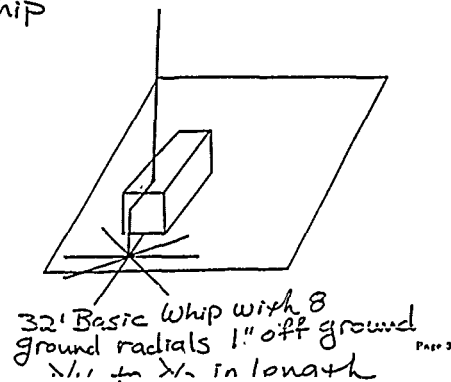
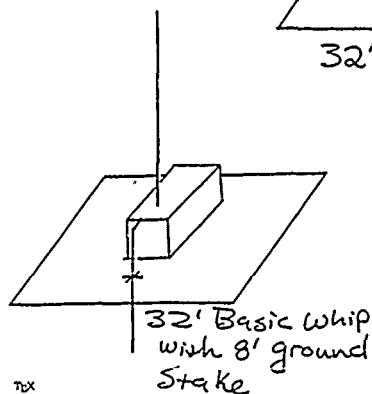
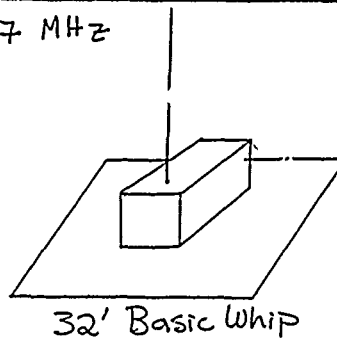
72X

Page 4

BASIC WHIP CONFIGURATIONS



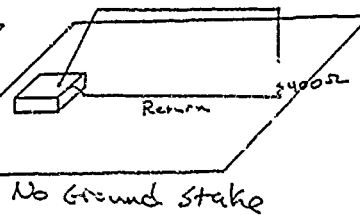
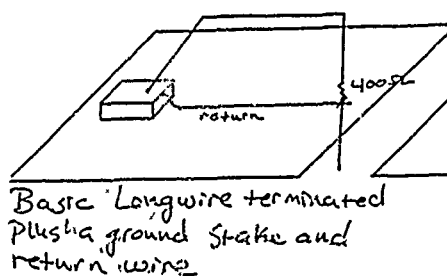
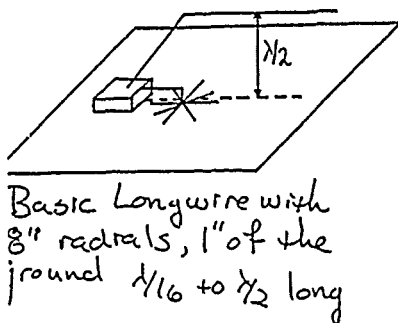
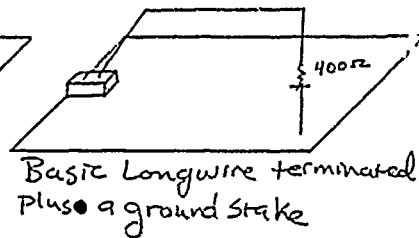
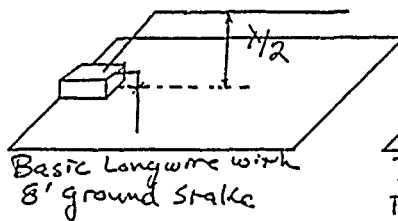
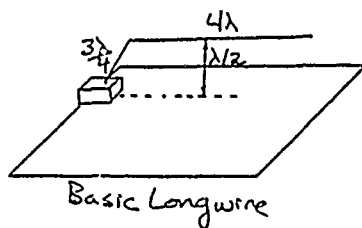
Frequencies: 5 & 17 MHz



72X

Page 5

LONG WIRE CONFIGURATIONS

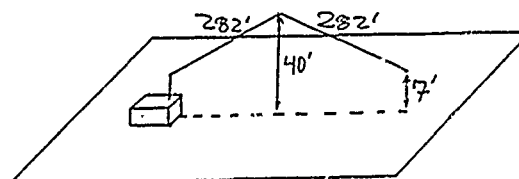
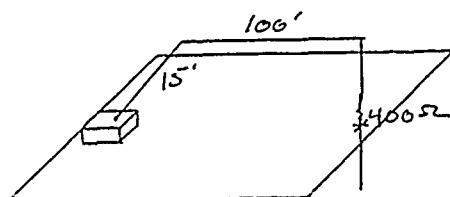
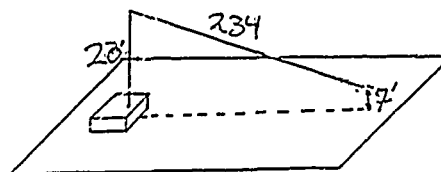
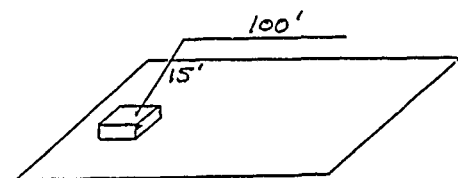


Frequencies: 17 MHz only

70x

Page 5

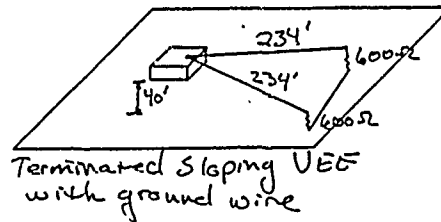
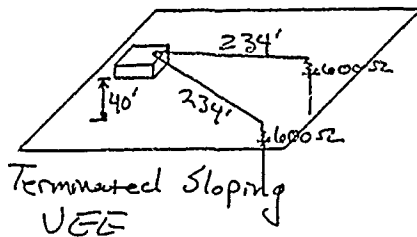
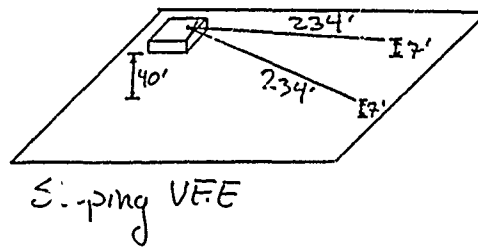
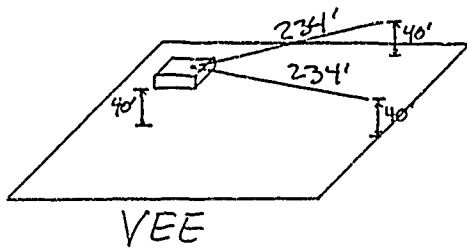
ADDITIONAL LONG WIRE CONFIGURATIONS



Also, on the above
vary lengths: 234' and 564'
vary heights: 6', 15', 20', 40'

70x

VEE CONFIGURATIONS



Also use 528' legs
Also look at Dipoles

Frequency: 17MHz

77X

Page 7

IMPORTANT CONCEPTS



- A command site can give field operators a range of take off angles and minimum gain at each angle required for reliable communication at the field site
- Field operators can then list the field antennas that meet or exceed this criteria
- They would then examine ease of construction data to choose which antenna to construct

77X

Page 8

FIELD PARAMETERS



SKY WAVE

- Find the maximum field gain and its associated azimuthal angle at each elevation angle
- Look at one degree increments in elevation and azimuth.
- Find the gain in dB over isotropic
- Also find the input impedance

TeX

Page 9

FIELD PARAMETERS



GROUND WAVE

- Use a 'fair' ground with $\epsilon = 10, \sigma = 0.003$
- Obtain E-field (in azimuth) at 1 mile, 25 feet off the ground with transmitter power of 15 watts :

Vertical		Horizontal	
max E	min E	max E	min E

TeX

Page 17

RESULTS



HALF SQUARE SKY WAVE

Antenna	10°	20°	30°	40°	50°	60°	70°	80°	90°
Half Square E	0.33	2.7	2.6	1.4	-0.6	3.3	-6.2	-9.7	—
Square ϕ	0,180	0,180	0,180	10,190	10,196	20,30 150,160	80,60 120,130	90	—
Half Square E	-3.4	-0.8	-0.5	-1.2	-2.7	-4.8	-7.4	-12	—
Inverted ϕ	0,180	0,180	0,180	0,180	10,190	30,160	80,90, 100	90	—
3EL Half Square E	2.0	4.3	4.2	3.0	0.8	-2.1	-6.2	-12	—
Square ϕ	0,180	0,180	0,180	0,180	0,180	0,180	0,180	90,270	—
3EL Half Square E	-0.5	2.1	2.4	1.7	0.2	-2.1	-5.6	-11	—
Inverted ϕ	0,180	0,180	0,180	0,180	0,180	0,180	0,180	90,270	—

Total field (gain in dBi) Frequency: 17 MHz Page 12

RESULTS



HALF SQUARE GROUND WAVE

	Vertical				Horizontal			
	ϕ	Max E	ϕ	Min E	ϕ	Max E	ϕ	Min E
Half Square	0 180	1.30	270	0.279 (-13 dB)	40 140	0.201	90 270	0
Inverted Half Square	0 180	0.84	250 290	0.155 (-15 dB)	40 140	0.031	90 270	0
3EL Half Square	0 180	1.57	90 270	0.010 (-44 dB)	30 150 210 330	0.155	0 90 180 270	0
Inverted 3EL Half Square	0 180	1.18	90,110 250,290	0.053 (-27 dB)	30 150 210 330	0.023	0 90 180 270	0

E fields in mV/m

OTHER DEVELOPMENTS



CURRENT OUTPUT

- Modified NEC3 to write out currents and related data to file using a CO card.
- Wrote a program that reads this file and does field calculations using a modified RDPAT routine
- Program also does radiation pattern plots

TpX

Page 13

OTHER DEVELOPMENTS

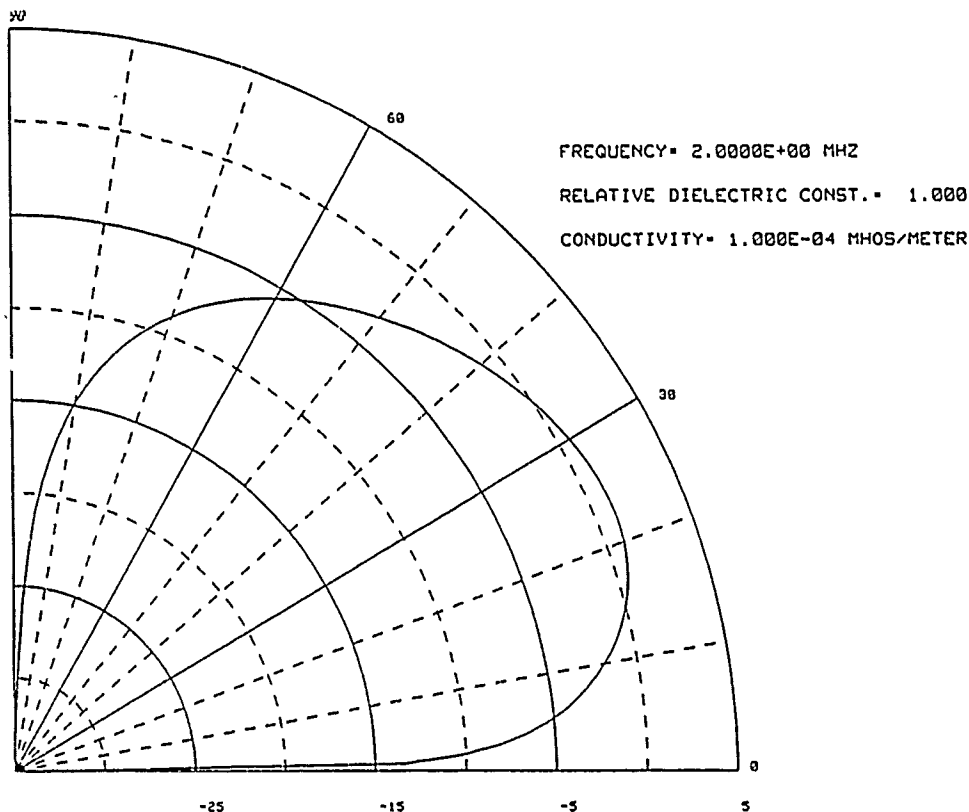


GROUND VARIATIONS

- Half wave dipole with lower edge .05 wavelengths above ground fed .3 wavelengths above the ground
- Used frequencies of 2,10 and 30 Mhz, dielectric constants of 1,15,30 and 100 and conductivities of .0001,.001,.01 and .1 S/M

TpX

Page 14



OTHER DEVELOPMENTS



GROUND VARIATIONS RESULTS (SURFACE WAVE)

2 MHz

	$\sigma = 10^{-4}$	$\sigma = 10^{-3}$	$\sigma = 10^{-2}$	$\sigma = 10^{-1}$	
$\epsilon = 1$	14.4	39.7	190.1	238.3	24.4
$\epsilon = 15$	54.3	62.6	179.3	237.8	12.8
$\epsilon = 30$	79.1	84.1	170.9	237.2	9.5
$\epsilon = 100$	128.8	130.6	160.8	234.7	5.2
dB VARIATION WITH $\epsilon \rightarrow$	19.0	10.3	1.5	.1	

dB VARIATION WITH σ

30 MHz

	$\sigma = 10^{-4}$	$\sigma = 10^{-3}$	$\sigma = 10^{-2}$	$\sigma = 10^{-1}$	
$\epsilon = 1$	11.9	3.9	2.1	11.4	15.1
$\epsilon = 15$	6.9	6.8	6.2	13.2	6.6
$\epsilon = 30$	10.7	10.7	10.2	15.6	3.7
$\epsilon = 100$	26.4	26.4	26.3	29.3	.9
	11.7	16.6	22.0	8.2	

dB VARIATION WITH σ

10 MHz

	$\sigma = 10^{-4}$	$\sigma = 10^{-3}$	$\sigma = 10^{-2}$	$\sigma = 10^{-1}$	
$\epsilon = 1$	10.9	3.2	10.3	143.4	33.0
$\epsilon = 15$	14.2	14.0	17.5	136.9	19.8
$\epsilon = 30$	24.2	24.2	26.8	131.2	14.7
$\epsilon = 100$	57.7	57.8	59.8	117.5	6.2
dB VARIATION WITH $\epsilon \rightarrow$	14.5	25.1	15.3	1.7	

dB VARIATION WITH σ

2 dB Variation in ϵ

OTHER DEVELOPMENTS



GROUND VARIATIONS RESULTS (SKY WAVE)

FREQ.	ELEV. ANGLE	MIN GAIN	MAX GAIN	VARIATION Δ
2 MHz	10°	-4	+5	9
"	20°	-2	+3	5
"	30°	-4	+1	5
10 MHz	10°	-3	+3	6
"	20°	-1	+3	4
"	30°	-4	+1	5
30 MHz	10°	-5	+3	8
"	20°	-3	+3	6
"	30°	-4	+1	5

TeX

Page 16

CONCLUSIONS



- Developed a tool for easier antenna analysis
- Looked at the effect of varying ground parameters
- Developing an engineering handbook with an analysis of Army-Marine field antennas

TeX

Page 17

VALIDATION OF SCATTERING RESULTS FOR A THICK PERFECTLY
CONDUCTING DIPOLE USING NEC AND THE SPHERICAL-WAVE EXPANSION TECHNIQUE

A.C. Ludwig
General Research Corporation
Santa Barbara, California

The spherical-wave expansion (SPEX) technique recently developed at General Research Corporation (A.C. Ludwig, IEEE Trans., AP, to be published July 1986) has been validated using two procedures: (1) the boundary condition is checked, using a built-in test feature, on a point set independent of the point set used to obtain the solution, and (2) the internal fields are computed using an independent surface current integration program. The second validation method has also been applied to results obtained using NEC. Although NEC has a built-in near-field capability, it was found that the new surface integration program, which interpolates the NEC current, produces a lower internal field; however, the internal field produced by the SPEX solution is even lower.

Results using SPEX and NEC for surface currents, scattered fields, and internal fields will be presented and compared.

A Comparison of NEC and MININEC Results with Experimental Measurements (LLNL, R.W.P. King, NBS)*

J. K. Breakall and A. P. Ludwigsen
University of California

Lawrence Livermore National Laboratories, Livermore, CA

INTRODUCTION

The Lawrence Livermore National Laboratory (LLNL) has been making electromagnetic measurements on actual and scale model objects for the last several years to develop understanding of coupling phenomenology. This effort has resulted in a complete upgrade of experimental facilities and the purchase of some new and very sophisticated instrumentation for measuring various parameters. In testing and calibrating these facilities, various monopole standards were developed and the results were directly compared with the best theoretical and computer models available. We have used NEC directly in this work and achieved excellent agreement for both the antenna impedance and receiving cross-section versus frequency over some ten octaves.

In this paper we will present some of these results and discuss some of these new facilities and instrumentation for making antenna measurements. We will also compare the results with those classical measurements made by R.W.P. King and associates on similar antennas. A comparison between another similar but different formulation of the method-of-moments technique as used in the MININEC computer program will also be made with NEC and these measurements. We will present the effects of two different excitation feed methods (applied E-field and current-slope-discontinuity) on impedance results. Additionally results will be shown for comparisons of Yagi antenna patterns as measured by the National Bureau of Standards (NBS) and computed using NEC and MININEC. It has been found that results from MININEC agree with those of NEC and NBS when the frequency is shifted by some 1.7 percent.

COMPARISON WITH KING

NEC uses two types of feed excitations, the Applied E-Field and Current Discontinuity sources. Convergence properties were found for each to provide segmentation and accuracy requirements for the models chosen for this work. The results are shown in Figures 1a and 1b.

The antenna chosen is the .5 meter length, 7.022 millimeter radius dipole as reported by

* Work performed under the auspices of the U. S. Department of Energy by the Lawrence Livermore National Laboratory under Contract W-7405-Eng-48.

King (1967). This antenna has been used as a standard of comparison throughout the literature and in the present antenna textbooks. The impedance results are compared to measurements given by Mack for this antenna for each of the theoretical formulations, King, NEC (App. E-Field), NEC (Current Disc.), and MININEC and are shown in Figures 2a,b,c,d (Resistance) and 3a,b,c,d (Reactance). The original results from King were actually shown as admittance and we display the new computed comparisons in Figures 4a,b,c,d (Conductance) and 5a,b,c,d (Susceptance). It is interesting to note that the admittance results give better visual agreement than impedance even though the data is the same for each.

COMPARISON WITH LLNL

We also made measurements here at LLNL on our time domain (TDR) facility on a .3 meter (length), 1.5875 millimeter (radius) monopole on a perfectly conducting ground plane. The experimental setup and equations for the calculation of the impedance are shown in Figure 6. The impedance results for NEC and MININEC comparisons are shown in Figures 7a,b (Resistance) and 8a,b (Reactance). Agreement is excellent except for a slight shift in frequency for the MININEC results. Similarly admittance results are shown in Figures 9a,b (Conductance) and 10a,b (Susceptance). A similar comparison was made for the related property of measuring the voltage response across a 50 ohm load at the monopole terminals to an incident spherical wave using our time domain measuring range (EMPEROR), our frequency domain facility (BEAMS), and NEC computed results. The NEC model had to include spherical wave excitation instead of the usual plane wave and the incorporation of the wire conductivity and permeability since we used a steel piano wire monopole. The results are shown in Figure 11. As can be seen the EMPEROR range is good up to about 1.5 GHz while the BEAMS facility is in excellent agreement up to 18 GHz. We plan to use this facility for making impedance measurements in the future also up to 18 GHz and carrying out anechoic radiation pattern measurements.

COMPARISON WITH NBS

Finally, we have included some results and findings on some comparisons of radiation patterns made at the NBS on Yagi antennas. In Figure 12 is shown the pattern of a 3 element Yagi as measured and computed by NEC at a center frequency of 299.8 MHz. The agreement is excellent in absolute magnitude and sidelobe structure. The same 3 element Yagi pattern is shown in Figure 13 as compared with MININEC at the frequency of 299.8 MHz. Again, agreement is good except for some 2-4 dB discrepancies in the sidelobes. Similarly patterns are shown for a 5 element Yagi compared with NEC in Figure 14. Again agreement is excellent for every inflection of the sidelobe structure. The MININEC 5 element Yagi results are shown in Figure 15 for a frequency of 299.8 MHz. The agreement is here is good in the mainlobe but only qualitative in the sidelobe region. By sweeping frequencies on the MININEC model it was found that excellent agreement could be obtained at a frequency of 305 MHz (1.7 percent higher than center frequency)

and this is shown in Figure 16. By repeating the MININEC pattern for the 3 element Yagi at 305 MHz excellent agreement was also obtained and is shown in Figure 17. It is not known yet why this frequency shift effect is occurring but we hope to look into this problem and hopefully discover the reason for this anomaly.

CONCLUSIONS

We have presented some experimental results from past and present work as compared with the computer antenna codes of NEC and MININEC. Agreement has been generally excellent on some simple antenna structures for both impedance and patterns. It is hoped that this work will provide interest in experimental validation of computer code results and future effort will be able to be undertaken to carry out more sophisticated modeling and measurements.

CONVERGENCE

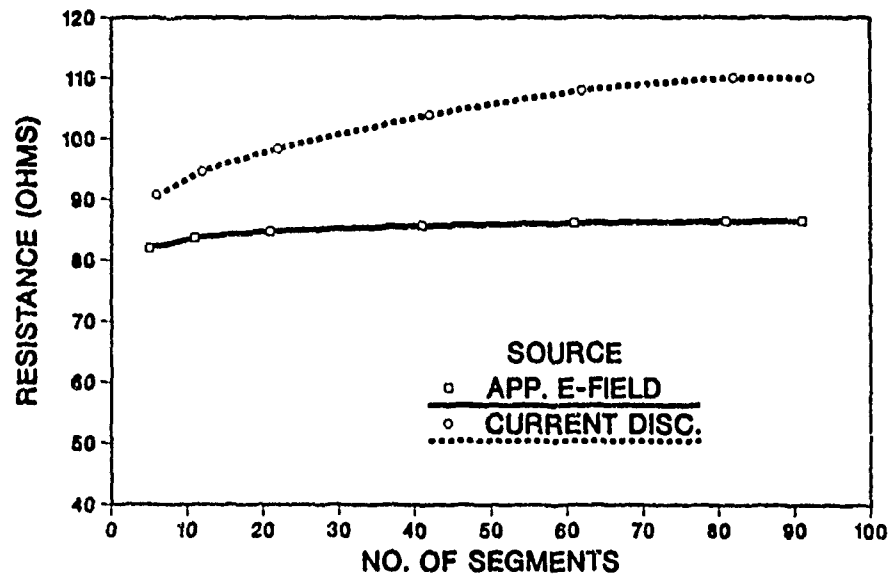


Figure 1a. NEC Feed Excitation Convergence Properties

CONVERGENCE

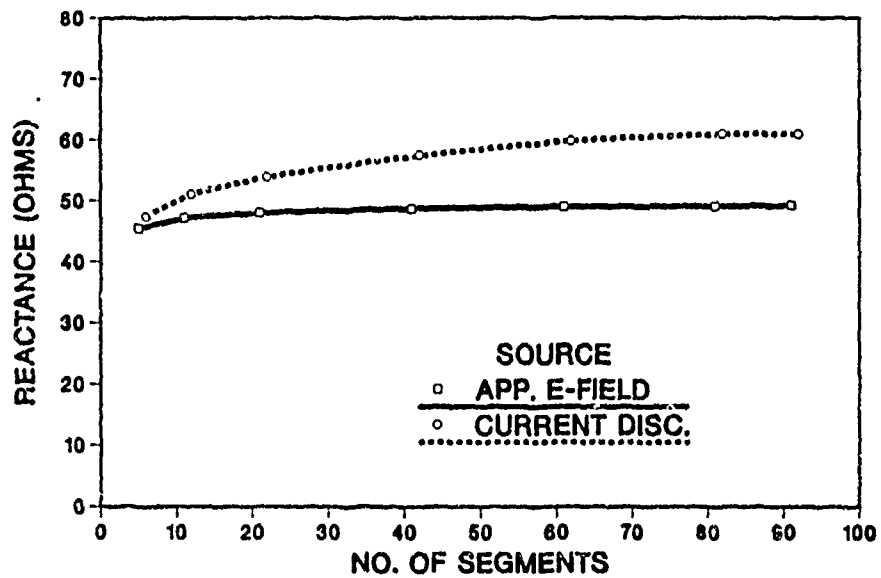


Figure 1b. NEC Feed Excitation Convergence Properties

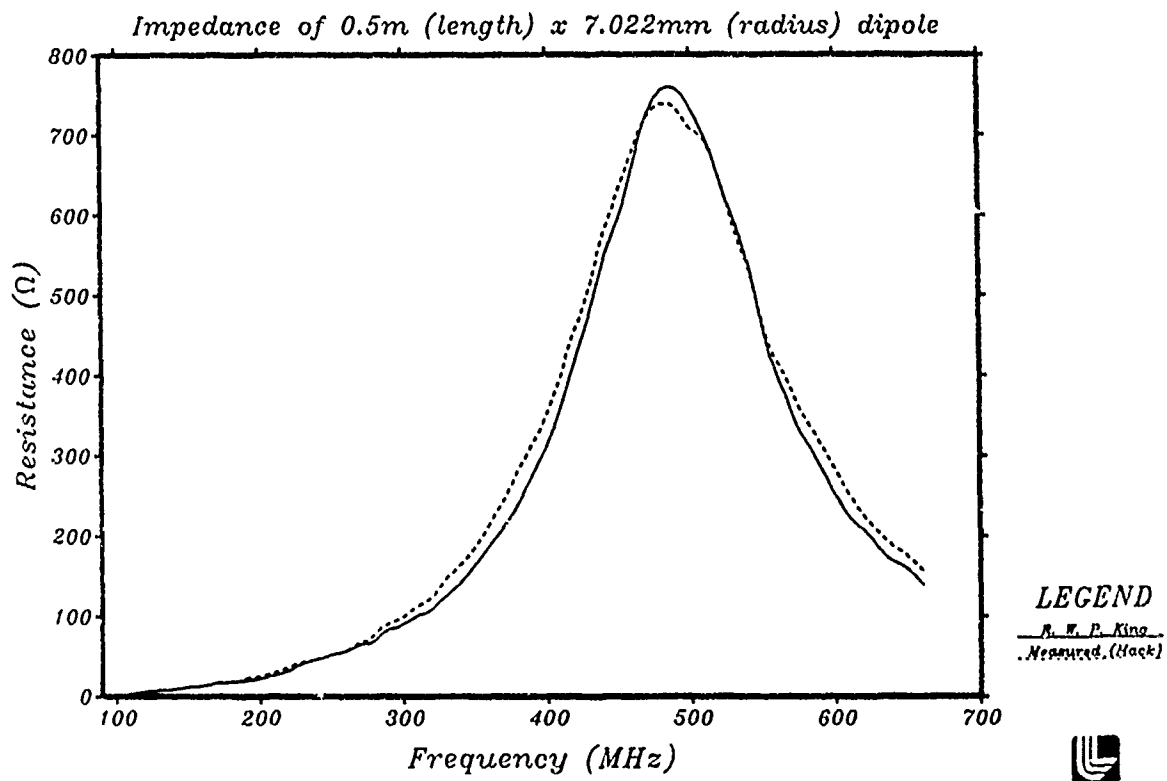


Figure 2a. R. W. P. King comparison

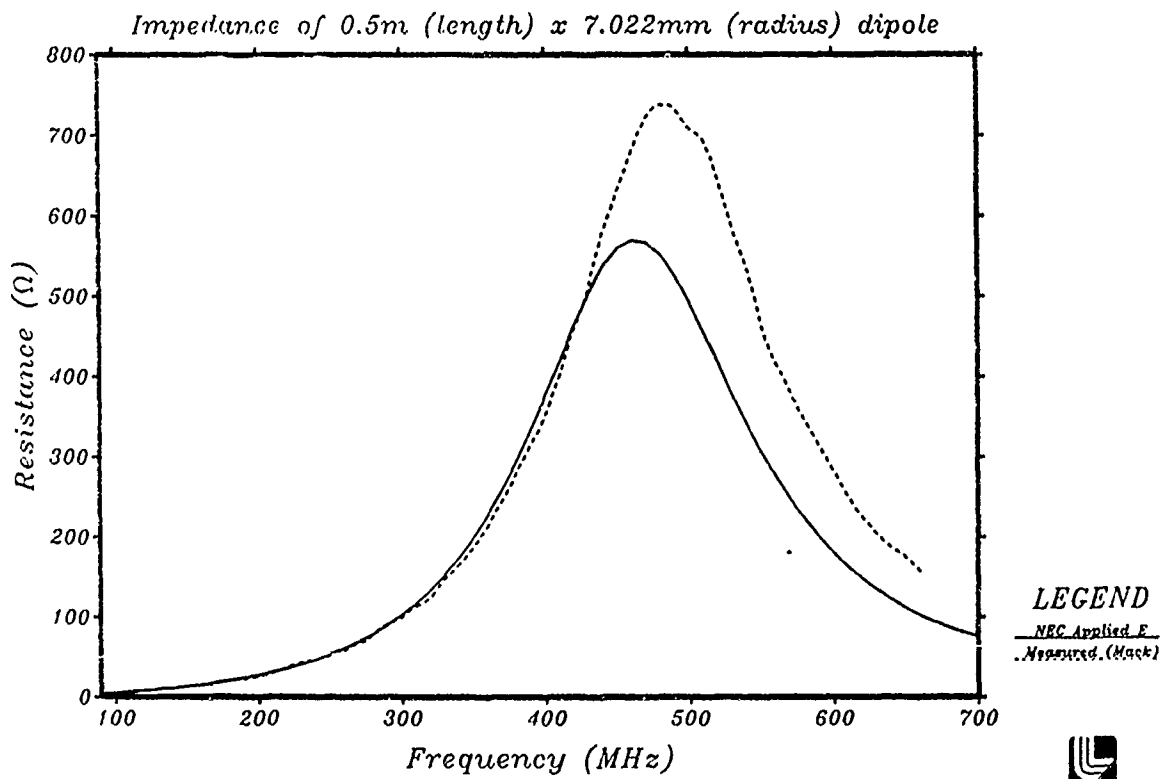


Figure 2b. NEC Applied E-field comparison

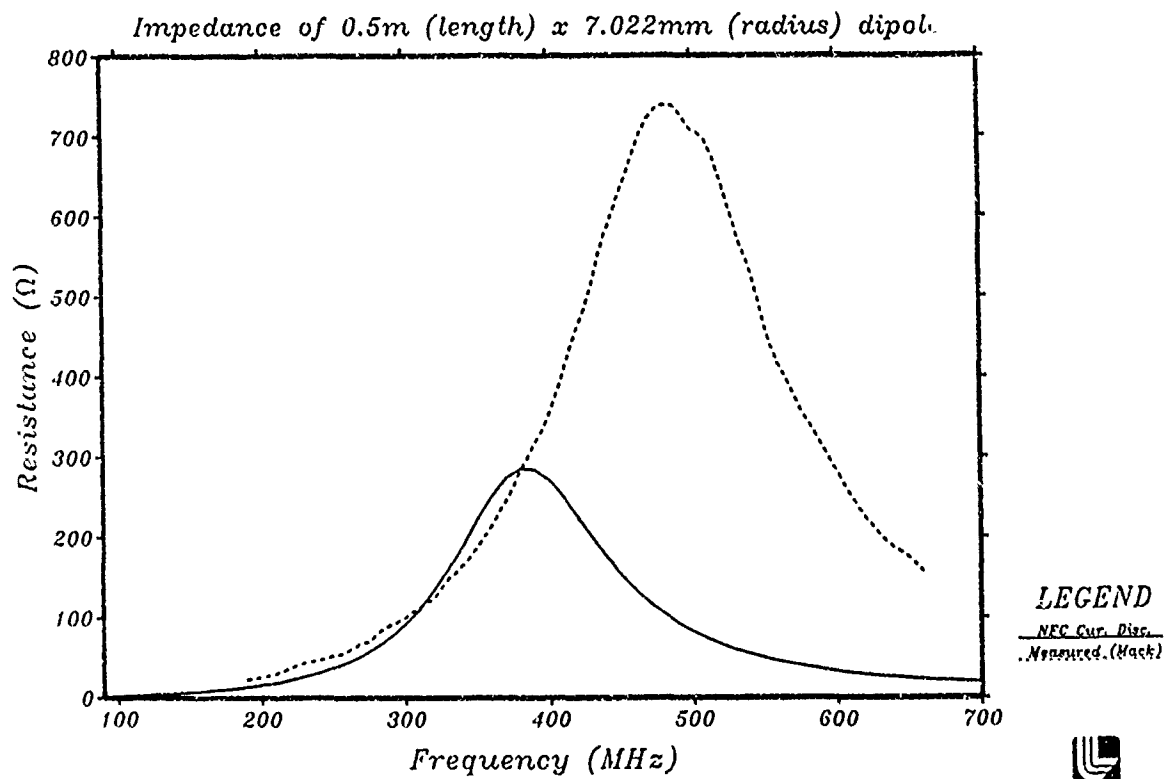


Figure 2c. NEC Current Discontinuity comparison

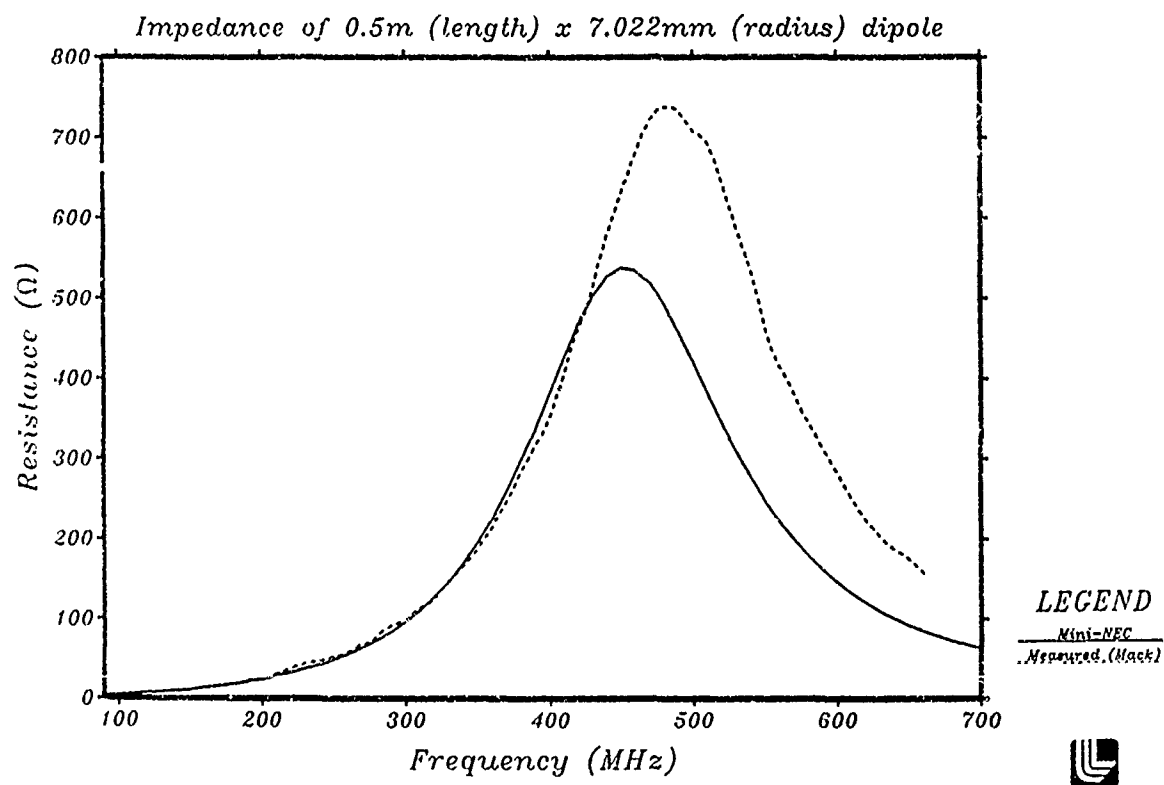


Figure 2d. Mini-NEC comparison

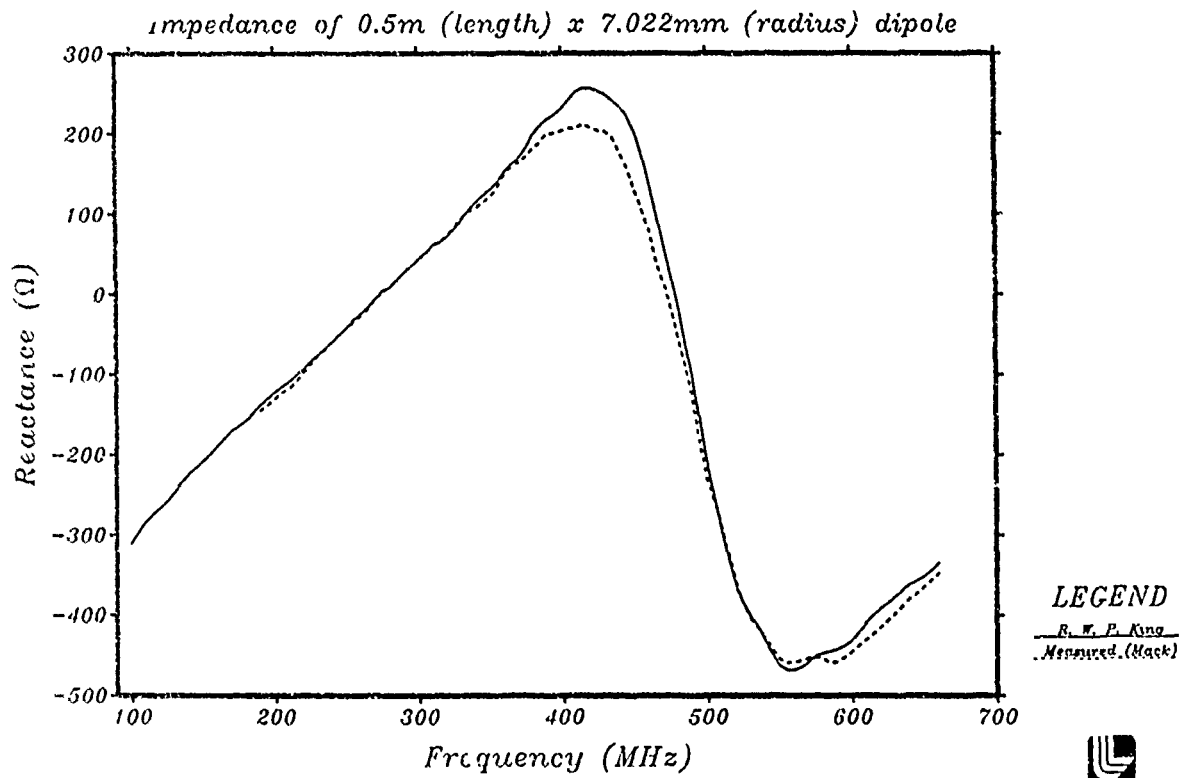


Figure 3a. R. W. P. King comparison

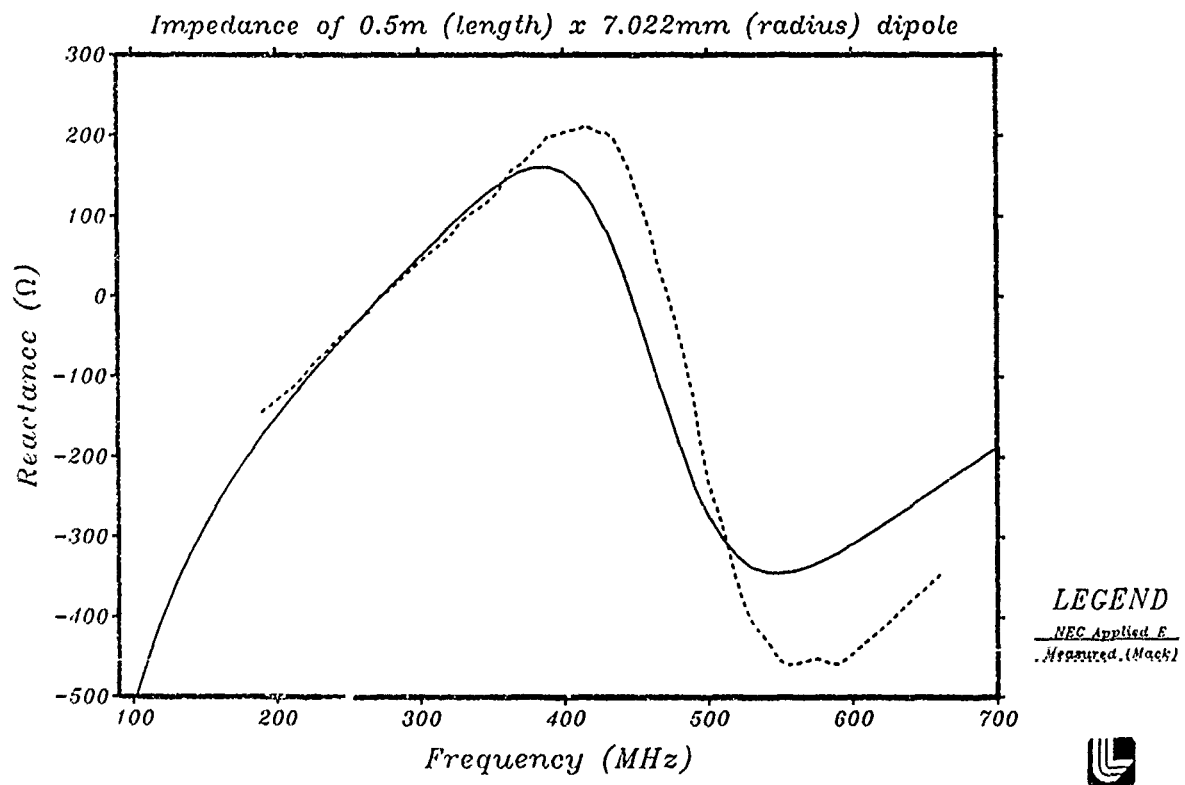


Figure 3b. NEC Applied E-field comparison

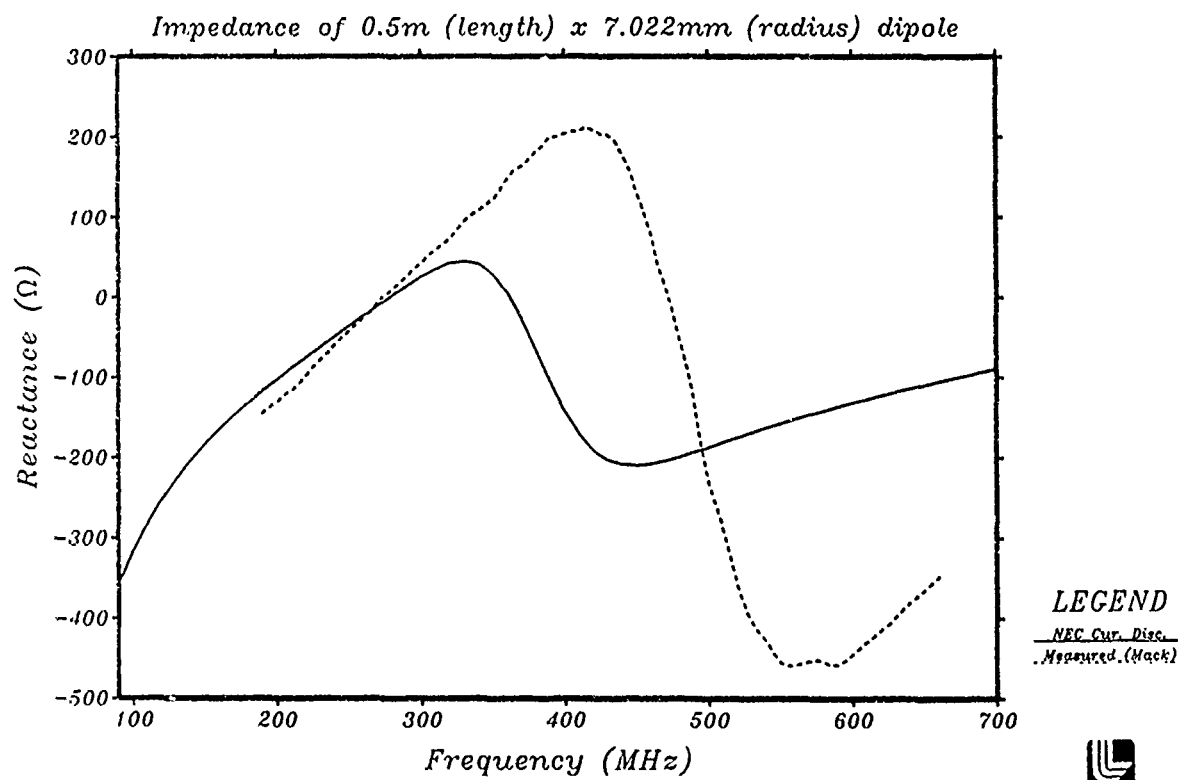


Figure 3c. NEC Current Discontinuity comparison

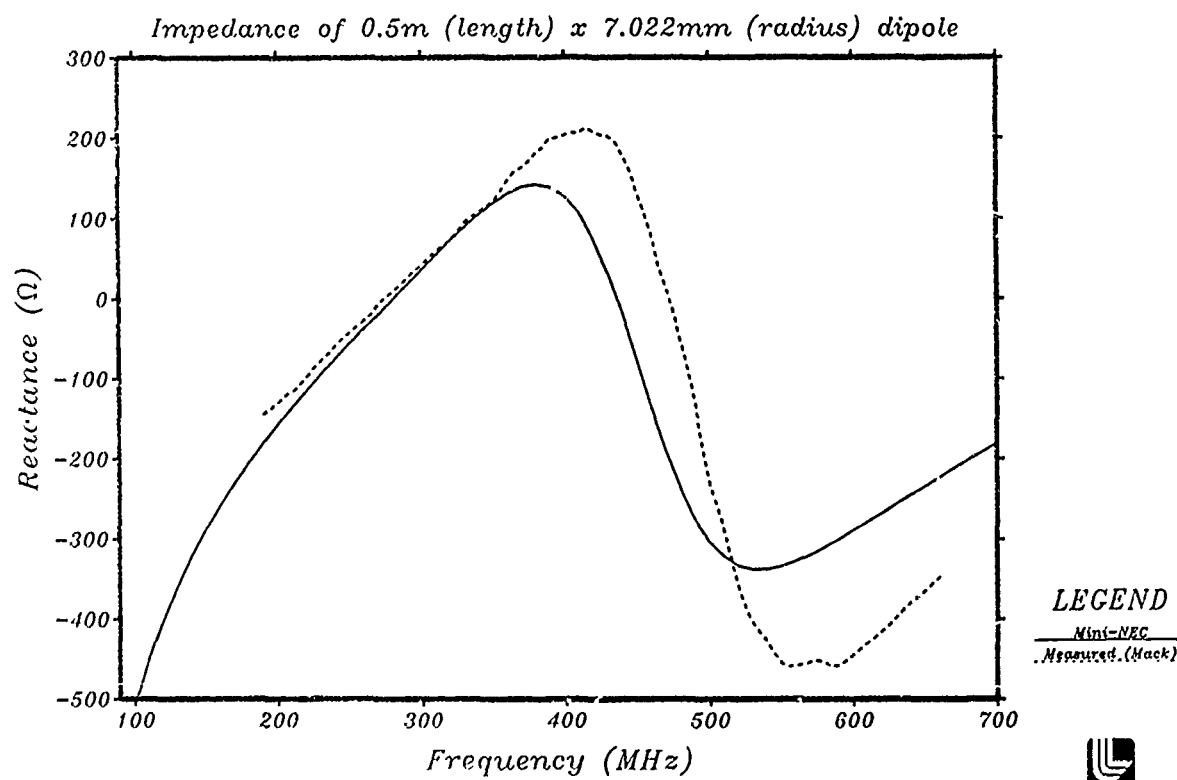


Figure 3d. Mini-NEC comparison

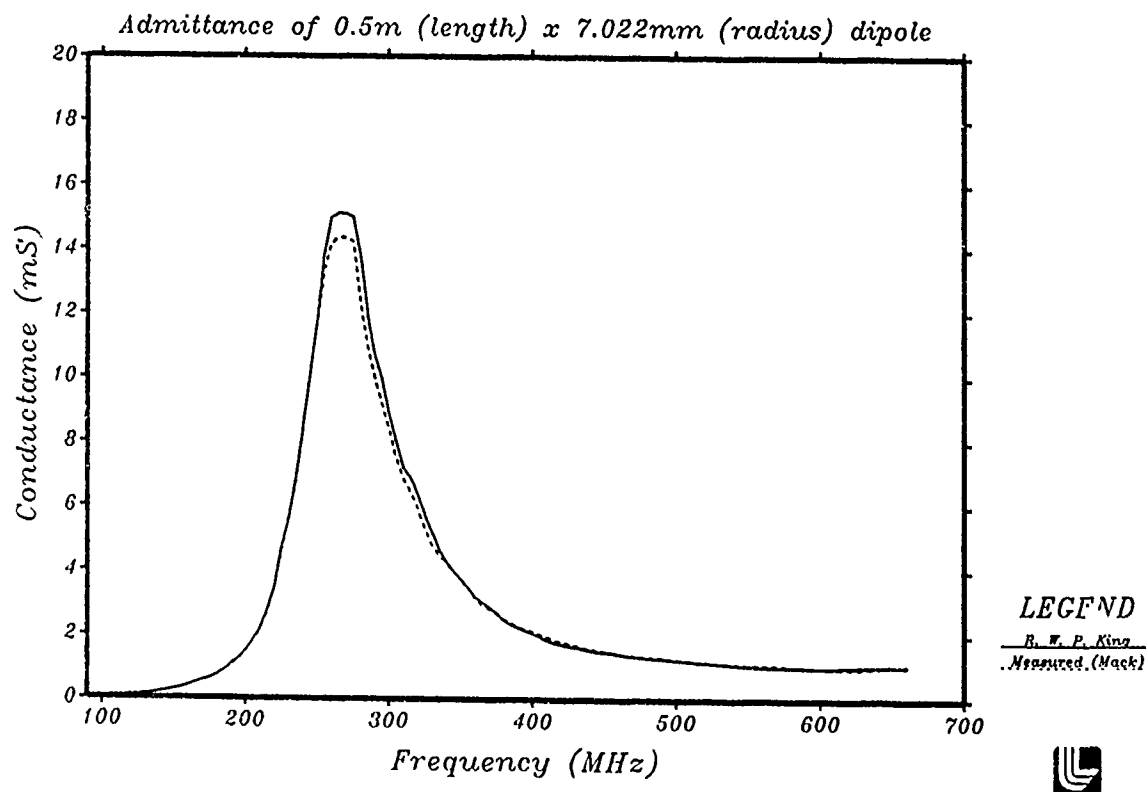


Figure 4a. R. W. P. King comparison

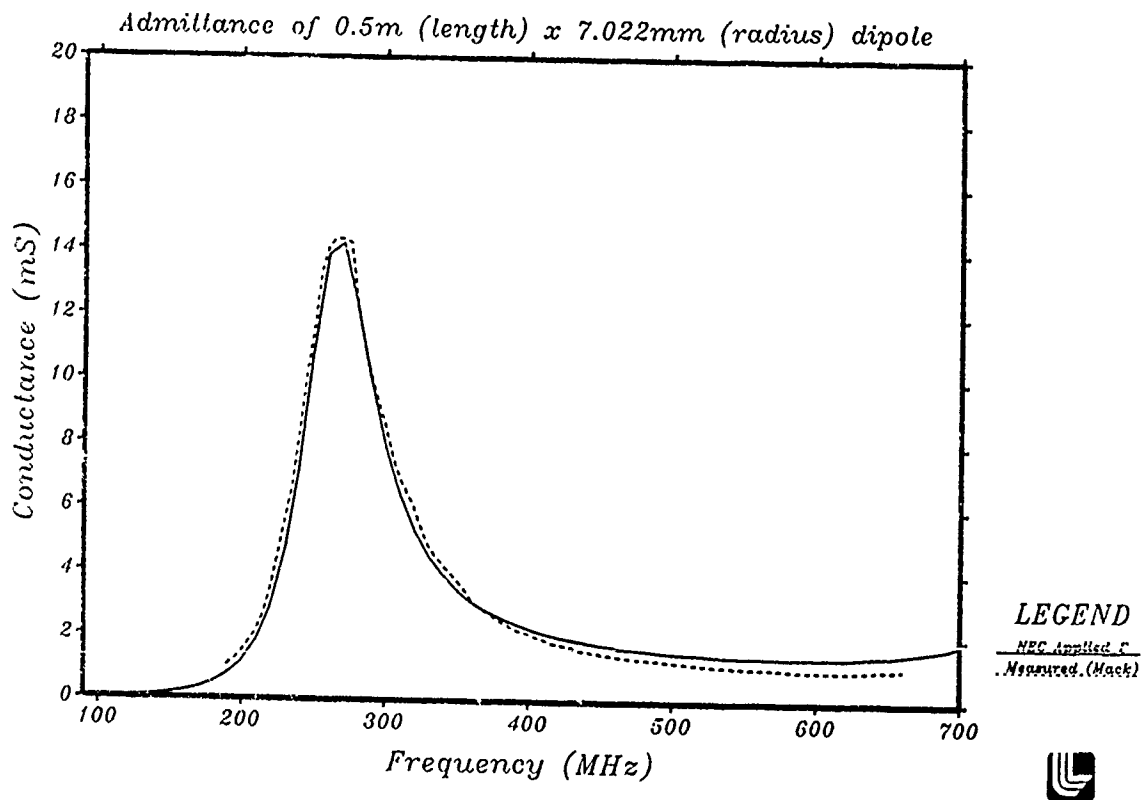


Figure 4b. NEC Applied E-field comparison

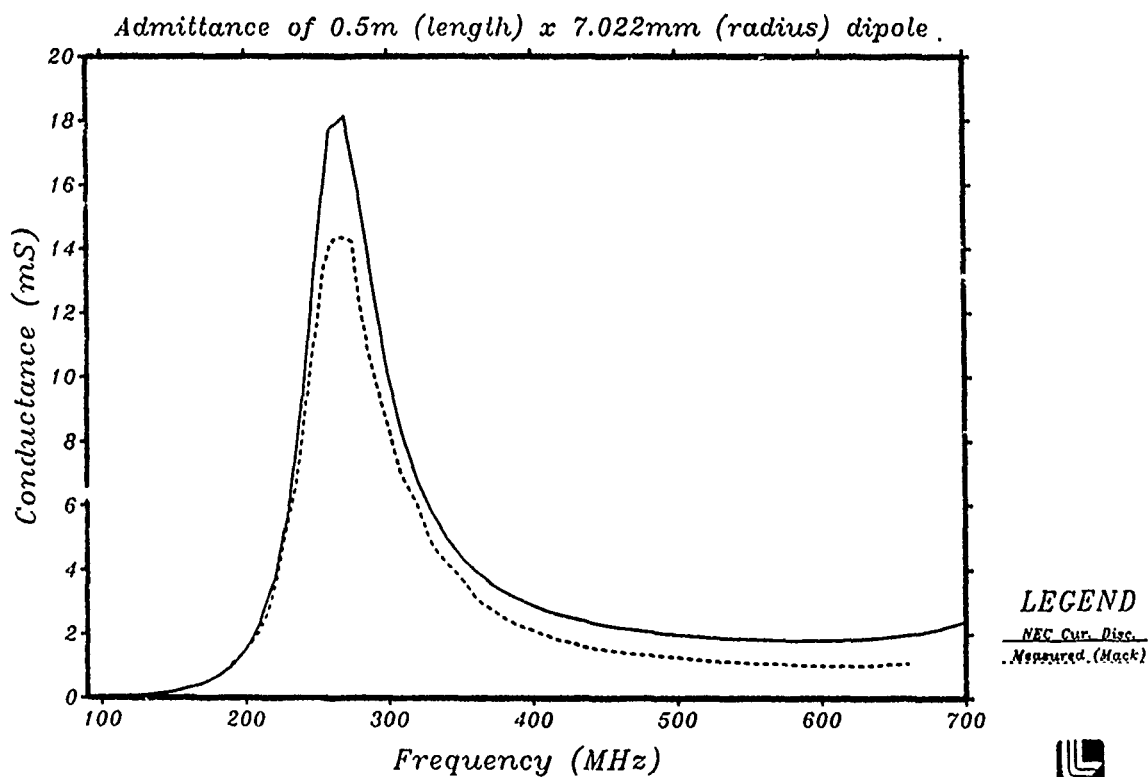


Figure 4c. NEC Current Discontinuity comparison

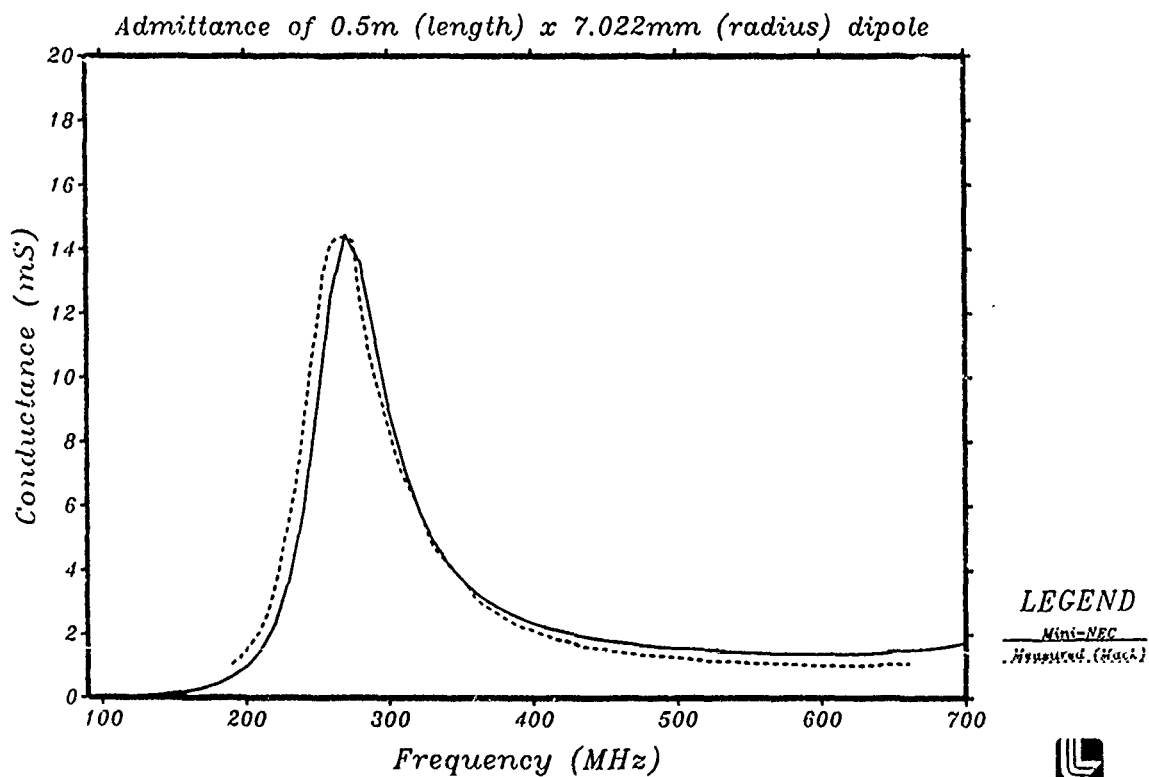


Figure 4d. Mini-NEC comparison

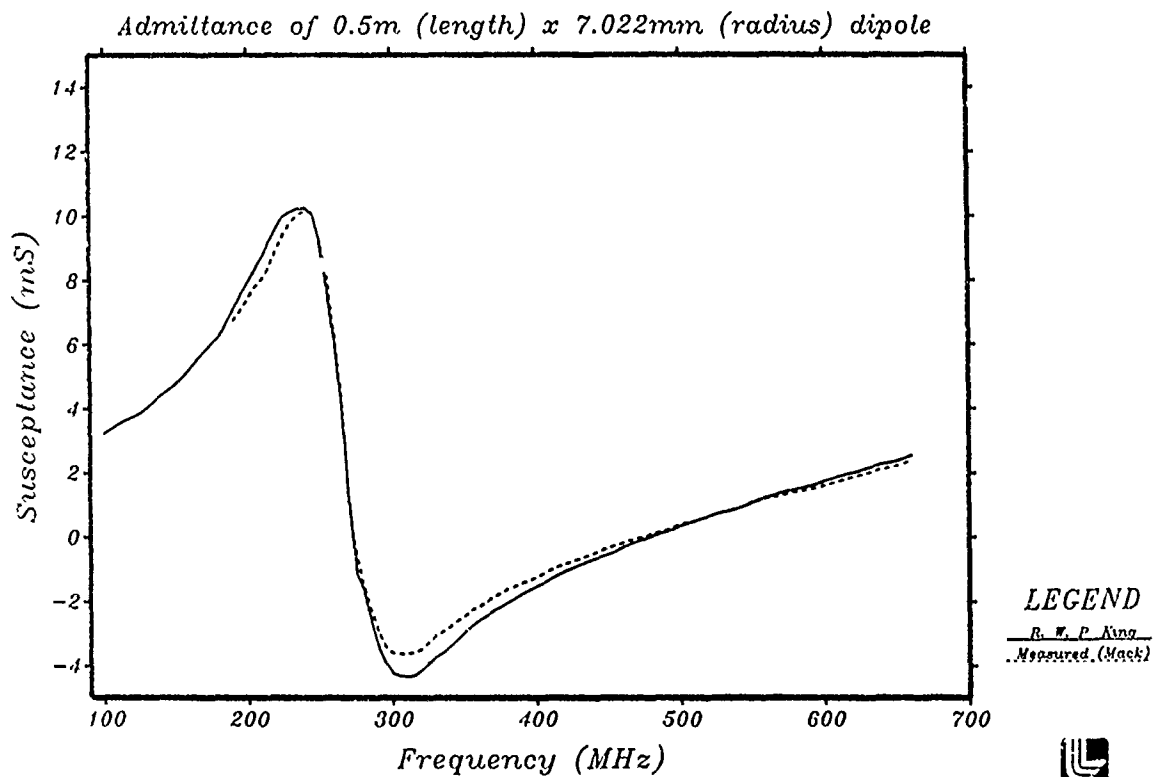


Figure 5a. R. W. P. King comparison

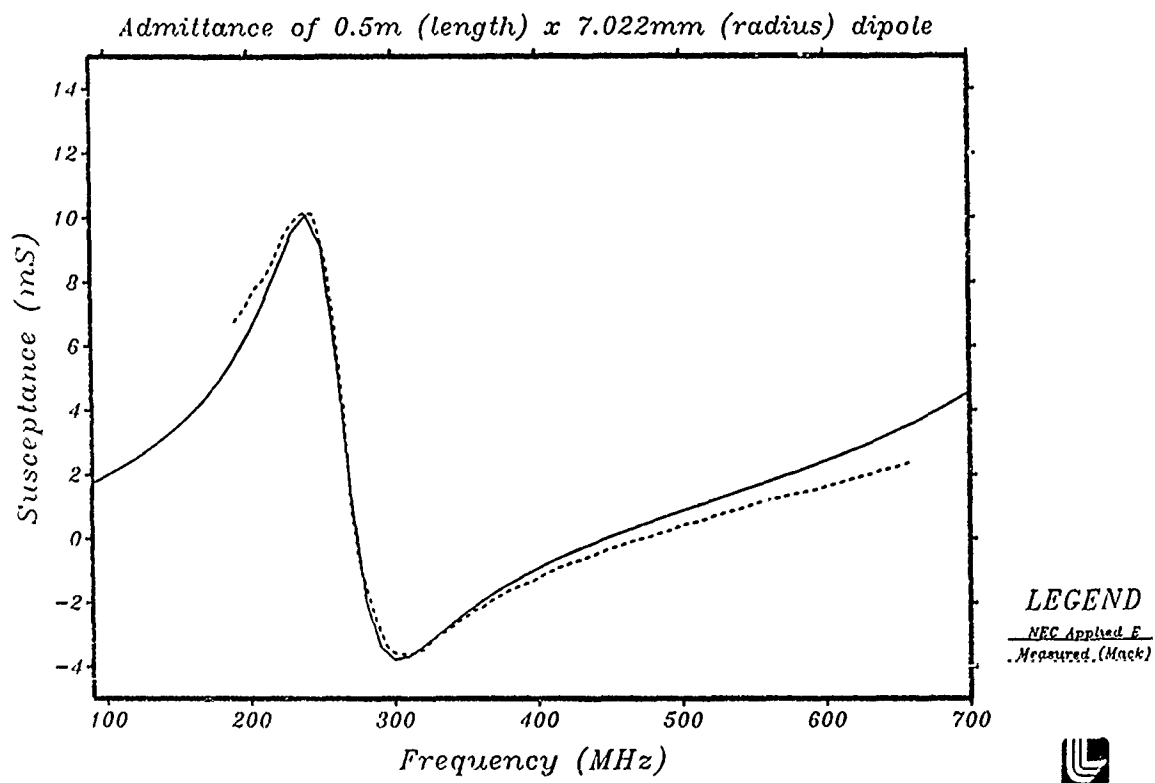


Figure 5b. NEC Applied E-field comparison

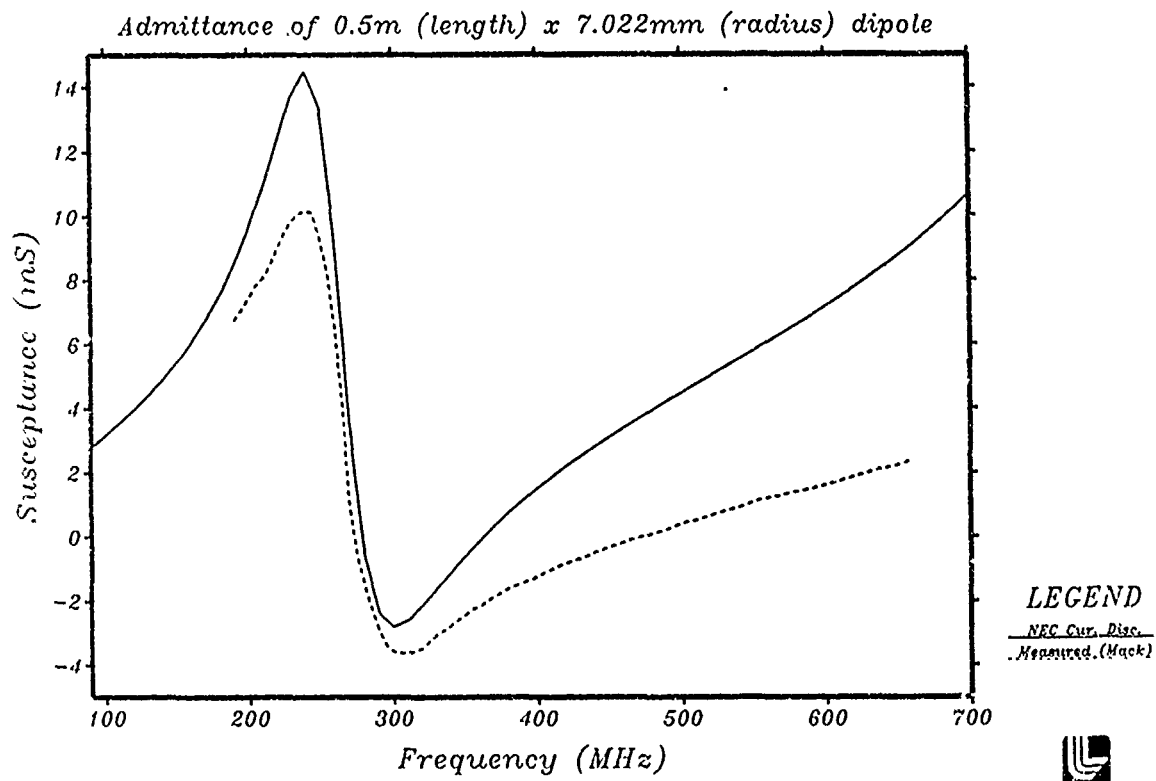


Figure 5c. NEC Current Discontinuity comparison

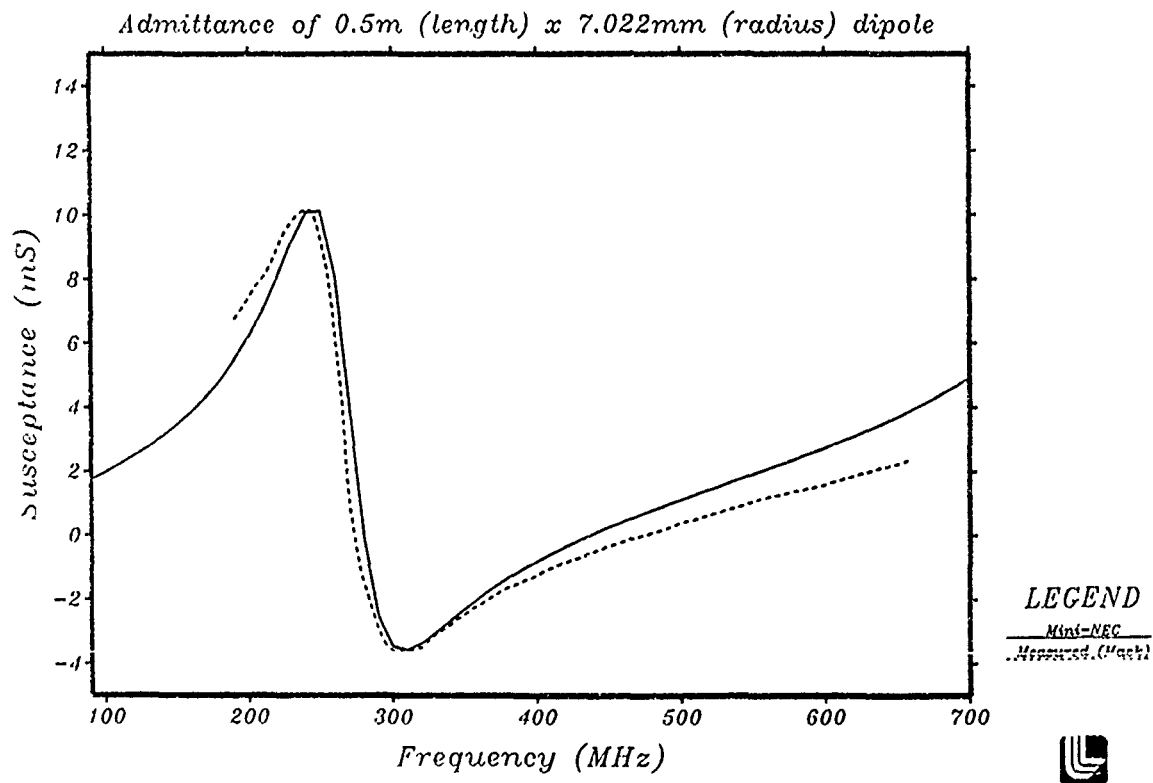


Figure 5d. Mini-NEC comparison

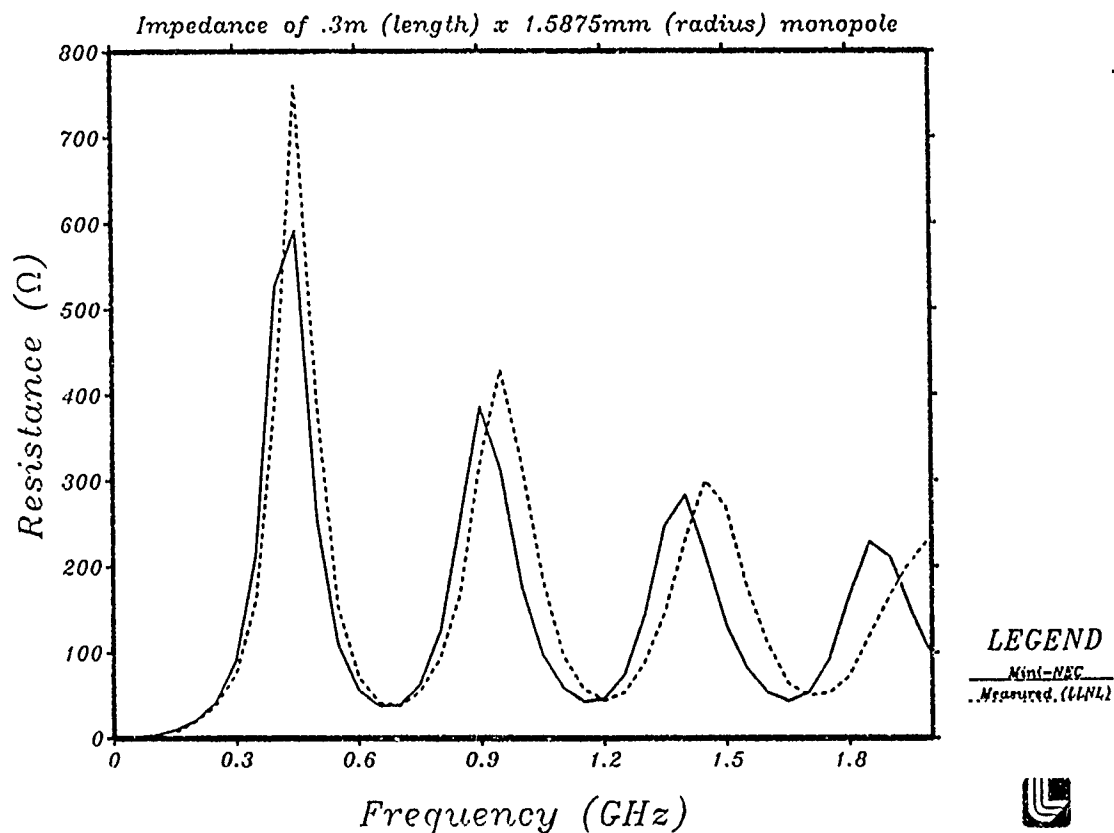


Figure 7b. Mini-NEC comparison

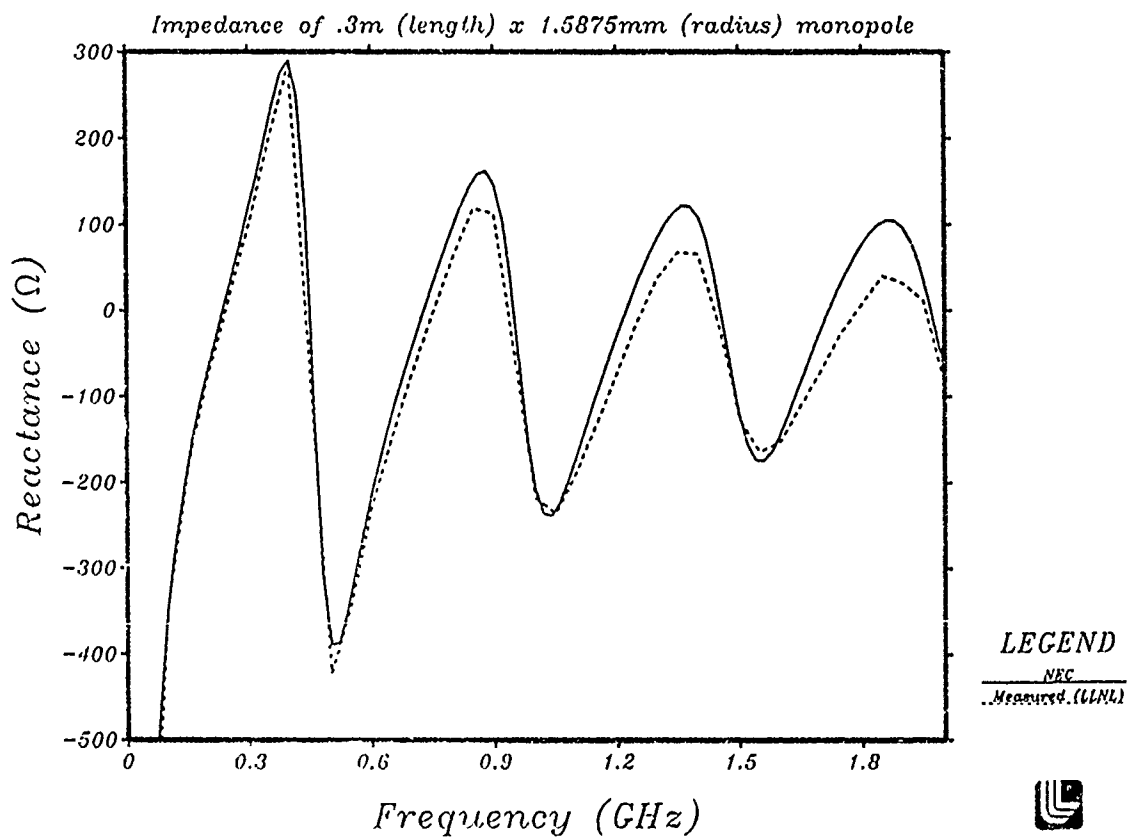


Figure 8a. NEC Applied E-field comparison

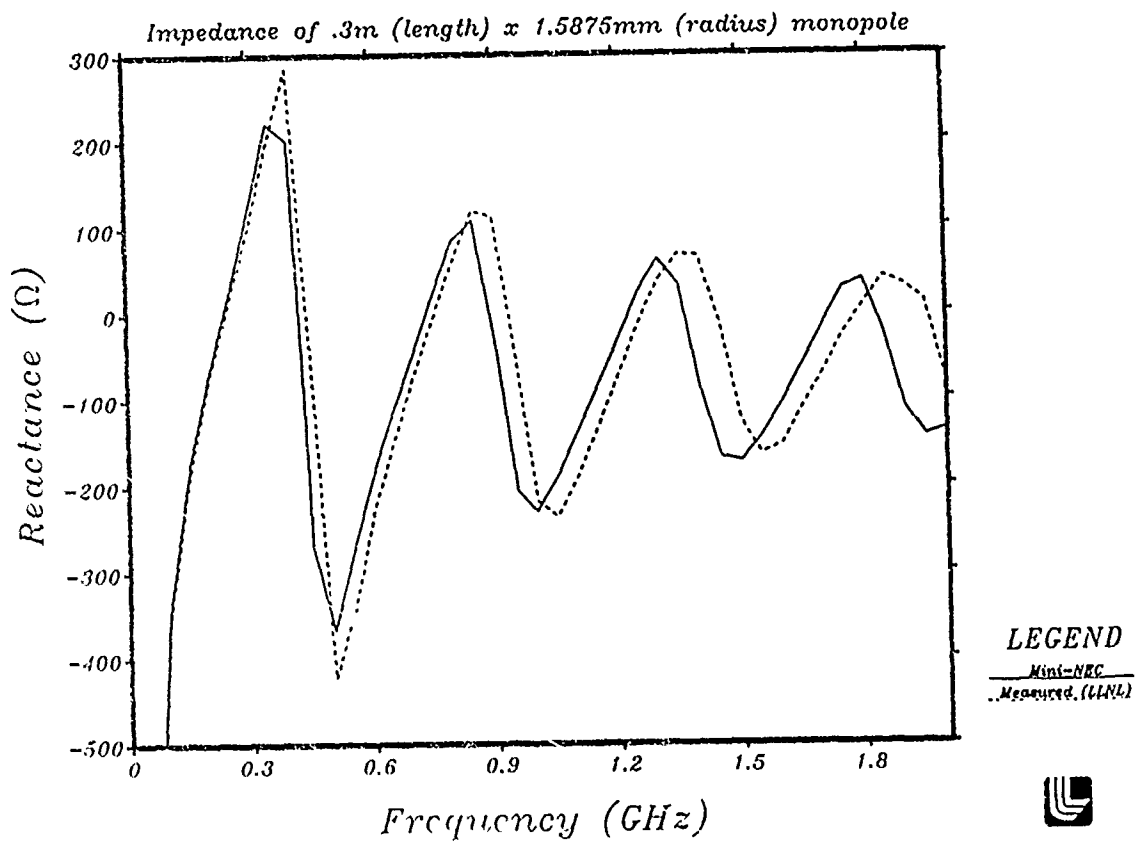


Figure 8b. Mini-NEC comparison

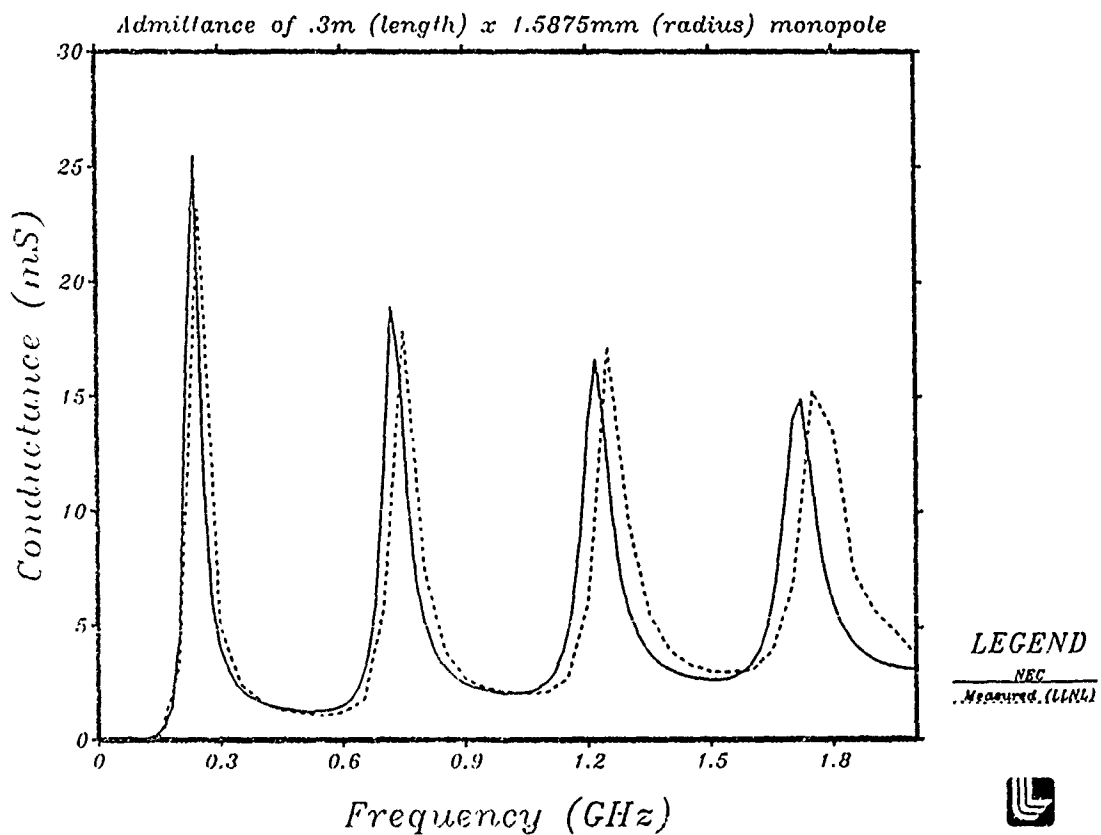


Figure 9a. NEC Applied E-field comparison

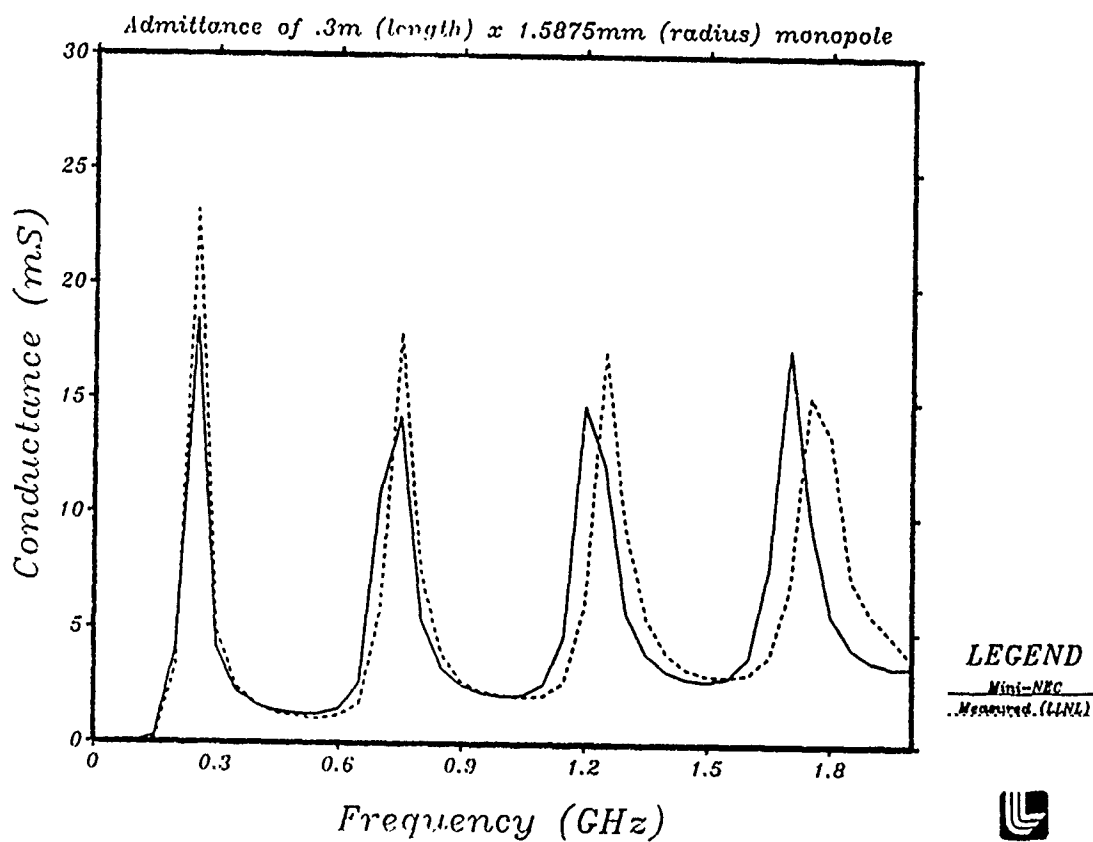


Figure 9b. Mini-NEC comparison

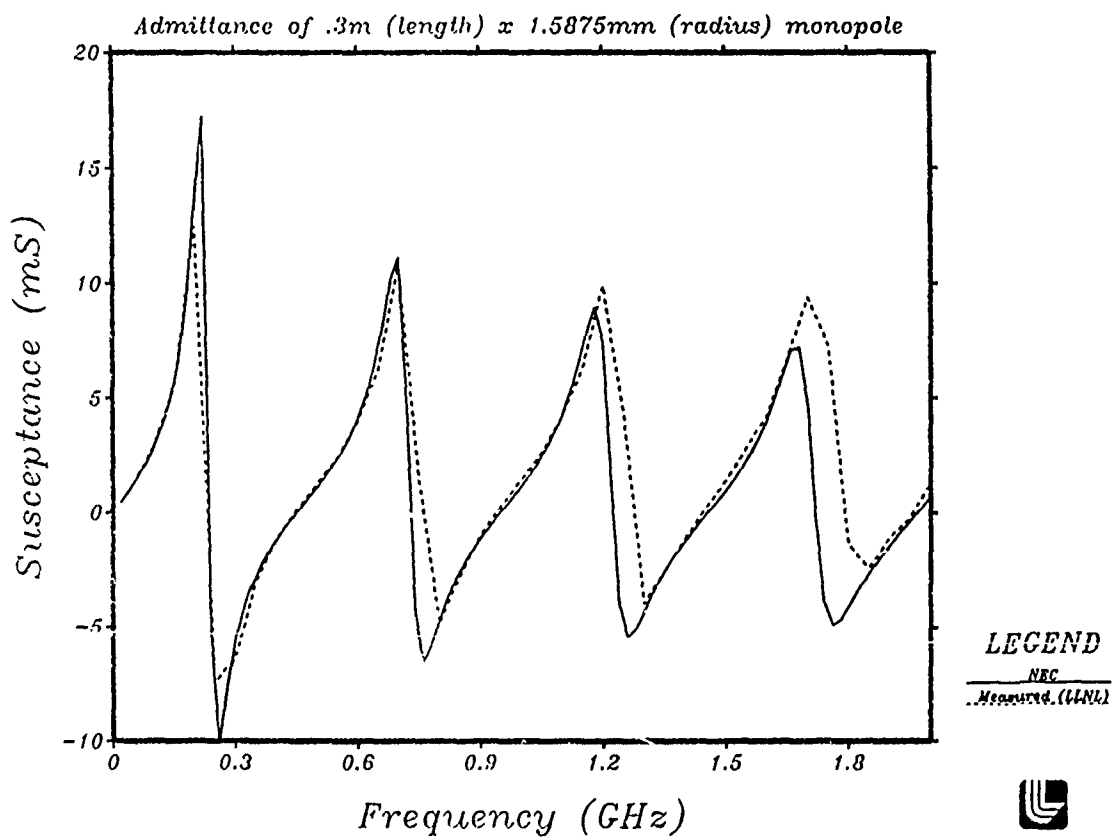


Figure 10a. NEC Applied E-field comparison

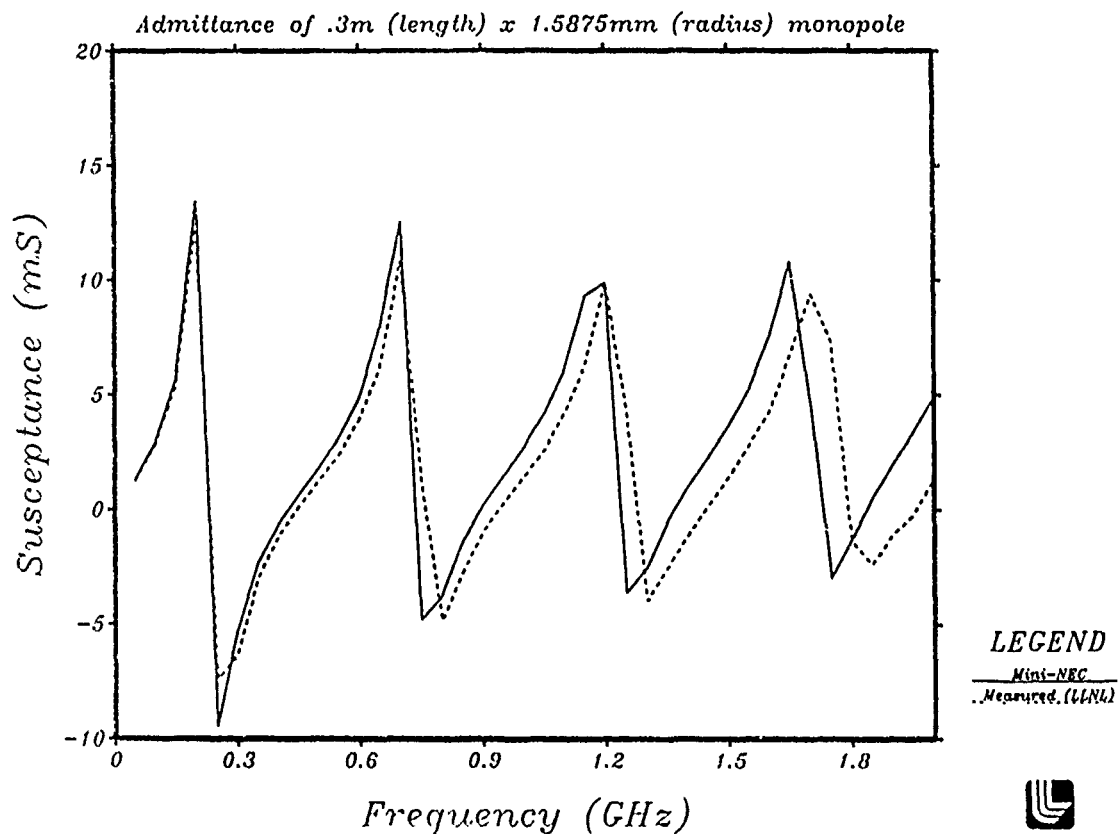


Figure 10b. Mini-NEC comparison

Comparison of NEC, EMPEROR, BEAMS

22.5cm Monopole, 45MHz to 18 GHz

VL(f)-50 Ohms/Einc(f) Spherical Wave
Conductivity and Permeability Modeled

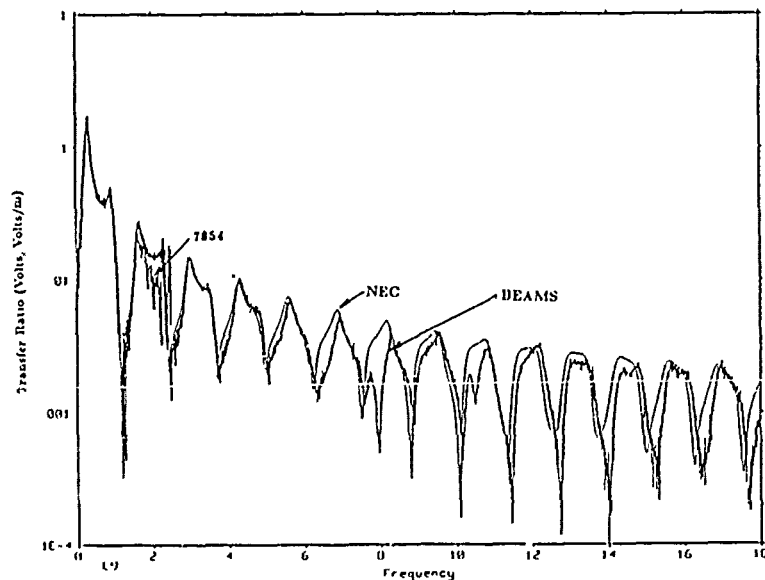


Figure 11. NEC, EMPEROR, and BEAMS comparison

3 Element Yagi

NEC (solid)



NBS - Measured (points)

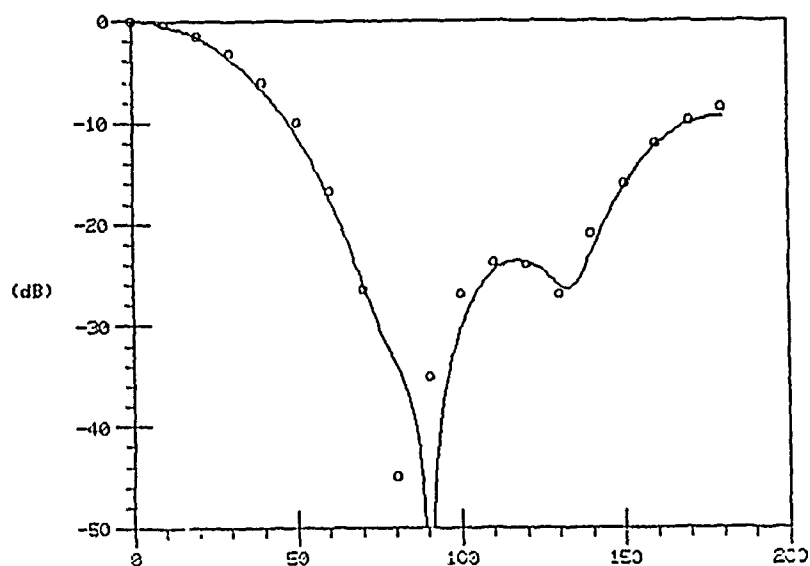


Figure 12. NEC Yagi Azimuth Pattern

3 Element Yagi

MININEC (solid), Freq = 299.8 MHz



NBS - Measured (points)

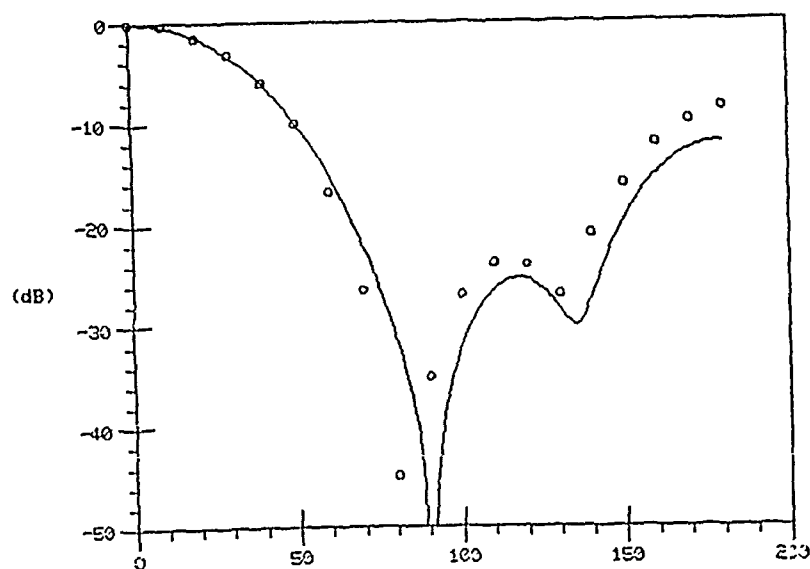


Figure 13. Mini-NEC Yagi Azimuth Pattern

5 Element Yagi

NEC (solid)



NBS - Measured (points)

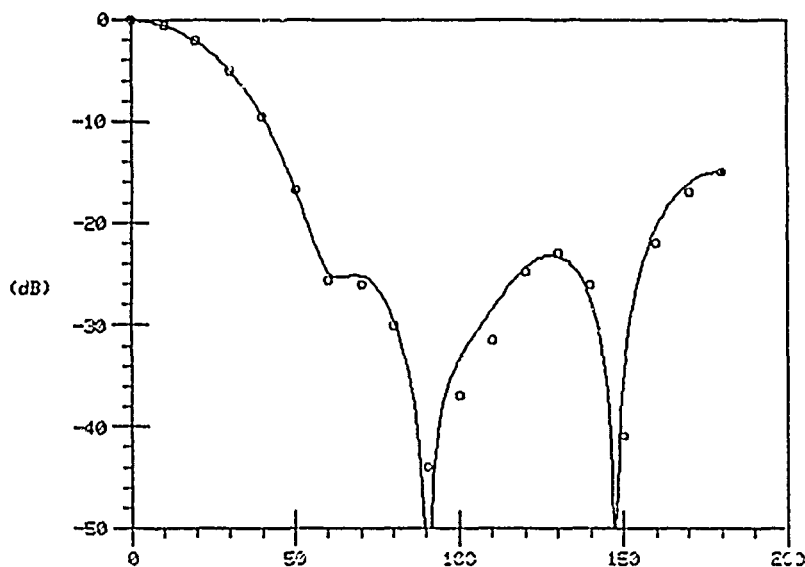


Figure 14. NEC Yagi Azimuth Pattern

5 Element Yagi

MININEC (solid), Freq = 299.8 MHz



NBS - Measured (points)

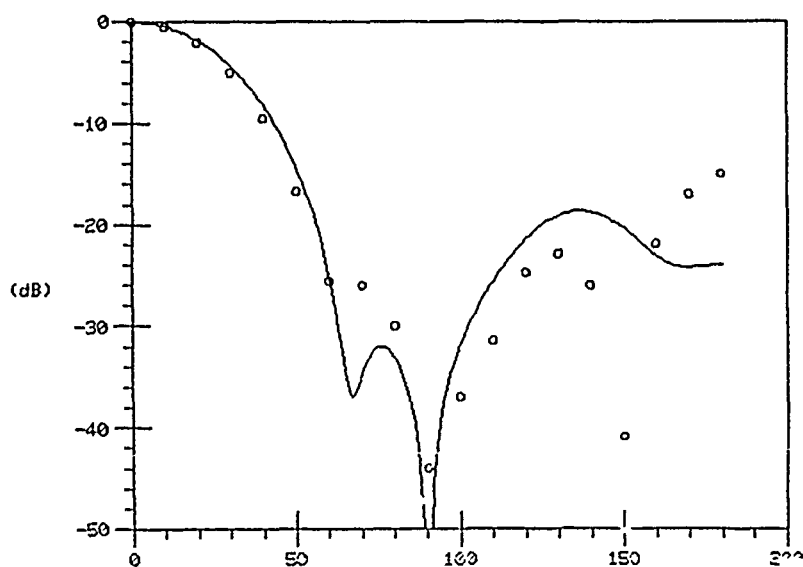


Figure 15. Mini-NEC Yagi Azimuth Pattern

3 Element Yagi

MININEC (solid), Freq = 305 MHz



NBS - Measured (points)

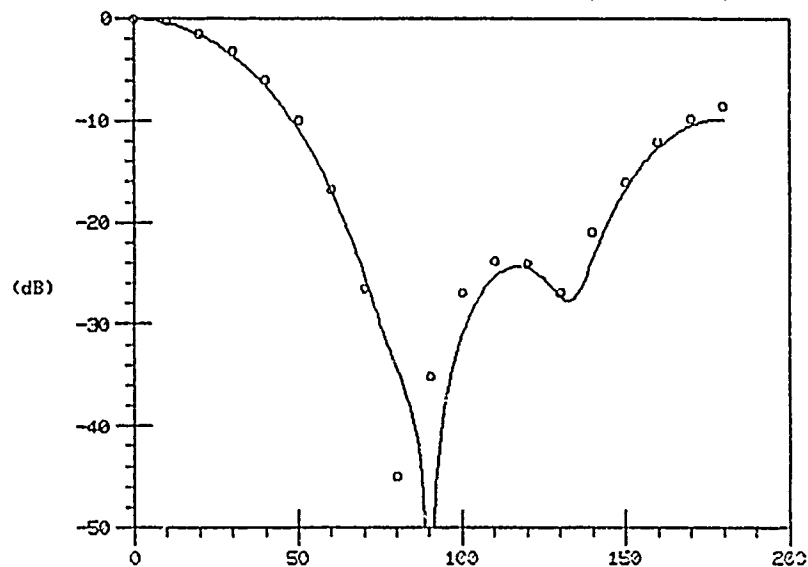


Figure 16. Mini-NEC Yagi Azimuth Pattern

5 Element Yagi

MININEC (solid), Freq = 305 MHz



NBS - Measured (points)

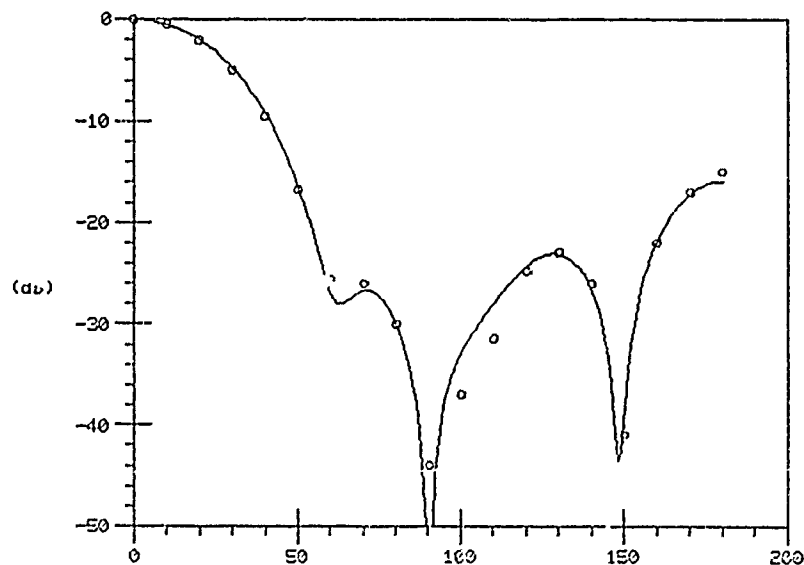


Figure 17. Mini-NEC Yagi Azimuth Pattern

USE OF IMPEDANCE PLOTS TO CHECK VALIDITY OF NEC MODELS

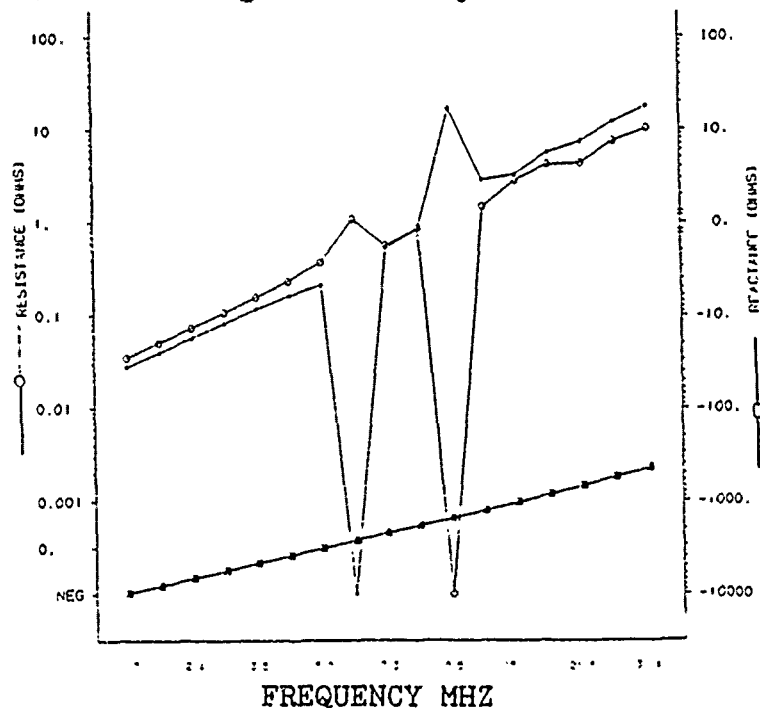
Don Rucker, Hang Lai, Helen Kwei
ESL ms205
495 Java Dr.
Sunnyvale Ca. 94086

It is usually desirable to design NEC wire grid models so that the widest possible bandwidth is useable. An impedance plot of a simple antenna on the model is a useful tool for both model building and for verification of models that have been developed. One can calculate the impedance of a linear monopole perpendicular to a ground plane using formulas such as equation 3-1 in (Jasik "Antenna Engineering Handbook" Mc Graw Hill. 1961). This data can be compared to a similar monopole attached to the model in locations where antennas to be evaluated will be placed.

For the case studied here impedance plots show the effect of the following modeling considerations:

- * using or not using double precision on the IBM 3083
- * the number of wires to used near the antenna,
- * number of sides on a solid body,
- * connectivity at wire junctions.

This typical impedance plot shows the effect of a segment not ending at a wire junction.



USE OF IMPEDANCE PLOTS TO CHECK VALIDITY OF
NEC MODELS

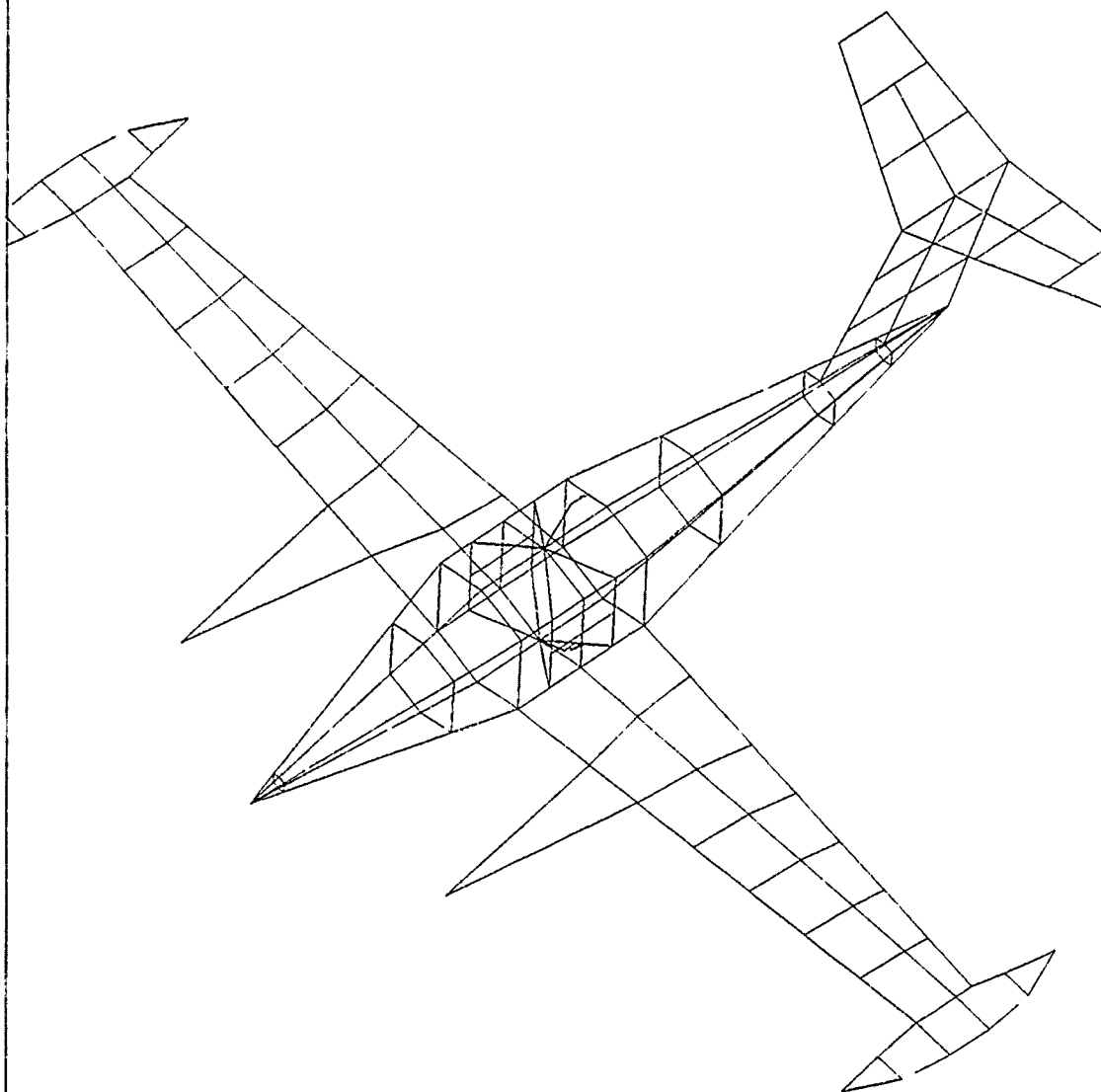
Don Rucker, Dr. Hang Lai, Helen Kwei
ESL ms205
495 Java Dr.
Sunnyvale Ca. 94086
Mar. 19, 1986

VIEW
GRAPH
#

SUBJECT

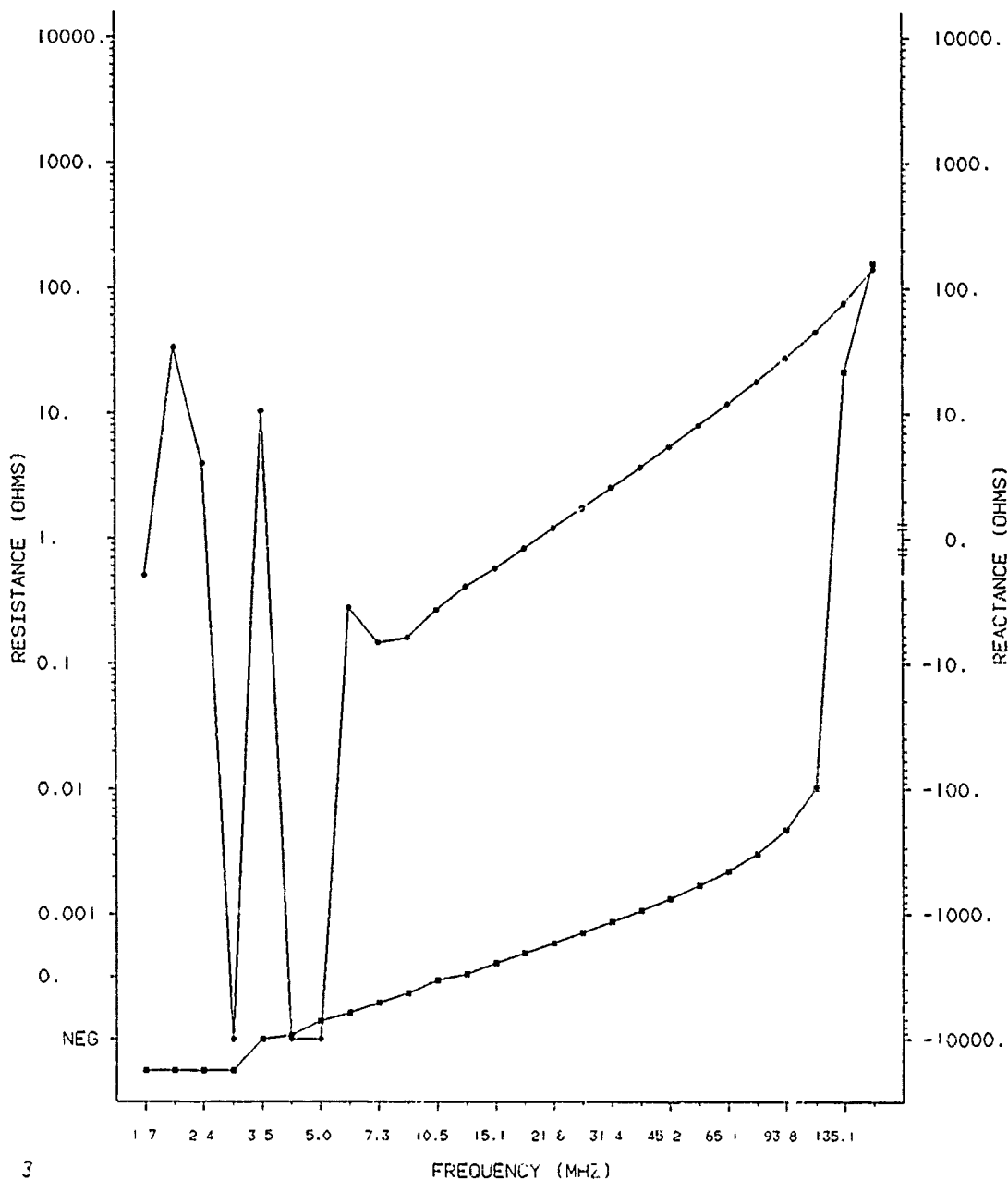
-
- 1 Title
 - 2 Aircraft with antenna shown in yellow, final model
 - 3 Dipole plot, single precision
 - 4 Dipole drawing
 - 5 Dipole plot, double precision, C.T. Tai's result shown in red
 - 6 Monopole plot w/ 3, 7" segments "
 - 7 Earlier monopole plot w/ error in GE card
 - 8 Monopole plot w/ 21, 1" segments "
 - 9 Aircraft center section drawing
 - 10 Impedance plot comparison to monopole
 - 11 Aircraft center section drawing, w/ transmission line feed
 - 12 Impedance plot w/ transmission line feed shows problem
 - 13 Impedance plot over ground free space comparison
 - 14 Aircraft center section drawing, 8 sided model
 - 15 Aircraft center section 8 sided model impedance plot
 - 16 Aircraft fuselage drawing
 - 17 Aircraft fuselage impedance plot compared to monopole
 - 18 Whole aircraft drawing
 - 19 Whole aircraft impedance plot shows problem
 - 20 Aircraft without tail impedance plot problem changed
 - 21 Aircraft without tail drawing with errors
 - 22 Whole aircraft impedance plot corrected
 - 23 summary and comments

SK-HHK888, -, 543: WHOLE AIRPLANE.
GOOD MODEL.



SK-H-K888 - 549
 DIPOL SK-H-K888-547. BAD RUN (SINGLE PRECISION RUN).
 FREE SPACE IMPEDANCE VOLTAGE SOURCE AT DIPOLE CENTER.

—●— RESISTANCE, TAG 1 SEG 4
 —●— REACTANCE, TAG 1 SEG 4

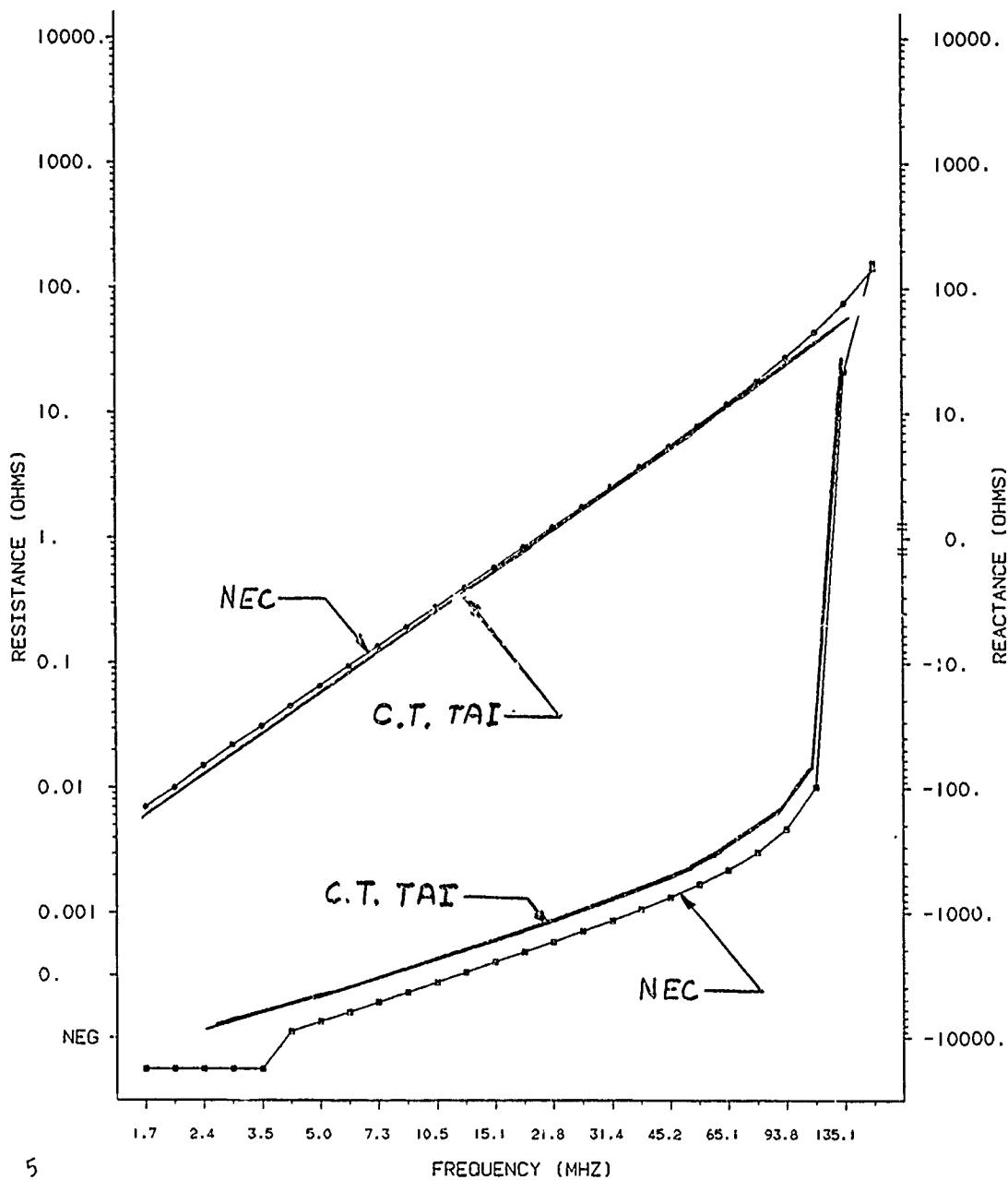


SK-HHK888,-,547: DIPOLE.



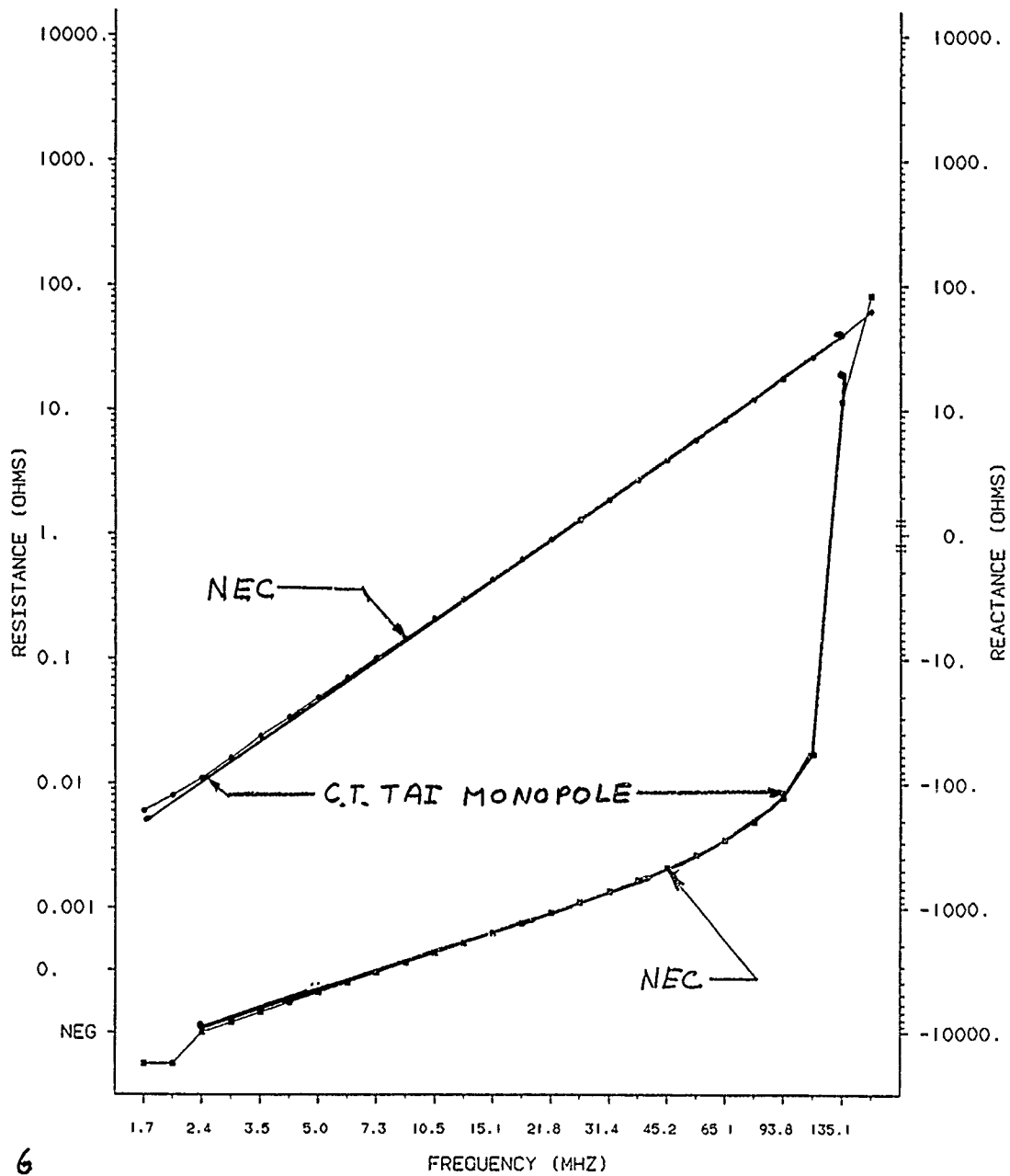
SK-HK888 - 548
 DIPOL SK-HK888-547: GOOD RUN (DOUBLE PRECISION RUN).
 FREE SPACE IMPEDANCE. VOLTAGE SOURCE AT DIPOLE CENTER.

—●— RESISTANCE, TAG 1 SEG 4
 —●— REACTANCE, TAG 1 SEG 4



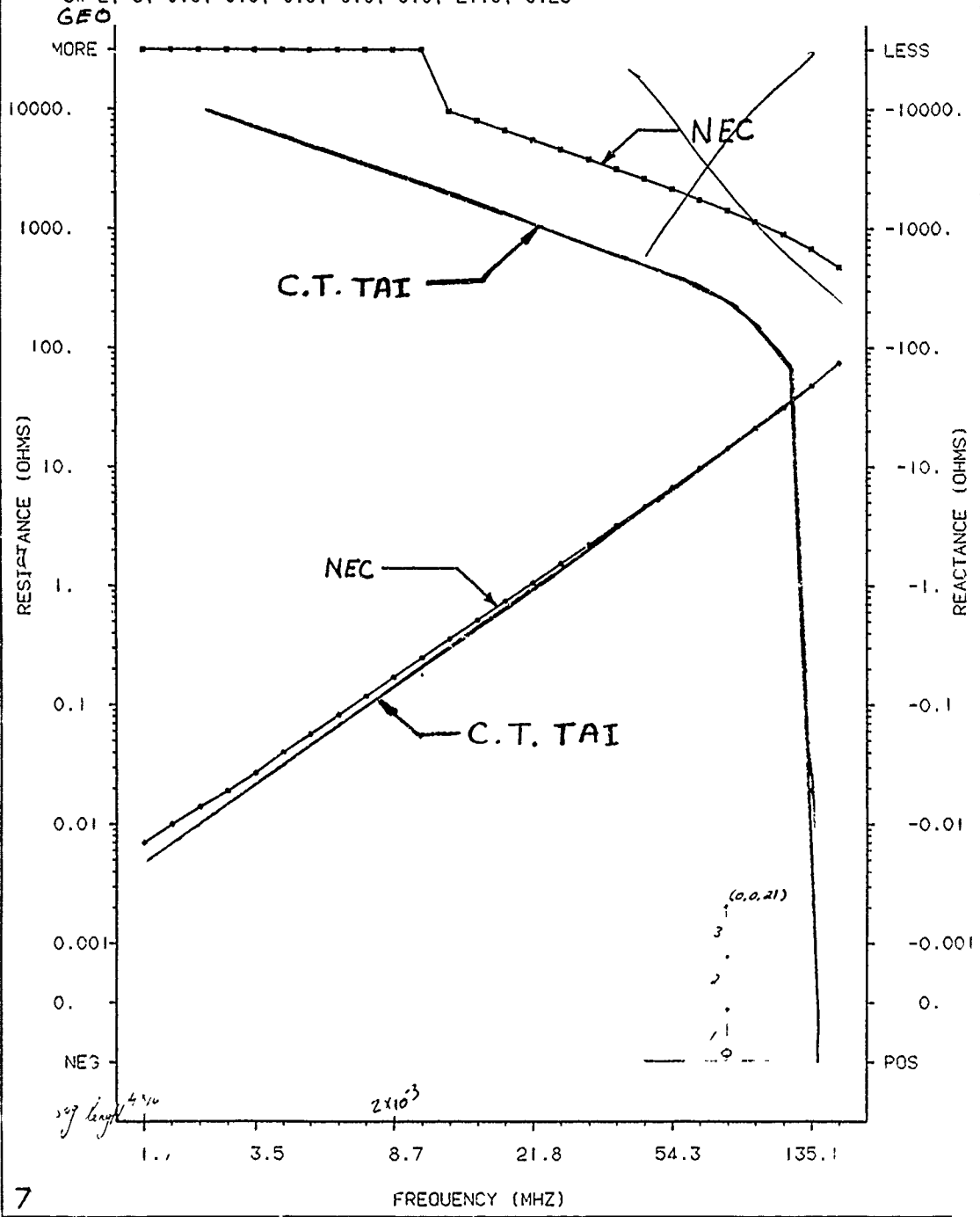
SK-HK888 - 552
 MONOPOLE: PERFECT GROUND, 7 INCHES PER SEGMENT
 GW 1. 3. 0.. 0.. 0.. 0.. 0.. 21.. 0.25

—●— RESISTANCE, TAG | SEG |
 —●— REACTANCE, TAG | SEG |



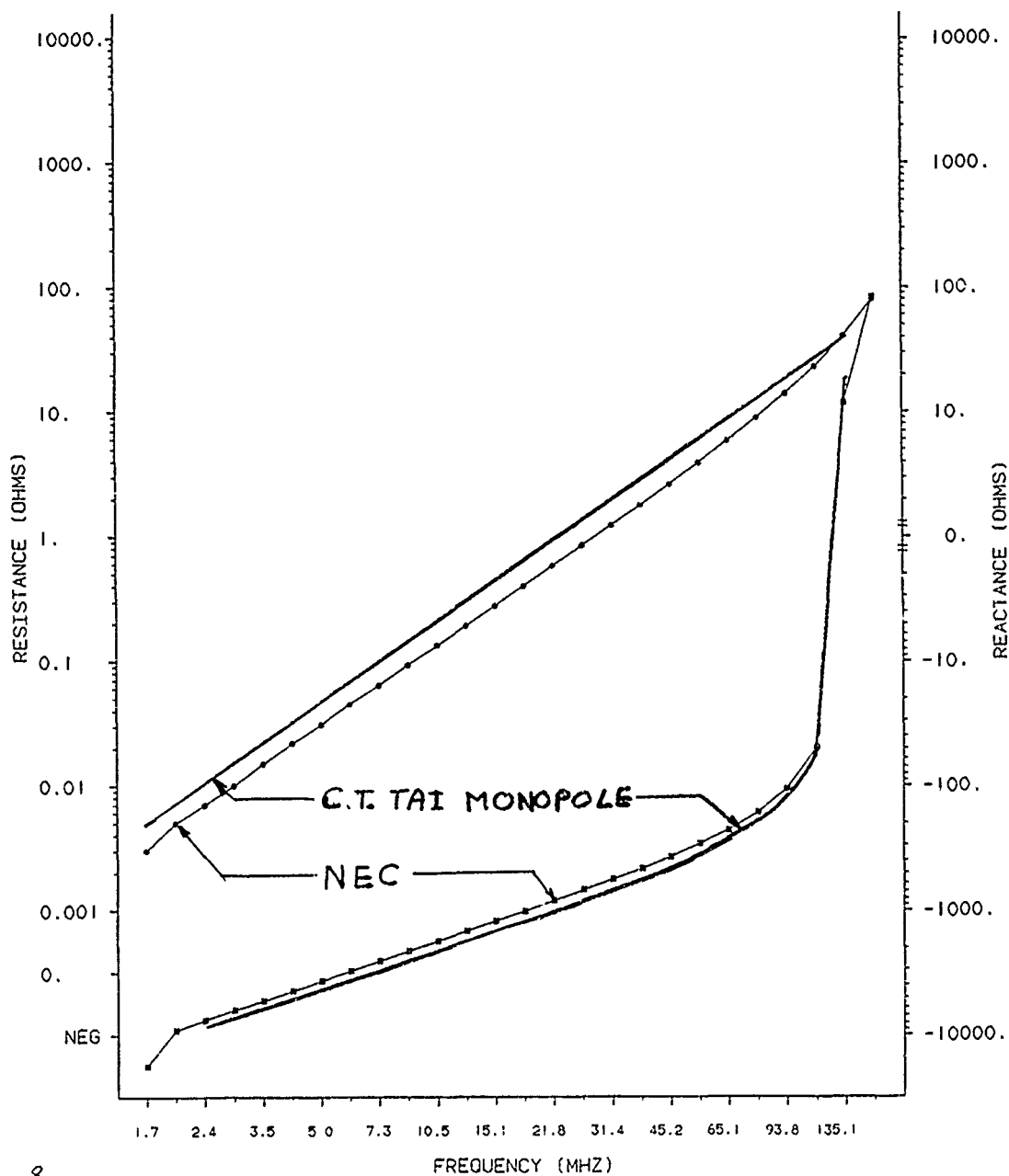
SK-HHK888,-,1
 MONOPOLE: GEOMETRY IN INCHES
 PERFECT GROUND WITH ERROR
 GW 2, 3, 0.0, 0.0, 0.0, 0.0, 0.0, 21.0, 0.25

— RESISTANCE, TAG 2 SEG 1
 — REACTANCE, TAG 2 SEG 1

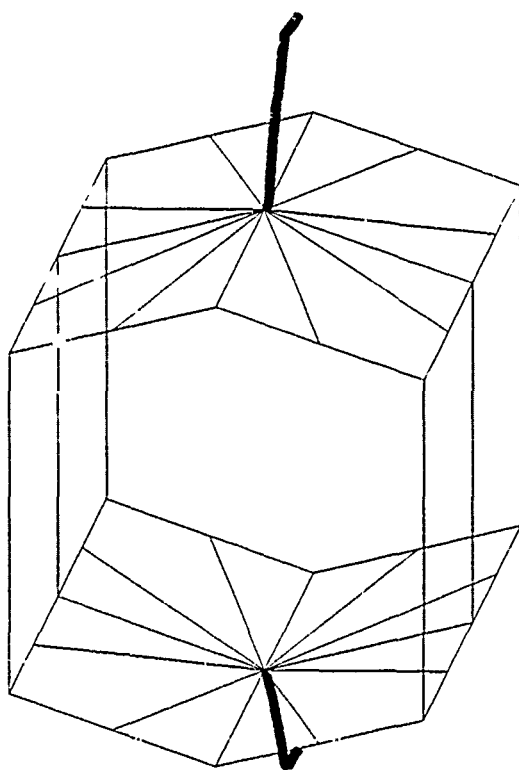


SK-HK888 - 557
 MONOPOLE: PERFECT GROUND, 1 INCH PER SEGMENT
 GW 1.21, 0., 0., 0., 0., 0., 21., 0.25

—●— RESISTANCE, TAG 1 SEG 1
 —●— REACTANCE, TAG 1 SEG 1

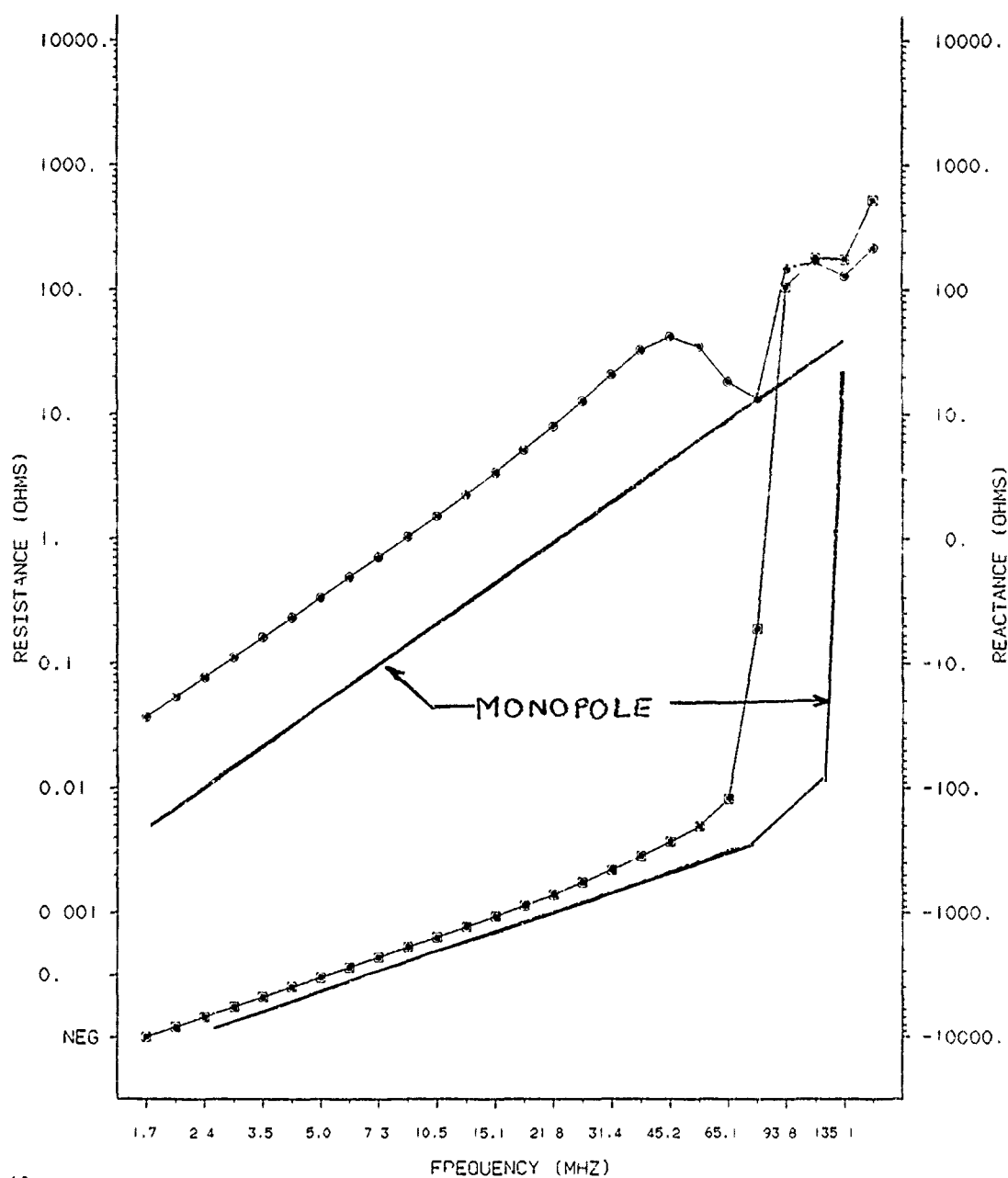


SK-HHK888,-.518: AIRPLANE CENTER.

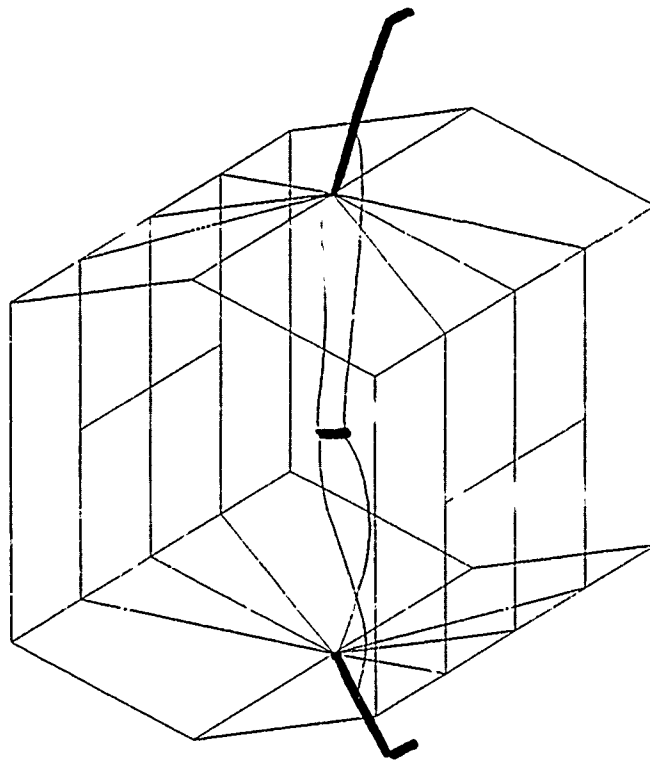


SK-HK888 - 529
 AIRPLANE CENTER SK-HK888-528: 6-SIDED FUSELAGE, 6
 EXTRA WIRES AT CENTER TOP AND BOTTOM BENT BLADES.
 8 WIRES AT BLADE JUNCTION, 10° PER SEGMENT
 FREE SPACE IMPEDANCE. VOLTAGE SOURCE AT BLADES.

—●— RESISTANCE, TAG 1 SEG 1
 —●— REACTANCE, TAG 1 SEG 1
 —○— RESISTANCE, TAG 33 SEG 1:9
 —□— REACTANCE, TAG 33 SEG 1:9

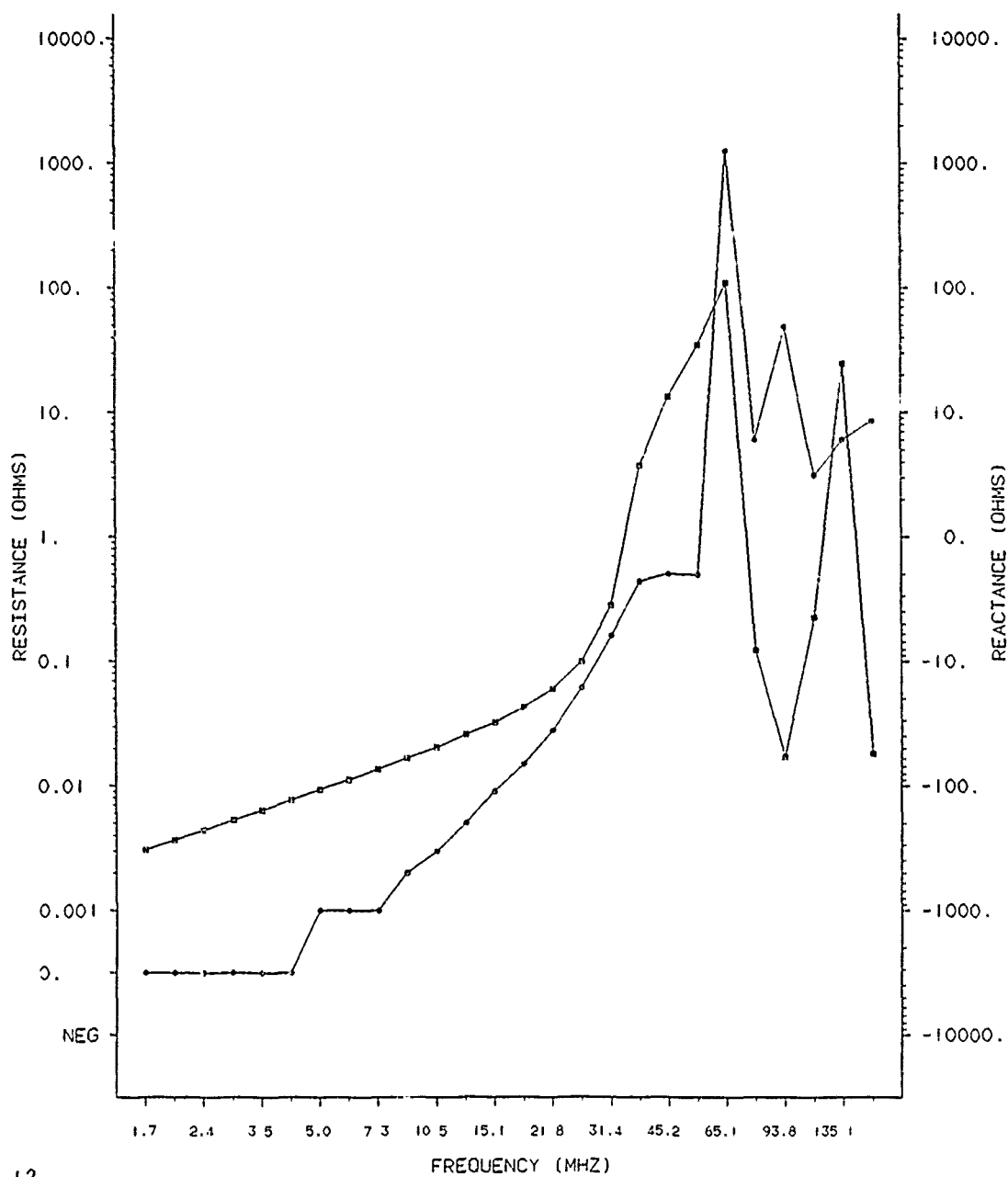


SK-HHK888, -,528: AIRPLANE CENTER.



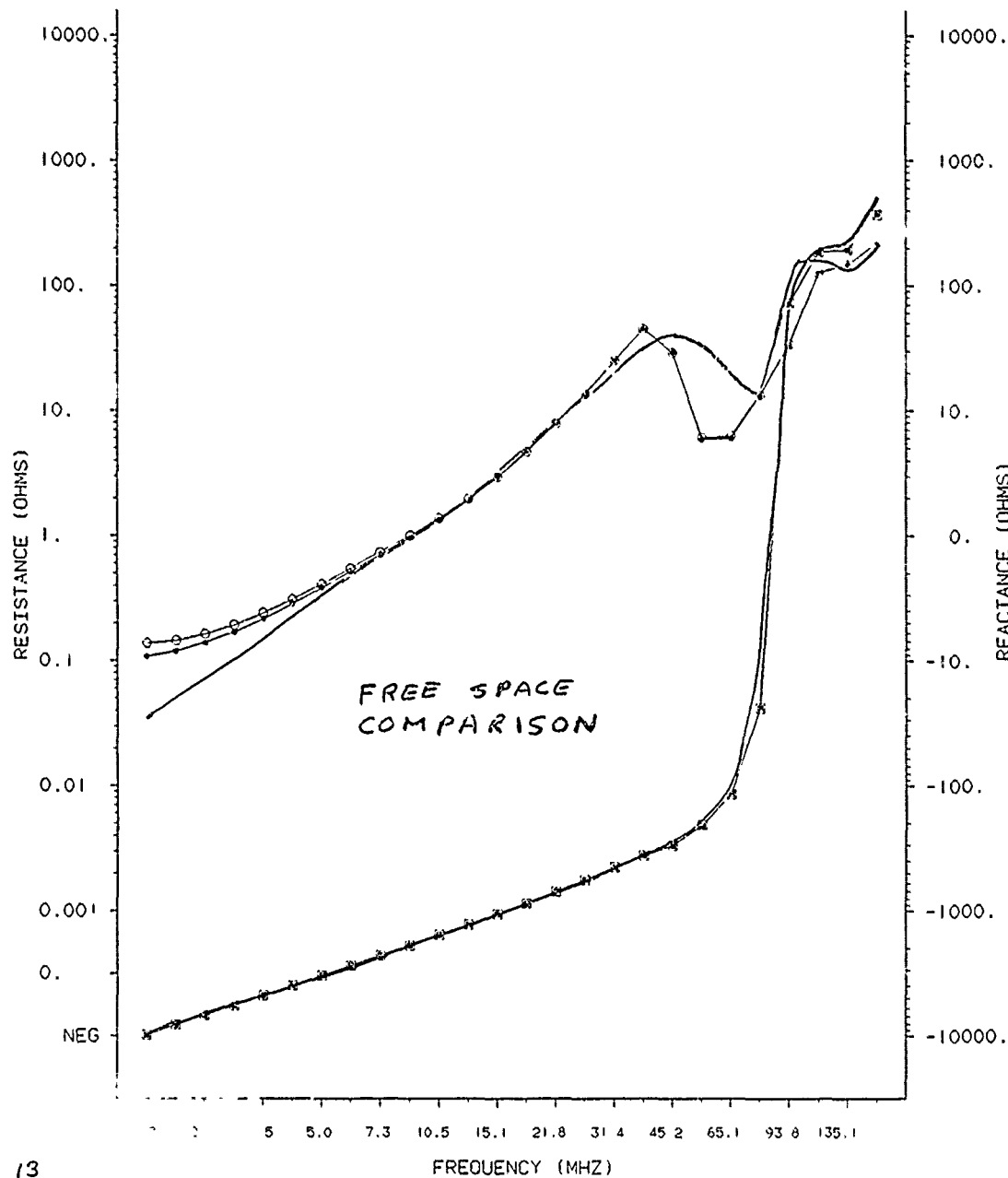
SK-HK888 - 530
 AIRPLANE CENTER SK-HK888-518: 6-SIDED FUSELAGE
 TOP AND BOTTOM BENT BLADES. 12 WIRES AT BLADE
 JUNCTION. 8" PER SEGMENT.
 FREE SPACE IMPEDANCE. TRANSMISSION LINE SOURCE.

—●— RESISTANCE, TAG 45 SEG 259
 —●— REACTANCE, TAG 45 SEG 259

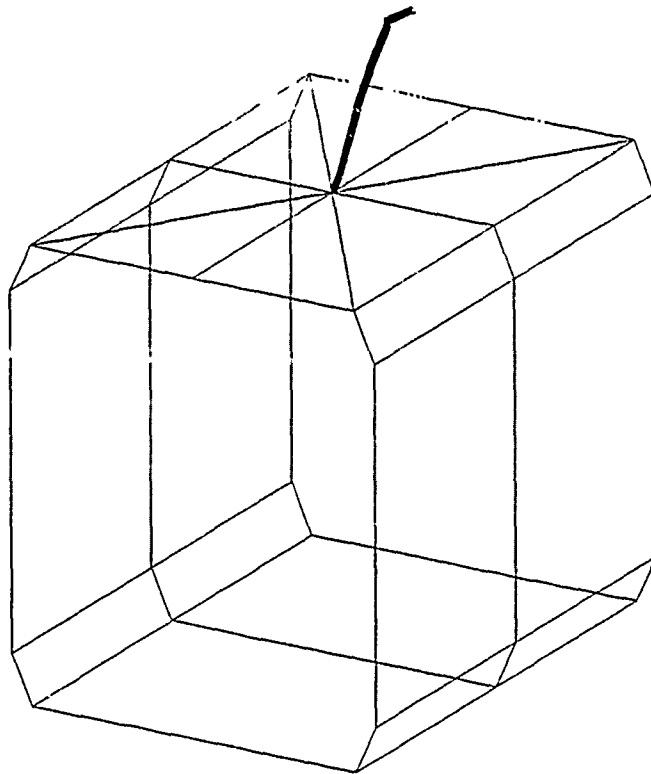


SK-HK888 - 527
 AIRPLANE CENTER SK-HK888-518: 6-SIDED FUSELAGE
 TOP AND BOTTOM BENT BLADES. 12 WIRES AT BLADE
 JUNCTION. 8" PER SEGMENT
 MODEL 30 FEET OVER PCR SOIL. VOLTAGE SOURCE AT
 BLADES.

—●—	RESISTANCE, TAG	1 SEG	1
—○—	REACTANCE, TAG	1 SEG	1
—x—	RESISTANCE, TAG	43 SEG	255
—□—	REACTANCE, TAG	43 SEG	255

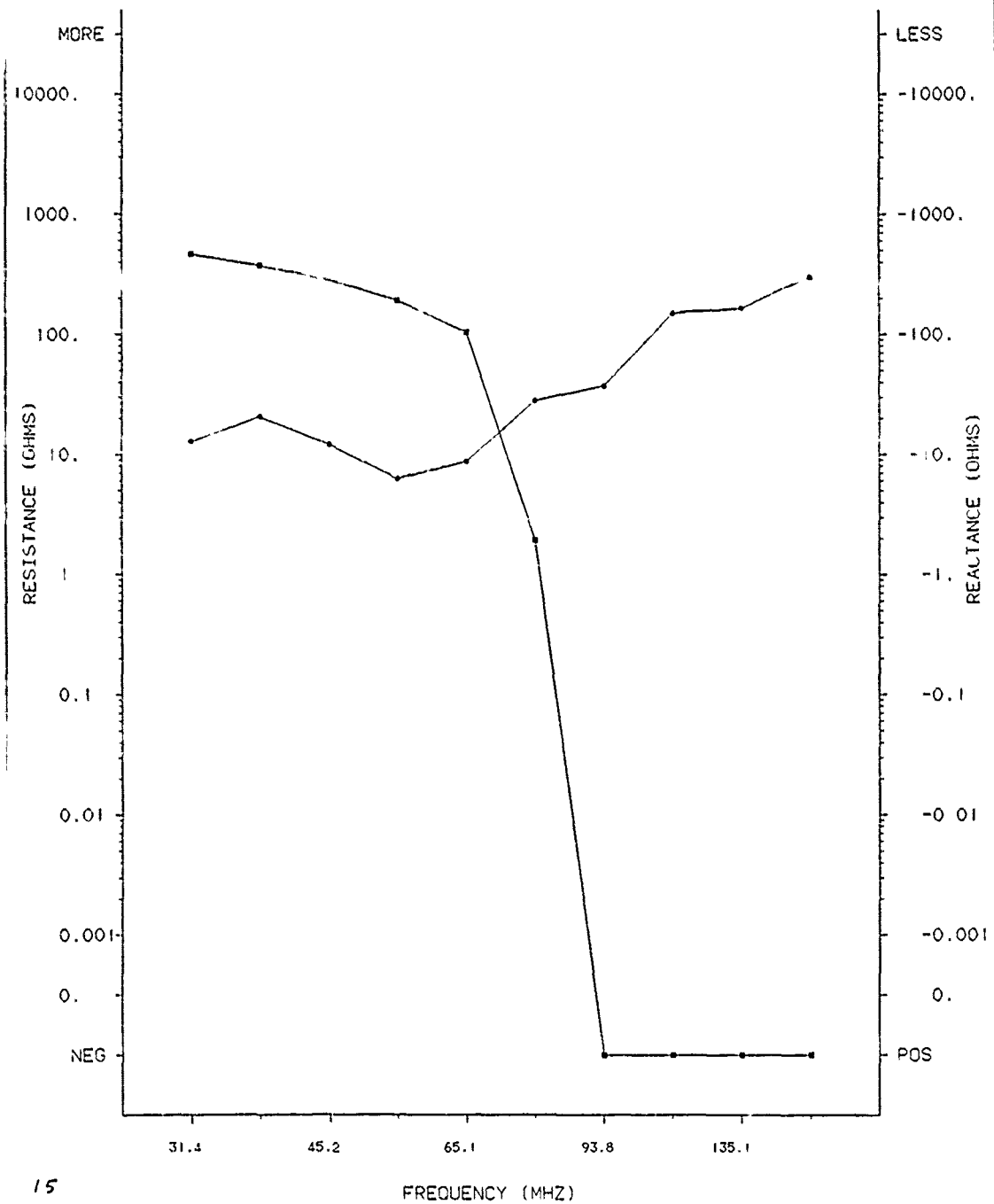


SK-HHK888,-,510: AIRPLANE CENTER.

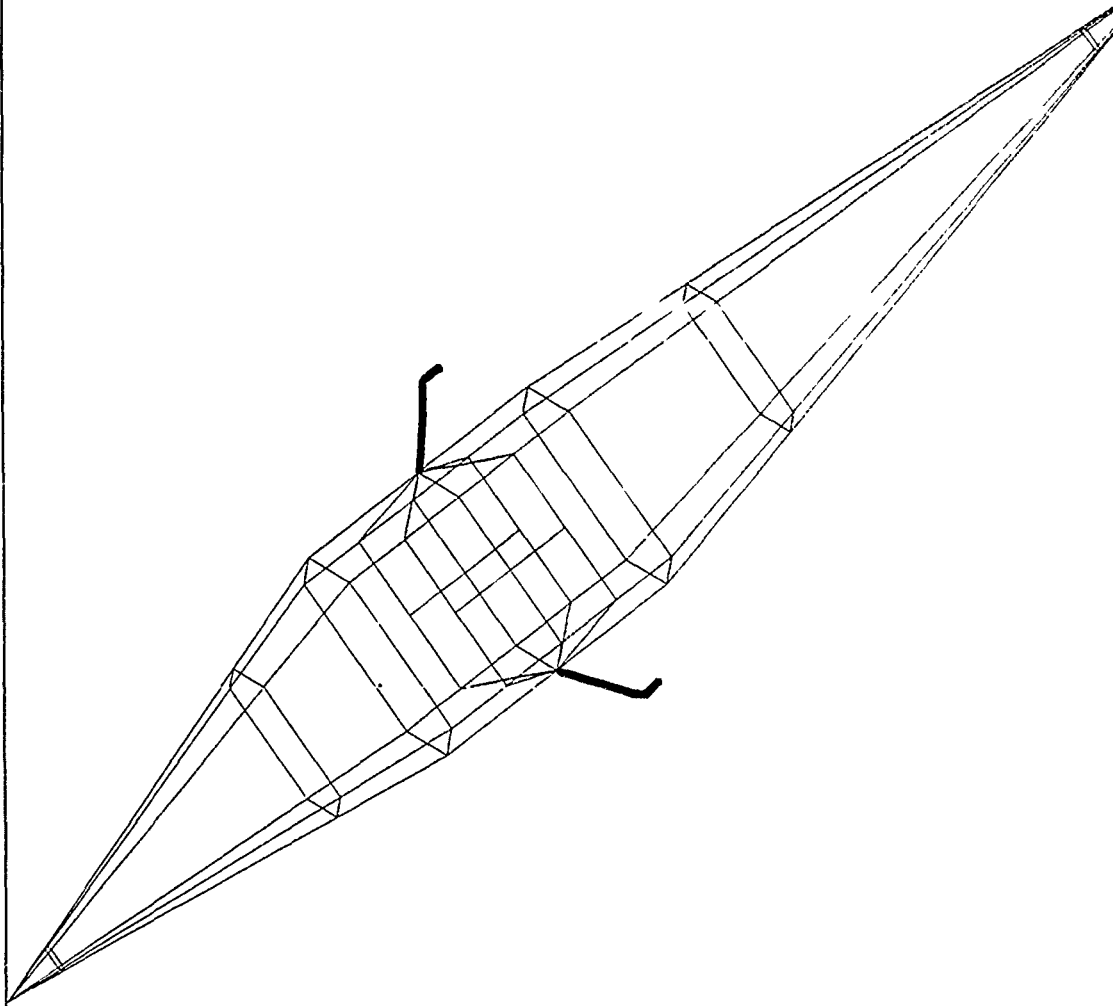


SK-HK888 - 511
 AIRPLANE CENTER SK-HK888-510: 8-SIDED, TCP BLADE.
 8 WIRES AT BLADE JUNCTION, 8" PER SEGMENT.
 FREE SPACE IMPEDANCE. VOLTAGE SOURCE AT BLADE. HIGH
 FREQUENCY RANGE.

—•— RESISTANCE, TAG 1 SEG 1
 —•— REACTANCE, TAG 1 SEG 1

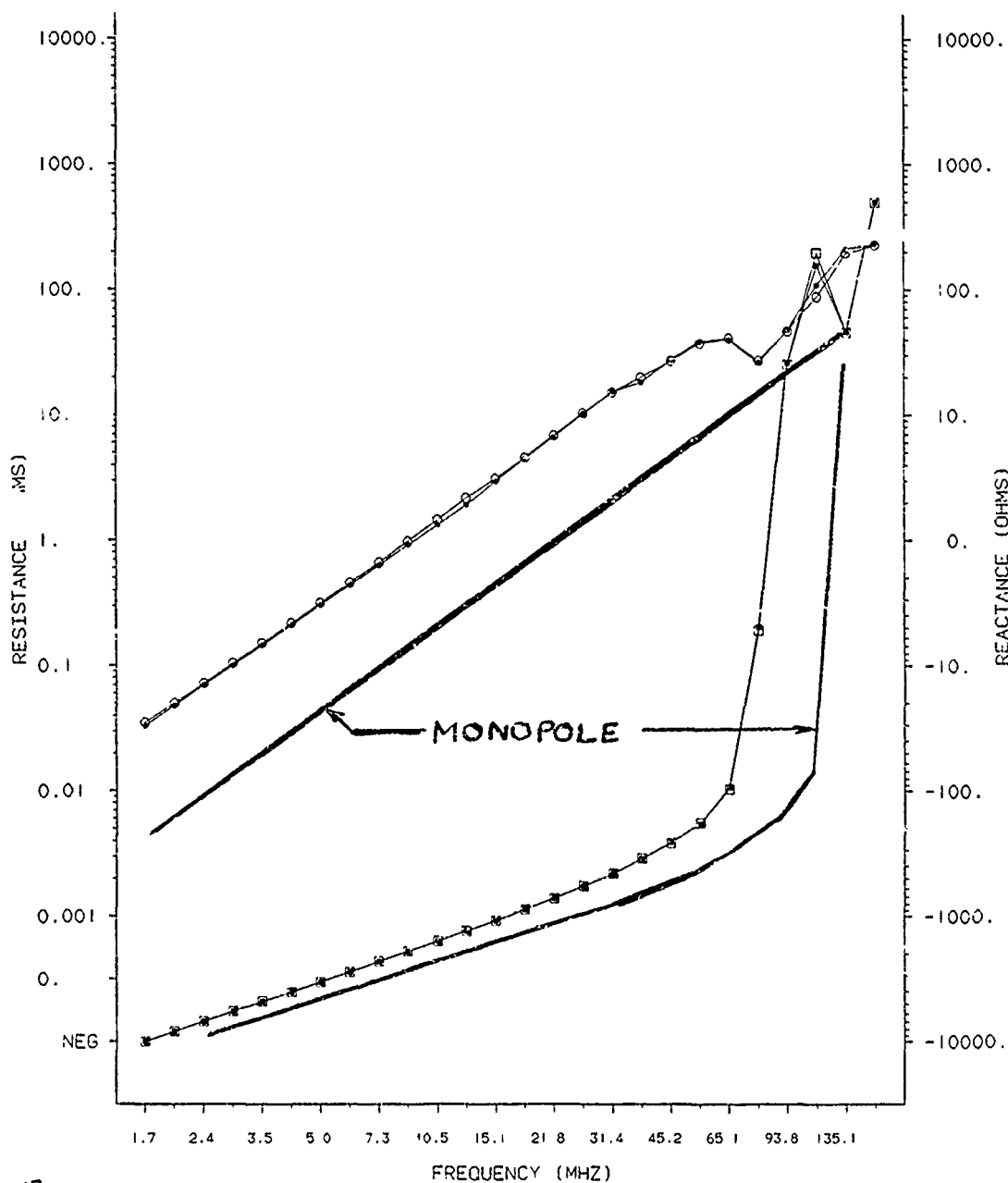


SK-HHK888, -,524: AIRPLANE FUSELAGE.

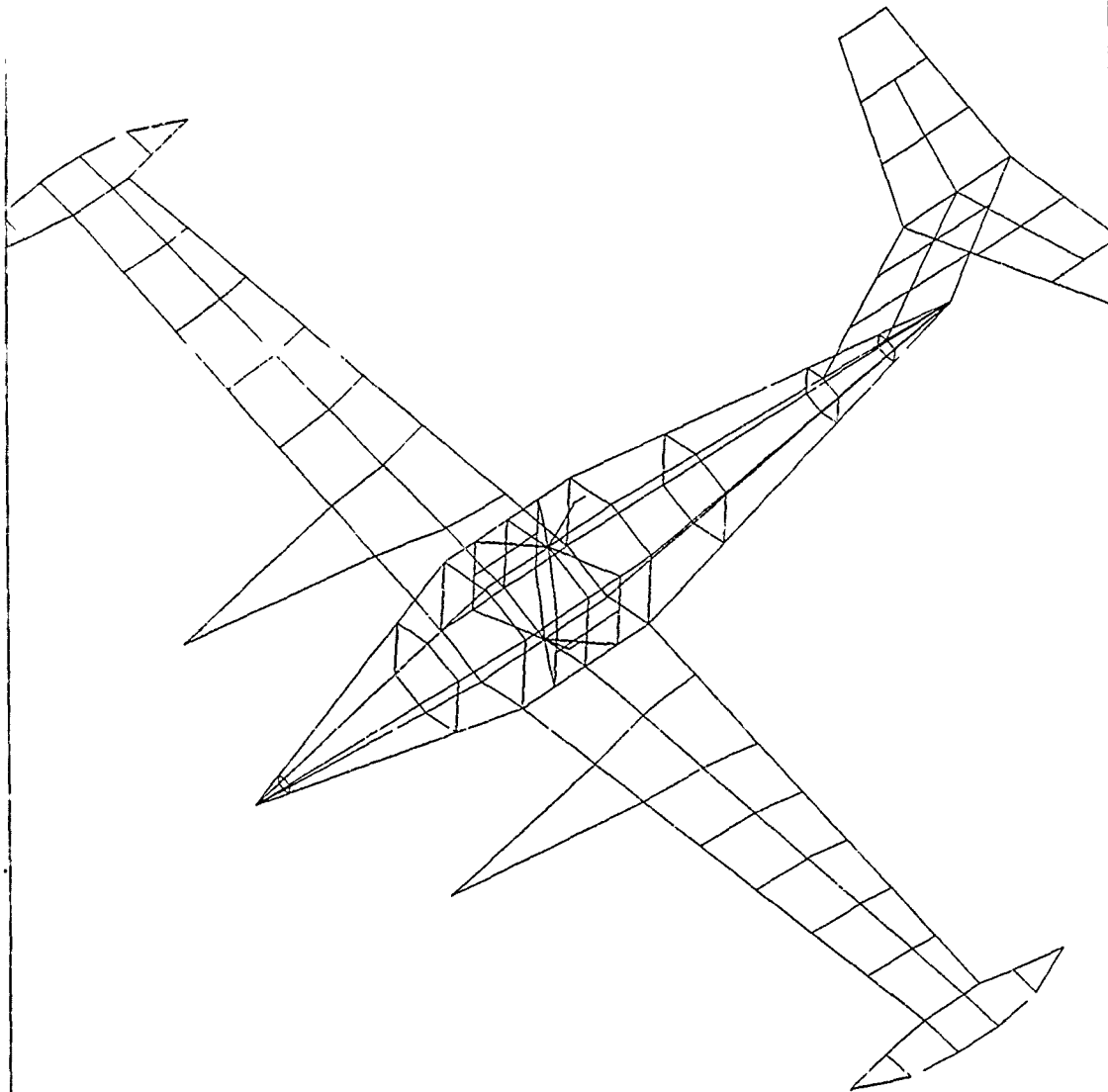


SX-HK888 - 533
 AIRPLANE FUSELAGE
 EXTENDED FUSELAGE AT SX-HK888-524: 6-SIDED FUSELAGE
 20" DIAMETER, 10" PER SEG AT CENTER, TOP AND BOTTOM BENT 31 DEG
 20" DIAMETER, 10" PER SEG AT CENTER, TOP AND BOTTOM BENT 31 DEG
 20" DIAMETER, 10" PER SEG AT CENTER, TOP AND BOTTOM BENT 31 DEG
 FREE SPACE IMPEDANCE. VOLTAGE SOURCE AT BLADES.

—●—	RESISTANCE, TAG	1 SEG	1
—○—	REACTANCE, TAG	1 SEG	1
—○—	RESISTANCE, TAG	33 SEG	119
—□—	REACTANCE, TAG	33 SEG	119

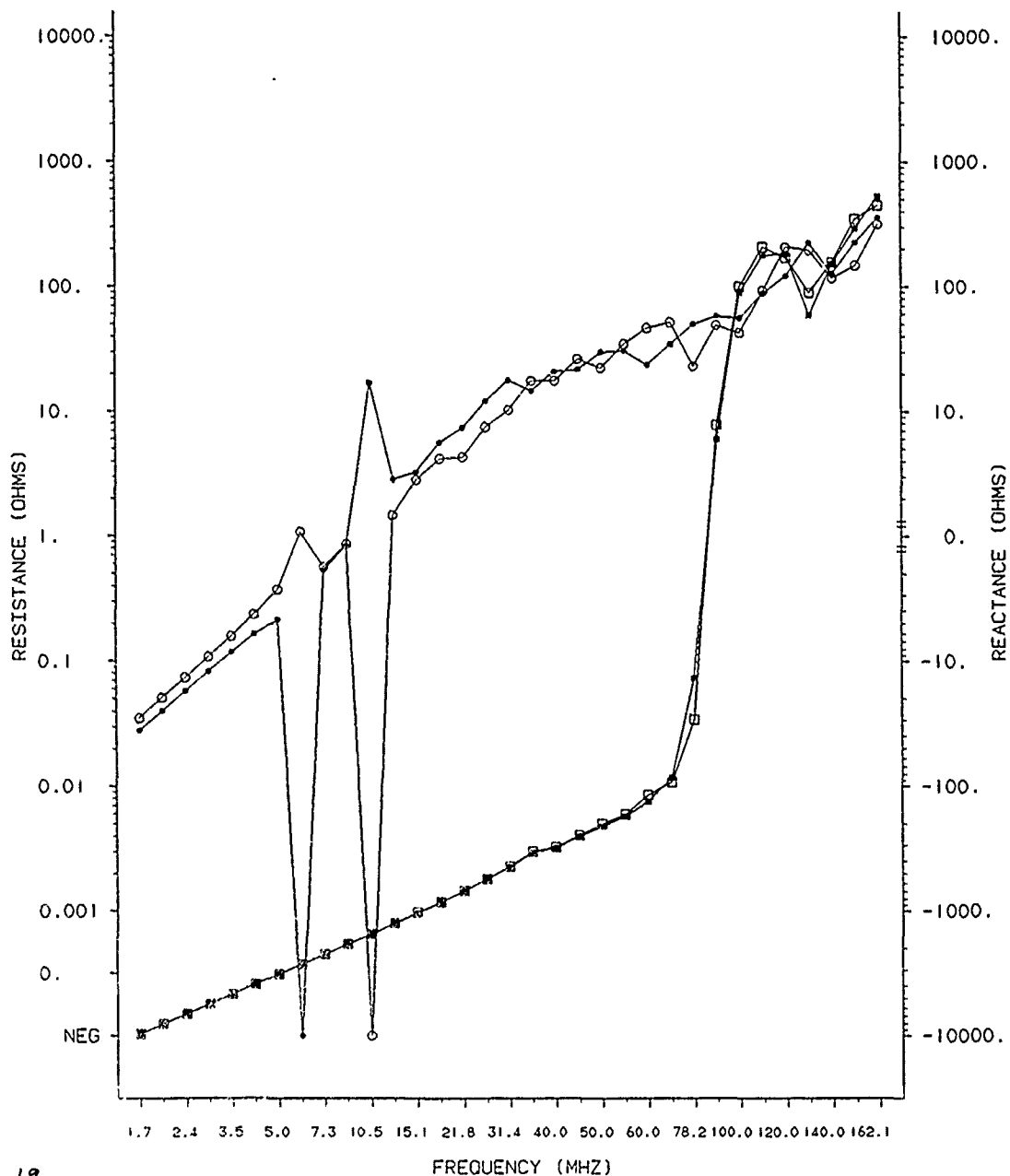


SK-HHK888, --, 543: WHOLE AIRPLANE.



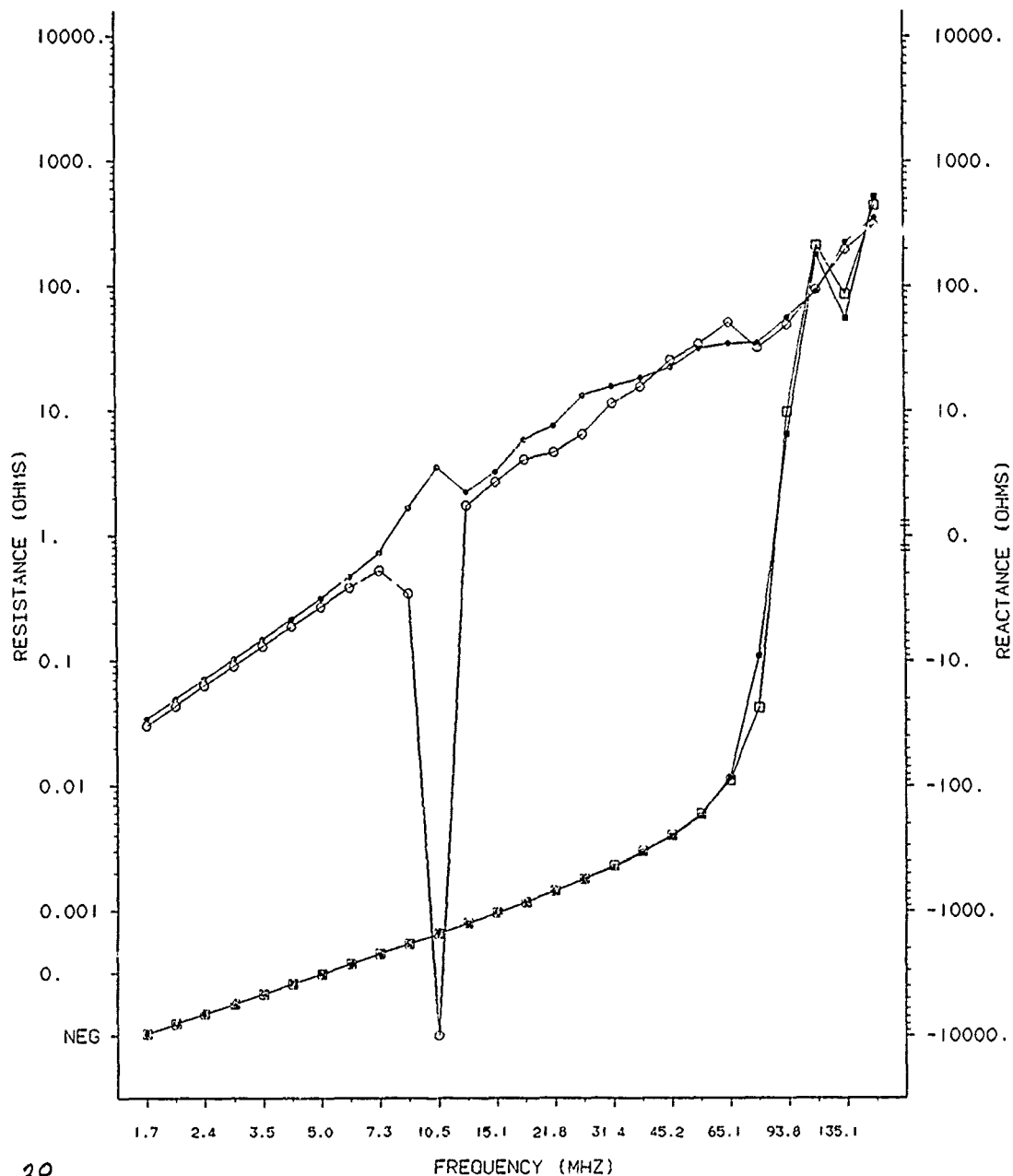
SK-H4K888 - 600
 WHOLE AIRPLANE SK-H4K888-538: BAD MODEL (SOME WING AND
 TAIL SEGMENTS DO NOT END AT WIRE JUNCTION). 6-SIDED
 FUSELAGE, 6 EXTRA WIRES AT CENTER, TOP AND BOTTOM
 BENT BLADES, 8 WIRES AT BLADE JUNCTION, 10 PER SEG
 AT CENTER, 20 TO 40 PER SEG ELSEWHERE.
 FREE SPACE IMPEDANCE. VOLTAGE SOURCE AT BLADES.

—●— RESISTANCE, TAG 1 SEG 1
 —●— REACTANCE, TAG 1 SEG 1
 —○— RESISTANCE, TAG 33 SEG 120
 —□— REACTANCE, TAG 33 SEG 120

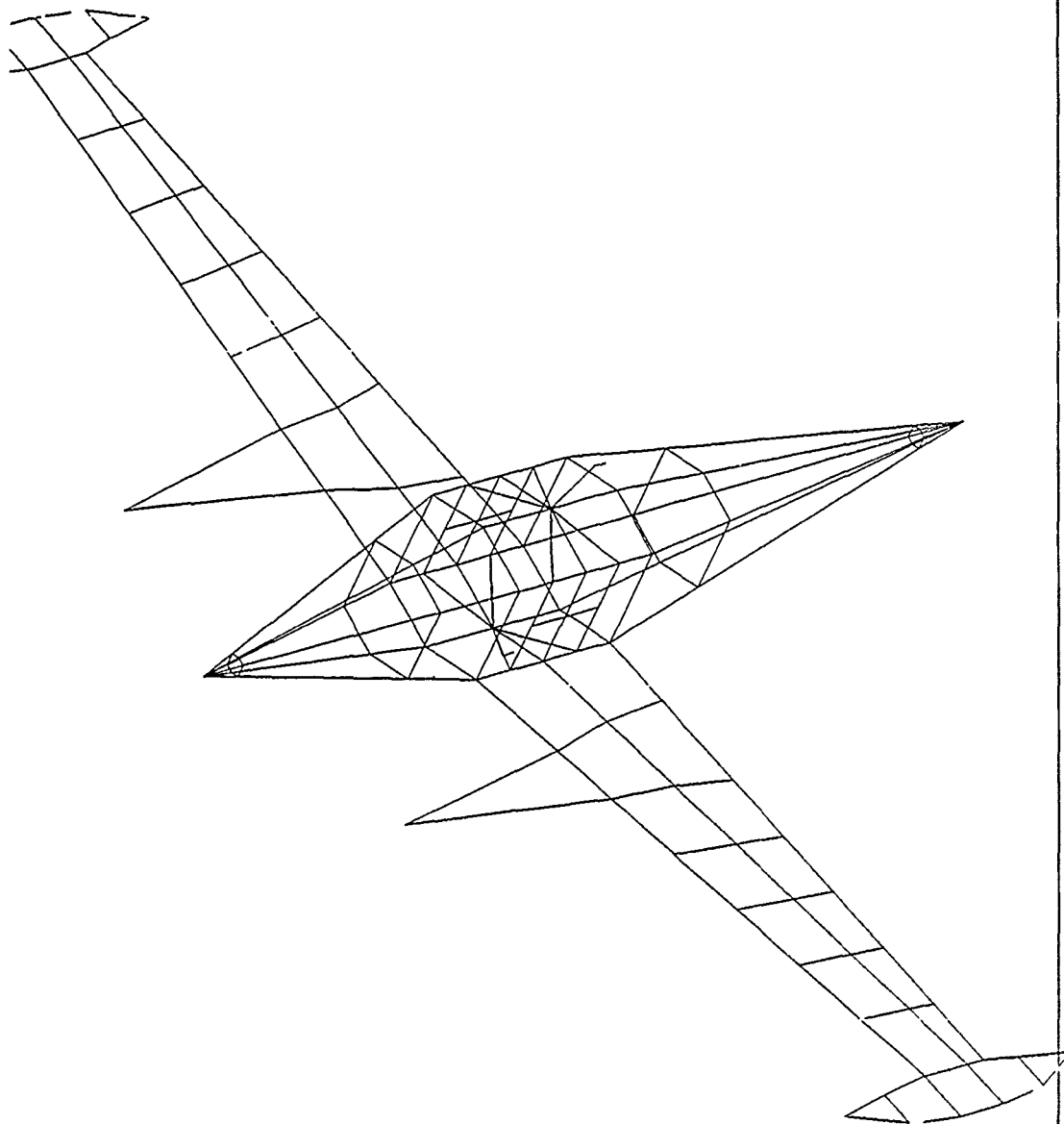


SK-H-K888 - 537
 AIRPLANE WITHOUT TAIL SK-H-K888-536: BAD MODEL (SOME
 WING SEGMENTS DO NOT END AT WIRE JUNCTION). 6-SIDED
 FUSELAGE, 6 EXTRA WIRES AT CENTER, TOP AND BOTTOM
 BENT BLADES, 8 WIRES AT BLADE JUNCTION, 10" PER SEG
 AT CENTER, 20" TO 40" PER SEG ELSEWHERE.
 FREE SPACE IMPEDANCE. VOLTAGE SOURCE AT BLADES.

—●— RESISTANCE, TAG 1 SEG 1
 —●— REACTANCE, TAG 1 SEG 1
 —○— RESISTANCE, TAG 33 SEG 120
 —□— REACTANCE, TAG 33 SEG 120

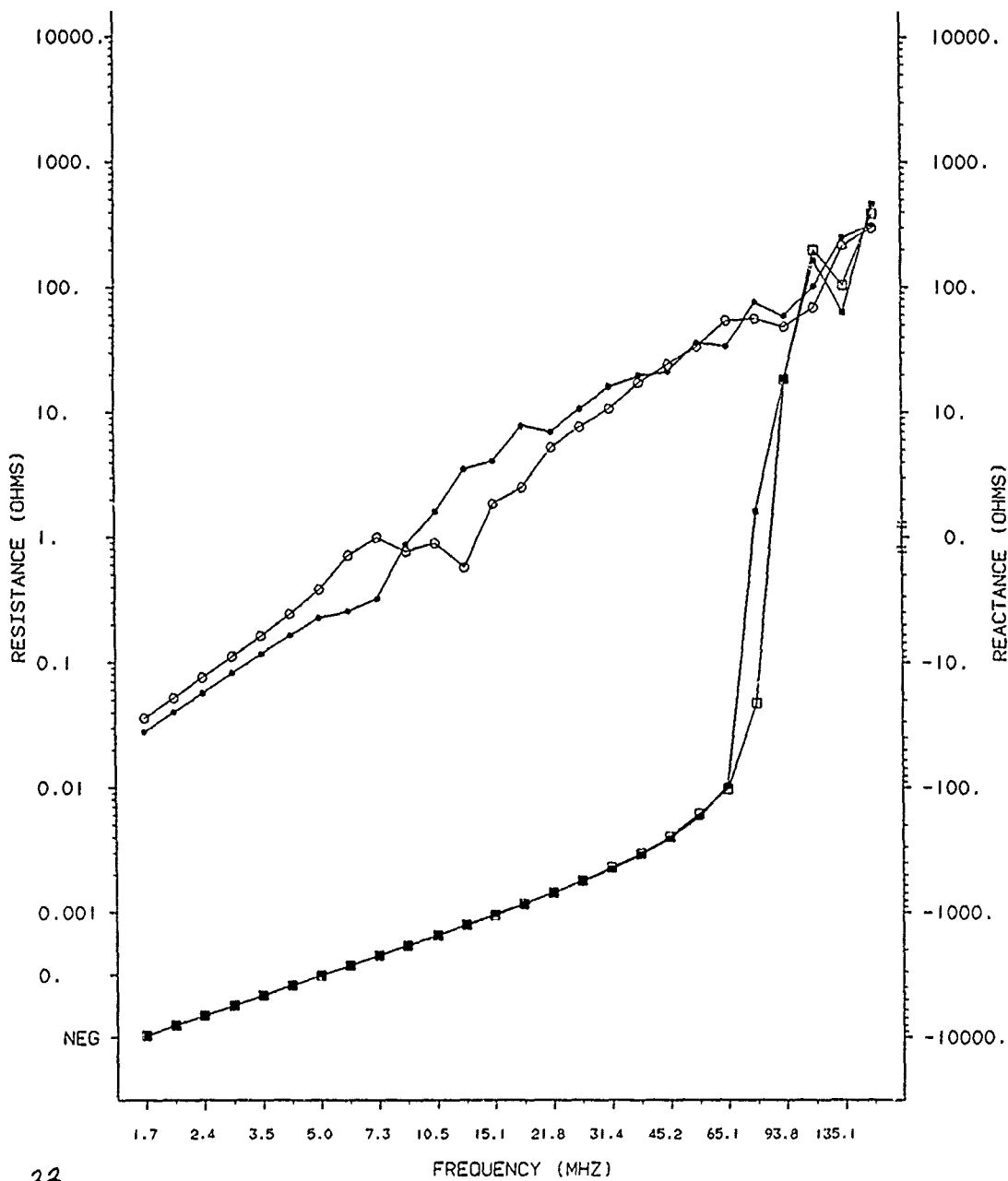


SK-HHK888,-,536: AIRPLANE WITHOUT TAIL.
BAD MODEL: SOME WING SEGMENTS DO NOT
END AT WIRE JUNCTION.



SK-HK888 - 551
 WHOLE AIRPLANE SK-HK888-543. GOOD MODEL. 6-SIDED
 FUSELAGE. 6 EXTRA WIRES AT CENTER, TOP AND BOTTOM
 BENT BLADES. 8 WIRES AT BLADE JUNCTION. 10" PER SEG
 AT CENTER. 20" TO 40" PER SEG ELSEWHERE.
 FREE SPACE IMPEDANCE. VOLTAGE SOURCE AT BLADES.

—●— RESISTANCE, TAG 1 SEG 1
 —●— REACTANCE, TAG 1 SEG 1
 —○— RESISTANCE, TAG 33 SEG 120
 —□— REACTANCE, TAG 33 SEG 120



SUMMARY AND COMMENTS

- Impedance plots are a good way to check a model during build.
- Impedance plots can check your procedures such as precision of calculation and model bandwidth.
- Graphical output files are as important as graphical input files.

FULL-SCALE HF ANTENNA TEST APPROACHES
APPLICABLE TO NUMERICAL MODEL VALIDATION

By

David L. Faust
Moray B. King

Advanced Systems Research Group
Eyring Research Institute
Provo, Utah 84601

Abstract

A broadband antenna test system (BATS) has been developed that allows the high accuracy differential or absolute measurement of full-scale HF (2-30 MHz) antenna parameters. The BATS was originally assembled as an antenna evaluation tool which provided design feedback to allow empirical development and optimization of broadband buried and low profile ground interactive antennas. This development approach was necessary since ground interactions in the HF region are quite difficult to model accurately and economically.

Two of the BATS protocols are particularly well suited for assisting in the validation of numerical electromagnetic code models addressing full-scale antennas in real ground conditions.

The closed loop sweep test protocol sequentially drives up to four antennas. The feed point parameters as well as radiated field strength are recorded for each antenna. The field strength pickup is isolated by a fiber optic link and can be located at ground level on the main beam axis of an antenna or anywhere within a 1-km hemisphere by the use of isolated cranes or tethered balloons. Differential accuracy can be on the order of $\pm .1$ dB in amplitude, $\pm .4$ degrees in phase and less than .1 m in position.

The open loop beacon test protocol maps the response of an antenna to the field radiated by an elementary dipole beacon towed below a helicopter. The BATS currently supports the simultaneous evaluation of 20 antennas with three types of flight paths, three beacon attitudes and 18 frequencies (2-66 Mhz).

All measurements are corrected for geometry to each antenna feedpoint, beacon emission pattern and feed cable attenuation. The absolute gain reference (in dBi) for the system is an adjustable horizontal dipole constructed over a reflecting ground screen. Absolute accuracy is on the order of ± 1 dB. Data examples will be presented for horizontal dipoles (1/2 wave) and vertical monopoles (1/4 wave or 35 foot tuned).

SCALE AND NUMERICAL MODELS FOR A LOW PROFILE HF SHIPBOARD ANTENNA

by

James C. Tertocha
Naval Postgraduate School

Shipboard HF antennas tend to protrude from the ship's silhouette and are quite fragile. This property increases the ship's profile and causes the antennas to be vulnerable to gun fire and bomb blast. One possible solution to this problem is to reduce the profile by making the antenna an integral part of the ship's structure.

This study approximates a section of a ship's superstructure as a 12x12x12 meter metal box over a perfect ground plane. One face of the box is insulated and a "patch monopole" placed at the insulated face. The base of the patch monopole is driven by a voltage source and, in turn, excites the box structure. Figure 1 shows the box structure with a patch monopole in place.

Three sizes of patch monopoles were used. The three sizes are shown in Figure 2. These were selected to vary the distance between the edge of the box and the edge of the patch monopole. Note that the monopole's patch section is centered at the insulated face of the box.

The Numerical Electromagnetics Code (NEC) was used to model the box and patch structure (also referred to as the survivable antenna). Wire grid structures were used to model the antennas. The insulated face of the box was approximated by leaving one face of the box open.

To determine the effect of various parameters on the antenna models' impedances, several versions of the patch monopole were investigated. The parameters that varied in these models were: grid size, feed line segmentation, type of voltage source used, and the grid geometry itself. Due to computer storage and time constraints, these models were limited to the large ($W/H=10$) and small ($W/H=1$) patch monopoles and the frequencies 2, 6, and 10 MHz. These frequencies corresponded to below, near, and above resonance.

The grid separation for the small antenna was varied from 2 to 0.4 meters. The large antenna's grid size was varied from a 5 meter mesh spacing to a .625 meter spacing. Tables 1 and 2 present the grid spacings in wavelengths for the two antenna sizes. Figure 3 shows typical grid models of the small and large patch monopoles.

The feed segmentation of the large and small antenna models were varied. The small antenna's feed line was broken into three equal length segments. In addition, a second small antenna model was used whose feed line's segment lengths were equal to the grid separation of the model. Table 3 presents these feed segment lengths in wavelengths.

Two models of the large patch monopole with different sized feed segment lengths were also investigated. The feed line was broken into three equal segments; the second model used a single segment feed line. Table 4 presents these feed segment lengths in terms of wavelengths.

Two types of voltage sources were used with the two sizes of patch monopole models. These were the E-gap and current-slope-discontinuity voltage sources. The voltage sources were individually applied to the bottom-most segment of the feed line for the particular patch monopole model used.

Figures 4 and 5 are typical plots of resistance and reactance versus grid size for the large and small antenna models. These models used the E-gap voltage source. The $W/H=1$ model had a three segment feed while the $W/H=10$ had a one segment feed line.

From these plots it is seen that, with the exception of the $W/H=1$ antenna resistance values, it is not apparent to what value of resistance or reactance the computer models will converge or if they will ever converge as grid size is reduced. Also it is seen that the grid density has much greater effect on the large antenna's impedance than on that of the small antenna.

Figures 6 and 7 are typical graphs showing how the resistance and reactance values change with grid size for the models with different numbers of feed segments. Figure 6 is the resistance and reactance graphs of the $W/H=1$ antenna and Figure 7 is the resistance and reactance graphs of the $W/H=10$ antenna.

From Figure 6 it is seen that for the small antenna the number of feed segments used in the two models has little affect on the resistance as a function of grid size. The number of feed segments does affect the reactance of the model as the grid size is varied. It is also noted that the three segment models have the greatest variation in reactance versus grid size.

The graphs of Figure 7 indicate that the two large antenna models with different feed segmentation tend to converge in resistance and reactance as grid size is reduced. Note also that the convergence takes place at a grid separation which is less than the .1 wavelength criteria commonly considered adequate for wire grid models.

Figures 8 and 9 are typical graphs of resistance and reactance as a function of grid size for the large and small antenna models with the E-gap and current-slope-discontinuity voltage sources.

The two voltage sources produce different impedances. However, for the large ($W/H=10$) antenna, the two values tend to converge as grid size is decreased. For the $W/H=1$ antenna, the two voltage sources result in impedances that tend to track each other at a fairly constant separation as the grid size is varied. In both cases, the current-slope-discontinuity voltage source produces greater resistance and reactance values than the E-gap source.

The large and small patch monopoles were also modeled with the three sparse geometries shown in Figure 10, along with their respective acronyms. These models utilized the E-gap voltage source. The small antenna's feed line had 3 segments while the large antenna's used 1 segment.

Tables 5 and 6 present the percent change in resistance and reactance of the sparse models with respect to the one meter grid separation, E-gap voltage source models.

The small antenna sparse models are relatively good over the frequency range 2-10 MHz with the worst case percent change in resistance being 2.97%. The reactances are less comparable, reaching a percent change of about 60% at 6 MHz. However, 6 MHz is the near resonance frequency of the grid model. The above and below resonance frequencies give a better correlation in reactance with a maximum percent change of 18.32%.

From Table 6 it is seen that the $W/H=10$ sparse models correlate less and less in impedance with the grid model as frequency increases and as the model becomes sparser, ie., the SPMVC model's impedance better than the SPMV model's impedance. It also reveals that reactances correlate worse than resistances.

From the graphs and tables presented, it was seen that the small antenna impedance has less variation as a function of grid size, feed segmentation and voltage source type. The large antenna's impedance was more dependent on these modeling parameters. The impedances for the various large antenna models tend to converge as the grid size is reduced. It was also noted that the sparse models were adequate in terms of impedance for electrically short antennas.

Scale physical models were built to provide a comparison between measured and calculated impedances. A standard monopole whose theoretical impedance characteristics have been tabulated was built for calibration (Ref 1). The physical models of the patch monopoles were scaled by 1/45. Two solid scale patch monopole models were constructed, one $W/H=10$ antenna and one $W/H=1$ antenna. In addition, a scale wire grid model was built for each of the three patch monopoles, ie., the $W/H=1$, $W/H=2$, and $W/H=10$ antennas. Figure 11 shows the solid and grid scale models of the $W/H=1$ antenna.

The frequency range (scaled by 45) used was 90-1080 MHz. At these frequencies the ground plane size ranged from 3.3 to 39.6 wavelengths. The radius of the feed transition used did not physically match that of the scale models, so each of the scale models and the monopole were tapered at their bases to fit the feed transition.

Figures 12 and 13 are plots of the resistance and reactance of the theoretical (KINGS), physical, and computer monopoles. These plots show good correlation in impedance between the computer model and the theoretical values. The physical model digresses from the theoretical impedance over the frequency range 350-700 MHz. The cause of this discrepancy is unknown. Above 900 MHz the physical and theoretical impedances also differ, however, this can be attributed to the taper at the base of the physical monopole.

Figures 14, 15, and 16 are plots of the measured resistance and reactance of the scale models. Included in these plots are the resistances and reactances calculated with NEC for the corresponding patch monopoles. The NEC models used the E-gap voltage source with the one meter grid separation. The $W/H=1$ and 2 models used 3 segment feed lines while the $W/H=10$ model used a 1 segment feed line.

From Figures 14 and 16, it is evident that the solid and grid models have similar impedance characteristics. Figures 14 and 15 show that the computer models' resistance deviates from the measured resistances in the frequency range around 350-700 MHz; which was also the range for which the physical monopole measurements deviated from the theoretical values. Thus, this discrepancy is attributed to experimental error rather than to the computer model. The measured and calculated reactances of the $W/H=1$ and $W/H=2$ antennas do track each other well.

Figure 16 shows plots of measured and calculated resistances and reactances of the $W/H=10$ antenna. Here the computed resistance and reactance track the measured values well except at the high frequency end, above 900 MHz. This is attributed to the taper on the physical models.

A computer model of the large patch monopole at the open face of the box was run over the frequency range 2-24 MHz. The patch monopole model was the one used in the impedance comparison with the scale models. The box was modeled as a wire grid structure. Figure 17 shows the wire grid structure used for the survivable antenna computer model.

Typically a 3:1 SWR is considered an adequate bandwidth criteria for broadband antennas. Figure 18 shows the 3:1 SWR circle. The shaded area of this figure represents the region which can be matched to a 3:1 SWR by use of a series impedance network. Impedances falling in this region will be considered acceptable for this study's application.

Figure 19 is the Smith Chart impedance plot of the large antenna at the box face. Comparing this plot to Figure 18, it is seen that at the frequencies 6-7.5 MHz and 8.5-22 MHz, the impedance lie within the 3:1 SWR circle or are series matchable to a 3:1 SWR. Thus the survivable antenna model possesses an adequate impedance over the above frequencies.

The radiation pattern of the survivable antenna for heights less than a tenth of a wavelength closely resemble those of an electrically short monopole. As the frequency increases, the box height nears .25 wavelengths and the patterns become cardioidal in the direction of the box face. Figure 20 is a horizontal pattern showing the cardioidal slope. Figure 21 is the corresponding vertical pattern. (Note this directionality might be removed by use of opposing patches on the box). At electrical heights greater than .5 wavelength, the patterns become more lobe. Figures 22 and 23 are typical patterns displaying these properties.

Following are some conclusions of this study. Solids may be approximated nicely by grid structures. The NEC model results agree with scale model measurements within experimental error. Sparse patch monopole models are adequate for electrically short antennas. When selecting a computer model, many modeling parameters must be considered. The large patch monopole computer model produced results which correlated better with physical measurements than did the smaller antennas. The impedance bandwidth of the survivable antenna is acceptable.

Some recommendations for future work:

The survivable antenna should be run over a higher frequency range; the VHF range may prove interesting. Investigate the use of a sparse geometry for the box structure. The patch monopole model with the current-slope-discontinuity source should be run over the 2-24 MHz frequency range for comparison with the E-gap voltage source. Finally, a scale model of the box-patch combination should be built and measurements made for comparison to the computed values.

REFERENCES

1. KING, Ronald W.P., Tables of Antenna Characteristics, pp. 46-48, IFI/Plenum, 1971.

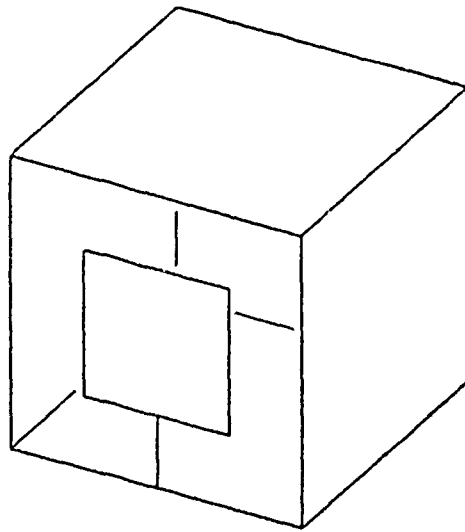


Figure 1. Box structure with patch monopole at face.

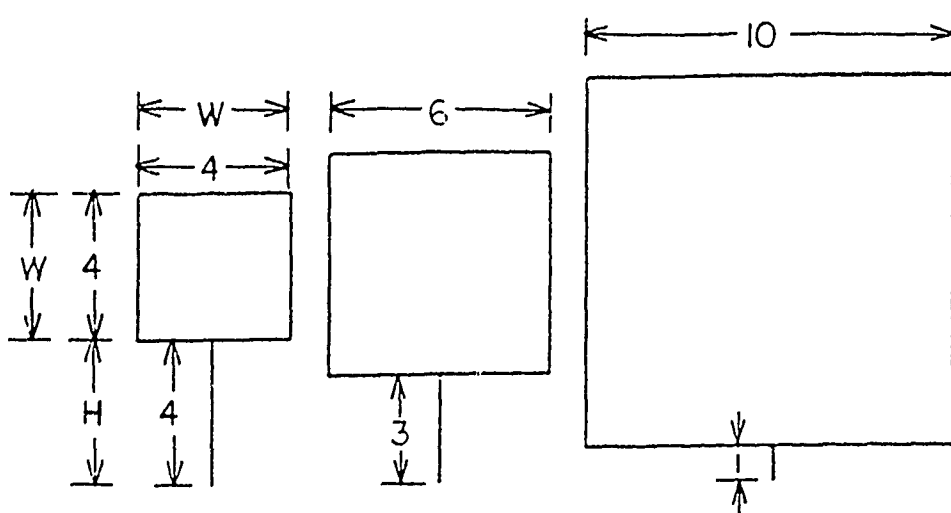


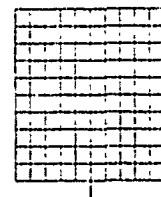
Figure 2. Three sizes of patch monopoles.

Table 1.
Grid Densities of W/H=1 Antenna Model.



Grid Spacing in Meters	Grid Spacing in Wavelengths		
	f = 2 MHZ	f = 6 MHZ	f = 10 MHZ
2	.0133	.0400	.0667
1	.0067	.0200	.0336
.5	.0033	.0100	.0167
.4	.0027	.0080	.0133

Table 2.
Grid Densities of W/H=10 Antenna Model.



Grid Spacing in Meters	Grid Spacing in Wavelengths		
	f = 2 MHZ	f = 6 MHZ	f = 10 MHZ
5	.0334	.1001	.1668
2.5	.0167	.0500	.0834
1.25	.0083	.0250	.0417
1	.0067	.0200	.0334
.625	.0042	.0125	.0209

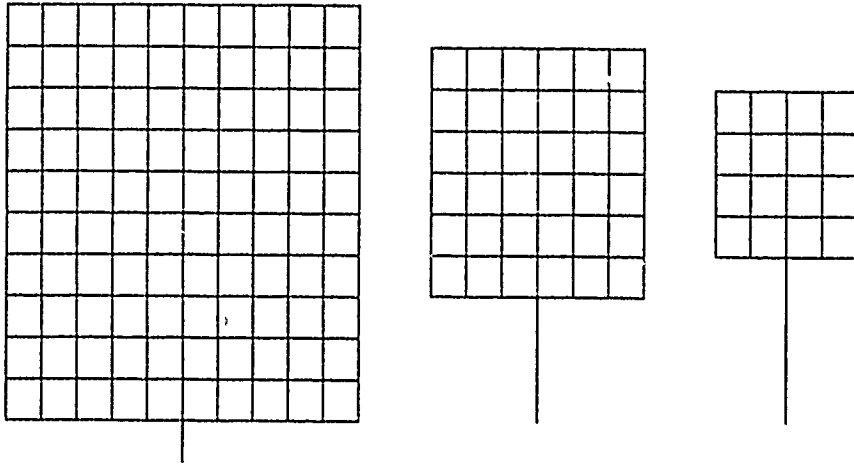


Figure 3. Typical grid models of patch monopoles.

Table 3.

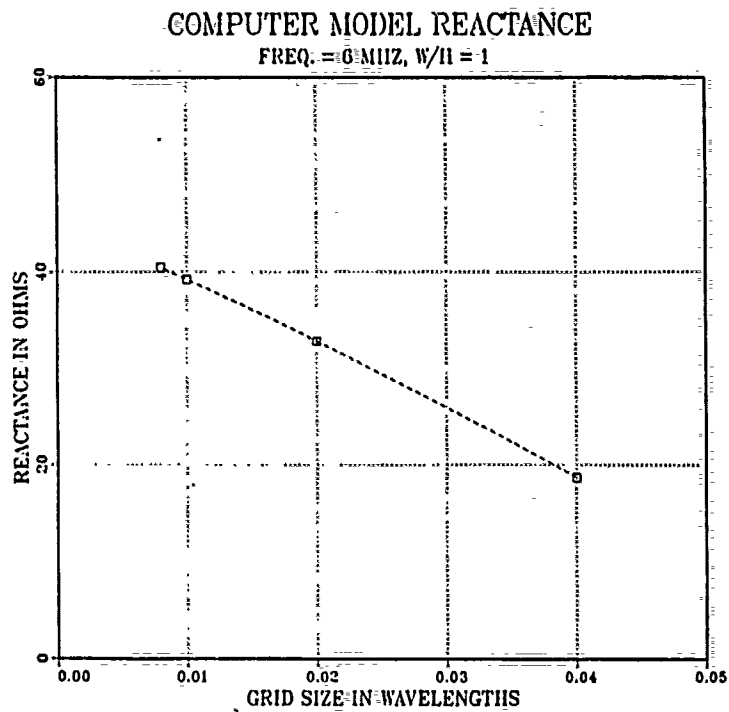
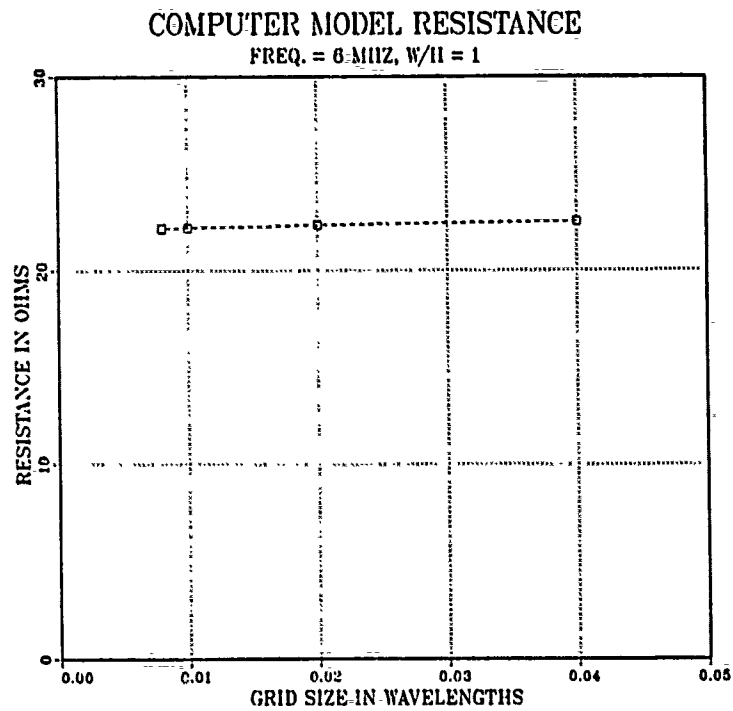
Number of Feed Segments Used & Their Length
in Wavelengths for the W/H=1 Antenna Models.

Number of Feed Segments	Feed Segment Length in Wavelengths		
	f = 2 MHZ	f = 6 MHZ	f = 10 MHZ
2	.0133	.0400	.0667
3	.0089	.0267	.0444
4	.0067	.0200	.0333
8	.0033	.0100	.0167
10	.0027	.0080	.0133

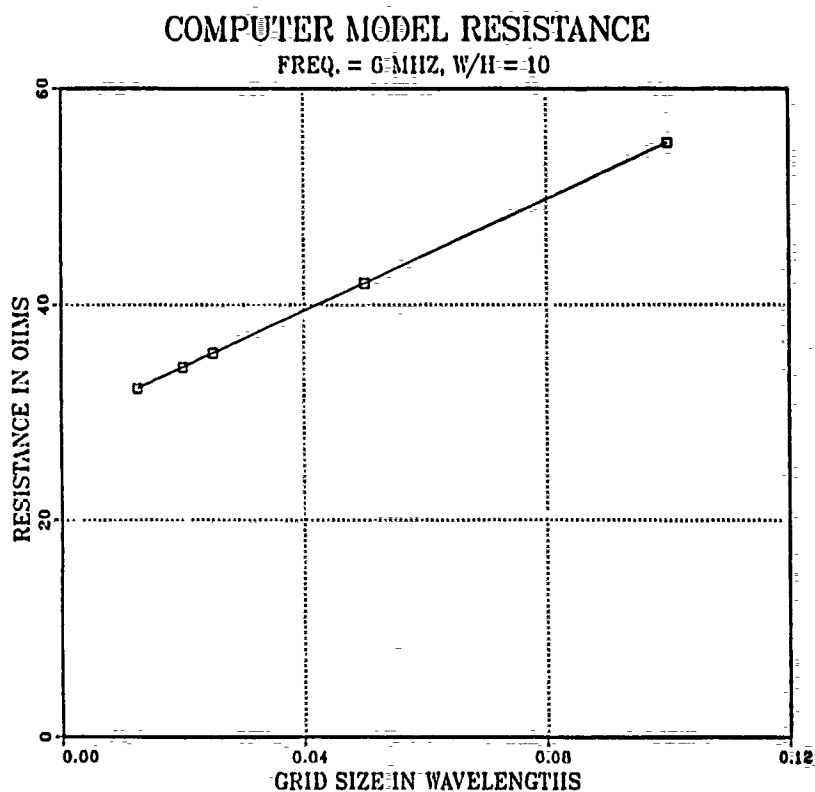
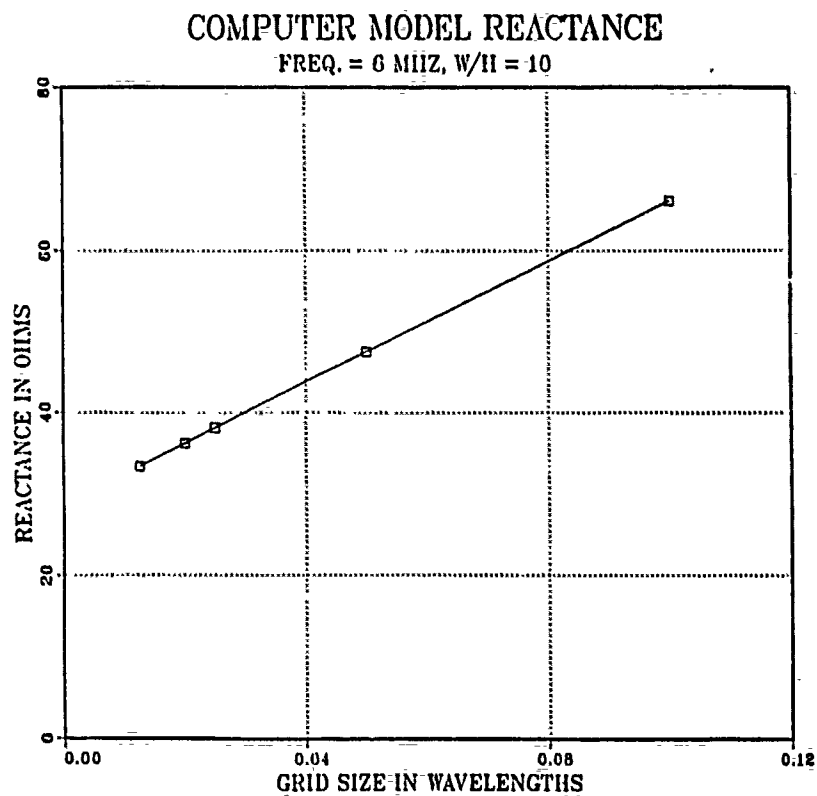
Table 4.

Number of Feed Segments Used & Their Length
in Wavelengths for the W/H=10 Antenna Models.

Number of Feed Segments	Feed Segement Length in Wavelengths		
	f = 2 MHZ	f = 6 MHZ	f = 10 MHZ
1	.0067	.0200	.0333
3	.0022	.0067	.0111



**Figure 4. Resistance & reactance versus grid size
for the W/H=1 antenna model at 6 Mhz.**



**Figure 5. Resistance & reactance versus grid size
for the W/H=10 antenna model at 6 Mhz.**

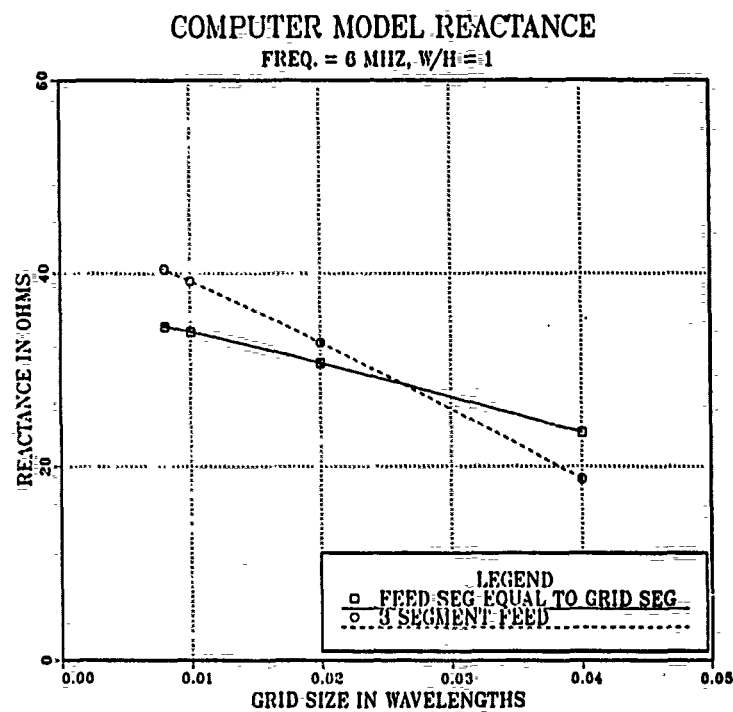
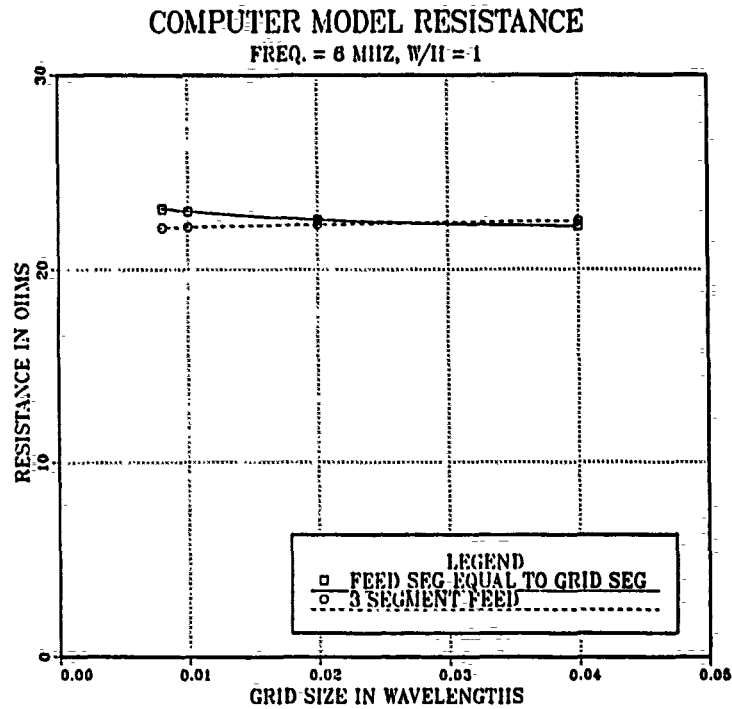


Figure 6. Comparison of different length feed line segments on resistance & reactance versus grid size for the W/H=1 antenna.

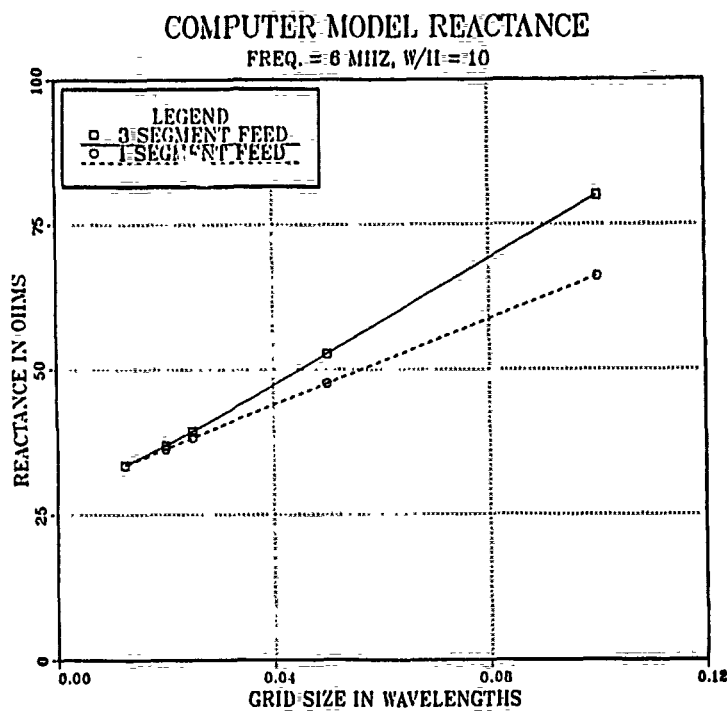
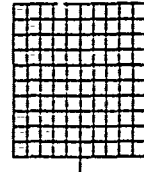
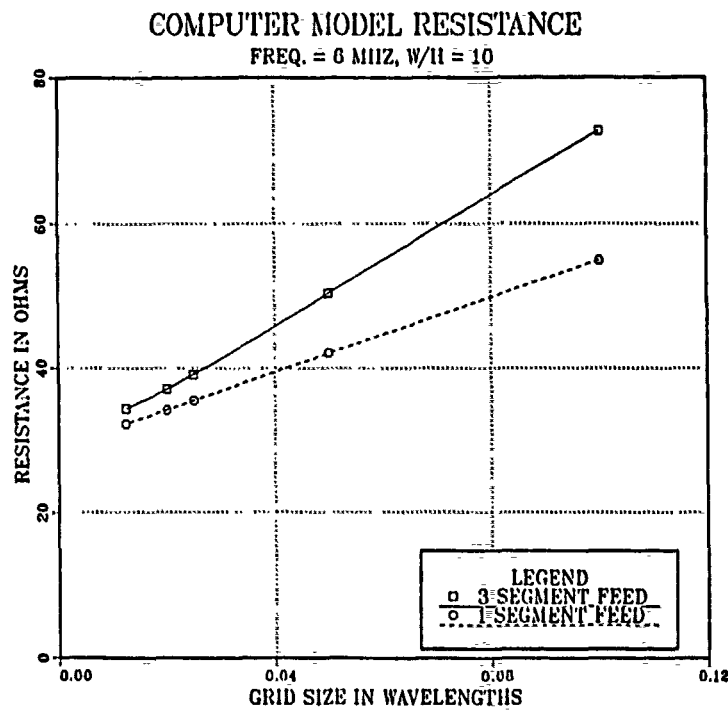


Figure 7. Comparison of different length feed line segments on resistance & reactance versus grid size for the W/H=10 antenna.

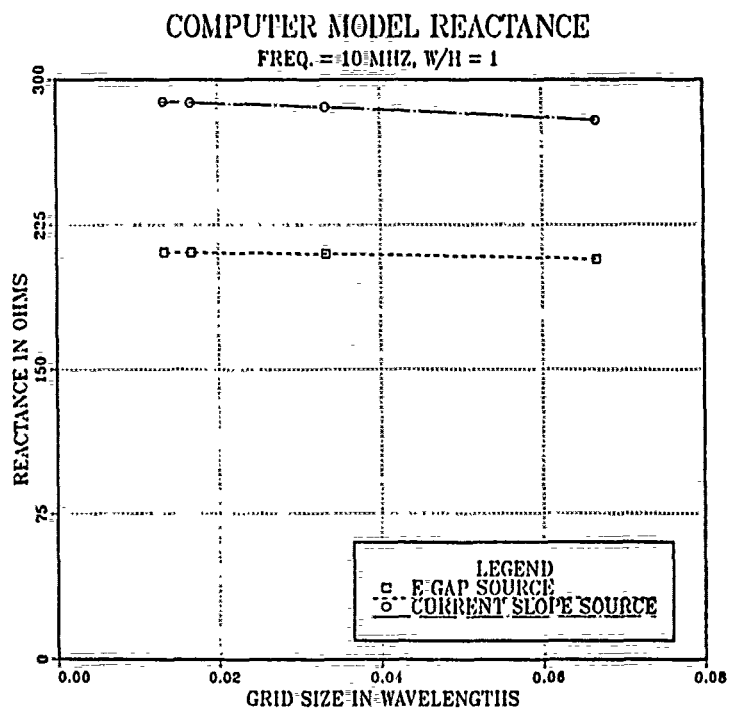
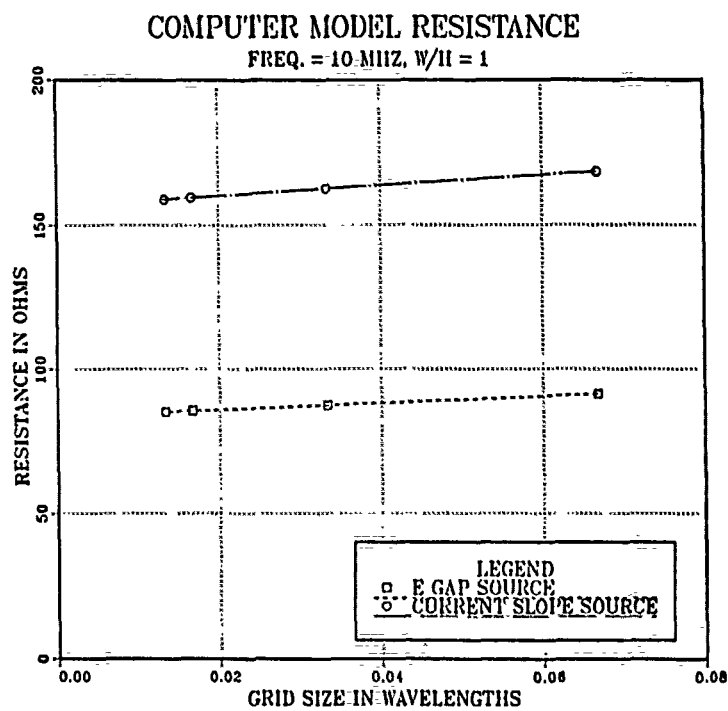


Figure 8. Comparison of voltage sources on resistance & reactance versus grid size for the W/H=1 antenna model.

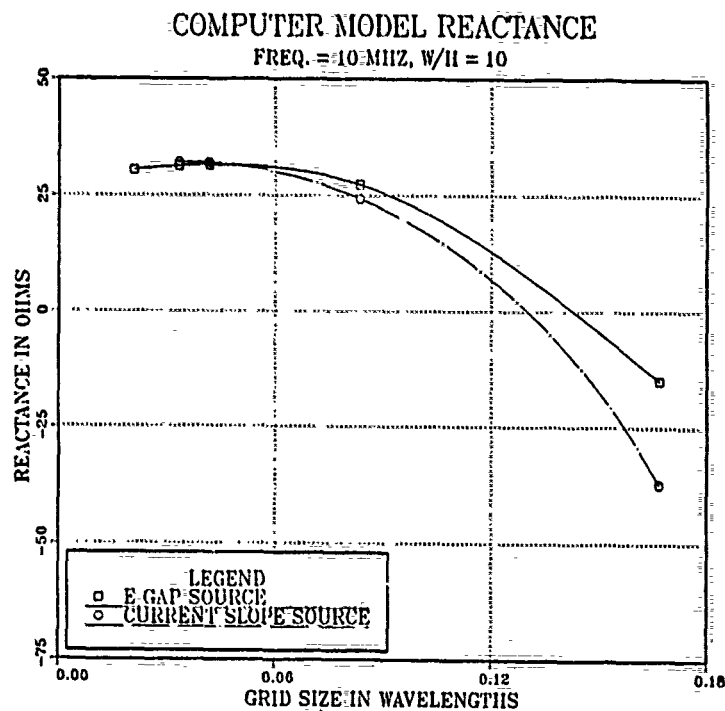
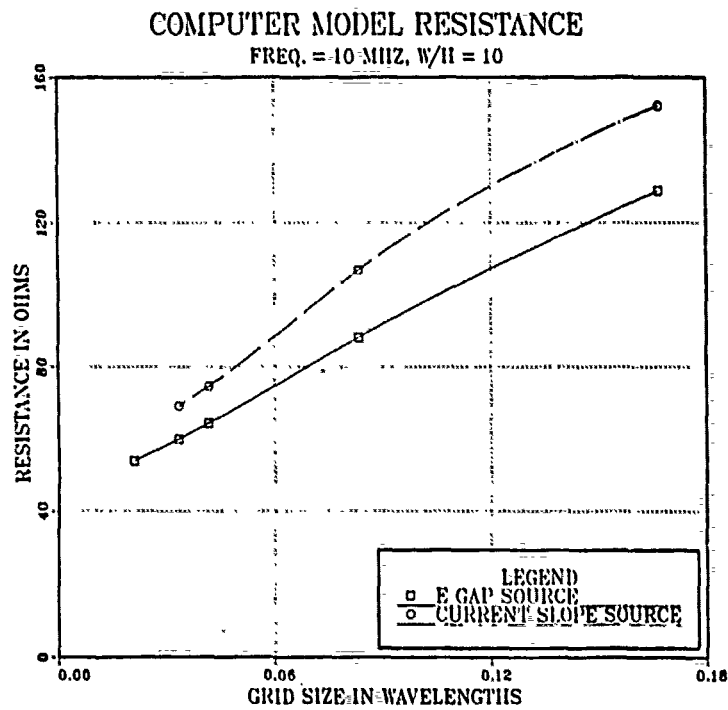


Figure 9. Comparison of voltage sources on resistance & reactance versus grid size for the W/H=10 antenna model.

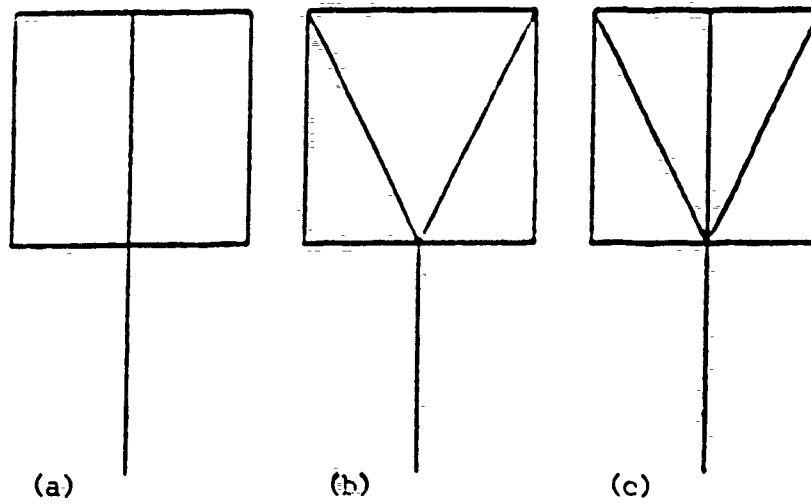


Figure 10. Sparse model geometries

a) SPMNV, b) SPMV, c) SPMVC.

Table 5.

PERCENT CHANGE IN RESISTANCE AND REACTANCE OF SPARSE MODELS
FROM WIRE GRID MODEL, $W/H = 1$



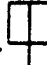



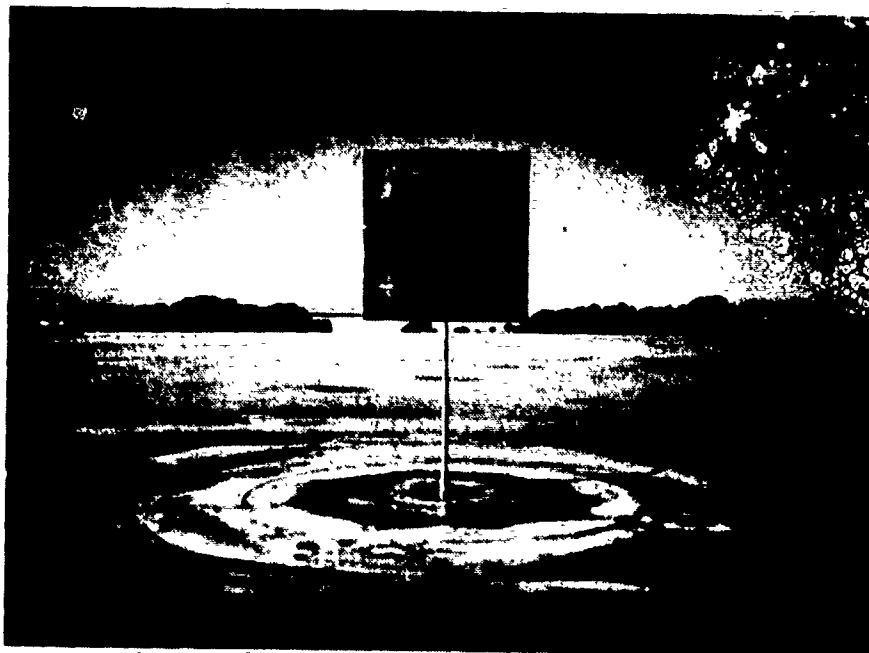
Freq in MHZ	SPMVC 		SPMV 		SPMNV 	
	$\Delta\%R$	$\Delta\%X_j$	$\Delta\%R$	$\Delta\%X_j$	$\Delta\%R$	$\Delta\%X_j$
2	.53	3.89	2.16	12.3	1.15	18.3
6	.89	19.2	2.26	45.6	.29	59.5
10	1.15	2.21	1.75	4.93	2.97	3.70

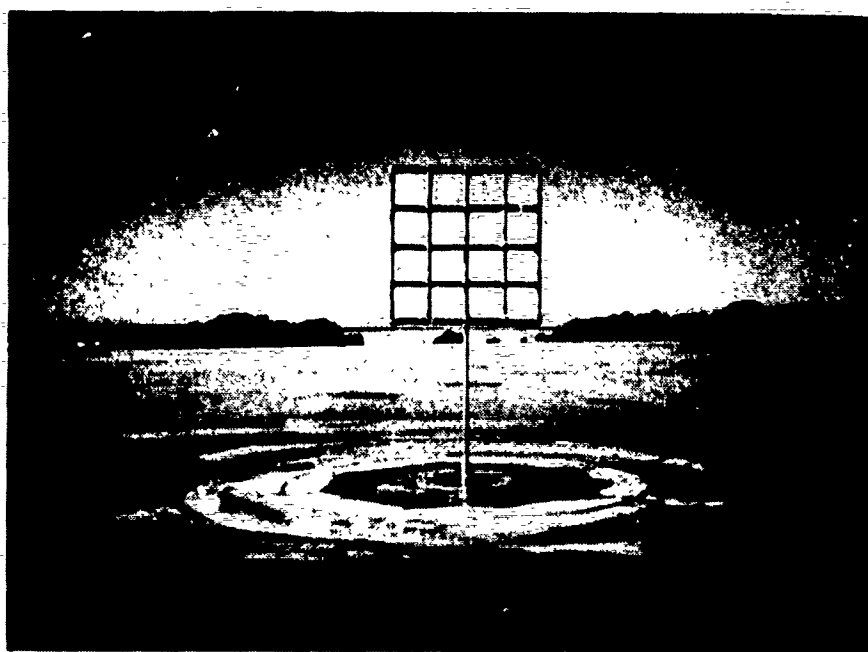
Table 6.

PERCENT CHANGE IN RESISTANCE AND REACTANCE OF SPARSE MODELS
FROM WIRE GRID MODEL, $W/H = 10$

Freq in MHZ	SPMVC 		SPMV 		SPMNV 	
	$\Delta\%R$	$\Delta\%X_j$	$\Delta\%R$	$\Delta\%X_j$	$\Delta\%R$	$\Delta\%X_j$
2	6.96	21.1	10.0	43.7	18.6	58.9
6	8.38	8.55	19.2	18.3	33.3	38.2
10	23.4	28.9	48.9	94.9	94.1	103.



a) $W/H=1$ Solid scale model.



b) $W/H=1$ Grid scale model.

Figure 11. Scale models.

MONOPOLE COMPARISON RESISTANCE

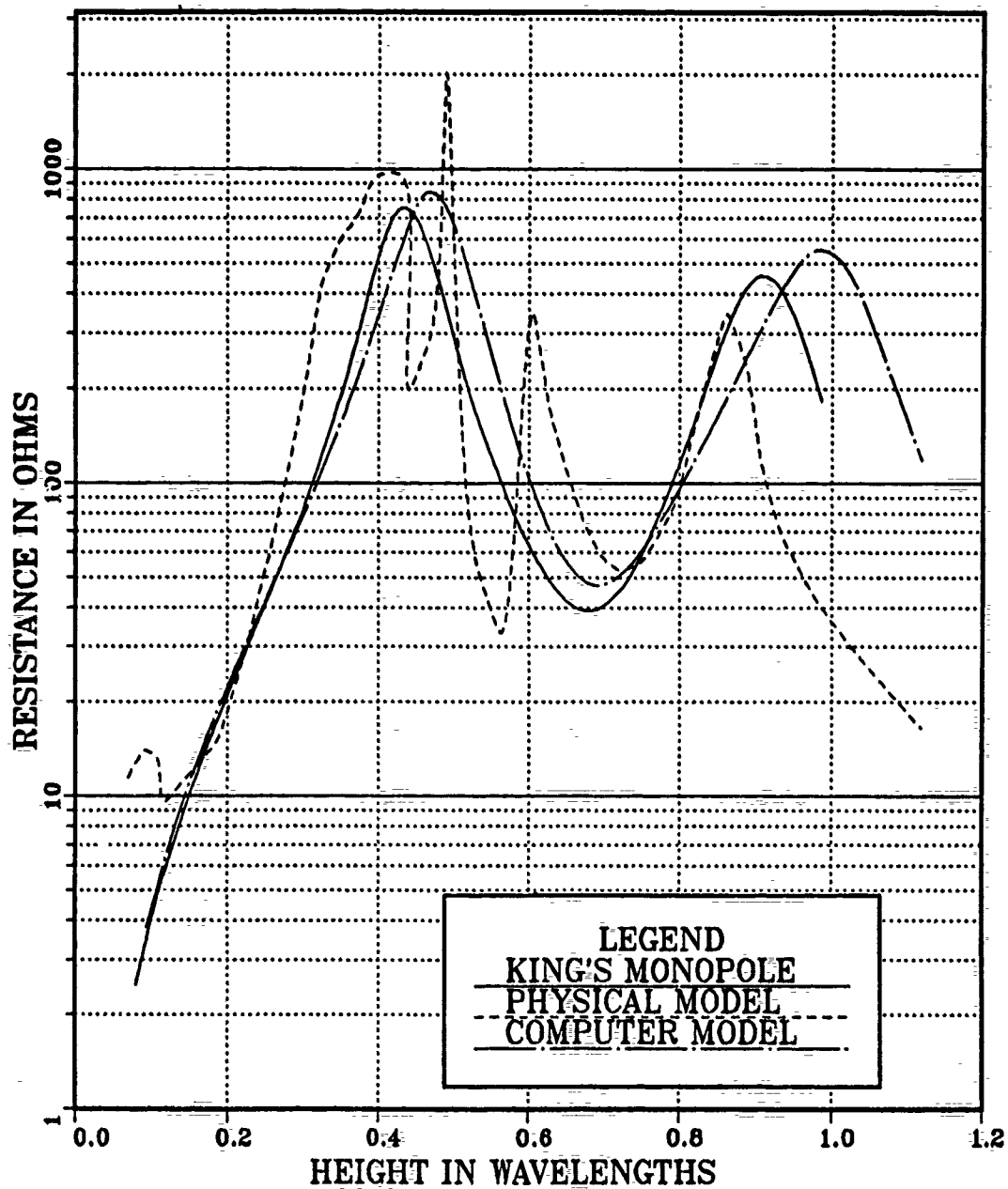


Figure 12. Monopole resistances.

MONOPOLE COMPARISON

REACTANCE

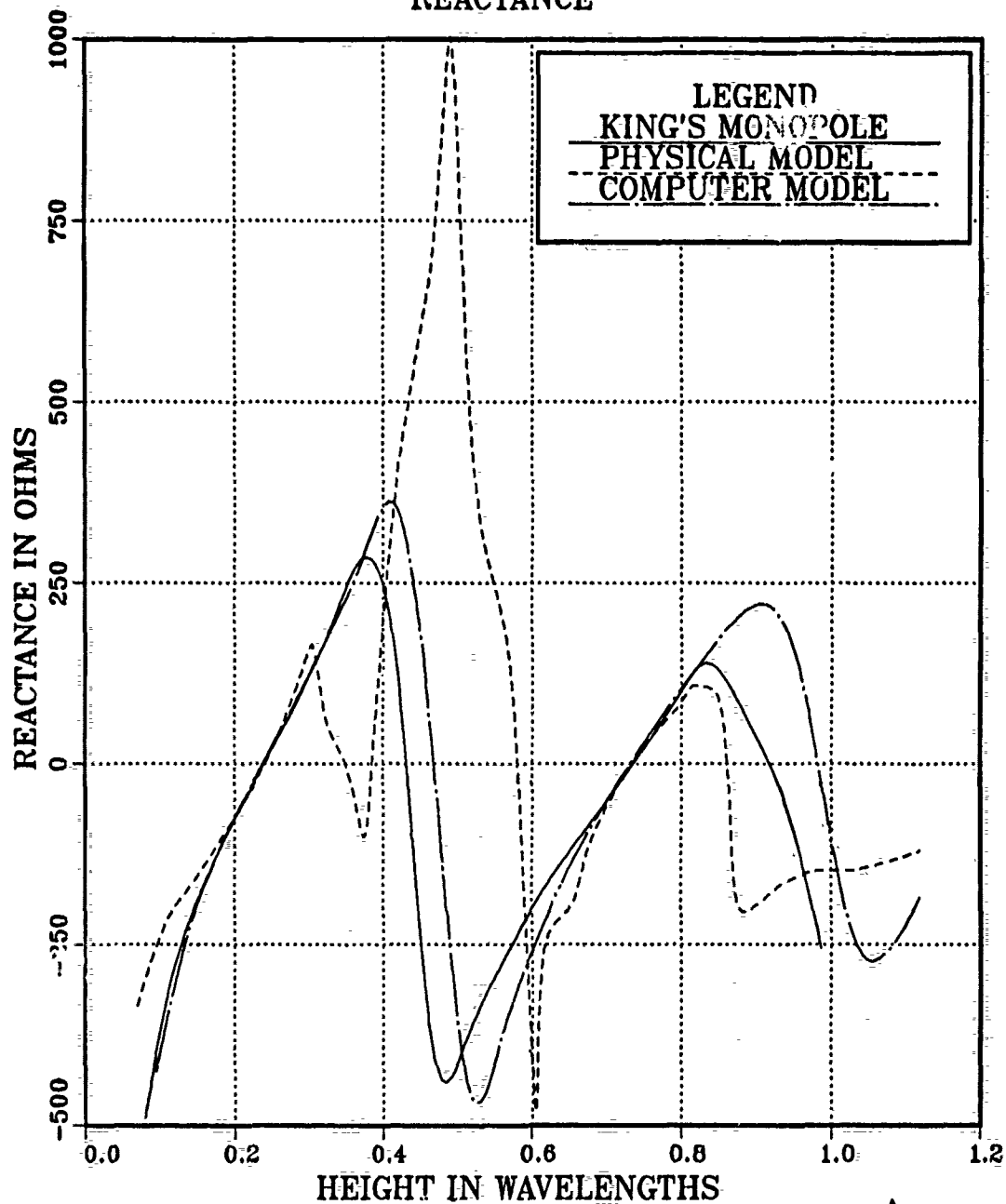
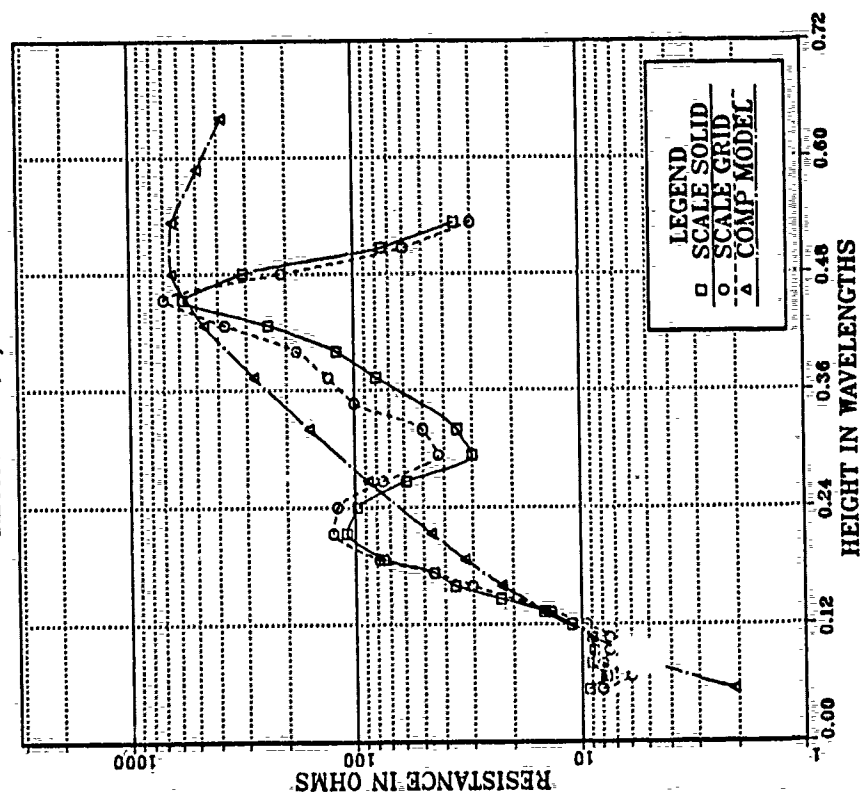


Figure 13. Monopole reactances.



PATCH MONOPOLE
RESISTANCE, $W/H = 1$



PATCH MONOPOLE
REACTANCE, $W/H = 1$

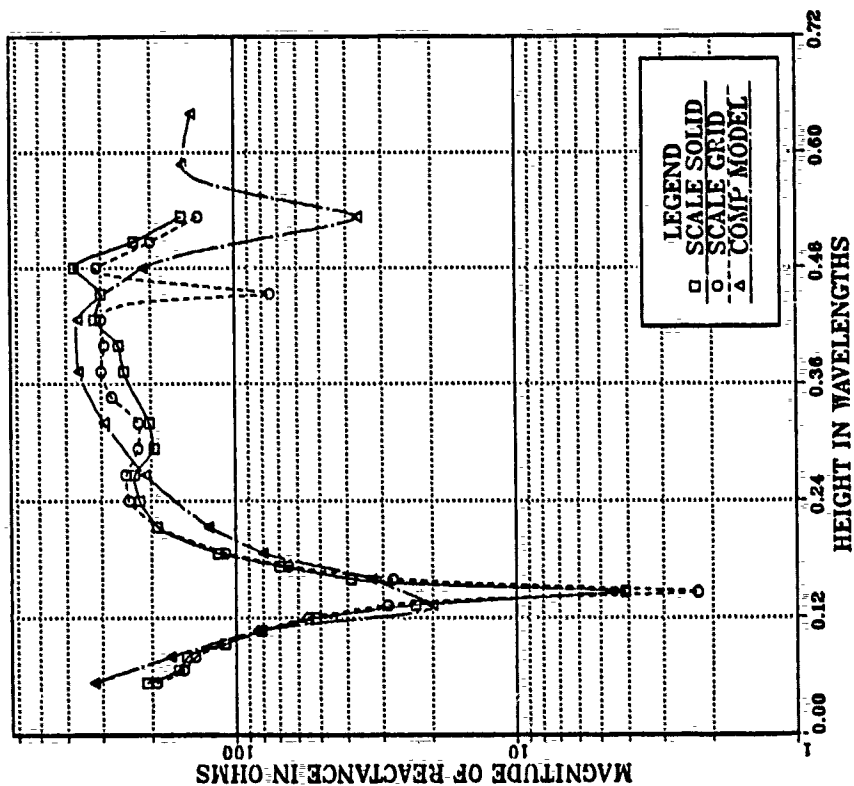
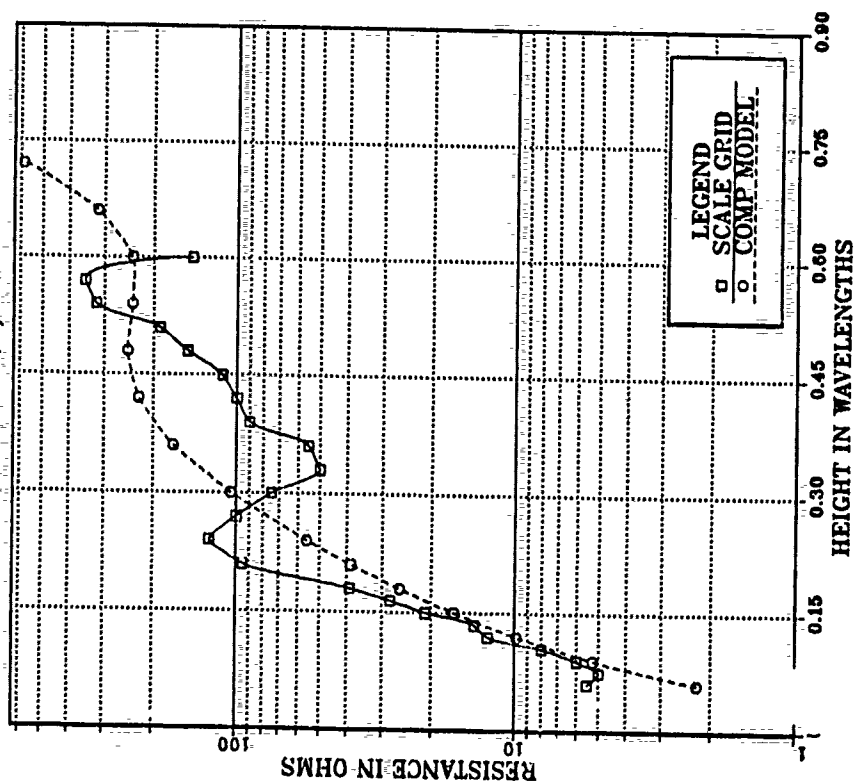


Figure 14. Resistance & reactance plots
of $W/H=1$ antenna models.

1	2	3	4	5	6	7	8	9	10
11	12	13	14	15	16	17	18	19	20
21	22	23	24	25	26	27	28	29	30
31	32	33	34	35	36	37	38	39	40
41	42	43	44	45	46	47	48	49	50
51	52	53	54	55	56	57	58	59	60
61	62	63	64	65	66	67	68	69	70
71	72	73	74	75	76	77	78	79	80
81	82	83	84	85	86	87	88	89	90
91	92	93	94	95	96	97	98	99	100

PATCH MONOPOLE
RESISTANCE, $W/H = 2$



PATCH MONOPOLE
REACTANCE, $W/H = 2$

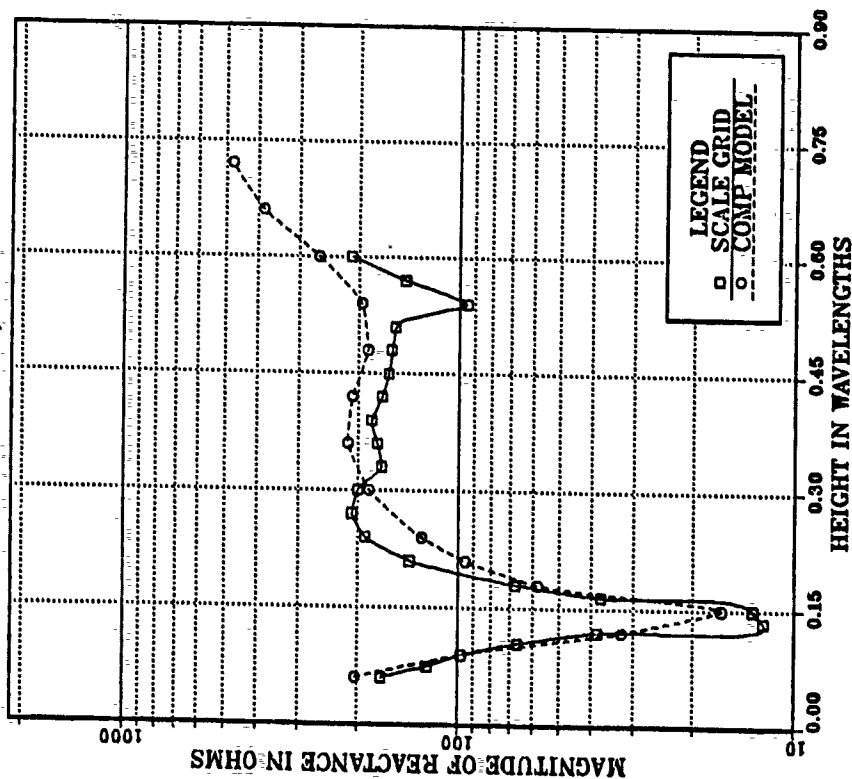
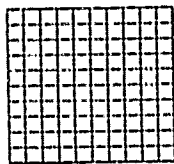
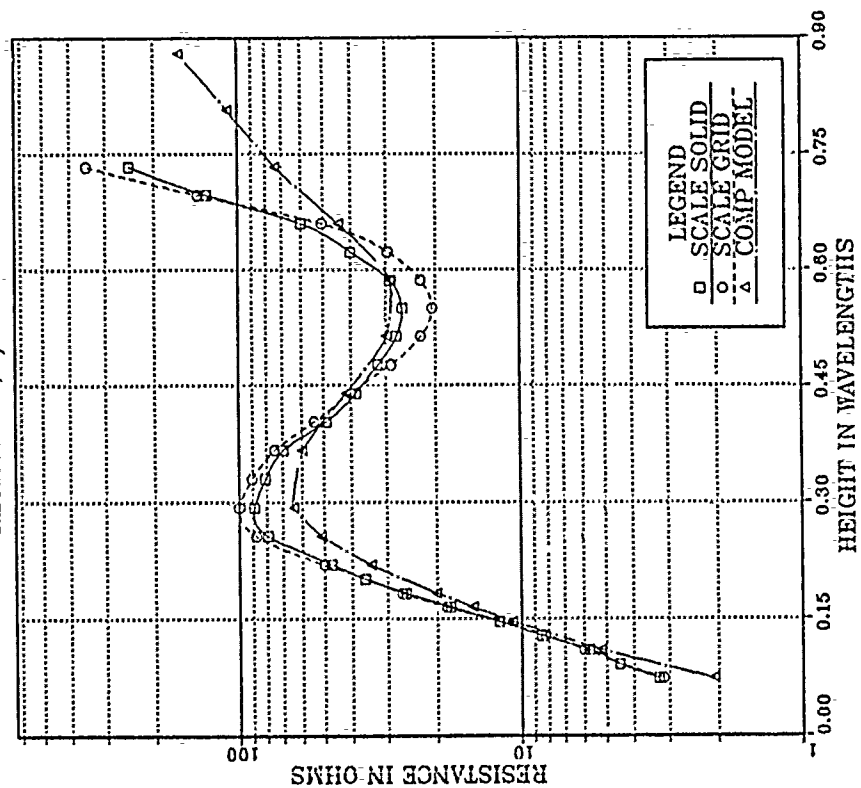


Figure 15. Resistance & reactance plots
of $W/H=2$ antenna models.



PATCH MONOPOLE
RESISTANCE, $W/H = 10$



PATCH MONOPOLE
REACTANCE, $W/H = 10$

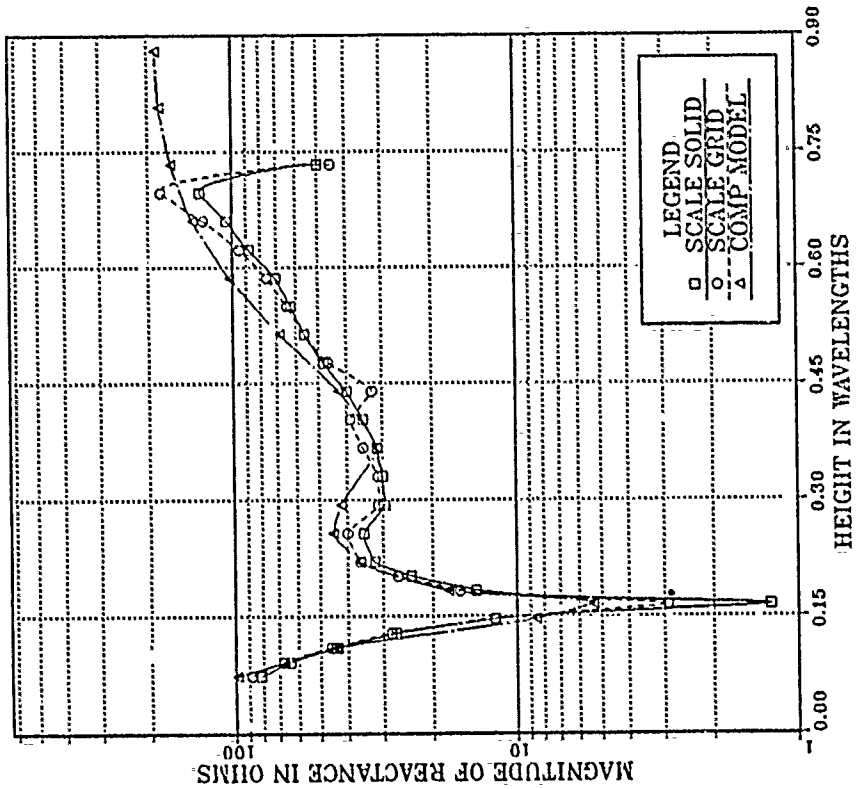


Figure 16. Resistance and reactance plots of $W/H=10$ antenna models.

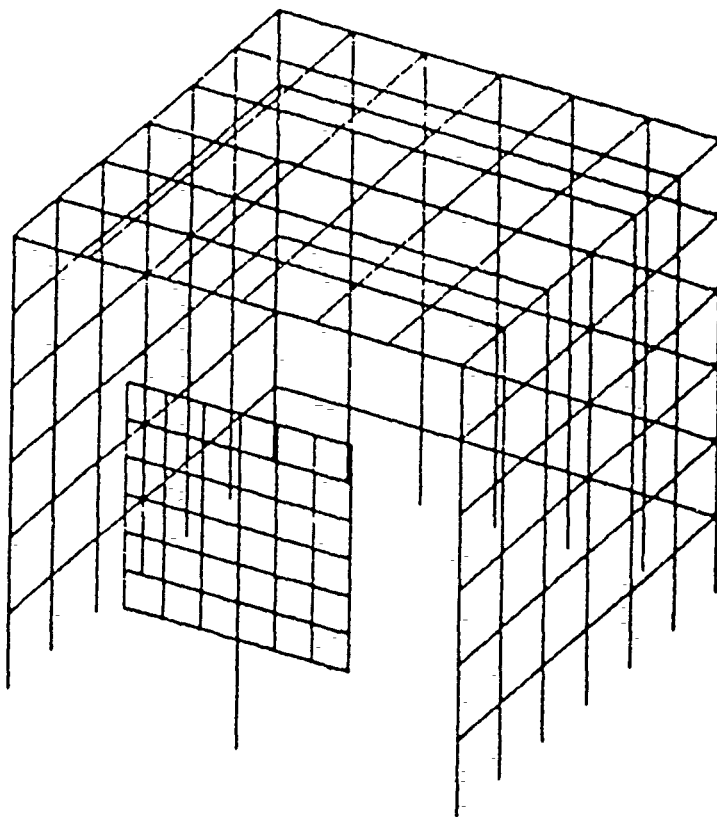


Figure 17. Patch monopole at the box face – grid model.

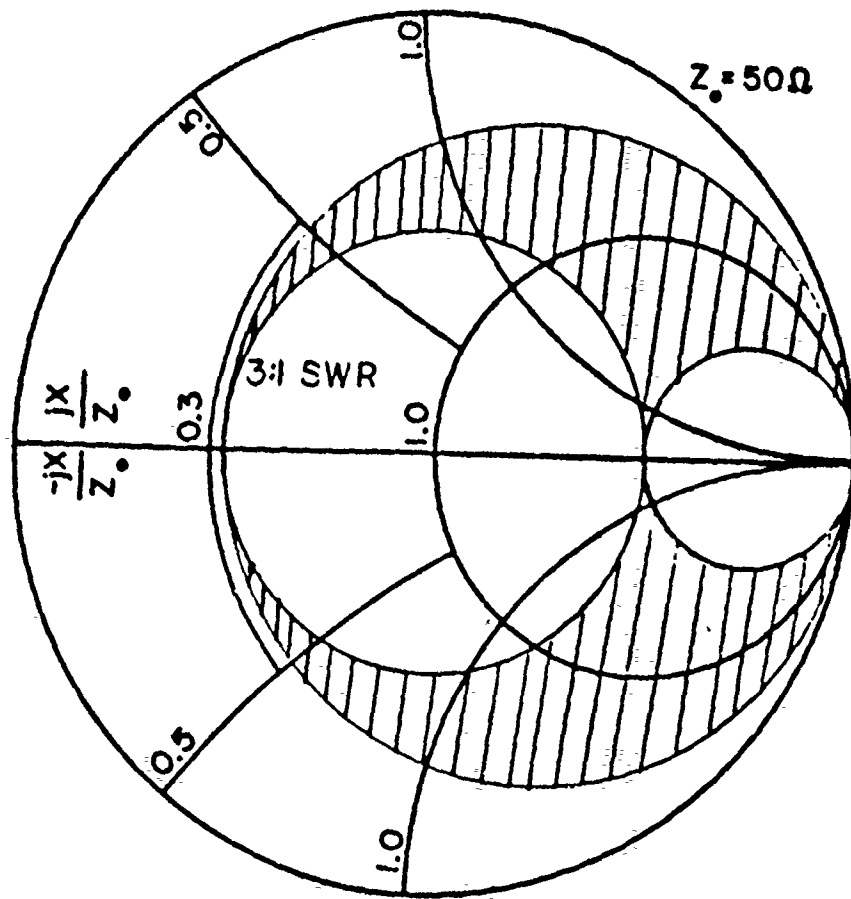


Figure 18. Smith Chart of 3:1 SWR
plus series matchable region.



LARGE ANTENNA AT BOX FACE

FREQ = 6 MHz, THETA = 60 DEG, PHI = 1 - 360 DEGS.

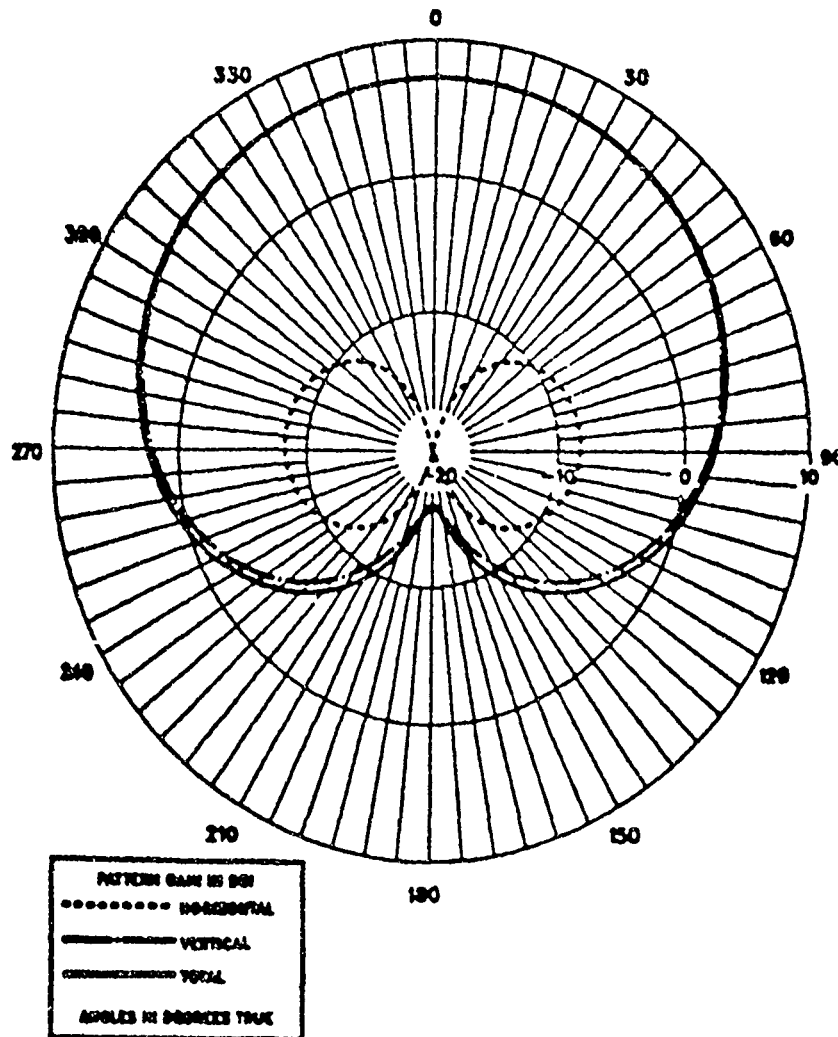


Figure 20. Horizontal pattern
for box height near .25 wavelength.

LARGE ANTENNA AT BOX FACE

FREQ = 6 MHZ, THETA = -90 - 90 DEGS, PHI = 0 DEG.

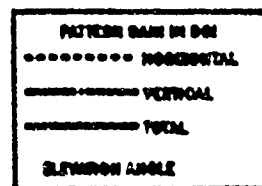
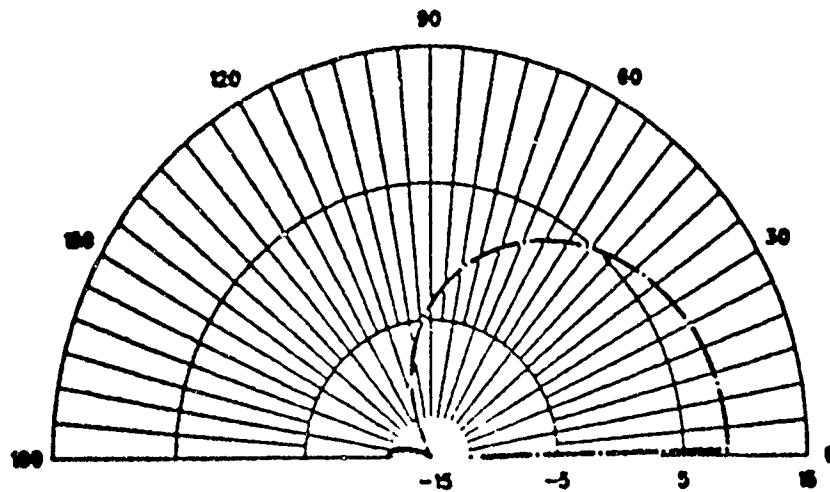


Figure 21. Vertical pattern
for the box height near .25 wavelength.

LARGE ANTENNA AT BOX FACE

FREQ = 20 MHz, $\theta = 60$ DEG, $\phi = 1 - 360$ DEGS.

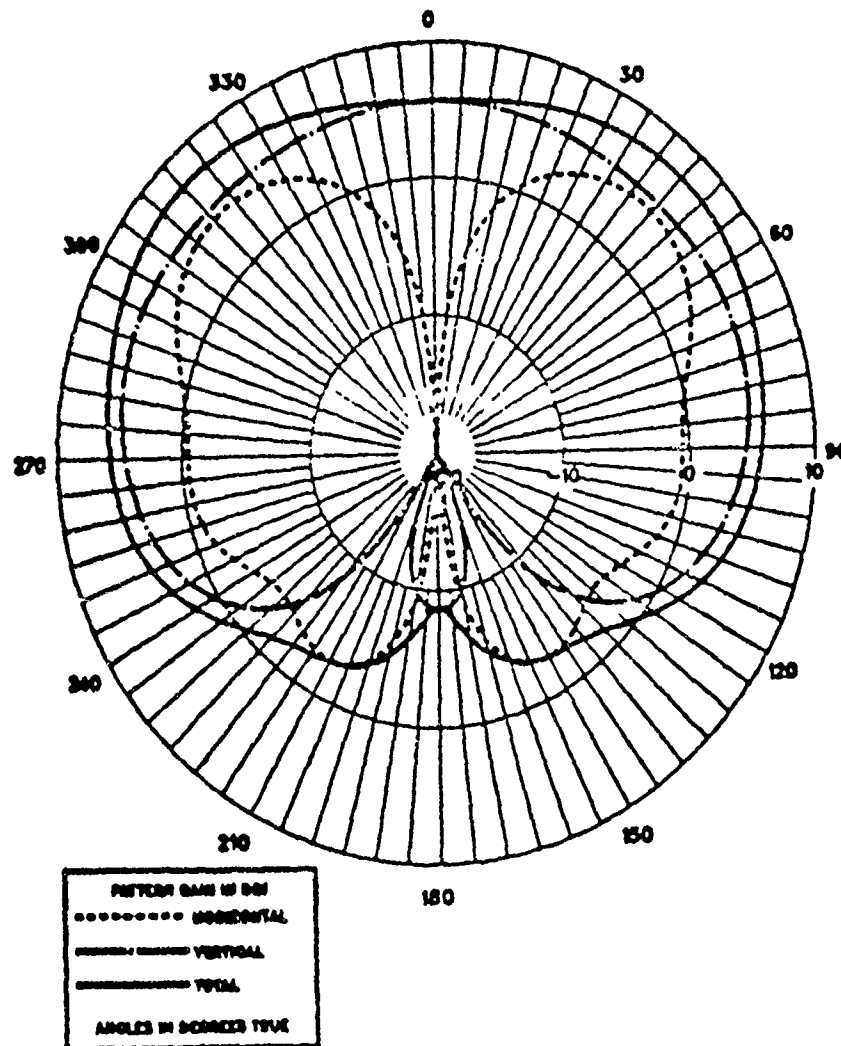


Figure 22. Typical horizontal patterns for box height greater than .5 wavelength.

LARGE ANTENNA AT BOX FACE

FREQ = 20 MHZ, THETA = -90 - 90 DEGS, PHI = 0 DEG.

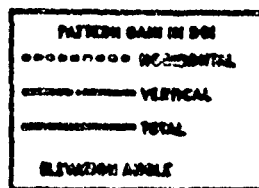
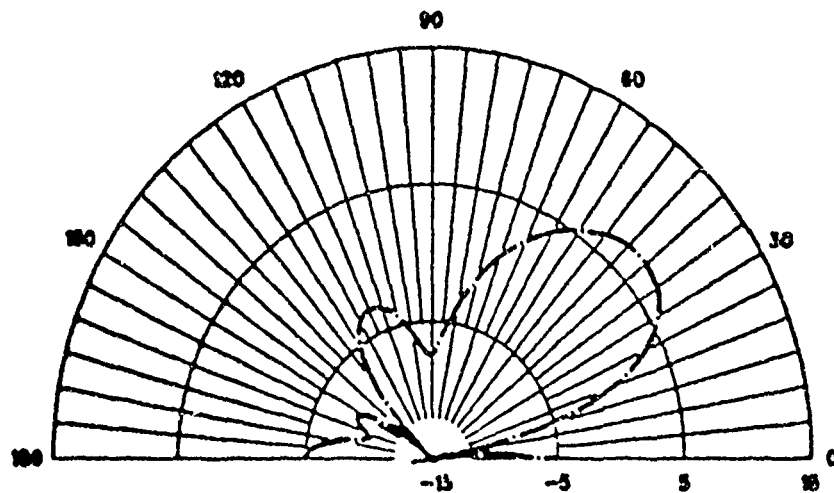


Figure 23. Typical vertical pattern for the box height greater than .5 wavelength

GROUND TREATMENT TO ENHANCE LOW
ANGLE RADIATION OF HIGH FREQUENCY
VERTICALLY POLARIZED ANTENNAS

by

Carl E. Smith
Harold J. Braschwitz
Smith Electronics, Inc.
Cleveland, Ohio

For
The Second Annual Review of Progress
in
Applied Computational Electromagnetics Society
meeting at
Naval Postgraduate School
Monterey, California
March 18-20, 1986

Smith Electronics, Inc.
8200 Snowville Road
Cleveland, Ohio 44141

GROUND TREATMENT TO ENHANCE LOW
ANGLE RADIATION OF HIGH FREQUENCY
VERTICALLY POLARIZED ANTENNAS

Carl E. Smith
Harold J. Braschwitz
Smith Electronics, Inc.
Cleveland, Ohio

ABSTRACT

The objective of the antenna engineer in designing a high frequency array for maximum range ionospheric communications is to place maximum signal as near to the horizon as possible. A second objective is often to eliminate pattern minimums in the elevation plane up to some maximum useable elevation angle, say twenty degrees.

A vertically polarized array placed close to the ground will eliminate minimums and over a perfectly conducting ground surface will place maximum signal at ground level. However, a vertically polarized array placed over a typical ground surface usually yields very disappointing results at low elevation angles, i.e. below 20°.

In this paper, a vertical polarized log periodic array over and artificial ground screen has been studied and computational results indicate good performance for various arrangements of the ground system both for high gain at low elevation angles and the absence of minimums in the elevation plane at useable low take off angles.

Computational procedures and results for obtaining array patterns over various size ground systems surrounded by typical earth conductivities are described.

GROUND TREATMENT TO ENHANCE LOW ANGLE RADIATION OF HIGH FREQUENCY VERTICALLY POLARIZED ANTENNAS

1.0 INTRODUCTION

Long Range point-to-point communications in the high frequency portion of the electromagnetic spectrum require, placing the maximum possible signal along or close to the horizon.

Propagation modes at extreme ranges are quite complex and do not always follow the same elevation and/or azimuth angle at every instant of time.

A wide range of operating frequencies are also required to achieve reliable point-to-point circuit performance over an extended period of time.

A large amount of antenna gain is also necessary to reduce transmitter power requirements or increase circuit reliability with maximum transmitter powers.

To place quantitative values on the above listed general requirements we have established the following antenna system specifications:

- (1) Elevation coverage from near zero to 20 degrees without pattern nulls or deep minimums in this sector.
- (2) Azimuthal coverage of plus or minus 8 degrees.
- (3) Antenna system gains of 10 to 20 dB/iso.
- (4) Operating frequencies of 3 to 30 MHz.
- (5) Ground conductivity of 1 to 13 mmho/m.

To achieve this result we have studied arraying five vertically polarized log periodic antennas horizontally or in the H plane. Radiating phase centers were spaced 0.7 wavelength resulting in an aperture width of about 2.8 wavelengths. Radiating phase center heights of 0.25 to 0.6 wavelengths were considered with sample curves for 0.25, 0.35 and 0.5 wavelengths presented herein. Vertical or E plane stacking of the log periodic element antennas was not desired. Arraying in this fashion would narrow the beam in the elevation plane and would make it difficult or impossible to avoid pattern minimums in the elevation sector from 0 to 20 degrees.

Vertical polarization was selected to produce maximum signal along or near the ground. We recognize that a vertically polarized signal over a real earth environment in the HF range at low elevation angles is severely attenuated. A major portion of this paper is devoted to this problem.

Horizontal polarization was also considered and discarded because of the problems involved in achieving low angle coverage along with eliminating minimums in the elevation sector up to 20 degrees. High radiating phase centers are required for obtaining low angle coverage and this also results in beam splitting problems at relatively low elevation angles.

To improve the low angle performance of vertically polarized radiators studies were made to determine the effect of placing conductive ground screens below and in front of the antenna.

Common practice in medium frequency broadcast antenna applications is to use 120 quarter wavelength radials extending from the base of the vertical radiating element. Such a ground system is used primarily to stabilize the antenna impedance.

Our work considered the effect of placing highly conductive ground screens extending a considerable distance from the radiator to not only stabilize impedance characteristics but to alter and improve low elevation angle radiation pattern performance.

Ground screens extending up to 5000 feet from the radiator were studied and some of the results are presented in this paper. The effect of high and low conductivity earth beyond the end of the various conductive ground screens have been included.

The primary results shown in this paper are the elevation patterns of an isotropic, vertically polarized radiator over the various composite conductive screen and real earth combinations.

Procedures and a sample calculation for combining this data with free space array characteristics are also included.

2.0 VERTICAL RADIATION PATTERN CHARACTERISTICS OF AN ISOTROPIC VERTICALLY POLARIZED RADIATOR

In this section sample pattern characteristics are shown where f = frequency in MHz, L = distance in feet or wavelengths λ to edge of conducting screen, σ = conductivity in mmho/m, ϵ = inductivity in farad per meter and h = vertical height of isotropic radiator in λ . Figure 1 shows the elevation and plan sketch of the physical layout.

Figures 2 through 9 show samples of the pattern characteristics for two values of frequency f , two values of conducting screen length L , two values of conductivity σ with corresponding inductivity ϵ combinations, and three values of height h . The pattern characteristics are also plotted showing the interesting effect of various ground screen lengths on the antenna radiating performance as shown in Figs. 10 through 17.

SMITH ELECTRONICS, INC.

These patterns can be multiplied by a directional antenna free space pattern to obtain the elevation patterns of a combined antenna ground system arrangement by means of the procedure in Appendix A of this paper.

3.0 LOG PERIODIC ARRAY GENERALIZED DESIGN EQUATION

3.1 Introduction

In a directional antenna design there are two problems to be solved, namely; (1) control the pattern shape by proper selection of pattern parameters and (2) the size of the pattern for a given amount of power depends upon the antenna system losses. This section will be devoted to molding the pattern shape by proper application of the generalized design equation.

The field strength, at a given point (P) in space, is a function of the placement of the radiating current elements along with magnitude and phase of the field strength produced by each radiating element. In other words we must know the space configuration of the radiation current elements and the individual vectors of field strength that they produce. This information can be expressed in equation form as a vector equation or only as a magnitude of the resultant field strength at unit distance which is commonly called the directional antenna pattern formula.

It is common practice to treat each radiating current element over a perfectly conducting ground plane earth and select the observation point, P, far enough away from the radiating system to assume that lines joining the radiating current elements and the observation point are parallel. This assumption, simplifies the mathematics and does not introduce appreciable error except when it is desired to deal with the near by radiation field. For near field study an even more general equation must be employed. For the far field study we will employ the above approximation.

After developing the generalized design equation for the far field and a three dimensional array of log periodic antennas (LPA's) over a perfectly conducting ground plane earth consideration will be given to the effects of various types of ground under and out in front of the LPA array in the direction of the major lobe. Also, consideration will be given to radiation pattern effects resulting from various highly conducting ground screens placed under and to various lengths out in front of the LPA array.

3.2 Space Configuration

In order to establish a system for specifying the location of each radiating current element in such a manner that the information can be used in the design equations refer to Fig. 18, which gives the azimuth plan view and the elevation plan view of the kth radiating current element with respect to the

SMITH ELECTRONICS, INC.

virtual apex. This figure clearly shows:

- (1) Space reference point, which is also the LPA virtual apex, and is the space origin point from which all distances are measured.
- (2) Space reference axis, which is a line passing through the space reference point and virtual apex. In this instance it is the azimuth center of the major lobe. In other applications it may be desirable to assign ϕ a value corresponding to the azimuth direction of the major lobe different from true north.
- (3) Azimuth of k^{th} radiating current element, ϕ_k , as shown in Fig. 18 (a) is measured clockwise in degrees from the space reference axis.
- (4) Spacing of k^{th} radiating current element, S_k , from the space reference point or virtual apex, is measured in electrical degrees along the line joining the radiating element and the virtual apex as shown in Fig. 18 (b). The horizontal plane projection of this distance is, $S_k \cos \theta_k$ as shown in Fig. 18 (b).

3.3 Three Dimension Array Configuration

Consider m in line LPA radiation current elements arranged in a horizontal circular array of n single LPA's all having the same virtual apex as shown in Fig. 19 (a). To make the design equation general we add l , the total number of stacked arrays, as shown in Fig. 19 (b). The total number of radiation elements in an array is then the product,

$$S_{lmn} = l m n \quad (1)$$

where:

S_{lmn} = total sum of radiation elements in
three dimension array

l = number of stacked radiating elements

m = number of in line radiating elements

n = number of single LPA's per layer

To clarify the radiating element numbering system the k^{th} element has a three digit subscript. As an example in Fig. 19 the k^{th} element is in the 2nd layer (of l), it is the 4th in line element (of m), and it is in the 3rd single LPA (of n). This three dimensional sketch in both plan and elevation views shows 1 to m in line elements in a single LPA. In the plan view the 1 to n single LPA's are shown and in the elevation view the 1 to l stacked $m n$ arrays are shown.

3.4 Voltage Vector Diagram

The field strength at the point P in space can be expressed as the sum of the voltage vectors in the diagram of Fig. 20. These vectors depend upon the space configuration of the three dimensional array, the vertical radiation characteristic of each radiating element, and the maximum field strength radiated

from each radiation current element.

(a) Phase Angle β_k of k^{th} Vector

The vector for the k^{th} radiating element makes an angle β_k with respect to the voltage vector reference as shown in Fig. 20. The angle β_k is a function of space phasing and time phasing. The space phasing toward observation point P in the vertical plane as shown in Fig. 18 (b) is,

$$S_k \cos (\theta + \theta_k)$$

and in the horizontal plane is,

$$S_k \cos (\phi - \phi_k + 180)$$

or since the cosine is the same for a positive or negative angle this term can be written

$$S_k \cos (\phi_k - \phi)$$

while the time phase term is simply ψ_k .

The k^{th} radiating element then appears to have the space phasing, to a plane through the virtual apex and perpendicular to the direction of the observation point P, of

$$S_k \cos (\theta + \theta_k) \cos (\phi_k - \phi)$$

Adding the time phase term, ψ_k , we have,

$$\beta_k = S_k \cos (\theta + \theta_k) \cos (\phi_k - \phi) + \psi_k \quad (2)$$

where:

β_k = phase relation of the field strength at the observation point P for the k^{th} radiating element taken with respect to the voltage reference axis, degrees.

S_k = electrical length of spacing of k^{th} radiating element to the space reference point, or virtual apex, degrees,

θ = elevation angle of observation point P measured up from horizon, degrees,

θ_k = elevation angle of k^{th} radiating element measured up from horizon, degrees,

ϕ = horizontal azimuth angle of the direction to the observation point P measured from the space reference axis, degrees,

ϕ_k = horizontal azimuth angle of k^{th} radiating element measured from the space reference axis, degrees,

ψ_k = time phasing of k^{th} radiating element taken with respect to the voltage vector reference axis, degrees.

B_k in Eq. (2) is the complete expression for the space and time phasing of the k^{th} radiating element and for any observation point P in the hemisphere.

(b) Magnitude $E_k f_k (\phi', \theta)$ of k^{th} Vector

The vector for the k^{th} radiating element, as shown in Fig. 20, has a magnitude of,

$$E_k f_k (\phi', \theta)$$

where:

E_k = magnitude of the field strength at unit distance, P , of the k^{th} radiating element taken in the direction of the voltage reference axis which is usually the maximum field, volts per meter

$f_k (\phi', \theta)$ = vertical radiation characteristic of the k^{th} radiating element.

This function has a value of unity in the direction of the maximum field.

In the case of vertical polarization each vertical radiating element can be assumed to be omnidirectional in the azimuth plane, hence the vertical radiation characteristic of each radiating element will be a function of only the elevation angle θ and the magnitude E_k will be a maximum when the elevation angle $\theta = 0$. The azimuth angle ϕ' can be omitted.

However, in the case of horizontal polarization the pattern is omnidirectional in the vertical plane perpendicular to the axis of the dipole where the magnitude E_k will be maximum, and the radiation characteristic will be a function only of the azimuth angle ϕ' measured from the vertical plane bisecting the dipole. Referring to Fig. 18 (a) the horizontal dipole radiation characteristic azimuth angle from the observation point P is,

$$\phi' = \phi - \phi_k + 180$$

3.5 Generalized Three Dimension Array Equation

The three dimension geometry is shown in Figs. 18 and 19 and the voltage vector summation is shown in Fig. 20. Combining the magnitude term given above and the phase relation term of Eq. (2) we can write,

$$E = \sum_{k=1}^{l m n} E_k f_k (\phi, \theta) \angle \beta_k \quad (3)$$

where: E = total effective field strength vector at unit distance (P) from the three dimension LPA array with respect to the voltage reference axis, volts per meter,

$k = k^{\text{th}}$ radiating element in LPA,

m = total number of in line radiating elements in single LPA,

n = total number of single LPA's in each layer,

l = total number of stacked $m n$ array layers,

and the other terms are defined above following Eq. (2)

4.0 EXAMPLE OF A LOG PERIODIC ANTENNA ARRAY

Consider the array composed of five log periodic antennas arrayed as shown in Fig. 19 (a). Each LPA has an alpha angle of 2° , a Tau ratio of 0.975, and height of radiating phase center of 0.5λ . The LPA's are arranged in a circular configuration with a horizontal or H plane spacing of 0.7 wavelengths. Experimental pattern range measurements show that the single element pattern in the elevation plane is given by Fig. 21 and the single LPA pattern in the azimuth plane is given by Fig. 22. The calculated azimuthal array pattern over an infinite expanse perfect ground is shown in Fig. 23. We assume that the array azimuthal pattern is unchanged over a conductive ground screen - real earth environment. We also assume that the free space elevation pattern of the array is the same as the free space pattern of a single LPA.

The array described is then placed over a conductive ground screen - real earth arrangement shown in Fig. 24. The predicted antenna-ground system elevation pattern at zero degrees azimuth is shown in Figs. 25, 26, 27 and 28.

5.0 CONCLUSIONS

This paper is a contribution to the state-of-the art with regard to the influence of the ground system design on high frequency vertically polarized antenna pattern control at low elevation angles. The importance of the ground system design in achieving satisfactory performance from a LPA array of this nature can not be over emphasized. The ground screen design used in the example illustrates an approach to obtain good performance over the high frequency range.

In preparing this paper it has been necessary to restrict our selection to only a few examples of ground system and LPA array combinations. Considerable additional data is available at Smith Electronics, Inc. for other antenna-ground system combinations at frequencies within the high frequency range.

6.0 REFERENCES

- (1) Smith, Carl E., "Theory and Design of Directional Antennas", Cleveland, Institute of Electronics, Cleveland, Ohio, 1959.
- (2) Smith, Carl E., Editor, "Log Periodic Antenna Design Handbook". Smith Electronics, Inc., Cleveland, Ohio, 1966.
- (3) Wait, J. R., "Electromagnetic Waves in Stratified Media", The MacMillan Company, New York, 1962.
- (4) Smith Electronics, Inc., "Navy VLF Site Location Project". November 1956.
- (5) Smith Electronics, Inc., "Navy VLF Ground System Design". May 1957.
- (6) Gustafson, W. M., Chase, W. M., and Balli, N. H., "Ground System Effects on High Frequency Antenna Propagation", U. S. Navy Electronics Laboratory, 4 January 1966.
- (7) Bernard, G. D., Gustafson, W. E., and Chase, W. M., "HF Extended Ground Systems: Results of Numerical Analysis". U. S. Navy Electronics Laboratory, 24 February 1966.
- (8) Maley, S. W. and King, R. J., "Impedance of a Monopole Antenna with a Radial-Wire Ground System on an Imperfectly Conducting Half Space, Part I, J. Research NBS, 66D (Radio Propagation) No. 2, pp 175-180, March-April 1962.
- (9) Larson, Tove, "The E-Field and H-Field Losses Around Antennas With a Radial Ground Wire System", J. Research NBS, 66D, (Radio Propagation) No. 2, pp 189-204, March-April 1962.
- (10) Beckman, Petr and Spizzichino, Andre, "The Scattering of Electromagnetic Waves from Rough Surfaces", The MacMillan Company, New York 1963
- (11) Watt, A. D., "VLF Radio Engineering", International Series of Monographs in Electromagnetic Waves Vol. 14, Pergamon Press, Inc. 1967.
- (12) P. C. Clemmow, "Radio propagation over a flat earth across a boundary separating two different media", Phil Trans., Roy Soc. (London) Vol 246, pp 1-55, 1954.
- (13) I. Carswell & C. Flammer, "Ground Antenna phase behavior in a differential phase measuring system" 1957 IRE Convention Rec. pt. 1 pp 49-56.
- (14) Kosta, S. P., "A Theory of the Log-Periodic Dipole Antenna", International Journal of Electronics, 1967, Vol. 23, No. 5, 473-483.

SMITH ELECTRONICS, INC.

7.0 ACKNOWLEDGEMENTS

We wish to take this opportunity to acknowledge the contributions of Mr. Carman Malagisi of RADC, the SEI staff and especially the Heavy Military Electronics Department of the General Electric Company for providing computer results that were used extensively in this study.

APPENDIX A

8.0 PROCEDURE FOR GENERATING PRINCIPAL PLANE PATTERNS

The following step procedure was used to generate the principal plane elevation patterns shown in this report.

Step 1 Obtain the array free space E plane pattern. Assume that the free space vertical plane pattern of the array is the same as the free space vertical plane element antenna pattern. Rotate the axis of this pattern downward by the amount of the array θ_k angle.

Step 2 Calculate the free space gain of the array by use of the formula:

$$G = \frac{31,800}{W_E \times W_H} \quad (A-1)$$

Where:

G = gain

W_E = free space half-power E plane beamwidth, degrees

W_H = free space half-power H plane beamwidth, degrees

The gain G allows for 23% loss in maximum lobe power to supply energy to side lobes and losses in the antenna system. The azimuth beamwidth W_H will not be altered when the array is placed over an infinite conductivity ground.

Step 3 Convert the gain value obtained in Eq. (A-1) to a decibel value by use of the expression

$$\text{dB} = 10 \log G \quad (A-2)$$

Step 4 Multiply the array free space E plane pattern (Step 1) by the array free space gain obtained in Step 2 and tabulate the array gain as a function of the elevation angles of interest.

To accomplish this express the array element free space pattern (Step 1) in terms of decibels and add this result to the gain value in decibels obtained in Step 3 for all of the vertical elevation angles of interest.

Step 5 Multiply the tabulated values obtained in Step 4 by the value of the ground multiplying factor for the specific elevation angle of interest to obtain the elevation pattern of the array over the particular ground situation selected. Use the decibel values of the array free space gain at a specific elevation angle and to this add the decibel value of the ground multiplying factor at this same elevation angle to obtain the elevation pattern of the array over the particular ground conditions to be studied.

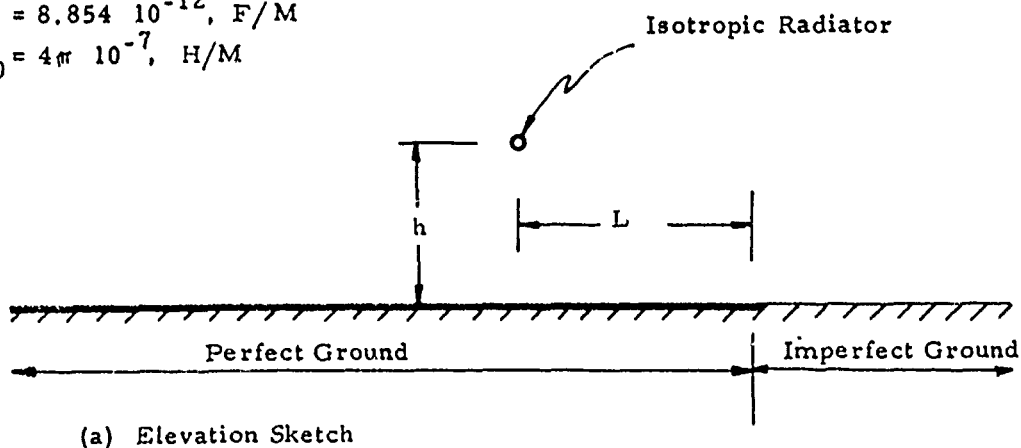
SMITH ELECTRONICS, INC.

Free Space Constants:

$$\sigma_0 = 0, \text{ mho/m}$$

$$\epsilon_0 = 8.854 \cdot 10^{-12}, \text{ F/M}$$

$$\mu_0 = 4\pi \cdot 10^{-7}, \text{ H/M}$$



Ground Constants:

$$\sigma_1 = \text{infinity, mho/m}$$

$$\epsilon_1 = \text{infinity, F/M}$$

$$\mu_1 = \mu_0, \text{ H/M}$$

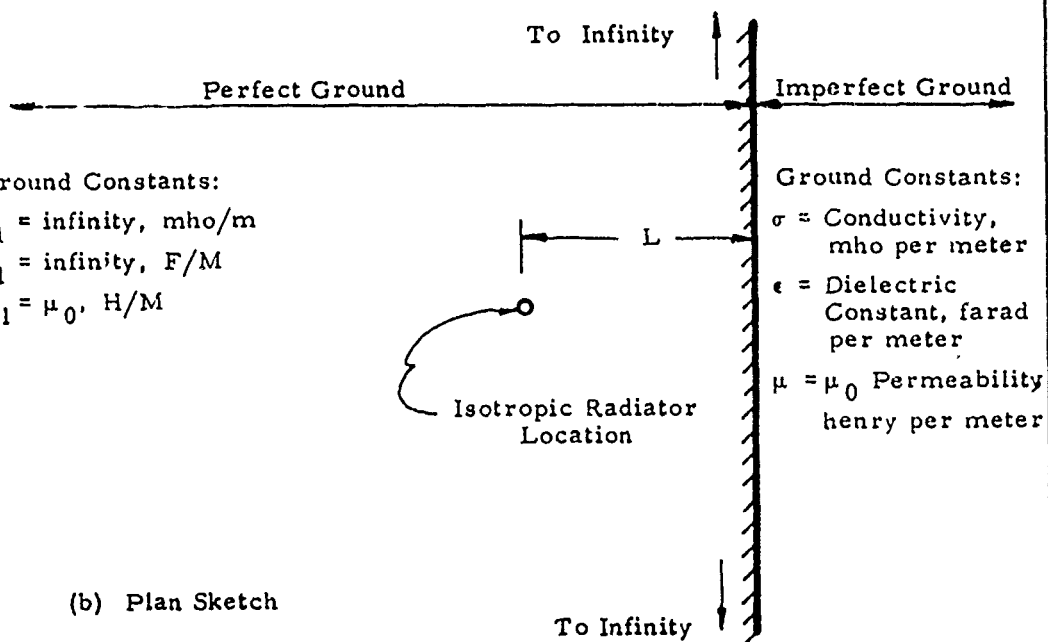


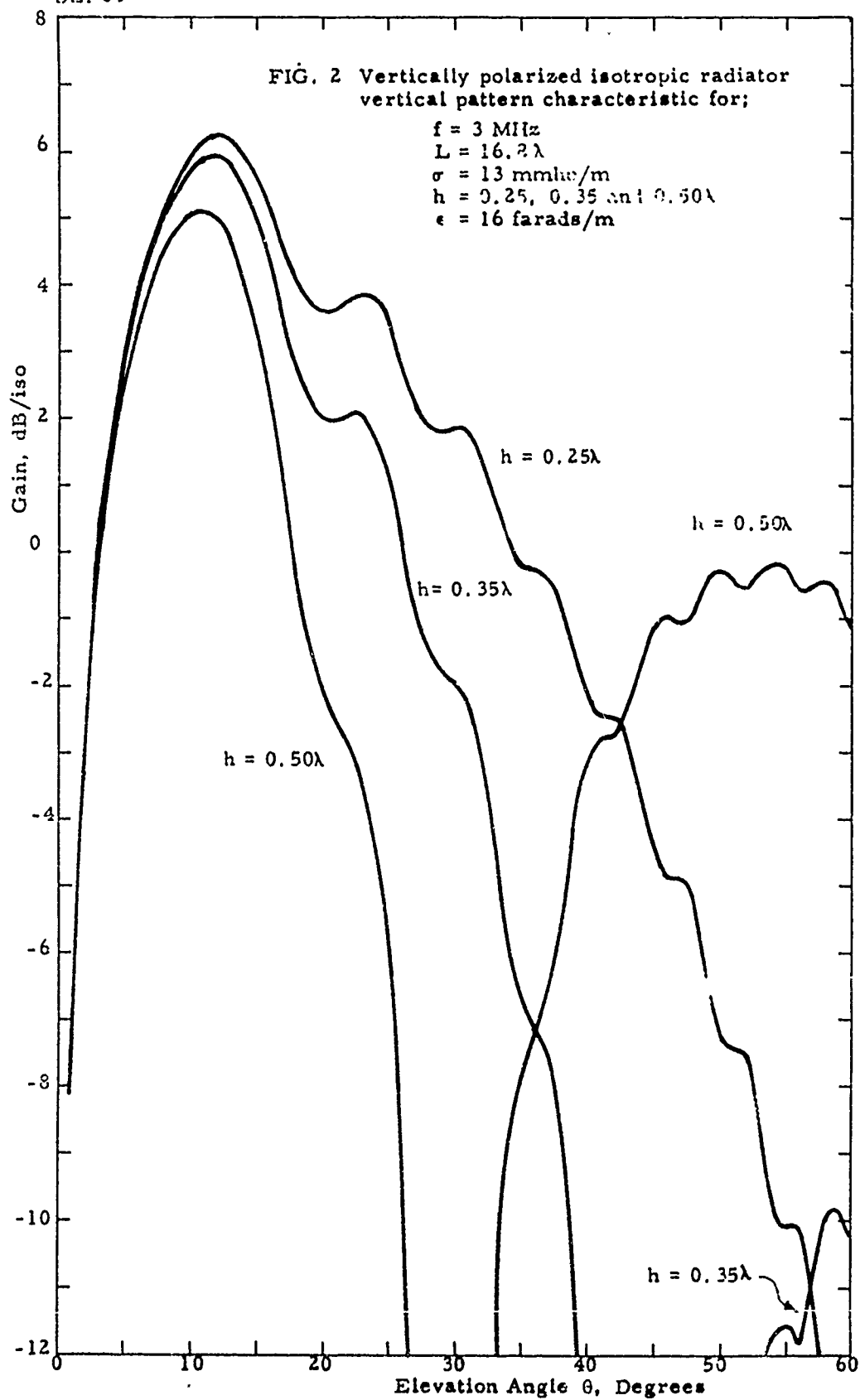
FIG. 1

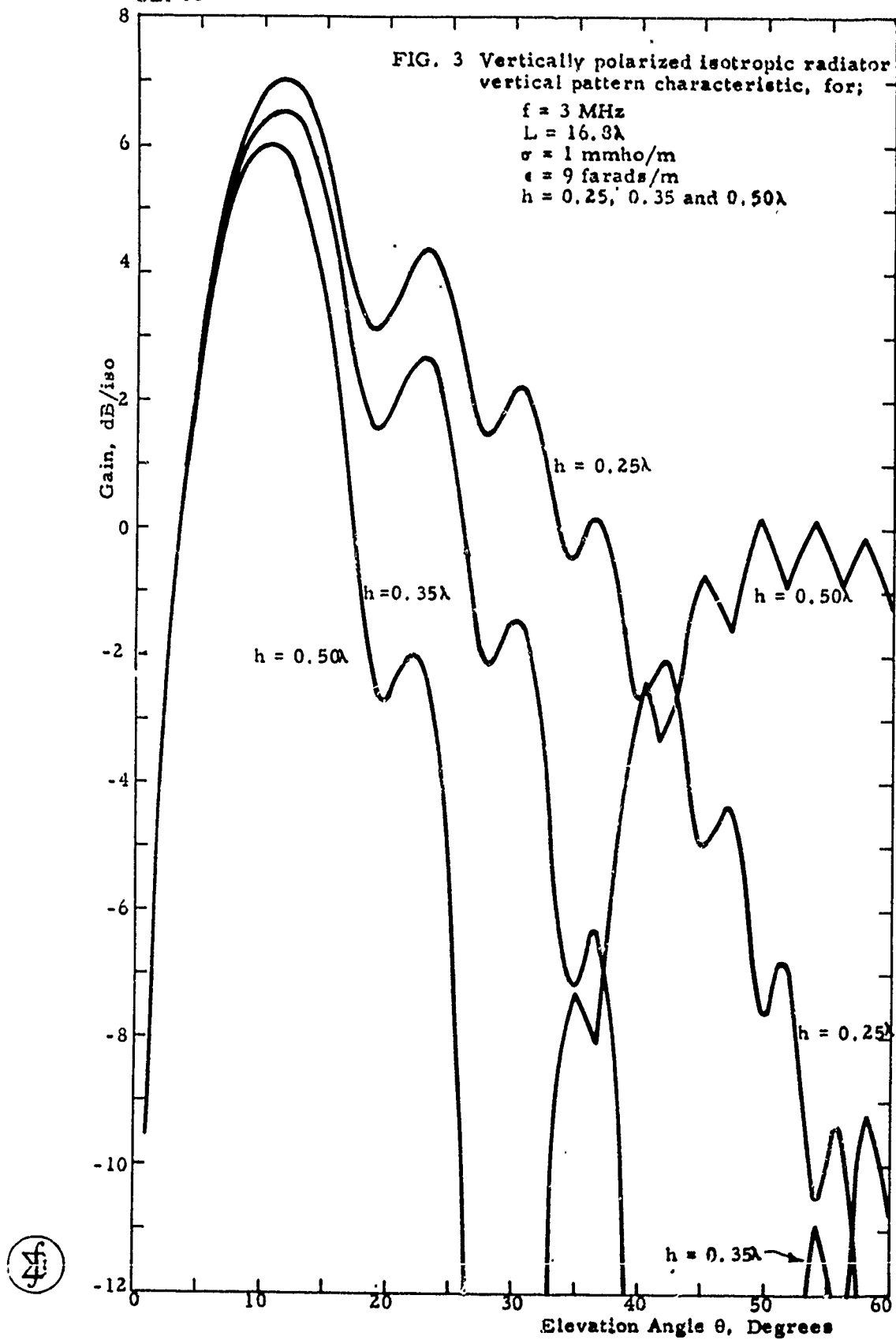
Sketch of isotropic radiator located at a height h above perfect ground and a horizontal distance L from imperfect ground

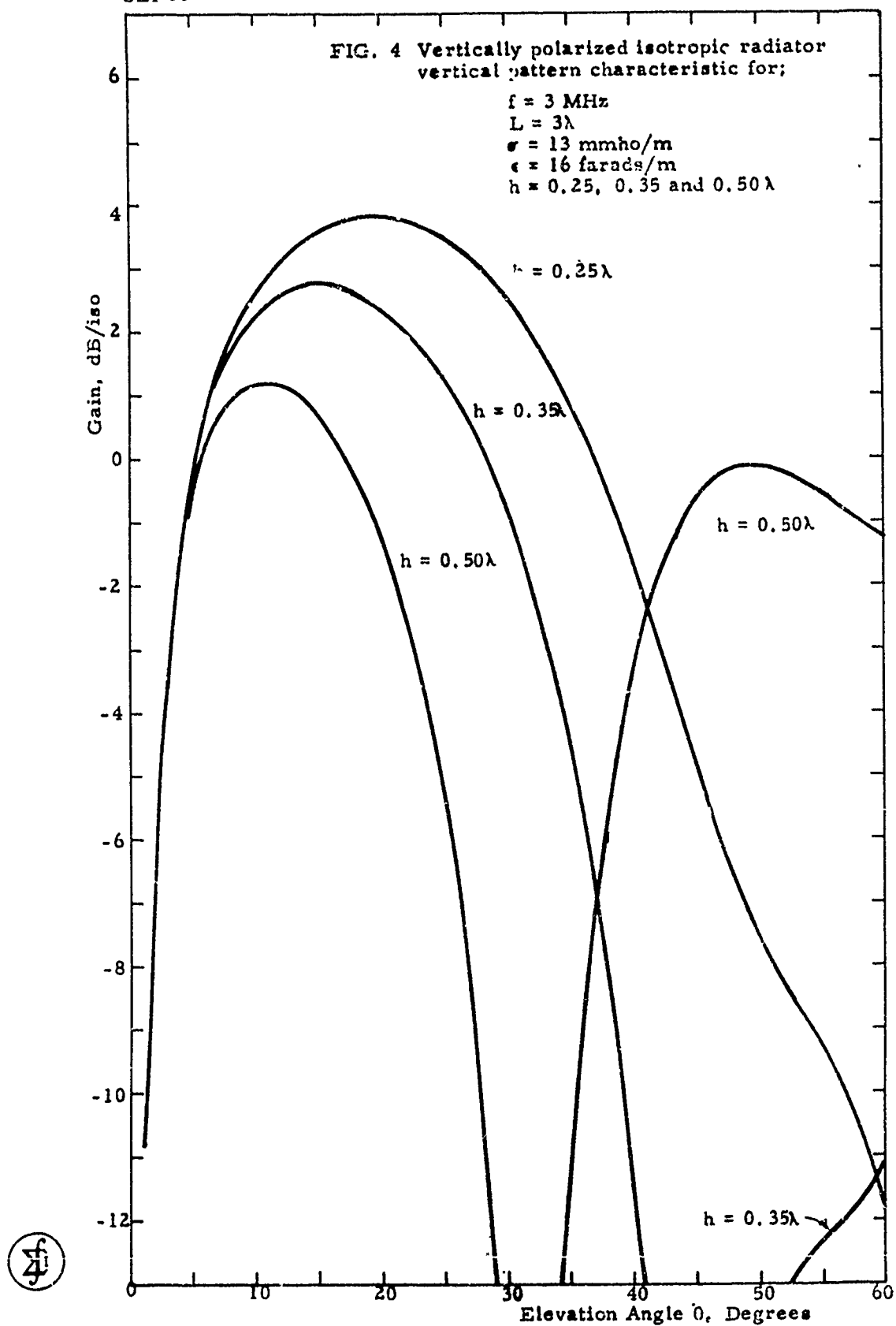


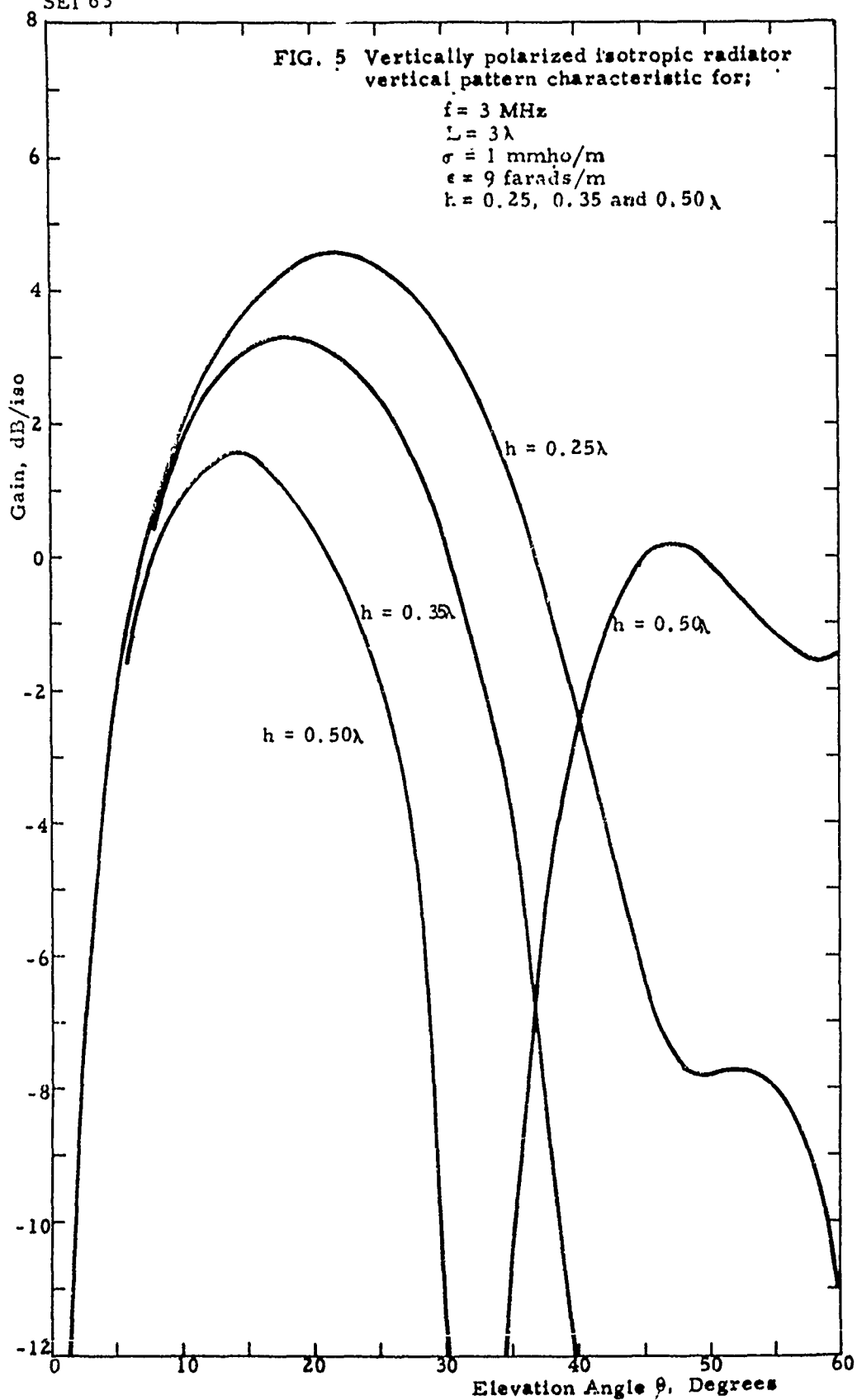
670428

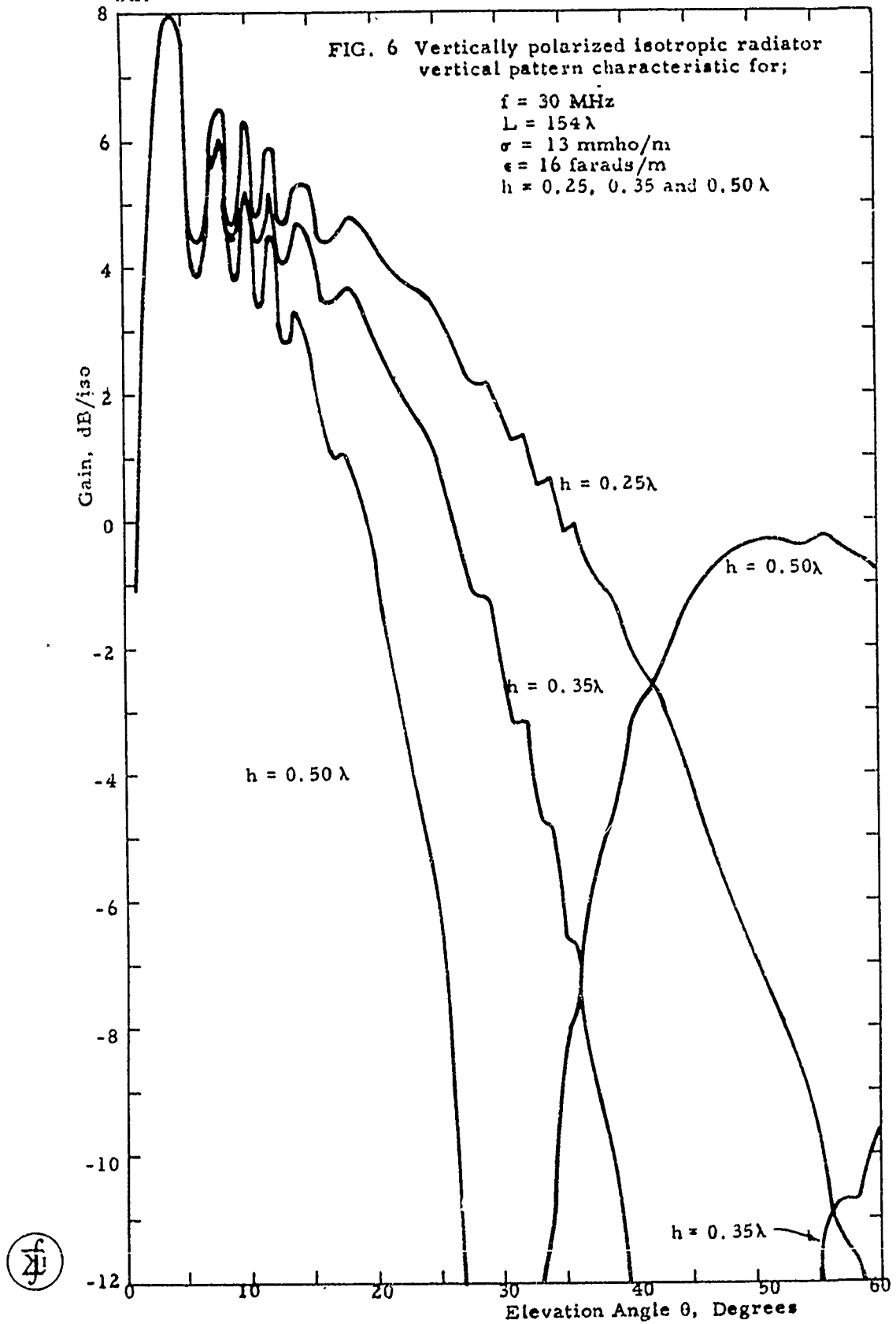
SEI 63



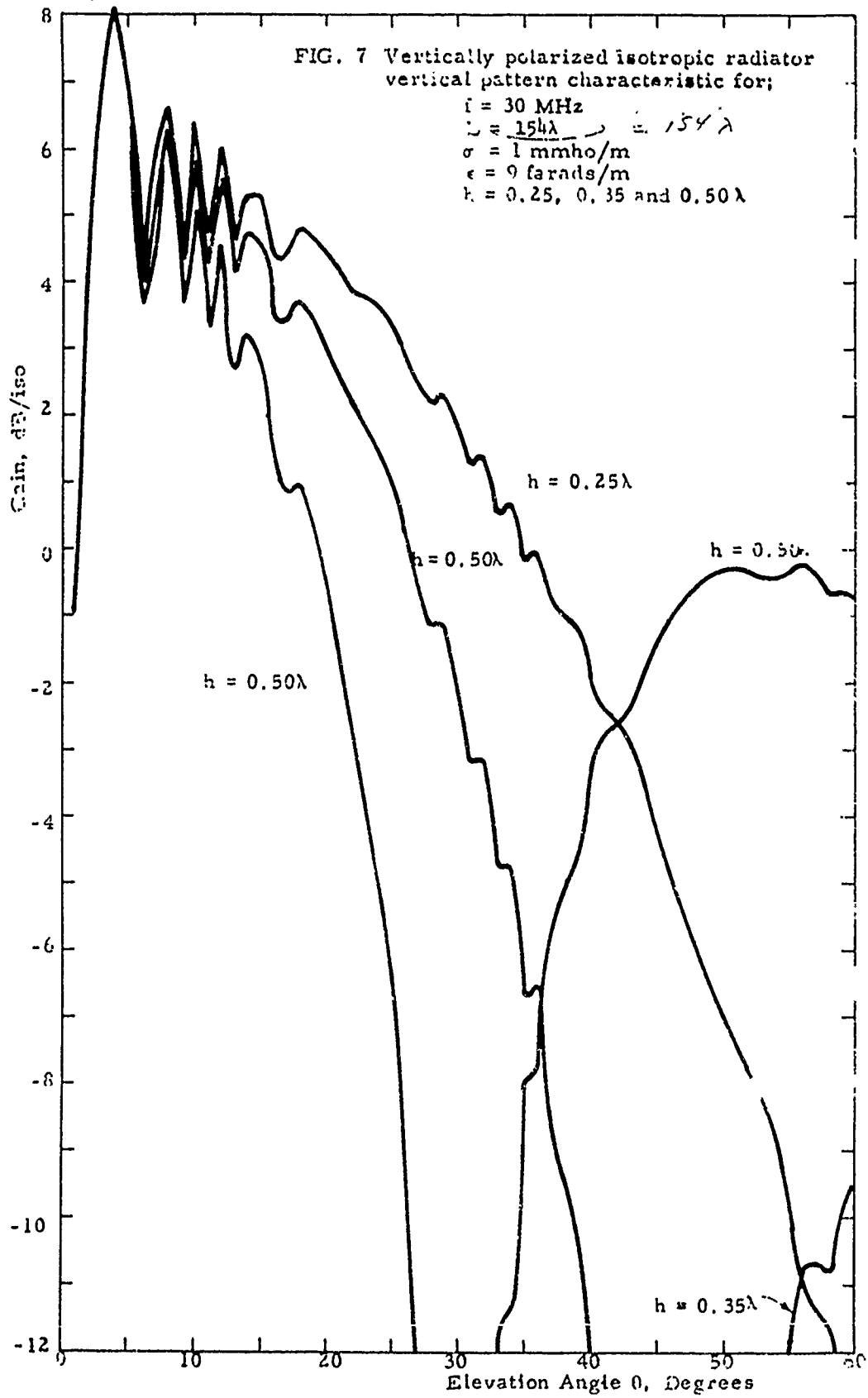


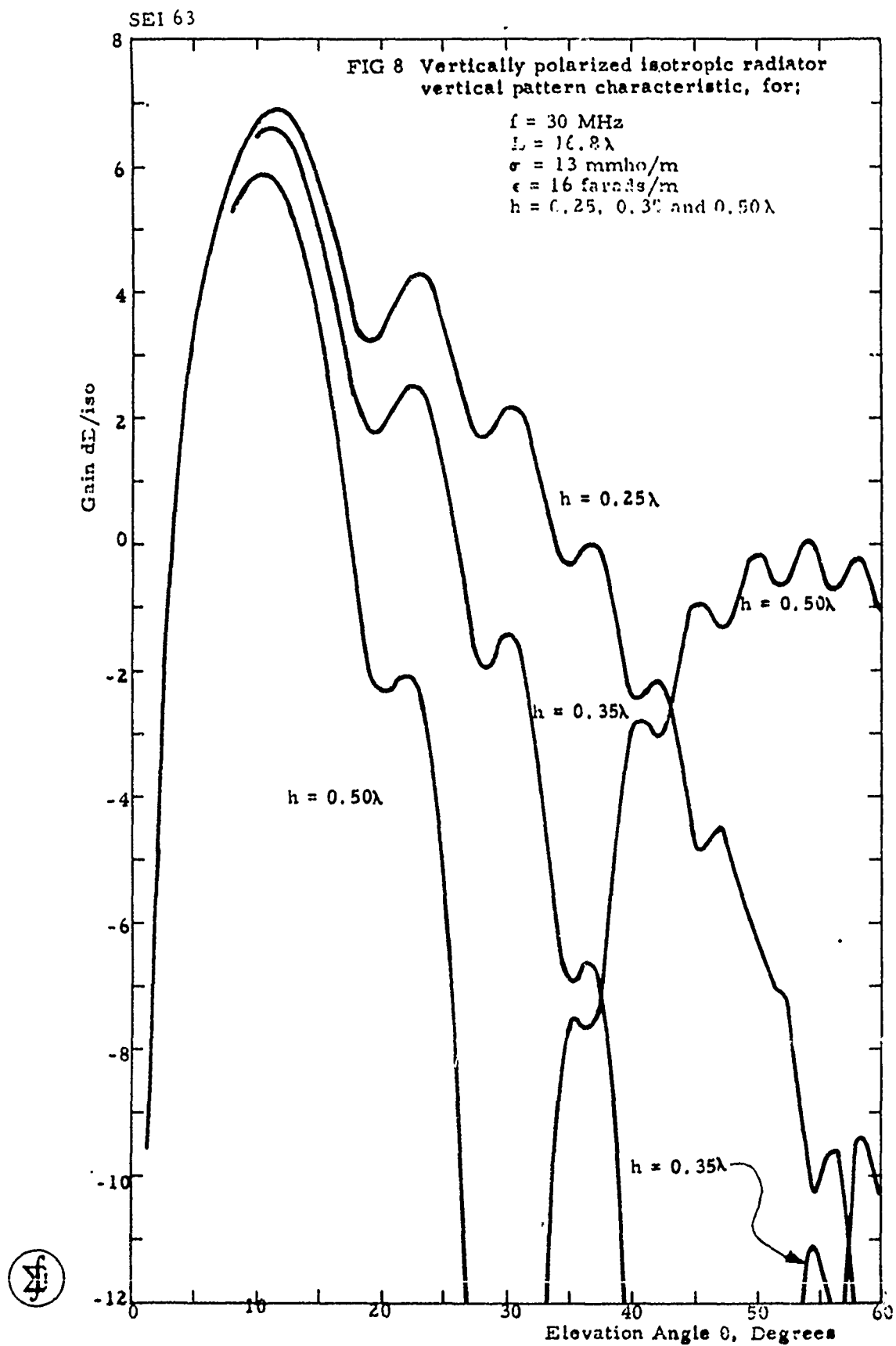






SET 63







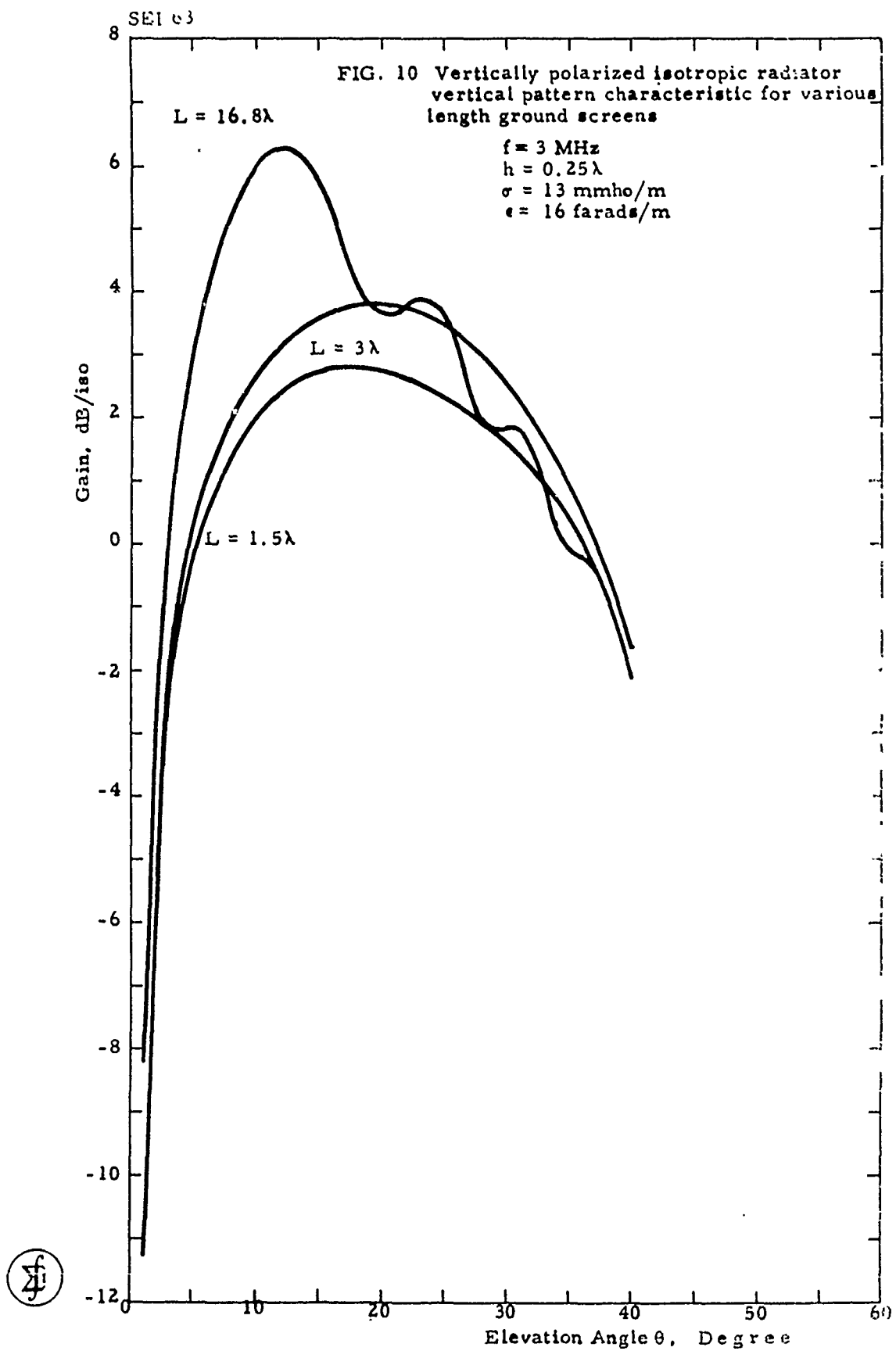
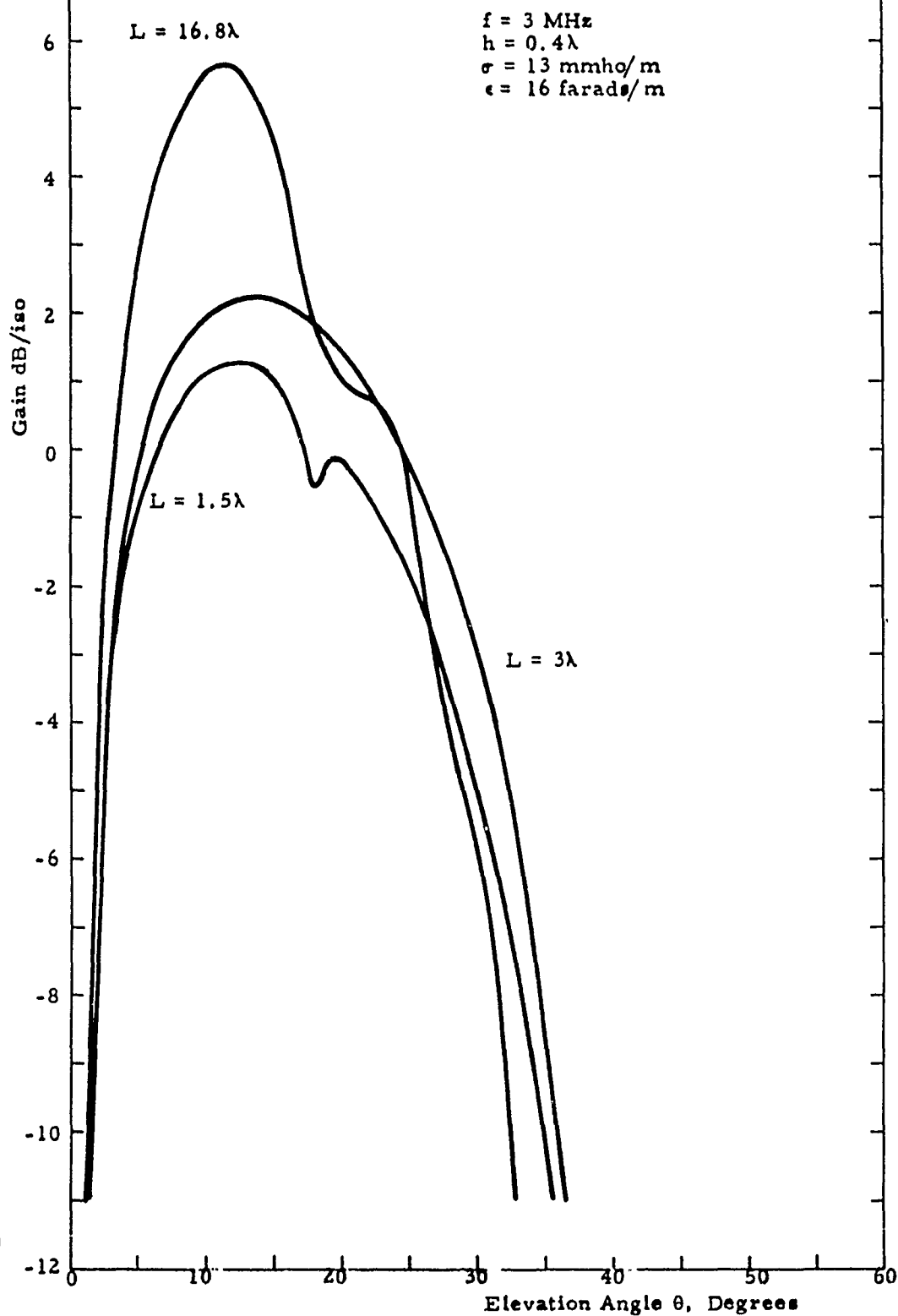
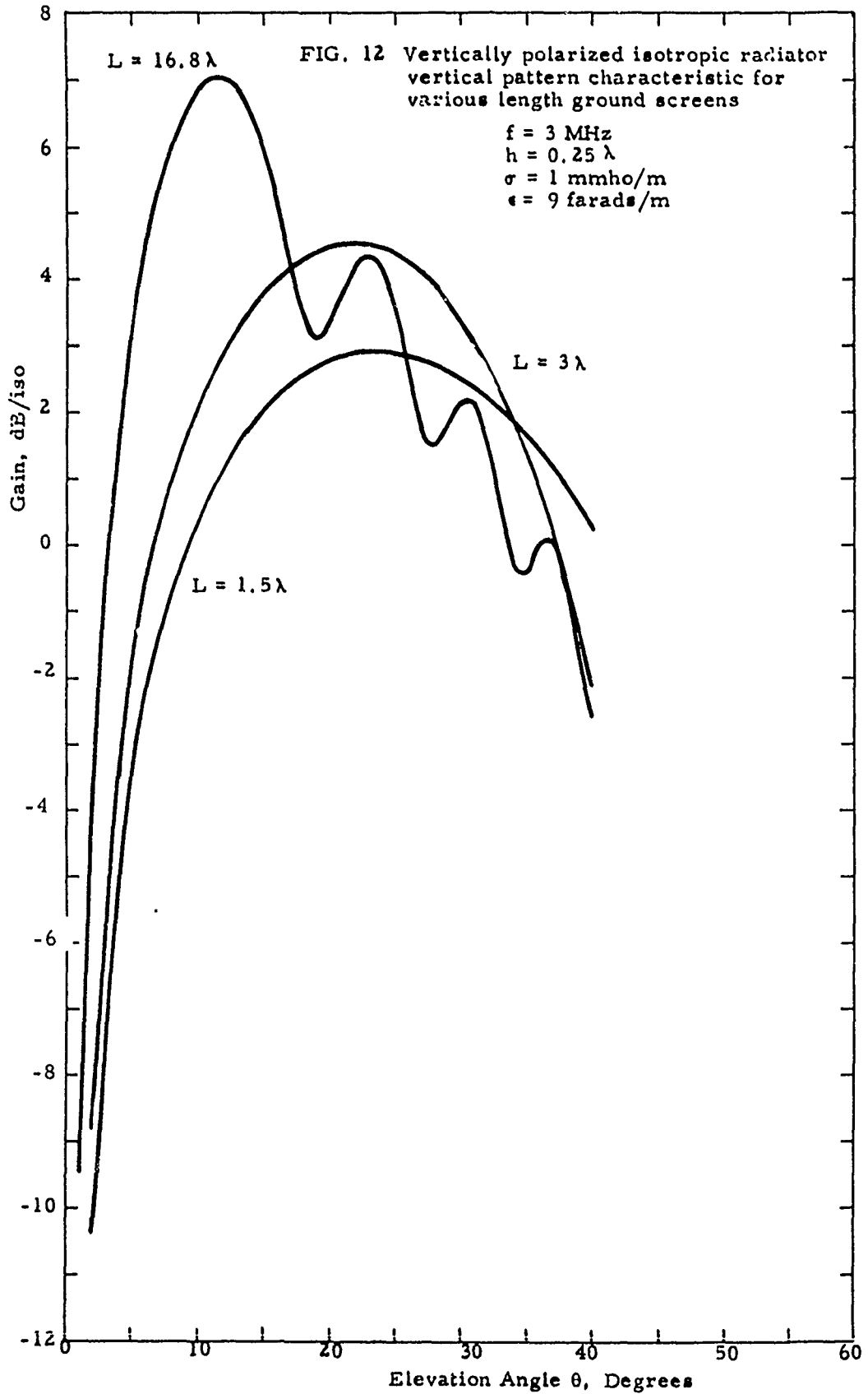
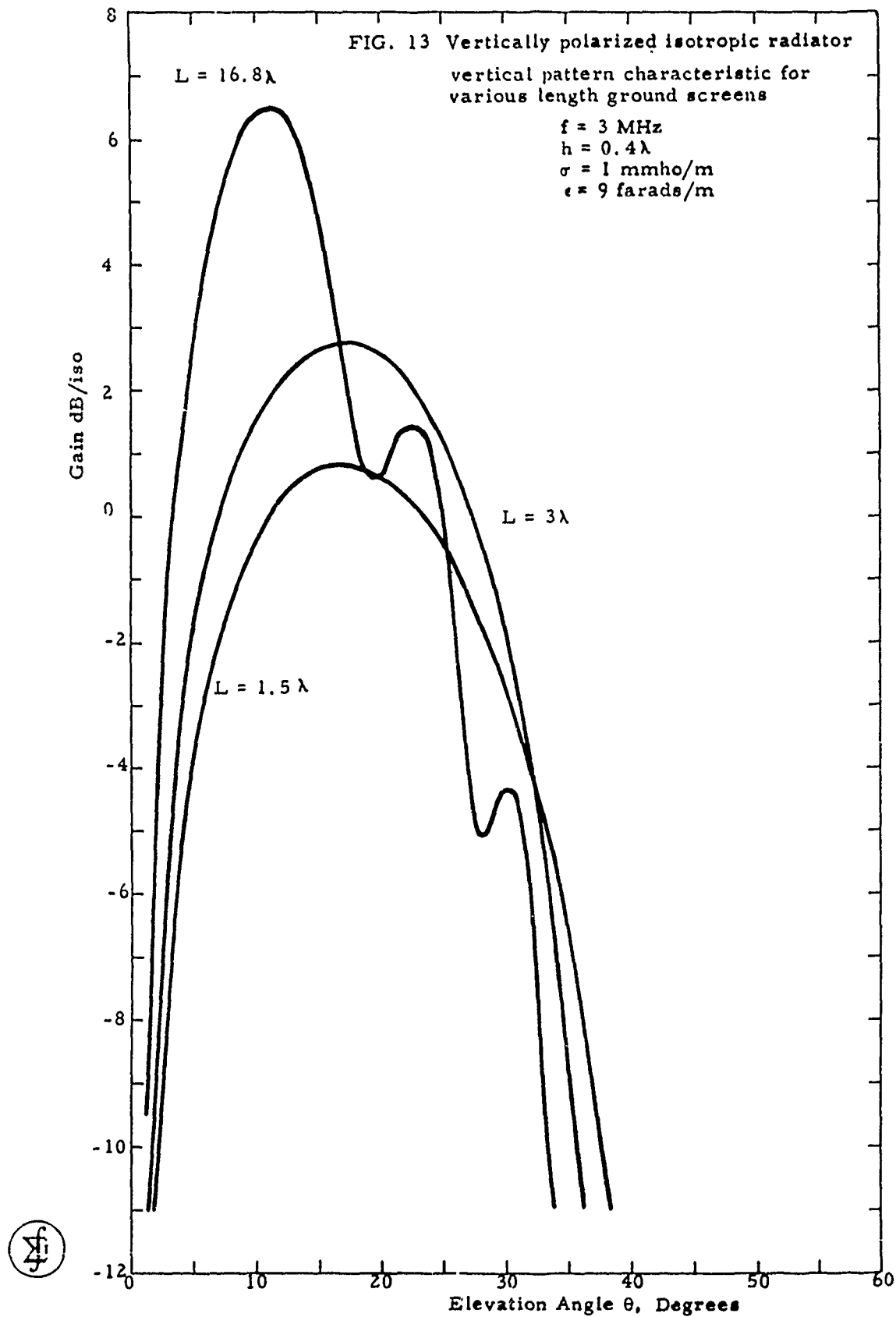


FIG. 11 Vertically polarized isotropic radiator
vertical pattern characteristic for
various length ground screens

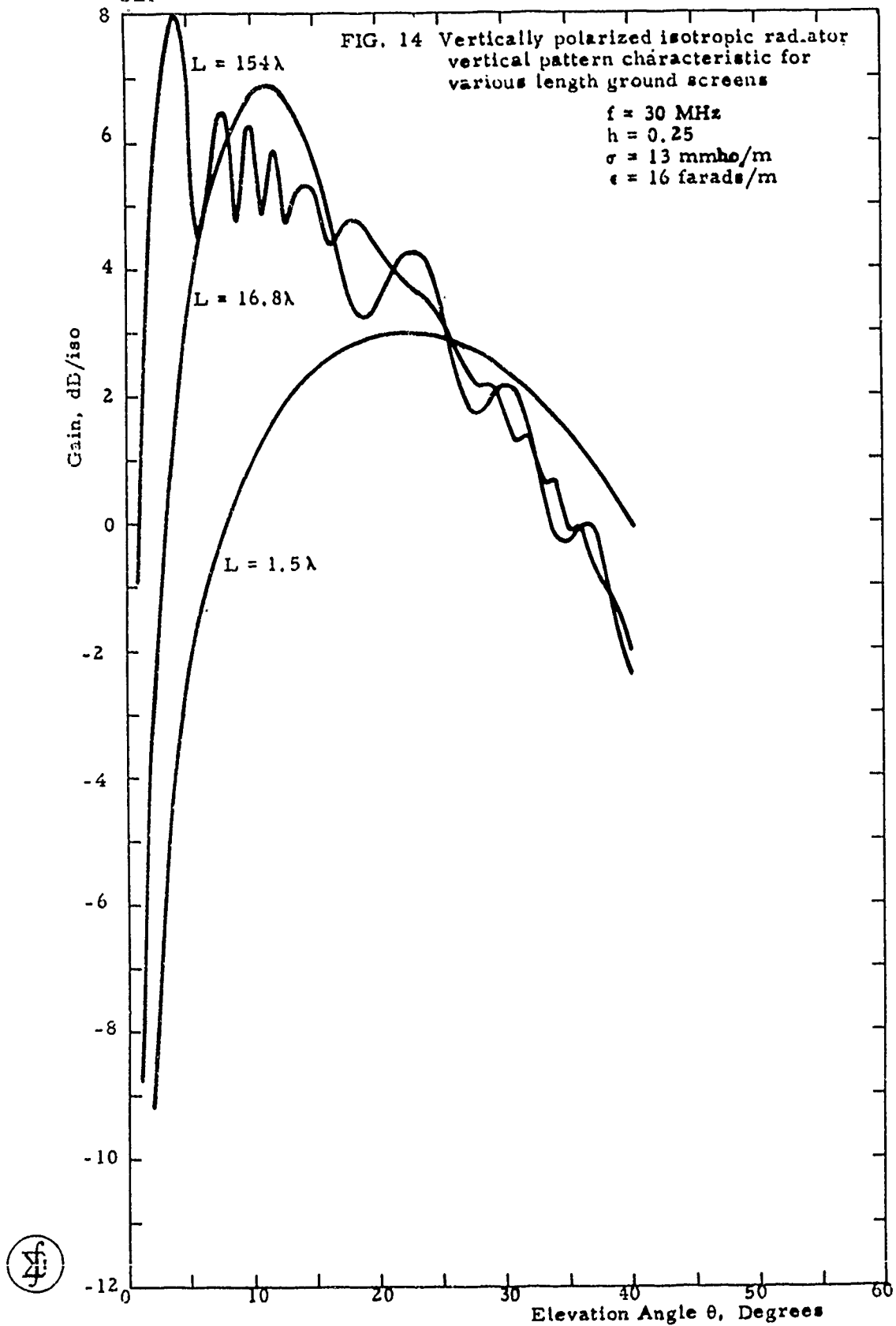


SEI 63

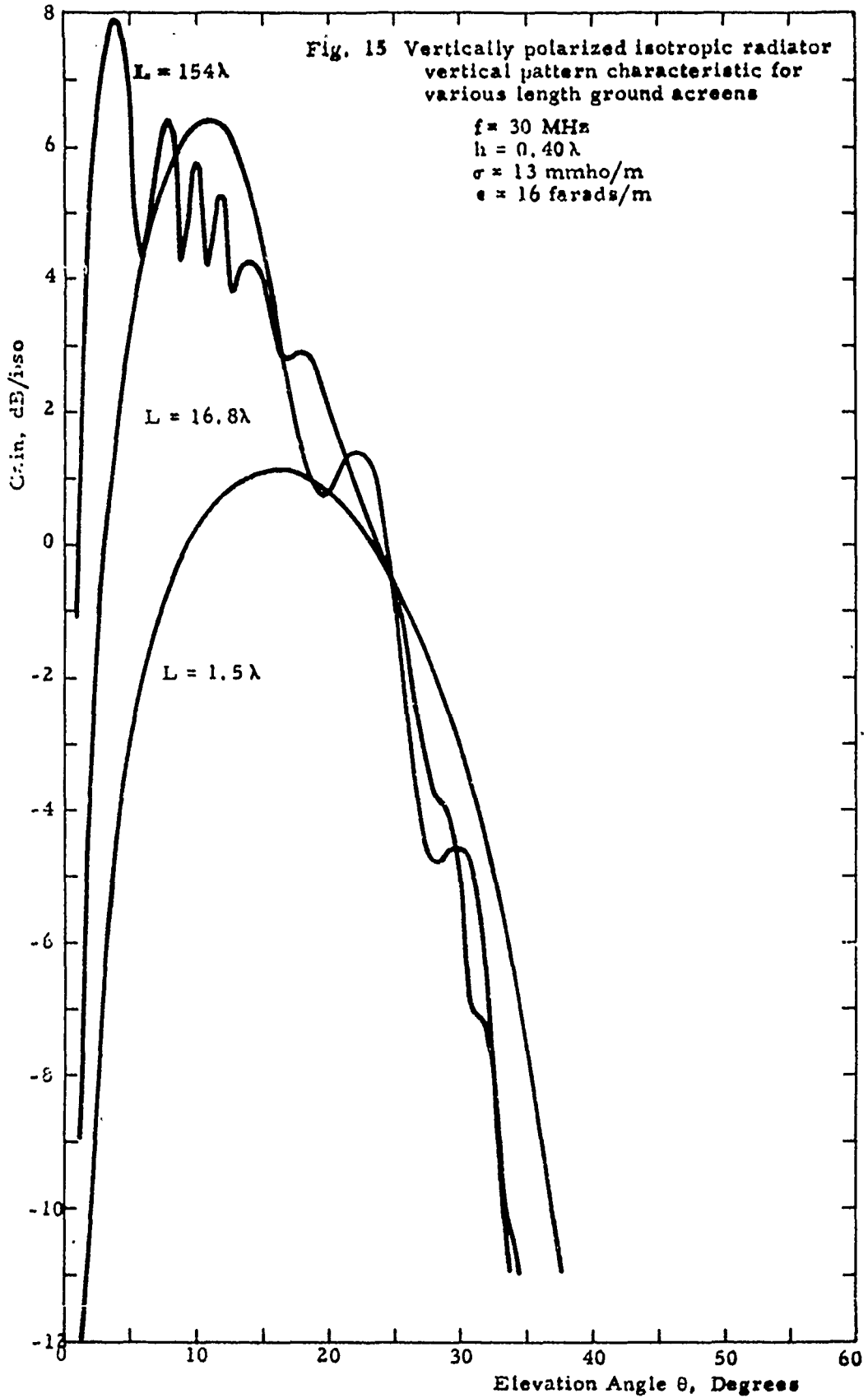




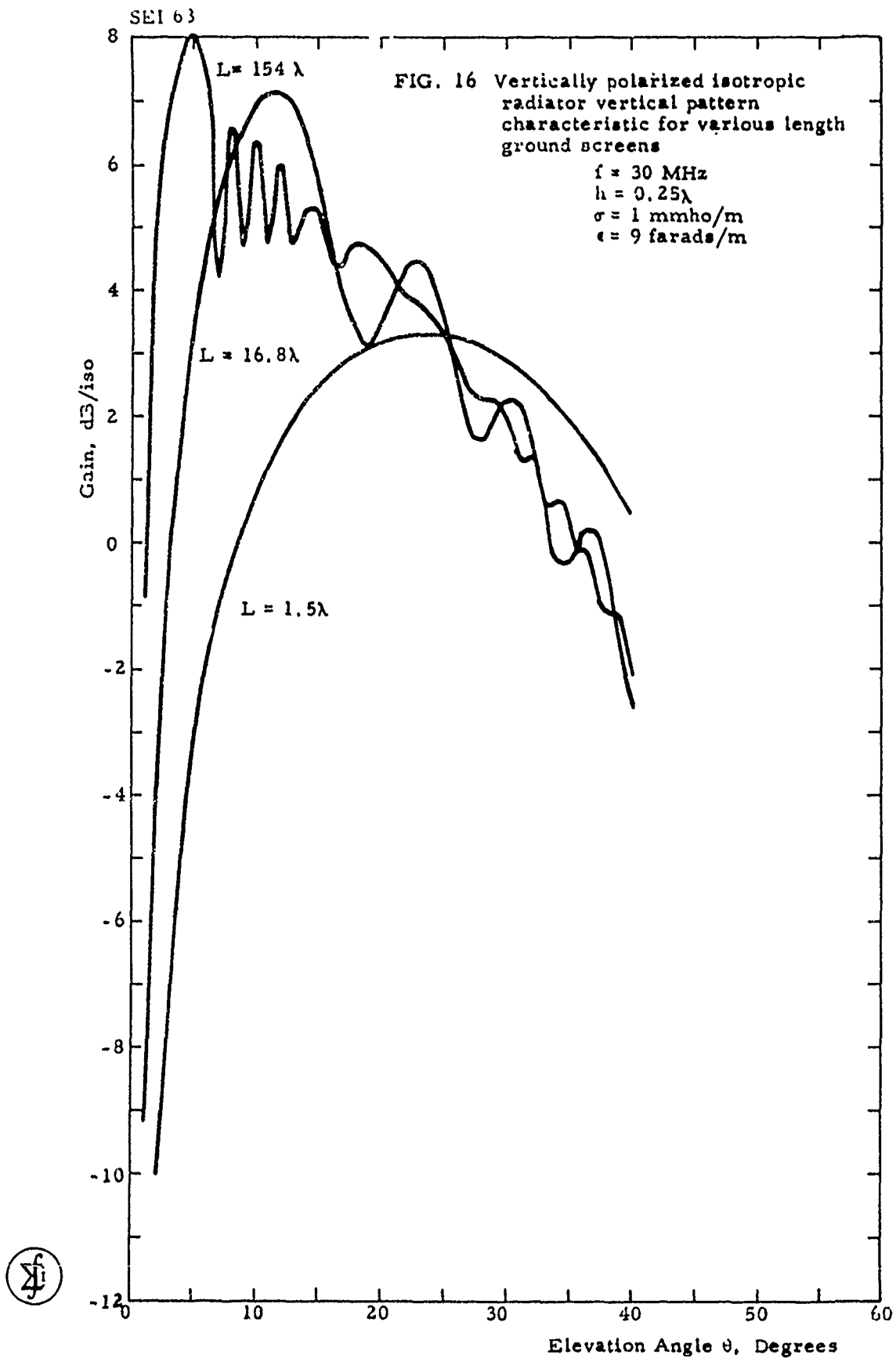
SEI 63



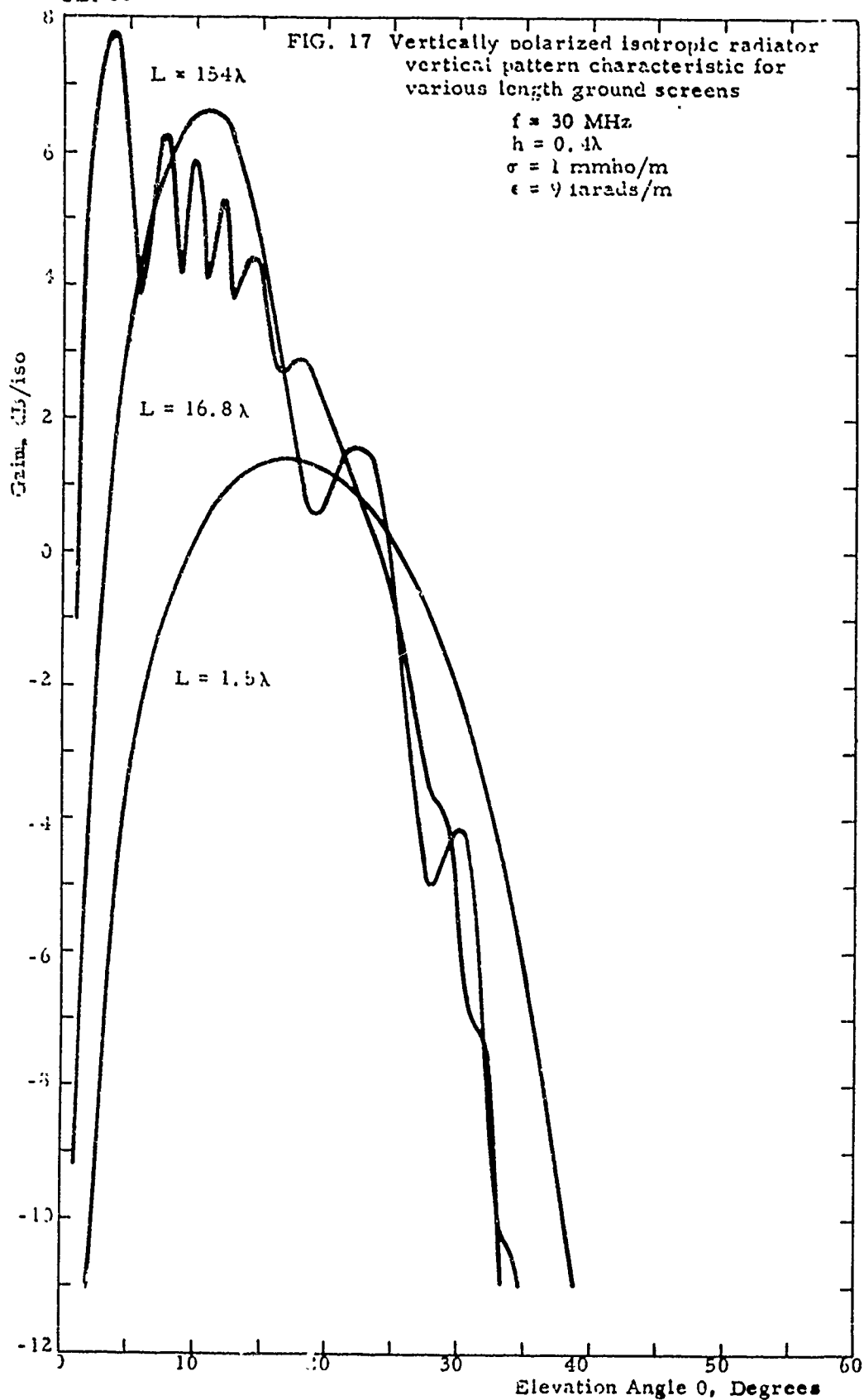
SEI 63

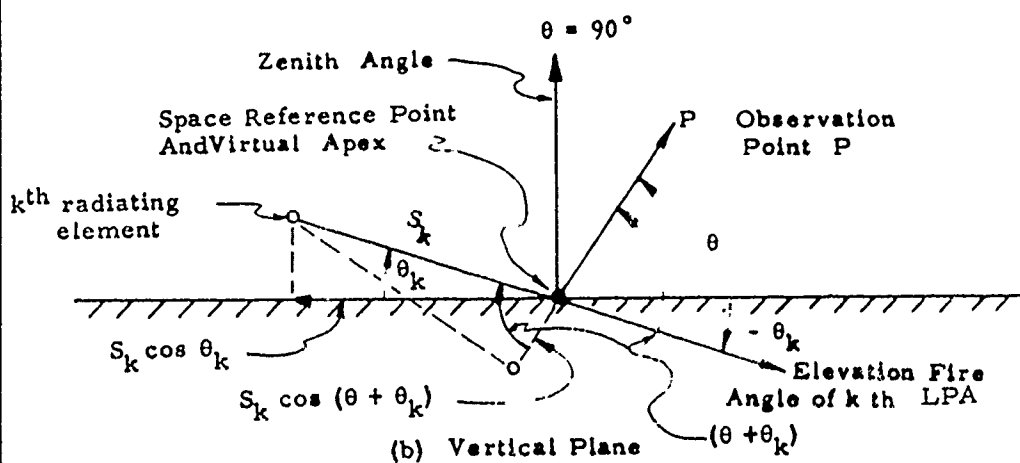
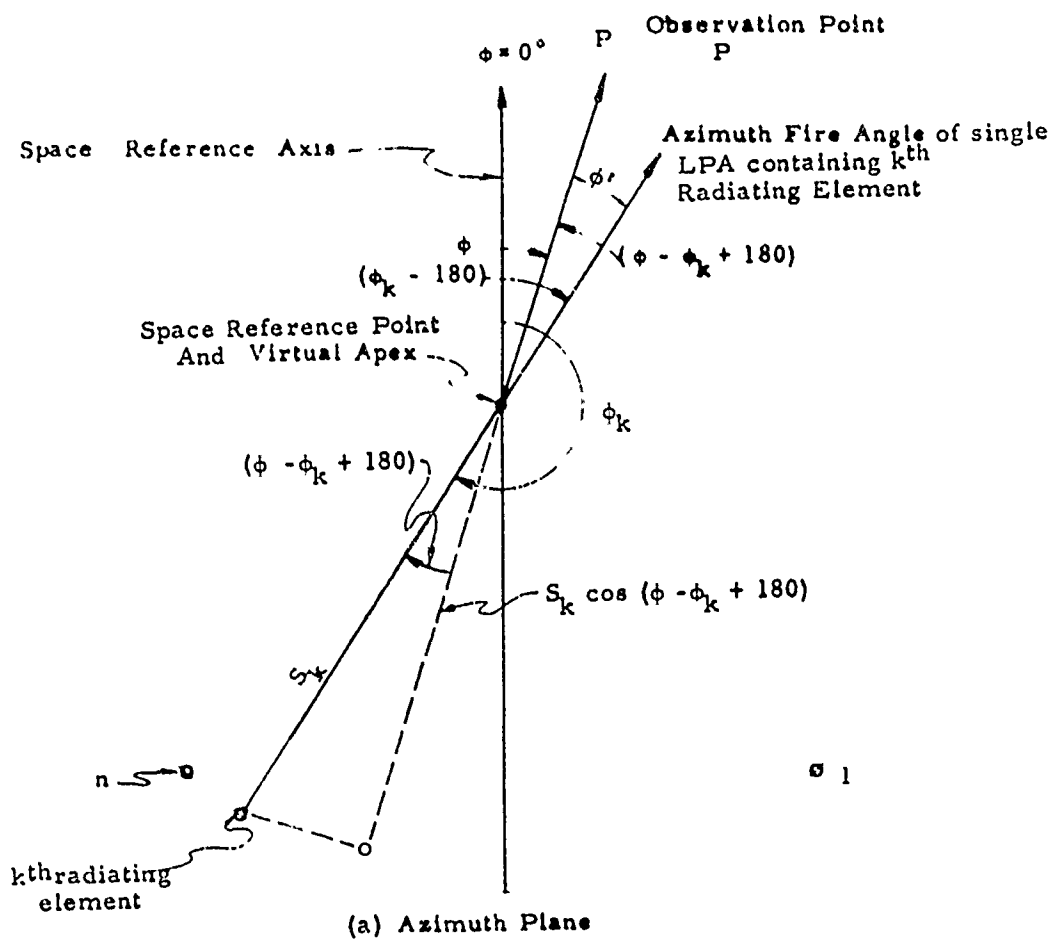


(4)



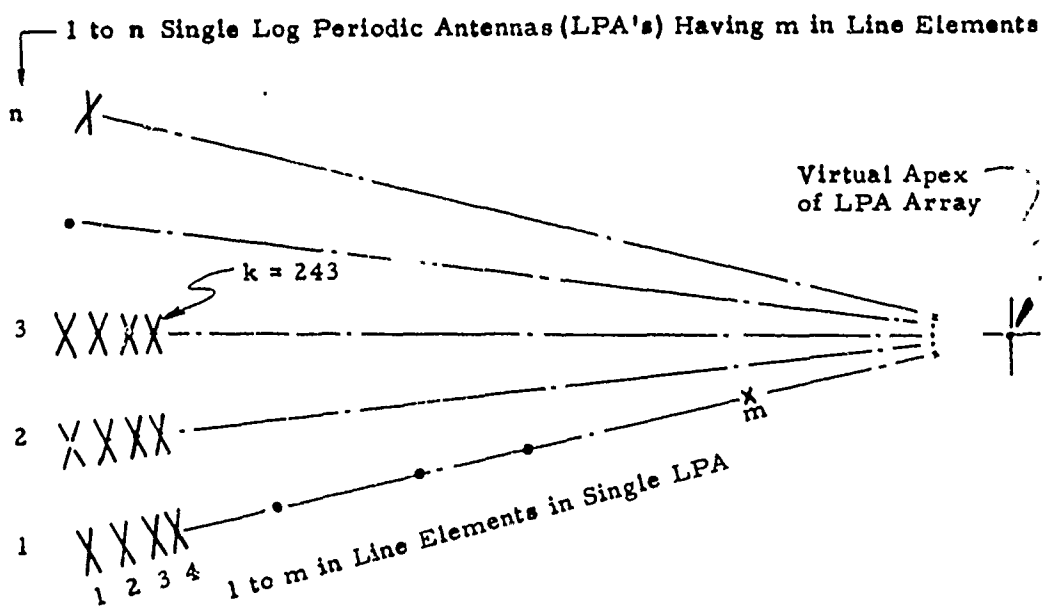
SEI 63



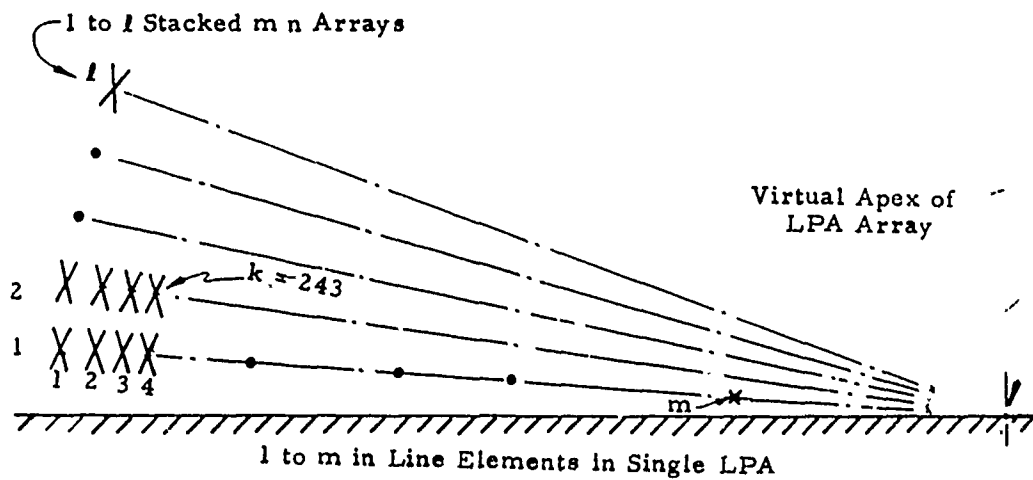


670427

FIG. 18 Plan and elevation sketch of K^{th} radiating element



(a) PLAN VIEW

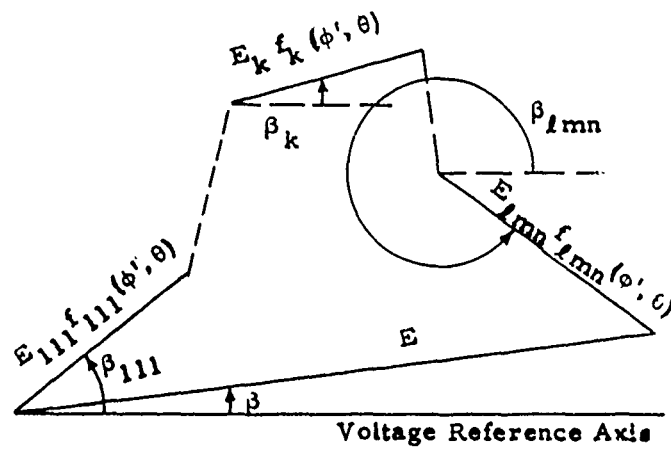


(b) ELEVATION VIEW



670427

FIG. 19 Three dimension circular array of log periodic crossed-dipole radiating elements



Smith Electronics, Inc.
680830

FIG 20 Summation for
 S_{lmn} Elements

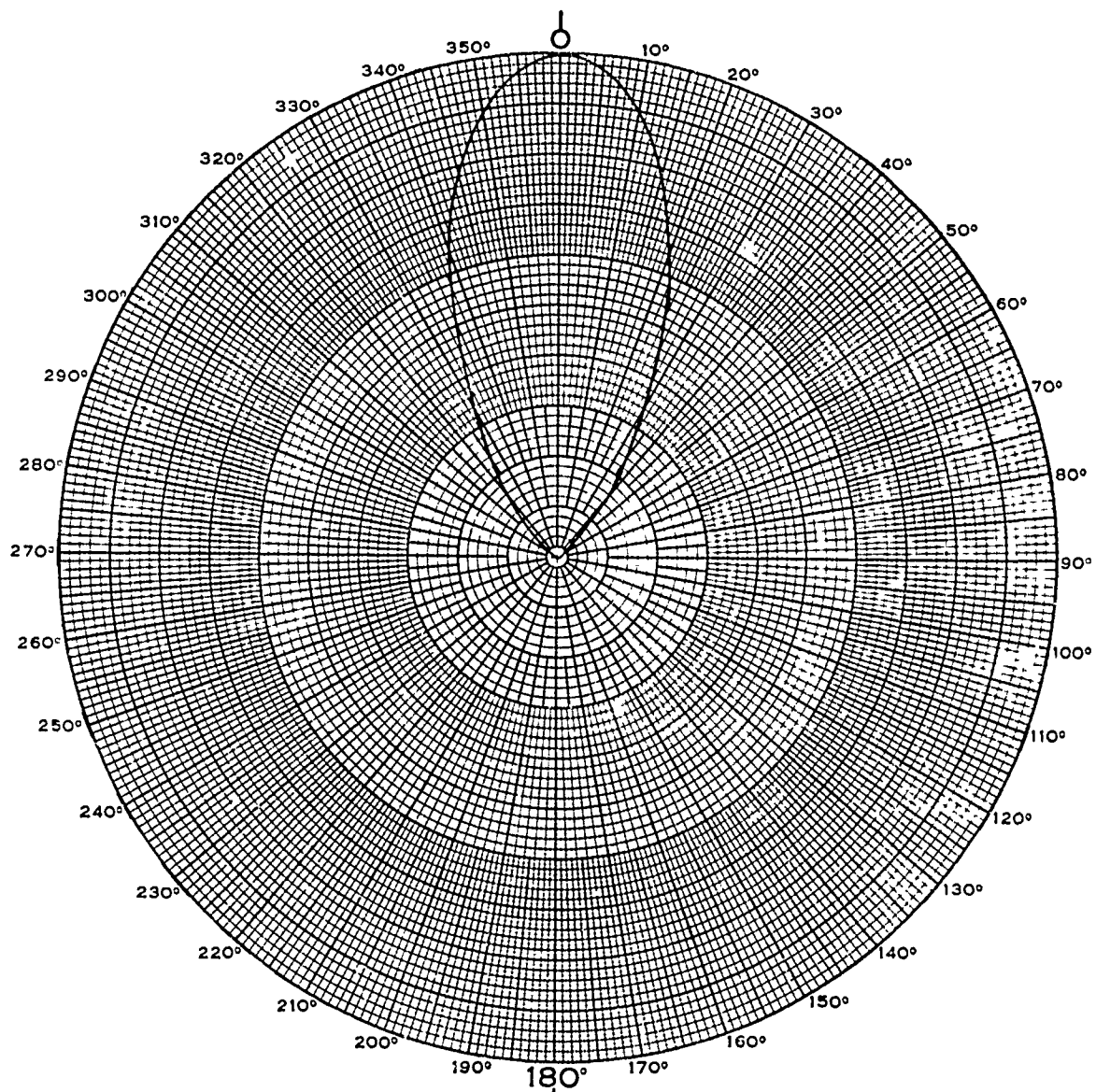


FIG. 21 Single LPA E field pattern
when located in an array
environment

$$E = \cos^{7.5} \theta$$

SMITH ELECTRONICS, INC.

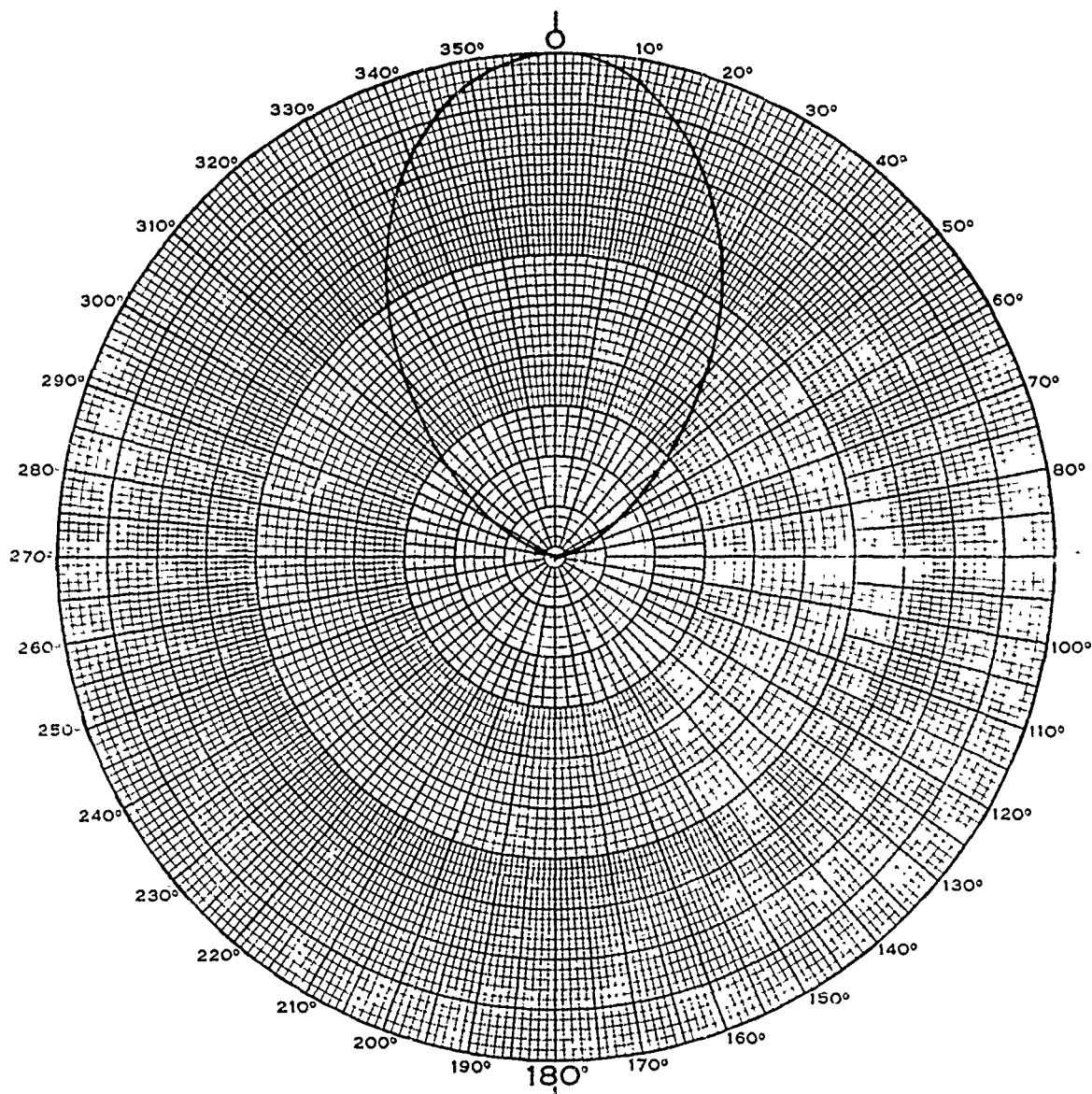


FIG. 22 Single LPA H field pattern when located in an array environment

$$E = \cos^{2.88} \theta$$

SMITH ELECTRONICS, INC.

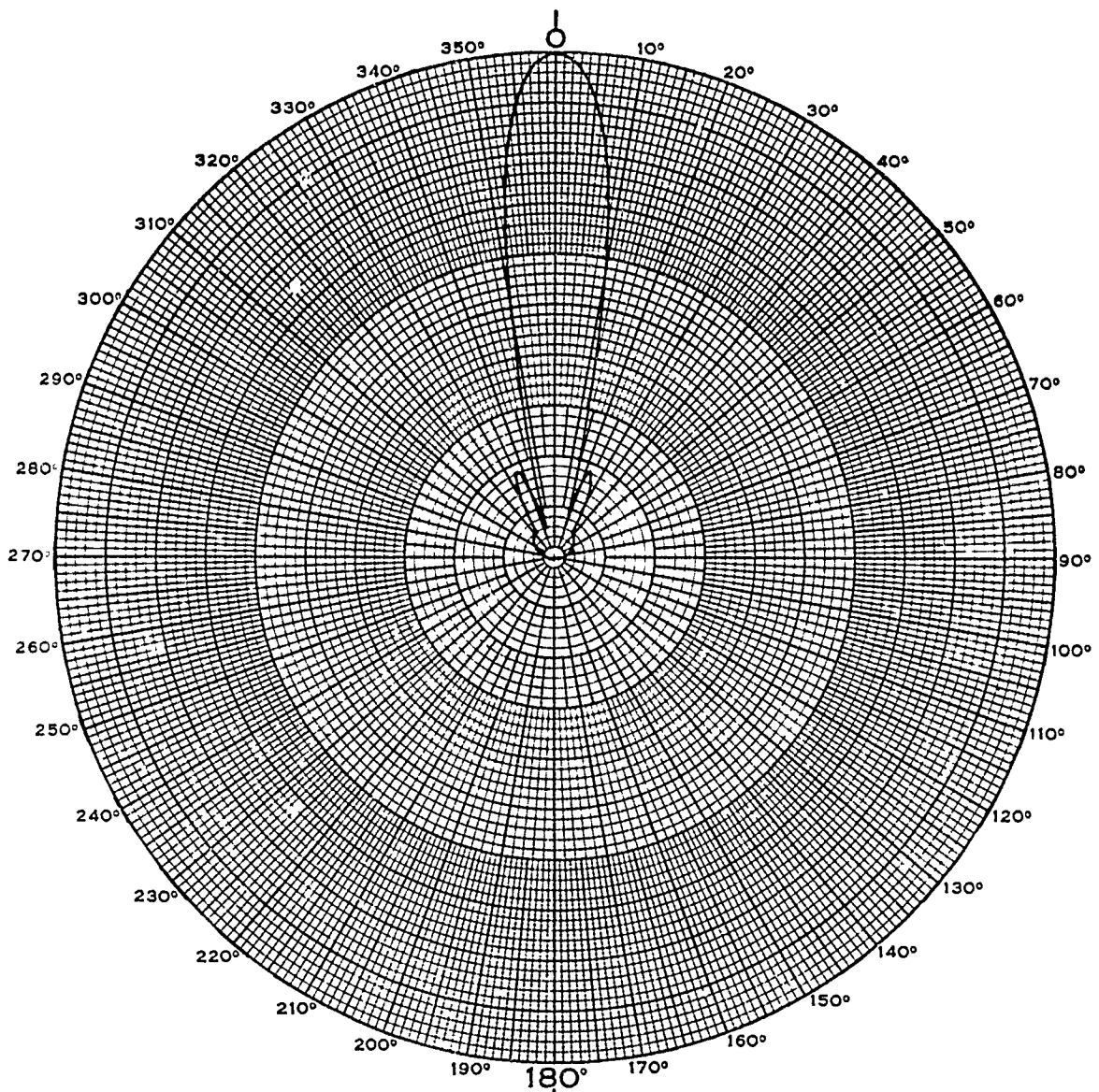


FIG. 23 Example of array azimuth pattern

Single LPA Patterns
 FIG. 21 for E Plane
 FIG. 22 for H Plane

$n = 5$ LPA's
 $a = 2$
 $\Gamma = 0.975$
 $h = 0.5\lambda$

SMITH ELECTRONICS, INC.

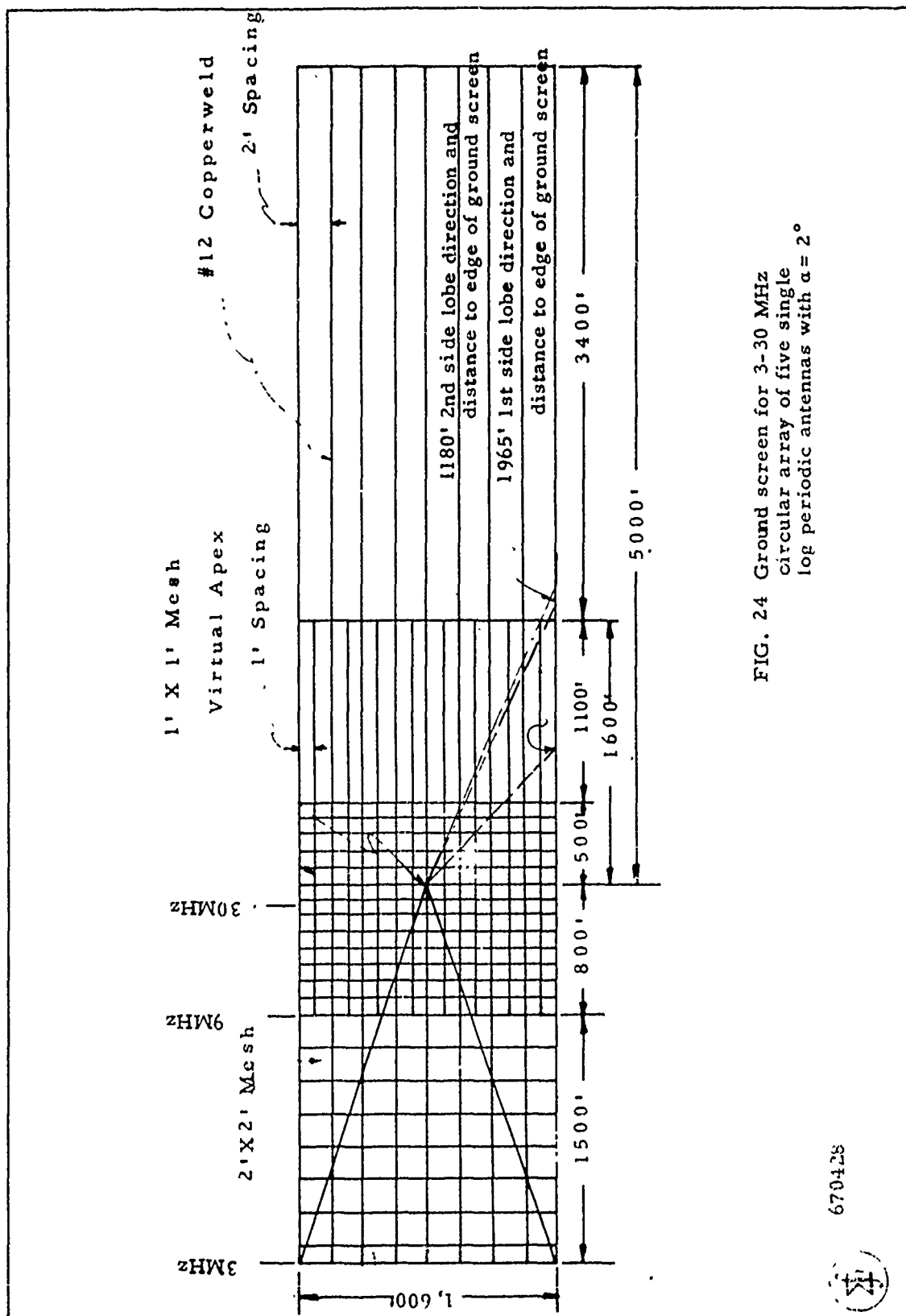


FIG. 24 Ground screen for 3-30 MHz
circular array of five single
log periodic antennas with $\alpha = 2^\circ$

670428

SEI 65

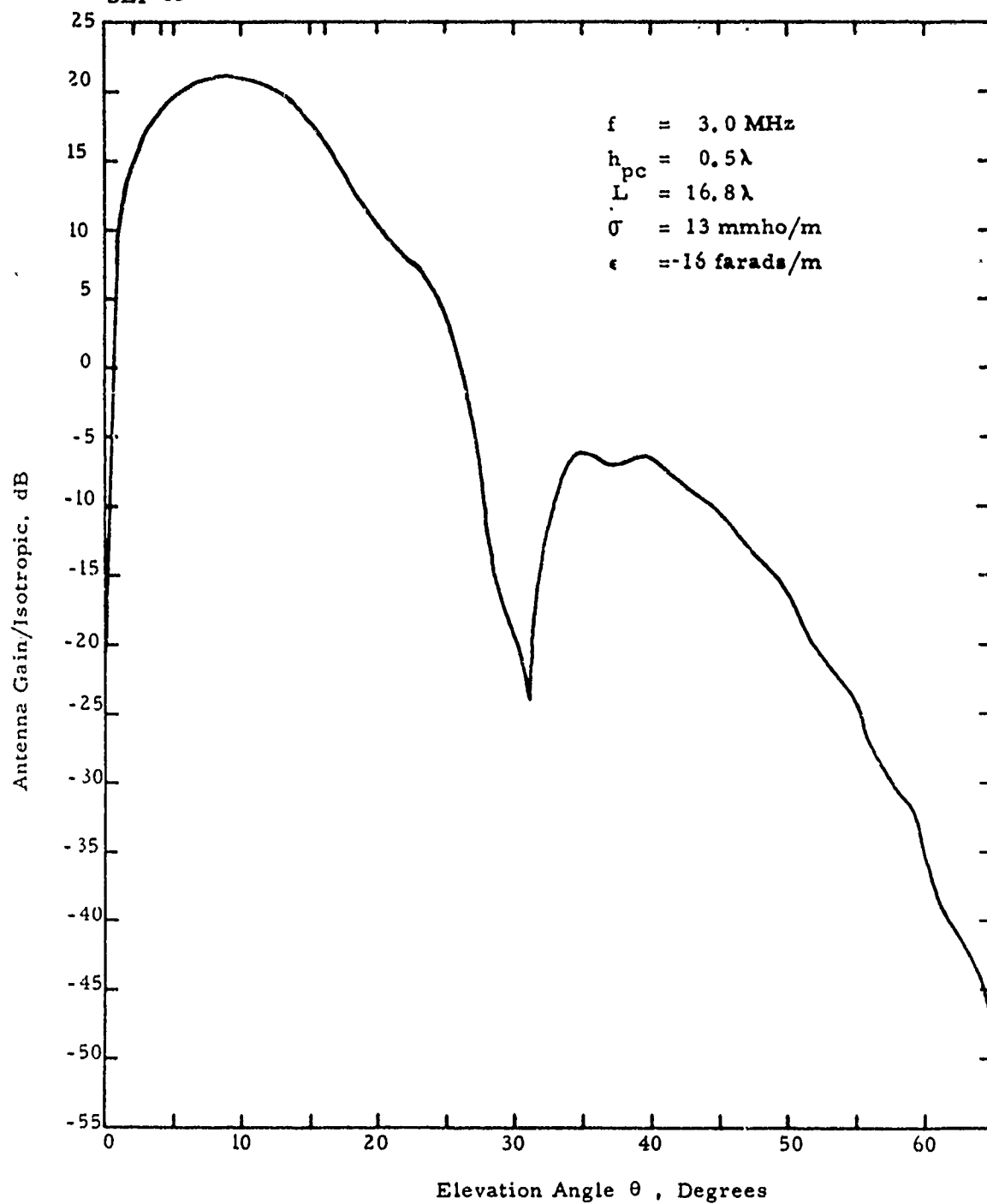


FIG. 25 Example of array elevation pattern for indicated parameters



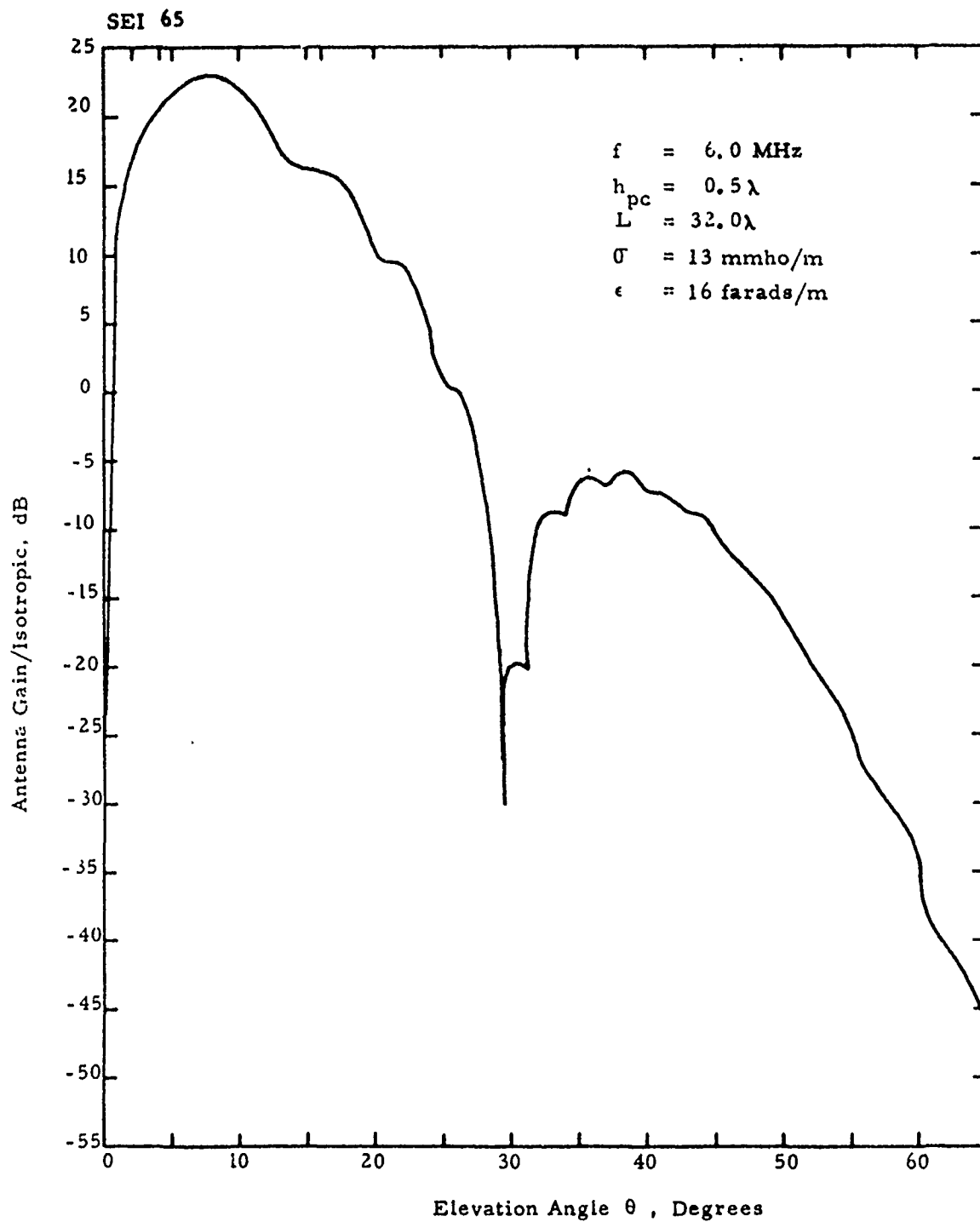


FIG. 26 Example of array elevation pattern
for indicated parameters



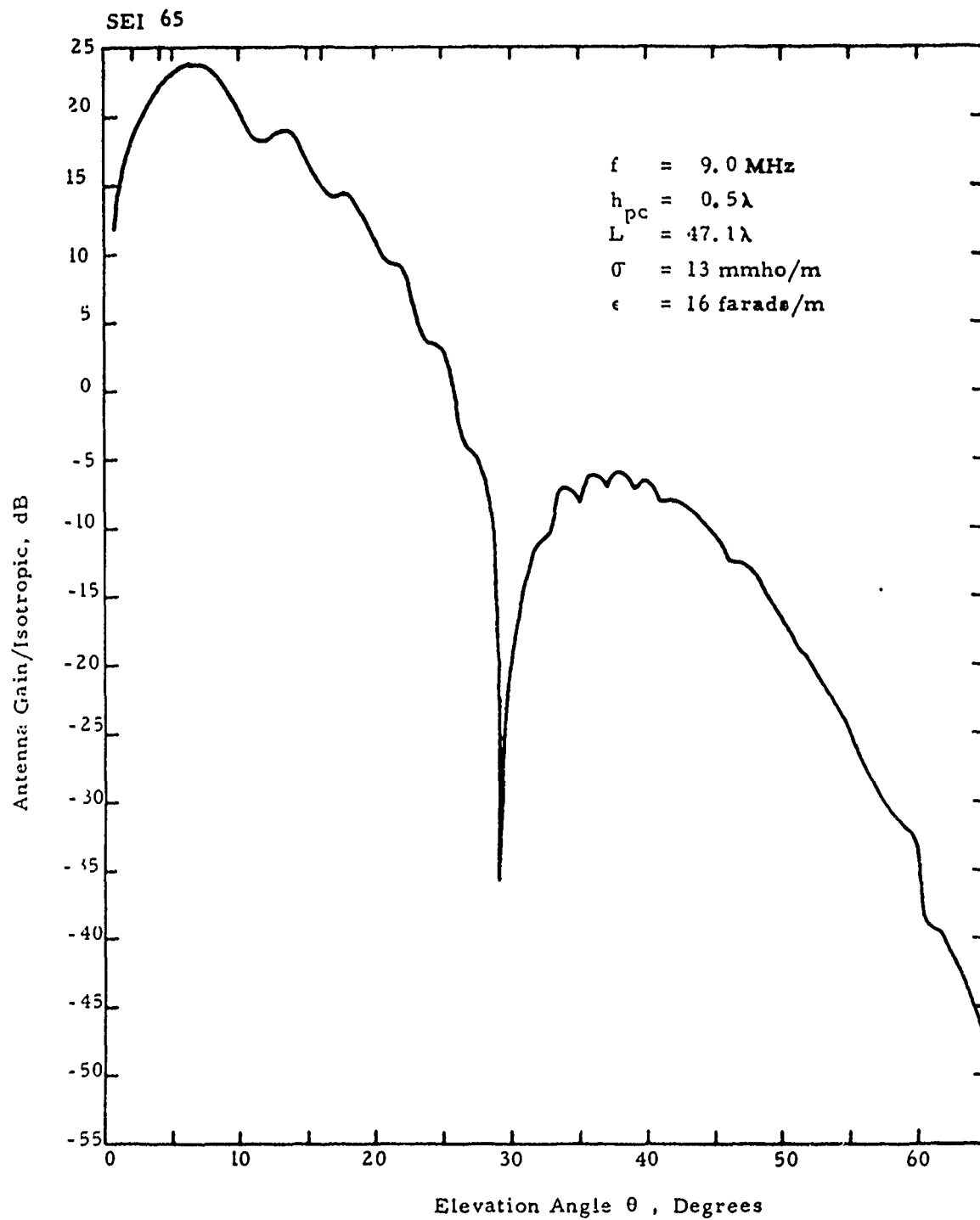


FIG. 27 Example of array elevation pattern
for indicated parameters



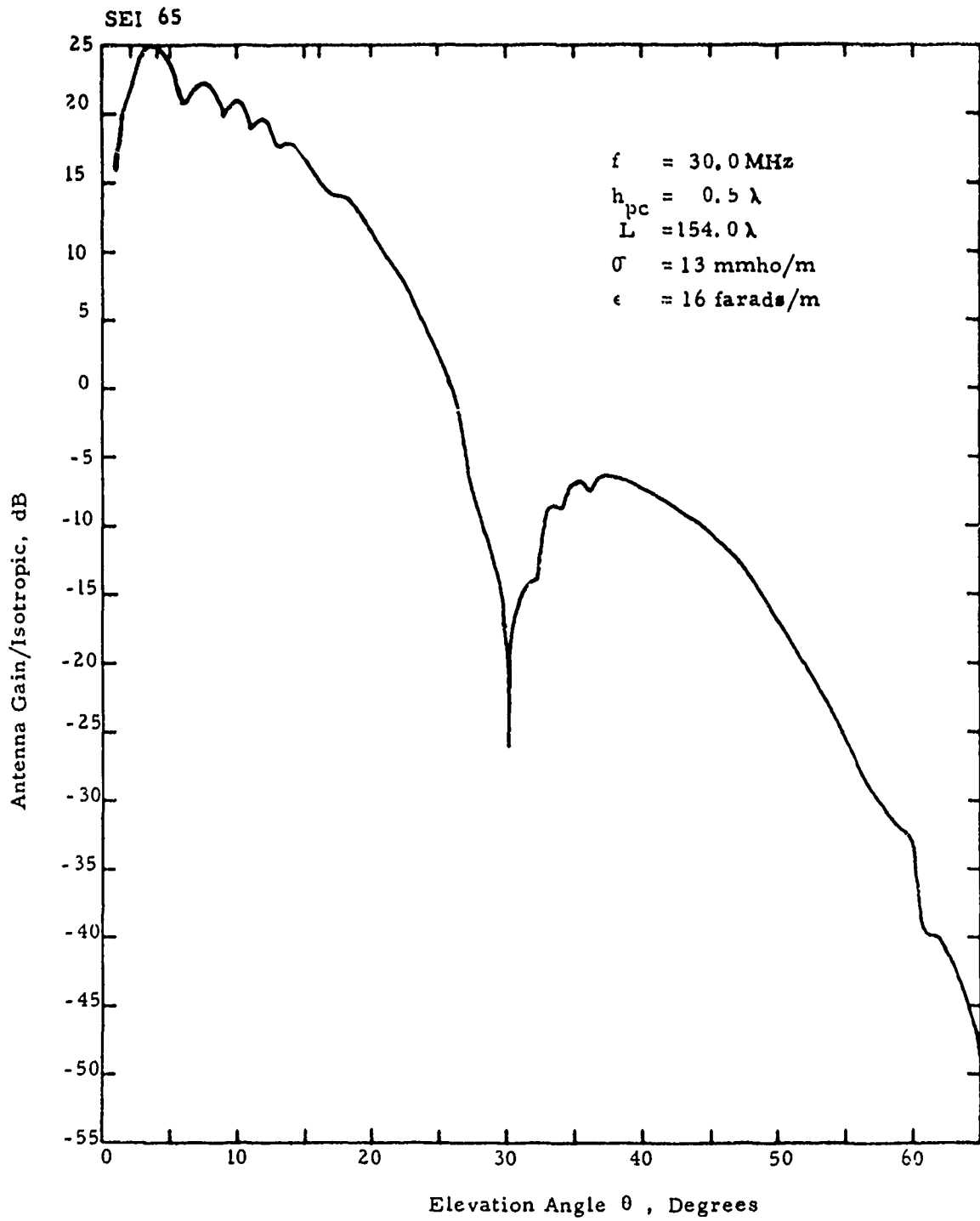


FIG. 28 Example of array elevation pattern
for indicated parameters



TIME-DOMAIN TREATMENT OF MAXWELL'S EQUATIONS
IN FREQUENCY DEPENDENT MEDIA

Richard Holland
Applied Physics, Inc.
5353 Wyoming Blvd., NE, Suite 3
Albuquerque, NM 87109

ABSTRACT

Longmire and Longley (DNA report 3167F, 1973) have described a method for representing certain types of frequency-dependent media in time-domain finite difference codes. They assumed the media could be described by a series of relaxation phenomena, one phenomenon per decade. Each phenomenon contributes a "current" to the $\nabla \times H$ equation, although these "currents" do not conveniently fit either the concept of conduction or displacement.

Recent discussions with ONR personnel have raised interest in more general types of media characterization. Specifically, there is now a desire to input the SEM or Prony parameters of a medium's σ and ϵ to time-domain codes. In other words, we now wish to work with the actual poles and residues of σ and ϵ rather than assuming the poles are uniformly spaced one per decade. The present work describes how this may be done.

It also goes beyond the work of Longmire and Longley in permitting use of complex as well as real poles. Prony "currents" associated with complex poles obey a temporally second-order differential equation, as opposed to the Prony "currents" of real poles. In both this formulation, and of the Longmire-Longley formulation, the latter obey temporally first-order differential equations.

In actual time-domain finite-difference codes, it is most exact to evaluate the Prony "currents" as well as the electric fields at the same spatial and temporal points. In the past, this simultaneous solution has not been implemented, due to the peculiar coupling of the equations for electric fields and Prony "currents". For the case of all poles real, we here also describe how to perform this exact solution using state theory;

Work was sponsored by Office of Naval Research and DARPA under Contract No. N00014-85-C-0852

i.e., by exponentiating the matrices coupling all the electric fields and Prony "currents".

INTRODUCTION

Consider a medium with anisotropic, frequency-dependent electrical properties. The electrical response of such a material may be fairly generally described by

$$\nabla \times \underline{H} = \underline{J}(t) + \underline{J}_f(t) \quad (1)$$

where $\underline{J}_f(t)$ is a forced current and

$$\underline{J}(t) = \underline{\sigma}_0 \cdot \underline{E}(t) + \underline{\epsilon}_\infty \cdot D\underline{E}(t) + \int_0^t \underline{K}(t-t') \cdot D\underline{E}(t') dt' \quad (2)$$

with D indicating the time-derivative operator. In this formulation, $\underline{\sigma}_0$, $\underline{\epsilon}_\infty$, and $\underline{K}(t-t')$ are second-rank tensors.

The frequency-domain form of eq. (2) is

$$\underline{J}(\omega) = \left[\underline{\sigma}_0 + i\omega \underline{\epsilon}_\infty + i\omega \int_0^\infty e^{-i\omega u} \underline{K}(u) du \right] \cdot \underline{E}(\omega) \quad (3)$$

Separation of eq. (3) into real and imaginary parts gives representations for the frequency-dependent conductivity and permittivity tensors,

$$\underline{\sigma}(\omega) = \underline{\sigma}_0 + \text{Re} \left[i\omega \int_0^\infty e^{-i\omega u} \underline{K}(u) du \right] \quad (4)$$

$$\underline{\epsilon}(\omega) = \underline{\epsilon}_{\infty} + \text{Re} \left[\int_0^{\infty} e^{-i\omega u} \underline{K}(u) du \right] \quad (5)$$

Longmire and Longley¹ have considered the scalar version of this formulation for the special case when $K(u)$ can be expressed as an exponential series,

$$K(u) = \sum_{m=1}^M a_m e^{-\beta_m u} \quad (6)$$

For this situation, eq. (2) may be rewritten

$$\underline{J}(t) = \sigma_0 \underline{E}(t) + \epsilon_{\infty} D \underline{E}(t) + \sum_{m=1}^M a_m \underline{J}_m(t) \quad (7)$$

with

$$\underline{J}_m(t) = e^{-\beta_m t} \int_{-\infty}^t D \underline{E}(t') e^{\beta_m t'} dt' \quad (8)$$

Equation (8) is equivalent to the differential equation

$$D \underline{J}_m(t) = D \underline{E}(t) - \beta_m \underline{J}_m(t) \quad (9)$$

Longmire and Longley assumed that materials could be represented by the exponential series of eq. (6) with one term for each decade of frequency over the spectrum of interest. This is equivalent to doing a Prony expansion of $K(u)$ [or $\sigma(\omega)$ and $\epsilon(\omega)$] with the poles forced to be spaced at

$$s_m = 10^{m+m_0} = \beta_m \quad (10)$$

While this assumption has been claimed to be reasonably accurate for wet soil, it would seem generally more correct to determine the poles from a Prony analysis of the medium's measured frequency-dependent characteristics. This is especially likely to be true if the material exhibits rapid variation in σ and ϵ with frequency.

STATE THEORY APPLICATIONS

Let us first assume the Prony analysis reveals no complex-conjugate pole pairs. In general, the \underline{a}_m will be second rank tensors, but the β_m will only be scalars. Then for every pole, each component of \underline{J}_m will obey

$$DE_i - DJ_{mi} - \beta_m J_{mi} = 0 \quad m = 1 - M, i = 1 - 3 \quad (11)$$

Additionally, the tensor form of eq. (7) gives

$$\epsilon_{\omega ij} DE_j + \sigma_{\omega ij} E_j + \sum_{m=1}^M a_{mij} J_{mj} = J_j \quad i, j = 1 - 3 \quad (12)$$

where

$$J_j = (\nabla \times \underline{H} - \underline{J}_f)_j \quad (13)$$

Equations (11) and (12) constitute a set of $3(M+1)$ coupled first order differential equations.

If anisotropy and frequency dependence were not present, the usual method of numerical solution would be explicit time-domain finite differencing. In this method, \underline{E} and \underline{H} evaluation points alternate both spatially and temporally using a well-tested leapfrog arrangement.²⁻⁴ In this arrangement, no two equations are coupled, and $E_x^{n+1/2}(I,J,K)$ means E_x evaluated at $((I + 1/2)\Delta X, J\Delta Y, K\Delta Z, (n + 1/2)\Delta t)$.

However, the present system of equations requires the three E_j 's and $3M J_{mj}$'s all to be evaluated simultaneously. While this cannot be done using conventional time-domain finite differencing, state theory does indicate an appropriate generalization of time-domain finite differencing.

First, let us consider the case where anisotropy, but not frequency dependence, is present,

$$[\epsilon_\infty] D[E] + [\sigma_0][E] = [J] \quad (14)$$

This matrix differential equation has a homogeneous solution

$$[E]_h = e^{-[\epsilon_\infty]^{-1}[\sigma_0]t} [A] \quad (15)$$

and a particular solution

$$[E]_p = [\sigma_0]^{-1}[J] \quad (16)$$

giving a general solution

$$[E] = e^{-[\epsilon_\infty]^{-1}[\sigma_0]t} [A] + [\sigma_0]^{-1}[J] \quad (17)$$

The constant vector $[A]$ may be evaluated at $(n - 1/2)\Delta t$:

$$[E]^{n-1/2} = [A] + [\sigma_0]^{-1}[J]^n \quad (18)$$

This gives the new E-field vector in terms of the old,

$$[E]^{n+1/2} = e^{-[\epsilon_\infty]^{-1}[\sigma_0]\Delta t} [E]^{n-1/2} + \left[1 - e^{-[\epsilon_\infty]^{-1}[\sigma_0]\Delta t}\right] [\sigma_0]^{-1}[J]^n \quad (19)$$

Similar exponential matrix techniques have been reported for time-domain solution of generalized multi-conductor transmission lines.⁵ In the previous work, one may see how to evaluate eq. (19) if $[\sigma_0]$ is singular or if $[\epsilon_\infty]^{-1}[\sigma_0]\Delta t$ has arbitrarily large elements. Basically, matrices are exponentiated using the power-series representation of an exponential.

If frequency dependence is present, the $[E]$ vector of eqs. (14)-(19) becomes replaced by

$$[E] \rightarrow \begin{bmatrix} \underline{E} \\ \underline{J}_1 \\ \vdots \\ \underline{J}_M \end{bmatrix} = [E'] \quad (20)$$

The $[\epsilon_\infty]$ matrix becomes

$$[\epsilon_\infty] \rightarrow \begin{bmatrix} \underline{\epsilon}_\infty & \underline{0} & \cdots & \underline{0} \\ \underline{I} & -\underline{I} & \cdots & -\underline{I} \\ \vdots & \vdots & \ddots & \vdots \\ \underline{I} & -\underline{I} & \cdots & -\underline{I} \end{bmatrix} = [\epsilon'] \quad (21)$$

and the $[\sigma_0]$ matrix becomes

$$[\sigma_0] \rightarrow \begin{bmatrix} \underline{\sigma}_0 & \underline{a}_1 & \cdots & \underline{a}_M \\ 0 & -\beta_1 \underline{I} & \cdots & 0 \\ \vdots & \vdots & \ddots & \vdots \\ 0 & 0 & \cdots & -\beta_M \underline{I} \end{bmatrix} = [\sigma'] \quad (22)$$

Lastly, the forcing vector becomes

$$[J] \rightarrow \begin{bmatrix} \underline{J} \\ 0 \\ \vdots \\ 0 \end{bmatrix} = [\underline{J}'] \quad (23)$$

Then the matrix equation for simultaneous advancement of \underline{E} and the \underline{J}_m is

$$[\underline{E}']^{n+1/2} = e^{-[\epsilon']^{-1}[\sigma']\Delta t} [\underline{E}']^{n-1/2} + \left(1 - e^{-[\epsilon']^{-1}[\sigma']\Delta t}\right) [\sigma']^{-1} [\underline{J}']^n \quad (24)$$

In the past, time-domain finite differencing has not often considered anisotropy. Frequency-dependent effects have been included by using the old $\underline{J}_m^{n-1/2}$ to find the new $\underline{E}^{n+1/2}$. (This decouples \underline{E} from the \underline{J}_m in eq. (12).) Then the new $\underline{E}^{n+1/2}$ have been used to find the new $\underline{J}_m^{n+1/2}$ from eq. (11).

TREATMENT OF COMPLEX POLES

If Prony analysis of the material's frequency dependence reveals complex pole pairs, a more general treatment becomes necessary. In this case, $\underline{K}(u)$ will contain terms of the form

$$\begin{aligned}
\underline{K}(u) &= \underline{b}_m \sin(\gamma_m u + \phi_m) e^{-\beta_m u} \\
&= \underline{b}_m \cos \phi_m \sin \gamma_m u e^{-\beta_m u} + \underline{b}_m \sin \phi_m \cos \gamma_m u e^{-\beta_m u}
\end{aligned} \tag{25}$$

The $\underline{J}_m(t)$ of eq. (8) now becomes

$$\begin{aligned}
\underline{J}_m(t) &= \int_{-\infty}^t \underline{D}\underline{E}(t') (\cos \phi_m \sin \gamma_m (t-t') e^{-\beta_m (t-t')} \\
&\quad + \sin \phi_m \cos \gamma_m (t-t') e^{-\beta_m (t-t')}) dt' \\
&= \underline{J}_{mc}(t) \cos \phi_m + \underline{J}_{ms}(t) \sin \phi_m
\end{aligned} \tag{26}$$

where \underline{J}_{mc} and \underline{J}_{ms} are the parts of \underline{J}_m associated with $\cos \phi_m$ and $\sin \phi_m$, respectively:

$$\underline{J}_{mc}(t) = \int_{-\infty}^t \underline{D}\underline{E}(t') \sin \gamma_m (t-t') e^{-\beta_m (t-t')} dt \tag{27}$$

$$\underline{J}_{ms}(t) = \int_{-\infty}^t \underline{D}\underline{E}(t') \cos \gamma_m (t-t') e^{-\beta_m (t-t')} dt \tag{28}$$

Differentiation of $\underline{J}_{mc}(t)$ and $\underline{J}_{ms}(t)$ yields

$$D\underline{J}_{mc}(t) = -\beta_m \underline{J}_{mc}(t) + \gamma_m \underline{J}_{ms}(t) \tag{29}$$

$$DJ_{ms}(t) = DE(t) - \beta_m J_{ms}(t) + \gamma_m J_{mc}(t) \quad (30)$$

These equations can be solved for $J_{mc}(t)$ and $J_{ms}(t)$ using Heavyside algebra:

$$[(D + \beta_m)^2 + \gamma_m^2] J_{mc}(t) = \gamma_m DE(t) \quad (31)$$

$$[(D + \beta_m)^2 + \gamma_m^2] J_{ms}(t) = (D + \beta_m) DE(t) \quad (32)$$

Thus, $J_m(t)$ obeys the differential equation

$$[(D + \beta_m)^2 + \gamma_m^2] J_m(t) = [\sin\phi_m(D + \beta_m) + \cos\phi_m\gamma_m] DE(t) \quad (33)$$

In principle, equations like (33) could be added to the set of equations given by (11) and (12), and the entire ensemble solved by state theory. This approach, however, requires treatment of second-order matrix differential equations of the form

$$[A]D^2[E] + [B]D[E] + [C][E] = [F] \quad (34)$$

The homogeneous solution of this equations includes square roots and complex exponents of matrices; it is much more complicated than eqs. (14) - (19). (To the best of our knowledge, exponential differencing has never been applied even to scalar second-order differential equations.)

Consequently, when Prony analysis of the material data yields complex pole pairs, our present strategy is to fall back to the old technique for dealing with real poles: First find $\underline{E}^{n+1/2}$ using the old $\underline{J}_m^{n-1/2}$. Then use

the new $\underline{E}^{n+1/2}$ and the finite-difference form of eq. (33) to find the new $\underline{J}_m^{n+1/2}$.

REFERENCES

1. Longmire, C.L. and H.J. Longley, "Time Domain Treatment of Media with Frequency-Dependent Electrical Parameters," DNA 3167F, 23 September 1973.
2. Yee, K.S., "Numerical Solution of Initial Boundary Value Problems Involving Maxwell's Equations in Isotropic Media," IEEE Trans. Antennas & Propagat., Vol. AP-14, pp. 302-307, May 1966
3. Longmire, C.L., "State of the Art in IEMP and SGEMP Calculations," IEEE Trans. Nuc. Sci., Vol. NS-22, pp. 2340-2344, December 1975.
4. Holland, R., "THREDE: A Free-Field EMP Coupling and Scattering Code," IEEE Trans. Nuc. Sci., Vol. NS-24, pp. 2416-2421, December 1977.
5. Holland, R., "The EMP Tunnel Code DHTRANS," IEEE Trans. Nuc. Sci., Vol. NS-25, pp. 1404-1411, December 1978.

SESSION V - "NUMERICAL ASPECTS OF INPUT/OUTPUT"

"Requirements for Graphic Standards"

Stephen Lamont

Naval Postgraduate School

"Generating a Ray-like Description from a Numerical Knowledge of the Electromagnetic Field"

Francis X. Canning

Naval Weapons Center

"Computer-Aided Engineering in EM Technology"

John Kuras and Nazih Youssef

Boeing Aerospace Company

"Application of Computer Aided Design to Electromagnetic Modeling"

W.S. Nelson, P. Tulyathan and M. Wehling

Northrop Corp.

Requirements for Graphic Standards

Steve Lamont

Naval Postgraduate School

Monterey, California

March 19, 1986

Although graphics are generally acknowledged to be effective aids in analysis and presentation of data, heretofore there has been little or no standardization in the coding or usage of graphics applications either on mainframe computers or on workstations. Recently work has been done in standards organizations such as ISO and ANSI to promulgate a graphics standard allowing programmers to code applications for a wide range of dissimilar devices with little to no recoding.

The first standard to be accepted was the Graphical Kernel System (GKS) in October 1984. Three other proposals are receiving active consideration from ANSI: Programmer's Hierarchical Interactive Standard (PHIGS), Virtual Device Metafile (VDM), and Virtual Device Interface (VDI). This paper will discuss the desirability and applicability of these standards to various computational electromagnetic tasks.

OVERVIEW

- Introduction
- Issues
- Approaches
- Standards
- Conclusions

INTRODUCTION

- Graphics is an effective means of communication.
(*1picture = 10³words*)
- Hindered by lack of standards for graphics applications (especially in personal computing).
- Barriers.
 - ♦ Memory.
 - ♦ Unlike devices (plotters vs. raster devices).
 - ♦ Performance.
- Answer: standard interfaces to devices (BIOS is standard interface to microcomputer system.)

ISSUES

- Portability
- Obsolescence
- Performance
- Expansion/Extension
- Development Time/Costs
- Fluency of Expression

APPROACHES

- Software Specifically Tailored to Hardware
- Standards Based Software With Device Independence
- Standards Based Software With Extensions to Devices.

APPROACHES (1)

- Software Specifically Tailored to Hardware

Portability

Low. Locked into specific hardware.

Obsolescence

Likely when next gizmo comes along.

Performance

Very good.

Expansion/Extension

Difficult. Probably tricks involved.

Development Time/Costs

High.

Fluency of Expression

Probably low.

APPROACHES (2)

- Standards Based Software With Device Independence

Portability

High.

Obsolescence

Low (until next standard).

Performance

Lower (high overhead may be involved).

Expansion/Extension

Relatively straightforward if other modern programming practices adhered to as well.

Development Time/Costs

Moderate to low.

Fluency of Expression

High.

APPROACHES (3)

- Standards Based Software With Extensions to Devices.

Portability

Medium.

Obsolescence

Low (until next standard).

Performance

Moderate (some overhead will be involved).

Expansion/Extension

Relatively straightforward if other modern programming practices adhered to and tricks kept to a minimum.

Development Time/Costs

Moderate.

Fluency of Expression

Moderate.

STANDARDS

Core Graphics Standard (CORE)

ACM/SIGGRAPH – 1977, 1979 FORTRAN based standard for 2-D graphics. Hardware independent.

Graphical Kernel System (GKS)

ANSI/ISO standard – 1980, 1984, 1985.
Adaptation of CORE. 2-D standard. Hardware independent. Several language bindings (FORTRAN, Pascal, C, Assembler, BASIC)

Programmer's Hierarchical Interactive Graphical Standard (PHIGS)

ANSI standard – 1985, 1986. 2-D & 3-D standard. Based upon data structures and transformations upon those structures. Allows some interaction with hardware.

STANDARDS (CONTINUED)

Virtual Device Interface (VDI)

Single standard for relaying input to a program and graphics information to output devices. May be extended to support advanced features.

- Input devices
 - ◆ Keyboards
 - ◆ Joysticks
 - ◆ Trackballs
 - ◆ Rodentia
- Output devices
 - ◆ Monitors
 - ◆ Printers
 - ◆ Plotters
 - ◆ Cameras

Virtual Device Metafile (VDM)

File format for storage and transporting of graphics information. Processed by a postprocessor for a specific device.

CONCLUSIONS

- Advances in hardware must be met by similar advances in software technology.
- VDIs should exploit device intelligence where ever possible.
- VDIs should support in emulation features not supported directly by hardware.
- Use of standard software allows better flow of information within community.

GENERATING A RAY-LIKE DESCRIPTION FROM A NUMERICAL
KNOWLEDGE OF THE ELECTROMAGNETIC FIELD

Francis X. Canning
Code 3313
Naval Weapons Center
China Lake, CA 93555-6001

A new method of presenting the output of a numerical calculation of an electromagnetic field is described. A formula has been found which takes the electromagnetic field in a plane (roughly perpendicular to the overall direction of propagation) and generates a ray-like picture of that field. This method is applied to a simple case, that of the field due to scattering by a conducting circular cylinder. Graphs showing, to speak very imprecisely, the strengths of the rays (actually, a quantity related to the "rays") propagating in each direction, are produced. The usefulness of this graphical description of electromagnetic fields is illustrated by examining these graphs for various wavelengths, positions, and a parameter within the method.

N.001

□ □ □ □ □ 4 MAR 86 □ □ □ □ □

GER

A2393



GENERATING A RAY-LIKE DESCRIPTION FROM A NUMERICAL KNOWLEDGE OF THE ELECTROMAGNETIC FIELD

FRANCIS X. CANNING

CODE 3313

NAVAL WEAPONS CENTER

CHINA LAKE, CA

MARCH 1986

□ □ □ □ □ 5 MAR 86 □ □ □ □ □

GER

N.002

A2393



GENERATING A RAY-LIKE DESCRIPTION FROM A NUMERICAL KNOWLEDGE OF THE ELECTROMAGNETIC FIELD

INTRODUCTION

- A METHOD OF GENERATING RAY-LIKE PICTURES FROM NUMERICAL VALUES OF THE FIELD HAS BEEN FOUND
- THE PURPOSE OF THIS PRESENTATION IS TO ILLUSTRATE THE USE OF THIS METHOD
- THE THEORY OF THE METHOD WILL NOT BE DESCRIBED
- HOWEVER, THE PHILOSOPHY OF THE THEORY WILL BE PRESENTED, SO THE MEANING OF THE GRAPHS SHOWN CAN BE UNDERSTOOD

N.003

A2393



GENERATING A RAY-LIKE DESCRIPTION FROM A NUMERICAL KNOWLEDGE OF THE ELECTROMAGNETIC FIELD

INTERPRETATION OF THE METHOD

- ONE MIGHT HOPE TO DETERMINE THE DIRECTION OF PROPAGATION OF THE FIELD BY USING A SLIT AND A SCREEN
- THE NARROWER THE SLIT IS, THE MORE THE DESCRIPTION OBTAINED PERTAINS TO THE FIELD AT THE CENTER OF THE SLIT
- HOWEVER, THE NARROWER THE SLIT IS, THE MORE THAT DIFFRACTION SPREADS OUT THE "RAY" DIRECTIONS
- WHILE THE METHOD USED HERE IS ANALOGOUS TO A SLIT AND SCREEN, IT IS MORE SOPHISTICATED

N.004

A2393



GENERATING A RAY-LIKE DESCRIPTION FROM A NUMERICAL KNOWLEDGE OF THE ELECTROMAGNETIC FIELD

THE MATHEMATICAL IMPLEMENTATION OF A CONCEPTUAL SLIT

- THE "SLIT" SHOULD NOT HAVE SHARP (DISCONTINUOUS) EDGES
- A WEIGHTING FUNCTION OF $\exp[-\alpha (X - X_0)^2]$ WILL BE USED IN GENERATING A CONCEPTUAL SLIT CENTERED AT $X = X_0$
- THE QUANTITY $w = 1/\sqrt{\alpha}$ IS A MEASURE OF THE WIDTH OF THE SLIT. IN ALL OF THE GRAPHS PRESENTED, w IS AN IMPORTANT DISTANCE TO NOTICE

N.B.: THE METHOD USED TO DEVELOP THE THEORY WAS MORE SOPHISTICATED THAN THIS OVERSIMPLIFIED INTERPRETATION OF THE THEORY

N.005

A2393



GENERATING A RAY-LIKE DESCRIPTION FROM A NUMERICAL KNOWLEDGE OF THE ELECTROMAGNETIC FIELD

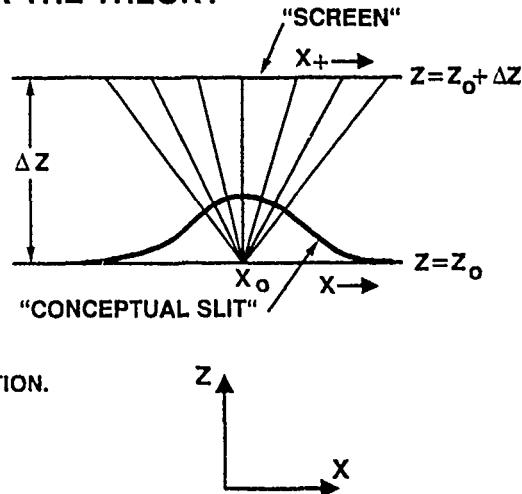
GEOMETRY FOR THE THEORY

CALL:
 $F^-(X)$ THE FIELD AS A FUNCTION OF X AT
 $Z=Z_0$ (AT THE SLIT).

CALL:
 $F^+(X_+)$ THE FIELD AS A FUNCTION OF X_+ AT
 $Z=Z_0+\Delta Z$ (AT THE SCREEN).

AND DEFINE:

$F(X_+|X)$ TO BE THE "PART OF" $F^+(X_+)$
DUE TO THE FIELD NEAR (WITHIN w OF) X .
"PART OF" IS AN APPROXIMATE INTERPRETATION.
A CAREFUL DEFINITION WOULD REQUIRE
GOING DEEPER INTO THE THEORY USED TO
DEVELOP THE METHOD



N.006

A2393



GENERATING A RAY-LIKE DESCRIPTION FROM A NUMERICAL KNOWLEDGE OF THE ELECTROMAGNETIC FIELD

THE EQUATION OF THE METHOD

- WE ASSUME THE FIELDS ARE PROPAGATING ROUGHLY UPWARDS, I.E. IN THE PLUS Z DIRECTION, WITH WAVE VECTOR K
- A SMALL ANGLE APPROXIMATION ABOUT THE POSITIVE Z -AXIS IS MADE
- THE RESULTING EQUATION IS:

$$F(X_+|X) = C \int_{-\infty}^{\infty} \underbrace{F^-(S)}_{\substack{\text{NUMERICAL VALUES} \\ \text{OF THE FIELD}}} \exp \left[-\alpha (X-S)^2 \right] \cdot \underbrace{\exp \left\{ \frac{ik}{2\Delta Z} [X_+^2 - X^2 + 2S(X-X_+)] \right\}}_{\substack{\text{MATHEMATICAL} \\ \text{WINDOW (SLIT)}}} dS$$

- IN THIS EQUATION, IT IS ASSUMED THAT IN SOME SENSE ΔZ IS SMALL

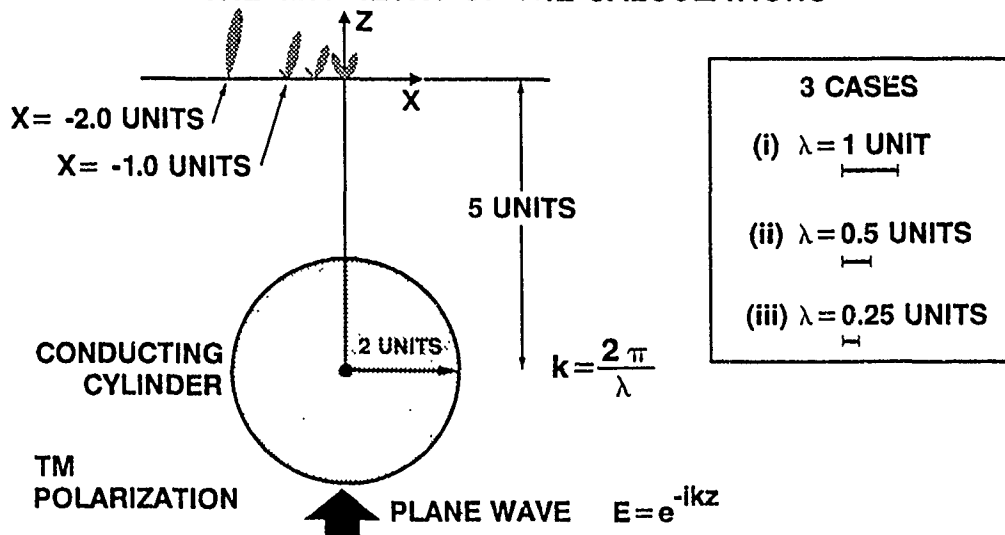
N.007

A2393



GENERATING A RAY-LIKE DESCRIPTION FROM A NUMERICAL KNOWLEDGE OF THE ELECTROMAGNETIC FIELD

THE GEOMETRY OF THE CALCULATIONS



N.008

A2393



GENERATING A RAY-LIKE DESCRIPTION FROM A NUMERICAL KNOWLEDGE OF THE ELECTROMAGNETIC FIELD

ABOUT THE GRAPHS

- THE NUMERICAL VALUES OF THE FIELD USED WERE GENERATED USING THE EIGENFUNCTION SOLUTION. HOWEVER, THE IMPORTANCE OF THIS METHOD LIES IN THAT THE NUMERICAL VALUES COULD HAVE COME FROM ANY ACCURATE CALCULATION. THUS, THIS METHOD CAN BE USED WHENEVER NUMERICAL RESULTS ARE AVAILABLE, FROM A NUMERICAL CODE
- THE GRAPHS SHOW A POLAR PLOT OF $|F(X_+, X)|$ FOR X FIXED, WHERE F REPRESENTS THE ELECTRICAL FIELD
- A LINEAR SCALE IS USED FOR ALL BUT THE LAST GRAPH

GENERATING A RAY-LIKE DESCRIPTION
FROM A NUMERICAL KNOWLEDGE OF THE ELECTROMAGNETIC FIELD



DISCUSSIONS OF GRAPH #1

WE BEGIN BY CONSIDERING THE CASE WHERE $\lambda = 1$ AND, INITIALLY, $X = 0$. FOR THIS PARTICULAR GEOMETRY AND WAVELENGTH, THE METHOD MAY BE APPLIED USING VARIOUS VALUES OF THE AVERAGING DISTANCE w (WHICH WAS DEFINED AS THE HALF-WIDTH AT $1/e$ HEIGHT FOR THE WEIGHTING FUNCTION) IN ORDER TO USE A NARROW AVERAGING FUNCTION, TAKE $w = 0.5$.

THE RESULTS OF THE CALCULATION ARE SHOWN ON THE FIRST GRAPH.

□ □ □ □ □ 6 MAR 86 □ □ □ □ □

GER

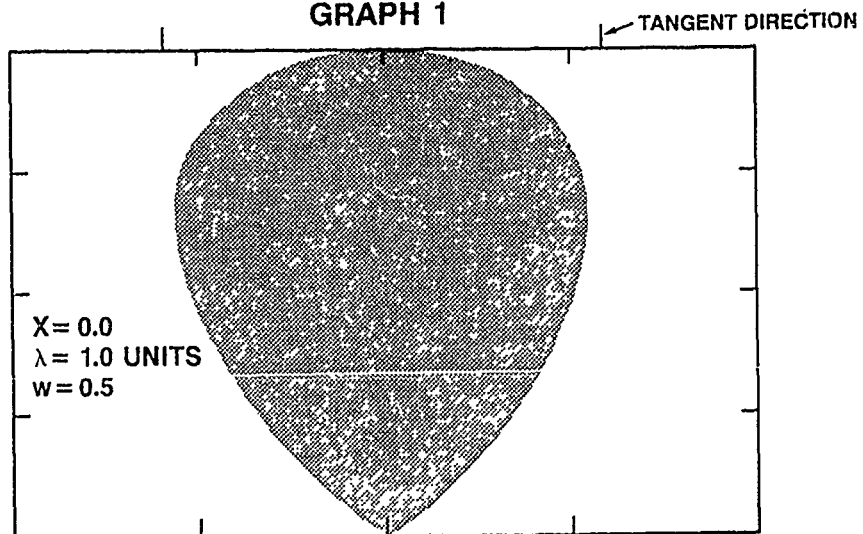
N.010

A2393



GENERATING A RAY-LIKE DESCRIPTION
FROM A NUMERICAL KNOWLEDGE OF
THE ELECTROMAGNETIC FIELD

GRAPH 1



GENERATING A RAY-LIKE DESCRIPTION
FROM A NUMERICAL KNOWLEDGE OF THE ELECTROMAGNETIC FIELD



DISCUSSIONS OF GRAPHS #1 AND #2

IT WAS SEEN THAT EXPECTED FEATURES OF THE SEPARATE RADIATION COMING AROUND EACH SIDE OF THE CYLINDER WERE NOT RESOLVED. THIS IS TO BE EXPECTED, SINCE THE AVERAGING WAS DONE OVER LESS THAN A WAVELENGTH. KEEPING THE GEOMETRY AND WAVELENGTH THE SAME, BUT INCREASING THE AVERAGING DISTANCE TO $w = 0.82$, THE SECOND GRAPH RESULTS.

NOTICE THAT ON GRAPH 2, THE DIRECTION OF A LINE TANGENT TO THE CYLINDER AND PASSING THROUGH THE OBSERVATION POINT HAS BEEN MARKED. ONE MAY CLEARLY SEE THAT THE DIRECTION OF THE PEAK IS APPROXIMATELY THAT OF THE TANGENT.

□ □ □ □ □ 6 MAR 86 □ □ □ □ □

GER

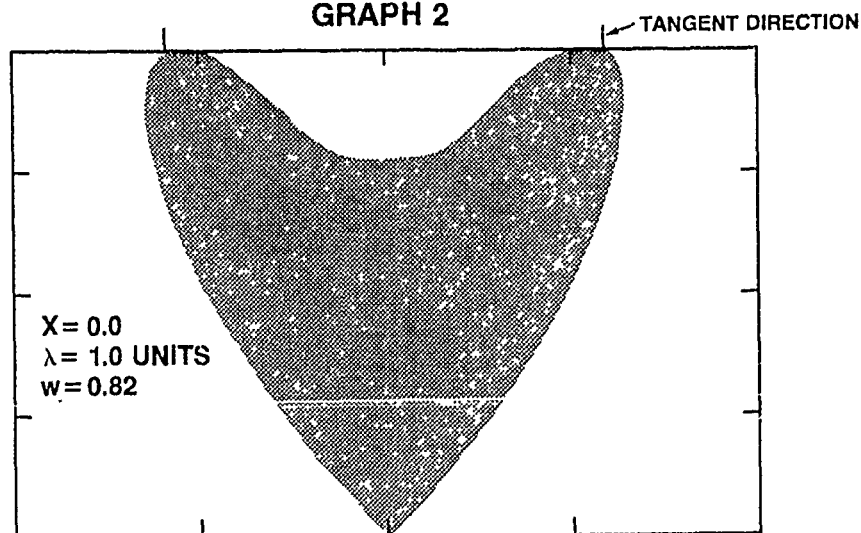
N.011

A2393



GENERATING A RAY-LIKE DESCRIPTION
FROM A NUMERICAL KNOWLEDGE OF
THE ELECTROMAGNETIC FIELD

GRAPH 2



GENERATING A RAY-LIKE DESCRIPTION
FROM A NUMERICAL KNOWLEDGE OF THE ELECTROMAGNETIC FIELD



DISCUSSIONS OF GRAPHS #2 AND #3

THE RADIATION FROM EACH SIDE NOW CAN BE CLEARLY RESOLVED. INCREASING THE AVERAGING DISTANCE TO $w = 1.0$, WE FIND GRAPH #3.

OVERLAYING GRAPHS 2 AND 3, THE INCREASED RESOLUTION ON GRAPH 3 IS APPARENT.

ONE ALSO CAN SEE THAT THE DIRECTIONS INDICATED ARE VERY SLIGHTLY DIFFERENT. WHEN ONE AVERAGES OVER A LARGER REGION, THAT AVERAGE INCLUDES THE REGION WHERE THE RAYS ARE HEADED TOWARDS THE CENTER AT A SHALLOWER ANGLE. THIS EFFECT IS OBSERVED ON THE GRAPHS.

□ □ □ □ □ 6 MAR 86 □ □ □ □ □

GER

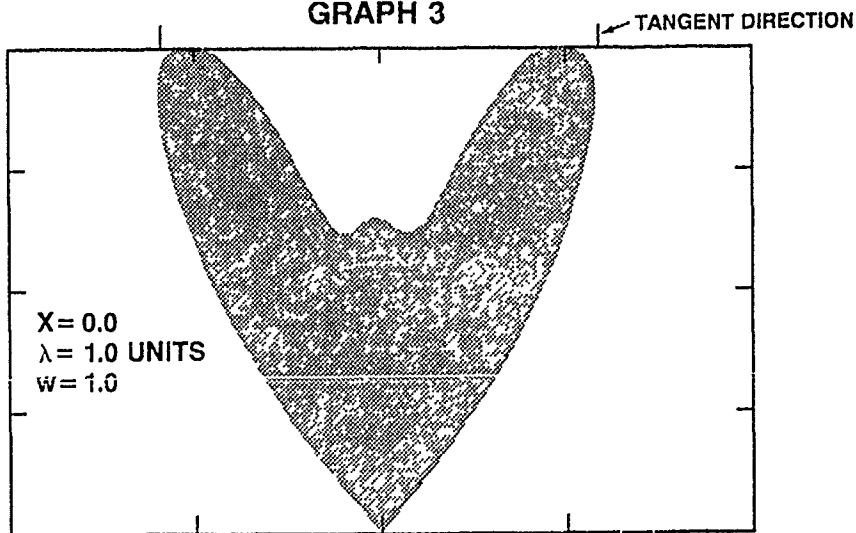
N.012

A2393



GENERATING A RAY-LIKE DESCRIPTION
FROM A NUMERICAL KNOWLEDGE OF
THE ELECTROMAGNETIC FIELD

GRAPH 3



GENERATING A RAY-LIKE DESCRIPTION
FROM A NUMERICAL KNOWLEDGE OF THE ELECTROMAGNETIC FIELD



DISCUSSIONS OF GRAPHS #4, #5, & #6

ON THE FOLLOWING THREE GRAPHS, WE MOVE THE OBSERVATION POINT FROM THE CENTER ($X = 0$), SUCCESSIVELY TO THE SIDE ($X = -0.5, -1.0, -2.0$).

NOTICE THAT AS WE DO SO, THE RADIATION GOING AROUND THE LEFT SIDE OF THE CYLINDER MUST CURVE LESS. THUS, THE RADIATION SHOULD BE HEADED MORE DIRECTLY UPWARD (I.E. SOMEWHAT LESS TO THE RIGHT) AND SHOULD BE STRONGER. THIS IS INDEED FOUND. SIMILARLY, THE RADIATION GOING AROUND THE RIGHT SIDE MUST CURVE MORE. THUS, IT SHOULD BE HEADED LESS DIRECTLY UPWARD (I.E. MORE TO THE LEFT), AND SHOULD BE WEAKER. THIS IS ALSO FOUND, UP TO GRAPH #6. WHERE IT IS SO WEAK THAT IT IS NOT DISTINGUISHABLE ON THE LINEAR PLOT SHOWN.

□ □ □ □ □ 6 MAR 88 □ □ □ □ □

GER

N.013

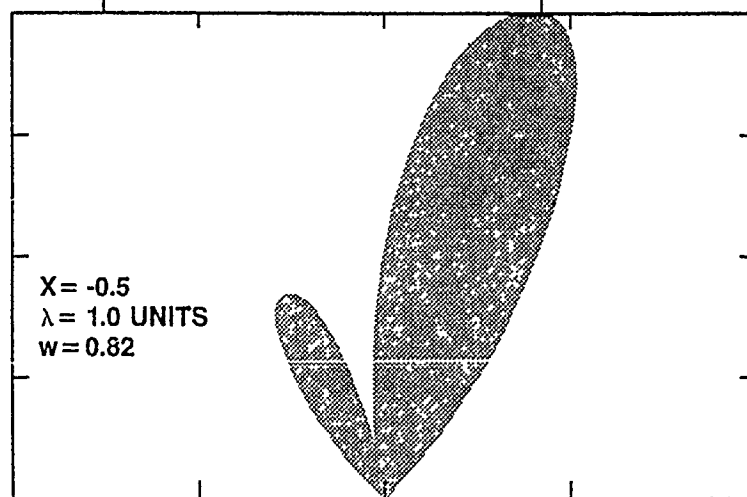
A2393



GENERATING A RAY-LIKE DESCRIPTION
FROM A NUMERICAL KNOWLEDGE OF
THE ELECTROMAGNETIC FIELD

TANGENT DIRECTION

GRAPH 4



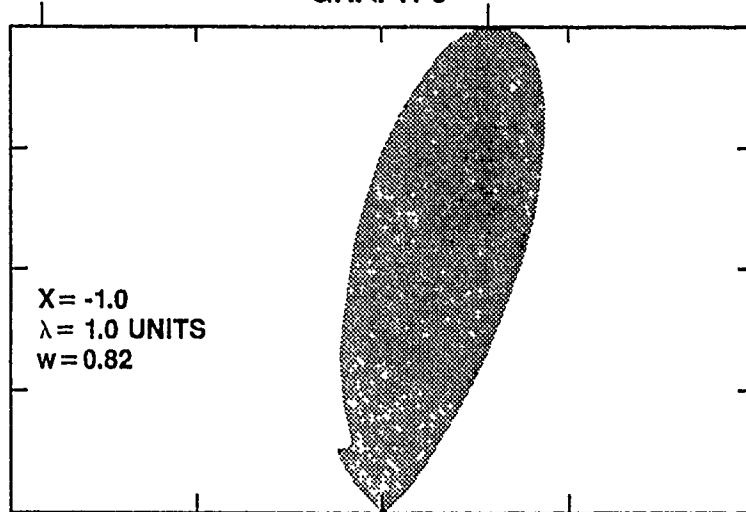
N.014

A2393



GENERATING A RAY-LIKE DESCRIPTION FROM A NUMERICAL KNOWLEDGE OF THE ELECTROMAGNETIC FIELD

GRAPH 5



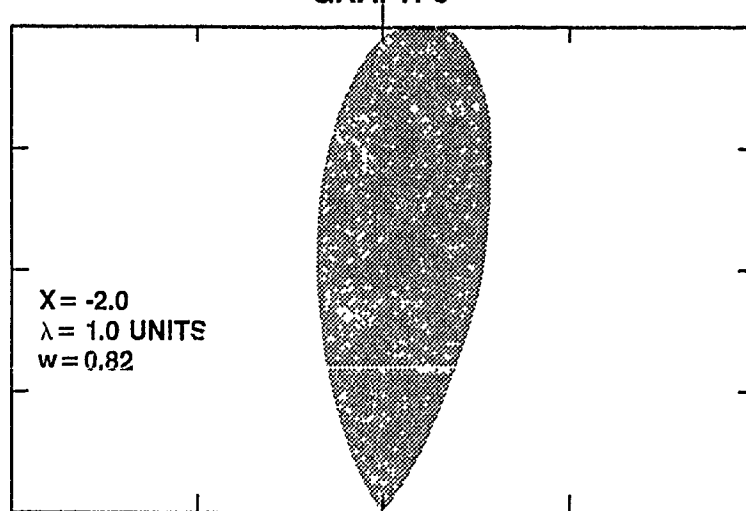
N.015

A2393



GENERATING A RAY-LIKE DESCRIPTION FROM A NUMERICAL KNOWLEDGE OF THE ELECTROMAGNETIC FIELD

GRAPH 6



GENERATING A RAY-LIKE DESCRIPTION
FROM A NUMERICAL KNOWLEDGE OF THE ELECTROMAGNETICAL FIELD



DISCUSSIONS OF GRAPHS #7 - #10

THE FOLLOWING GRAPHS RECONSIDER THE GEOMETRIES JUST SEEN, BUT FOR $\lambda = 0.5$.
ALL OF THE PREVIOUSLY MENTIONED FEATURES ARE PRESENT, WHILE THEY ALL ARE SHARPER.
IN OTHER WORDS, BECAUSE THE WAVELENGTH IS ONE HALF AS LARGE, THE LOBES ARE HALF
AS WIDE. AGAIN, IN THIS CASE, THE DIRECTIONS OF THE PEAK AMPLITUDES CHANGE AS
EXPECTED WHEN THE OBSERVATION POINT MOVES.

□ □ □ □ □ 5 MAR 86 □ □ □ □ □ GER

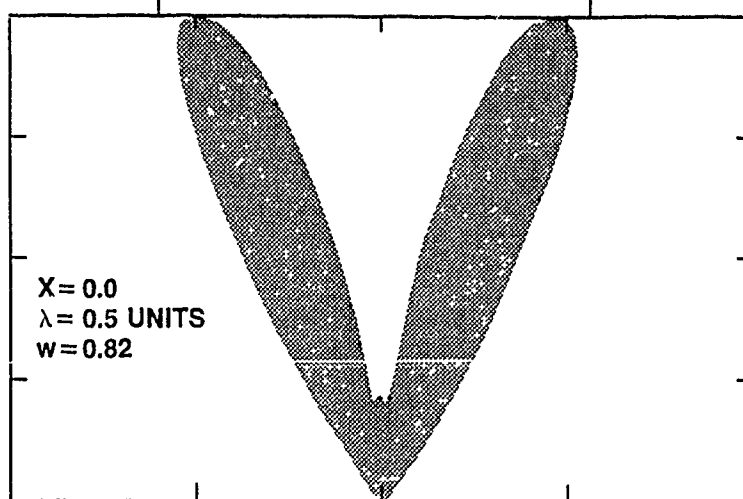
N.016

A2393



GENERATING A RAY-LIKE DESCRIPTION
FROM A NUMERICAL KNOWLEDGE OF
THE ELECTROMAGNETIC FIELD

GRAPH 7



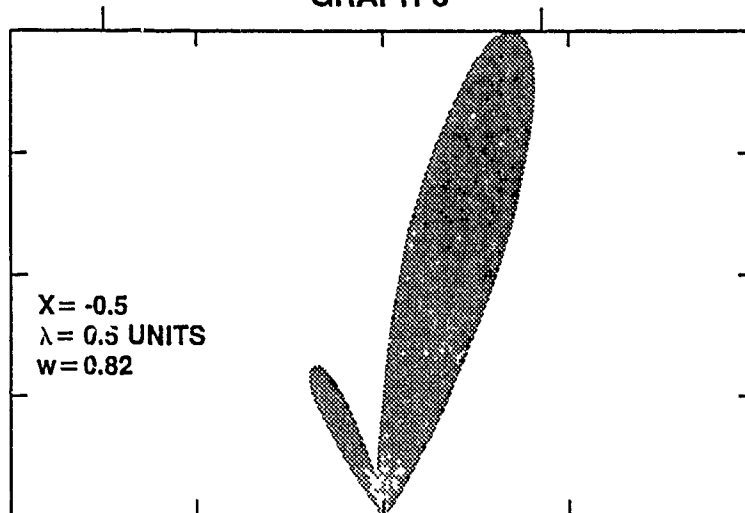
N.017

A2393



GENERATING A RAY-LIKE DESCRIPTION FROM A NUMERICAL KNOWLEDGE OF THE ELECTROMAGNETIC FIELD

GRAPH 8



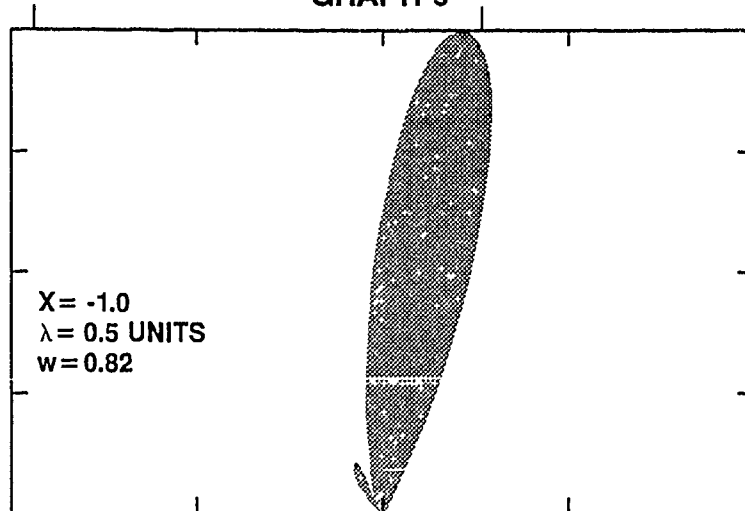
N.018

A2393



GENERATING A RAY-LIKE DESCRIPTION FROM A NUMERICAL KNOWLEDGE OF THE ELECTROMAGNETIC FIELD

GRAPH 9



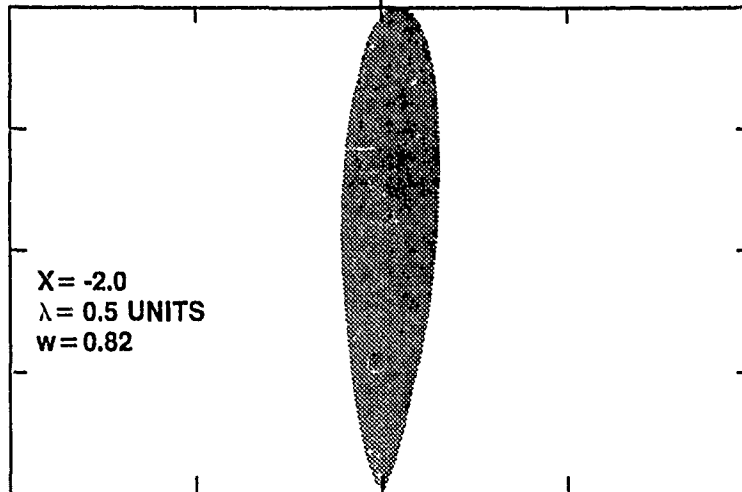
N.019

A2393



GENERATING A RAY-LIKE DESCRIPTION FROM A NUMERICAL KNOWLEDGE OF THE ELECTROMAGNETIC FIELD

GRAPH 10



GENERATING A RAY-LIKE DESCRIPTION FROM A NUMERICAL KNOWLEDGE OF THE ELECTROMAGNETIC FIELD



DISCUSSION OF GRAPH #11

ON THE NEXT GRAPH, #11, WE SEE THE EFFECT OF VARYING THE AVERAGING DISTANCE ON THE DIRECTIONS OF THE PEAKS. SINCE THE WAVELENGTH USED HERE IS VERY SHORT, ONLY ONE-QUARTER UNIT, THE PEAKS WILL BE OBSERVABLE FOR SMALL AVERAGING DISTANCES w . WHEN w IS FAIRLY LARGE, I.E. $w = 0.82$, THE PEAKS ARE QUITE NOTICEABLY MORE TOWARDS THE Z - AXIS THAN ARE THE TANGENT DIRECTIONS. THIS IS BECAUSE WHEN w IS THIS LARGE, WE ARE USING NOT ONLY THE FIELD AT THE CENTER, BUT ALSO QUITE FAR FROM THE CENTER. HOWEVER, AS w DECREASES TO 0.5 AND THEN TO 0.25, THE PEAKS BECOME VERY CLOSE TO LYING IN THE TANGENT DIRECTIONS. WHEN $w = 0.18$, THE GRAPH IS SO SPREAD OUT THAT THE PEAK CANNOT BE PRECISELY LOCATED. ALTHOUGH THIS METHOD IS DIFFERENT THAN GTD, THIS METHOD FINDS DIRECTIONS WHICH, FOR SHORTER WAVELENGTHS, ARE APPROXIMATELY IN THE TANGENT LINE DIRECTIONS FOUND IN GTD.

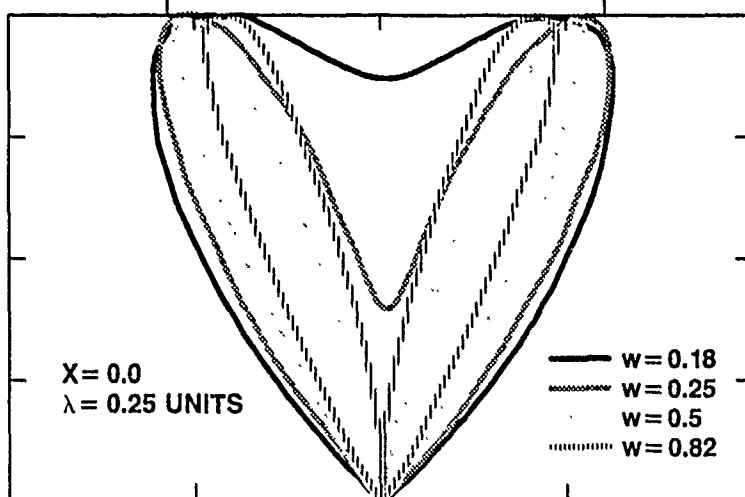
N.020

A2393



GENERATING A RAY-LIKE DESCRIPTION FROM A NUMERICAL KNOWLEDGE OF THE ELECTROMAGNETIC FIELD

GRAPH 11



GENERATING A RAY-LIKE DESCRIPTION FROM A NUMERICAL KNOWLEDGE OF THE ELECTROMAGNETIC FIELD



DISCUSSIONS OF GRAPHS #12 AND #13

THE LAST TWO GRAPHS, #12 AND 13, ILLUSTRATE THE DYNAMIC RANGE AVAILABLE USING THIS METHOD. FIRST, NOTICE THE POLAR PLOT OF THE ELECTRIC FIELD, USING A LINEAR SCALE TO SHOW THE ELECTRIC FIELD. THE ONE PEAK IS CLEARLY VISIBLE. HOWEVER, BECAUSE OF THE SHORT WAVELENGTH (λ IS ONE-QUARTER UNIT WHICH IS ONE-EIGHTH OF THE RADIUS OF THE CYLINDER), THE OTHER PEAK HAS A GREATLY REDUCED INTENSITY. HOWEVER, ON THE LOGARITHMIC PLOT, BOTH PEAKS ARE CLEARLY VISIBLE. OVER SIXTY DECIBELS OF DYNAMIC RANGE OF POWER ARE ATTAINED HERE. IT APPEARS THAT THE LIMITING FACTOR HERE IS THE ANGULAR RESOLUTION AS DETERMINED BY w^- . MUCH LARGER DYNAMIC RANGES ARE PROBABLY ATTAINABLE IN SITUATIONS THAT ALLOW MORE ANGULAR RESOLUTION (SUCH AS SHORTER WAVELENGTH).

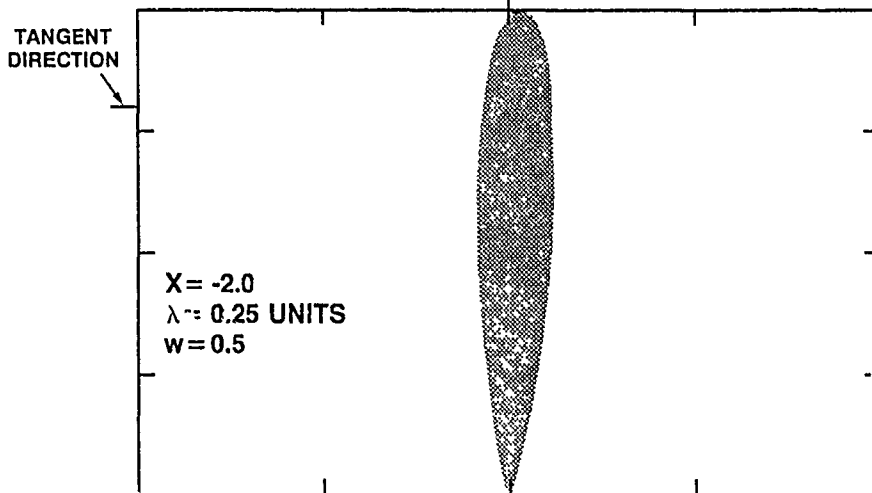
N.021

A2393



GENERATING A RAY-LIKE DESCRIPTION FROM A NUMERICAL KNOWLEDGE OF THE ELECTROMAGNETIC FIELD

GRAPH 12 LINEAR SCALE



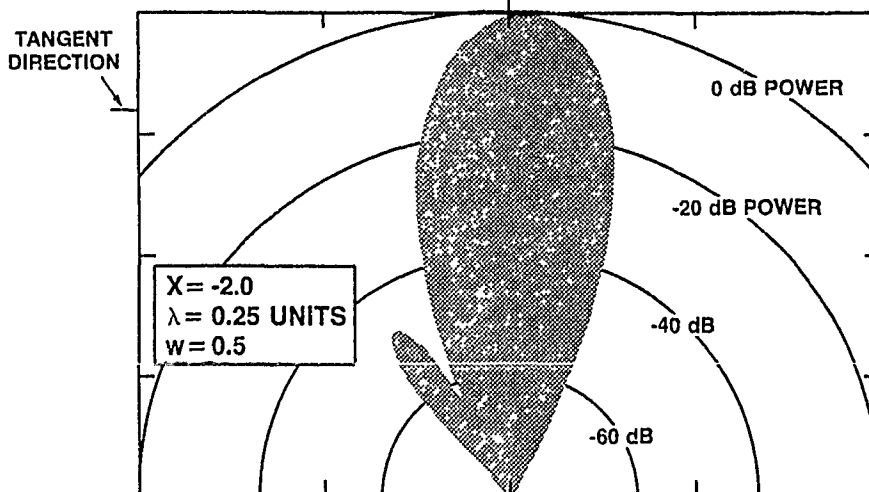
N.022

A2393



GENERATING A RAY-LIKE DESCRIPTION FROM A NUMERICAL KNOWLEDGE OF THE ELECTROMAGNETIC FIELD

GRAPH 13 LOG SCALE



N.009

A2393



GENERATING A RAY-LIKE DESCRIPTION FROM A NUMERICAL KNOWLEDGE OF THE ELECTROMAGNETIC FIELD

CONCLUSIONS

- A RAY-LIKE DESCRIPTION CAN BE GENERATED FROM NUMERICAL VALUES OF THE FIELD
- THIS METHOD CAN BE USED EVEN WHEN GTD CAN'T BE USED
- THE RESULTING PICTURES CAN BE A USEFUL DIAGNOSTIC
- THE MODIFICATIONS NECESSARY TO APPLY THIS METHOD NEAR CONDUCTING SURFACES, IN CAVITIES, AND IN GENERAL MATERIALS ARE BELIEVED UNDERSTOOD, AND THE COMPUTER CODE IS BEING WRITTEN
- THE METHOD PRESENTED HERE SHOULD PROVE USEFUL IN ANALYZING AND PRESENTING THE OUTPUT OF NUMERICAL CODES. IN PARTICULAR, WHEN MANY INTERACTIONS COMBINE TO CAUSE A FIELD, THIS METHOD WILL GIVE A USEFUL AND SIMPLE DESCRIPTION OF THAT NET FIELD

COMPUTER AIDED ENGINEERING IN EM TECHNOLOGY

John Kuras and Nazih Youssef
P. O. Box 3999
Boeing Aerospace Company
Seattle, WA 98124-2499

Rapid advances in detection technology combined with the continuous demand to lower RCS has forced RCS analysts to update and to improve their modeling codes. This is not a simple task, especially if a wide range of capabilities are desired while maintaining simplicity. In order to meet this challenge, Boeing Aerospace Company has been active in developing universal input/output formats for use in RCS codes. These formats consist of advanced tutorial methods combined with graphical capabilities. Highlights of the approach are:

1. User-friendly,
2. designer-oriented,
3. provide a fast learning process,
4. speed up code development,
5. increase data input versatility,
6. decrease problem turn-around time, as well as,
7. increase modeling accuracy.

Computer Aided Engineering in EM Technology

John C. Kuras, Boeing Aerospace Company

Nazih Youssef, Boeing Aerospace Company

The computer solution of radar scattering problems can be divided into three steps: 1) the preparation of input geometry and system parameters, 2) the execution of a code (or codes) to estimate the scattered fields, and 3) the interpretation of the results produced by those codes. A wide variety of computer techniques are used to perform the estimation step. High frequency/large body problems are usually solved using physical optics or physical theory of diffraction techniques, while the scattering from smaller bodies or body components is typically estimated via method of moment or finite element techniques. Regardless of the type of code used during the estimation step, all of these codes require some form of geometry description for input and produce some form of plotable parametric output data.

In the past (see Figure 1), the geometry data was generated by either entering one coordinate at a time on a keyboard, or by writing custom (geometry specific) programs to write the coordinate data to a file. The RCS engineer usually needs to run more than one of these codes for each analysis. Therefore, in the past, he needed to generate the geometry in several different formats, one for each code he desired to run. These methods were obviously quite time consuming and prone to error.

When performing a full body RCS analysis, the outputs from these codes must often be combined using method of component techniques. In the past this combining process was also done by hand.

The bottom line problems with the previous approach to computer aided RCS analysis at Boeing were that input generation and results interpretation were too labor intensive and running the various codes required excessive code specific knowledge. The effect of these problems was discouragement from using the available analytical codes.

The objectives (see Figure 2) of the RCS Computer Aided Engineering (CAE) project at Boeing Aerospace are to reduce the flow time required to perform an analysis from several weeks down to 1 or 2 days while retaining the full analytical capability of existing codes. Where necessary, new tools will be developed to aid the RCS design process. However, the overall system must remain tailorable to specific design

project needs, not only at the module level (codes added or deleted as needed), but at the user level as well. The latter implies some form of user programmability.

The approach (see Figure 3) taken was to interface the existing RCS codes into an integrated system called ISAT (Interfaced Scatter Analysis Tools). As analytical codes are incorporated into ISAT, they are interfaced to a common geometry and material properties database, a common output database, and interactive tutorial drivers are written to process the parametric data (frequencies, scatter angles, options, etc.) required by the code. The ISAT system includes utility programs that make full use of interactive graphics for geometry preparation and results display. A utility is provided to combine results from various sources using the method of components, and interfaces are also provided to assist in the transfer of geometry data between the various Boeing technology organizations.

The flexibility of file interfaced systems (see Figure 4) is an accepted fact within software engineering¹ circles. Due to the interfaced structure of ISAT, modules can be easily introduced or deleted as needed. If a particular design project within Boeing has their own computer and needs to run only a subset of the available analytical tools available in ISAT, the subset can be converted to the project's computer without concern for the remaining modules. Likewise, if a project has a special analytical tool that they wish to include in their copy of ISAT, it can be quickly and easily interfaced with maximum confidence that its inclusion will not affect the other codes in the system.

The engineer's productivity (and then, analysis flow time) is enhanced in three ways when using ISAT: via interactive tutorial drivers, via graphical input and output, and via the ISAT user document.

¹ E. Yourdon and L. Constantine, "Structured Design," Yourdon Press, N.Y., Second Edition, Page 324.

The interactive tutorial drivers can be thought of as a type of expert system that has evolved one step beyond the simple expression of a printed recommendation. Rather than printing a list of suggested execution options as previous systems have done,² Boeing's interactive tutorial drivers interface directly to the code to be executed. Not only do the drivers have sufficient artificial intelligence to ask the user all of the questions necessary to prepare a code for execution, but they are also able to check the data input by the user, and produce syntactically and semantically correct parameter data for the code.

Figure 5 contrasts interactive tutorial input with the more commonly used menu driven type of input. The tutorial system is task oriented: once the overall task is selected, the user is prompted with questions that will further refine the specific task to be performed. The menu driven system is option oriented: the lowest level menus in the hierarchy set options that are used to specify the task that the system is to perform. With menu driven systems, the hierarchy may need to be traversed from top to bottom level several times in order to select the proper options. It is up to the user to know which options must be set and which menus set those options. Therefore, the menu driven systems are not only more difficult to learn, but are also less likely to catch user errors. The menu driven system has little or no built-in intelligence.

In ISAT, the SDRC IDEAS package is currently used to perform the 3-D graphical input and output displays. It was selected for use within ISAT because it is the best commercially available package that suits our needs, and it can be licensed for far less than it would cost to develop a comparable capability.

The significant features of the IDEAS package are illustrated in Figure 6.

² B. Buchanan and E. Shortliffe, "Rule-Based Expert Systems, The MYCIN Experiments of the Stanford Heuristic Programming Project," Addison-Wesley Publishing, 1984, Page 315.

The GEOMOD module in IDEAS contains an excellent surface fitting routine, it can perform boolean operations on objects (to drill holes or add appendages), and has features which allow the user to easily position objects relative to one another. In addition, GEOMOD creates a faceted model of 3-D objects that is ideally suited for input into physical optics codes. The GEOMOD faceting (see Figure 7) is such that facet dimensions are short in directions of high surface curvature and long in directions of low curvature.

On the other hand, the SUPERTAB module of IDEAS creates meshes that are ideally suitable for input into method of moments codes (see Figure 8). Such codes generally require element dimensions to be less than a given value and with near unity aspect ratio. SUPERTAB can also produce meshes that become more dense in a particular area, thus allowing finer meshes around discontinuities or areas of high flux gradient. SUPERTAB can also create surface attached contour and surface attached X-Y plots. In ISAT, these are used to display field density within dielectrics (Figure 9) and surface current densities (Figures 10 and 11).

In addition, the IDEAS package supports a wide variety of graphics terminals, and makes full use of color, gray scales, and solid modeling features when they are available on the hardware. IDEAS is also user programmable (allowing the user to design custom commands) and is provided with considerable documentation. However, IDEAS is not tutorially driven, and thus it suffers from a higher learning curve than the other modules in ISAT.

Experience has shown that the importance of the user documentation for systems such as ISAT cannot be overstated. The user document is generally the first part of the system that new users are exposed to. The impression that the user document makes with the new user influences his view of the overall system during the entire learning phase and beyond. It is important for the user document to be thorough in its coverage of the basics such as login and file management so as not to leave the inexperienced computer user floundering. However, it is equally important for the document to not be flippant, contrite, or superfluous. Such documentation styles tend to irritate intelligent readers. The primary audience for the user document is engineers, and engineers generally appreciate compact factual documentation.

The organization of the ISAT manual is illustrated in Figure 12. It is logically organized such that the information goes from general to specific as the user proceeds thru the sections. Each code is documented independently in the ISAT manual, so that a user need not become acquainted with codes other than the specific code that he needs to use. This also allows for easy modification of the manual as codes are added or deleted from the system. The data within each section is presented in formats that are convenient for the interactive user during data preparation, processing, and review. The sections contain:

Section 1 Contains brief one or two line descriptions of each of the codes within ISAT. From these descriptions, the user can generally determine which analytical codes he will need to run to complete his analysis.

Section 2 Contains the ISAT procedures flow charts. From these charts the user can determine which pre- or post-processing utilities can be used with the codes he needs to run.

Section 3 Contains the "input-output files charts." One chart is provided for each procedure. These charts are used to determine the input files required by, and the output files produced by the codes and pre- or post-processors he needs to run. If only one code is to be run, the chart can also be used to keep track of the user's file names.

Section 4 Contains an introduction to the VAX VMS interactive operating system and CMEDIT, the portable text editor used within ISAT. The commands in this section help the user to create and manage his input and output files interactively.

Section 5 Contains a special form to help the user keep track of the names and places of disk files, magnetic tapes, and job names.

Section 6 Is divided into subsections, each subsection (or "Chapter") number corresponds to the procedure number for the code which the chapter describes. Each procedure subsection (or chapter) contains: 1) an introduction to the procedure, 2) a description of the procedure, problem size capabilities, and input and output data files, 3) aids for preparation of

input files, 4) aids for examination of output files, and explanations of diagnostics likely to be produced by the procedure, and 5) acknowledgements, references, consultation sources, and certification status.

The ISAT User's Manual is provided in a loose leaf three ring binder so that figures such as the file management chart and data preparation aids can be easily removed and reproduced by the user. Each section and procedure chapter is separated by labeled tab dividers for the user's convenience.

Figure 13 illustrates the current status of ISAT. The analytical codes include 2-D and body of revolution physical optics and method of moment codes and 3-D physical optics codes. Utilities are included for database management, tape management, file editing, micro-fiche generation, document quality plotting, and the IDEAS package. Interfaces are provided for transferring geometry data to and from other Boeing technology organizations and subsidiaries. The interactive tutorial capability is provided either by the INGEN utility or has been built directly into the analytical code. The method of components combining is performed by the RECOTA code.

As is illustrated in Figure 14, the RECOTA code is not only capable of performing a physical optics solution for bodies created in GEOMOD (including component shadowing and multi-scatter), but is also able to read in scattering results from other sources. Measured data from Boeing's RCS ranges or calculated data from any of the other ISAT analytical codes can be read into RECOTA via the "empirical data" input file. Data from the various RECOTA inputs can be switched on and off, windowed, and combined either coherently or incoherently as described by Crispin and Siegel.³

Although ISAT is far from complete, it is a working production tool. Since its initial release in 1983, it has been used on many design projects at Boeing, including several full body analyses and dozens of component analyses. In addition to the ongoing job of interfacing additional analytical codes, development tasks directly associated with ISAT are in progress in the following three areas.

³ J. Crispin and K. Siegel, "Radar Cross-Section Analysis," Academic Press, 1968, Chapter 9.

Portable Geometry Package

A need has been indentified within Boeing for a geometry generation and output display package that can be easily ported to various computers and graphics terminals. The package will be simpler than IDEAS in terms of display capability, but will use interactive tutorial input rather than menus.

Unification of Interface Definition

Currently, several different data file formats are used within ISAT to interface the various modules. This not only complicates maintenance, but can limit the versatility of the system as well. The long range goal for ISAT is to have all modules communicate via a common interface format using the RIM relational database manager that is already a part of the system (see Figure 15). Thus as new modules are added, they will be capable of communicating with every relevant part of ISAT via the single interface format.

Software Development Tools for Tutorial Generation

In 1985 MAC, Boeing's precompiler development tool, was installed on our VAX. Work will begin shortly to build a precompiler that will not only increase the productivity of programmers involved with interactive tutorial driver development, but will also allow the incorporation of certain enhancements into the drivers that are impractical now. These enhancements will increase the flexibility of the tutorial language, and permit the eventual development of a declarative format knowledge base for the tutorials. The declarative format is used by most LISP based expert systems, and is easier to define and maintain than the procedural format currently being used in ISAT.

In conclusion, Boeing Aerospace is actively involved in the development of a CAE system for use by the RCS design and analysis engineers. That system, ISAT, is an interfaced set of programs that make extensive use of interactive tutorial dialogues, graphics, and user friendly, compact document to greatly improve the productivity of the computer user. ISAT has seen considerable use at Boeing, and has proven itself in terms of reducing analysis flow times. The ISAT project is open ended; enhancements will continue to be made to the system and new codes will be added as they become available. Near term improvements will include a portable geometry generation package and enhanced flexibility in tutorial dialogues.

Existing RCS System (Examples)

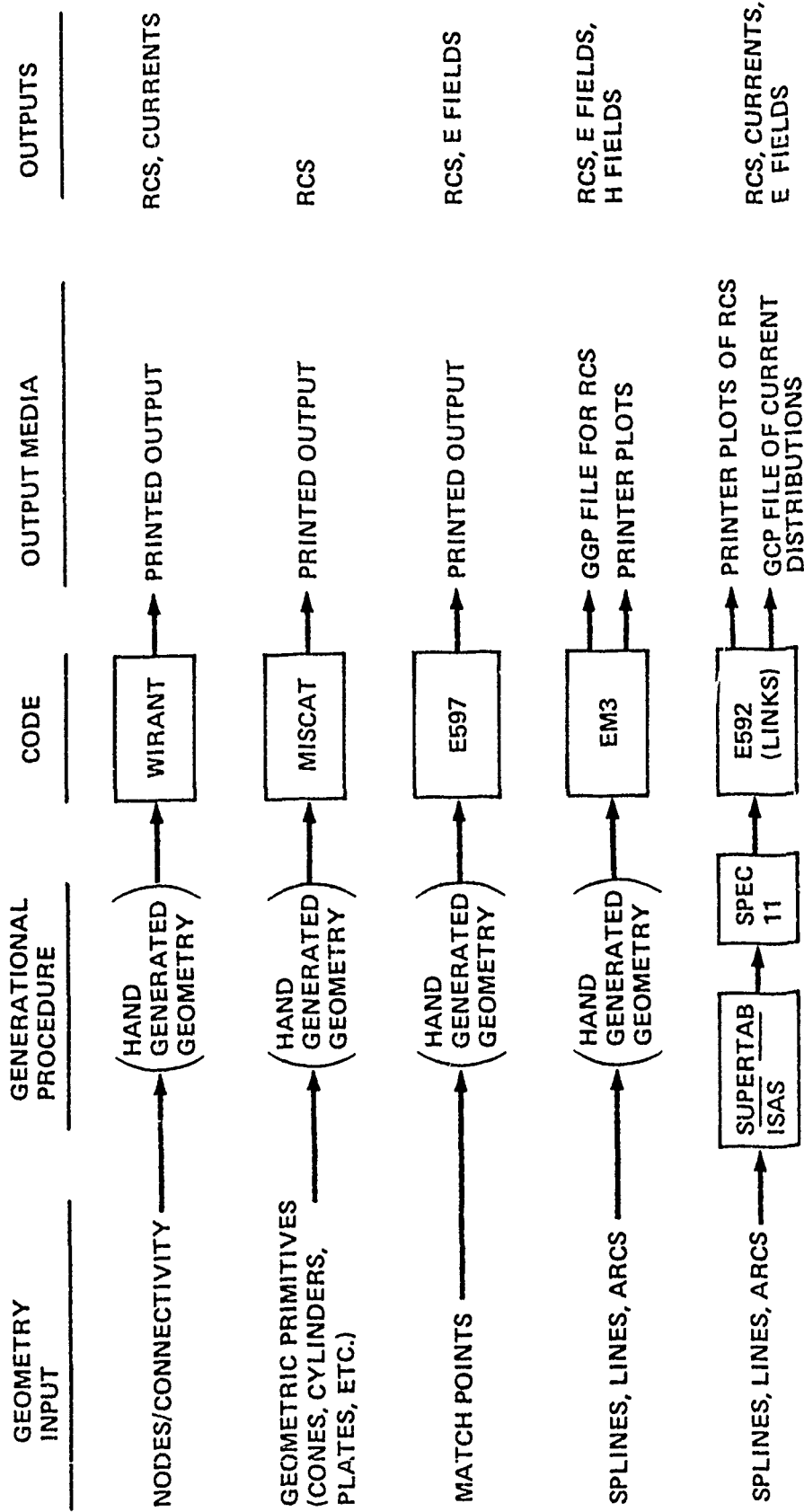


Figure 1:

UNCLASSIFIED

Objectives of ISAT (U)

- Reduce data processing flow times .
- Retain full capability of existing programs
- Develop new capability to aid design
- Open ended

Figure 2:

UNCLASSIFIED

UNCLASSIFIED

ISAT System Diagram (U)

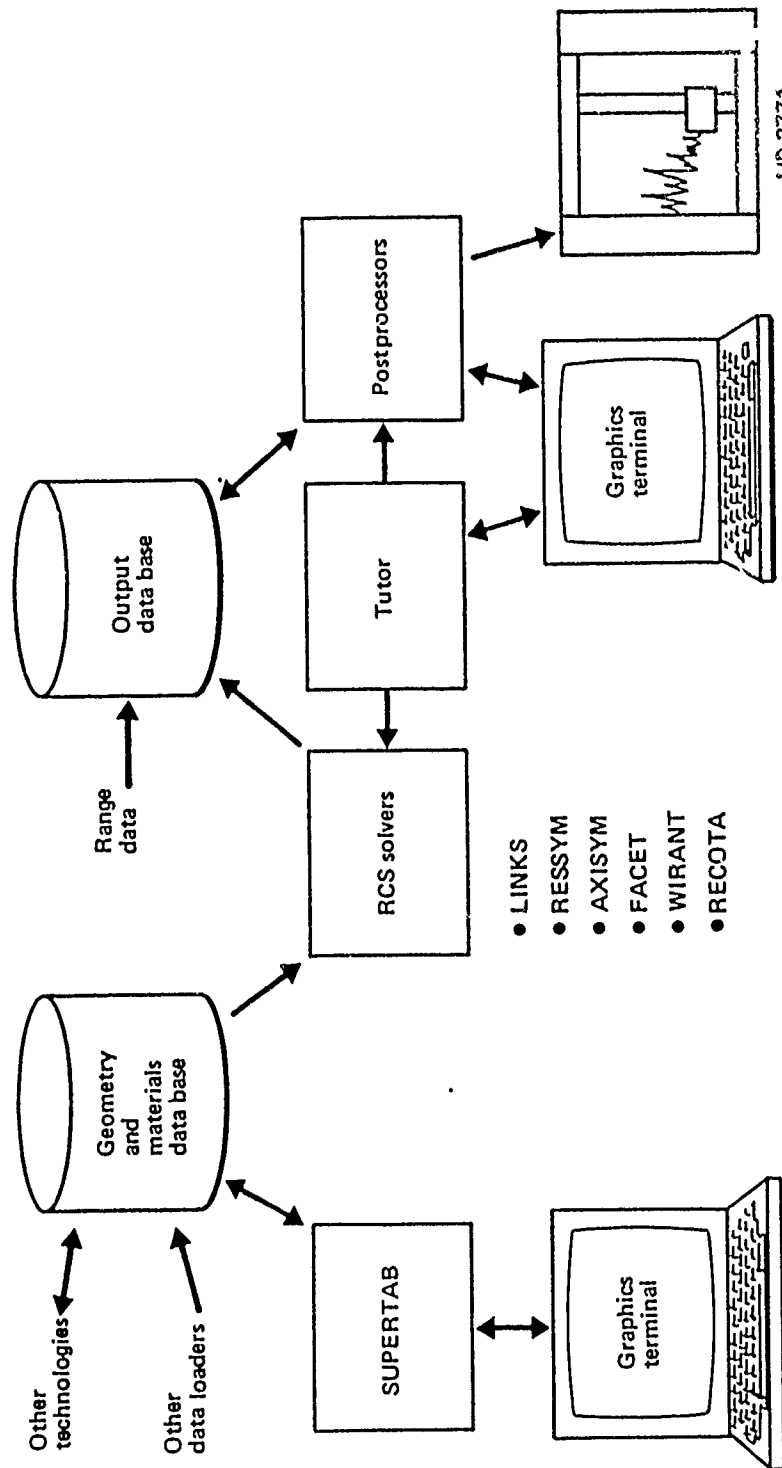


Figure 3:
UNCLASSIFIED

UNCLASSIFIED

Why “Interfaced”? (U)

- So that new modules, methods, or subsystems—

Can be simply introduced

Figure 4:
UNCLASSIFIED

UNCLASSIFIED

Tutorial Versus Menu Input (U)

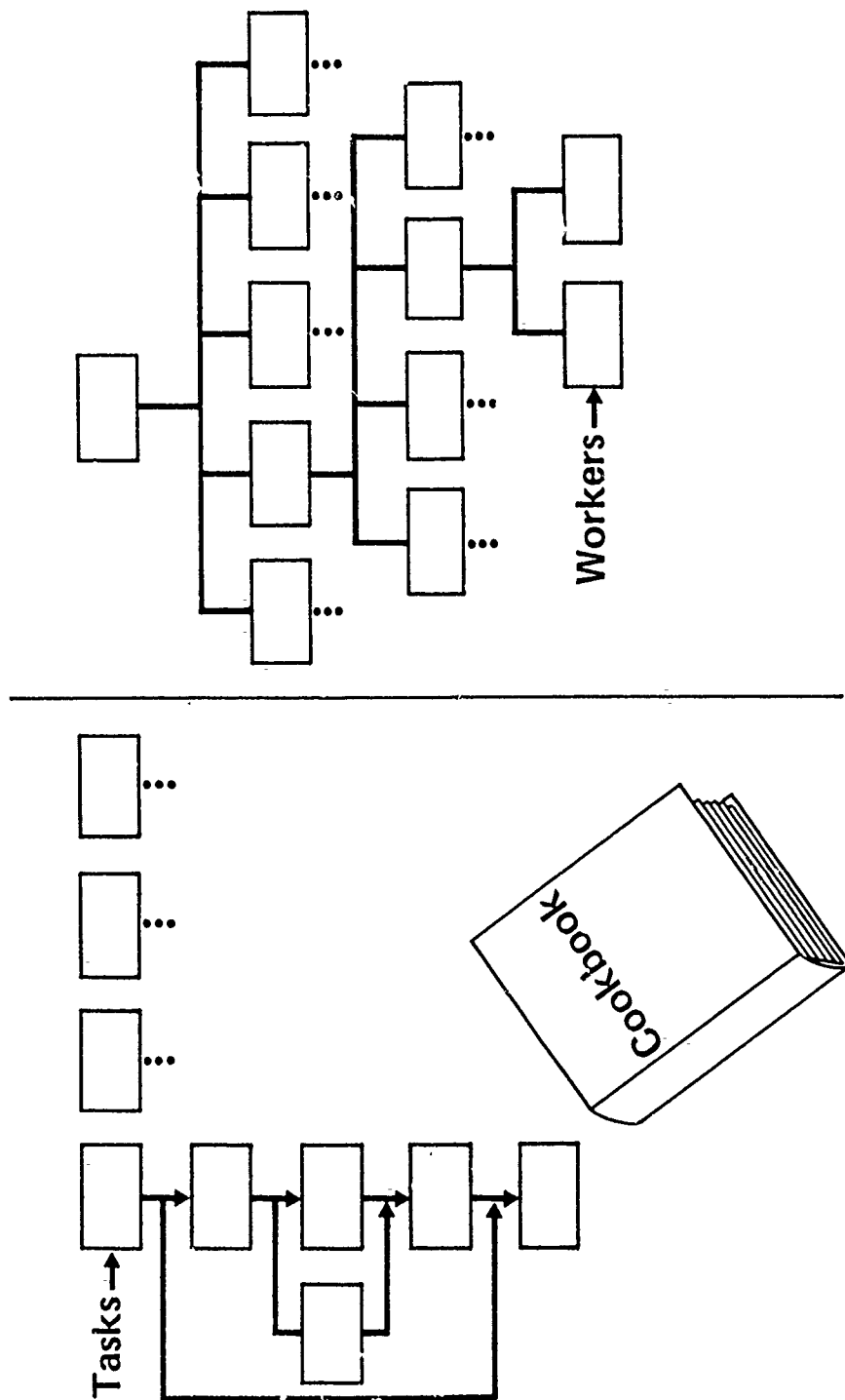


Figure 5:
UNCLASSIFIED

UNCLASSIFIED

Why SUPERTAB/GEOMOD? (U)

- Rational B-splines + geometric primitives
- Boolean operations on bodies
- Autopositioning of subbodies
- Mechanism definition and animation
- Interference checking and lines of intersection
- Auto (weighted) mesh generation and checking
- Ease of mesh modification
- Large library of element types (1D, 2D, and 3D)
- Contour (color optional) and X-Y result displays
- Ultrafast graphics generation
- Wide variety of graphics devices supported
- Programmability
- Documentation

Figure 6:
UNCLASSIFIED

Automatic Facet Generation (U)

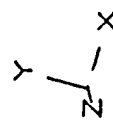
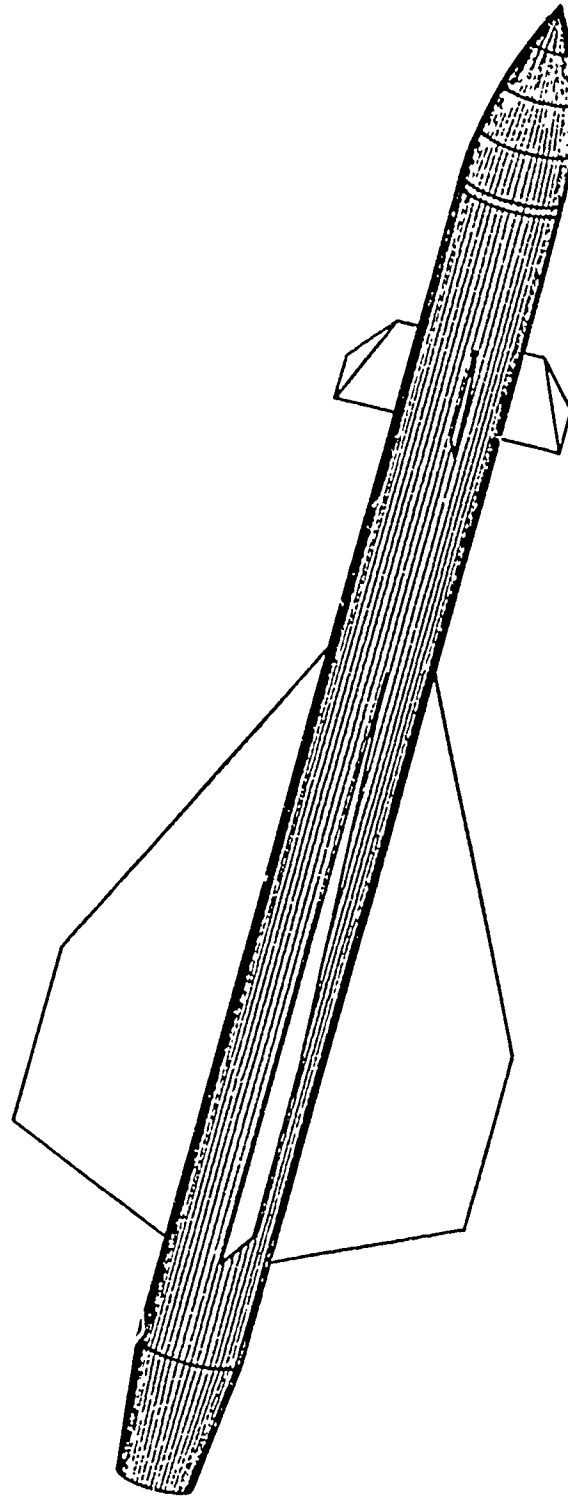
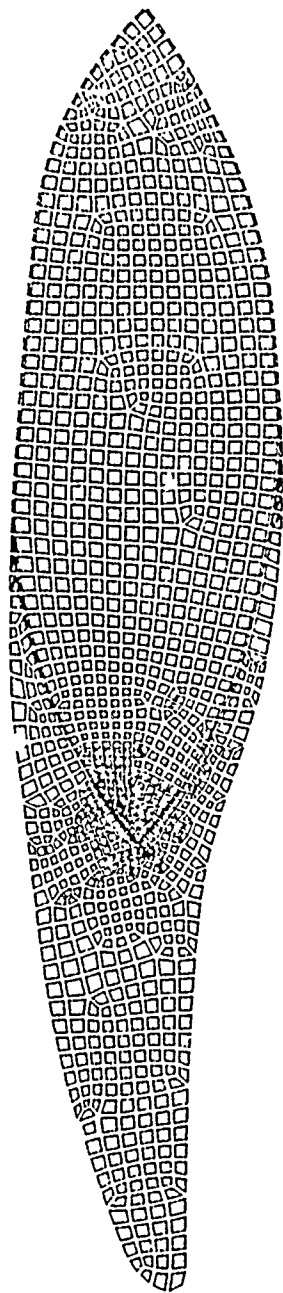


Figure 7:

JCK
03-14-86

Automatic Mesh Generation (U)

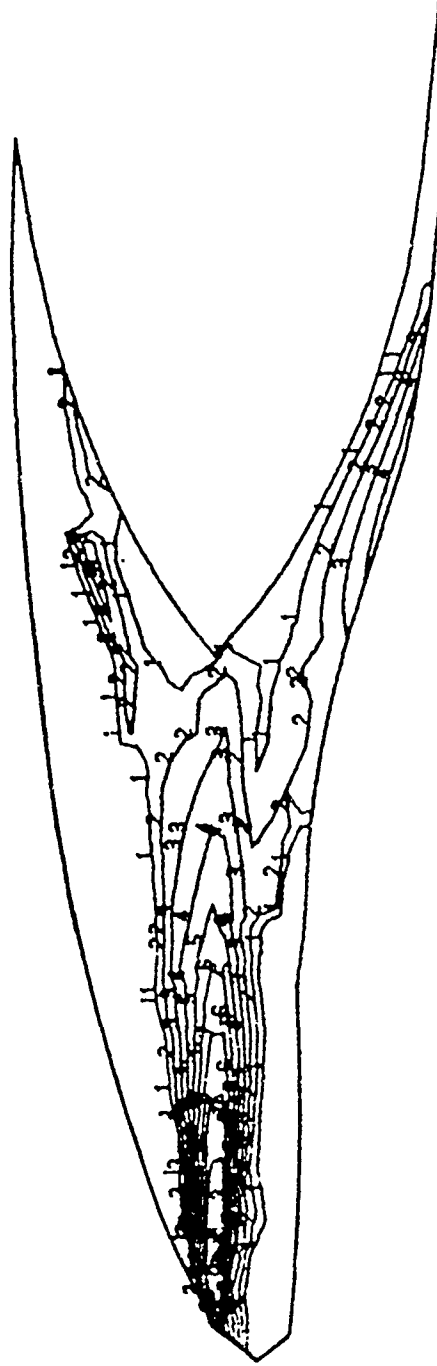


Y — X

Figure 8:

UNCLASSIFIED

Amplitude Contours (U)

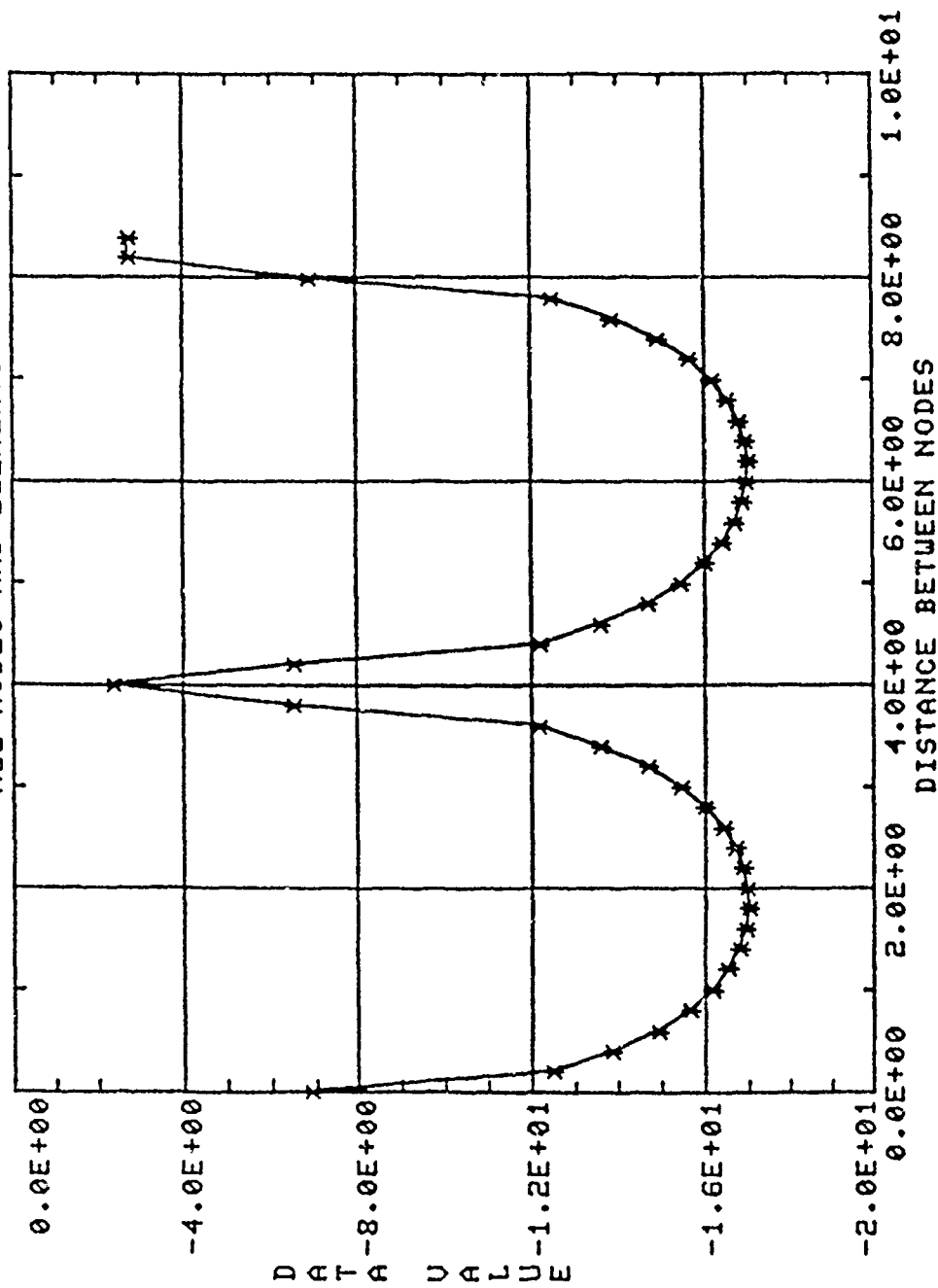


Y
└──┐
X

Figure 9:
UNCLASSIFIED

Segment Current Metal Box (U)

ALL NODES AND ELEMENTS



LOAD CASE: 1

SEGMENT CURRENTS
TOP SURFACE

Figure 10:

Surface Attached Contour Plots (U)

HOT 20 20 ONE
 THETA = 20 PHI = 20 AVERAGE BLADE POSITION = 6.3
 1--6.000E+00
 13--7.800E+01

LEVELS=13
 DELTA=+6.000E+00

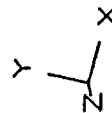
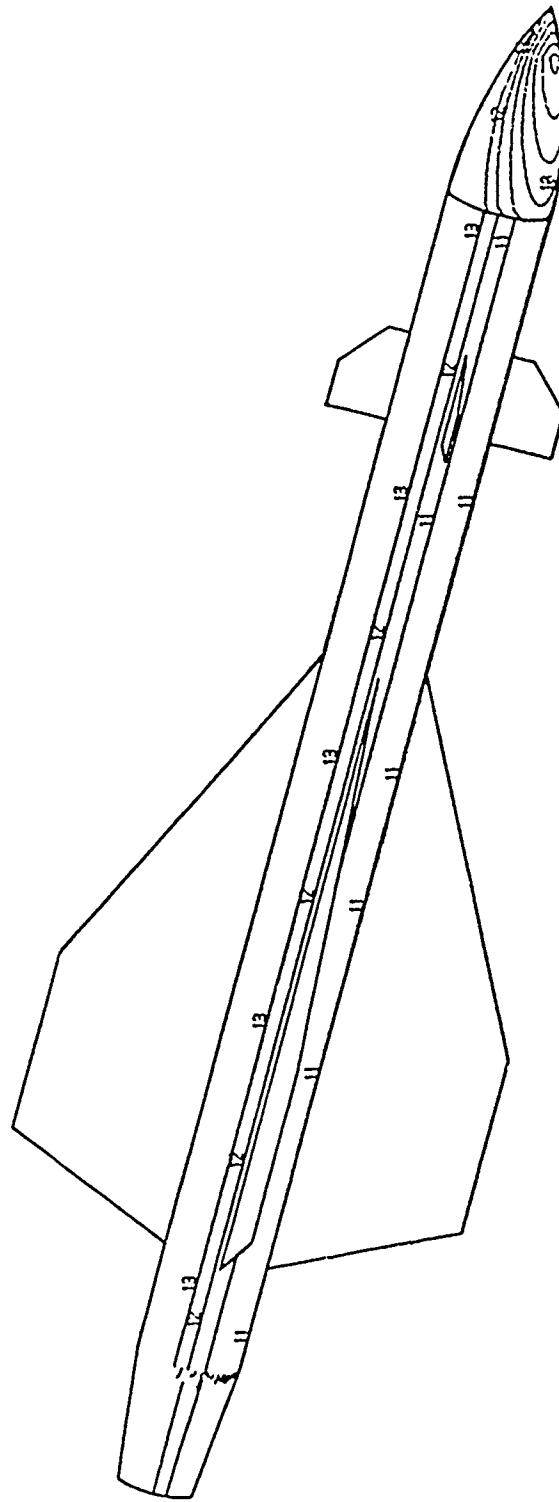


Figure 11:

UNCLASSIFIED

ISAT Users Manual Organization (U)

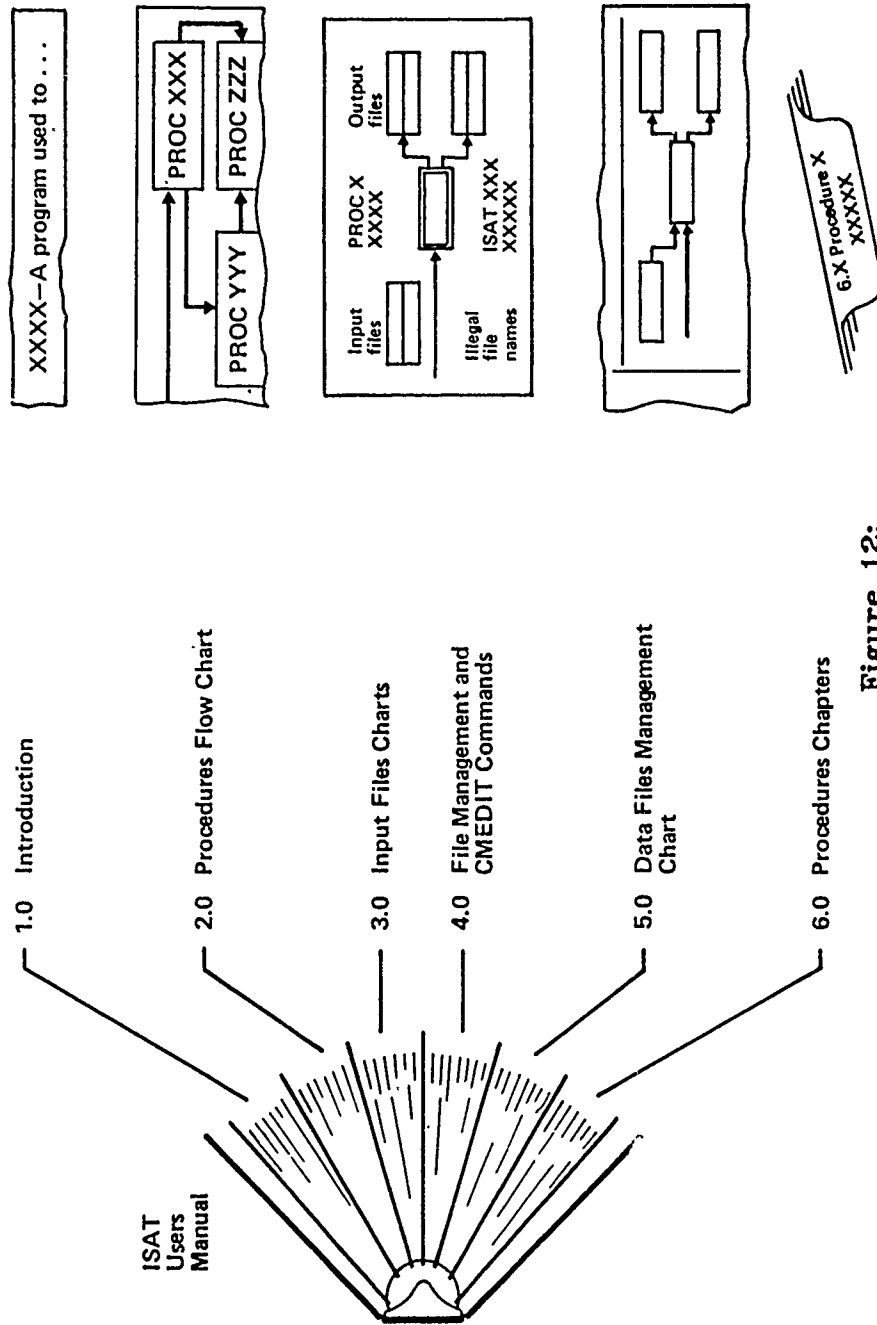


Figure 12:
UNCLASSIFIED

ISAT Block Diagram (U)

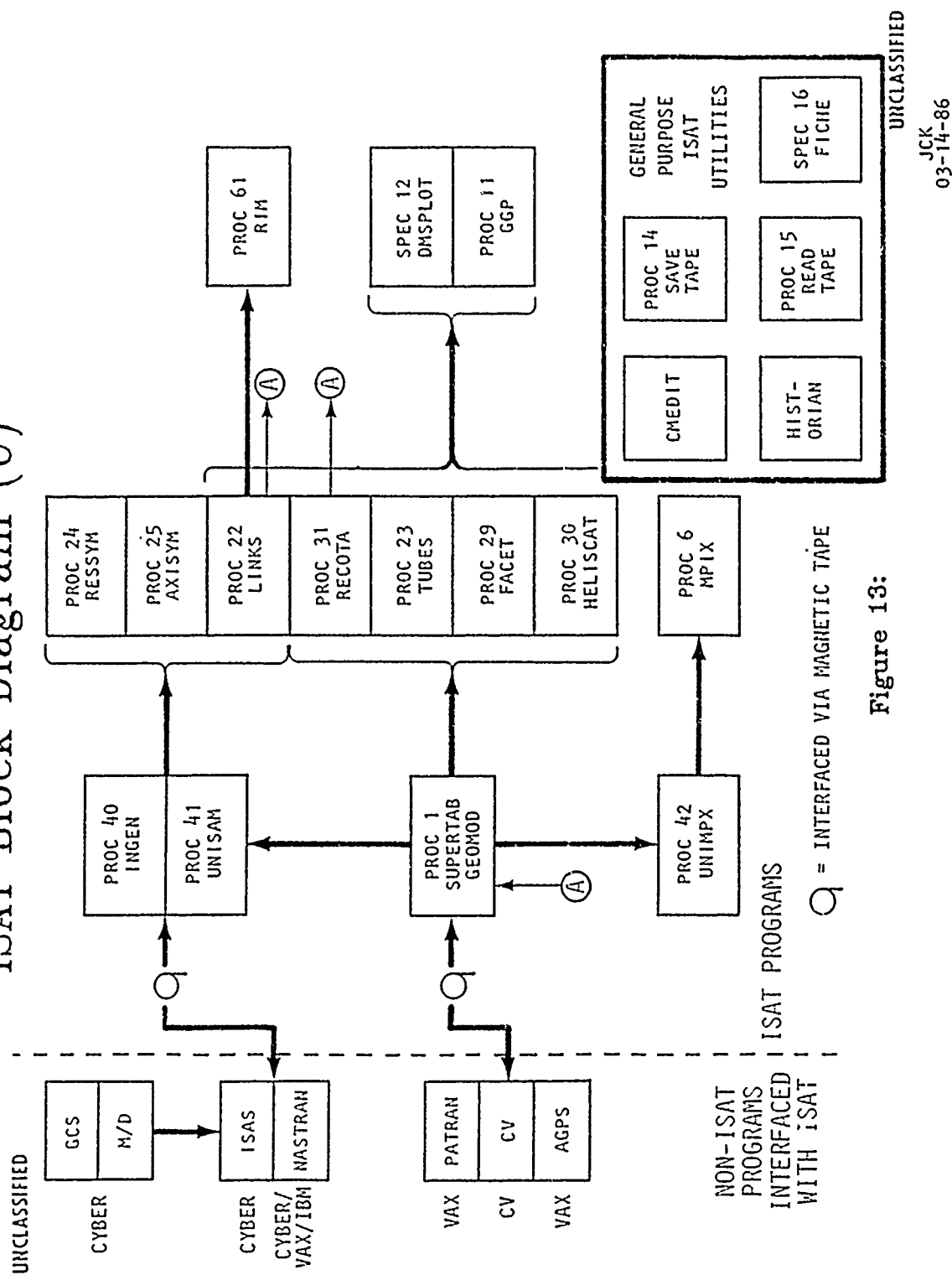


Figure 13:

Power Budget Analysis (U)

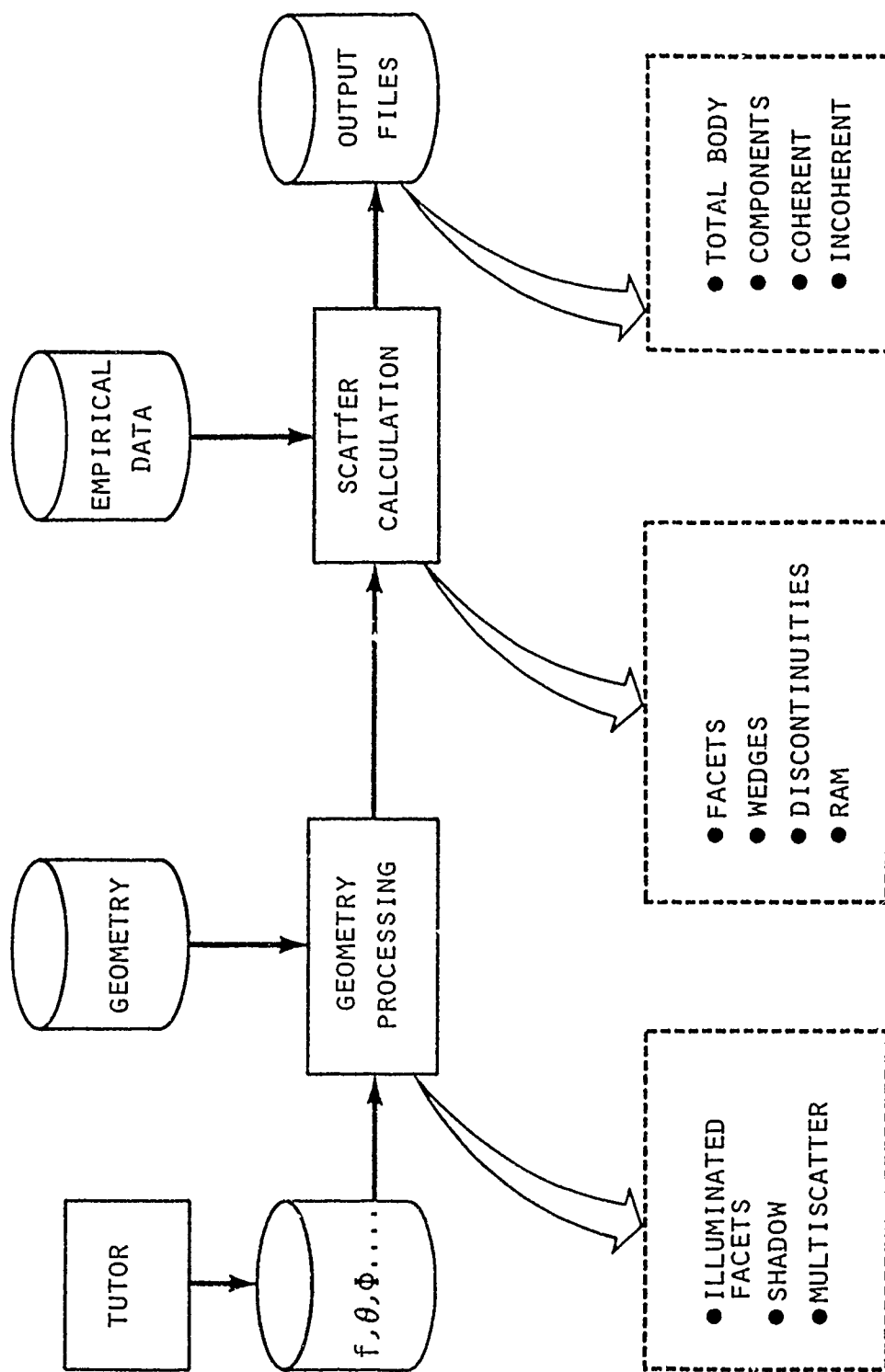


Figure 14:

Ideal Common Databus Design

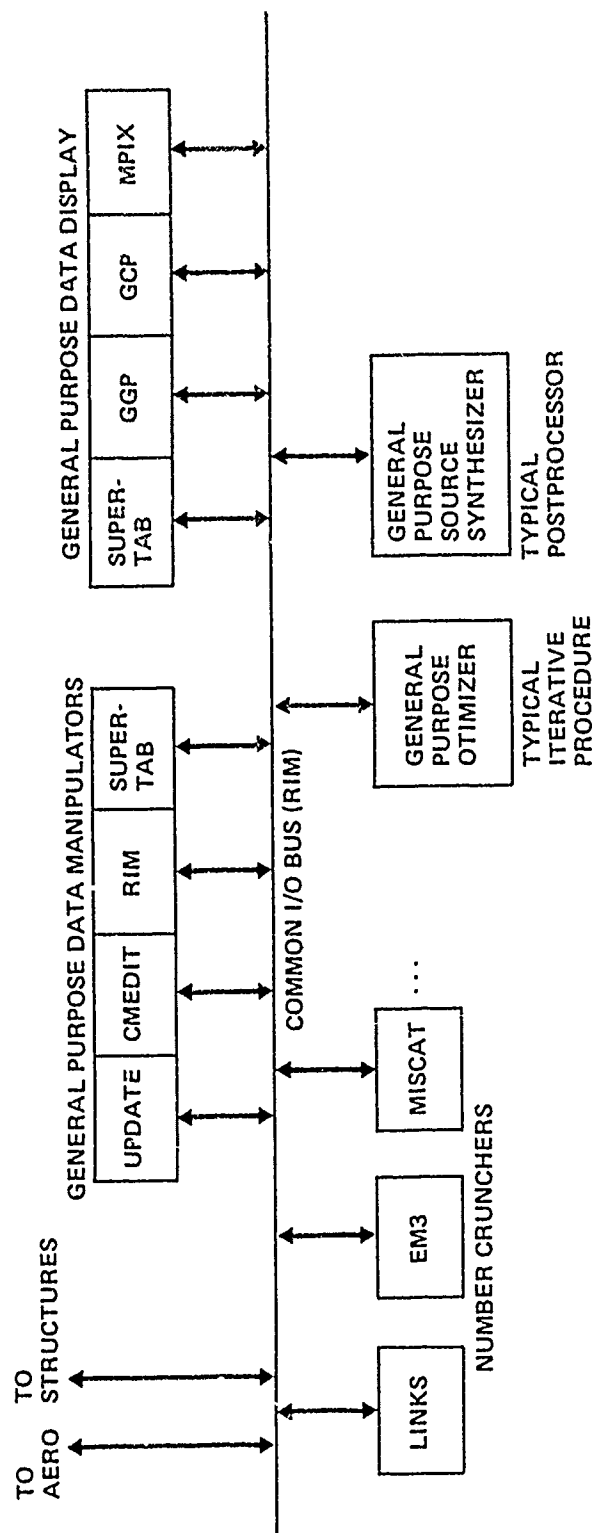


Figure 15:

APPLICATION OF COMPUTER-AIDED DESIGN TO ELECTROMAGNETIC MODELING

W. S. Nelson, P. Tulyathan, M. L. Wehling

INTRODUCTION

The Northrop Computer-Aided Design (NCAD) system is a tool that provides design engineers and other users with improved methods of designing and analyzing geometric objects in two- or three- dimensional space. A basic NCAD work station consists of a Cathode Ray Tube (CRT), light pen, function buttons, and alphanumeric keyboard. This workstation is connected to an IBM mainframe computer where the NCAD software and database reside. An NCAD model is the mathematical representation of an object or entity under study. It consists of a list of elements (see Figure 1) from which all visual displays, drawings, and engineering and manufacturing data are derived. The model contains the specific numerical values that uniquely define each element.

The surface description of a model is probably the most useful information required for electromagnetic analysis codes. Assuming that a model is already created by a designer in NCAD, this paper presents the techniques involved in tailoring the NCAD surface model to the specific form as required by analysis codes which reside on another computer system (TSO). General curves and surfaces are represented in NCAD by the rationalized parametric cubic (RPC) curve and the RPC bicubic surface patch. This allows the complete representation of the actual curves/surfaces to be used by an analysis code. The mathematics involved in the RPC curve and surface patch are first described. Next, the WRITE CAD GEOMETRY and NET functions are examined in the context of preparing a model in which only the elements essential to the analysis code are created and transferred to the TSO system. Three electromagnetic analysis codes: Radome Analysis Program, General Electromagnetic Model for the Analysis of Complex Systems (GEMACS), and Numerical Electromagnetic Code (NEC) are discussed to illustrate the facility of using the computer aided design techniques for creating the requisite geometric inputs.

RPC CURVE AND SURFACE PATCH [1]

The parametric cubic (PC) curve is represented as:

$$\begin{bmatrix} X(u) \\ Y(u) \\ Z(u) \end{bmatrix} = \begin{bmatrix} u^3 & u^2 & u & 1 \end{bmatrix} \begin{bmatrix} A_x & A_y & A_z \\ B_x & B_y & B_z \\ C_x & C_y & C_z \\ D_x & D_y & D_z \end{bmatrix} \quad (1)$$

or in a compact form as:

$$P(u) = Au^3 + Bu^2 + Cu + D \quad (2)$$

where $P(u)$ represents either the x , y , or z coordinate in the Cartesian system for a curve parameter u . The curve parameter u is defined to be in the region $0 \leq u \leq 1$. A , B , C , and D are the constants associated with the x , y , or z coordinate. Eq. (1) and (2) are called the algebraic form of the PC since it is the usual cubic polynomial representation of a function. The constants A ,

B, C, and D in the right hand side of Eq. (1) are referred to as the algebraic coefficients of the PC curve.

Taking the parametric derivative of Eq. (2), substituting the values $u=0$ and $u=1$, and solving for the algebraic coefficients will result in

$$\begin{bmatrix} A \\ B \\ C \\ D \end{bmatrix} = \begin{bmatrix} 2 & -2 & 1 & 1 \\ -3 & 3 & -2 & -1 \\ 0 & 0 & 1 & 0 \\ 1 & 0 & 0 & 0 \end{bmatrix} \begin{bmatrix} P(0) \\ P(1) \\ P'(0) \\ P'(1) \end{bmatrix} \quad (3)$$

Substituting Eq.(3) into (1) yields

$$\begin{bmatrix} X(u) \\ Y(u) \\ Z(u) \end{bmatrix} = [U] [M] \begin{bmatrix} P_X(0) & P_Y(0) & P_Z(0) \\ P_X(1) & P_Y(1) & P_Z(1) \\ P_X'(0) & P_Y'(0) & P_Z'(0) \\ P_X'(1) & P_Y'(1) & P_Z'(1) \end{bmatrix} \quad (4)$$

$$[U] = [u^3 \ u^2 \ u \ 1]$$

$$[M] = \begin{bmatrix} 2 & -2 & 1 & 1 \\ -3 & 3 & -2 & -1 \\ 0 & 0 & 1 & 0 \\ 1 & 0 & 0 & 0 \end{bmatrix}$$

Eq. (4) is the geometric form of the PC curve since it is defined in a point/slope form. The constants $P(0)$, $P(1)$, $P'(0)$, and $P'(1)$ are referred to as the geometric coefficients. The functions $[U][M]$ in the right hand side of Eq. (4) are known as "blending functions" since they blend the effects of the end point coordinates and tangent vectors to produce the intermediate point coordinates values over the domain of u .

A RPC curve is defined as the ratio

$$\bar{P}(u) = \frac{P(u)}{W(u)} = \frac{Au^3 + Bu^2 + Cu + D}{A_W u^3 + B_W u^2 + C_W u + D_W} \quad (5)$$

where the denominator term is called the "weighting function." Thus the RPC curve is represented by 16 coefficients with 12 being the algebraic or geometric coefficients and 4 additional constants (A_W , B_W , C_W , D_W) describing the weighting function. Since a conic is a ratio of two quadratic expression, it is represented in the RPC curve format with the leading cubic coefficient term equal to zero, i.e., a rational quadratic.

A parametric bi-cubic (PC) surface patch can be expressed in the algebraic form as a bi-cubic polynomial representation

$$P(u,w) = \sum_{i=0}^3 \sum_{j=0}^3 A_{ij} u^i w^j \quad (6)$$

or in the matrix form

$$P(u,w) = [U] [A] [W]$$

The surface parameters u and w are defined to be in the region $0 \leq u \leq 1$ and $0 \leq w \leq 1$. Eq. (6) describes a mapping from the unit square in the (u,w) space to the real space bi-cubic surface patch as shown in Figure 2. The algebraic coefficients Eq. (6) can be shown to be related to the geometric coefficients by

$$[A] = [M] [G] [M]^T \quad (7)$$

where $[M]$ and $[M]^T$ are the matrix and the transpose of the matrix described in Eq. (4) and

$$[G] = \begin{bmatrix} P(0,0) & P(0,1) & P^u(0,0) & P^u(0,1) \\ P(1,0) & P(1,1) & P^u(1,0) & P^u(1,1) \\ P^w(0,0) & P^w(0,1) & P^{uw}(0,0) & P^{uw}(0,1) \\ P^w(1,0) & P^w(1,1) & P^{uw}(1,0) & P^{uw}(1,1) \end{bmatrix} \quad (8)$$

The superscript for ! in Eq. (8) denote a partial derivative with respect to the parameters u or w . A close inspection of the matrix G will show that the first two rows are the boundary curves at $u=0$ and $u=1$, respectively. Similarly, the first two columns are the boundary curves at $w=0$ and $w=1$, respectively. The blending functions are $[U][M]$ and $[M]^T[W]$.

The RPC surface patch representation is the ratio

$$\bar{P}(u,w) = \frac{P(u,w)}{W(u,w)} = \frac{\sum_{i=0}^3 \sum_{j=0}^3 A_{ij} u^i w^j}{\sum_{i=0}^3 \sum_{j=0}^3 A_{wij} u^i w^j} \quad (9)$$

where A_{ij} and A_{wij} are constants determined during the creation of the RPC patch. Thus a RPC patch is represented by a 16×4 matrix of constant coefficients and the fourth column being the constants describing the weighting functions.

In summary, general curves and surfaces are defined mathematically by a set of coefficients from which all geometric properties can be evaluated. Thus the exact description of a model is retained in these coefficients and can be transferred to an analysis code.

WRITE CAD GEOMETRY

The NCAD interface module (WRITE CAD GEOMETRY) provides a means of writing the geometry of an NCAD model to the TSO system where the analysis programs reside. Figure 3 shows a menu of the elements that can be written to a pre-allocated TSO data set. These elements are parametric patches, parametric lines, random points, and groups of patches, lines, or points. A

combined output of patches and lines is allowed. Other SPECIAL FORMATS selections allow the designer/analyst to output CAD geometry into the specific geometry formats required by various analysis programs.

NCAD surface models are represented by either the RPC surface patches or a set of loft lines (string of wires). The loft line data can be transformed into a net surface by the use of the NET function. The net surface is a group of continuous surface patches that act as one surface. To create a net, each string may contain one or more wires. If a string contains more than one wire, each wire must share one and only one end point with another wire. Although the NET function can create RPC surface plates, it can also create a wire net which is a group of straight lines which connect interpolated points. A wire net is created by dividing a string of wires equally (in terms of arc length or parametric increment) and storing the x, y, z coordinates and the wire number. Thus a database containing $(M+1) \times (N+1)$ points is used to represent an (MXN) net. The following two examples illustrate the procedure of creating the appropriate model for the analysis code input geometry.

EXAMPLE 1. The Radome Analysis Program which will be discussed in the next section, uses the RPC patch as the mathematical representation of the radome surface. The NCAD drawing of an arbitrarily shaped radome configuration is shown in Figure 4(A). RPC surface patches Figure 4(B) are created by using the loft lines and the NET function. The RPC surface patches coefficients are written to the TSO file by the WRITE CAD geometry feature.

EXAMPLE 2. This example illustrates the steps involved in creating a wire net for the GEMACS or NEC code. RPC surface patches are used to model the surface of an aircraft model, Figure 5(A). Since this model is too complicated for a wire grid structure, cross sections of the aircraft are first isolated, Figure 5(B) and 5(C). The net function was applied to these cross sections, Figure 5(D). Note also that several nets are created as shown in Figure 5(E). The advantage of keeping the data in the wire net format is that the surface information (i.e., flat panels) can be extracted and drawn using the hidden line algorithm. GEMACS or NEC geometry can be easily transformed from the wire net data.

RADOME ANALYSIS PROGRAM

Central to the radome analysis is the ray tracing algorithm which is the ray surface intersection calculation. Rays are traced from the antenna aperture to the radome wall to determine angles of incidence to be used in calculating radome effects. The angle of incidence is the angle formed by a ray and the surface normal at the intersection point. In this analysis, a radome surface is described by a set of RPC patches, Figure 4(B). The ray surface intersection is solved by an algorithm based on an iterative process on small planar approximation to the surface and will be described in the following. The fact that the rays emanating from the antenna are all parallel simplifies the intersection algorithm. Each RPC patch and the rays are rotated so that the rays are parallel with one of the principal axes. A patch is checked against all the rays to determine if any ray or rays intersect it. Viewing the patch and rays from the principal plane orthogonal to the rays (i.e. viewing along the ray axis), the patch becomes a bounded plane (y-z plane) and the rays are transformed to points. A "min/max" rectangle is formed around the 2-D projection of the patch and those points (2-D projection of the rays) which lie exterior to the rectangle are eliminated from the intersection point search for the particular patch. If there is no point within the "min/max" rectangle, the procedure is repeated for the next patch. The next procedure is used when a point is determined to be within the

"min/max" rectangle of a patch. To localize the area of the patch where an intersection is likely to occur, the patch is divided into small rectangles with the parametric side length of DU and DW. Each rectangle is further divided into two triangles as shown in Figure 6(A). The 2-D projection of a triangle is shown in Figure 6(B). In this figure, \underline{n}_1 , \underline{n}_2 , and \underline{n}_3 are vectors perpendicular to the three sides of the triangle and \underline{v}_1 and \underline{v}_2 are vectors from the two apexes of the triangle to the point. If the three dot products $\underline{n}_1 \cdot \underline{v}_1$, $\underline{n}_2 \cdot \underline{v}_2$, and $\underline{n}_3 \cdot \underline{v}_1$ have the same sign, then the point lies within the triangle.

Once a triangle is found to contain the intersection point, an iteration is done to locate the actual coordinates of the point. On a parametric surface, this is equivalent to locating the u and w values of the intersection point. The iterative method begins by finding the point (P_0) which is the intersection of the ray with a plane formed by the three vertices (P_1 , P_2 and P_3) of the triangle as shown in Figure 7. The distance (d) between P_0 and P_2 is then calculated. If this distance is less than a given tolerance (1×10^{-8}) then the ray surface intersection point (P_I) is considered found, that is, P_0 , P_2 and P_I coincides. If the distance is greater than the tolerance, then the iteration process continues.

The next step in the iteration is to calculate the parametric values of P_0 (i.e. u_0 , w_0) by

$$u_0 = u_2 + du \quad (10-a)$$

$$w_0 = w_2 + dw \quad (10-b)$$

where (u_2 , w_2) are the parametric values of the point P_2 . The values of du and dw are approximated by using the parallelogram plane method as expressed by the following equations:

$$y_0 = \frac{(y_1 - y_2)}{DU} \cdot du + \frac{(y_3 - y_2)}{DW} \cdot dw + y_2 \quad (11-a)$$

$$z_0 = \frac{(z_1 - z_2)}{DU} \cdot du + \frac{(z_3 - z_2)}{DW} \cdot dw + z_2 \quad (11-b)$$

Solving for du and dw in equations (11-a) and (11-b) yields

$$du = DU \cdot \frac{(y_0 - y_2)(z_3 - z_2) - (y_3 - y_2)(z_0 - z_2)}{(y_1 - y_2)(z_3 - z_2) - (y_3 - y_2)(z_1 - z_2)} \quad (12-a)$$

$$dw = DW \cdot \frac{(y_1 - y_2)(z_0 - z_2) - (y_0 - y_2)(z_1 - z_2)}{(y_1 - y_1)(z_3 - z_2) - (y_3 - y_2)(z_1 - z_2)} \quad (12-a)$$

The values of u and w are then used to calculate the x, y, z coordinates on the patch surface which will be the new P_2 in the next iteration. New values of P_1 and P_3 are calculated using the following parameters:

$$\begin{array}{ll} u_1 = u_0 + 0.1*DU & (13-a) \\ w_1 = w_0 & (13-b) \\ u_3 = u_0 & (13-c) \\ w_3 = w_0 + 0.1*DW & (13-d) \end{array}$$

Typically 3 to 4 iterations are required to locate the intersection point. The surface normal is approximated by the normal to the parallelogram plane used at the time the convergence criteria is met.

The speed of the above intersection algorithm is illustrated in Figure 8. An IBM 370/3084 mainframe computer is used to determine the ray surface intersection solution of a tangent ogive radome using the RPC representation and that of the exact solution [2]. In this case, the fineness ratio of the tangent ogive is 3 and the base diameter is 16.27 inches. The rays are arranged in a rectangular grid and spaced 0.6 inch apart. Although only 2 RPC patches are required to represent exactly a tangent ogive surface, the surface is divided into 162 patches. This large number of patches are typically required to represent a general radome shape with a similar dimension.

GEMACS AND NEC PROGRAMS

GEMACS and NEC codes are generalized software packages to solve exterior radiation and scattering problems. These codes implement the Geometrical Theory of Diffraction (GTD) and the Method of Moments (MOM) solution techniques. In addition GEMACS supports the hybrid MOM/GTD technique for solving the problem of antenna radiating in the presence of large conducting structures. The following discussion is primarily concerned with the creation and manipulation of the GTD and MOM models, using interactive computer graphics. A model will be referred to as a GTD or MOM model with the implication that the exact geometry input format can be written by a processor for either code.

GTD Model

GTD employs ray optical techniques to determine components of the fields reflected and diffracted by various structures. Complex geometrical shapes are modeled by multisided flat plates and finite elliptical cylinders. In constructing a GTD model, an analyst is concerned with the selection of plates and cylinders to represent the overall physical object. Plates simulate shapes which have relatively flat surfaces such as aircraft wings and horizontal and vertical stabilizers. Elliptical cylinders simulate curved areas such as an aircraft fuselage.

Figures 9(A) and 9(B) illustrate the simplification of an aircraft for the analysis of the coupling between a transmit antenna mounted in the fairing below the vertical stabilizer and a receive antenna mounted to the outboard pylon. The electrical fields are perturbed by the shadowing due to the fuselage, the wing and the horizontal stabilizer. The NCAD system provides a means for constructing and visualizing a GTD model.

The GTD model consists of an elliptical cylinder and two flat plates. Figure 9(C) illustrates the actual cross sectional cuts of the fuselage close to the vicinity of the antenna and the elliptical cylinder used in the GTD model. The bottom half of the fuselage is shadowed and is not modeled. Figure 9(D) illustrates the determination of the corners of the plates and the intersections with the cylinder. The coordinates of the points and dimensions of the cylinder are input to the GEMACS and NEC codes.

MOM MODEL

Methods for solving the surface current density of a radiating or scattering object for the MOM formulations of the GEMACS or NEC codes are the Magnetic Field Integral Equation (MFIE) or the Electrical Field Integral Equation (EFIE). Simultaneous linear equations are derived for the currents on a structure which has been subdivided into small wire segments (EFIE) or surface patches (MFIE). Smooth closed bodies may be modeled as surface patches or wire nets while thin bodies are only modeled as wire nets. The currents for each wire segment or surface patch are integrated over the entire geometry either analytically or numerically. In consideration of computational time, the structures are, of necessity, small relative to wavelength.

The coordinates for the endpoints of the wires or the corners of the patches required for MOM models can be obtained rapidly from databases of RPC patches with NCAD. Figure 10 illustrates the subdivision of the RPC patches of a stylized airplane. A wire grid, Figure 10(B) is created by subdividing the patches of the model, Figure 10(A), into a regular pattern with segment lengths in a range appropriate for the frequency. The model makes use of its axial symmetry by only modeling half of the structure. The coordinates of the wire net are readily passed to a TSO dataset for further processing to the specifications of the individual codes. A processing code written for the GEMACS program subdivides larger flat plates into regular (triangular or) quadrilateral wire grids and automatically eliminates all small segments, Figure 10(C).

GRAPHICAL OUTPUT

In addition to the processing code referred to above, several routines are used with the GEMACS program to present the output graphically. Field pattern and current distribution by wire or patch number are available in rectangular or polar plots using the DISSPLA graphics software.

An innovative code produces color current graphs using the DISSPLA software. This interactive program obtains current and geometry information from output files to establish a color table and a current scale. The components of a wire-grid structure are plotted in the colors corresponding to the magnitudes of the surface current density. A wire-grid model of an aircraft with a wire antenna attached to the fuselage and is shown in Figure 11. The radiation from the antenna excites the surface current on the wire segments. A color display of Figure 11 will show the wires with high current density in the "hot" color and the wires carrying less current in "cold" color. The wire-grid model of Figure 11(B) is plotted in Figure 12 with the wire segments carrying higher and lower current density plotted in Figure 12(A) and 12(B) respectively.

CONCLUSION

NCAD and DISSPLA software are the basis of several graphical codes to create the geometries and to display the outputs of electromagnetic codes such as GEMACS and NEC. RPC patches are used by NCAD to define general surfaces. An algorithm is described from a radome code to solve the intersection of a ray with an RPC surface. NCAD with the NET option is used to visualize an electromagnetic problem and to simplify complex geometries into basic geometrical shapes, wire grids or flat patches. Finally, a code used with DISSPLA is used to graph the complex problem of the distribution of currents on a surface.

ACKNOWLEDGEMENT

The authors would like to recognize the efforts of M. Yankulich, E. G. Proft, and D. L. Parker of Northrop Corporation, Aircraft Division, Hawthorne, California for their developement and implementation of several of the computer codes used in this presentation.

REFERENCES

- [1] A. R. R. Forest, "On Coon's and Other Method for the Representation of a Surface," Iterative Computer Graphics (Herbert Freeman, editor).
- [2] G. K. Huddleston, H. L. Bassett, & J. M. Newton, "Computer-Aided Radome Analysis Using Geometric Optics and Lorentz Reciprocity," Report AFOSR-TR-81-0460, Feb. 1981, Georgia Institute of Technology. (ADA099182)

LEVEL	ELEMENT	ELEMENT SYMBOL
POINTS	POINTS X-PAIRS	PT PT
WIRES	LINES ARCS CIRCLES CONIC: ELLIPSE PARABOLA HYPERBOLA CUBIC RATIONAL LINE RATIONAL CURVE	LN CA CI EL PA HY PC LR RC
SURFACES	UNBOUNDED SPHERE RATIONAL PATCH NETS	PL SP RP GP
SOLIDS	(UNDEFINED)	
NONGEOMETRIC	TEXT GENERAL GROUPS PICTURE PLANES: PRIMARY VIEW AUXILLIARY VIEW FULL SECTION MATRICES 1 THROUGH 12	TX GP PV AV FS ..

Figure 1. NCAD model elements

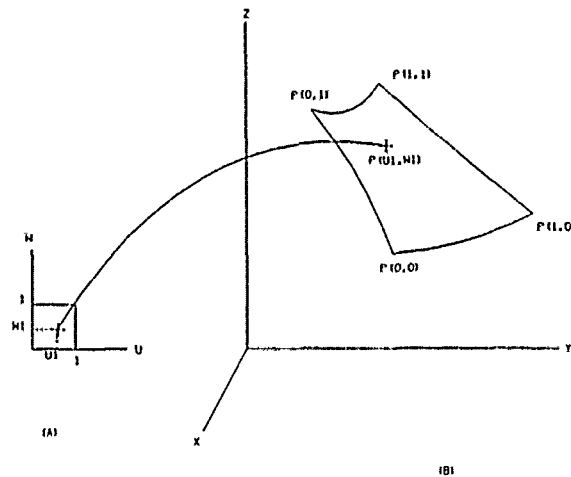


Figure 2. The mapping from a unit square in the U, W coordinate (A) to the corresponding point on the surface patch (B).

***** WRITE CAD GEOMETRY TO OUTPUT FILE *****

* PARAMETRIC PATCHES *

CUBIC PATCH (PC)

RATIONAL PATCH (RPC)

OTHER PATCH TYPES

* PARAMETRIC CURVES *

CUBIC LINE

RATIONAL LINE

OTHER LINE TYPES

* SPECIAL FORMATS (ONE PICK ONLY) *

POINTS (DISPLAYED POINTS ONLY)

GROUPS

USSAERO

PANAIR

ORACLE

(M+1) X (N+1) POINTS

(1XN) POINT NET

FROM (MXN) WIRE NET

FROM PINT STRING

LANGLEY WAVE DRAG

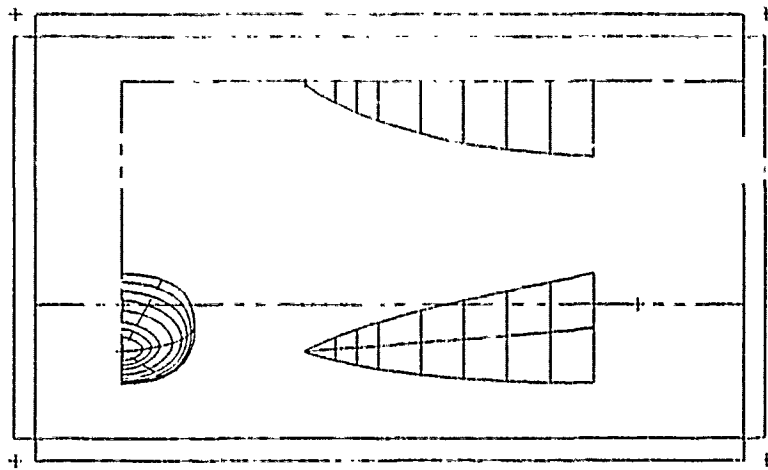
S/V MODELING

NASTRAN SOLIDS, PLATES, LINES, GRIDS

* START OVER AND DELETE ALL PICKS *

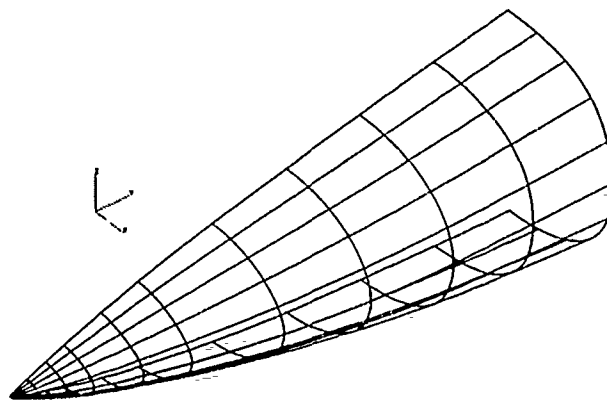
ACCEPT EXIT

Figure 3. Write CAD Geometry Menu



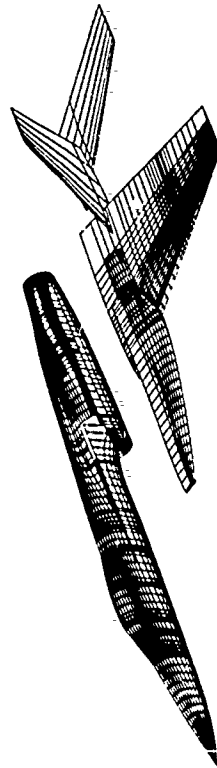
(A)

ENTER MENU ITEM NO. ON A PAD MENU

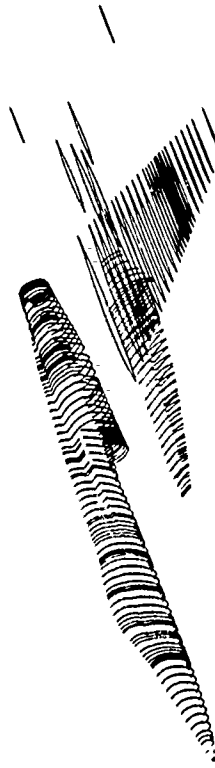


(B)

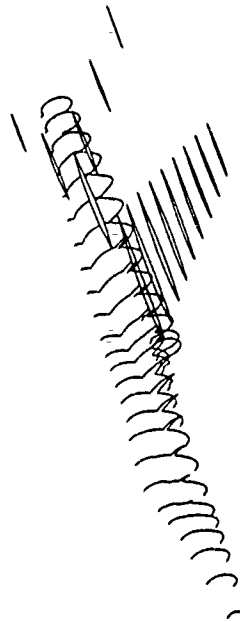
Figure 4. (A) Three view drawing of a general radome configuration.
(B) RPC representation of the radome surface.



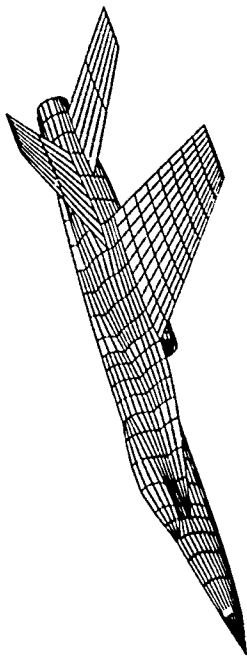
A) NORLOFT SURFACES RESIDING IN TSO DATASETS



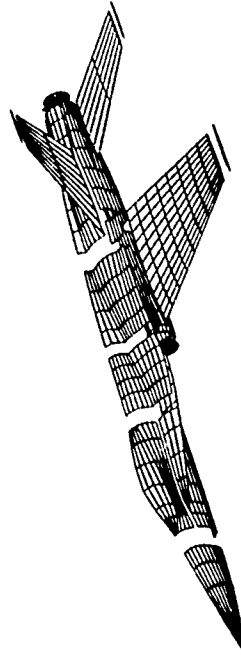
B) PATCH CORNER POINTS TAKEN FROM NORLOFT DATA AND USED TO DEFINE CROSSECTIONS



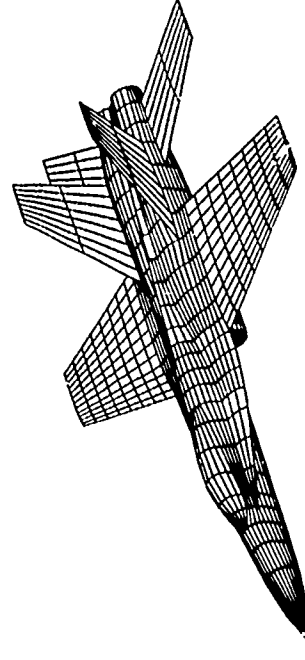
C) WIRE CROSSESECTION CREATED ON NCAD FROM POINT INPUT



D) PANELS GENERATED USING NCAD "NET" FUNCTION



E) SHRINK BY NET PLOT USING ICAD "HIDLIN" PROGRAM



F) PLOT USING SYMMETRY OPTION IN "HIDLIN"

Figure 5. Wire-Grid Model generation from lofted surface model.

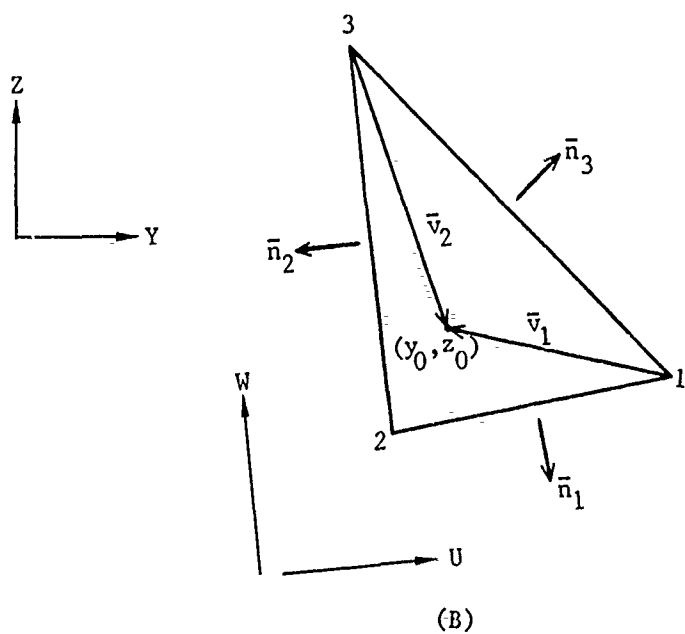
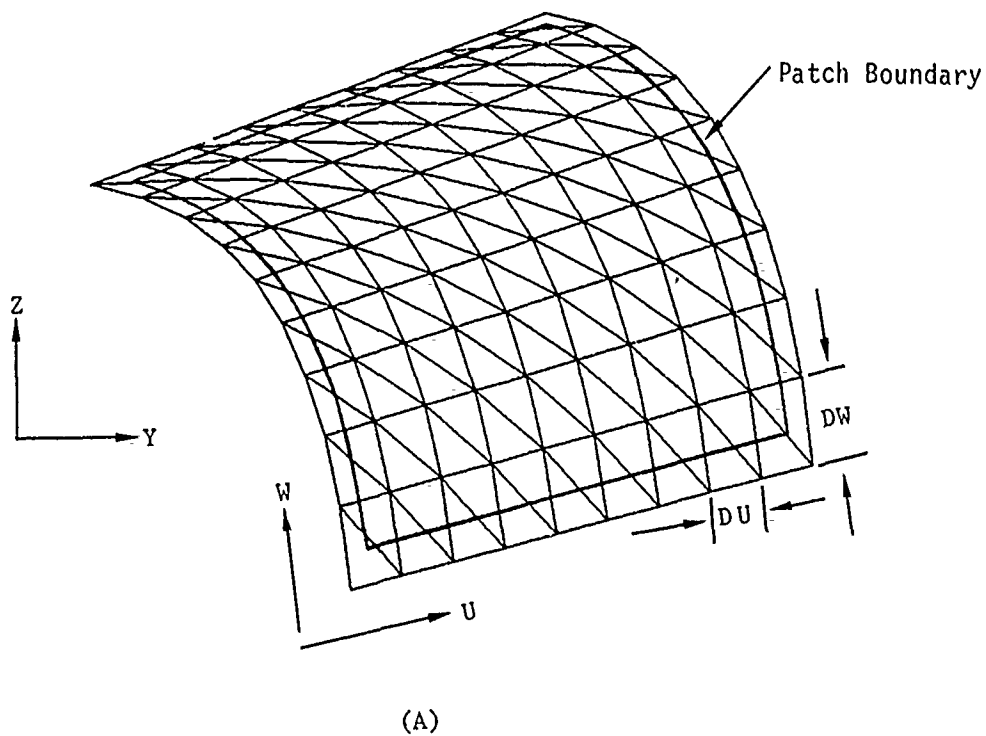


Figure 6. (A) Triangular Grid Covering a Patch
 (B) Vectors Used to Determine Shotline Containment Within a Triangle.

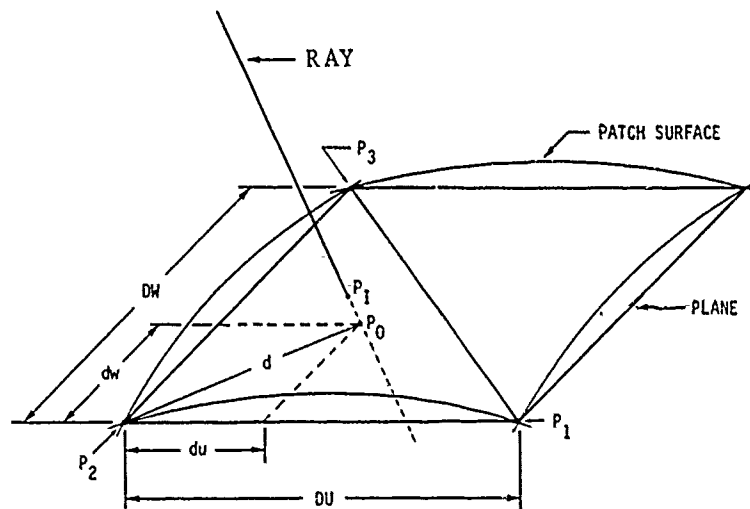


Figure 7. Schematic for the intersection point iteration.

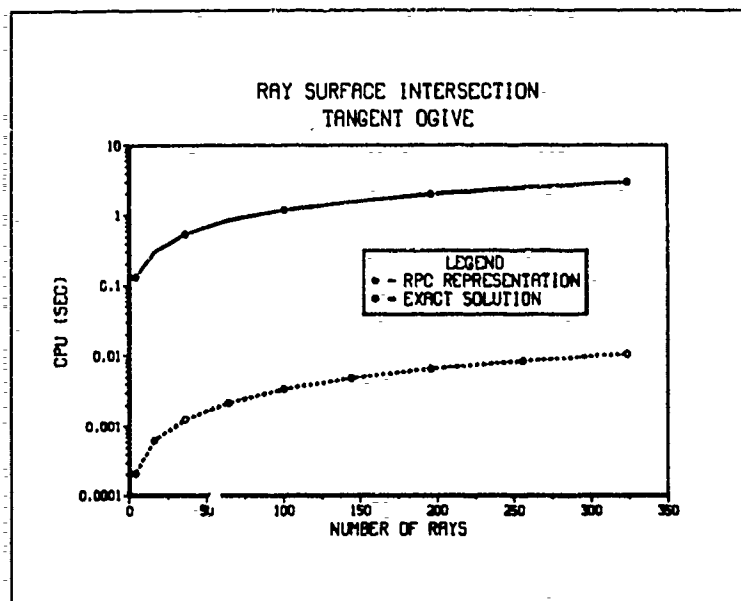
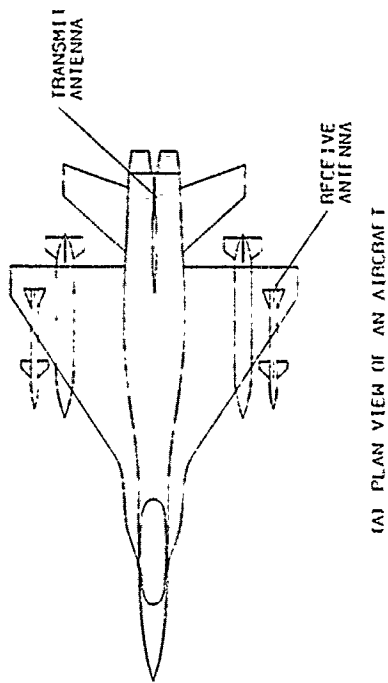
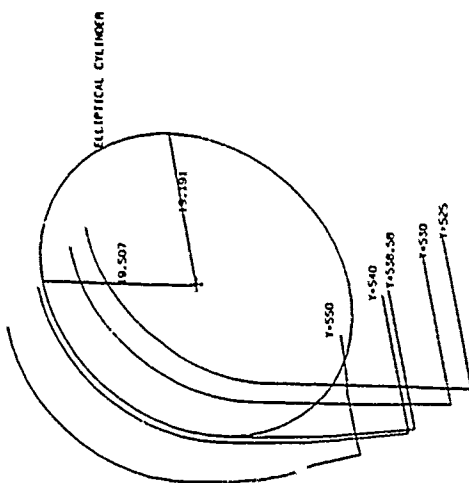


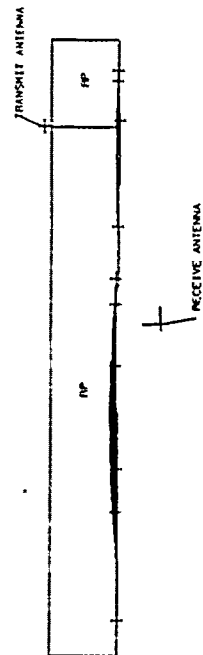
Figure 8. CPU time required for ray surface intersection.



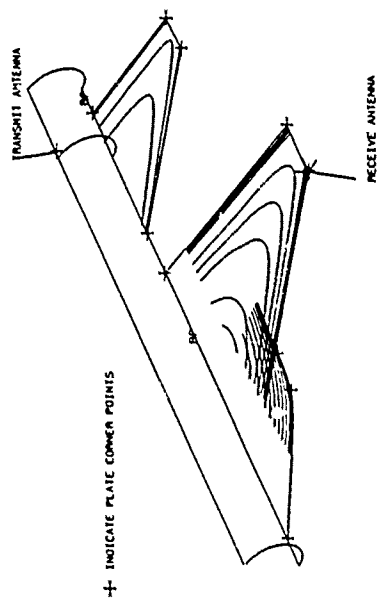
(A) PLAN VIEW OF AN AIRCRAFT



(C) TRIMETRIC VIEW OF FUSELAGE IN THE VICINITY OF THE TRANSMIT ANTENNA

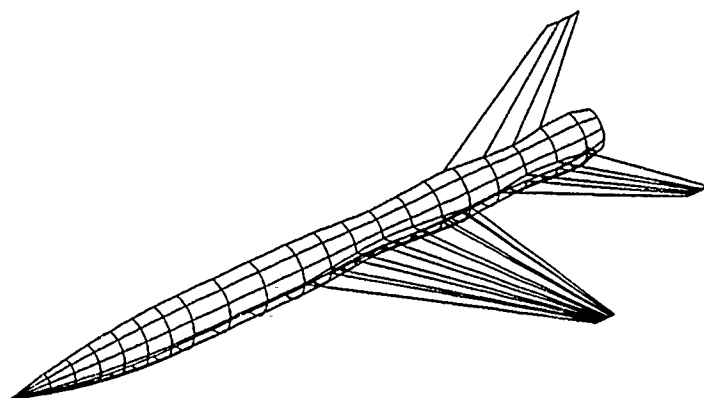


(B) PROFILE VIEW OF GTD MODEL

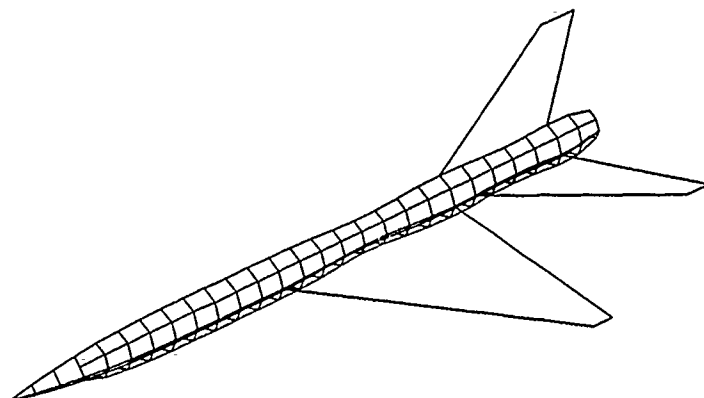


(D) TRIMETRIC VIEW OF GTD MODEL

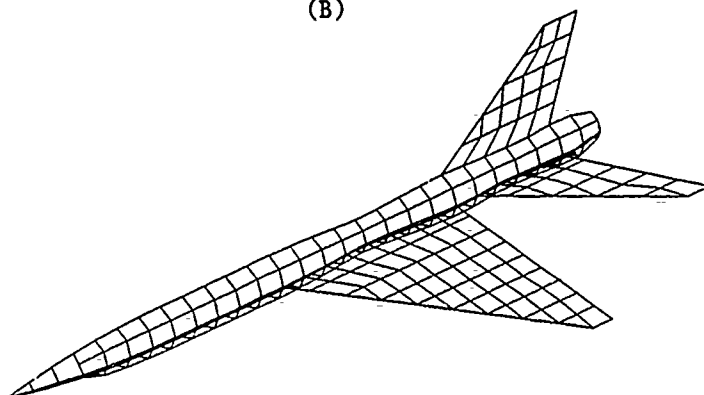
Figure 9. GTD model for an antenna coupling analysis.



(A)

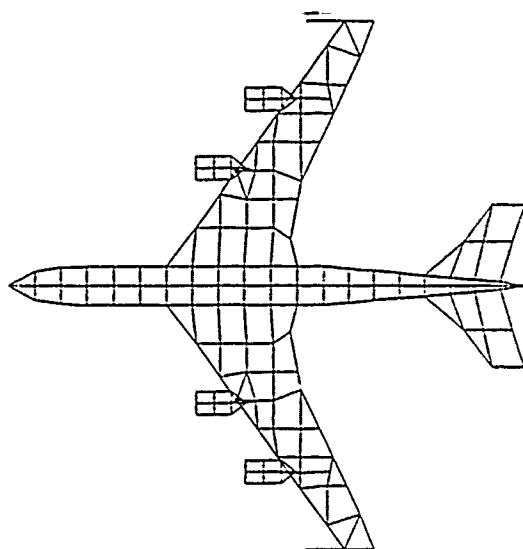


(B)



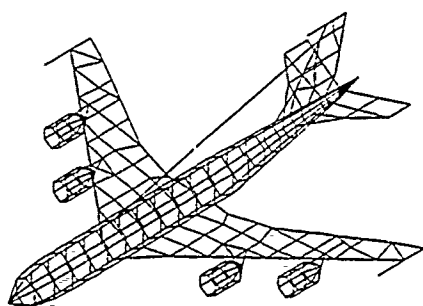
(C)

Figure 10. (A) RPC patch and (B) (C) wire frame representations of a "coke bottle" airplane



(A)

0.0 dB
 RED
 -30.0 dB
 BLUE
 -60.0 dB



(B)

0.0 dB
 RED
 -30.0 dB
 BLUE
 -60.0 dB

Figure 11. (A) Plan View and (B) Trimetric View of a wire-frame model with color current maps.

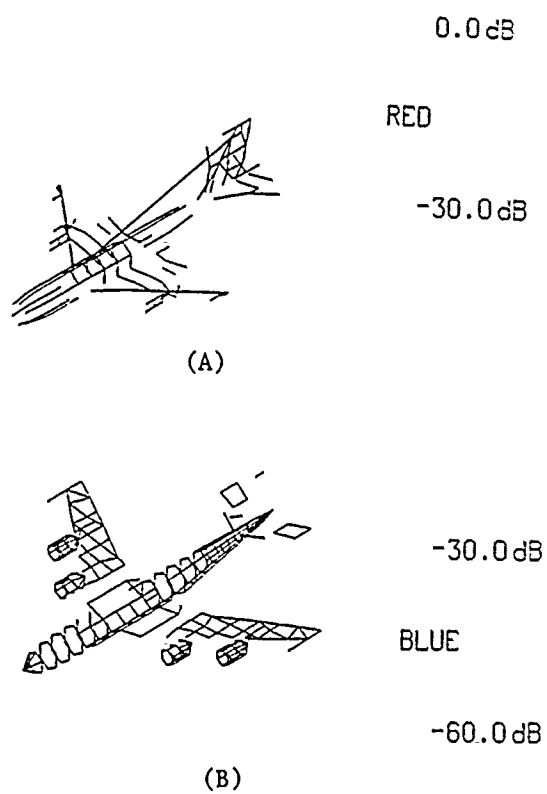


Figure 12. Example of Layered Plots for High Resolution Black and White Current Maps

SESSION VI - "MININEC APPLICATIONS"

"Extensions to MININEC"

James Logan and J.W. Rockway

Naval Ocean Systems Center

"Modification to MININEC for the Analysis of Wire Antennas with Small Radius to Wavelength Ratio"

Todd Poston and Steve Kershner

Kershner, Wright & Hagaman

"Analysis of Stepped-Radius Colinear Dual Antenna Arrays"

Donn Campbell

US Army GENCOMS

"Design Approach for Electrically Small Transmitting Antennas Using the Microcomputer"

Peder Hansen and James Logan

Naval Ocean Systems Center

EXTENSIONS TO MININEC

J. C. Logan and J. W. Rockway
Naval Ocean Systems Center, Code 822
271 Catalina Blvd.
San Diego, CA 92152-5000

INTRODUCTION:

The "MINI" ELECTROMAGNETICS Code, or MININEC, is a method of Moments computer program for analysis of thin wire antennas [1]. A Galerkin procedure is applied to an electric field integral equation to solve for the wire currents following an approach suggested by Wilton [2]. This formulation results in an unusually short computer program suitable for implementation on a microcomputer. Hence, MININEC is written in a BASIC language compatible with many popular microcomputers.

MININEC solves for impedance and currents on arbitrarily oriented wires, including configurations with multiple wire junctions, in free space and over a perfectly conducting ground plane. Options include lumped parameter impedance loading of wires and calculation of near zone and far zone fields. Both near electric fields and near magnetic fields can be determined for free space and over a perfectly conducting ground. The far zone electric fields and radiation pattern (power pattern) can also be determined for free space and perfectly conducting ground.

Additional radiation pattern options include a Fresnel reflection coefficient correction to the patterns, for finite conducting grounds (real earth surface impedance). Up to five changes in surface impedance due to real ground are allowed in a linear or circular "cliff" model. The cliff may take on any elevation (including zero, i.e., a flat surface), however, there is no correction for diffraction from cliff edges. In the case of a circular cliff model, the first media may include a correction for the surface impedance of a densely spaced, buried, radial wire ground screen.

The first version of MININEC given by NOSC TD 516 (reference [13]), calculated currents and radiation patterns for wire antennas in free space and on a perfectly conducting ground plane. Wires attached to ground were required to intersect at a right angle and could not be impedance loaded at the connection point. Subsequent revisions corrected these shortcomings culminating in Version 2 or MININEC(2), given by Li, et al [3]. The first two versions of MININEC require user specification of wire end connections. However, MININEC(3) determines connection information for itself from user defined wire end coordinates. MININEC(3) also displays the currents wire by wire and at all wire ends, including wire junctions. MININEC(3) features an improved, faster solution routine and has been completely restructured using a more modular programming style, including the use of helpful comment statements.

PERFORMANCE DATA:

Insight for effective application of MININEC is gained from comparisons with measured data or analytic solutions (when available). In this manner, modeling guidelines are derived and updated from simple antenna problems for which there is reliable measured data or generally accepted theoretical data.

The theoretical behavior of the dipole has been studied intensively and the literature is rich with examples that include measured and theoretical data. In the following, data published by R. W. P. King [4] is used for reference. Figures 1, 2, and 3 show convergence tests for an electrically short dipole, a dipole near resonance and a dipole near anti-resonance, respectively. The admittance versus number of segments and the percent difference between MININEC and R. W. P. King admittance data are shown in each figure. Definite signs of convergence are evident for the short dipole and the resonant dipole (Figures 1 and 2), but no sign of convergence is seen for the anti-resonant dipole (Figure 3). Similar convergence behavior of other codes (e.g. NEC for anti-resonant dipoles) have also been observed by the authors. Never-the-less, acceptably

accurate dipole data can be predicted by MININEC. Figure 4 shows the admittance of a MININEC dipole model compared to the theory of R. W. P. King for a wide band.

The shortest segment limit of MININEC is demonstrated in figure 5. Shown is the dipole admittance as a function of dipole length for a 10 segment dipole. The conductance begins to oscillate wildly for dipoles smaller than 10^{-3} wave length. This implies a short segment length, for a 16-bit machine and single precision, of 10^{-4} wavelengths.

Figure 6 shows MININEC behavior as a functions of wire radius. Shown also for comparison is a limited amount of data from King for radii between 10^{-3} and 10^{-2} wave lengths. Earlier versions of MININEC show proper behavior between 10^{-2} and 10^{-5} wave lengths. MININEC (3) is good for radii as low as 10^{-8} as can be seen in the figure. Smaller radii are possible, but the lower limit has not yet been identified.

Figure 7 is a comparison of a MININEC loop antenna model to the theory of R. W. P. King. A convergence test was performed for a one wavelength circumference loop to select 22 segments for the model. It can be seen that the agreement is very good for a wide range of loop size. Figure 8 demonstrates the size of the smallest loop which gives satisfactory loop behavior. When the loop circumference is smaller than 10^{-2} wavelengths, the conductance becomes unstable and appears to oscillate.

The limited amount of MININEC data given here illustrates some of the practical limits of the latest version of MININEC.

DISTRIBUTION:

A formal report on Version 3 of MININEC is being prepared. The data shown here along with other validation data and a complete source listing will be included in the report. The plans are to publish MININEC with unlimited distribution. An announcement of the publication date and instructions on how to obtain a copy will be announced in the ACES newsletter.

REFERENCES

1. A. J. Julian, J. C. Logan, J. W. Rockway, "MININEC; A Mini-Numerical Electromagnetic Code", NOSC TD 516, September 1982
2. D. R. Wilton, "Wire Problems", Lecture Notes for Short Course on Computational Methods in Electromagnetics, 1981
3. S. T. Li, J. C. Logan, J. W. Rockway, D. W. Tam, "Microcomputer Tools for Communications Engineering", Artech House, Inc., Dedham, MA, 1983
4. R. W. P. King, "Tables of Antenna Characteristics", IFI/Plenum Data Corporation, New York, 1971

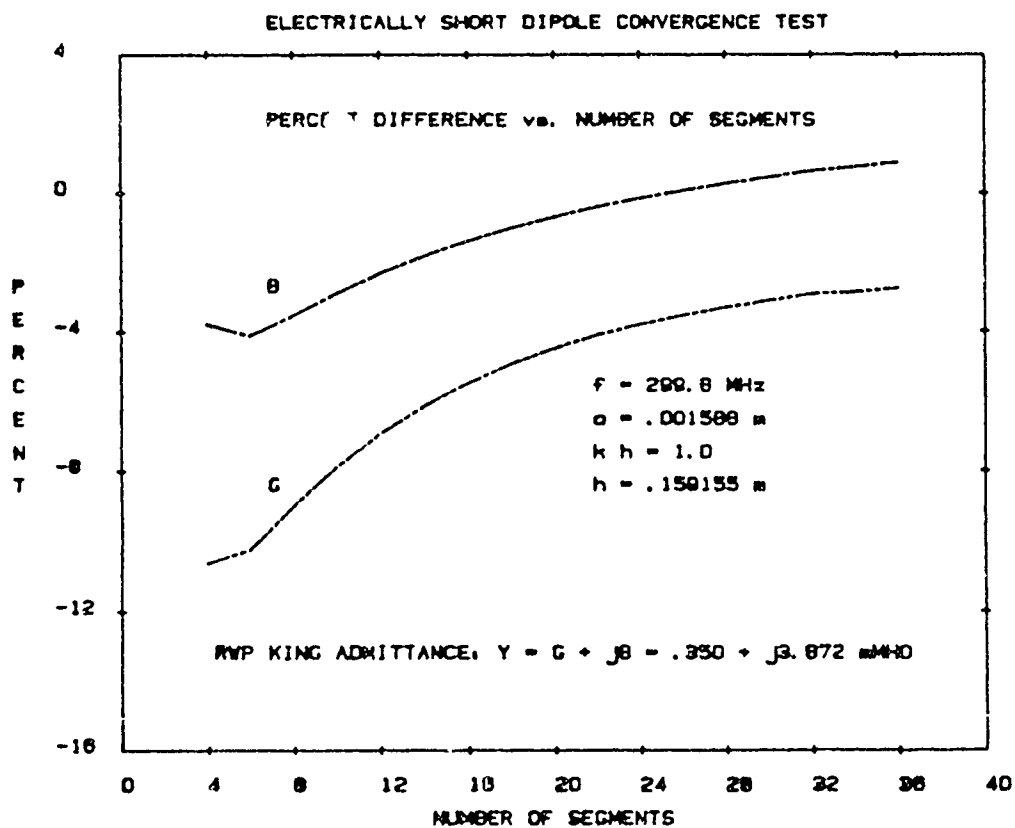
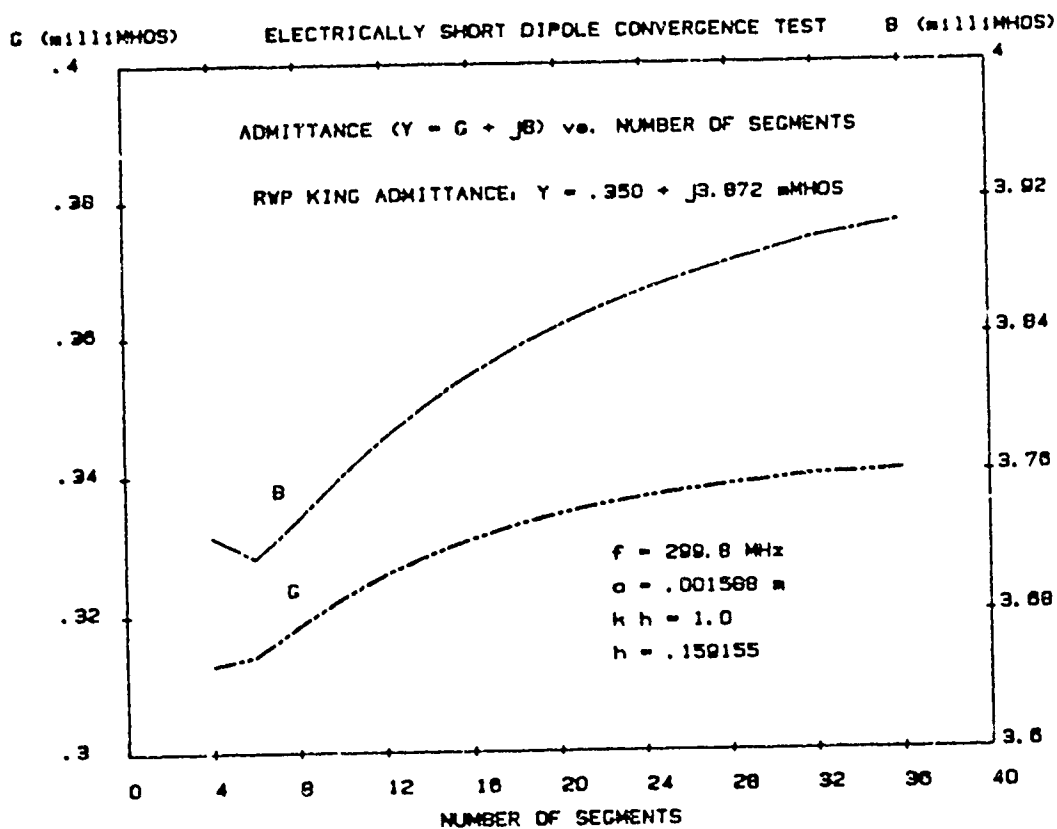


Figure 1

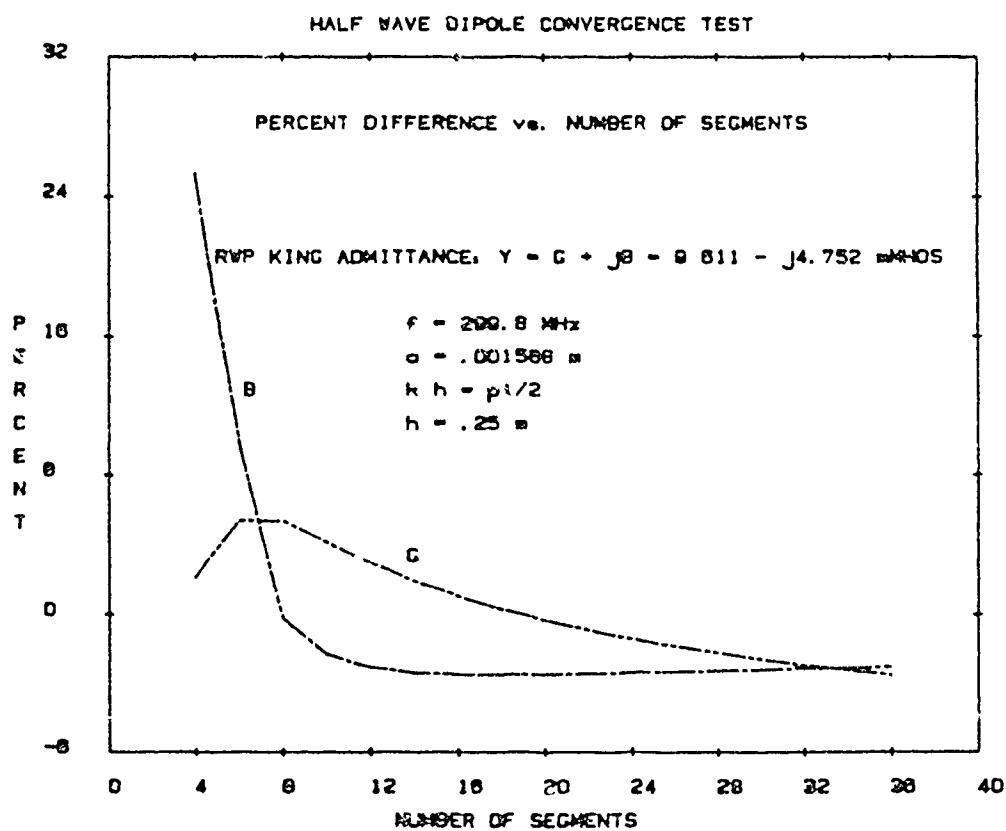
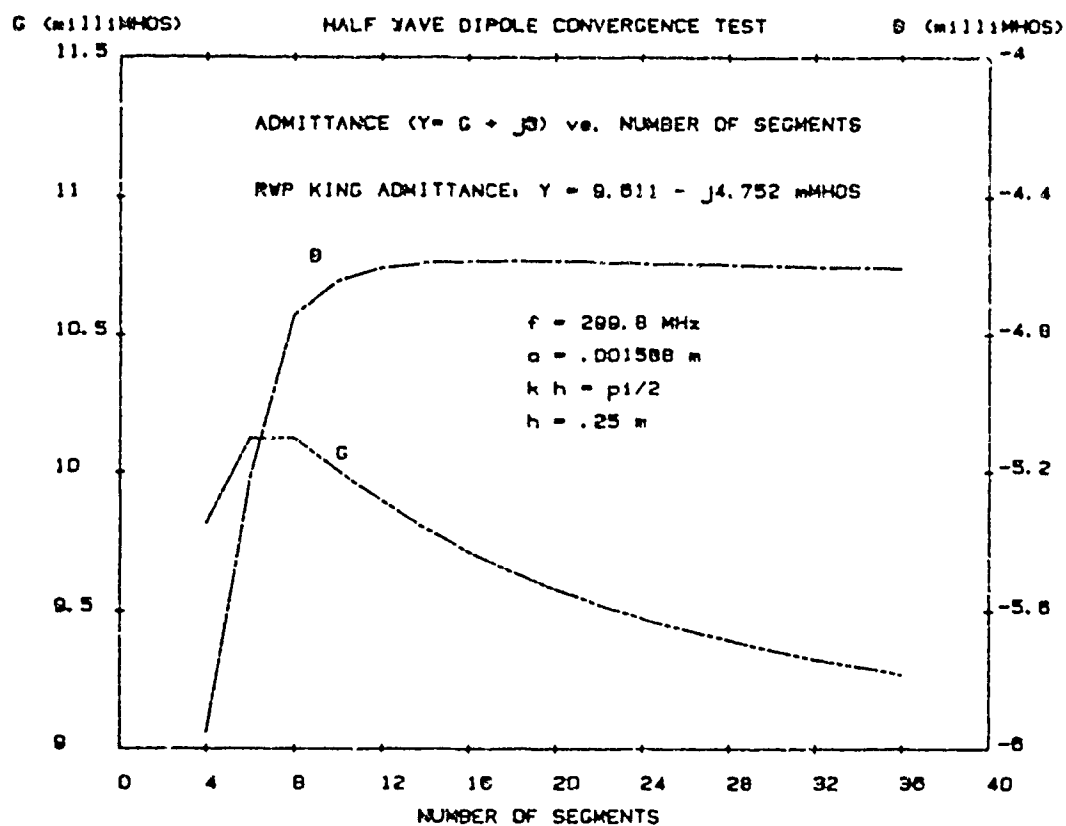


Figure 2

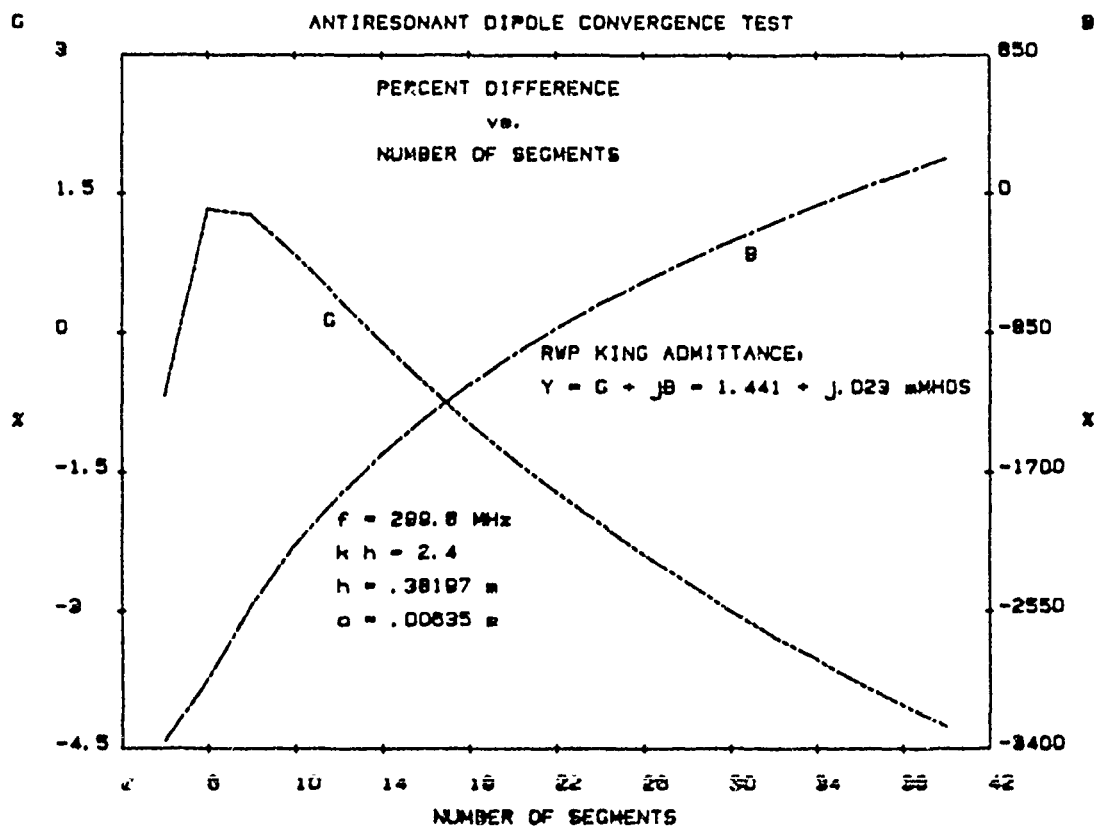
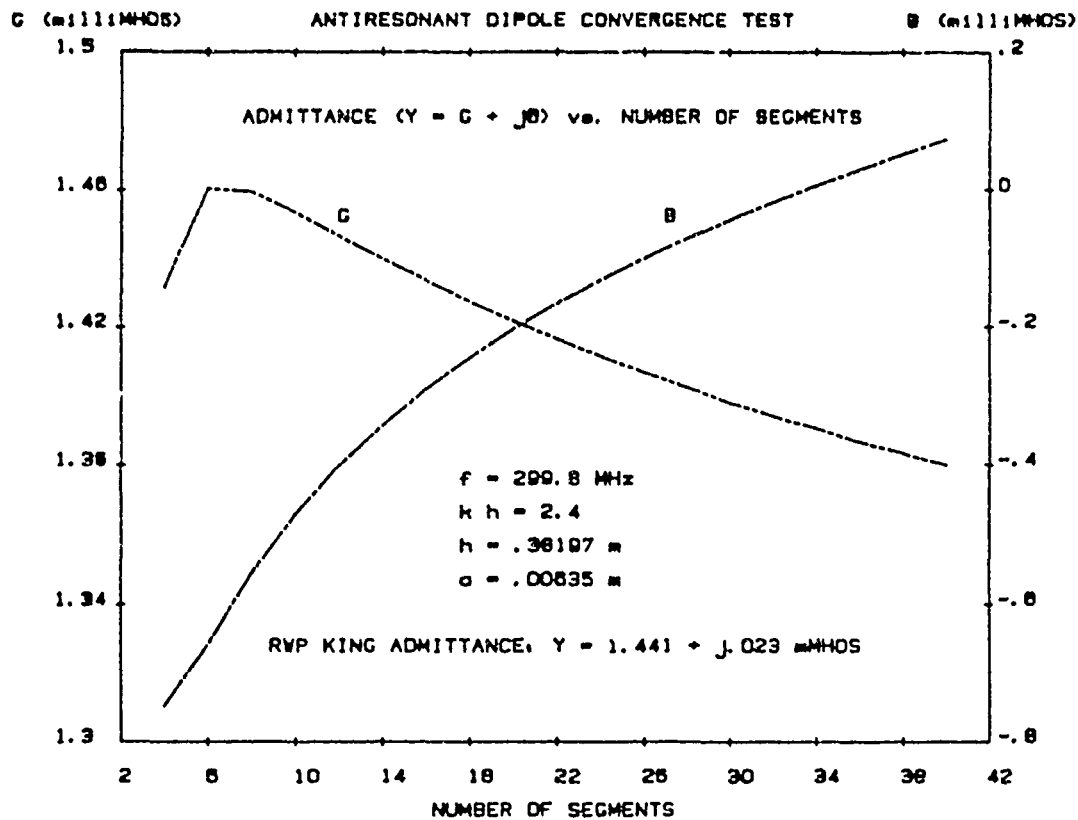


Figure 3

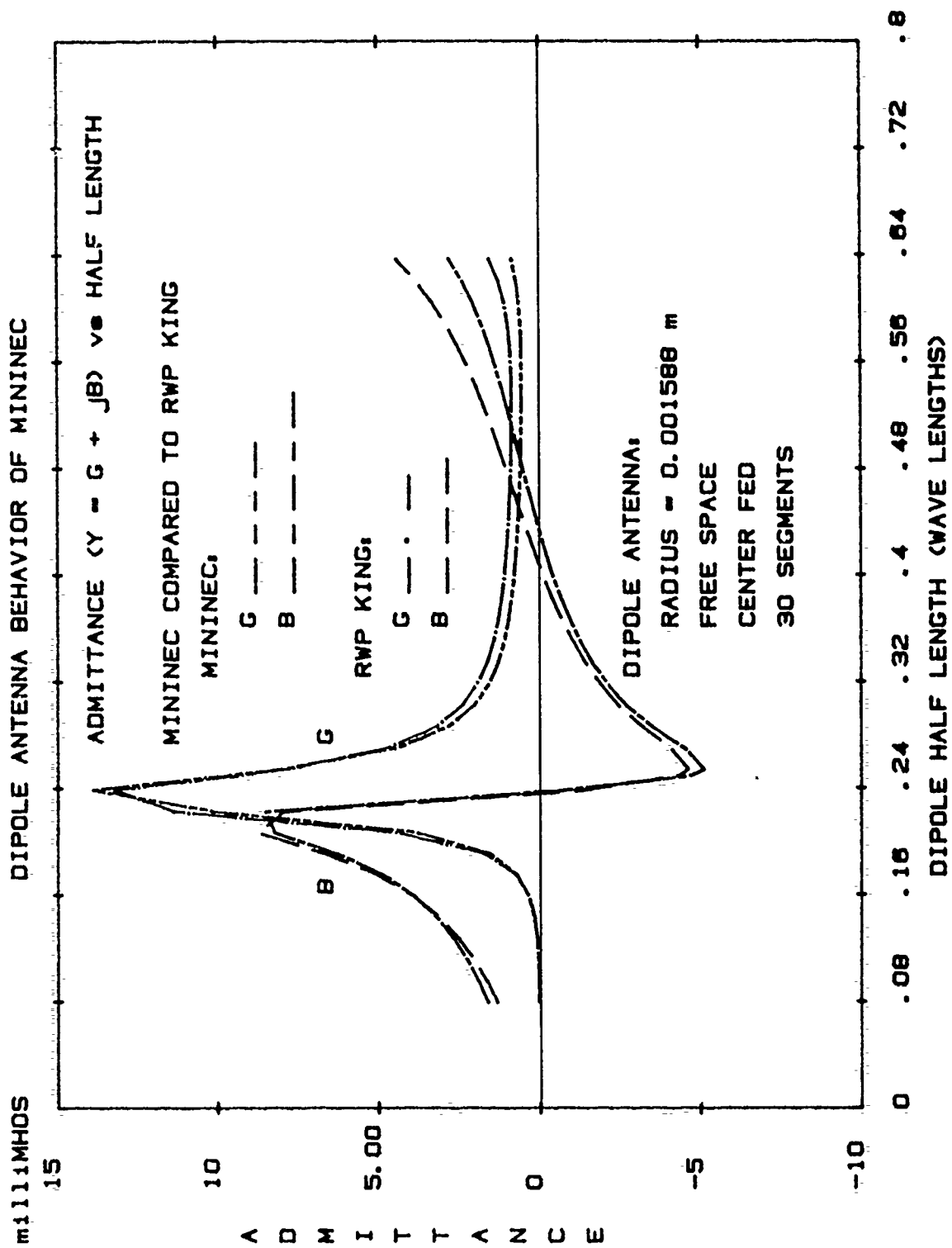


Figure 4

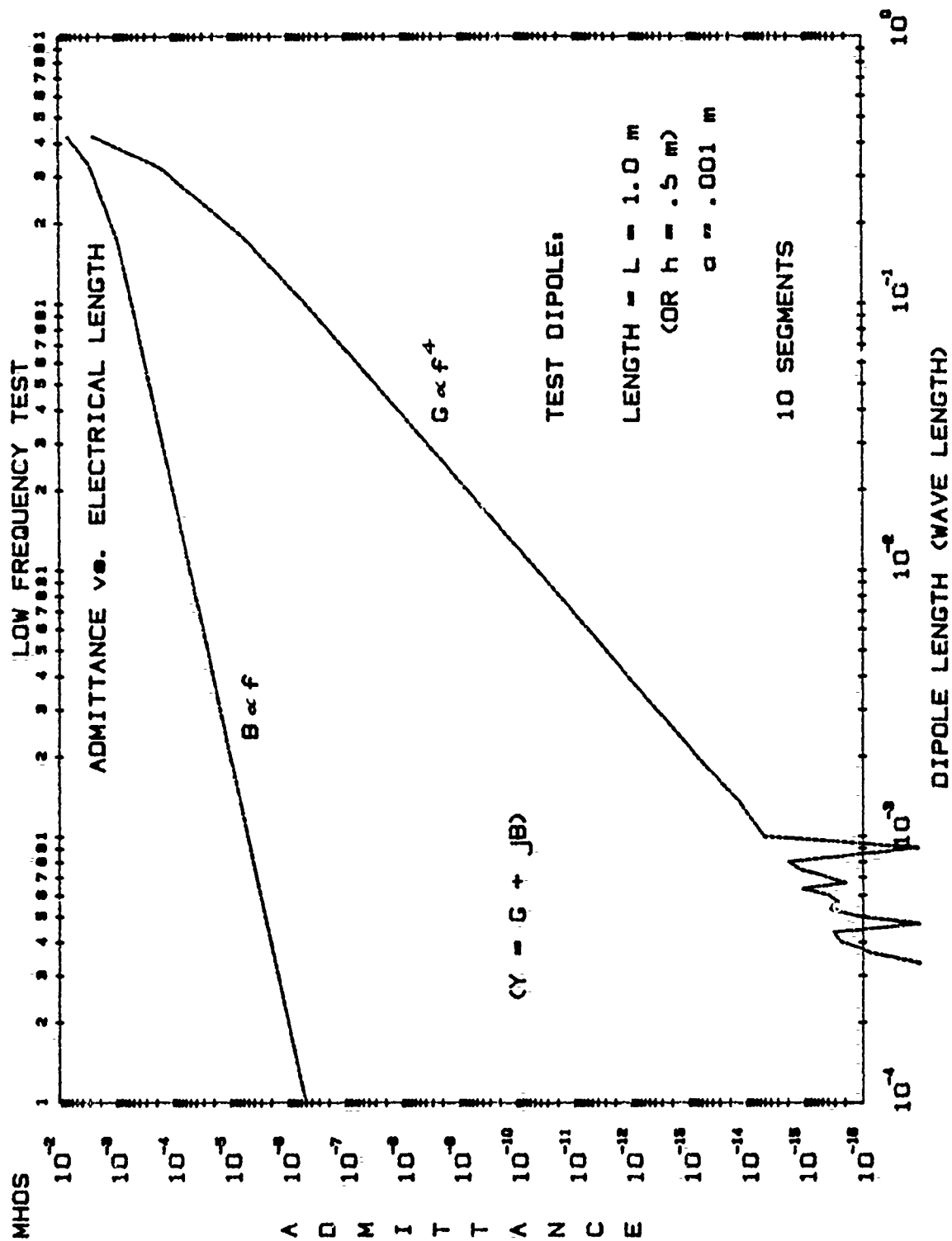


Figure 5.

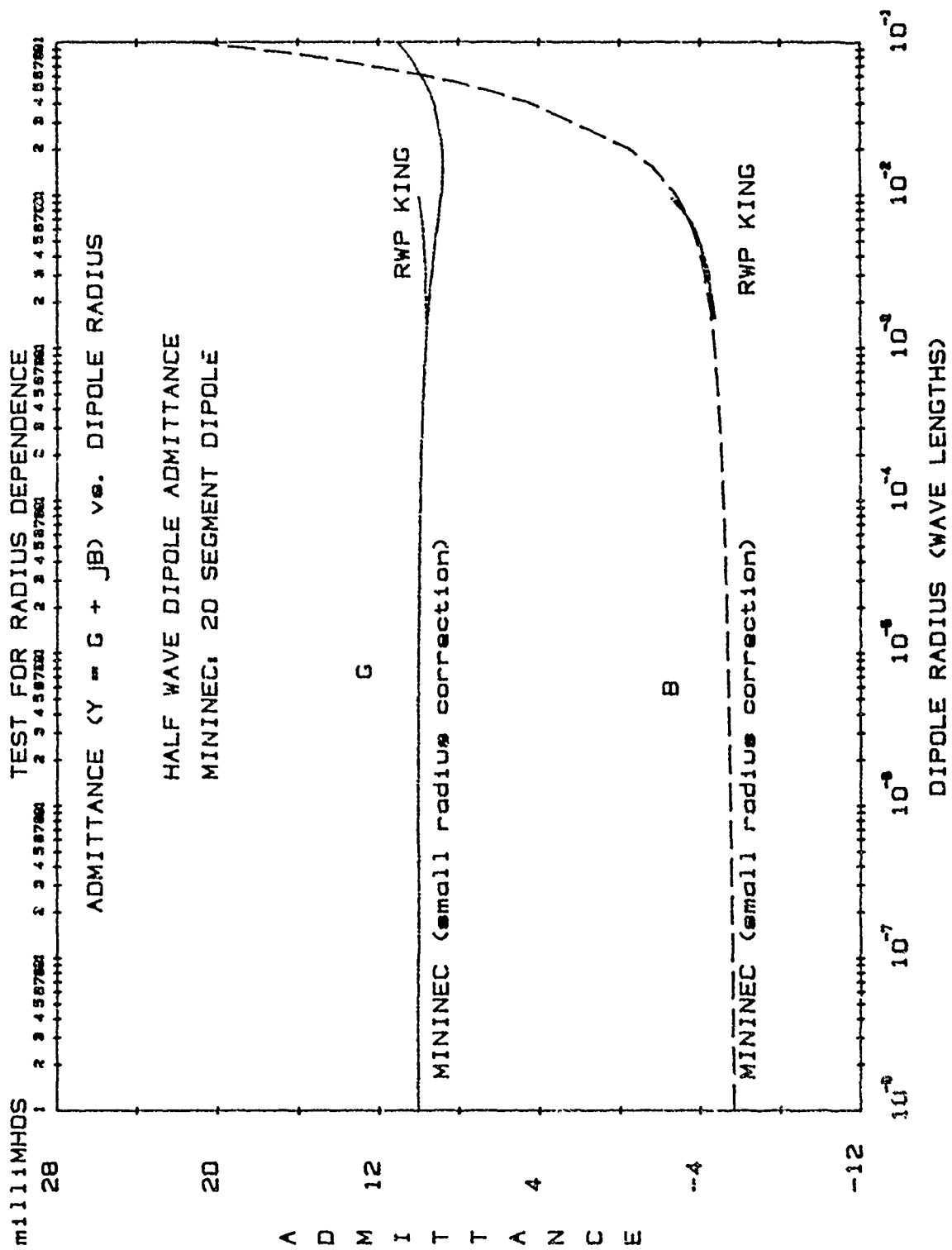


Figure 6

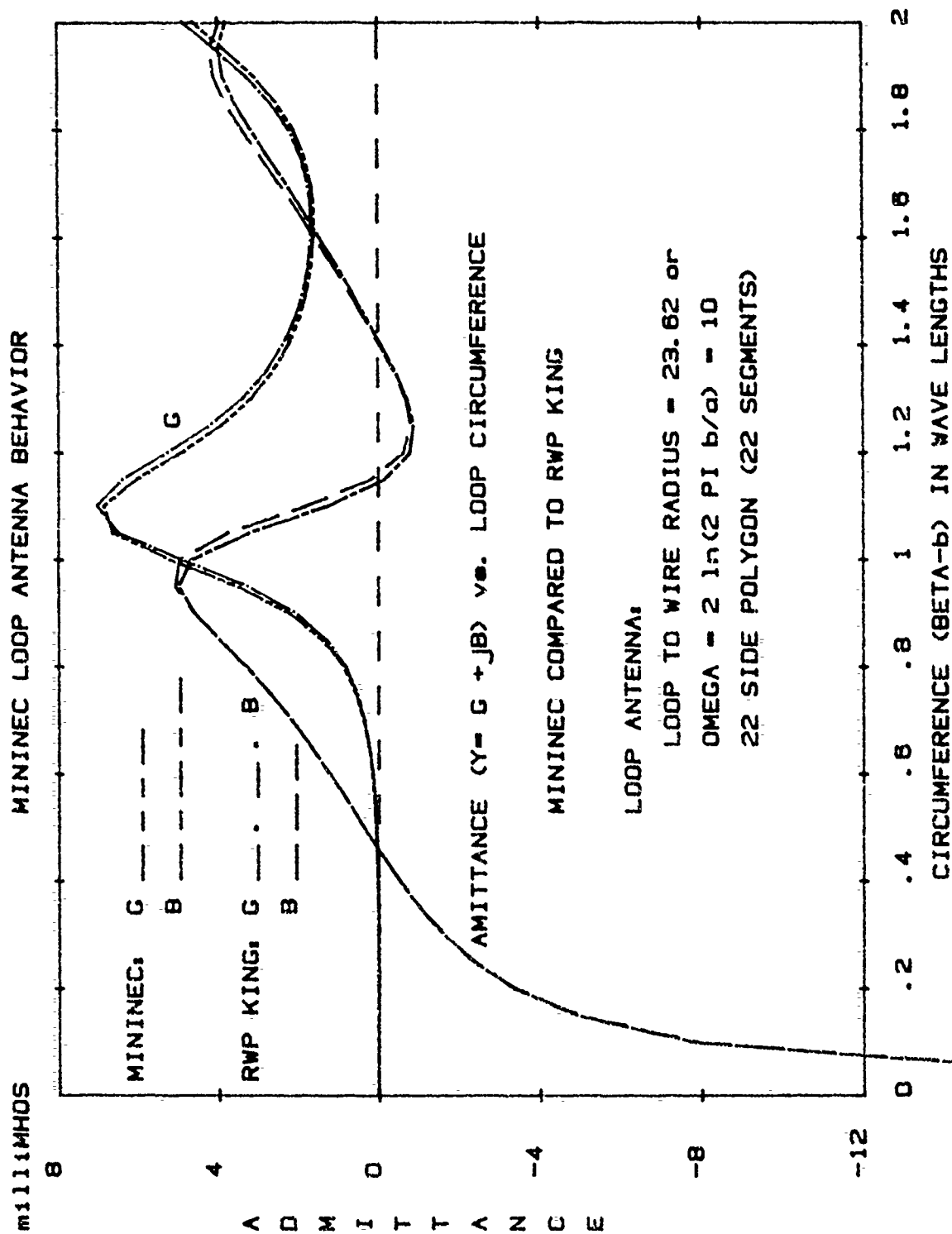


Figure 7

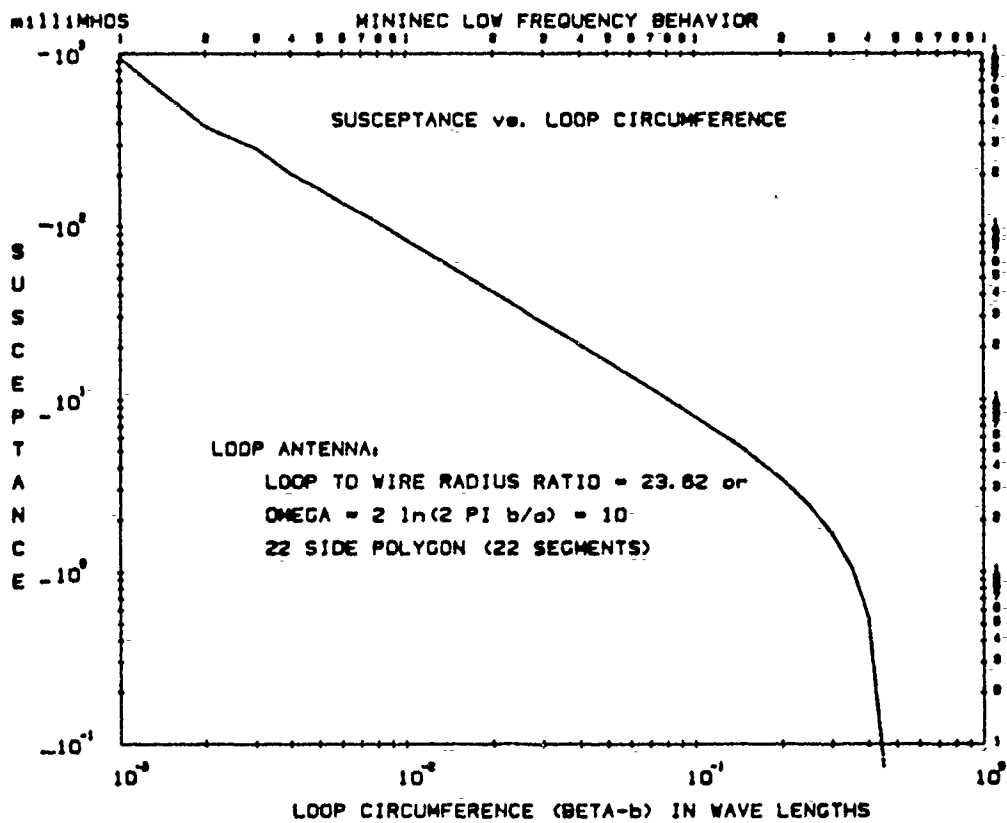
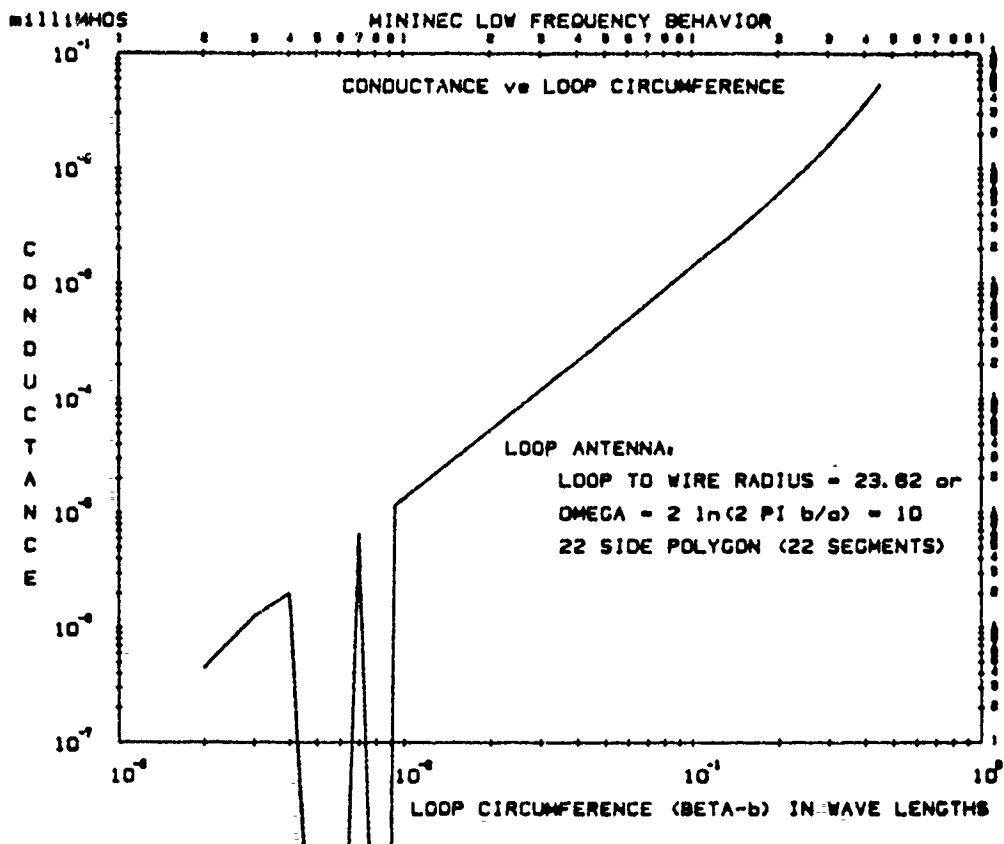


Figure 8

Modification to MININEC for the Analysis of Wire Antennas With Small Radius to Wavelength Ratios

Todd D. Poston
Stephen W. Kershner

Kershner, Wright & Hagaman, P.C.
5730 General Washington Drive
Alexandria, VA 22312

ABSTRACT

MININEC is a useful and compact method of moments antenna program, but MININEC does not give reasonable values for the input reactance of very thin wires at low frequencies. This problem greatly restricts the use of MININEC in the design and analysis of vlf and lf antennas. A modification to the program which eliminates this restriction is discussed. The modification consists of treating the currents as filaments and only considering the wire radius when computing the self impedance of a segment. A listing of the changed computer code is included.

INTRODUCTION

MININEC is a method of moments microcomputer program, written in BASIC, that analyzes thin-wire antennas [1]. This compact code is based on a modified Galerkin procedure that was described by D. R. Wilton to solve an integral equation for the electric field [2,3]. With proper modeling, MININEC can solve accurately for the current and impedance on most arbitrarily oriented wires.

However, the input reactance given by MININEC (MININEC (2)) for an electrically short, thin monopole begins to diverge from the expected value for wire radii less than approximately $10^{-5}\lambda$,

where λ is the wavelength. Wires with radii less than $10^{-5}\lambda$ are commonly used in vlf/lf antennas. This limitation of the program is evident in Figure 1, which displays the input reactance X_a calculated by MININEC and the expected values for a 90.5 m monopole at 150 kHz for $10^{-6} < a/\lambda < 10^{-4}$ where a is the wire radius. The expected value is the input reactance for a short vertical radiator given by the equation

$$X_a = -Z_0 \cot \frac{2\pi h}{\lambda} \quad \text{ohms}, \quad (1)$$

where h is the height of the radiator. The characteristic impedance Z_0 is given by

$$Z_0 = 60 \left[\log \left(\frac{h}{a} \right) - 1 \right] \quad \text{ohms} \quad (2)$$

which fits experimentally measured values [4]. The above expression gives approximately the same value as the more complicated equation for the input reactance from the induced emf method using a sinusoidal current distribution [5].

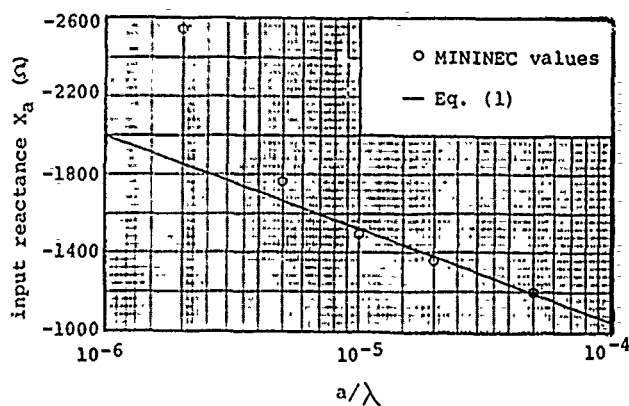


Figure 1. Input reactances from MININEC for a 90.5 m monopole divided into five segments at 150 kHz.

The exact a/λ value where MININEC is no longer valid depends on the particular microcomputer, whether double precision variables are being used, and the number of segments chosen. This limitation prevents MININEC from being used to design vlf and lf antennas that use wires with small radius to wavelength ratios.

A modification to the program has been developed which replaces the code for the integral psi with code that treats the current as a filament on the wire axis. This change has resulted in reactances that differ by less than 1% from the values given by Eq. (1) and that are in excellent agreement with experimental values for a top-loaded monopole. This new code provides a low frequency extension to MININEC.

MODIFICATION AND VERIFICATION

MININEC is based on the assumptions that the wire radius is very small in comparison to a wavelength and that the radius is small with respect to the segment length so that there will be no azimuthal component of the current [1]. Evidently from Fig. 1, the assumption on a/λ is overpowered by a computational error for values less than approximately 10^{-5} .

In order to determine the vector and scalar potentials from a current carrying wire, MININEC evaluates an integral psi given by

$$\psi_{m,v} = \int_{s_v}^{s_u} k (s_m - s') ds' \quad (3)$$

where

$$k (s_m - s') = \frac{1}{2\pi} \int_{-\pi}^{\pi} \frac{e^{-jk r_m}}{r_m} d\phi, \quad (4)$$

$$r_m = \left[(s_m - s')^2 + 4a^2 \sin^2 \frac{\phi}{2} \right]^{\frac{1}{2}} \quad (5)$$

s_m is the observation point, s_v and s_u are the upper and lower endpoints respectively of the source segment and a is the wire radius. Equation (3) results in an elliptical integral of the first kind due to a singularity at $r_m=0$. Since the wires are very thin in terms of a wavelength when MININEC becomes unreliable, the current and charge densities can be approximated by filaments of current and charge on the wire axis following Harrington. Thus, the double integral is simplified to a single integral [6]

$$\psi(m,n) = \frac{1}{4\pi \Delta l_n} \int_{\Delta l_n} \frac{e^{-jk R_m}}{R_m} dl, \quad (6)$$

where the distance between the source segment and observation point is

$$R_m = \begin{cases} \sqrt{\rho_m^2 + (z - z_m)^2} & m \neq n \\ \sqrt{a^2 + z^2} & m = n \end{cases}, \quad (7)$$

Δl_n is the length of the source segment, n is the center of source segment, m is the observation point, ρ_m is the horizontal distance between m and n , z is the vertical coordinate (along the source with the origin at the center of segment n), and z_m is the vertical distance between z and m . The integral can be approximated by expanding $e^{-jk R_m}$ with a Maclaurin series to two terms. For $m=n$, this approximation yields

$$\psi(m,n) \approx \frac{1}{2\pi \Delta l_n} \log\left(\frac{\Delta l_n}{a}\right) - j \frac{k}{4\pi}, \quad (8)$$

For $m \neq n$, use the crudest approximation with R_m constant so that

$$\psi(m,n) \approx \frac{e^{-jk R_m}}{4\pi R_m}. \quad (9)$$

This simplifying modification was incorporated into MININEC by changes to the two subroutines in lines 20-880 [2].

Most of the elliptical integration subroutine was deleted (specifically lines 70-220). The remaining integral is still performed numerically with the Gaussian quadrature subroutine. In addition, other statements had to be changed in order to adapt this modification into the program without changing the variables. These changes included the deletion of the variable I6 in lines 650 and 860, and the square of the wire radius A2 is no longer necessary in line 730. Also lines 281-288 were inserted to treat the $m=n$ case, including when a half segment is being calculated, and two lines (60 and 785) were added to direct the program to the proper lines based on the value of distance D. The modified subroutines of an IBM Personal Computer version of MININEC are listed in the Appendix.

Figure 2 displays the results of the modified MININEC along with the same expected values of input reactance that were displayed in Figure 1. The agreement is within 1% for $10^{-7} < a/\lambda < 10^{-4}$. This modification has a slight affect on the resistance values. The modified program gives resistance values that are 2% lower than the results from MININEC for $a/\lambda \approx 10^{-7}$.

This modified MININEC was also used to determine the input impedance at 50 kHz of a 192 m top-loaded monopole with six-radial wires. The tower was divided into five segments, and the radials wires were each divided into three segments. The tower had a radius of 0.48 m and the six top radials each had a radius of 0.0127 m ($a/\lambda \approx 2 \times 10^{-6}$) which gave an input reactance of $0.621 - j625$ ohms, or within 3% of the value obtained from experimental data ($0.636 - j609$ ohms) [7].

Another example to check the modified version is a comparison to NEC for a 365 m top-loaded monopole operating at 27 kHz. There were twelve 0.0143 m radius radials. Each wire was divided into three segments. The tower had a radius of 0.88 m and was divided into five segments. The two programs gave the following values of input impedance

NEC	0.632 - j419 ohms
Modified MININEC	0.614 - j393 ohms

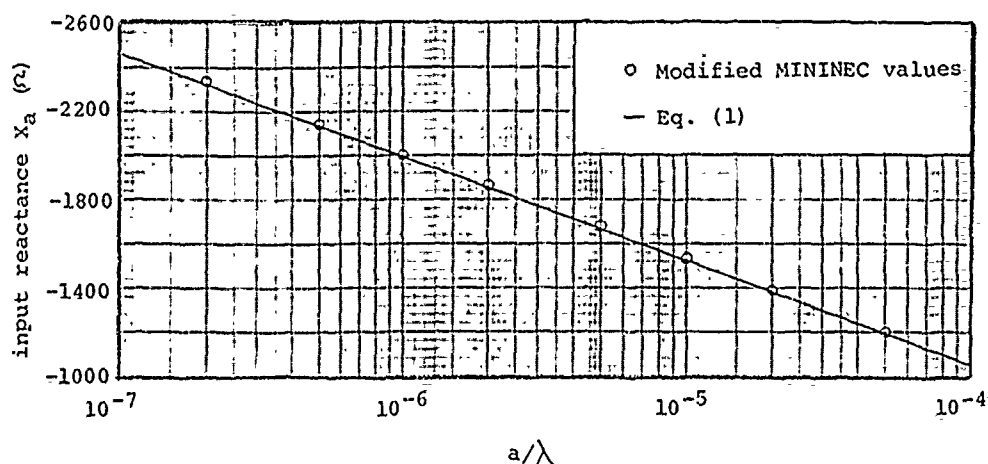


Figure 2. Input reactances from modified MININEC compared to expected values for a 90.5 m monopole divided into five segments at 150 kHz.

CONCLUSIONS

A quick modification to MININEC has been presented that allows the program to analyze vlf and lf antennas. The adapted program yields reasonable values for the input reactance of wires with very small radius to wavelength ratios, without introducing significant error in the resistance values. This low-frequency extension could be implemented as an option in the program instead of replacing the valid code for larger wires, similar to the thin-wire and the extended thin-wire kernels in NEC.

ACKNOWLEDGEMENTS

The authors would like to thank J. C. Logan of the Naval Ocean Systems Center and A. W. Glisson of the University of Mississippi for helpful conversations. We would also like to thank J.C. Logan for providing us a copy of MININEC for the IBM PC.

REFERENCES

1. A.J. Julian, J.C. Logan, and J.W. Rockway, MININEC: A mini-numerical electromagnetics code, Technical Document 516, Naval Ocean Systems Center, San Diego, Calif., 1982.
2. S.T. Li, J. W. Rockway, J.C. Logan, and D.W.S. Tam, Microcomputer Tools for Communications Engineering, Artech House, Dedham, Mass., Chapter 4, 1983.
3. D. R. Wilton, Wire problems, Lecture notes for short course on computational methods in electromagnetics, 1981.
4. H. Jasik, Antenna Engineering Handbook, McGraw-Hill, New York, pp. 19-2 - 19-3, 1961.
5. E. C. Jordan, and K. G. Balmain, Electromagnetic Waves and Radiating Systems, Prentice-Hall, Englewood Cliffs, Chapter 14, 1968.
6. R.F. Harrington, Field Computation by Moment Methods, Macmillan, New York, Chapter 4, 1968.
7. T.E. Devaney, R.F. Hall, and W.E. Gustafson, Low frequency top-loaded antenna, U.S. Navy Electronics Lab., San Diego, Calif., 1966.

APPENDIX

LISTING OF MODIFIED MININEC SUBROUTINES

```

20 X3=T*D(P4)
30 Y3=T*F(P4)
40 Z3=F*T*G(P4)*F0
50 D=SQR(D4-F3*(X3*X2+Y3*Y2+Z3*Z2)*X3*X3+Y3*Y3+Z3*Z3)
60 IF D<1 THEN RETURN
210 D1=D*W
240 T3=T3+COS(B1)/D
250 T4=T4+SIN(B1)/D
260 RETURN
270 F1=1
280 F0=1
300 IF K=1 AND P3-P2=1 AND P1=(P3+P2)/2 THEN GOTO 282 ELSE GOTO 285
282 T1=2*LOG(S(P4)/A(P4))
283 T2=-(W*S(P4))
284 GOTO 880
285 IF I=J AND K=1 AND P3-P2=.5 AND 1-P1/INT(P1)=0 THEN GOTO 286
    ELSE GOTO 290
286 T1=LOG(S(P4)/A(P4))
287 T2=-(W*S(P4)/2)
288 GOTO 880
290-IF C(J,1)=C(J,2) THEN F0=SGN(C(J,P1))
300 F3=2*SGN(C(J,P1))
310 IF P1=INT(P1)+.H0 GOTO 440
320 I4=INT(P1+1)
330 I5=INT(P1)
340 X1=(X(I4)+X(I5))/2
350 Y1=(Y(I4)+Y(I5))/2
360 Z1=(Z(I4)+Z(I5))/2
370 X2=X1-X(P2)
380 Y2=Y1-Y(P2)
390 Z2=Z1-Z(P2)*F
400 X3=X1-X(P3)
410 Y3=Y1-Y(P3)
420 Z3=Z1-Z(P3)*F
430 GOTO 530
440 I4=INT(P2+1)
450 IF P2=INT(P2)+.H0 THEN I4=P2
460 I5=INT(P2)
470 X2=X(P1)-(X(I4)+X(I5))/2
480 Y2=Y(P1)-(Y(I4)+Y(I5))/2
490 Z2=Z(P1)-(Z(I4)+Z(I5))/2
500 X3=X(P1)-X(INT(P3))
510 Y3=Y(P1)-Y(INT(P3))
520 Z3=Z(P1)-Z(INT(P3))
530 D0=X2*X2+Y2*Y2+Z2*Z2
540 D3=X3*X3+Y3*Y3+Z3*Z3
550 S4=(P3-P2)*S(P4)
560 F2=1
570 N3=7
580 T1=H0
590 T2=T1
600 T=S(P4)+.801*A(P4)
610 A2=A(P4)*A(P4)
620 IF SQR(D3)+SQR(D0)>T GOTO 680
630 I6=16*A(P4)/S(P4)
640 IF P1=INT(P1)+.H0 THEN F2=2
650 IF P1=INT(P1)+.H0 THEN S4=S(P4)/2
670 GOTO 720
680 T=SQR(D0)/ABS(S4)
690 IF T>3 THEN N3=2
700 IF T>5 THEN N3=1
710 I6=H0
720 I5=N3*2
730 D0=D0
740 L=N3
750 T3=H0
760 T4=T3
770 T=S4*(Q(L)+.5)
780 GOSUB 20
785 IF D<1 THEN GOTO 282
790 T=S4*(.5-Q(L))
800 GOSUB 20
810 L=L+1
820 T1=T1+Q(L)*T3
830 T2=T2+Q(L)*T4
840 L=L+1
850 IF L<15 GOTO 750
860 T1=F2*T1*S4
870 T2=F2*T2*S4
880 RETURN

```

ANALYSIS OF STEPPED-RADIUS COLINEAR DUAL ANTENNA ARRAYS

D.V. Campbell

I. INTRODUCTION

Mutual coupling of cosited antennas can adversely impact the performance of communication systems involving a number of radios operating on adjacent frequencies. Antennas are colocated, for example, in transportable military air-traffic control systems where simultaneous transmission and reception is required. Crosstalk interference due to strong mutual coupling of the antennas is often very difficult to mitigate in these systems.

This paper is concerned with the analysis of a COLINEAR DUAL ANTENNA ARRAY designed to provide very high interdipole isolation from 225 to 400 MHz. This array incorporates two independently fed colinear broadband dipoles and a feed line isolator section to suppress parasitic rf current coupling.

The MINI-NUMERICAL ELECTROMAGNETICS CODE (MININEC) (1) is used to model the array and the feed line isolator section. The analysis shows that the isolator section design significantly affects the interdipole coupling. Antenna arrays incorporating stepped-radius conductors have been modeled with MININEC and it has been found that the effect of the step in wire radius, while not pronounced, may be significant.

II. TECHNICAL APPROACH

Transportable military air-traffic control centrals incorporate communication systems operating at HF, VHF, and at UHF. Air traffic controllers must communicate simultaneously on adjacent channels. Because of strong mutual coupling of the cosited antennas, it can be very difficult to prevent receiver overload, desensitization, and crosstalk.

Interference can be reduced by means of selective filters. In the investigation reported here, which is concerned only with the UHF system, the coupling between the two UHF antennas was minimized by employing the colinear antenna arrangement and by incorporating a transmission line isolator section in the feed line of the upper dipole to suppress parasitic rf currents on the feed line. See Fig. 1.

The colinear antenna arrangement minimizes the field coupling between the dipoles. For example, the isolation between a pair of colinear dipoles in free space separated by 1.5 wavelengths would be -36 decibels. Interantenna isolation is defined as the fraction of the total power radiated by one antenna which is intercepted by the other. Another factor favoring vertical stacking of antennas is the improved azimuthal radiation pattern which results from reduced shadowing effects.

III. FEED LINE ISOLATOR SECTION

By providing adequate spacing of the colinear antennas, radiation coupling can, in principle, be reduced to acceptable levels. At 300 MHz, for example, a vertical spacing of 1.5 meters may provide adequate isolation. The isolation between colinear dipoles can be estimated from the following formula

$$\text{Frec./Ptrans.} = \frac{4}{9} (kr)^4$$

where k is the free-space wavenumber and r is the antenna spacing.

A second coupling effect, i.e., interdipole coupling due to parasitic rf currents induced on the feed line of the upper dipole, is much more difficult to control than radiation coupling and, with radiation coupling minimized, is the dominant coupling effect. A design objective is the reduction of this current coupling to a level smaller than that caused by radiation (field) coupling. An additional requirement is to accomplish this reduction in coupling over an octave frequency range.

In a previous theoretical and experimental investigation (2) it has been shown that parasitic currents can be suppressed over an octave frequency range by means of an isolator section incorporated in the feed line of the upper antenna.

The isolator section consists of a sequence of high impedance cable chokes placed in the coaxial cable feed line at quarter-wavelength intervals. A cable choke is made of coaxial cable coiled to form an inductor and which can be approximated by an inductance, L in parallel with a self capacitance, C . The reactance of the choke is

$$X = 2\pi f_0 L / (f_0/f - f/f_0)$$

where

$$f_0 = 1/2\pi(LC)^{1/2}$$

A cable choke has been constructed having L/C constants of .44 microhenry and .72 picofarad and resonating at 280 MHz. The reactance of this choke is 1128, -5603, and -1061 ohms at 200, 300, and 400 MHz respectively and is extremely high at resonance.

Considerable skill and ingenuity is needed in constructing a cable choke to secure a high L/C ratio and to establish the self resonance frequency near the middle of the frequency band. Moreover, the self capacitance of the cable choke must be kept to a minimum to secure high reactance over a broad bandwidth.

The isolator section behaves as a band rejection filter which eliminates the interdipole coupling due to conducted parasitic currents on the transmission line outer surface. The high impedance cable chokes suppress the parasitic current by enforcing a sequence of near zeros in the current distribution over a broad frequency range.

IV. STEPPED-RADIUS COLINEAR DUAL ANTENNA

In the original investigation the antenna array was treated theoretically as an electrically long loaded wire of constant diameter and a three-term expression for the current was used to simplify the analysis (3). In a practical antenna system, however, the dipoles would probably be somewhat larger in diameter than the coaxial cable of the feed line isolator section.

In the present paper MININEC is used to investigate the effect of stepped-radius conductors on the current distribution and isolation of the colinear dual antenna system. Current distributions on stepped-radius antennas having radius ratios of 1.25, 10, and 100 have been previously computed while validating MININEC and found to compare quite favorably with very accurate distributions obtained by Glisson and Wilton (4). Since MININEC is based on Wilton's formulation, it is believed that this thin-wire moment method code is quite capable of accurately treating the stepped-radius wire antenna problems considered here.

The current amplitude distribution along the antenna array has been used as a performance measure because it provides a very good indication of the effectiveness of the isolator section in suppressing parasitic current on the feed line. Ideally, the current should be confined to the driven dipole and be greatly suppressed along the rest of the array at all frequencies within the rejection band of the isolator section. Theoretically, the isolator section can be extremely effective. In practice, however, the filtering properties of the isolator section are limited because of the difficulty in fabricating the broadband high impedance cable chokes.

In this investigation, antenna current distribution and interdipole isolation has been computed for an antenna-isolator section of constant radius and for an antenna having an isolator section of reduced radius. The L/C constants of practical UHF cable chokes have been used in the simulations so that realistic results are obtained. Each of the antennas modeled incorporates an isolator section containing a sequence of five identical cable chokes placed in the feed line at .25 meter intervals. This spacing corresponds to a quarter-wavelength at the midband frequency (300 MHz) and has been found to provide effective broadband suppression of current. Additional chokes could be included in a longer antenna.

A. CONSTANT-RADIUS ANTENNA

The current distribution at 200 MHz on a constant-radius (1.58 cm) colinear dual antenna array with high impedance cable chokes ($L/C = .44/.72$) is given in Fig. 2. At 200 MHz each cable choke has an inductive reactance of 1128 ohms. In this model the "receiving" dipole is on the left between the origin and .5 meters and is connected to a 50 ohm load at its center. The "transmitting" dipole is on the right between 1.5 and 2 meters, and the isolator section extends from .5 to 1.5 meters. It is seen that the current is essentially confined to the transmitting dipole. The filtering provided by the isolator section, in this case, is highly effective.

The antenna current distribution at 300 MHz is shown in Fig. 3. At this frequency, the dipoles are approximately a half-wavelength long and the choke reactance is -5603 ohms. The sinusoidal current on the driven dipole is evident. The weak current along the isolator section is a indication of its effectiveness in suppressing induced parasitic current.

The current distribution at 400 MHz is given in Fig. 4. Although the chokes are highly reactive (-1061 ohms) at 400

MHz, the effectiveness of the isolator section is somewhat diminished as evidenced by the current amplitude. The use of additional chokes or chokes with higher reactance would provide more current suppression if required.

B. STEPPED-RADIUS ANTENNA

In the stepped-radius antenna, the dipoles are 1.58 cm in radius and the isolator section is .18 cm in radius, corresponding to RG-58 coaxial cable transmission line. As in the constant-radius antenna discussed above, five high impedance cable chokes ($L/C = .44/.72$) are placed at .25 meter intervals in the feed line to form the isolator section. Except for its smaller radius isolator section, the stepped-radius antenna is identical to the constant-radius antenna.

The current distribution at 200 MHz is given in Fig.5. It is seen that the feed line current is highly suppressed and that the distribution is practically identical to that of the constant-radius antenna (Fig.2).

At 300 MHz the current distribution (Fig.6) along the stepped-radius antenna is very similar to that of the constant-radius antenna (Fig.3).

At 400 MHz the current amplitude (Fig.7) along the isolator section of the stepped-radius antenna is somewhat weaker than that of the constant-radius antenna (Fig.4), indicating that the current coupling to the receiving dipole is correspondingly reduced.

C. INTERDIPOLE ISOLATION

The interdipole isolation provides a good performance measure of an isolator section and has been calculated for the constant-radius antenna and for the stepped-radius antenna. See Fig.8. Evidently, the stepped-radius antenna provides somewhat better isolation above 350 MHz than the constant-radius antenna in keeping with its current suppression characteristic. The interdipole isolation has also been tabulated in Fig.9. At 400 MHz, the stepped-radius antenna provides about -55 dB isolation in comparison with -44 dB provided by the constant-radius antenna.

V. CONCLUSION

MININEC has been used to study the effect of stepped-radius wires on the performance of colinear dual antenna systems. It has been found that large steps in wire radius (for example 9/1 steps) do not significantly alter the current distribution but may significantly affect the interdipole isolation at some frequencies. Computer simulations indicate that a colinear dual antenna system incorporating an isolator section of reduced wire radius can provide a high degree of current suppression and high interdipole isolation over an octave frequency range. Current distributions on these antennas obtained with MININEC agree well with distributions obtained previously using a three-term expression for the antenna current.

REFERENCES

1. S.T. Li, J.W. Rockway, L.C. Logan and D.W.S. Tam (1983) Microcomputer Tools for Communications Engineering, Artech House, Inc., Dedham, Mass.
2. D.V. Campbell, S. Fich and F.K. Schwering, "Suppression of Parasitic Currents on Feed Lines of Colinear Dual Antenna Systems", IEEE Trans. Antennas Propagat., Vol. AP-28, pp. 658-662, Sept 1980.
3. L.C. Shen, T.T. Wu, and R.W.P. King, "A Simple Formula of Current in Dipole Antennas", IEEE Trans. Antennas Propagat., Vol. AP-16, pp. 542-547, Sept 1968.
4. A.W. Glisson and D.R. Wilton, "Numerical Procedures for Handling Stepped-Radius Wire Junctions", University of Mississippi, Final Report for Contract No. N66001-77-C-0156, March 1979.

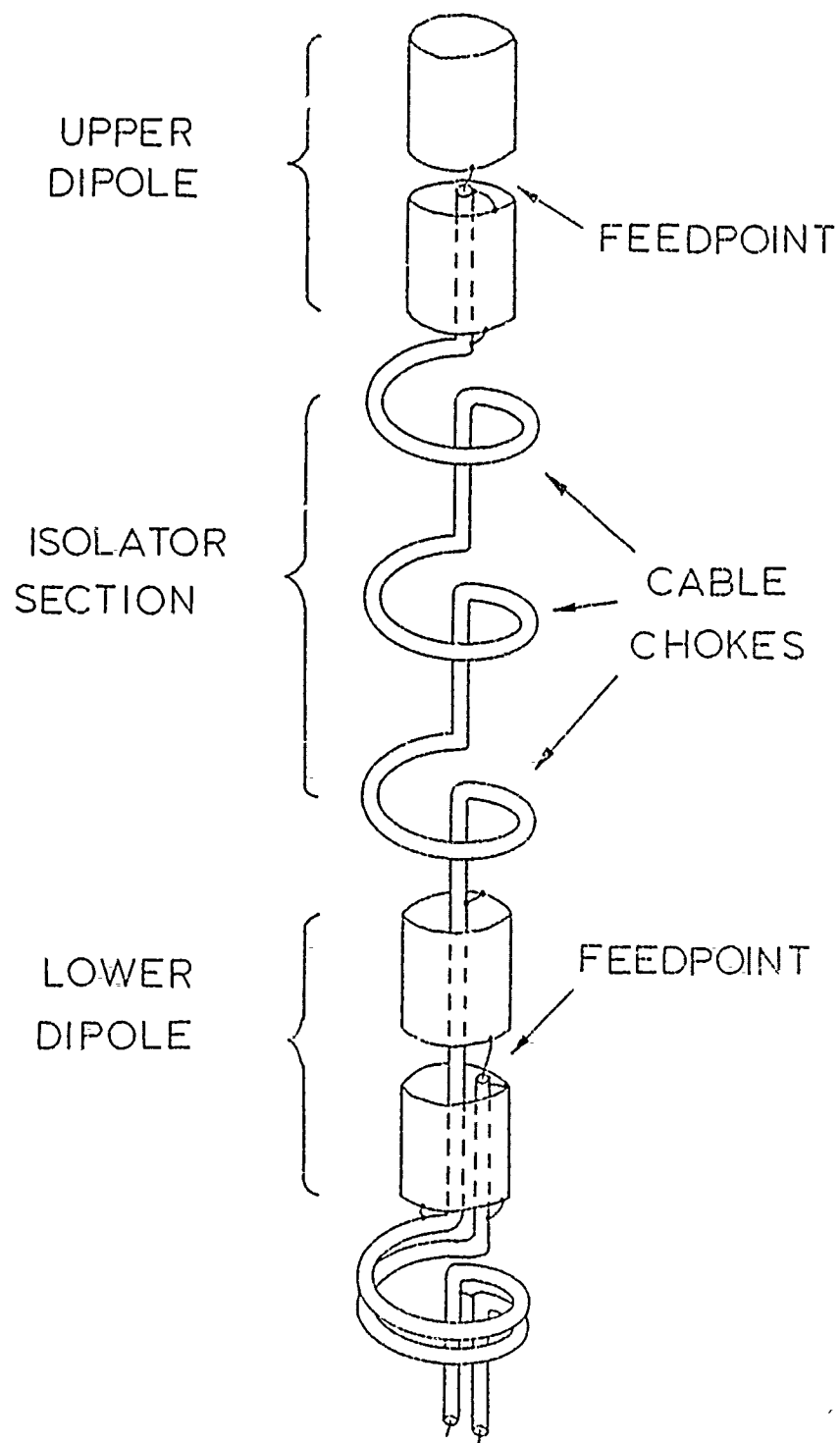


FIGURE 1

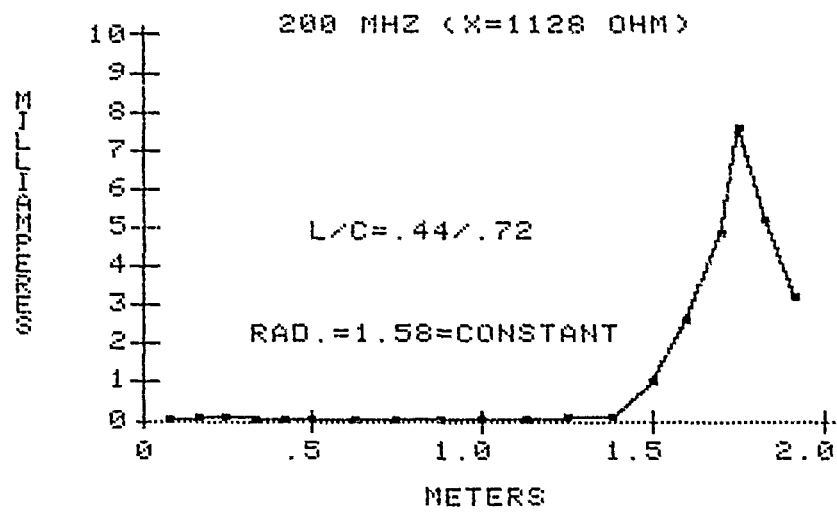


Figure 2

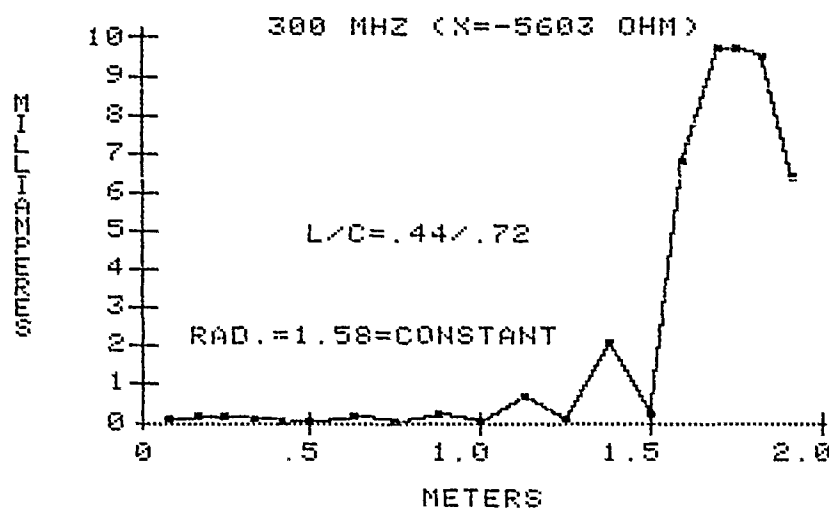


Figure 3

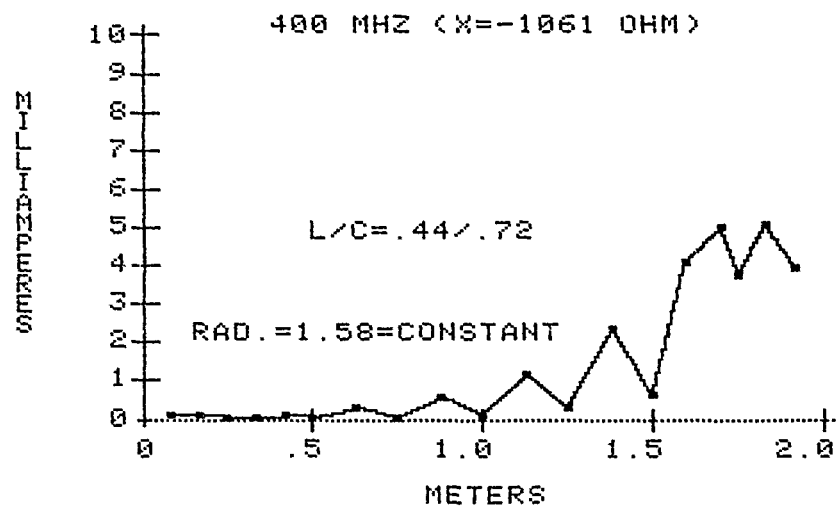


Figure 4

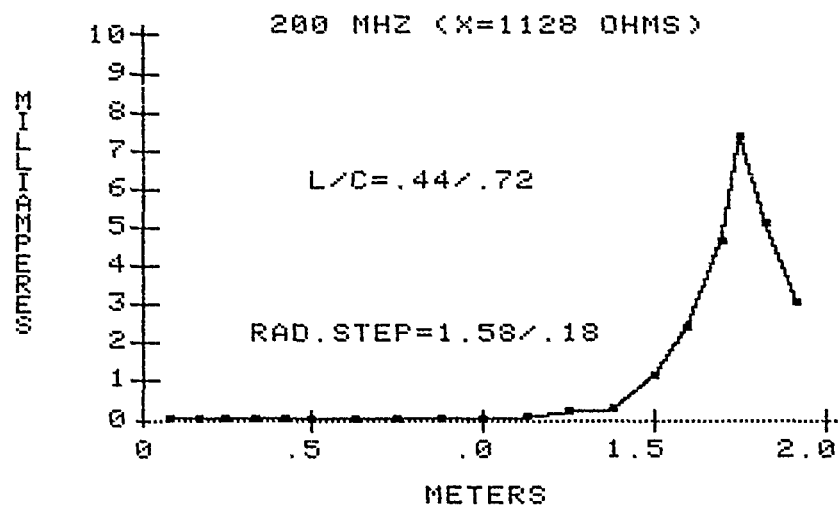


Figure 5

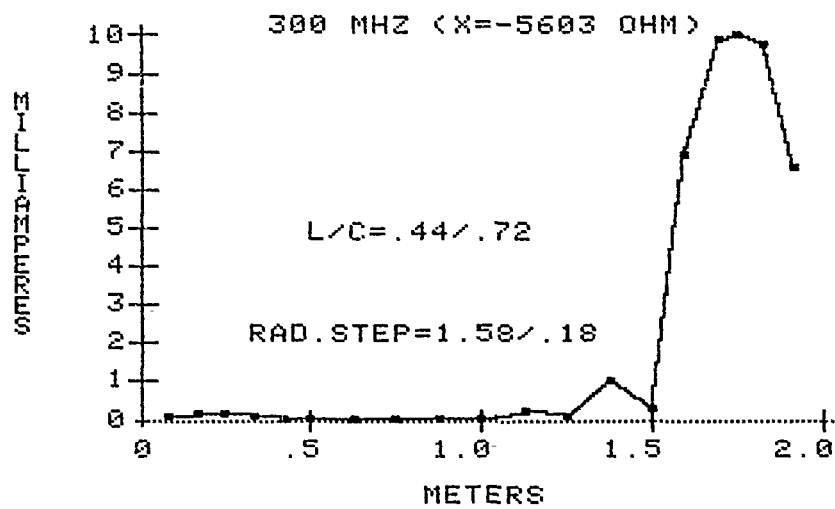


Figure 6

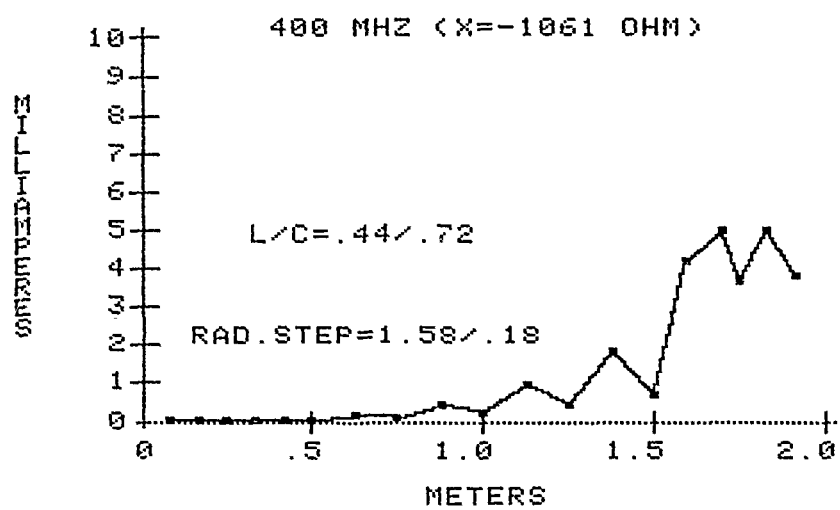


Figure 7

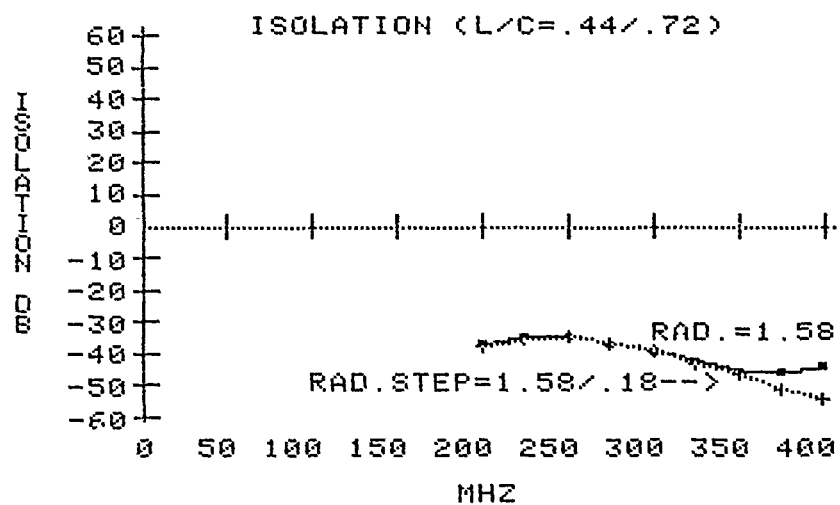


Figure 8

INTERDIPOLE ISOLATION

<u>FREQUENCY</u>	<u>CONSTANT-RADIUS ANTENNA (1.58 cm)</u>	<u>STEPPED-RADIUS ANTENNA (1.58/.18 cm)</u>
200 MHz	-37 dB	-37.5 dB
225	-34.9	-35.3
250	-34.8	-34.9
275	-36.6	-36.6
300	-39.5	-39.5
325	-42.6	-43.1
350	-45.3	-46.6
375	-45.3	-51.0
400	-43.9	-54.3

Figure 9

DESIGN APPROACH FOR ELECTRICALLY SMALL TRANSMITTING ANTENNAS USING THE MICROCOMPUTER

Peder M. Hansen and James C. Logan
(U.S. Naval Ocean Systems Center, San Diego,
California, USA)

INTRODUCTION

The practical parameters of interest for a transmitting antenna are: (1) power limitation (radiated power), (2) bandwidth, and (3) efficiency. For electrically small antennas these parameters become severely limited. The problems with electrically small antennas stem from the fact that they have a large amount of reactive energy stored in the region immediately surrounding the antenna, resulting in a high value of input reactance and a small value of radiation resistance (high Q).

The high Q results in small bandwidth (varies with frequency cubed), large voltage required for a given radiated power (varies with frequency to the fourth power), and reduced efficiency due to losses in the tuning elements and surrounding media. The frequency variation of efficiency is more complicated but generally increases with frequency. Consequently, the design problem usually boils down to meeting the system requirements at the lowest frequency, and they will be exceeded for higher frequencies. The antenna self-resonance is usually designed to be above the highest operating frequency so that one type of element (capacitance or inductance) will suffice for tuning. Excellent articles and discussions on electrically small antenna designs are contained in references 1, 2, and 3.

Until recently, the electrical design of such antennas was based on approximate (electro-static) solutions and empirical data [3]. In order to ensure performance, relatively large safety factors were used and the antenna structures often were larger than required. Also, if nonstandard configurations were to be used, model measurements were required. There now exists a computer program, Mini-Numerical Electromagnetics Code (MININEC) [4], which can be run on

various microcomputers and give acceptably accurate calculations of the characteristics of arbitrarily shaped antennas, including current distribution, impedance, and radiated fields. A design approach for electrically small antennas based on MININEC will be developed.

MININEC

The MINI-NUMERICAL ELECTROMAGNETICS CODE is a frequency domain Method of Moments computer code for the analysis of wire antennas. MININEC is written in the BASIC language for use on microcomputers with as little as 64k memory. The MININEC program is based on the numerical solution of an integral representation of the electric fields. A modified Galerkin procedure is used to solve the integral equation. This formulation results in a uniquely compact (i.e., requiring little core computer storage) code suitable for implementation on a microcomputer. The MININEC code solves for the impedance and currents on arbitrarily oriented wires in free space and over a flat perfectly conducting ground plane. Configurations with multiple wire junctions can also be used. Options include lumped parameter impedance loading of the wires and calculation of far-field patterns.

The solution to an antenna problem generated by a thin wire method of moments computer program is at best an approximation. Nonetheless, highly accurate answers can be obtained by careful modeling of the antenna configuration, taking into account the inherent limitations of the computer code.

POWER LIMITATION

The power limitation of a device is limited by voltage (breakdown, or corona), or current (heating). In the case of electrically small antennas, it is usually a voltage. There are voltage limits associated with all of the insulators in the antenna system. The structure itself will have a voltage limit above which the fields on it will be strong enough to cause local breakdown of the air (corona). In general, the overall limit is usually the feed through insulator (bushing) or base insulator. The structure and other insulators are designed to withstand at least the corresponding voltage.

BASE VOLTAGE LIMIT

For electrically small antennas, the input reactance is much greater than the radiation resistance. This results in a very useful inequality

$$\frac{X_b^2}{R_r} = \frac{V^2}{P_r} \leq \frac{V_{\max}^2}{P_r} \quad (1)$$

where

X_b = antenna feed reactance

R_r = Radiation resistance

P_r = Radiated power

V_{\max} = Bushing or base insulator voltage limit

Equation 1 indicates that for a given feed voltage limit, and radiated power requirement, a maximum allowable limit of X_b^2/R_r is determined.

BANDWIDTH

The radiation of Q of an antenna is defined by

$$Q_r = X_{co}/R_r$$

where X_{co} is the reactance at the operating frequency of the antenna static capacitance [3].

In the absence of losses, the 3 dB bandwidth of the tuned antenna will be

$$BW_o = f/Q_r \quad (2)$$

where f is the operating frequency.

BW_o is termed the antenna bandwidth efficiency product. Since for a real antenna there will be losses, the actual antenna bandwidth will be greater than BW_o and given by

$$BW_{as} = BW_o/n_{as} \quad (3)$$

where BW_{as} is antenna system unloaded bandwidth (Hz) and n_{as} is antenna system efficiency.

MININEC can be used to calculate Q_r by using the reactance slope technique. This is done by calculating X_b at two frequencies near the operating frequency and calculating the slope X'_b . Then

$$X_{co} = (X_b - f X'_b)/2$$

ANALYSIS OVER PERFECTLY CONDUCTING EARTH

MININEC cannot solve problems that include finitely conducting earth. However, for electrically small antennas that have ground systems in contact with the earth, the antenna feed reactance, radiation resistance, and charge distribution do not change significantly if the earth is replaced by a perfect conductor. Thus, MININEC can be used to obtain X_b , R_r , X_{co} over a perfectly conducting ground and the values applied to antenna design.

EXAMPLE

The example chosen illustrates the application of the above design procedure to a 550 kHz balloon supported emergency AM broadcast antenna. The balloon supports a wire tether which is also the antenna. The design requires 1,000 watts radiated, feed voltage less than 10,000 volts, an unloaded antenna system bandwidth of 3 kHz, and an antenna system efficiency of 80%. Using MININEC, curves of X_b^2/R_r and Q_r versus wire length have been generated and are given in Figures 1 and 2. To illustrate the flexibility of MININEC, calculations have been made for a perfectly vertical wire, corresponding to no wind, and for a catenary corresponding to the worst-case winds to be encountered operationally.

From equation 1, X_b^2/R_r must satisfy

$$X_b^2/R_r \leq 10^5$$

from equations 2 and 3, Q_r must satisfy

$$Q_r \leq 183.3/.8 = 229$$

Examination of Figures 1 and 2 indicates that the constraints are most severe for the case involving the catenary. The minimum required wire length obtained from the figures is given in Table 1.

Table 1. Minimum Wire Length (Meters)

	Without Catenary	With Catenary
Feed Voltage	63.0	67.9
Bandwidth	54.9	57.2

The limiting case is the feed voltage requirement for the configuration with the catenary and calls for a minimum wire length of 67.9 meters.

SUMMARY

Calculating antenna characteristics over perfectly conducting ground with MININEC and application of the appropriate relationships allow the designer to determine the required size of an electrically small antenna.

REFERENCES

1. Wheeler HA, "Fundamental Limitations of Small Antennas," Proceedings IRE, V35 (December 1947), 1479-1484 .
2. Wheeler HA, "Small Antennas," IEEE Transactions Antennas and Propagation, 4 (July 1975), 462-469.
3. Watt, AD. VLF Radio Engineering, Pergamon Press, New York (1967).
4. Li ST et al., Microcomputer Tools for Communication Engineering, Artech House, Inc., Dedham, Massachusetts (1983).

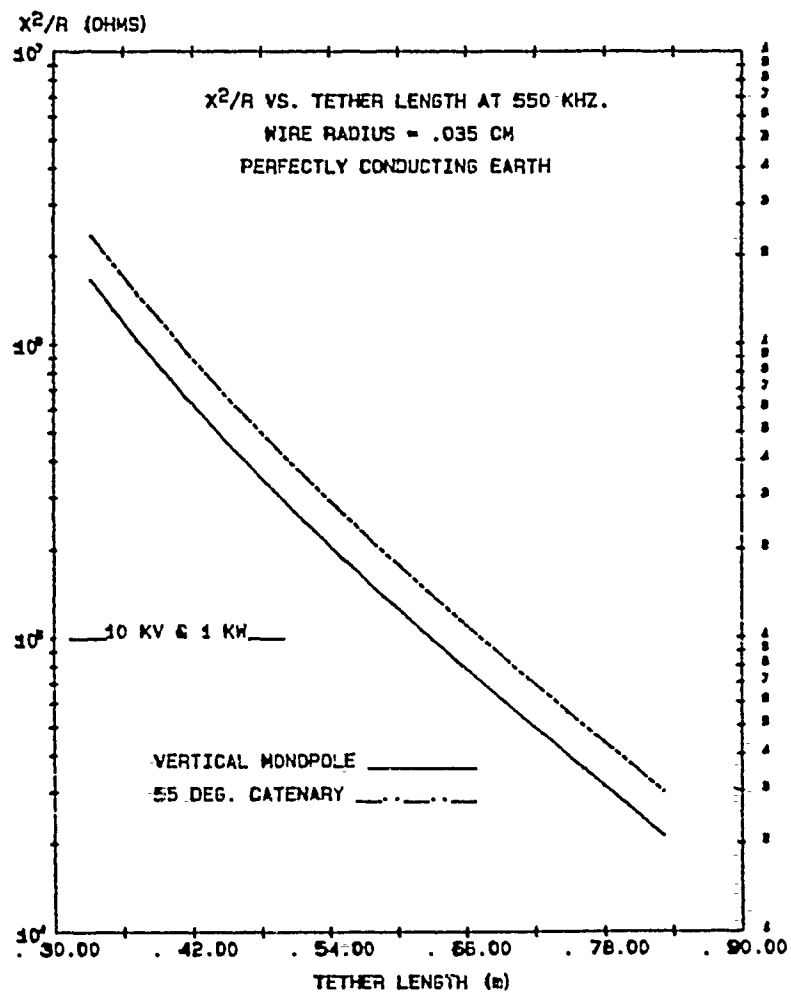


FIGURE 1.

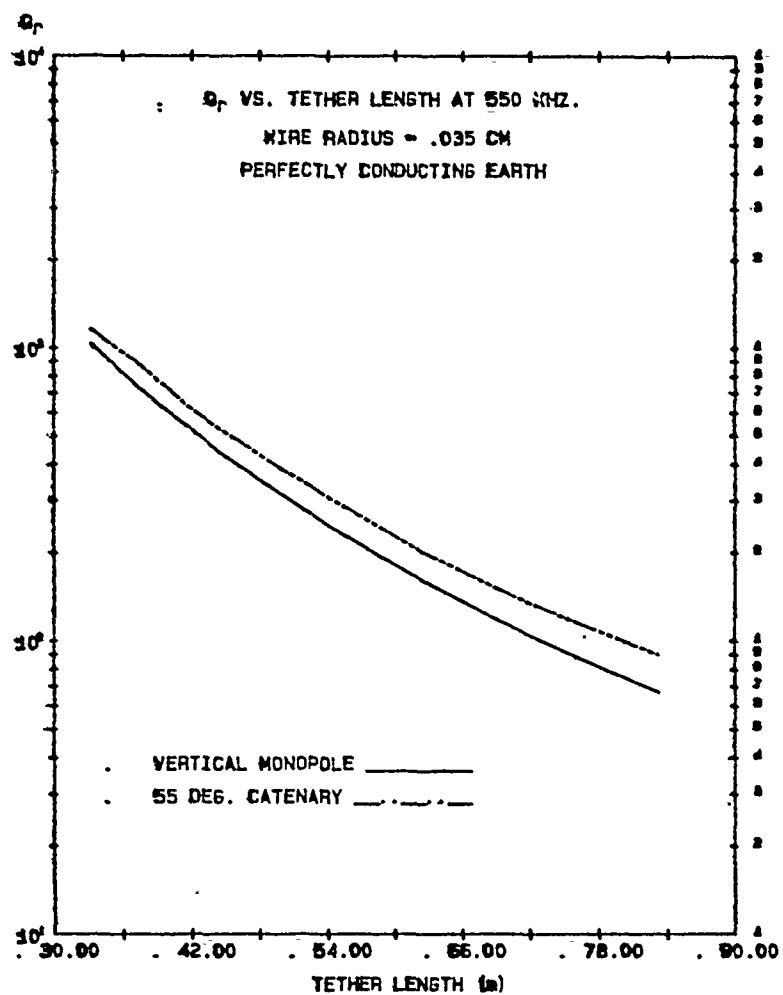


FIGURE 2.

SESSION VII - "COMPUTATIONAL EM MODELING"

"NEC3 on a PC"
Stephen Lamont

Naval Postgraduate School

"A Computational Model for Electromagnetic Interactions with Advanced Composites"
Harold Sabbagh, Thomas Roberts & David Sabbagh Sabbagh Associates

"MAXWELL - A User Friendly PC-Based Finite Element Program for Electromagnetics"
Z.J. Cendes Carnegie-Mellon University

NEC3 ON A PC

Stephan Lamont

Naval Postgraduate School

Monterey, California

Abstract

This paper presents the results of efforts to implement the full mainframe version of NEC3 on three microcomputer based workstations, the IBM RT PC, the IBM PC AT, and the IBM PC AT/370¹. The architecture and configuration of each of the three systems will be briefly described and conversion and implementation experiences will be discussed. Benchmark results of sample problems will be presented.

Introduction

Considerable progress has been made in recent years toward placing advanced computational power upon the desktop of an engineer or scientist. For the first time it is feasible to consider implementing a full or reasonably complete subset version of the Numerical Electromagnetic Code (NEC3) on a small and affordable computer system.

Three small systems were chosen as targets for implementation:

- the IBM PC AT, as an example of a commonly available "off the shelf" microcomputer,
- the IBM PC AT/370, as a middle to high end micro-mainframe, and
- the IBM RT PC, as an example of a high performance, high function workstation embodying a novel architecture and with capabilities outside the range of "personal" computers.

¹ IBM, IBM PC, IBM PC AT, IBM PC AT/370 and IBM RT PC are trademarks of the International Business Machines Corporation.

The FORTRAN compiler for each machine is a native code compiler and was chosen based upon availability and/or compatibility with the compiler resident on the Naval Postgraduate School IBM 3033 mainframe computer.

Hardware and Operating Systems

IBM PC AT

The IBM PC AT used in this study is an "off the shelf" system with 1152 kilobytes of memory, 2-20 megabyte fixed disks, the 16 bit Intel 80286 processor and Intel 80287 numeric coprocessor, and IBM Professional Graphics Controller and Display. The numeric coprocessor provides 32 and 64 bit IEEE standard floating point operations, including several trigonometric and exponential functions. The used operating system is PC-DOS Version 3.1.

IBM PC AT/370

The IBM PC AT/370 is a single user implementation of the venerable IBM 360/370 hardware architecture which runs on a standard IBM PC AT as a "host" system.

The full 370 instruction set is implemented with the exception of certain Supervisor state instructions specifically relating to multiprocessing or multitasking. The board set consists of a coprocessor board, containing two Motorola 68000 microprocessors remicrocoded to recognize native 370 instruction codes and an Intel 8087 numeric coprocessor with microcode revisions allowing it to process standard 370 hardware floating point (32 bit single and 64 bit double precision hexadecimal), and a 512 kilobyte dual ported random access memory shared by the AT host and the 370 coprocessor. When the 370 coprocessor is running, the AT's 80286 processor is used to handle all I/O and other housekeeping tasks and is not, in general, available for user tasks.

The AT/370 was configured with the maximum 8 megabytes of virtual memory, paged to and from a paging dataset resident on one of the AT'S 20 megabyte fixed disks.

The operating system is a subset with extensions of the mainframe VM/CMS operating system. The extensions provide transfer to and from the PC-DOS file system and the CMS file system as well as host connectivity.

IBM RT PC

Perhaps the most interesting of the three systems is the recently announced IBM RT PC. This machine is a departure for IBM in a number of ways.

First, the Reduced Instruction Set Computer (RISC) architecture is novel, at least for conservative IBM. A RISC instruction set is based upon statistics showing that approximately 80 percent of the machine instructions executed in normal program code are composed of 20 percent of a computer's total instruction set. It follows then that performance over a large set of applications may be improved if that 20 percent of the instruction set is optimized and the balance of the instructions are emulated in software.

Second and perhaps more apparent is the commitment of IBM to the UNIX² System V operating system with extensions. The operating system, called AIX³, provides a PC-DOS like shell, as well as the more familiar UNIX shell, to allow migration from the PC environment to the UNIX environment.

The machine supports a virtual address space of 1 terabyte in real memory of up to 16 megabytes and provides for a floating point accelerator option. Floating point arithmetic is done according to the IEEE standard. A PC AT-like coprocessor may be added for PC compatibility and this coprocessor may have its own memory or share virtual memory with the RT host. Shared memory will seriously degrade the AT performance; adding AT memory

² UNIX is a trademark of AT&T Bell Laboratories.

³ AIX is a trademark of INTERACTIVE Systems Corporation

will bring the performance up to an estimated 80 percent of a stand alone AT. Announced processors will support up to 210 megabytes of fixed disk (up to 3-70 megabyte drives), and 4 megabytes of real memory.

Performance of the RT PC is in the 1.8 to 2.0 million instruction per second (mips) range with a Whetstone benchmark figure of roughly 250 kWhets claimed by IBM. True multitasking is also possible on the RT PC.

The machine tested was equipped with 4 megabytes of real memory, a floating point accelerator (a necessity for scientific or engineering work), 140 megabytes of hard disk (2-70 megabyte drives), and a 1.2 megabyte floppy disk drive.

FORTRAN Compilers

IBM PC AT

The FORTRAN compiler chosen for the IBM PC AT was IBM's Professional FORTRAN written by the Ryan-McFarland Corporation. It is an implementation of the ANSI 1977 FORTRAN standard (X3.9-1978) with extensions. It supports the REAL, DOUBLE PRECISION, and COMPLEX datatypes found in most FORTRAN implementations. However, it does not support DOUBLE PRECISION COMPLEX. The 8087 or 80287 numeric coprocessor is a mandatory hardware prerequisite feature for computers running programs compiled by Professional FORTRAN.

A library manager is provided with the compiler which allows the user to build object code libraries for use in linking large modules. The standard PC-DOS linker is used.

IBM PC AT/370

On the PC AT/370 mainframe IBM VS/FORTRAN Version 4.1 was used. It supports all datatypes required by NEC3 including DOUBLE PRECISION COMPLEX. Due to cer-

tain technical reasons and to avoid licensing questions, the NEC3 program was compiled and linked on the host IBM 3033AP machine under VM/CMS and transferred to the AT/370 using a VM/PC file transfer utility.

IBM RT PC

The FORTRAN compiler on the RT PC is based upon the UNIX F77 compiler with extensions. It supports all datatypes required by NEC3 including DOUBLE PRECISION COMPLEX. The compiler performs two compilation passes, a code generation pass, and a "peephole" code optimization pass.

Implementation Experiences

IBM PC AT

The lack of the DOUBLE PRECISION COMPLEX datatype required double precision complex summation, division, and multiplication algorithms to be coded in two subroutines to provide the required accuracy.

Because of the 640 kilobyte DOS limitation, the segment limit and the in core matrix partitioning blocks had to be reduced. The present number of segments and/or patches allowable on the PC AT implementation is 300. The in core matrix partition was set to 1000 complex numbers.

One "error" that cropped up while processing an out of core solution was a message indicating a record length too long on a variable length file. This error was actually traced to an awkward construction in a function having an auxiliary entry point. When the routine was rewritten as two separate functions, the record length error vanished.

The record length error cropped up again, however, as soon as the program attempted actual variable length (unformatted) I/O. This error was eliminated by including a run time parameter specifying the maximum record length allowable. The

documentation, at least to this reader, is somewhat less than lucid on this point and the error message makes no reference whatever to the run time parameter. As a result, considerable time was spent attempting to circumvent a problem which could have been easily recognized and rectified.

The library manager supplied, while a very helpful aid, especially with a program with over 90 subroutine and function units, is very slow, especially when handling large libraries. This appears to be because it makes a copy of the entire library when adding or deleting a member. When the library is nearly 100 kilobytes in size, this can be quite a chore.

As implied above, the program was broken down into component files, each encompassing only one subroutine or function, and each program unit was compiled separately. This was to reduce compile time required whenever a module had to be changed and also because the text editor, KEDIT⁴, would not handle the entire NEC3 code in one chunk. While this improved performance in compilation of individual modules, a secondary effect having to do with the file and directory architecture of PC-DOS degraded disk access times. Because a subdirectory is treated by DOS as a standard DOS file, when a large number of members are added, the directory may not be located in contiguous storage but rather scattered over several "extents" of disk memory. This causes significant degradation in performance since when DOS does a directory search it begins at the start of the directory and searches sequentially. Hence, a large number of "seeks" may be needed to find an entry in the directory. This became quite annoying as disk space became more and more fractionalized. A disk optimizer would have been a helpful utility.

As of this writing a major "bug" still remains in NEC3 on the PC AT. Out of core solutions do not produce the correct currents and hence completely erroneous answers. Hexadecimal dumps of the out of core temporary files have been checked against mainframe files, and after allowing for inevitable differences due to the different floating point algorithms, they appear to be the same based upon extensive spot checking. The right hand side of the

matrix solution has been printed out and, again, they appear to be correct. "In core" solutions agree to the precision of the machines, so further explorations will be carried out to determine the root of this problem.

At runtime, all scratch files were redirected to a 512 kilobyte virtual disk allocated in unused high AT memory.

IBM PC AT/370

The "conversion" of NEC3 for the AT/370 was actually only a trivial process of recompiling the code and relinking it using a special library, since the AT/370 does not support a feature known in IBM parlance as a Discontiguous Shared Segment which allows specially coded re-entrant libraries to be shared by a number of users, thus reducing the virtual memory requirement of an individual user's machine and enhancing overall system performance slightly. The load module was then copied from the host system over to the AT/370's file space and the host connection severed. It is fortunate that this process needed to be done only once as the file transfer, even with a high speed coaxial connection, took nearly a half hour. File transfer is not one of the AT/370's strong points.

IBM RT PC

Minimal changes had to be made in the NEC3 code on the RT. These changes were mostly related to inadvertent deviations from the FORTRAN 77 standard when local enhancements were made on the NPS version of NEC3 much earlier. Less than a dozen errors were generated in the first compiler run and these were corrected by recoding a few initialization statements.

More severe was a problem encountered when running the optimization step of compilation. The intermediate assembly language generated by the F77 code generator was over 5 megabytes in size and, because the system's minidisks were generated with insufficient size, the optimizer abnormally terminated when it ran out of minidisk space. This difficulty was circumvented by simply breaking the source code into four smaller segments and recompiling.

⁴ KEDIT is a trademark of the Mansfield Software Group

Benchmark Times and Results

The complete set of NEC3 test problems as detailed in the NEC User's Manual and included with IBM distribution tapes were run on each machine. Run times for Example 1 (center fed linear antenna), Example 4 (T antenna on a box over perfect ground), and the rhombic antenna are compared in Tables 1 - 3. As discussed above, the out of core solutions (Example 4 and the rhombic antenna) on the PC AT are erroneous. Results from runs on the NPS 3033AP and a Cray 1S (using NEC2) are presented for comparison with the microcomputer runs. No timings are available for the Cray runs.

Table 1: Example 1

7 segments, center fed linear antenna, free space.

System	Fill (sec)	Factor (sec)	Impedance (Ohms)
PC AT	4.4	0.1	0.82698E+02 j0.46306E+02
AT/370	4.2	0.2	0.82696E+02 j0.46294E+02
RT PC	3.0	Note 1	0.82698E+02 j0.46306E+02
3033AP	0.07	0.003	0.82698E+02 j0.46306E+02
Cray1	n/a	n/a	0.82698E+02 j0.46306E+02

Notes:

- 1) Timing not available. Timer resolution: 1 second.

Table 2: Example 4

8 segments, 12 patches, T antenna on a box over perfect ground.

System	Fill (sec)	Factor (sec)	Impedance (Ohms)
PC AT	31.03	13.8	Note 1
AT/370	17.0	2.1	0.12154E+03 j0.26261E+03
RT PC	15.0	3.0	0.12154E+03 j0.26263E+03
3033AP	0.393	0.033	0.12154E+03 j0.26261E+03
Cray1	n/a	n/a	0.18073E+03 j0.21765E+03

Notes:

- 1) Out of core solution.

Table 3: 160 segment rhombic.

160 segments, 1 plane of symmetry, finite ground.

System	Fill (sec)	Factor (sec)	Impedance (Ohms)
PC AT	1097.	171.	Note 1
AT/370	448.	78.	0.35216E+03 j0.17195E+03
RT PC	513.	92.	0.35206E+03 j0.17297E+03
3033AP	11.3	1.3	0.35216E+03 j0.17195E+03
Cray1	n/a	n/a	0.35206E+03 j0.17206E+03

Notes:

- 1) Out of core solution.

Conclusions

It has been shown that it is feasible to implement and run the NEC3 code on three small to medium size systems in the workstation category of computers. Of the three systems examined, the IBM RT PC makes the strongest showing by far.

Comparing run times, the RT PC and the PC AT/370 are virtually equal. Indeed, in terms of the size of problems solvable, because of their similar virtual memory architectures, they are comparable. However, in the author's opinion, the RT PC is a stronger contender in a number of ways.

First, IBM has shown a commitment to support the RT PC in both service and software and it is expected to be a mainstream product in the engineering workstation area. This is an enthusiasm which has not been shown for the AT/370.

Second, the UNIX operating system has support outside the IBM community and a large number of software applications may be easily "ported" to it.

Third, host connectivity is not mandatory for the RT PC. This is a strong point against the AT/370, for unless it is run in an IBM 370 network environment, it is next to useless as all of the important software, such as VS/FORTRAN, must be downloaded to the AT/370.

Fourth, AIX is a multitasking operating system, which VM/PC is not. Therefore, an application may be started, either in the foreground or in background mode, and then the user may proceed in another context to perform other work, even to the extent of another NEC run.

Finally, since the architecture of the RT PC, with the exception of the proprietary RISC processor chip itself, is an open one and already one sees the beginnings of a vigorous second source market in support of the system with software and hardware options.

All of this is not to say that NEC3 on a PC AT is a dead issue. It could be feasible to run the program on the AT if the software problem of out of core matrix manipulation is solved. However, the system is slow and since the DOS operating system does not yet support multitasking in any effective manner, one must be willing to commit the processor to a single task for long periods of time for large problems.

Acknowledgements.

The author wishes to thank Professor Richard Adler of NPS and Mr Gerald J Burke of Lawrence Livermore National Laboratories for their advice and consultation in the conversion process, Ms Mary Ann DeVecchio and Mr Dennis Campbell of IBM Monterey and Mr Javed S Kahn of IBM San Jose for their kind assistance in providing an IBM RT PC for the benchmark studies, and Mr Gary F Aberle of IBM Information Systems for his assistance in porting NEC3 to the RT PC. Also, the author wishes to express his appreciation to Professor Douglas G Williams, Director of the Naval Postgraduate School Computer Center for his support in this effort.

Bibliography

- (1) G.J. Burke and A.J. Poggio, *Numerical Electromagnetic Code (NEC) -- Method of Moments NOSC TD-116, January 1981.*
- (2) F. Waters, ed., *IBM RT Personal Computer Technology* IBM Corporation, Form No. SA23-1057, 1986.
- (3) International Business Machines Corporation *IBM Virtual Machine/Personal Computer User's Guide* Order No. 6137739, December 1965.

- (4) Ryan-McFarland Corporation, *Ref-*
erence: IBM Personal Computer Profes-
sional FORTRAN Order No. 6138815,
November 1984

A COMPUTATIONAL MODEL FOR ELECTROMAGNETIC INTERACTIONS WITH ADVANCED COMPOSITES

Harold A. Sabbagh
Thomas M. Roberts*
L. David Sabbagh

Sabbagh Associates, Inc.
2634 Round Hill Lane
Bloomington, IN 47401

Composite materials in the form of fiber-reinforced matrix materials as, for example, graphite epoxy, are being increasingly used in critical structures and structural components because of their high strength-to-weight ratio. In order to assess the integrity of these structures, it is necessary to employ suitable methods for quantitative nondestructive evaluation (NDE). One such method is to use electromagnetics (eddy-currents), but the problem is that composite materials are inherently anisotropic, which means that much of the classical eddy-current technology and design procedures are not applicable. In this paper we apply a rigorous model of electromagnetic interactions with graphite-epoxy composites, which is based on a continuum approach. In this approach the graphite fibers produce a macroscopic conductivity tensor that has different conductivities along and transverse to the fiber direction.

A method for computing electromagnetic fields within anisotropic media, which is based on a matrix form of Maxwell's equations in Fourier transform space, is then described. By using this approach we compute the tensor Green's function for a plane-parallel slab of graphite-epoxy. With the Green's tensor we can compute the fields interior to the slab, produced by such excitation sources as current-dipoles, current-loops and current-sheets, efficiently by using the Fast Fourier Transform algorithm. We show specific results, in the form of three-dimensional plots, for several such sources.

*Permanent address: Department of Physics, Indiana University, Bloomington, IN 47405.

Supported by Naval Surface Weapons Center (White Oak Labs) under Contract No. N60921-85-C-0046 with Sabbagh Associates.

CHAPTER 1

IDENTIFICATION AND SIGNIFICANCE OF THE PROBLEM

The present research problem is to develop a model for electromagnetic interactions with advanced composite materials, especially eddy-currents. Composite materials in the form of fiber-reinforced matrix materials as, for example, graphite-epoxy, are being increasingly used in critical structures and structural components because of their high strength-to-weight ratio. In order to assess the integrity of these structures, it is necessary to employ suitable methods for quantitative NDE. One method uses eddy-currents; composite materials, however, are inherently anisotropic, which means that many of the classical eddy-current technology and design procedures are not applicable. In addition, composite materials vary widely in their permittivities and conductivities, which means that new analyses must be carried out to develop effective strategies for using eddy-currents in quantitative NDE. A final problem is that there is a variety of potential failure modes in composites, such as delaminations, fiber-breakage due to impact damage, flaws, etc., some of which may not be readily detectable by eddy-currents [1]. In order to complement the empirical studies of [1] it is necessary to embark upon a rigorous quantitative NDE program for composites to assess the role that eddy-currents play in it. Our purpose in this paper is to develop a model describing the interaction of induced eddy-currents and the conducting graphite fibers in graphite epoxy.

This objective can be met by accomplishing the following:

1. Apply rigorous electromagnetic theory to determine a Green's function for a stratified half-space, or a finite slab, of anisotropic composite materials.
2. Write a computer program to execute the model.

Electromagnetic theory and the Green's function are dealt with in Chapters 2-4, and in Appendices A, B and C.

CHAPTER 2

AN ELECTROMAGNETIC MODEL FOR GRAPHITE-EPOXY

BACKGROUND

Eddy-current methods for the examination of carbon fiber reinforced epoxy resins and other composite materials have been discussed and analyzed by Owston and Prakash [2]-[5]. These analyses have been based on an *ad hoc* equivalent circuit in which the composite test piece is regarded as being inductively coupled to the probe, much as in the classical treatment of eddy-current evaluation of metals. Though the technique gives a useful indication of the form of the results, a more satisfactory approach, as Owston [4] points out, is to use a field-theoretic analysis which is capable of giving exact results for a given model. A field-theoretic analysis is also desirable when computing electromagnetic interactions for shielding effectiveness of advanced composites in aircraft [6].

The heart of the problem is to determine a Green's function for the composite material. (The Green's function is the electromagnetic field produced by a point-source of current.) Much work has been done in recent years on the subject of electromagnetic interactions with composite materials, mostly in the context of electromagnetic shielding of avionics equipment from electromagnetic pulses [6]-[10]. Some of this work is directly applicable to the problem of computing eddy-current flow within composites, but the Green's function problem must be attacked by applying rigorous electromagnetic theory to anisotropic media.

CONSTITUTIVE RELATIONS FOR ADVANCED COMPOSITES

Advanced composite materials are laminates made up of a number of individual layers bonded together. Each layer consists of a unidirectional array of long fibers embedded in, and firmly bonded to, a matrix. The basic building blocks of any specific composite are defined by the types of fibers and matrix involved. Some fiber-matrix systems are: boron-epoxy, graphite-epoxy, Kevlar-epoxy, graphite-polymide and graphite-thermoplastic [7].

The matrix for each of these materials is normally a good dielectric, whereas the fibers vary in electrical conductivity from modest (graphite) to a poor dielectric (boron) to a good dielectric (Kevlar). These materials are nonmagnetic, so that the magnetic permeability is μ_0 .*

Composites have anisotropic conductivities because of the unidirectional arrays of fibers within. For example, for graphite-epoxy the average macroscopic conductivity along the fiber direction is 20,000 mhos/m, whereas in the direction transverse to the fibers, the conductivity is 100 mhos/m. It may be surprising to find a nonzero transverse conductivity

* These, and other facts about electromagnetic constitutive relations, are taken from [7], which is the most complete reference on electromagnetic modeling of composite materials that we have found.

in graphite-epoxy, in view of the earlier statement that the matrix is a good dielectric. The fact is that there is enough local fiber-to-fiber contact that the average macroscopic conductivity is not zero. (See Figure 1(a).) Other materials, of course, have different longitudinal and transverse conductivities, as shown in Table 1 [7]:

TABLE 1. SUMMARY OF ELECTRICAL PROPERTIES OF SOME COMPOSITES

	<u>Graphite-Epoxy</u>	<u>Boron-Epoxy</u>	<u>Kevlar</u>
Permeability μ_R	1	1	1
Permittivity ϵ_R	indeterminate	5.6	3.6
DC Conductivity (mhos/m)			
longitudinal σ_L	2×10^4	30	6×10^{-9}
transverse σ_T	100	2×10^{-8}	6×10^{-9}
Anisotropy Ratio (σ_L/σ_T)	200	1.5×10^9	1

The reason that ϵ_R for graphite-epoxy is indeterminate is because the fiber-to-fiber contact effectively shunts the capacitance between fibers with a fairly low resistance path, making it impossible to measure dielectric permittivities at frequencies less than 100 megahertz, or so. Thus, in Figure 1(b), which shows a possible ac equivalent circuit for eddy-current flow, the capacitors are effectively shorted by the fiber-to-fiber resistors at the lower frequencies.

The anisotropy of the composite manifests itself in a complex permittivity tensor, the tensor being diagonal in a coordinate system (ξ_1, ξ_2, ξ_3), where ξ_1 is parallel to the average fiber direction, ξ_2 is perpendicular to the average fiber direction, but lies in the plane of the composite layer, and ξ_3 is perpendicular to both fibers and the plane of the layer:

$$\bar{\epsilon} = \begin{pmatrix} \hat{\epsilon}_{11} & 0 & 0 \\ 0 & \hat{\epsilon}_{22} & 0 \\ 0 & 0 & \hat{\epsilon}_{33} \end{pmatrix}. \quad (1)$$

Here, $\hat{\epsilon}_{ii} = \epsilon_{ii} - j \frac{\sigma_{ii}}{\omega}$, with $j = \sqrt{-1}$, and ω is the angular frequency. The coordinate system just defined, for which the complex permittivity tensor is diagonal, is not necessarily the laboratory coordinate system, (x, y, z), in which the electromagnetic field vectors are defined. In any case, the tensor symbol will be used, and the components in a particular coordinate system may be computed by applying the usual rules for transforming Cartesian tensors.

From here on we will consider only graphite-epoxy, for which $\epsilon_{11} = \epsilon_{22} = \epsilon_{33} = \epsilon_0$, $\sigma_{11} = 2 \times 10^4$ mhos/m, and $\sigma_{22} = \sigma_{33} = 100$ mhos/m.

MATRIX WAVE EQUATIONS FOR GRAPHITE-EPOXY

Maxwell's equations are the fundamental equations for electromagnetic analysis. Using the constitutive relations just defined for graphite-epoxy, these equations become, in

the sinusoidal steady-state:

$$\begin{aligned}\nabla \times \bar{E} &= -j\omega\mu_0\bar{H} \\ \nabla \times \bar{H} &= j\omega\bar{\epsilon} \cdot \bar{E} + \bar{J}^{(i)}.\end{aligned}\quad (2)$$

Because of the anisotropy of graphite-epoxy, it is convenient to work with a matrix formulation of these equations that has been useful in crystal optics, plasmas and microwave devices [11]-[19]. We start by writing (2) in the 6×6 matrix form

$$\begin{pmatrix} j\omega\bar{\epsilon} & -\nabla \times \bar{I} \\ \nabla \times \bar{I} & j\omega\mu_0\bar{I} \end{pmatrix} \begin{pmatrix} \bar{E} \\ \bar{H} \end{pmatrix} = \begin{pmatrix} -\bar{J}^{(i)} \\ \bar{0} \end{pmatrix}, \quad (3)$$

where the permittivity tensor includes a conductivity term, as in (1), except that the matrix is not necessarily diagonal. \bar{I} is the identity matrix, and $\bar{0}$ is the zero vector.

We write the matrix of partial derivatives as

$$\begin{pmatrix} \bar{0} & -\nabla \times \bar{I} \\ \nabla \times \bar{I} & \bar{0} \end{pmatrix} = \bar{U}_1 \partial/\partial x + \bar{U}_2 \partial/\partial y + \bar{U}_3 \partial/\partial z, \quad (4)$$

where

$$\begin{aligned}\bar{U}_1 &= \begin{pmatrix} \bar{0} & 0 & 0 & 0 \\ 0 & 0 & 0 & 1 \\ 0 & 0 & -1 & \bar{0} \\ 0 & 1 & 0 & \bar{0} \end{pmatrix}, & \bar{U}_2 &= \begin{pmatrix} \bar{0} & 0 & 0 & -1 \\ 0 & 0 & 1 & 0 \\ 0 & 0 & 0 & \bar{0} \\ -1 & 0 & 0 & 0 \end{pmatrix}, \\ \bar{U}_3 &= \begin{pmatrix} \bar{0} & 0 & 1 & 0 \\ 0 & -1 & 0 & 0 \\ 1 & 0 & 0 & \bar{0} \\ 0 & 0 & 0 & \bar{0} \end{pmatrix}.\end{aligned}\quad (5)$$

When these matrices are substituted into (3), along with the definitions

$$\bar{e} = \begin{pmatrix} \bar{E} \\ \bar{H} \end{pmatrix}, \quad \bar{j}^{(i)} = \begin{pmatrix} \bar{J}^{(i)} \\ \bar{0} \end{pmatrix}, \quad \bar{K} = \begin{pmatrix} \bar{\epsilon} & \bar{0} \\ \bar{0} & \mu_0\bar{I} \end{pmatrix}, \quad (6)$$

we get

$$\left[j\omega\bar{K} + \bar{U}_1 \partial/\partial x + \bar{U}_2 \partial/\partial y + \bar{U}_3 \partial/\partial z \right] \bar{e} = -\bar{j}^{(i)}. \quad (7)$$

Upon defining the two-dimensional Fourier transforms in (x,y) by

$$\tilde{e}(k_x, k_y, z) = \frac{1}{4\pi^2} \iint_{-\infty}^{\infty} \bar{e}(x, y, z) e^{j(k_x x + k_y y)} dx dy \quad (8)(a)$$

$$\bar{e}(x, y, z) = \iint_{-\infty}^{\infty} \tilde{e}(k_x, k_y, z) e^{-j(k_x x + k_y y)} dk_x dk_y, \quad (8)(b)$$

we take the Fourier transform of (7):

$$\left[j\omega \bar{K} - jk_x \bar{U}_1 - jk_y \bar{U}_2 + \bar{U}_3 d/dz \right] \tilde{e} = -\tilde{j}^{(i)}. \quad (9)$$

To get this result we assume that the composite material is homogeneous in the (x,y) plane, so that \bar{K} is independent of (x,y).

The third and sixth rows of (9) are independent of z-derivatives. Thus, we can use these two equations to solve for \tilde{e}_3 and \tilde{e}_6 in terms of the remaining variables:

$$\tilde{e}_3 = -\frac{K_{31}}{K_{33}} \tilde{e}_1 - \frac{K_{32}}{K_{33}} \tilde{e}_2 + \frac{k_y}{\omega K_{33}} \tilde{e}_4 - \frac{k_x}{\omega K_{33}} \tilde{e}_5 - \frac{\tilde{j}_3^{(i)}}{j\omega K_{33}} \quad (10)(a)$$

$$\tilde{e}_6 = -\frac{k_y}{\omega\mu_0} \tilde{e}_1 + \frac{k_x}{\omega\mu_0} \tilde{e}_2 \quad (10)(b)$$

When we use these two equations to eliminate the z-components from the remaining equations in (9) we end up with system of four first-order differential equations in the four transverse electromagnetic field components. This system is written as the 4×4 vector-matrix equation:

$$\frac{d\tilde{e}_t}{dz} = \bar{S} \tilde{e}_t + \bar{U} \tilde{j}^{(i)}, \quad (11)$$

where

$$\tilde{e}_t = [\tilde{e}_1, \tilde{e}_2, \tilde{e}_4, \tilde{e}_5] = [\tilde{E}_x, \tilde{E}_y, \tilde{H}_x, \tilde{H}_y]; \quad (12)$$

the subscript, 't', denotes transverse field variables.

The components of \bar{S} and \bar{U} are:

$$\begin{aligned} S_{11} &= \frac{jk_x K_{31}}{K_{33}}, & S_{12} &= \frac{jk_x K_{32}}{K_{33}}, & S_{13} &= \frac{-jk_x k_y}{\omega K_{33}}, & S_{14} &= -j\omega\mu_0 + j\frac{k_x^2}{\omega K_{33}} \\ S_{21} &= \frac{jk_y K_{31}}{K_{33}}, & S_{22} &= \frac{jk_y K_{32}}{K_{33}}, & S_{23} &= j\omega\mu_0 - j\frac{k_y^2}{\omega K_{33}}, & S_{24} &= j\frac{k_x k_y}{\omega K_{33}} \\ S_{31} &= j\omega K_{21} - j\omega \frac{K_{23} K_{31}}{K_{33}} + j\frac{k_x k_y}{\omega\mu_0}, & S_{32} &= j\omega K_{22} - j\omega \frac{K_{23} K_{32}}{K_{33}} - j\frac{k_x^2}{\omega\mu_0} \\ S_{33} &= \frac{jk_y K_{23}}{K_{33}}, & S_{34} &= \frac{-jk_x K_{23}}{K_{33}}, & S_{41} &= -j\omega K_{11} + j\omega \frac{K_{13} K_{31}}{K_{33}} + j\frac{k_y^2}{\omega\mu_0} \\ S_{42} &= -j\omega K_{12} + j\omega \frac{K_{13} K_{32}}{K_{33}} - j\frac{k_x k_y}{\omega\mu_0}, & S_{43} &= \frac{-jk_y K_{13}}{K_{33}}, & S_{44} &= \frac{jk_x K_{13}}{K_{33}} \end{aligned} \quad (13)$$

$$\begin{aligned} U_{11} &= 0, & U_{12} &= 0, & U_{13} &= \frac{k_x}{\omega K_{33}} \\ U_{21} &= 0, & U_{22} &= 0, & U_{23} &= \frac{k_y}{\omega K_{33}} \\ U_{31} &= 0, & U_{32} &= 1, & U_{33} &= -\frac{K_{23}}{K_{33}} \\ U_{41} &= -1, & U_{42} &= 0, & U_{43} &= \frac{K_{13}}{K_{33}}. \end{aligned} \quad (14)$$

CHAPTER 3

DERIVATION OF A GREEN'S FUNCTION FOR A GRAPHITE-EPOXY SLAB

The formal solution of (11) defines the Green's function, $\tilde{\tilde{G}}$:

$$\tilde{e}_i(z) = \int \tilde{\tilde{G}}(z|z') \cdot \tilde{j}^{(i)}(z') dz'. \quad (15)$$

The double bars over G denote a tensor, and the tilde over any variable means a transverse Fourier transform, as before. Clearly, the Green's function is the transverse field at z due to a point current source at z' . Thus, it is a 4×3 tensor, because there are four transverse field components, as shown in (12), and the point current source can be oriented in the x-, y-, or z-direction. Because the current flow in the models studied in this report are confined to the transverse plane, i.e., the (x,y)-plane, we will be interested in only the first two columns of $\tilde{\tilde{G}}$.

The calculation of the Green's function requires a knowledge of the eigenmodes of (11) for a nonstratified medium. These are solutions of the homogeneous form of (11), with $\tilde{\tilde{S}}$ constant with respect to z . The eigenmode theory is developed in Appendix A.

In order to compute $\tilde{\tilde{G}}$ we must know the geometry of the composite material. In this report we will work with the plane-parallel slab that is shown in Figure 2, with the x-axis parallel to the fiber direction, and the y-direction transverse. Thus, the region of interest consists of three parts: the region above the slab (which is free space), the composite slab, and the region below the slab. Call these regions 1, 2, 3, respectively, as shown in Figure 2, and introduce the following notation for the Green's function:

$$\begin{aligned} \tilde{\tilde{G}}_{ij}(z|z') &= \text{Field produced at } z \text{ in region } i, \text{ due to a} \\ &\quad \text{point source of current at } z' \text{ in region } j; \\ &\quad i, j = 1, 2, 3. \end{aligned}$$

As we will see later, the only Green's functions that are needed are $\tilde{\tilde{G}}_{21}$ and $\tilde{\tilde{G}}_{12}$.

In order to compute $\tilde{\tilde{G}}_{21}$, consider Figure 3(a), in which the point-source of current is located at z' in region 1. We further subdivide the three regions into four regions, called A-D, and expand the vector field solutions in each of these four regions in terms of the eigenvectors of Appendix A:

$$A: \quad a \begin{pmatrix} -\alpha_{10} \\ -\alpha_{20} \\ 0 \\ 1 \end{pmatrix} e^{-\lambda_0(z-z')} + b \begin{pmatrix} 0 \\ -\beta_{10} \\ 1 \\ -\beta_{20} \end{pmatrix} e^{-\lambda_0(z-z')} \quad (16)(a)$$

$$B: \quad c \begin{pmatrix} \alpha_{10} \\ \alpha_{20} \\ 0 \\ 1 \end{pmatrix} e^{\lambda_0(z-z')} + d \begin{pmatrix} -\alpha_{10} \\ -\alpha_{20} \\ 0 \\ 1 \end{pmatrix} e^{-\lambda_0(z-z')} + e \begin{pmatrix} 0 \\ \beta_{10} \\ 1 \\ -\beta_{20} \end{pmatrix} e^{\lambda_0(z-z')} + f \begin{pmatrix} 0 \\ -\beta_{10} \\ 1 \\ -\beta_{20} \end{pmatrix} e^{-\lambda_0(z-z')} \quad (16)(b)$$

$$C: \quad c' \begin{pmatrix} \alpha_1 \\ \alpha_2 \\ 0 \\ 1 \end{pmatrix} e^{\lambda_1 z} + d' \begin{pmatrix} -\alpha_1 \\ -\alpha_2 \\ 0 \\ 1 \end{pmatrix} e^{-\lambda_1 z} + e' \begin{pmatrix} 0 \\ \beta_1 \\ 1 \\ -\beta_2 \end{pmatrix} e^{\lambda_3 z} + f' \begin{pmatrix} 0 \\ -\beta_1 \\ 1 \\ -\beta_2 \end{pmatrix} e^{-\lambda_3 z} \quad (16)(c)$$

$$D: \quad g \begin{pmatrix} \alpha_{10} \\ \alpha_{20} \\ 0 \\ 1 \end{pmatrix} e^{\lambda_0(z+z_0)} + h \begin{pmatrix} 0 \\ \beta_{10} \\ 1 \\ -\beta_{20} \end{pmatrix} e^{\lambda_0(z+z_0)}, \quad (16)(d)$$

where $\alpha_1 = S_{14}/\lambda_1$, $\alpha_2 = S_{24}/\lambda_1$, $\beta_1 = \lambda_3/S_{32}$, and $\beta_2 = S_{31}/S_{32}$. The subscript '0' denotes quantities defined in isotropic free-space.

Equations 16(a) and 16(d) contain only outgoing waves at $\pm\infty$. In order to determine the unknown expansion coefficients a through h , c' through f' , we must satisfy certain boundary conditions. The fields must be continuous at the two boundaries, $z = 0$, and $z = -z_0$, which do not contain current singularities. At $z = -z'$, which does contain a point singularity, there must be a discontinuity. The amount of discontinuity can be inferred from (11), in which the imposed source current has the form:

$$\hat{j}^{(i)} = \hat{j} e^{jk_z x'} e^{jk_y y'} \delta(z - z'), \quad (17)$$

where \hat{j} is the unit vector in the direction of current flow.

Upon integrating (11) an infinitesimal distance across the plane $z = z'$, we get

$$\tilde{e}_t^{(+)} - \tilde{e}_t^{(-)} = \bar{U} \hat{j} e^{jk_z x'} e^{jk_y y'}, \quad (18)$$

where (+) denotes the limit immediately above z' , and (-) denotes the limit immediately below.

In order to find the response to x-directed currents (the first column of the Green's tensor) we let $\hat{j} = \bar{a}_x$. The right-hand side of (18) becomes

$$\begin{pmatrix} 0 \\ 0 \\ 0 \\ -1 \end{pmatrix} e^{jk_z x'} e^{jk_y y'}. \quad (19)$$

Similarly, for a y-directed current, which will produce the second column of the Green's tensor, we let $\hat{j} = \bar{a}_y$, and get

$$\begin{pmatrix} 0 \\ 0 \\ 1 \\ 0 \end{pmatrix} e^{jk_z x'} e^{jk_y y'} \quad (20)$$

for the right-hand side of (18).

Once we obtain the boundary conditions, the solution for the expansion coefficients becomes a straight-forward problem in linear algebra.

The computation of $\tilde{\tilde{G}}_{12}$ proceeds in a similar manner, except that the four subregions are shifted downward, as shown in Figure 3(b). The field expansions are given by:

$$A: \quad a \begin{pmatrix} -\alpha_{10} \\ -\alpha_{20} \\ 0 \\ 1 \end{pmatrix} e^{-\lambda_0 z} + b \begin{pmatrix} 0 \\ -\beta_{10} \\ 1 \\ -\beta_{20} \end{pmatrix} e^{-\lambda_0 z} \quad (21)(a)$$

$$B: \quad c \begin{pmatrix} \alpha_1 \\ \alpha_2 \\ 0 \\ 1 \end{pmatrix} e^{\lambda_1(z+z')} + d \begin{pmatrix} -\alpha_1 \\ -\alpha_2 \\ 0 \\ 1 \end{pmatrix} e^{-\lambda_1(z+z')} + e \begin{pmatrix} 0 \\ \beta_1 \\ 1 \\ -\beta_2 \end{pmatrix} e^{\lambda_3(z+z')} \\ + f \begin{pmatrix} 0 \\ -\beta_1 \\ 1 \\ -\beta_2 \end{pmatrix} e^{-\lambda_3(z+z')} \quad (21)(b)$$

$$C: \quad c' \begin{pmatrix} \alpha_1 \\ \alpha_2 \\ 0 \\ 1 \end{pmatrix} e^{\lambda_1(z+z')} + d' \begin{pmatrix} -\alpha_1 \\ -\alpha_2 \\ 0 \\ 1 \end{pmatrix} e^{-\lambda_1(z+z')} + e' \begin{pmatrix} 0 \\ \beta_1 \\ 1 \\ -\beta_2 \end{pmatrix} e^{\lambda_3(z+z')} \\ + f' \begin{pmatrix} 0 \\ -\beta_1 \\ 1 \\ -\beta_2 \end{pmatrix} e^{-\lambda_3(z+z')} \quad (21)(c)$$

$$D: \quad g \begin{pmatrix} \alpha_{10} \\ \alpha_{20} \\ 0 \\ 1 \end{pmatrix} e^{\lambda_0(z+z_0)} + h \begin{pmatrix} 0 \\ \beta_{10} \\ 1 \\ -\beta_{20} \end{pmatrix} e^{\lambda_0(z+z_0)}, \quad (21)(d)$$

and the current singularity is at z' , which is within the slab.

The boundary conditions, including the discontinuity condition, (18), are the same as before. In particular, the inhomogeneous terms, (19) and (20), corresponding to an x-directed and y-directed current source, respectively, continue to hold.

In Appendix B we sketch the application of the boundary conditions for solving for the expansion coefficients for $\tilde{\tilde{G}}_{12}$. The process for $\tilde{\tilde{G}}_{21}$ is similar. After the coefficients have been determined, we substitute c' through f' into (16)(c) to complete the computation of $\tilde{\tilde{G}}_{21}$; for $\tilde{\tilde{G}}_{12}$ we substitute (a, b) into (21)(a). These steps complete the solution of the Green's tensor.

CHAPTER 4

CALCULATION OF THE ELECTROMAGNETIC FIELD WITHIN A GRAPHITE-EPOXY SLAB

Having computed a Green's function for the graphite-epoxy slab, it is possible to determine the field within the slab due to currents above the slab (by using $\tilde{\tilde{G}}_{21}$), or to determine the field above the slab due to currents within the slab (by using $\tilde{\tilde{G}}_{12}$). The latter operation will be used in the inverse problem. The method of determining the fields, given the currents, is to use (15).

We have considered four different impressed current sources, $\tilde{j}^{(i)}$: an infinite current sheet, a filamentary circular current loop, and two finite circular current sheets with distributed windings, one with a uniform distribution, and the other with a linearly increasing distribution. Each of the current sources is parallel to the surface of the slab. The three circular currents simulate, to a degree, flat 'pancake' coils.

The infinite current sheet plays a significant role in the inversion process, which will be presented in the next two chapters, and will be discussed first.

INFINITE CURRENT SHEET

The problem is illustrated in Figure 4. In the Fourier transform domain, the current sheet is given by

$$\tilde{j}^{(i)}(k_x, k_y, z') = I_0 \delta(k_x) \delta(k_y) \delta(z' - z'') (\bar{a}_x \cos \theta + \bar{a}_y \sin \theta), \quad (22)$$

where I_0 is the surface current density in amperes per meter, and θ is the direction of current flow. The delta function at the origin of (k_x, k_y) space is due to the fact that the current sheet is uniform over the entire (x, y) plane. The principal axes are the x- and y-axes, the x-axis being along the fiber direction, and the y-axis transverse. We will compute the field within the slab when the current is oriented along either of these axes (i.e., $\theta = 0^\circ$ or 90°), and then use a simple tensor transformation to compute the fields when the current sheet is oriented at any other angle.

Because the spectrum of $\tilde{j}^{(i)}$ is concentrated at the origin, we can simply put $k_x = k_y = 0$ in computing the Green's function, $\tilde{\tilde{G}}_{21}$. Of course, the evaluation of the integral in (15) is simplified because of the delta function at z'' . These facts allow us to write down a simple analytic expression for the transverse fields within the slab:

current in x-direction:

$$\begin{pmatrix} \tilde{E}_x \\ \tilde{E}_y \\ \tilde{H}_x \\ \tilde{H}_y \end{pmatrix} = c' \begin{pmatrix} -\eta_{11} \\ 0 \\ 0 \\ 1 \end{pmatrix} e^{\lambda_1 z} + d' \begin{pmatrix} \eta_{11} \\ 0 \\ 0 \\ 1 \end{pmatrix} e^{-\lambda_1 z}; \quad (23)(a)$$

current in y-direction:

$$\begin{pmatrix} \tilde{E}_x \\ \tilde{E}_y \\ \tilde{H}_x \\ \tilde{H}_y \end{pmatrix} = e' \begin{pmatrix} 0 \\ \eta \\ 1 \\ 0 \end{pmatrix} e^{\lambda_3 z} + f' \begin{pmatrix} 0 \\ -\eta \\ 1 \\ 0 \end{pmatrix} e^{-\lambda_3 z}, \quad (23)(b)$$

where

$$\begin{aligned} c' &= g \left(\frac{\eta_{11} + \eta_0}{2\eta_{11}} \right) e^{\lambda_1 z_0}, & d' &= g \left(\frac{\eta_{11} - \eta_0}{2\eta_{11}} \right) e^{-\lambda_1 z_0} \\ g &= \frac{e^{-\lambda_0 z''}}{2\alpha_{11}} I_0 \\ \alpha_{11} &= \frac{(\eta_{11} + \eta_0)^2 e^{\lambda_1 z_0} - (\eta_{11} - \eta_0)^2 e^{-\lambda_1 z_0}}{(\eta_{11} + \eta_0)^2 - (\eta_{11} - \eta_0)^2} \\ e' &= h \left(\frac{\eta + \eta_0}{2\eta} \right) e^{\lambda_3 z_0}, & f' &= h \left(\frac{\eta - \eta_0}{2\eta} \right) e^{-\lambda_3 z_0} \\ h &= \frac{-e^{-\lambda_0 z''}}{2\alpha_{22}} I_0 \\ \alpha_{22} &= \frac{(\eta + \eta_0)^2 e^{\lambda_3 z_0} - (\eta - \eta_0)^2 e^{-\lambda_3 z_0}}{(\eta + \eta_0)^2 - (\eta - \eta_0)^2} \\ \lambda_0 &= j\omega(\mu_0 \epsilon_0)^{1/2}, \lambda_1 = j\omega(\mu_0 K_{11})^{1/2}, \lambda_3 = j\omega(\mu_0 K)^{1/2}, \\ \eta_0 &= (\mu_0 / \epsilon_0)^{1/2}, \eta_{11} = (\mu_0 / K_{11})^{1/2}, \eta = (\mu_0 / K)^{1/2}. \end{aligned} \quad (24)$$

We see from (23) that an x-directed uniform current sheet produces an x-directed electric field and a y-directed magnetic field, whereas a y-directed current sheet produces a y-directed electric field and an x-directed magnetic field. This is what we expect from an isotropic medium; it occurs in an anisotropic medium when the x- and y-directions are principal axes for the medium.

For an "off-axis" orientation of the current sheet, however, the results are much different and must be calculated by using a simple tensor transformation. Let T_{xx} and T_{yy} be the electric fields produced within the slab due to a current sheet above the slab. Then in the principal coordinate system, (x, y) , we have

$$\begin{pmatrix} \tilde{E}_x \\ \tilde{E}_y \end{pmatrix} = \begin{pmatrix} T_{xx} & 0 \\ 0 & T_{yy} \end{pmatrix} \begin{pmatrix} \tilde{j}_x^{(i)} \\ \tilde{j}_y^{(i)} \end{pmatrix}, \quad (25)$$

so that

$$\begin{pmatrix} \tilde{j}_x \\ \tilde{j}_y \end{pmatrix} = \begin{pmatrix} \sigma_{11} T_{xx} & 0 \\ 0 & \sigma T_{yy} \end{pmatrix} \begin{pmatrix} \tilde{j}_x^{(i)} \\ \tilde{j}_y^{(i)} \end{pmatrix}. \quad (26)$$

Let (x', y') be the rotated coordinate system. Then

$$\begin{pmatrix} x' \\ y' \end{pmatrix} = \begin{pmatrix} \cos \theta & \sin \theta \\ -\sin \theta & \cos \theta \end{pmatrix} \begin{pmatrix} x \\ y \end{pmatrix}. \quad (27)$$

Hence, the relationship between the induced current and the exciting current, in the (x', y') coordinate system, is

$$\begin{aligned}
 \begin{pmatrix} \tilde{J}_{x'} \\ \tilde{J}_{y'} \end{pmatrix} &= \begin{pmatrix} \cos \theta & \sin \theta \\ -\sin \theta & \cos \theta \end{pmatrix} \begin{pmatrix} \tilde{J}_x \\ \tilde{J}_y \end{pmatrix} \\
 &= \begin{pmatrix} \cos \theta & \sin \theta \\ -\sin \theta & \cos \theta \end{pmatrix} \begin{pmatrix} \sigma_{11} T_{xx} & 0 \\ 0 & \sigma T_{yy} \end{pmatrix} \begin{pmatrix} \cos \theta & -\sin \theta \\ \sin \theta & \cos \theta \end{pmatrix} \begin{pmatrix} \tilde{j}_x^{(i)} \\ \tilde{j}_y^{(i)} \end{pmatrix} \\
 &= \begin{pmatrix} \sigma_{11} T_{xx} \cos^2 \theta + \sigma T_{yy} \sin^2 \theta & (-\sigma_{11} T_{xx} + \sigma T_{yy}) \sin \theta \cos \theta \\ (-\sigma_{11} T_{xx} + \sigma T_{yy}) \sin \theta \cos \theta & \sigma_{11} T_{xx} \sin^2 \theta + \sigma T_{yy} \cos^2 \theta \end{pmatrix} \begin{pmatrix} \tilde{j}_x^{(i)} \\ \tilde{j}_y^{(i)} \end{pmatrix}.
 \end{aligned} \tag{28}$$

The magnitudes of the currents that are induced at the surface of the slab are plotted in Figure 5(a), for a frequency of 10^6 Hz, and $\sigma_{11} = 2 \times 10^4$, $\sigma = 100$. The slab thickness, z_0 , is 1.27 cm (0.5 inches), and z'' , the height of the current sheet above the slab, is 2.54 mm (0.1 inch). We assume that the current sheet carries current in the x' direction only; the angular variable shown in Figure 5(a) is the angle between the x' and x axes. Now we see that, generally, there is a component of current (the smaller loop) that flows transverse to the direction of the current sheet. The larger curve is the component of current that flows parallel to the exciting current. For an isotropic medium, the smaller loop would vanish, and the larger curve would be an arc of a circle.

These results are in qualitative agreement with those of Prakash and Owston [3], who used a simple theoretical analysis that was based on an equivalent circuit. We can extend the field model that has been developed in this report to include slabs that consist of graphite-epoxy laminates of differing "lay-up order", i.e., in which the laminates have their principal axes differing from one-another. In addition, we can include the effects of non-simple excitation sources, such as the "horse-shoe" eddy-current probe of Prakash and Owston [3]. An advantage of the more extensive field-theoretic analysis is that it more clearly suggests the limits of simpler equivalent circuit models.

CIRCULAR CURRENT DISTRIBUTIONS

The circular currents produce more interesting field distributions than does the infinite current sheet. Expressions for $\tilde{j}^{(i)}(k_x, k_y, z)$ for each of the distributions are derived in Appendix C. We note, now, that the spectrum of each current distribution is no longer concentrated at the origin, so that we must compute $\tilde{\tilde{G}}_{21}$ for all k_x, k_y , as described in Chapter 3. When $\tilde{\tilde{G}}_{21}$ and $\tilde{j}^{(i)}$ are substituted into (15), we obtain the transverse Fourier transform of the transverse field vector at any level, z , within the slab. Then, upon taking the inverse Fourier transform, say by using the Fast Fourier Transform (FFT) algorithm, we get the fields in physical space, at each level, z . We have done this for each of the current distributions, and have found that the results are qualitatively similar in all three cases; hence, we will display results of the filamentary loop, only. The parameters, dimensions and frequency are the same as for the current sheet; the radius of the current loop is 0.5 inch (1.27 cm).

Before going into the anisotropic problem, we illustrate, in Figure 5(b), the fields induced into an isotropic medium (with conductivity 2×10^4 mhos/m) at a depth of 0.05 inch (0.127 cm). The isotropic nature of the response is clearly apparent; if we were to look vertically downward we would see a circular response region. Each pixel is a square, whose side is 0.05 inch. Thus, the response region has a diameter of about 1.0 inch, which is the diameter of the current loop. Therefore, the result agrees with our intuition.

The situation in an anisotropic material is changed dramatically, however. In this case the fibers will 'guide' the field, so that it will die out much less rapidly in the x-direction (along the fibers) than in the y-direction. This is illustrated quite clearly in Figure 5(c), where the complex values of the x- and y-components of the electric field at a depth of 0.05 inch are shown. The response region in this figure is highly elongated in the x-direction, when viewed from directly above. The x-component of the induced electric current field is obtained by multiplying the x-component of the electric field by σ_{11} , which is equal to 2×10^4 mhos/m, and the y-component of the current is given by the product of the y-component of electric field with σ_{22} (100 mhos/m). Therefore, the eddy-currents do not flow in the usual circular paths of an unbounded isotropic medium, as suggested by Figure 5(b), but, rather, flow in highly elongated quasi-elliptical paths. The degree of eccentricity of the paths depends upon the degree of anisotropy, as measured by the ratio, σ_{11}/σ_{22} .

In many applications it is important to know how rapidly the induced field dies out with depth into the slab. In an anisotropic medium there is no unique skin-depth, because the conductivity varies with direction of the electric field. Therefore, the problem must be handled numerically in most cases. We present in Figure 5(d) model calculations of the induced electric field at a depth of 0.4 inches within the slab. The excitation source is the filamentary current loop of before, and the frequency remains 1 MHz. Upon comparing this figure with Figure 5(c), we draw the following conclusions: the field magnitude is reduced by about an order-of-magnitude, the field is much more spread out in the y-direction and is very uniform in the x-direction. These results are consistent with the notion of diffusion in isotropic media; they are an obvious manifestation of the filtering-out of the higher spatial frequencies, k_x , k_y , with depth, and the crowding of the spatial-frequency spectrum toward the origin. In addition, we note that the x-component of the electric field dies out much more rapidly with depth than does the y-component. This is due to the fact that in the principal axis coordinate system the x-component interacts with a much larger conductivity, σ_{11} , than does the y-component (which interacts with σ_{22} .) This supports our statement that there is no unique skin-depth in graphite-epoxy.

Model computations of the type presented in this chapter can be very useful in setting up eddy-current experiments in graphite-epoxy, and interpreting the results.

REFERENCES

- [1] M. L. Phelps, "In-Service Inspection Methods for Graphite-Epoxy Structures on Commercial Transport Aircraft," (NASA-CR-165746), Final Report (Boeing Commercial Airplane Co., Seattle).
- [2] C. N. Owston, "Carbon Fibre Reinforced Polymers and Non-Destructive Testing," British Journal of NDT, Vol. 15, No. 6, January 1973, pp. 2-11.
- [3] R. Prakash and C. N. Owston, "Eddy-current method for the determination of lay-up order in cross-ply crfp laminates," Composites, vol. 7, No. 2, April 1976, pp. 88-92.
- [4] C. N. Owston, "Eddy Current Methods for the Examination of Carbon Fibre Reinforced Epoxy Resins," Materials Evaluation, November 1976, pp. 237-250.
- [5] R. Prakash, "Non-destructive Testing of Composites," Composites, October 1980, pp. 217-224.
- [6] Vincent Volpe, "Conductivity and Electromagnetic Shielding Characteristics of Graphite/Epoxy Laminates," J. Composite Materials, Vol. 14 (July 1980), pp. 189-197.
- [7] J. L. Allen, et al., "Electromagnetic Properties and Effects of Advanced Composite Materials: Measurement and Modeling," RADC-TR-78-156, Phase Report, June 1978 (ADA 058041).
- [8] J. Allen, et al., "A Technology Plan for Electromagnetic Characteristics of Advanced Composites," Rochester Institute of Technology, prepared for Rome Air Development Center, May 1976.
- [9] C. D. Skouby, "Electromagnetic Effects of Advanced Composites," McDonnell Aircraft Company, prepared for Office of Naval Research, January 1975 (ADA 010882).
- [10] W. Graf, J. Hamm, J. E. Nanevich, and D. E. Tremain, "Engineering Effects of Advanced Composite Materials on Avionics," SRI International, prepared for U. S. Army Avionics R & D Command, July 1981 (ADA 104015).
- [11] Dwight W. Berreman, Journal of the Optical Society of America, Vol. 62, Number 4, April 1972, pp. 502-510.
- [12] C. Altman and A. Schatzberg, Appl. Phys. B28, pp. 327-333 (1982).
- [13] C. Altman and A. Schatzberg, Appl. Phys. B26, pp. 147-153 (1981).
- [14] C. Altman, A. Schatzberg, and K. Suchy, IEEE Trans. Ant. Prop., vol. AP-32, No. 11, November 1984.
- [15] A. Schatzberg and C. Altman, J. Plasma Physics (1981), Vol. 26, Part 2, pp. 333-344.
- [16] Kurt Suchy and Colman Altman, J. Plasma Physics (1975), Vol. 13, Part 3, pp. 437-449.

- [17] C. M. Krowne, IEEE Antennas Propagation Symp. Dig., Boston, NE, June 25-29, 1984, pp. 569-572.
- [18] C. M. Krowne, IEEE Trans. Microwave theory Tech., Vol. MTT-32, No. 12, December 1984, pp. 1617-1625.
- [19] C. M. Krowne, IEEE Trans. Ant. Prop. Vol. AP-32, No. 11, November 1984, pp. 1224-1230.

APPENDIX A

EIGENMODE ANALYSIS OF ANISOTROPIC MEDIA

Start with the homogeneous form of (11), i.e., with $\tilde{j}^{(i)} = 0$. Since the matrix, $\bar{\bar{S}}$, is constant with respect to z for a nonstratified medium, we look for eigenvector solutions of the form:

$$\tilde{e}_t(z) = \tilde{e}_0 \exp(\lambda z), \quad (A1)$$

where \tilde{e}_0 is a constant vector, and λ is a parameter to be determined. Upon substituting (A1) into (11), we get the eigenvalue problem:

$$\bar{\bar{S}} \tilde{e}_0 = \lambda \tilde{e}_0. \quad (A2)$$

The eigenvalues are the solutions of the secular equation

$$\det[\bar{\bar{S}} - \lambda \bar{\bar{I}}] = 0. \quad (A3)$$

There will be four eigenvalues, and the eigenvector corresponding to each eigenvalue can be computed from the two independent equations arising out of the four simultaneous equations in (A2).

In the principal coordinate system, the generalized permittivity tensor, $\bar{\bar{\epsilon}}$, is diagonal, as in (1). Hence, the only nonzero K_{ij} in (13) are $K_{11} \neq K_{22} = K_{33}$. Upon letting $K_{22} = K_{33} = K$, we get:

$$\begin{aligned} S_{13} &= -j \frac{k_x k_y}{\omega K}, & S_{14} &= -j \omega \mu_0 + j \frac{k_x^2}{\omega K}, & S_{23} &= j \omega \mu_0 - j \frac{k_y^2}{\omega K}, \\ S_{24} &= j \frac{k_x k_y}{\omega K}, & S_{31} &= j \frac{k_x k_y}{\omega \mu_0}, & S_{32} &= j \omega K - j \frac{k_x^2}{\omega \mu_0}, \\ S_{41} &= -j \omega K_{11} + j \frac{k_y^2}{\omega \mu_0}, & S_{42} &= -j \frac{k_x k_y}{\omega \mu_0}. \end{aligned} \quad (A4)$$

When these coefficients are substituted into (A3), and the determinant expanded, we obtain a quartic equation for λ :

$$\lambda^4 - a\lambda^2 + b = 0, \quad (A5)$$

where

$$\begin{aligned} a &= -\omega^2 \mu_0 (K + K_{11}) + 2k_y^2 + k_x^2 (1 + K_{11}/K) \\ b &= \omega^4 \mu_0^2 K K_{11} - \omega^2 \mu_0 (2K_{11} k_x^2 + (K + K_{11}) k_y^2) \\ &\quad + k_x^2 k_y^2 (1 + K_{11}/K) + k_x^4 (K_{11}/K) + k_y^4. \end{aligned} \quad (A6)$$

Hence, the eigenvalues (the roots of (A5)) are:

$$\begin{aligned} \pm \lambda_1 &= \pm j (\omega^2 \mu_0 K_{11} - (K_{11}/K) k_x^2 - k_y^2)^{1/2} \\ \pm \lambda_3 &= \pm j (\omega^2 \mu_0 K - k_x^2 - k_y^2)^{1/2}. \end{aligned} \quad (A7)$$

Note that λ_3 corresponds to an isotropic medium, and that the anisotropy is manifest in λ_1 . Clearly, if $K_{11} = K$, then $\lambda_1 = \lambda_3$, which agrees with the results for an isotropic medium.

Corresponding to each eigenvalue, λ , is an eigenvector that satisfies (A2). We have some liberty in choosing the two independent equations that generate the eigenvectors; hence, there is some arbitrariness in choosing the eigenvectors. We choose the following:

$$\begin{aligned} \bar{v}_1 = \begin{pmatrix} S_{14}/\lambda_1 \\ S_{24}/\lambda_1 \\ 0 \\ 1 \end{pmatrix}, \quad \bar{v}_2 = \begin{pmatrix} -S_{14}/\lambda_1 \\ -S_{24}/\lambda_1 \\ 0 \\ 1 \end{pmatrix}, \quad \bar{v}_3 = \begin{pmatrix} 0 \\ \lambda_3/S_{32} \\ 1 \\ -S_{31}/S_{32} \end{pmatrix}, \quad \bar{v}_4 = \begin{pmatrix} 0 \\ -\lambda_3/S_{32} \\ 1 \\ -S_{31}/S_{32} \end{pmatrix}. \quad (A8) \\ (+\lambda_1) \qquad \qquad (-\lambda_1) \qquad \qquad (+\lambda_3) \qquad \qquad (-\lambda_3) \end{aligned}$$

The second and fourth vectors are the two (+)-going modes, and the first and third are the two (-)-going modes, in the z-direction.

These results are used in computing the Green's function in Chapter 3.

APPENDIX B

COMPUTATION OF COEFFICIENTS FOR $\tilde{\tilde{G}}_{12}$

In this appendix we want to fill in a few of the steps outlined in Section III for $\tilde{\tilde{G}}_{12}$. The computations for $\tilde{\tilde{G}}_{21}$ are similar.

Referring to Figure 3(b), together with (21), we have for the boundary conditions at $z = 0$ and $z = -z_0$:

$$a \begin{pmatrix} -\alpha_{10} \\ -\alpha_{20} \\ 0 \\ 1 \end{pmatrix} + b \begin{pmatrix} 0 \\ -\beta_{10} \\ 1 \\ -\beta_{20} \end{pmatrix} = c \begin{pmatrix} \alpha_1 \\ \alpha_2 \\ 0 \\ 1 \end{pmatrix} e^{\lambda_1 z'} + d \begin{pmatrix} -\alpha_1 \\ -\alpha_2 \\ 0 \\ 1 \end{pmatrix} e^{-\lambda_1 z'} \\ + e \begin{pmatrix} 0 \\ \beta_1 \\ 1 \\ -\beta_2 \end{pmatrix} e^{\lambda_3 z'} + f \begin{pmatrix} 0 \\ -\beta_1 \\ 1 \\ -\beta_2 \end{pmatrix} e^{-\lambda_3 z'}; \quad (B1)(a)$$

$$c' \begin{pmatrix} \alpha_1 \\ \alpha_2 \\ 0 \\ 1 \end{pmatrix} e^{\lambda_1 (z' - z_0)} + d' \begin{pmatrix} -\alpha_1 \\ -\alpha_2 \\ 0 \\ 1 \end{pmatrix} e^{-\lambda_1 (z' - z_0)} \\ + e' \begin{pmatrix} 0 \\ \beta_1 \\ 1 \\ -\beta_2 \end{pmatrix} e^{\lambda_3 (z' - z_0)} + f' \begin{pmatrix} 0 \\ -\beta_1 \\ 1 \\ -\beta_2 \end{pmatrix} e^{-\lambda_3 (z' - z_0)} = g \begin{pmatrix} \alpha_{10} \\ \alpha_{20} \\ 0 \\ 1 \end{pmatrix} + h \begin{pmatrix} 0 \\ \beta_{10} \\ 1 \\ -\beta_{20} \end{pmatrix}. \quad (B1)(b)$$

The boundary condition at $z = z'$ is the discontinuity induced by the point current-source. For an x-directed current the equation is:

$$c \begin{pmatrix} \alpha_1 \\ \alpha_2 \\ 0 \\ 1 \end{pmatrix} + d \begin{pmatrix} -\alpha_1 \\ -\alpha_2 \\ 0 \\ 1 \end{pmatrix} + e \begin{pmatrix} 0 \\ \beta_1 \\ 1 \\ -\beta_2 \end{pmatrix} + f \begin{pmatrix} 0 \\ -\beta_1 \\ 1 \\ -\beta_2 \end{pmatrix} \\ = c' \begin{pmatrix} \alpha_1 \\ \alpha_2 \\ 0 \\ 1 \end{pmatrix} + d' \begin{pmatrix} -\alpha_1 \\ -\alpha_2 \\ 0 \\ 1 \end{pmatrix} + e' \begin{pmatrix} 0 \\ \beta_1 \\ 1 \\ -\beta_2 \end{pmatrix} + f' \begin{pmatrix} 0 \\ -\beta_1 \\ 1 \\ -\beta_2 \end{pmatrix} - \begin{pmatrix} 0 \\ 0 \\ 0 \\ 1 \end{pmatrix}, \quad (B2)(a)$$

and for the y-directed current it is:

$$c \begin{pmatrix} \alpha_1 \\ \alpha_2 \\ 0 \\ 1 \end{pmatrix} + d \begin{pmatrix} -\alpha_1 \\ -\alpha_2 \\ 0 \\ 1 \end{pmatrix} + e \begin{pmatrix} 0 \\ \beta_1 \\ 1 \\ -\beta_2 \end{pmatrix} + f \begin{pmatrix} 0 \\ -\beta_1 \\ 1 \\ -\beta_2 \end{pmatrix}$$

$$= c' \begin{pmatrix} \alpha_1 \\ \alpha_2 \\ 0 \\ 1 \end{pmatrix} + d' \begin{pmatrix} -\alpha_1 \\ -\alpha_2 \\ 0 \\ 1 \end{pmatrix} + e' \begin{pmatrix} 0 \\ \beta_1 \\ 1 \\ -\beta_2 \end{pmatrix} + f' \begin{pmatrix} 0 \\ -\beta_1 \\ 1 \\ -\beta_2 \end{pmatrix} + \begin{pmatrix} 0 \\ 0 \\ 1 \\ 0 \end{pmatrix}. \quad (B2)(b)$$

Because the boundary conditions at $z = 0$ and $z = z'$ are independent of current direction, it is best to work with them first and solve for $(c - f)$ in terms of (a, b) , using (B1)(a), and $(c' - f')$ in terms of (g, h) , using (B1)(b). The results, after some straightforward algebra, are:

$$\begin{aligned} c &= \frac{a(\alpha_1 - \alpha_{10}) + b\alpha_1(\beta_2 - \beta_{20})}{2\alpha_1} e^{-\lambda_1 z'} \\ d &= \frac{a(\alpha_1 + \alpha_{10}) + b\alpha_1(\beta_2 - \beta_{20})}{2\alpha_1} e^{\lambda_1 z'} \\ e &= \frac{a(\frac{\alpha_2\alpha_{10} - \alpha_1\alpha_{20}}{\alpha_1}) + b(\beta_1 - \beta_{10})}{2\beta_1} e^{-\lambda_3 z'} \\ f &= \frac{-a(\frac{\alpha_2\alpha_{10} - \alpha_1\alpha_{20}}{\alpha_1}) + b(\beta_1 + \beta_{10})}{2\beta_1} e^{\lambda_3 z'}, \quad (B3)(a) \\ c' &= \frac{g(\alpha_1 + \alpha_{10}) + h\alpha_1(\beta_2 - \beta_{20})}{2\alpha_1} e^{-\lambda_1(z' - z_0)} \\ d' &= \frac{g(\alpha_1 - \alpha_{10}) + h\alpha_1(\beta_2 - \beta_{20})}{2\alpha_1} e^{\lambda_1(z' - z_0)} \\ e' &= \frac{g(\frac{\alpha_1\alpha_{20} - \alpha_2\alpha_{10}}{\alpha_1}) + h(\beta_1 + \beta_{10})}{2\beta_1} e^{-\lambda_3(z' - z_0)} \\ f' &= \frac{-g(\frac{\alpha_1\alpha_{20} - \alpha_2\alpha_{10}}{\alpha_1}) + h(\beta_1 + \beta_{10})}{2\beta_1} e^{\lambda_3(z' - z_0)}. \quad (B3)(b) \end{aligned}$$

Now we substitute these expressions into the remaining boundary condition at $z = z'$, for either the x- or y-directed current source. For the x-directed source:

$$(c - c') \begin{pmatrix} \alpha_1 \\ \alpha_2 \\ 0 \\ 1 \end{pmatrix} + (d - d') \begin{pmatrix} -\alpha_1 \\ -\alpha_2 \\ 0 \\ 1 \end{pmatrix} + (e - e') \begin{pmatrix} 0 \\ \beta_1 \\ 1 \\ -\beta_2 \end{pmatrix} + (f - f') \begin{pmatrix} 0 \\ -\beta_1 \\ 1 \\ -\beta_2 \end{pmatrix} = \begin{pmatrix} 0 \\ 0 \\ 0 \\ -1 \end{pmatrix}, \quad (B4)(a)$$

and for the y-directed source:

$$(c - c') \begin{pmatrix} \alpha_1 \\ \alpha_2 \\ 0 \\ 1 \end{pmatrix} + (d - d') \begin{pmatrix} -\alpha_1 \\ -\alpha_2 \\ 0 \\ 1 \end{pmatrix} + (e - e') \begin{pmatrix} 0 \\ \beta_1 \\ 1 \\ -\beta_2 \end{pmatrix} + (f - f') \begin{pmatrix} 0 \\ -\beta_1 \\ 1 \\ -\beta_2 \end{pmatrix} = \begin{pmatrix} 0 \\ 0 \\ 1 \\ 0 \end{pmatrix}. \quad (B4)(b)$$

The solutions of these equations are:

x-directed source:

$$(c - c') = -1/2, \quad (d - d') = -1/2, \quad (e - e') = 0, \quad (f - f') = 0; \quad (B5)(a)$$

y-directed source:

$$(c - c') = \beta_2/2, \quad (d - d') = \beta_2/2, \quad (e - e') = 1/2, \quad (f - f') = 1/2. \quad (B5)(b)$$

Upon using (B3), we eliminate $(c - f), (c' - f')$, in favor of (a, b, g, h) :

$$a(\alpha_1 - \alpha_{10}) + b\alpha_1(\beta_2 - \beta_{20}) - g(\alpha_1 + \alpha_{10})e^{\lambda_1 z_0} - h\alpha_1(\beta_2 - \beta_{20})e^{\lambda_1 z_0} = v_1 \quad (B6)(a)$$

$$a(\alpha_1 + \alpha_{10}) + b\alpha_1(\beta_2 - \beta_{20}) - g(\alpha_1 - \alpha_{10})e^{-\lambda_1 z_0} - h\alpha_1(\beta_2 - \beta_{20})e^{-\lambda_1 z_0} = v_2 \quad (B6)(b)$$

$$a\left(\frac{\alpha_2\alpha_{10} - \alpha_1\alpha_{20}}{\alpha_1}\right) + b(\beta_1 - \beta_{10}) - g\left(\frac{\alpha_1\alpha_{20} - \alpha_2\alpha_{10}}{\alpha_1}\right)e^{\lambda_3 z_0} - h(\beta_1 + \beta_{10})e^{\lambda_3 z_0} = v_3 \quad (B6)(c)$$

$$-a\left(\frac{\alpha_2\alpha_{10} - \alpha_1\alpha_{20}}{\alpha_1}\right) + b(\beta_1 + \beta_{10}) + g\left(\frac{\alpha_1\alpha_{20} - \alpha_2\alpha_{10}}{\alpha_1}\right)e^{-\lambda_3 z_0} - h(\beta_1 - \beta_{10})e^{-\lambda_3 z_0} = v_4, \quad (B6)(d)$$

where the vector on the right side is given by

$$\begin{pmatrix} -\alpha_1 e^{\lambda_1 z'} \\ -\alpha_1 e^{-\lambda_1 z'} \\ 0 \\ 0 \end{pmatrix}, \text{ for x-directed source; } \quad (B7)(a)$$

$$\begin{pmatrix} \alpha_1 \beta_2 e^{\lambda_1 z'} \\ \alpha_1 \beta_2 e^{-\lambda_1 z'} \\ \beta_1 e^{\lambda_3 z'} \\ \beta_1 e^{-\lambda_3 z'} \end{pmatrix}, \text{ for y-directed source. } \quad (B7)(b)$$

(B6) and (B7) are the final analytic expressions; (a, b, g, h) are computed numerically, and the results used in the Green's function. Note that we have not used the exponential term, $e^{j(k_x x' + k_y y')}$, that appears in (19) and (20). This is due to the fact that in computing the transverse Fourier transform of the Green's function, as defined in (15), we divide by $\frac{z^{(i)}}{j}$, which is the exponential term.

APPENDIX C

COMPUTATION OF $\tilde{j}^{(i)}$ FOR CIRCULAR CURRENT SHEETS

If the sheet lies in the plane $z = z''$, and has a coil-turns density of $f(r)$, where r is the radial coordinate, then the current density is given by

$$\bar{J}^{(i)}(x, y, z) = I_0 \delta(z - z'') (-\bar{a}_x \sin \theta + \bar{a}_y \cos \theta) f(r), \quad (C1)$$

where I_0 is the total current carried by the coil. Then

$$\tilde{j}^{(i)}(k_x, k_y, z) = \frac{I_0 \delta(z - z'')}{4\pi^2} \iint_{-\infty}^{\infty} (-\bar{a}_x \sin \theta + \bar{a}_y \cos \theta) f(r) e^{j(k_x x + k_y y)} dx dy. \quad (C2)$$

Upon transforming to cylindrical coordinates:

$$\begin{aligned} \tilde{j}^{(i)}(k_x, k_y, z) &= \frac{I_0 \delta(z - z'')}{4\pi^2} \int_0^{2\pi} d\theta \int_0^{\infty} r f(r) (-\bar{a}_x \sin \theta + \bar{a}_y \cos \theta) e^{jr(k_x \cos \theta + k_y \sin \theta)} dr \\ &= \frac{I_0 \delta(z - z'')}{4\pi^2} \int_0^{\infty} f(r) \left[\int_0^{2\pi} r (-\bar{a}_x \sin \theta + \bar{a}_y \cos \theta) e^{jr(k_x \cos \theta + k_y \sin \theta)} d\theta \right] dr \\ &= \frac{-j I_0 \delta(z - z'')}{4\pi^2} \int_0^{\infty} f(r) \left[(-\bar{a}_x \frac{d}{dk_y} + \bar{a}_y \frac{d}{dk_x}) \int_0^{2\pi} e^{jr(k_x \cos \theta + k_y \sin \theta)} d\theta \right] dr. \end{aligned} \quad (C3)$$

The θ -integral can be easily calculated by first transforming into cylindrical coordinates in Fourier-space:

$$\begin{aligned} k_x &= k_r \cos \phi \\ k_y &= k_r \sin \phi \\ k_r &= (k_x^2 + k_y^2)^{1/2}. \end{aligned} \quad (C4)$$

Thus, the integrand becomes $e^{jk_r r \cos(\theta - \phi)}$, which, according to a well-known identity involving Bessel functions, is

$$e^{jk_r r \cos(\theta - \phi)} = J_0(k_r r) + 2 \sum_{k=1}^{\infty} j^k J_k(k_r r) \cos k(\theta - \phi). \quad (C5)$$

Only the first term survives the integral over 2π radians, so that (C3) becomes

$$\begin{aligned} \tilde{j}^{(i)}(k_x, k_y, z) &= \frac{-j I_0 \delta(z - z'')}{2\pi} (-\bar{a}_x \frac{d}{dk_y} + \bar{a}_y \frac{d}{dk_x}) \int_0^{\infty} f(r) J_0(k_r r) dr \\ &= \frac{j I_0 \delta(z - z'')}{2\pi} (-\bar{a}_x \frac{k_y}{k_r} + \bar{a}_y \frac{k_x}{k_r}) \int_0^{\infty} r f(r) J_1(k_r r) dr. \end{aligned} \quad (C6)$$

The final integral is the Bessel transform of the coil-turns density, $f(r)$. This transform can be easily computed for a number of interesting practical coil configurations. For example, if the coil consists of a single filamentary loop of radius r_0 , then $f(r) = \delta(r - r_0)$, so that the Bessel transform is simply $r_0 J_1(k_r r_0)$. Hence,

$$\frac{\tilde{z}^{(i)}}{\tilde{j}} = \frac{j I_0 r_0 \delta(z - z'')}{2\pi} J_1(k_r r_0) \left(-\bar{a}_x \frac{k_y}{k_r} + \bar{a}_y \frac{k_x}{k_r} \right). \quad (C7)$$

For a coil with a uniform distribution of turns, whose density is N_c , and extends to a radius of r_0 , the Bessel transform reduces to $N_c \int_0^{r_0} r J_1(k_r r) dr$, which can only be computed numerically. Therefore, for such a coil

$$\frac{\tilde{z}^{(i)}}{\tilde{j}} = \frac{j N_c I_0 \delta(z - z'')}{2\pi} \left(-\bar{a}_x \frac{k_y}{k_r} + \bar{a}_y \frac{k_x}{k_r} \right) \int_0^{r_0} r J_1(k_r r) dr. \quad (C8)$$

Finally, for a coil of radius r_0 , whose density of turns linearly increases, i.e., for which $f(r) = N_c r$, the Bessel transform can be explicitly computed, with the result that

$$\frac{\tilde{z}^{(i)}}{\tilde{j}} = \frac{j N_c r_0^3 I_0 \delta(z - z'')}{2\pi} \left(-\bar{a}_x \frac{k_y}{k_r} + \bar{a}_y \frac{k_x}{k_r} \right) \left(\frac{J_2(k_r r_0)}{k_r r_0} \right). \quad (C9)$$

CAPTIONS FOR FIGURES

Figure 1.

- (a) Showing how fiber-to-fiber contact allows transverse conduction (after [4]).
- (b) A possible ac equivalent circuit for eddy-current flow (after [4]).

Figure 2. A plane-parallel slab and regions defined for computation of the Green's function.

Figure 3.

- (a) A vector point-source of current at (x', y', z') in region 1; for computation of $\tilde{\tilde{G}}_{21}$.
- (b) A vector point-source of current at (x', y', z') in region 2; for computation of $\tilde{\tilde{G}}_{12}$.

Figure 4. An infinite current sheet parallel to, and above, the anisotropic slab.

Figure 5.

- (a) Vector current induced within anisotropic slab, as a function of orientation of current with respect to fibers. The large curve is the magnitude of the current component parallel to the sheet, and the small curve is the magnitude of the current component transverse to the sheet. Frequency = 10^6 Hz; $\sigma_{11} = 2 \times 10^4$, $\sigma = 100$.
- (b) Electric field induced into an isotropic medium, by a circular filamentary current loop, at a depth of 0.05 in. Frequency = 10^6 Hz; $\sigma_{11} = \sigma = 2 \times 10^4$. RE and IM denote real and imaginary parts, respectively; X and Y denote x and y components.
- (c) Electric field induced into an anisotropic medium, by a circular filamentary current loop, at a depth of 0.05 in. Frequency = 10^6 Hz; $\sigma_{11} = 2 \times 10^4$, $\sigma = 100$. Same nomenclature as Figure 5(b).
- (d) Same as Figure 5(c) except that the depth is 0.4 in.

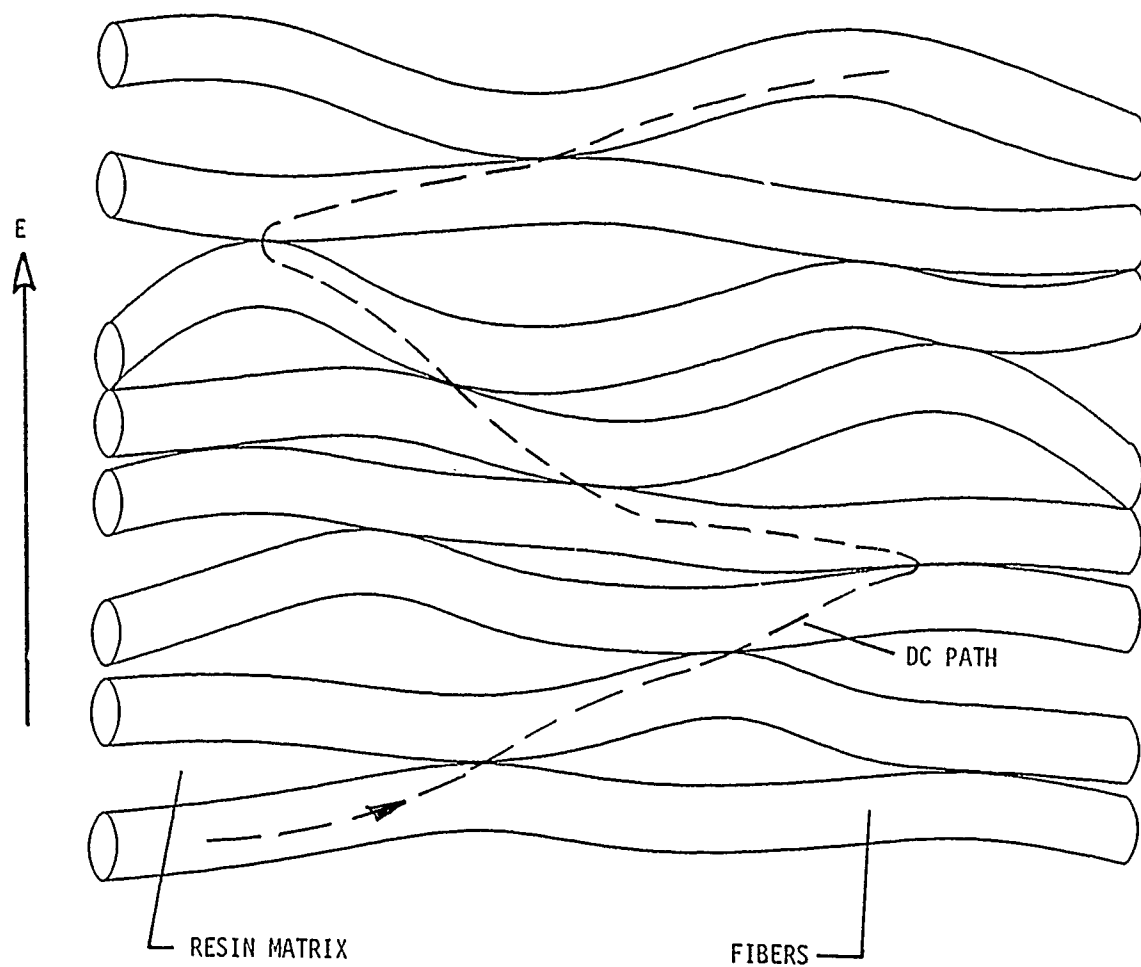


Figure 1. (a)

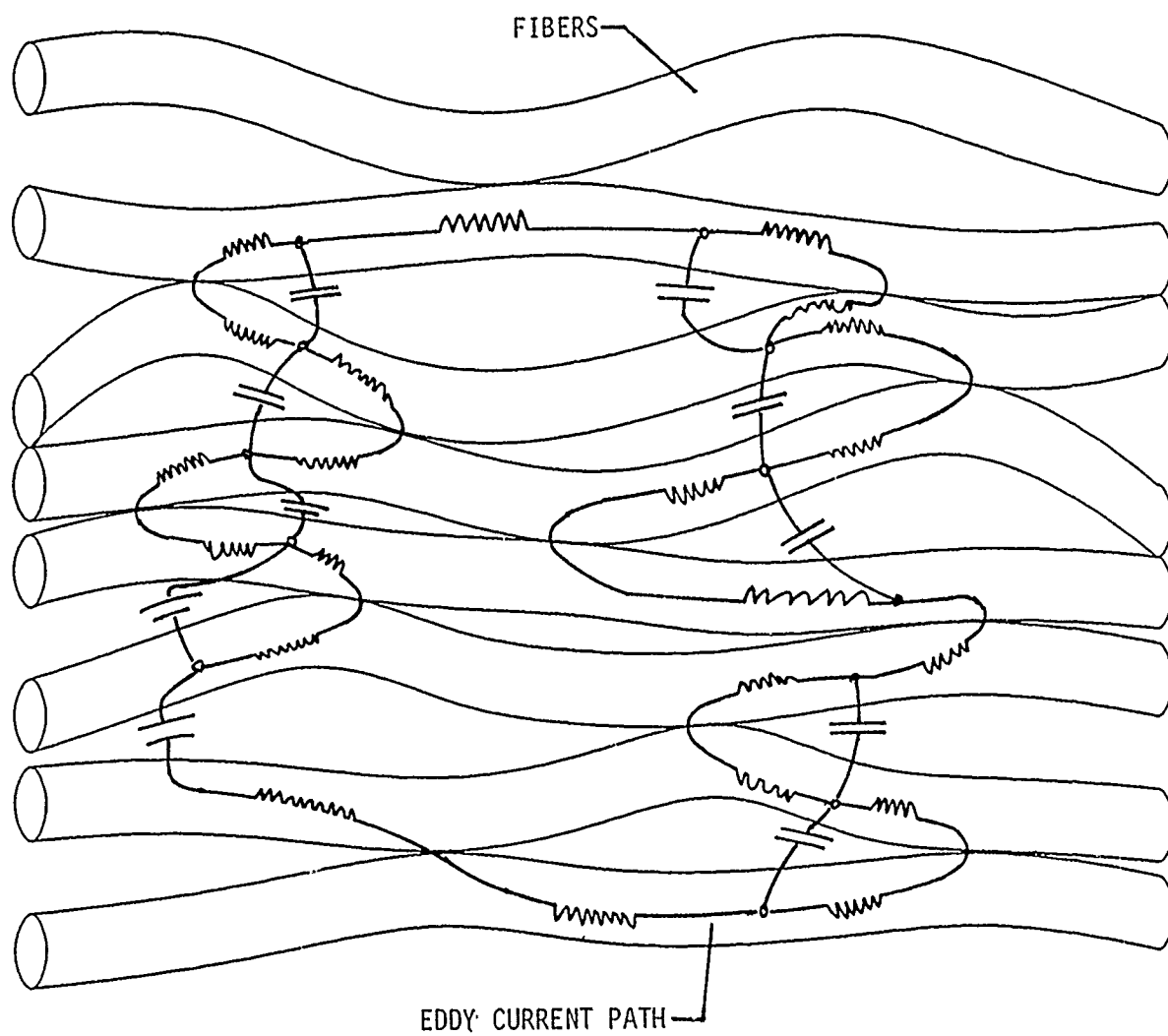


Figure 1. (b)

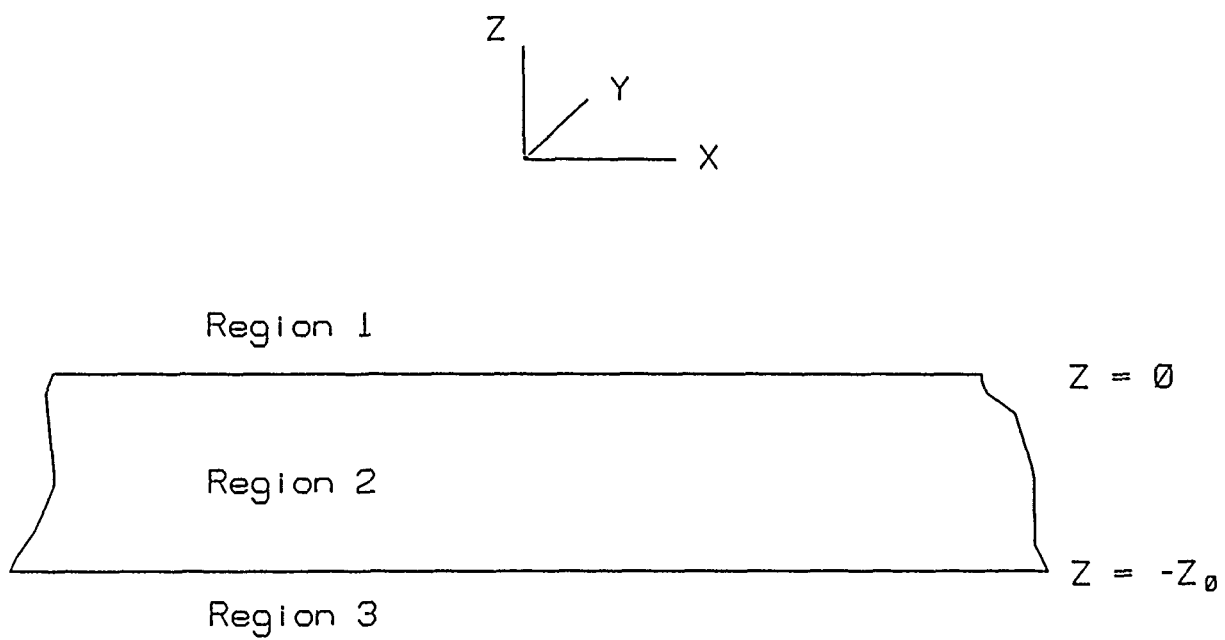


Figure 2.

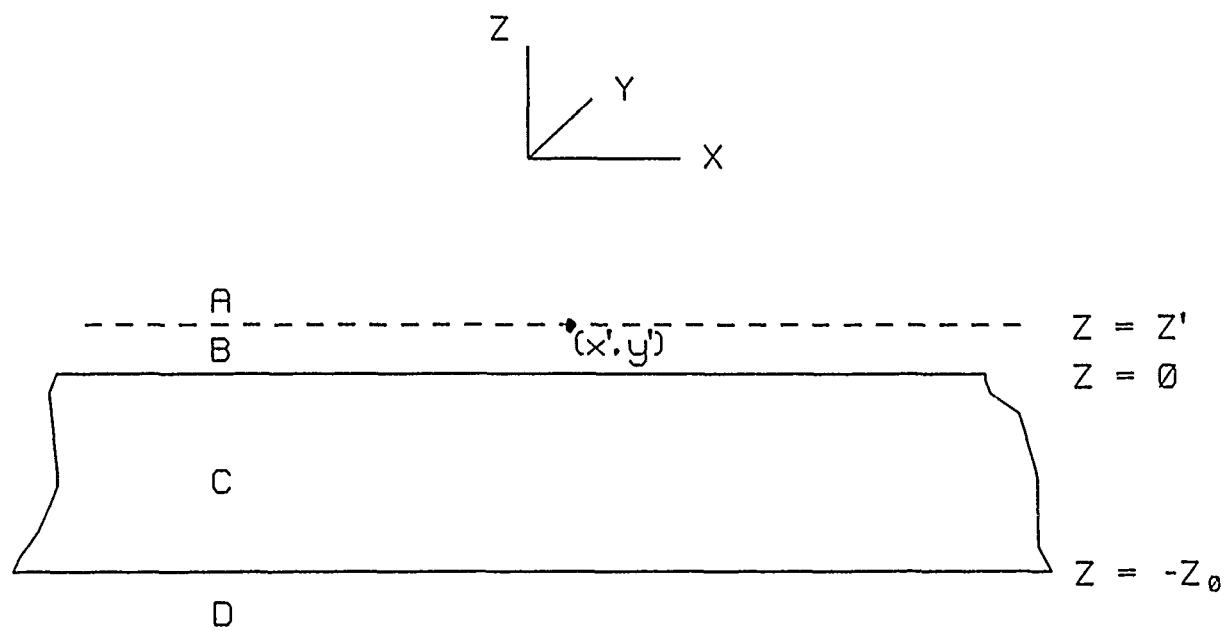


Figure 3. (a)

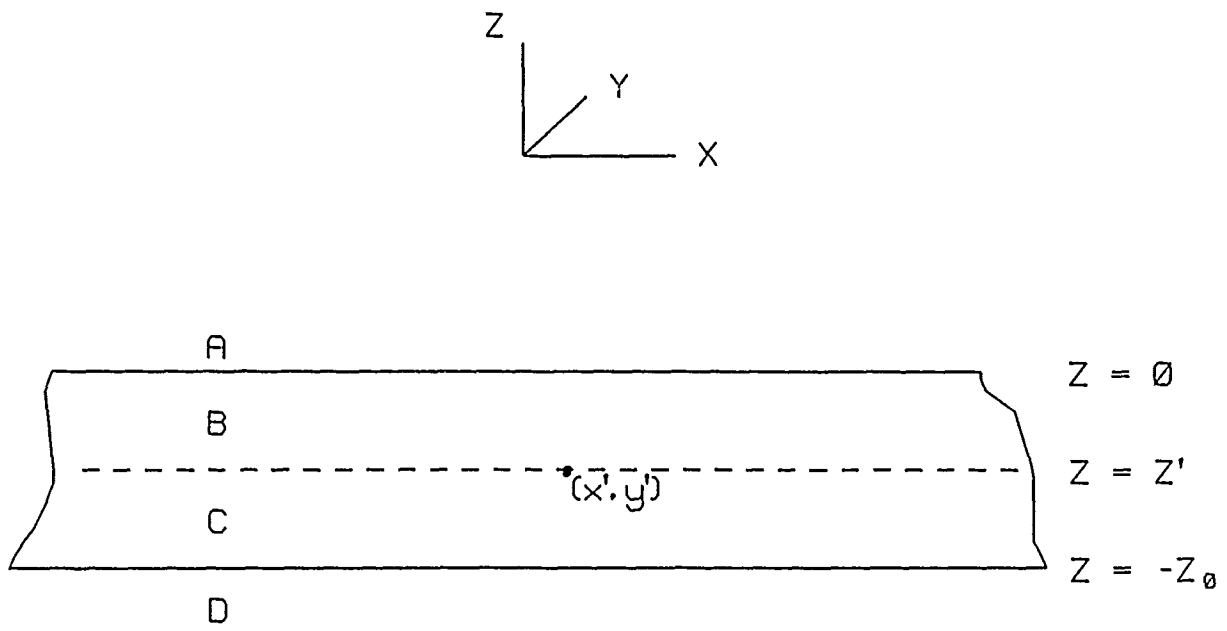


Figure 3. (b)

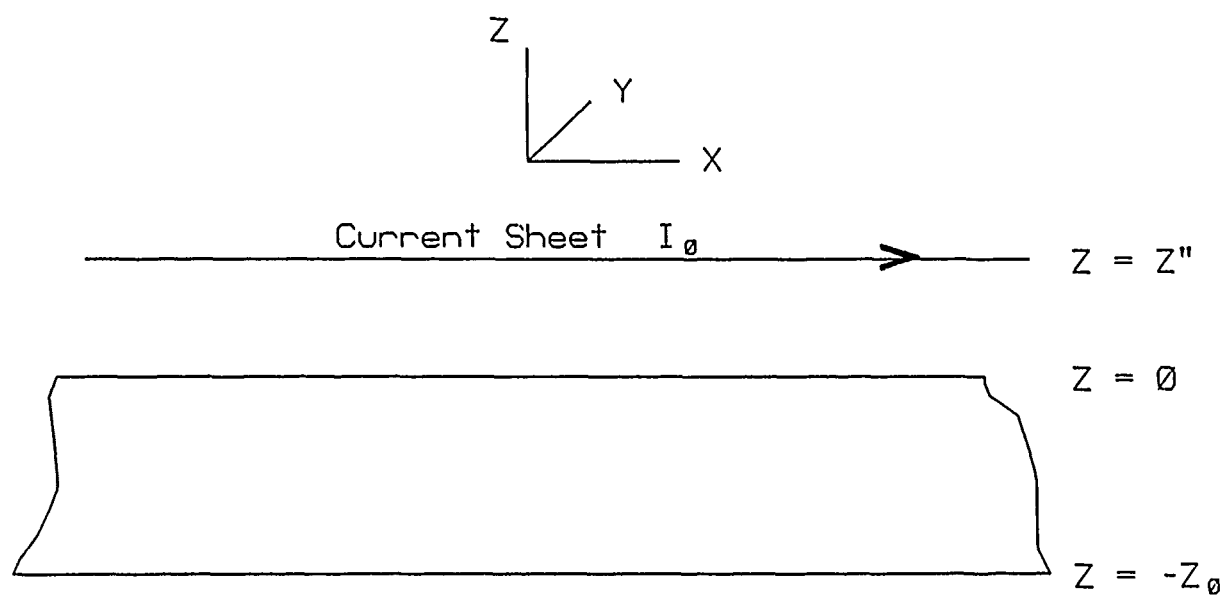


Figure 4.

46 4410

K&E POLAR CO-ORDINATE
KEUFFEL & ESSER CO. MADE IN U.S.A.

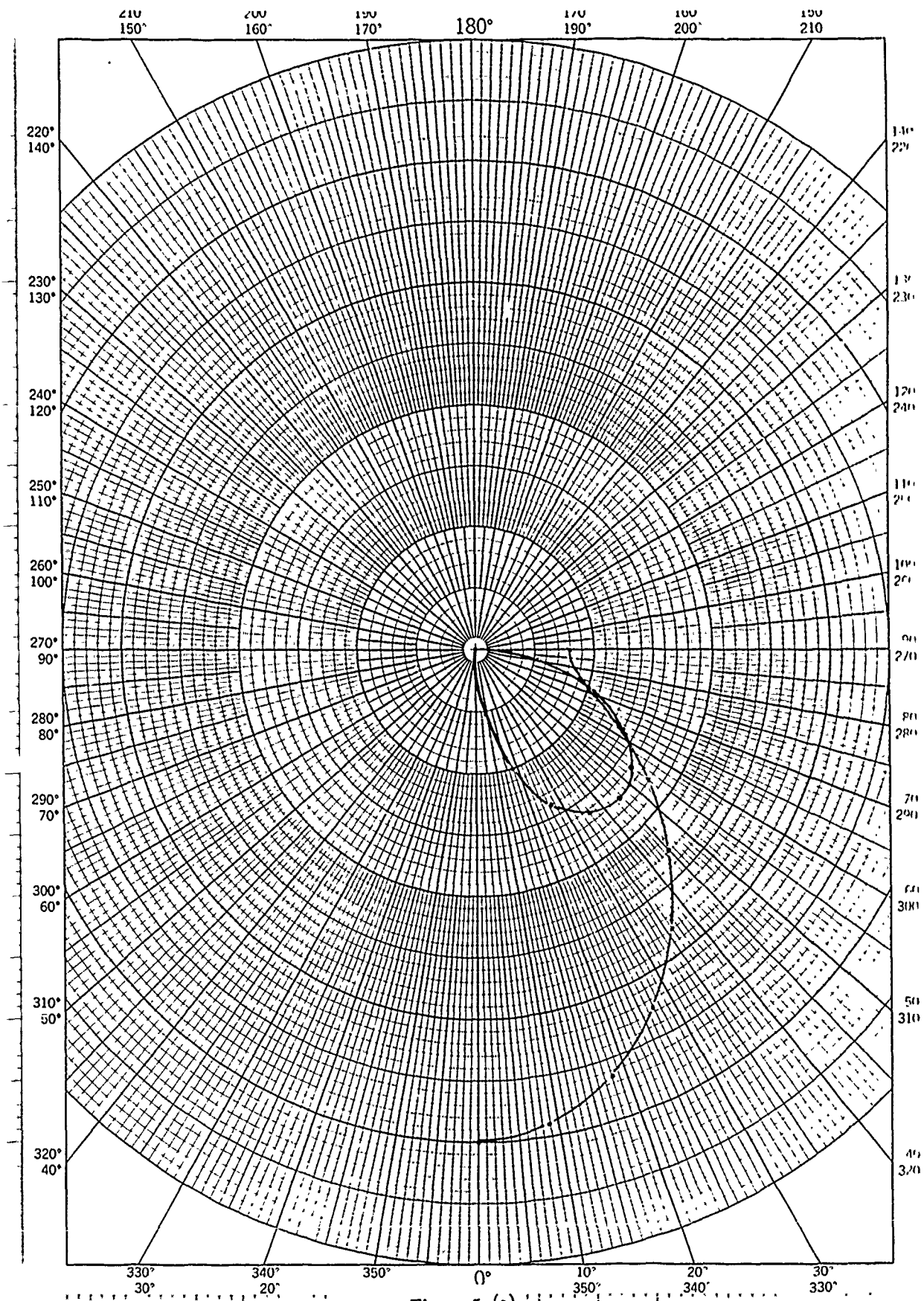
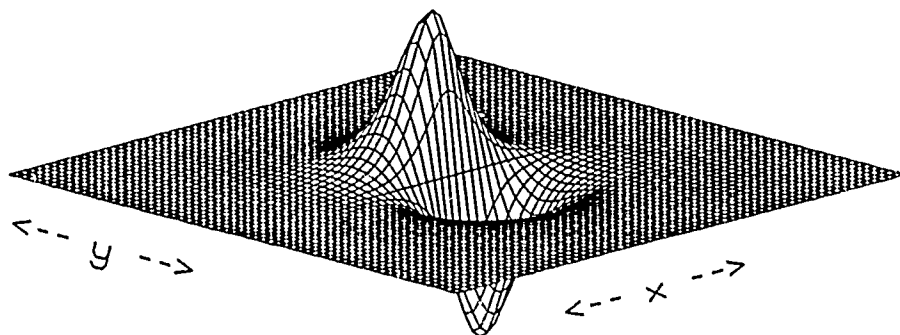


Figure 5. (a)



$0.61973E-01$
 $x=15.000$
 $y=15.000$

$e_{min} = -0.61973E-01$

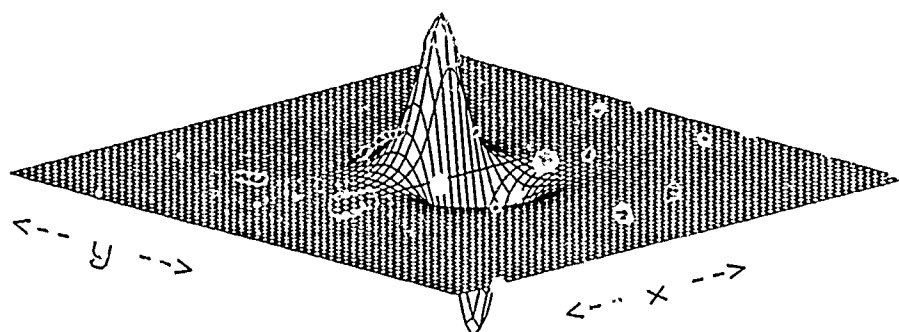
$e_{max} = 0.61973E-01$

TUE, JUL 16 1985

09:45:30

REFLD1X

Figure 5. (b)
real



0.14119E+00

x=15.000

y=15.000

emin = -0.14119E+00

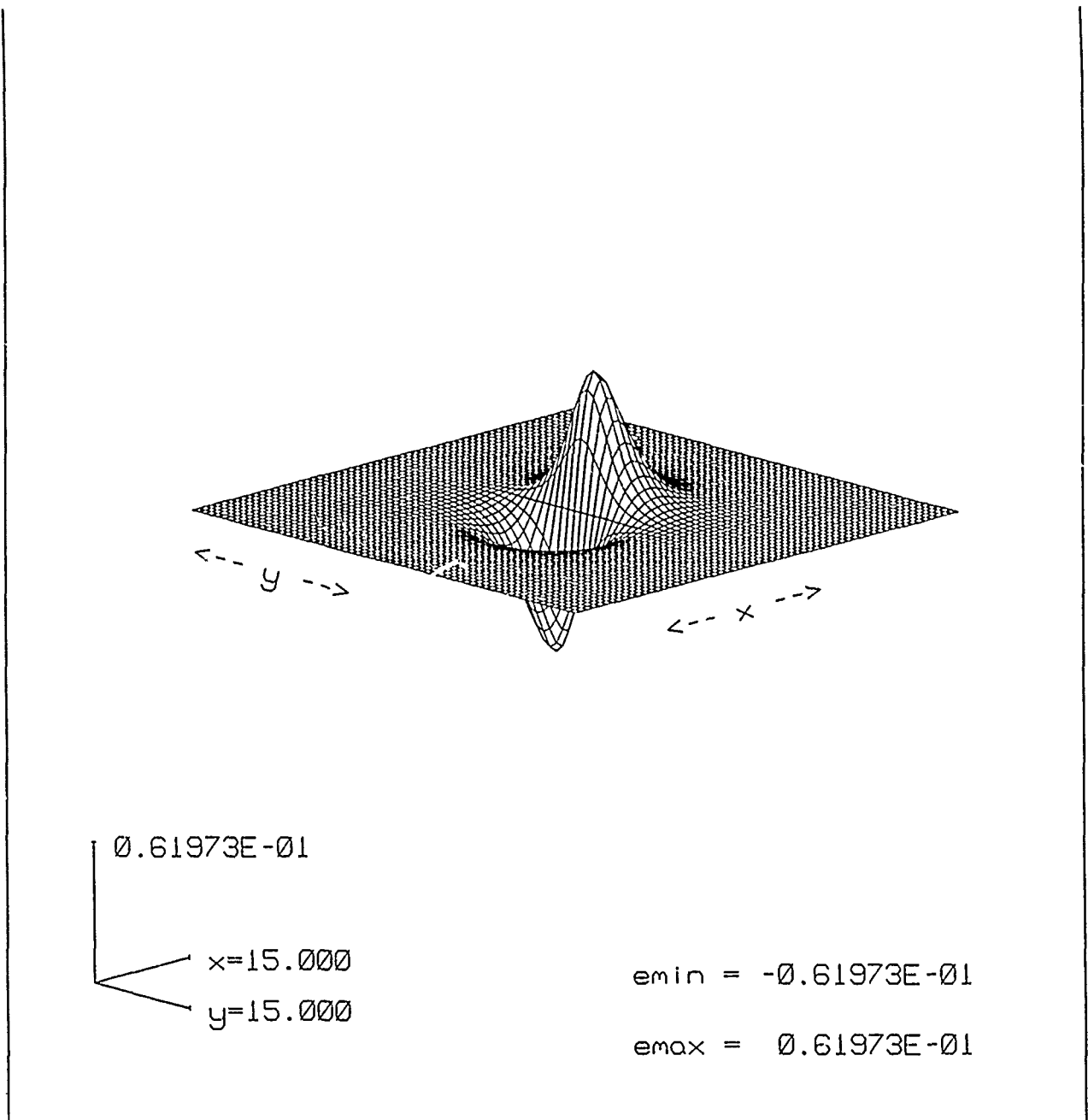
emax = 0.14119E+00

TUE, JUL 16 1985

09:48:34

IMFLD1X

Figure 5. (b)
imaginary

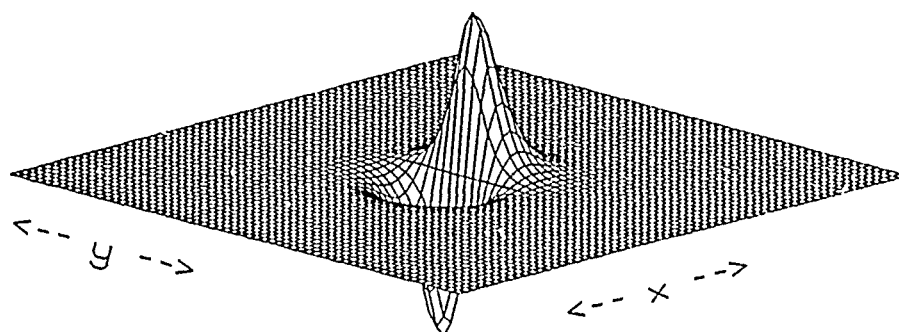


TUE, JUL 16 1985

09:59:38

CREATED BY PROGRAM EFLDPLT
REFLDIY

Figure 5. (b)
real



$0.14119E+00$
 $x=15.000$
 $y=15.000$

$emin = -0.14119E+00$

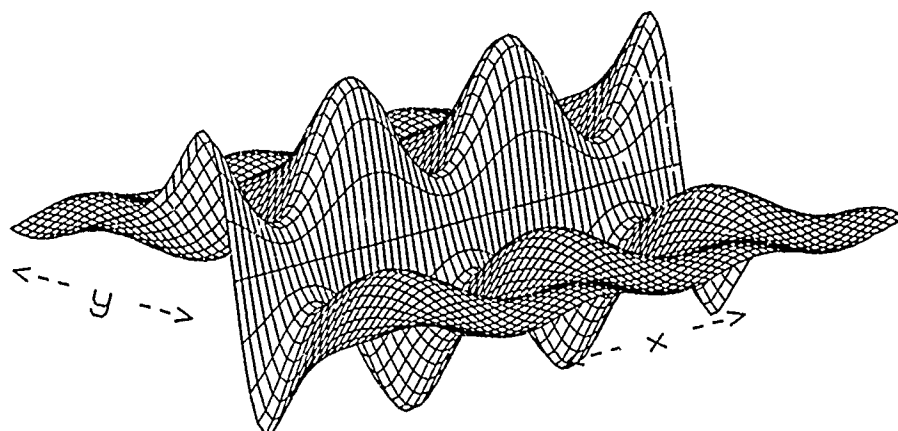
$emax = 0.14119E+00$

TUE, JUL 16 1985

09:55:40

IMFLD1Y

Figure 5. (b)
imaginary



$0.15169E-01$
 $x=15.000$
 $y=15.000$

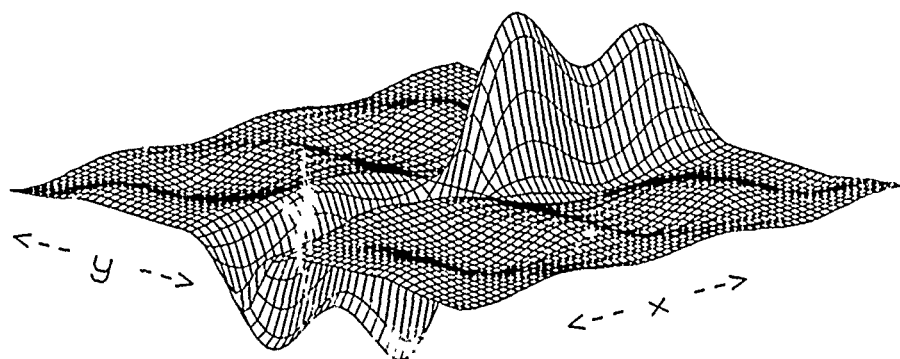
$emin = -0.15169E-01$
 $emax = 0.15169E-01$

MON, JUL 15 1985

21:37:57

REFLD1X

Figure 5. (c)
real



0.17900E-01

x=15.000

y=15.000

emin = -0.17900E-01

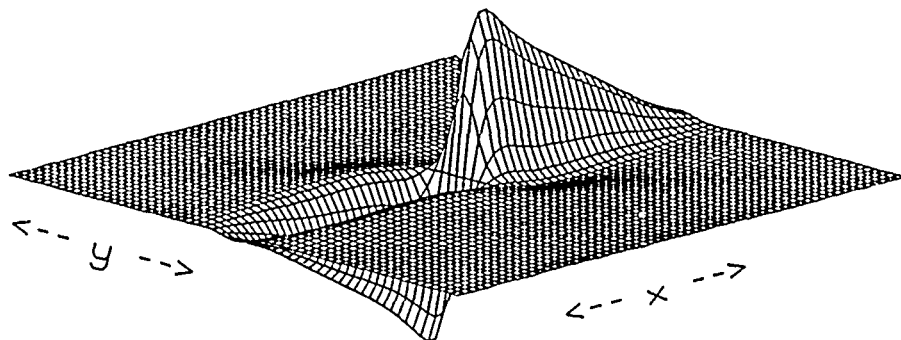
emax = 0.17900E-01

MON, JUL 15 1985

21:44:17

REFLD1Y

Figure 5. (c)
real



0.41955E+00

x=15.000
y=15.000

emin = -0.41955E+00

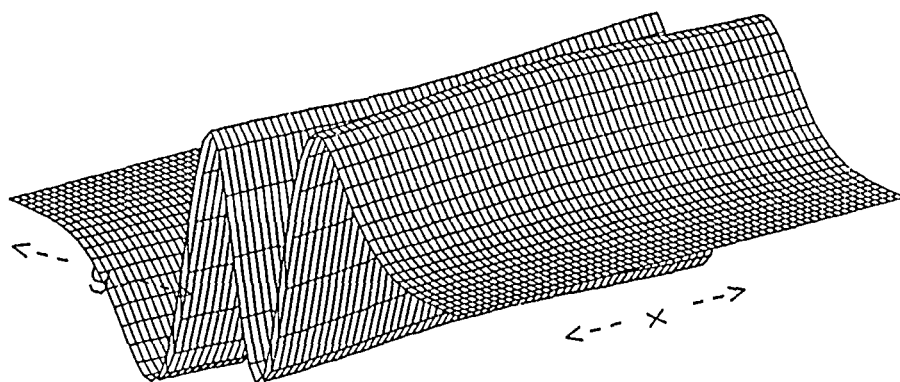
emax = 0.41955E+00

MON, JUL 15 1985

21:47:26

IMFLD1Y

Figure 5. (c)
imaginary



$0.24519E-03$
 $x=15.000$
 $y=15.000$

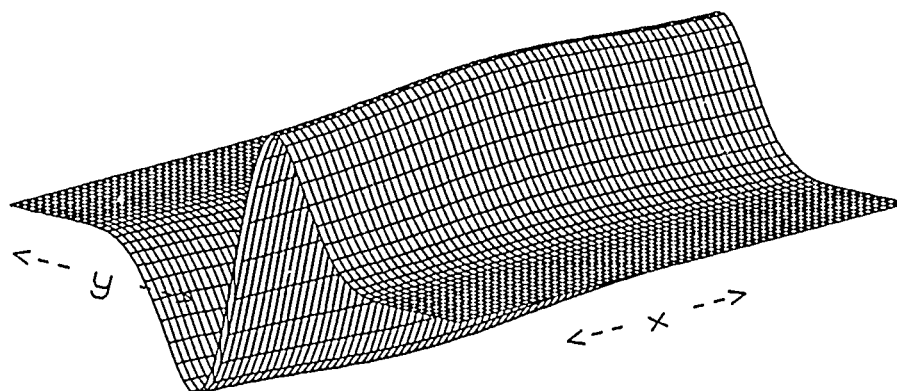
$e_{min} = -0.24519E-03$
 $e_{max} = 0.24519E-03$

WED, JUL 17 1985

09:40:03

REFLD1X

Figure 5. (d)
 real



$0.73733E-03$
 $x=15.000$
 $y=15.000$

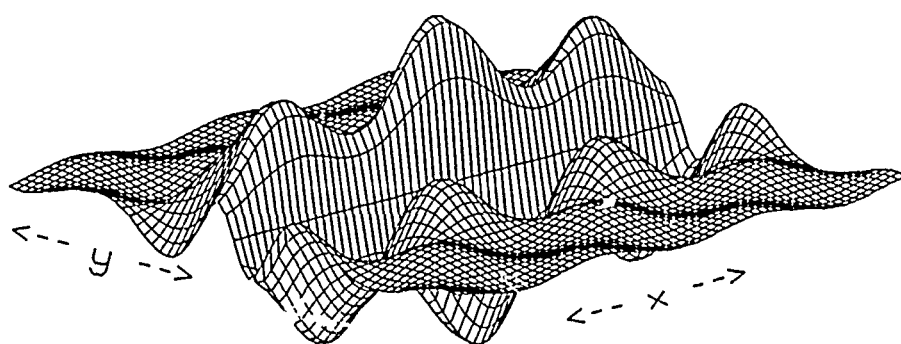
$e_{min} = -0.73733E-03$
 $e_{max} = 0.73733E-03$

WED, JUL 17 1985

09:42:32

IMFLD1X

Figure 5. (d)
imaginary



0.25104E-01

x=15.000

y=15.000

emin = -0.25104E-01

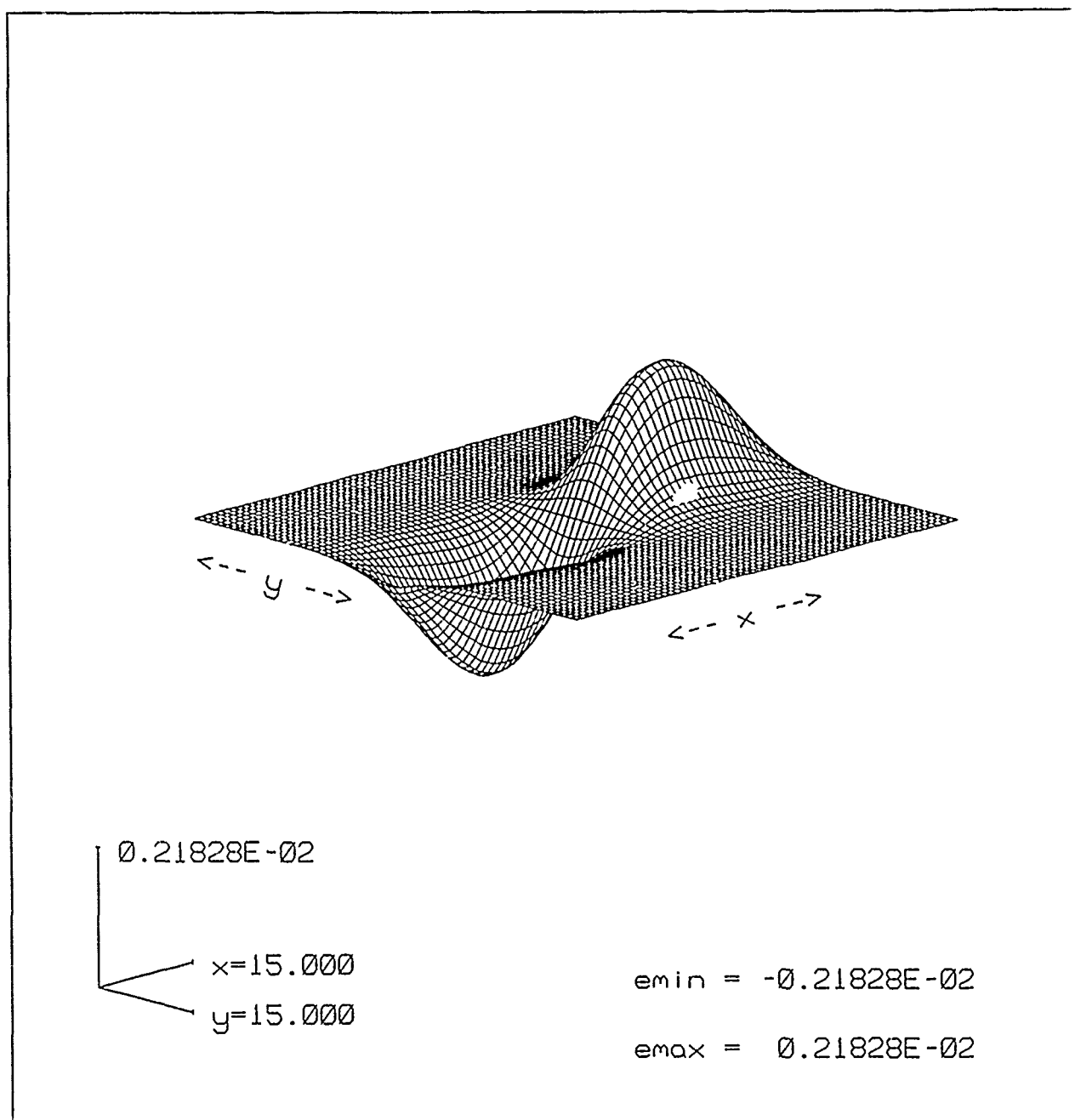
emax = 0.25104E-01

MON, JUL 15 1985

21:40:21

IMFLD1X

Figure 5. (c)
imaginary

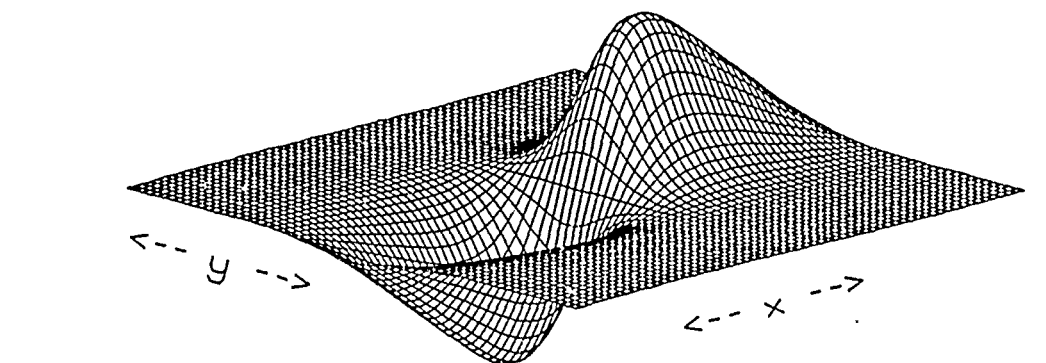


WED, JUL 17 1985

09:51:29

REFLD1Y

Figure 5. (d)
real



$0.36688E-01$
 $x=15.000$
 $y=15.000$

$emin = -0.36688E-01$
 $emax = 0.36688E-01$

WED, JUL 17 1985

09:54:25

IMFLD1Y

Figure 5. (d)
imaginary

"MAXWELL - A USER FRIENDLY PC-BASED FINITE ELEMENT PROGRAM FOR ELECTROMAGNETICS"

Z.J. Cendes
Department of ECE
Carnegie-Mellon University
Pittsburgh, PA 15213

A user friendly computer program called MAXWELL is described for solving electromagnetic field problems. The program is based on the concept that numerical procedures in a CAD package should be transparent to the user. It allows microwave and antenna engineers to solve field problems by simply drawing the problem's geometry on the computer graphics screen and specifying a few device parameters. Solutions, field plots, field values, capacitances, inductances, scattering coefficients, and other device parameters are obtained interactively as if the computer were an easy to use "pocket calculator", powerful enough to manipulate field variables.

At the present time MAXWELL solves problems involving transmission lines, microwave planar integrated circuits, wave guide discontinuities, and two dimensional dielectric and antenna scatterers. It is based on the finite element method, employs the powerful and efficient Delaunay triangulation algorithm (Z. Cendes, D. Shenton, and H. Shannaffer IEEE Trans, MAG-19, 2551-2554, 1983) for mesh generation and the highly efficient preconditioned conjugate gradient algorithm for matrix solution. Typical problems that involve the neighborhood of 100-300 second order finite elements require approximately 10-30 minutes to set up and solve on an IBM AT personal computer.

The approach used in MAXWELL to model the open boundary condition is also highly efficient. MAXWELL employs a novel one-step technique in which the exterior boundary condition is introduced by directly evaluating the variational principle for the exterior region. In this way the finite element matrix equation is solved only once. Previous approaches (S.K. Chang and K.K. Mei IEEE Trans, AP-24, 35-42, 1976) for incorporating the exterior field boundary condition into finite element solutions required that N boundary value problems be solved corresponding to N possible field variations on the boundary.

Provided the equipment is available, the presentation will include a live demonstration of MAXWELL in action.

TOTAL SCATTERING FROM A LONG CYLINDER

F C. Paddison, J. W. Follin, Jr.
R. Mitchel, A.L. Maffett
John Hopkins University
Applied Physics Laboratory
John Hopkins Road
Laurel, Maryland 20707

A brief overview of this paper was presented at the First Annual Review of NEC in March 1985. The complete paper is to be published in Volume 5, No. 1 - 1985 of Electromagnetics, published in cooperation with Electromagnetics Society, P.L.E. Uslenghi, Editor. Electromagnetics was published by Hemisphere Publishing Co., 1010 Vermont Avenue, NW, Washington D. C. 20005. Hemisphere has been sold to Harper and Row.

LARGE BISTATIC ANGLE RADAR CROSS SECTION OF A RIGHT CIRCULAR CYLINDER

F. C. Paddison, J. W. Follin, Jr., and F. Mitchell, *The Johns Hopkins University Applied Physics Laboratory, Laurel, Maryland 20707*, and A. L. Maffett, *consultant*

1. INTRODUCTION AND DISCUSSION

The monostatic radar cross section (MRCS) of simple shapes has been a subject of much interest for more than three decades, from both a theoretical and an experimental point of view. Over that time span, exact solutions have been achieved for some shapes [1], and useful approximate estimates have been developed [2] [3] [4]. Monostatic measurement methods are state of the art, are well understood, and are relatively easy to carry out (see, for example [5] or [6]).

Bistatic radar cross-section (BRCS) results, in either theoretical or experimental form, are somewhat more difficult to come by. Of course, the exact solutions hold for both MRCS and BRCS situations, although convergence problems may partially negate their bistatic usefulness, but some of the approximation methods become invalid in bistatic applications, and measurement difficulties increase significantly. The latter remarks are particularly true for large bistatic angles, β . For example, the bistatic theorem, which relates BRCS to MRCS for small-to-moderate sized values of β , no longer holds for large β . This statement has been verified by measurement data, as will be shown below.

The theoretical approximation picture for BRCS began to improve, and continues to do so, with the advent and rapid advancement of high-speed digital computers. Numerical methods based on integral equation representations for scattered fields have been introduced and developed by, for example, Oshiro [7], Harrington [8], and Poggio and Miller [9]. In particular, the numerical electromagnetic code (NEC) [10], which is based on the method of moments [8], represents a valuable outgrowth of much of this work. Although the NEC has been used for some scattering problems, its chief use has been in calculating antenna patterns. The scattering application of NEC is continued herein with the determination of BRCS for a finite right circular cylinder at, in particular, large bistatic angles. The cylinder configuration and the variety of bistatic angles are chosen so that numerical results can be compared with the existing measured data.

2. DISCUSSION

2.1 Bistatic Measurement Results

Under the sponsorship of the Rome Air Development Center and under the direction of The Johns Hopkins University Applied Physics Laboratory, BRCS measurements of selected simple and complex shapes were made by the Delco Electronics Division of General Motors Corp. [11]. The measurements were CW at a frequency of 35 GHz for both parallel and perpendicular polarizations. The targets were made of aluminum; the cylinders, which are of interest here, were right circular (closed ends), 1.85 cm in diameter and 16 and 8 cm long.

The measurements were made and the data recorded as follows. For a transmitter and receiver separated by a fixed bistatic angle β , the target, located at the apex of β , is rotated. The BRCS is then recorded as a function of the angle measured from the bisector of β , that is, just as if the MRCS were being recorded with both the transmitter and the receiver located at that aspect. The aspect angle origin (i.e., 0°) is located at the cylinder axis. Figure 1 shows the configuration for the measurement and data recording. The arrangement is immediately recognizable as the one pertinent to the bistatic theorem; indeed, it permits the overlay of BRCS and MRCS results. Table 1 shows the range of bistatic data obtained.

Table 1—Cylinder and bistatic angle specifications.

Cylinder Length, L		Diameter, D		Bistatic Angle, β (deg)
(cm)	(L/λ)	(cm)	(D/λ)	
16	18.7	1.85	2.16	0, 140, 160, 170, 175.4
8	9.3	1.85	2.16	175.4

Figure 2 shows the MRCS for the cylinder and Fig. 2b the BRCS for $\beta = 140^\circ$. These results confirm immediately the remark above that the bistatic theorem no longer holds for large β . The complete set of experimental data reviewed here is outlined in Table 2.

Table 2—Experimental BRCS for a finite circular cylinder.

Figure Number	Cylinder Length (cm)	β (deg)	Polarization
2a	16	0	HH
2b	16	140	HH
3a	16	160	HH
3b	16	165	HH
3c	16	170	HH
4a	16	175.4	HH
4b	16	0	VV
4c	16	140	VV
5a	16	160	VV
5b	16	165	VV
5c	16	170	VV
6	16	175.4	VV
7a	8	175.4	HH
7b	8	175.4	VV

2.2 Calculations

As is true for any set of experimental data, it is desirable to compare results with theoretical calculations. Also, for a consideration of BRCS versus β , rather few experimental points are available. Therefore, it is intended that theory be used to supply the complete curve (of BRCS versus β), with the experimental data confirming or not confirming its validity at the points for which measured data exist. Our intuition with regard to MRCS, which explains scintillation as interference of returns from cylinder ends, avails little in the bistatic case, where the returns seem more to be governed by intercepted area considerations that offer few if any scintillations.

To check out and supplement the measured data, the NEC seemed to offer the best available tool. As was mentioned above, it is based on an integral equation representation that can be inverted (numerically) to find the current distribution induced on the cylinder by an illuminating plane wave. Depending on whether an electric-field or a magnetic-field integral equation is used, the cylinder must be modeled by a mesh of wires or a collection of facets, respectively. In either case, the wire lengths and separations and the facet dimensions must be held to $\lambda/10$ or less. The original code could handle 600 wires or facets; the current one can use 1000.

Both the wire mesh and the facet configurations have been used to model the finite cylinder. The wire mesh model used 12 lines of 63 wires, each 0.254λ long, on the cylindrical portion. Each end was closed with 12 radial wires of four segments each plus two circumferential rings, separated by $\lambda/2$; each ring consisted of 12 segments. A third ring of a similar nature was required to yield results that were symmetric under an interchange of transmitter and receiver. Altogether, 996 wire segments were required for this model (Fig. 8).

BRCS computations were made for horizontal polarization only. For $\beta = 175.4^\circ$, the fit of computed results to measured data was quite good. For smaller bistatic angles, it was not as good and so those comparisons are not included here. The facet model results are used instead.

The facet model used 16 rows of 59 facets, each with a dimension of 0.316 cm, or 0.113λ , on the cylindrical surface. Each end of the cylinder was modeled by 24 pie-shaped facets arranged in an outer ring of 16 and an inner ring of 8. Both HH and VV BRCS calculations were made using the facet model.

2.3 Calculated Data

The BRCS results from the NEC calculations for the 16-cm cylinder are compared with measured data in figures as enumerated in Table 3. Calculations have not been made for the 8-cm cylinder.

Table 3—Figures of calculated and measured BRCS for the 16-cm cylinder.

Figure Number	β (deg)	Polarization
9	140	HH
10a	160	HH
10b	165	HH
10c	170	HH
11a	175.4	HH
11b	140	VV
11c	160	VV
12a	165	VV
12b	170	VV
12c	175.4	VV

2.4 Additional Calculated Data

The NEC lends itself nicely to calculations for a variety of receiver positions corresponding to a fixed transmitter position. Under those circumstances, the numerical inversion of the integral equation to find the current distribution needs to be carried out only once. Then from the current distribution, the scattered field (and hence the BRCS) in any direction (i.e., for any receiver position) can be computed. BRCS computations have been made for the transmitter located at 5° , 45° , and 90° from the cylinder axis, with the receiver position covering a complete circular cut in 5° steps for each transmitter position. The results are shown in Figs. 13a through 13c.

BRCS as a function of β for fixed aspect angles is also available. Figure 14a shows HH BRCS (σ/λ^2) versus β for fixed aspect angles 0° , 30° , 45° , 60° , and 90° (recall that the aspect angle is measured from the cylinder axis). Figure 14b gives similar results for VV polarization.

SUMMARY

The experimental data presented here show a marked decrease in the amplitude and frequency of the RCS destructive and constructive interference pattern with increasing β . Further, the average level of RCS steadily increases with increasing β until, in the forward scattering lobe, the RCS becomes equal to $4\pi A^2/\lambda^2$, where A is the projected cross-sectional area of the cylinder. The resolution of the calculated RCS is limited because a new computation is needed for each angle of incidence; however, the correlation of measured and calculated data is very good considering that the integral equation code is being pressed to its current limits. In order to keep within the limits of 100 facets, their size had to be 0.3λ instead of the recommended 0.2λ , which accounts for the somewhat large errors at $\beta = 140^\circ$, although the numerical results are within several decibels of the experimental data for the larger β .

Although the comparisons are very good, the NEC usefulness remains limited by the need to keep the ratio of target size to wavelength fairly small. This limitation on a powerful tool raises the question of whether, and by how much, it could be alleviated by combining NEC with another method, such as the variational.

ACKNOWLEDGMENTS

The Delco measurements were sponsored by the U.S. Air Force Rome Air Development Center (Griffiss AFB, N.Y., Mr. James Michels, Program Director) and were performed under the subcontractual direction of The Johns Hopkins University Applied Physics Laboratory. The NEC computations were supported by the Laboratory's IR&D program.

REFERENCES

- [1] J. J. Bowman, T. B. A. Senior, and P. L. E. Uslenghi, eds., *Electromagnetic and Acoustic Scattering by Simple Shapes*, North-Holland Publishing Co., Amsterdam (1969).
- [2] J. W. Crispin, Jr., and A. L. Maffett, "Radar Cross-Section Estimation for Simple Shapes," *Proc. IEEE*, Vol. 53, No. 8, pp. 833-848 (1965).
- [3] J. W. Crispin, Jr., and K. M. Siegel, eds., *Methods of Radar Cross-Section Analysis*, Academic Press, New York (1968).
- [4] G. T. Ruck, *Radar Cross-Section Handbook*, Plenum Press, New York (1970).
- [5] P. Blacksmith, Jr., R. E. Hiatt, and R. B. Mack, "Introduction to Radar Cross-Section Measurements," *Proc. IEEE*, Vol. 53, No. 8, pp. 901-920 (1965).
- [6] R. B. Mack, *Basic Design Principles of Electromagnetic Scattering Measurement Facilities*, RADC-TR-81-40 Rome Air Development Center, Griffiss AFB, N.Y. (1981).
- [7] F. K. Oshiro, "Source Distribution Techniques for the Solution of General Electromagnetic Scattering Problems," *Proc. First GISAT Symp.*, Mitre Corp., Vol. 1, pp. 83-107 (1965).
- [8] R. F. Harrington, *Field Computation by Moment Methods*, Macmillan, New York (1968).
- [9] A. J. Poggio and E. K. Miller, ch. 4 in R. Mittra, *Computer Techniques for Electromagnetics*, Pergamon Press, Oxford (1973).
- [10] G. J. Burke and A. J. Poggio, *Numerical Electromagnetic Code (NEC)—Method of Moments*, Naval Ocean Systems Center, San Diego (1981).
- [11] Delco Electronics, *Radar Cross-Section Measurements*, Report R81-152, Delco Electronics Division, General Motors, Santa Barbara (1981).

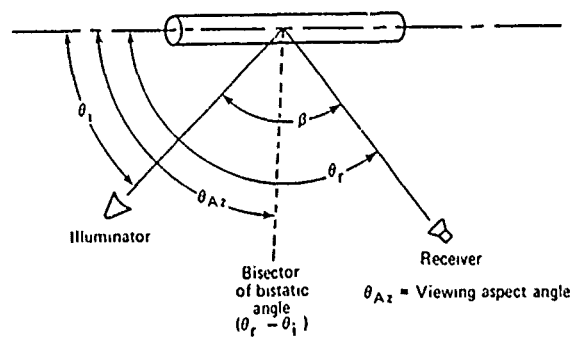
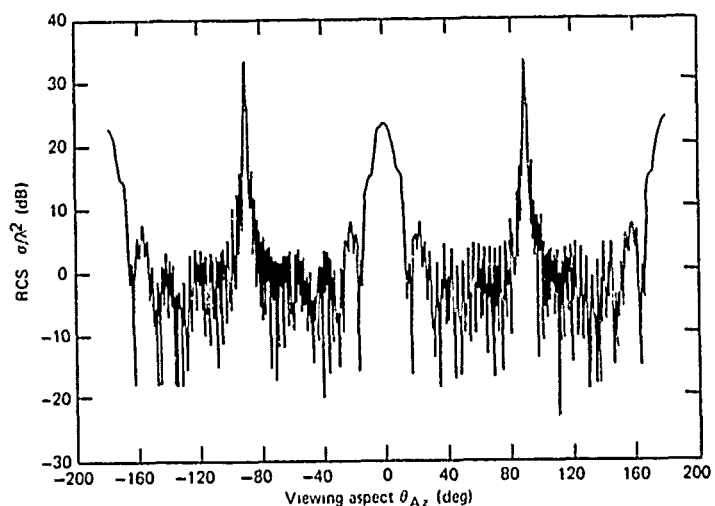
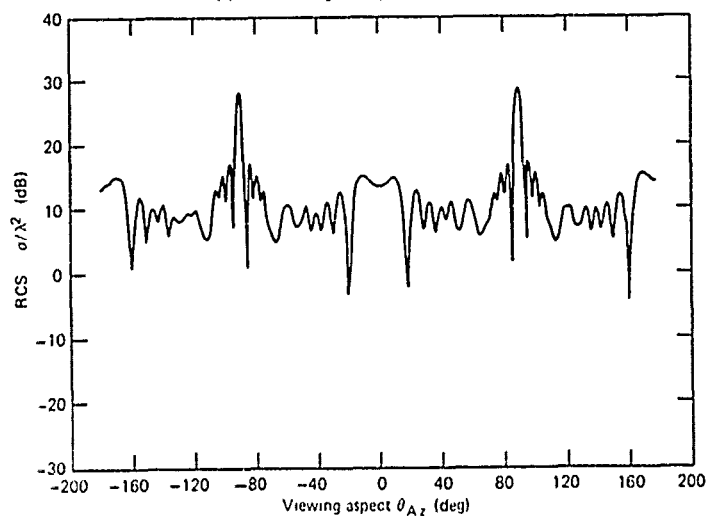


Fig. 1 The bistatic geometry.

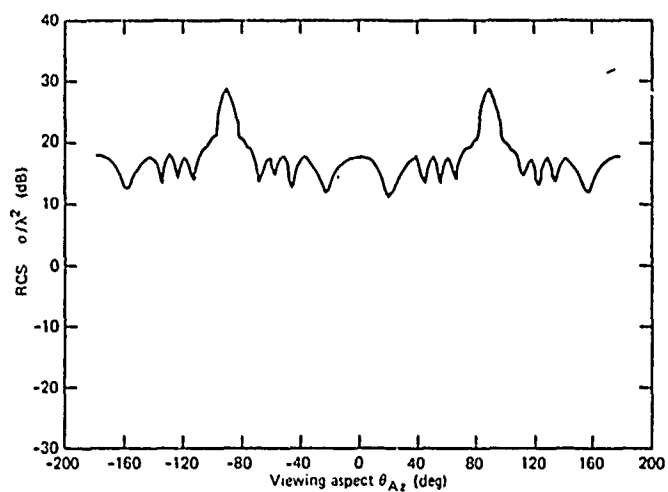


(a) Bistatic angle 0° , polarization HH

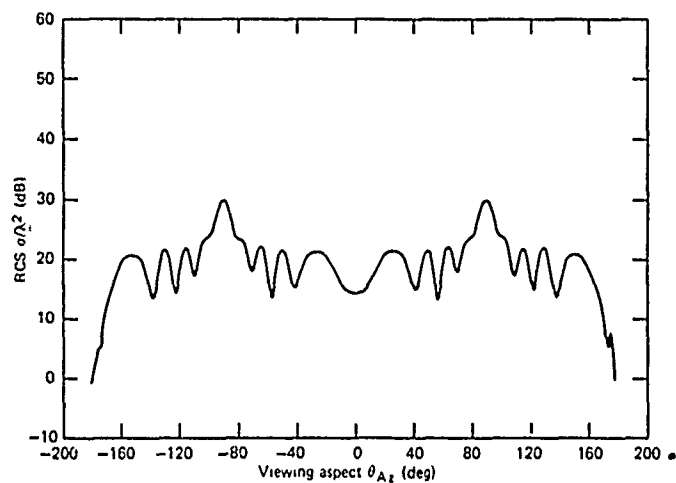


(b) Bistatic angle 140° , polarization HH

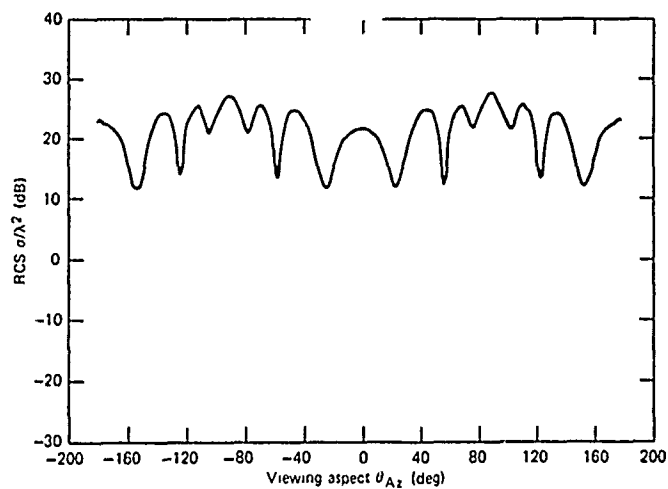
Fig. 2 Measured RCS, 16×1.85 cm cylinder at 35 GHz.



(a) Bistatic angle 160° , polarization HH

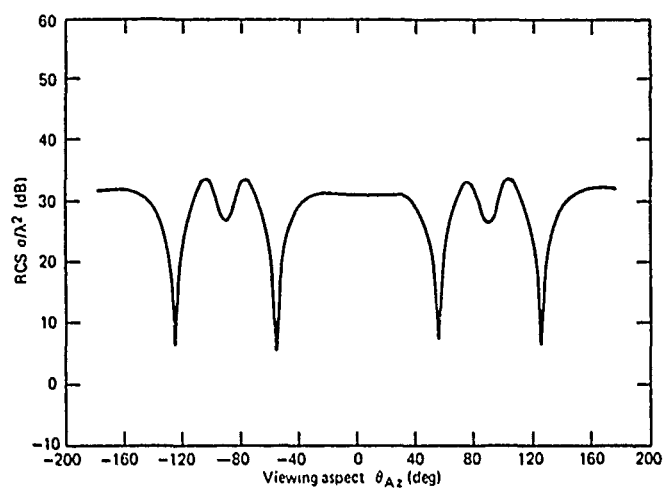


(b) Bistatic angle 165° , polarization HH

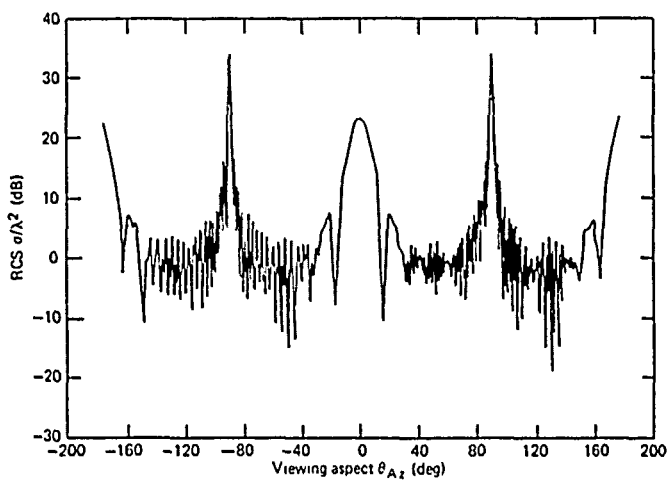


(c) Bistatic angle 170° , polarization HH

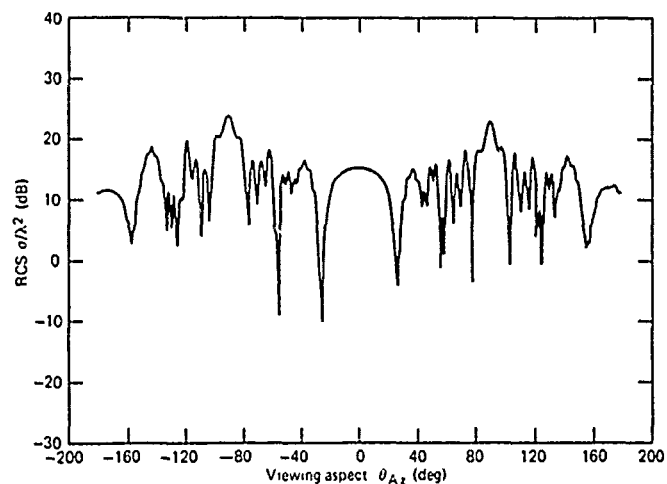
Fig. 3 Measured RCS, 16×1.85 cm cylinder at 35 GHz.



(a) Bistatic angle 175.4° , polarization HH

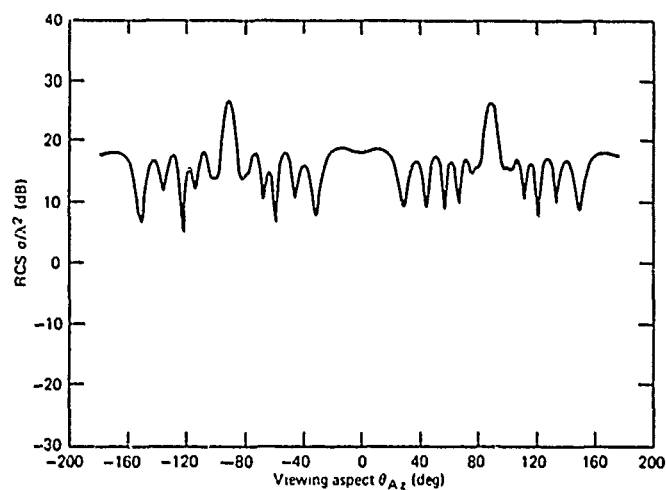


(b) Bistatic angle 0° , polarization VV

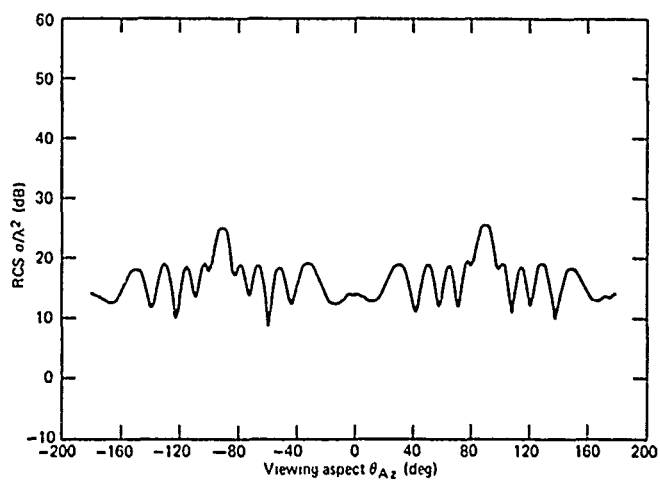


(c) Bistatic angle 140° , polarization VV

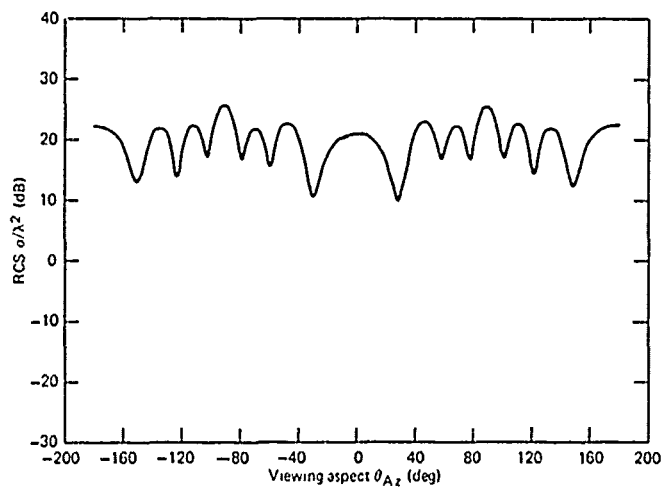
Fig. 4 Measured RCS, 16×1.85 cm cylinder at 35 GHz.



(a) Bistatic angle 160° , polarization VV



(b) Bistatic angle 165° , polarization VV



(c) Bistatic angle 170° , polarization VV

Fig. 5 Measured RCS, 16×1.85 cm cylinder at 35 GHz.

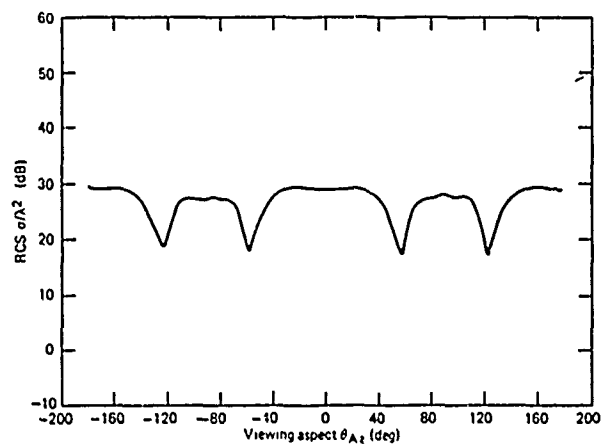


Fig. 6 Measured RCS, 16×1.85 cm cylinder at 35 GHz, bistatic angle 175.4° , VV polarization.

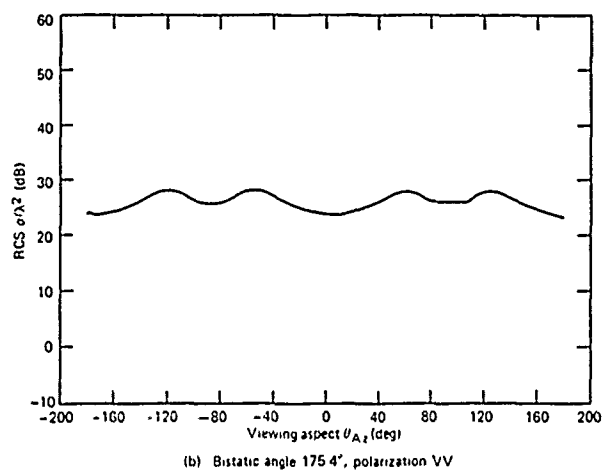
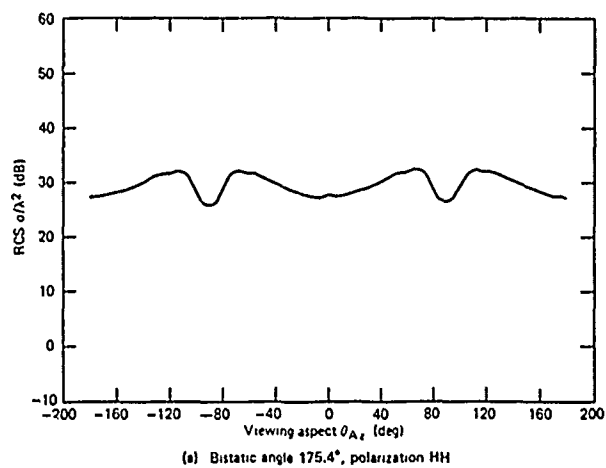


Fig. 7 Measured RCS, 8×1.85 cm cylinder at 35 GHz.

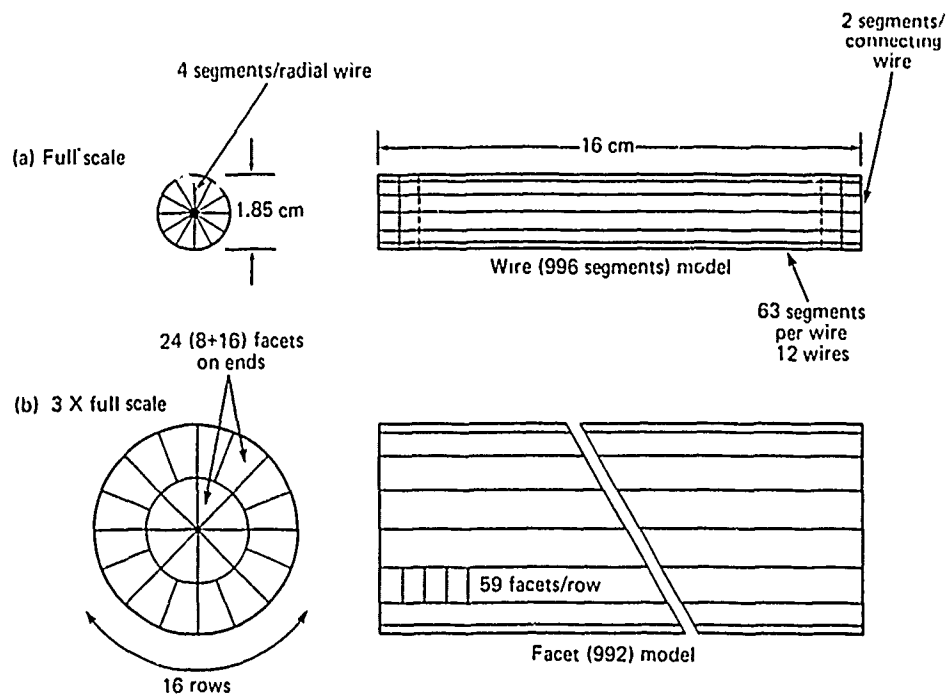


Fig. 8 Illustration of method of representing a right circular cylinder with (a) 42 wires composed of a total of 996 fractional wavelength segments and (b) 20 rows of a total of 992 square fractional wavelength facets.

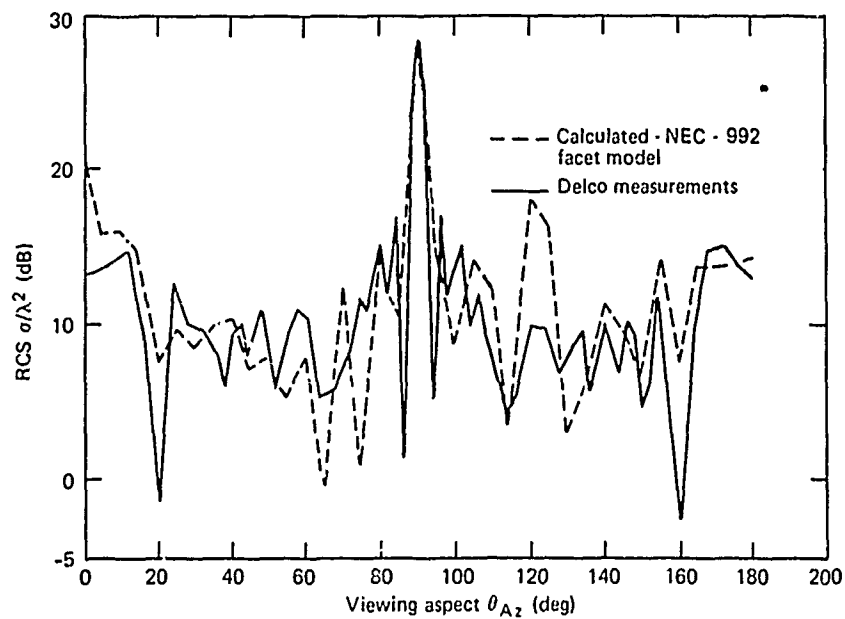


Fig. 9 Comparison of measured and calculated bistatic RCS, 16×1.85 cm cylinder at 35 GHz, bistatic angle 140° , HH polarization.

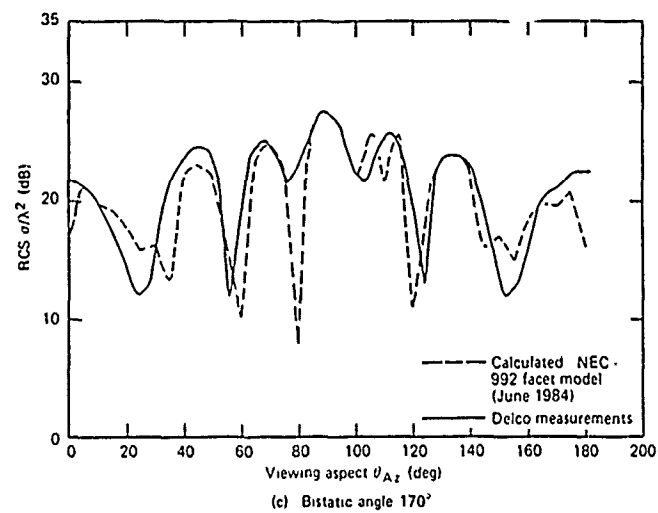
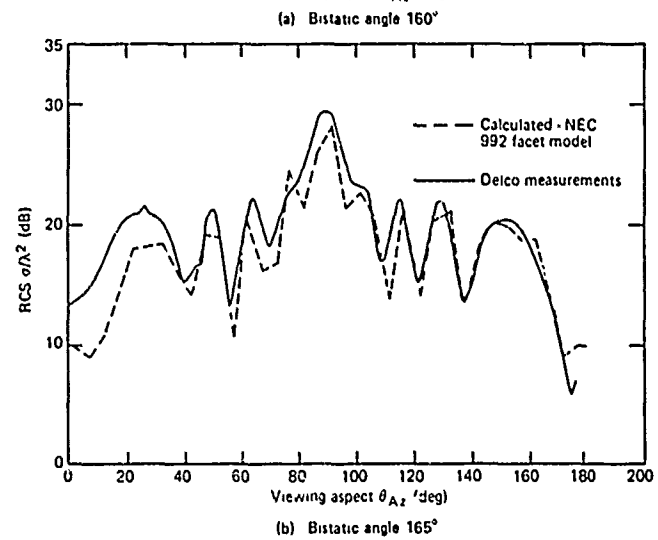
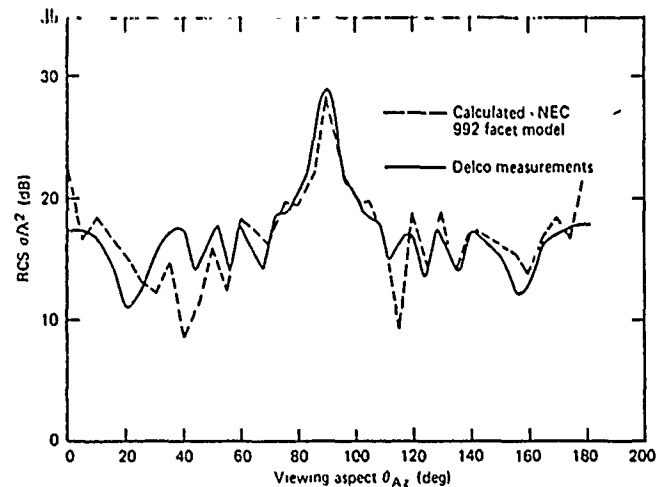
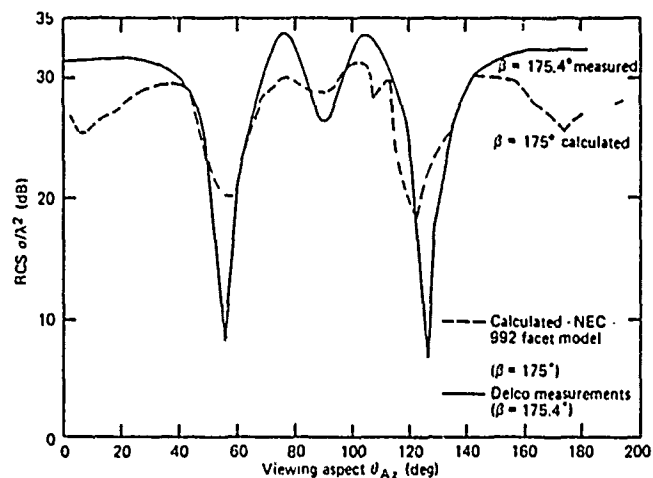
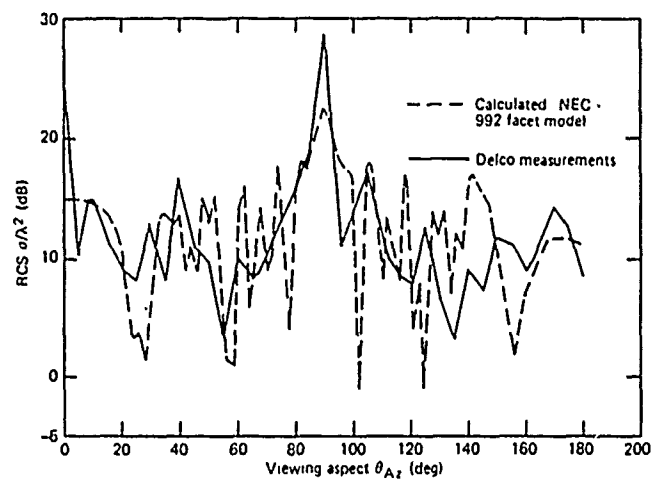


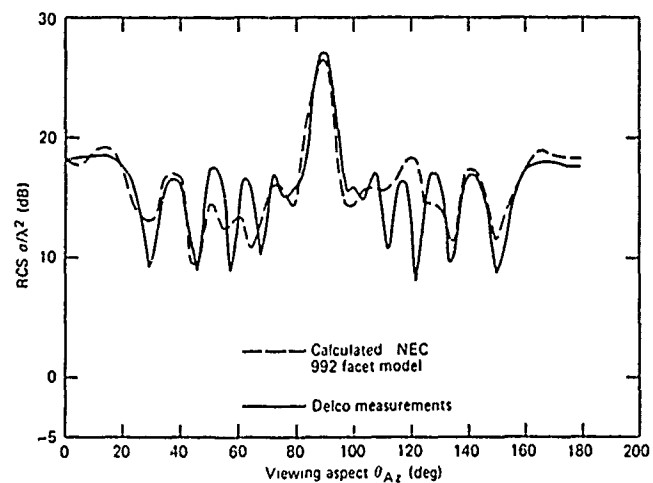
Fig. 10 Comparison of measured and calculated bistatic RCS, 16×1.85 cm cylinder at 35 GHz, HH polarization.



(a) Bistatic angle 175.4°, HH polarization

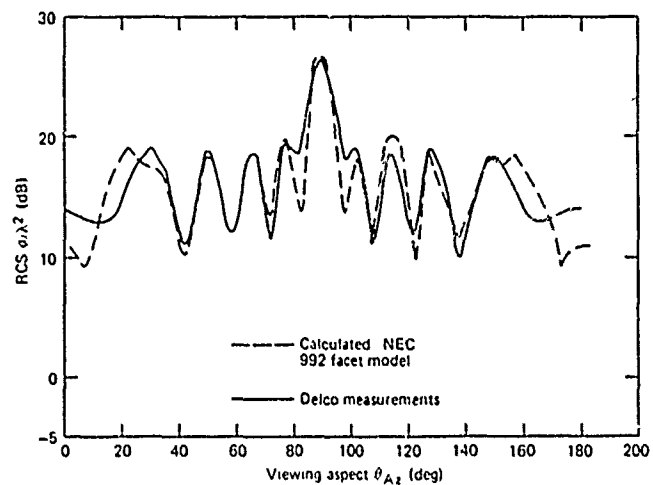


(b) Bistatic angle 140°, VV polarization

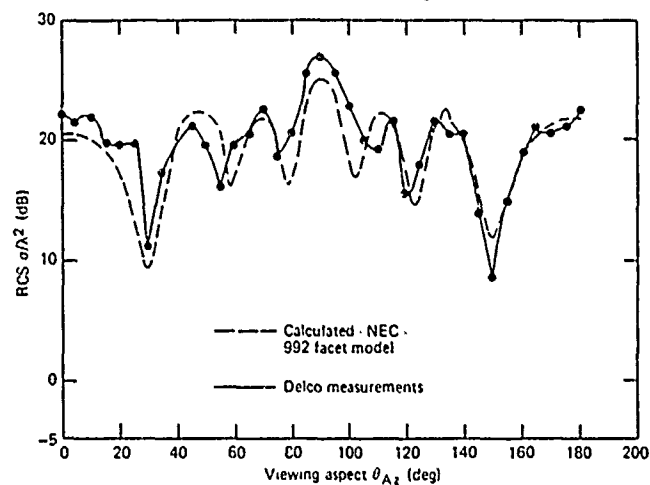


(c) Bistatic angle 160°, VV polarization

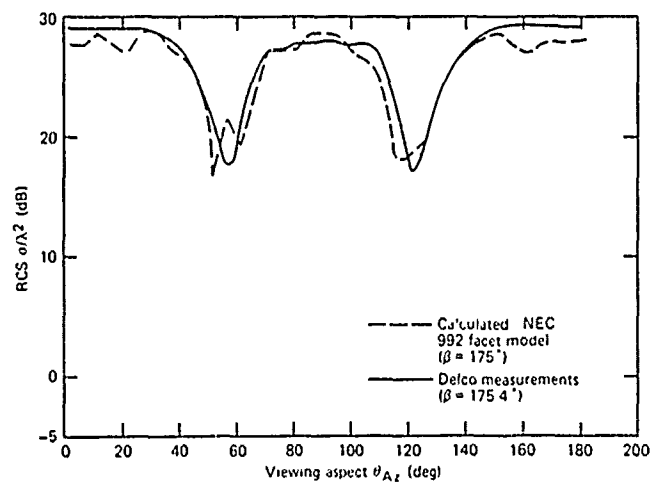
Fig. 11 Comparison of measured and calculated bistatic RCS, 16×1.85 cm cylinder at 35 GHz.



(a) Bistatic angle 165° , VV polarization

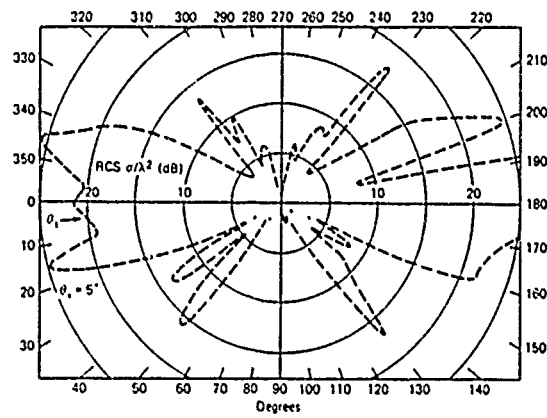


(b) Bistatic angle 170° , VV polarization

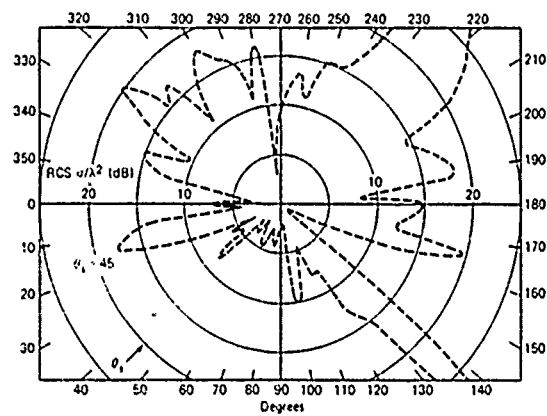


(c) Bistatic angle 175° , VV polarization

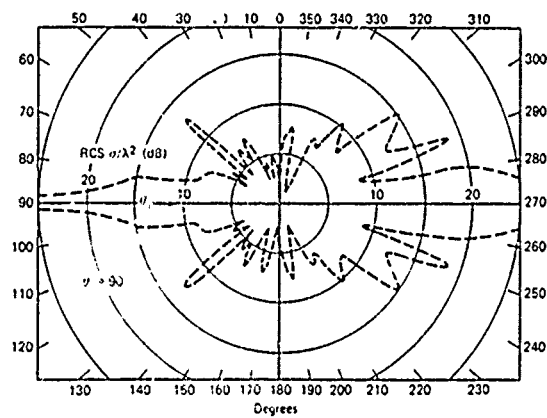
Fig. 12 Comparison of measured and calculated bistatic RCS, 16×1.85 cm cylinder at 35 GHz.



(a) Total scatter: illumination angle $\theta_i = 5^\circ$



(b) Total scatter: illumination angle $\theta_i = 45^\circ$



(c) Total scatter: illumination angle $\theta_i = 90^\circ$

Fig. 13 Calculated normalized electromagnetic scatter around a 16×1.85 cm conducting cylinder at 35 GHz. The electric vector is in the plane parallel to the longitudinal axis of the cylinder. 992 facet model. HH polarization.

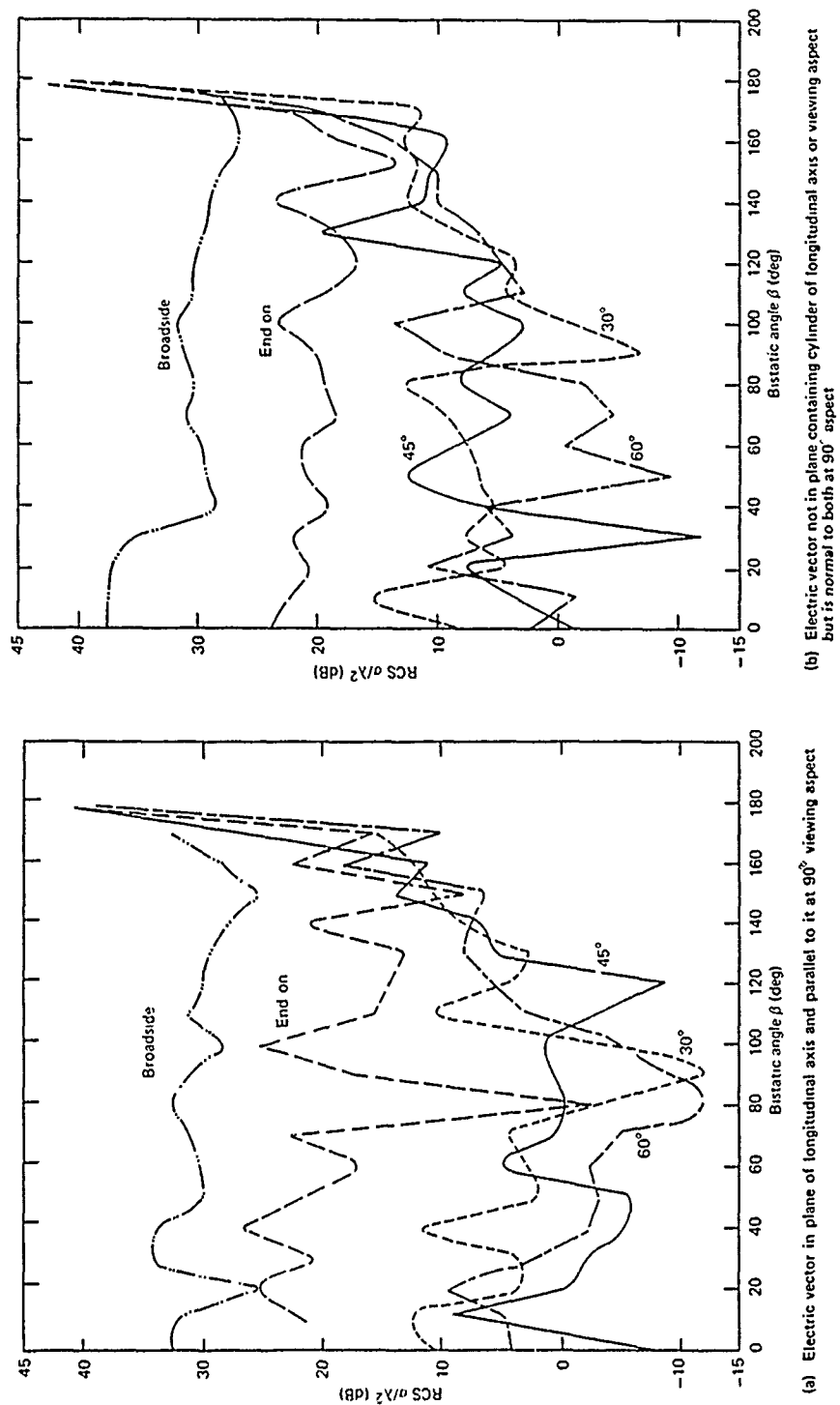


Fig. 14 Calculated normalized electromagnetic scatter from a 16×1.85 cm conducting cylinder at 35 GHz as a function of bistatic angle. The bisector of the angle is held fixed at 0° , 30° , 45° , 60° , and 90° from the cylinder's longitudinal axis. 992 facet model.